SIMS 2012

The 53rd Scandinavian Conference on Simulation and Modelling

OS-2012/06

ORKUSTOFNUN

SIMS 2012

The 53rd Scandinavian Conference on Simulation and Modeling

Reykjavík, Iceland
Orkugarður, Grensásvegur 9

4-6 October, 2012

Conference Proceedings

Organized by

Orkustofnun
National Energy Authority

Edited by
Jónas Ketilsson

Published by

Orkustofnun,

National Energy Authority, Iceland 2012

ISBN: 978-9979-68-318-6

Table of Contents

Session 5 - IEA-GIA work on Sustainable use of Geothermal Resources

Modelling sustainable geothermal utilization
Gudni Axelsson

Optimal and sustainable use of the Dogger aquifer geothermal resource: long-term management and new technologies
Simon Lopez, Hamm Virginie and Olivier Goyeneche

Sustainability analysis of the Berlin geothermal field, El Salvador
Manuel Monterrosa

Session 6 - Simulator Development & Optimization

Towards A Parallel Distributed Equation-Based Simulation Environment
Robert Braun and Petter Krus

A homogeneous two-phase flow model of an evaporator with internal rifled tubes
Axel Ohrt Johansen and Brian Elmegaard

Hydro Power Systems: Scripting Modelica Models for Operational Studies in Education
Dietmar Winkler and Bernt Lie

Session 7 - Modeling of Geothermal Systems

Modeling Fluid and Energy Flow in Liquid Dominated Hydrothermal Systems
Larus Thorvaldsson and Halldor Palsson

Long-term hydro and geothermal reservoir operation
Úlfar Linnet and Óli Grétar Blöndal Sveinsson

A coubled wellbore-reservoir simulator utilizing measured wellhead conditions
Halldora Gudmundsdottir, Magnus Thor Jonsson and Halldor Palsson

Session 8 - Modeling of energy systems

Comparison open modelica - dymola for power plant simulation
Erik Dahlquist, Elena Tomas Aparicio, Hailong Li, Peter Fritzson and Per Östlund

Development of a multi-level approach to model and optimise the Kalina Split Cycle for marine diesel engines
Ulrik Larsen and Tuong-Van Nguyen

Additional Papers (not presented during the conference)

A Globally-Implicit Computational Framework for Physics-Based Simulation of Coupled Thermal-Hydro-Mechanical Problems: Application to Sustainability of Geothermal Reservoirs

Robert Podgorney, Hai Huang, Mitch Plummer, Derek Gaston

June 2012

1 Introduction

Numerical modeling has played an important role in understanding the behavior of geothermal systems since as early as the 1970s. While capabilities of geothermal reservoir simulators have grown since then, the prospect of simulating more challenging classes of geothermal problems–such as reservoir creation and operation of engineered geothermal systems (EGS), high enthalpy supercritical magmatic systems, etc–pose additional, and very significant, computational challenges that the current generation of continuum or dual-continuum hydrothermal models are ill-equipped to describe.

Interest in multiphysics simulation techniques is growing rapidly with a focus on more realistic and higher fidelity analysis of geothermal and engineering systems. This increase in activity is typically attributed to increasing computer power and more robust computational schemes [9, 11, 12], but in truth, advanced numerical methods are playing an equal role. The phrase "multiphysics simulation" is used to describe analyses which include disparate physical phenomena–such as coupled multiphase, multicomponent fluid flow, enthalpy transport, and geomechanics *and their feedbacks*–are examined in a simultaneous manner. Examples of multiphysics problems in subsurface energy applications are numerous and include pressure and temperature driven permeability creation and evolution in geothermal reservoirs, temperature driven phase evolution of in-situ kerogen processing of oil shale reservoirs, kinetically controlled reactive transport in the flow of contaminants, etc. In addition to multiphysics coupling, most of these problems also have multiscale issues to resolve.

Examining coupled physics for fluid flow, energy transport, and geomechanical deformation is a relatively new area for the geothermal community; however, simulating coupled problems has been an important topic of study in the reactive transport community for

decades. Yeh and Tripathi [21] and Steefel and MacQuarrie [16] cite three major approaches that differ in the way coupling transport and reaction have been considered for reactive transport modeling: (1) GIA (fully-coupled) approach that solves all governing nonlinear equations simultaneously at each time step using various forms of Newton's method, (2) sequential iteration approach (SIA) that subdivide the reactive transport problem into transport and reaction subproblems, solves them sequentially, and then iterates, and (3) sequential non-iteration approach (SNIA) that solves the transport and reaction problems sequentially without iteration, which is often referred as operator-splitting. The operator-splitting approach is perhaps the simplest to implement and requires the least computational resources in terms of the memory and CPU time; thus, it became the method of choice for subsurface reactive transport modeling during the past three decades.

However, the drawback of the operator-splitting approach is the splitting error when the physics (either reactions-transport or flow-mechanics) are tightly coupled; the solution becomes inaccurate and requires very small time steps [17]. For most potential EGS reservoirs fluid flow, heat transport, and rock deformation will be strongly nonlinearly coupled. The changes in flow and energy transport properties due to fracturing and/or dissolution add further complexity and nonlinearity to the problem. For such situations, the global implicit approach (GIA) solves all solution variables simultaneously during each time step by seeking the solution of a large system of nonlinear equations via some form of Newton's method and is a more robust solution than the other two approaches [3, 8, 14].

One potential limitation of the GIA approach is the need to compute, store and invert the Jacobian matrix. This could become problematic for large systems which would be expected for reservoir-scale geothermal problems. As the number of solution variables grows, the matrix holding the Jacobian entries also grows. The increased size of the Jacobian matrix results in greater memory usage and more CPU time to solve the resulting system of linear equations within the Newton iterations. For highly nonlinear processes involving strong fluid-reservoir interactions and significant changes of flow and transport properties due to fracturing, the true Jacobian is often difficult to describe in analytical formulas. For reasons such as these, during the past three decades, despite its numerical merits of greater robustness and the ability to take larger time steps, the fully-coupled GIA method was considered to be too CPU-time and memory-intensive [21] or to be computationally inefficient [16]. It has been used primarily only as a research tool for small one- or two-dimensional problems with a few thousands of unknowns. Since the first attempts of implementing the GIA approach in the early 1980s [17, 13], only a handful of examples based on this approach have been reported in the literature, compared with numerous examples of applications based on an operator splitting approach [19, 20, 15].

This paper highlights the development of a fully-coupled and fully-implicit modeling tool for predicting the dynamics of fluid flow, heat transport, and rock deformation using a GIA named **FALCON** (**F**racturing **A**nd **L**iquid **CON**vection). The code is developed

on a parallel **M**ultiphysics **O**bject **O**riented **S**imulation **E**nvironment (**MOOSE**) computational framework developed at Idaho National Laboratory (INL) for providing finite element solutions of coupled system of nonlinear partial differential equations. In this paper, a brief overview of the governing equations numerical approach are discussed, and an example simulation of strongly coupled geothermal reservoir behavior is presented.

2 Architecture and Design

FALCON has been designed for the simulation of geothermal reservoirs, both conventional hydrothermal and EGS. The architecture of FALCON has a plug-and-play modular design structure based on representing each piece of the residual term in a weak form of the governing PDEs as a "Kernel". Kernels may be coupled together to achieve different application goals. All kernels are required to supply a residual, which usually involves summing products of finite element shape functions. The basic architecture of the code allows convenient coupling of different processes and incorporation of new physics.

Figure 1 shows the basic architecture of FALCON, with the Kernels at the uppermost level, directly underlain by the numerical framework and solver libraries used to couple the Kernels and perform reservoir simulations. Currently primary Kernels (primary variables) have been written to describe the following physics:

- Single-phase flow of water
- Two-phase flow of water and steam
- Conservative heat transport
- Enthalpy transport
- Fluid and Energy Sources/Sinks
- Displacement (all mechanics are solved in terms of displacement)

For any given simulation, any combination of the primary kernels can be applied to make the problem as simple or complex as necessary, with some exceptions. Single phase flow of water problems must be cast in terms of temperature, while steam-water flow problems must use enthalpy for energy transport. The option of single phase temperature formulation was the basis for early versions of FALCON and have been retained because of their computational and memory efficiency. As an example of the modular framework, one can simply choose only a single phase pressure kernel, and solve a simple LaPlace equation based on imposed boundary conditions, totally ignoring energy and mechanics kernels.

An auxiliary variable system has been built into FALCON to handle solving most

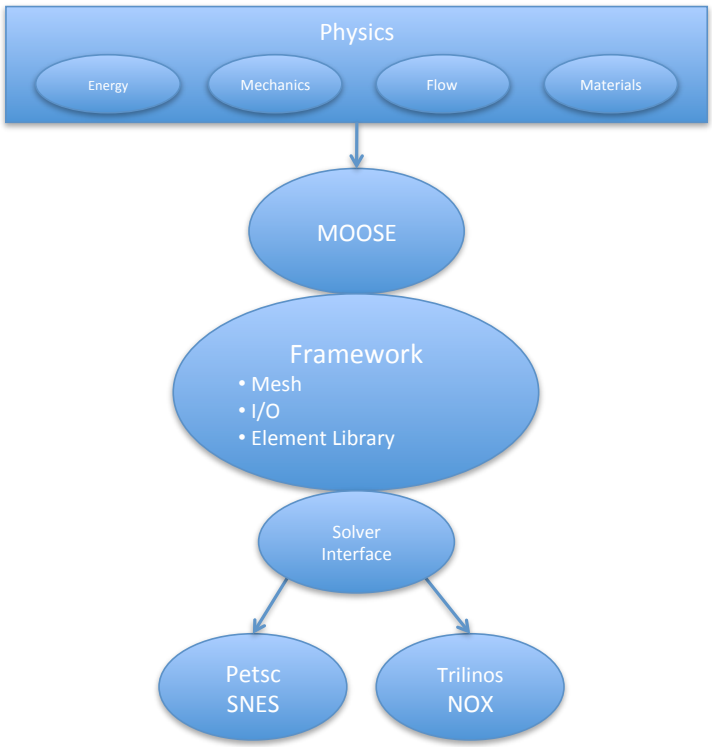

Figure 1: Kernel and Object Oriented Architecture used to develop the FALCON simulator.

all of the derived quantities and variables that are dependent on the primary kernels mentioned above. The number of auxiliary kernels needed for a given simulation depends on the choice of primary variables and whether they are formulated in terms of pressure-temperature or pressure-enthalpy. In general, a simulation run with the pressure-enthalpy formulation, considering geomechanical displacement and damaging, requires the most auxiliary kernels and has the highest computational burden. The auxiliary kernels consist of

- Equation of state calculations
  - Steam and water density
  - Steam and water viscosity
  - Derivatives of steam and water density to pressure, temperature, or enthalpy as required
- Stress and Strain
- Fluid Velocities
- Damage Mechanics (or fracturing)

In addition to the primary and auxiliary physics kernels, other kernels are required for the mesh, material properties (and some additional supporting calculations), boundary conditions, code execution/solver parameters, and data output.

2.1 Code Uses and Limitations

As stated above, the FALCON code has been developed to support simulation of both conventional hydrothermal and EGS reservoirs, with a primary design focus on EGS resources. While we are using the IAPWS-97 formulation [18], which has an quite an effective operating range of pressure ($\leqslant 100MPa$) and temperature($\leqslant 800C$), code development to date has focused on subcritical conditions.

Maximum mesh sizes are related to the number of kernels, and hence the total system wide Degrees of Freedom (DoFs), used in a simulation. In practice, the true limitations are based on computational power and available memory. The parallel scaling and performance example testing used 1 million grid blocks and more than 20 million DoFs, and showed remarkable scalability. Code tests have used computational meshes with greater than 30 million elements and also showed excellent scaling performance [7]. For any parallel simulation runs, a minimum of 20,000 DoFs per processor is recommended for good scalability.

3 Numerical Methodology

FALCON has been developed using INL's MOOSE framework [6]. This framework provides a strong numerical foundation for rapid development of multi-dimensional, parallel, fully implicit, fully-coupled, nonlinear simulation capabilities. MOOSE is based on a finite element discretization strategy and utilizes state-of-the-art preconditioned Jacobian-Free Newton-Krylov (JFNK) nonlinear solution method that requires only residual evaluations of the discrete system. Strategic use of this feature results in a modular, pluggable architecture that greatly simplifies adding new physics and coupling them together. The MOOSE framework incorporates multiple parallel solution capabilities including both Message Passing Interface (MPI) and threading utilizing the Intel Threading Building Blocks (TBB), which allows application codes developed upon MOOSE to run efficiently on multicore workstations, laptops and supercomputers. All parallel activities are completely hidden from application developers, enabling scientists and engineers to focus on the physics of problem they wish to solve instead of parallel programing practices. In addition, applications developed upon MOOSE also inherit many advanced computing capabilities such as dimension-independence, massive parallelism, high-order finite elements and adaptive mesh refinement/coarsening with both structured and unstructured meshes.

The MOOSE framework has a layered structure, as shown in Figure 2. The lower layer

interfaces with several open-source libraries from multiple universities and national laboratories. In particular, the libMesh finite element framework developed by the CFDLab at the University of Texas at Austin [10] provides a core set of parallel finite-element libraries. Coupled with interfaces to linear and nonlinear solvers from both PETSc [2] and Trilinos [9] along with other packages such as Hypre [4], MOOSE and application codes developed upon it provide considerable flexibility including the abilities to swap out solver libraries and to utilize diverse large scale parallel computing resources. The middle layer of MOOSE provides a set of core functionalities necessary for residual and Jacobian (more precisely, the preconditioner) evaluations required by the preconditioned JFNK approach, such as fetching the designated test and shape functions, numerical integration using Gaussian quadrature, and coupling physics. The top layer of MOOSE,

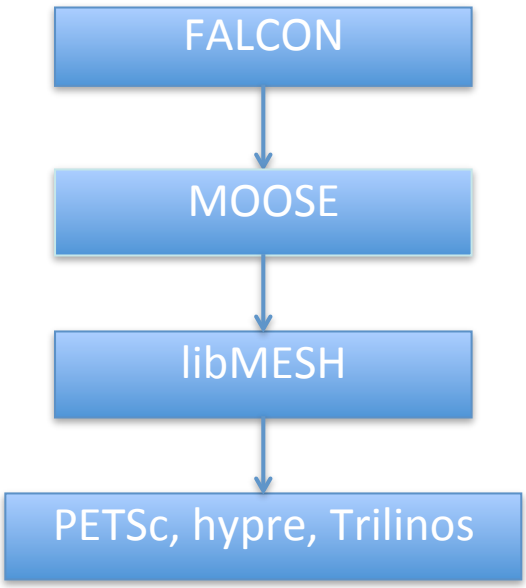

Figure 2: Hierarchical framework used to build the FALCON simulator, based up the INL developed MOOSE library [6]. The libMesh finite element framework developed by the CFDLab at the University of Texas at Austin [34] provides a core set of parallel finite-element libraries and couples with interfaces to linear and nonlinear solvers from both Petsc [2] and Trilinos [9] along with other packages such as Hypre [4].

referred as the kernel, is the interface with physics where the FALCON application is built (see Figure 2). It is convenient to think of a kernel as a piece of the residual term in the weak forms of PDEs, for example, the diffusion term, advection term, time accumulation term in the weak form of general enthalpy transport equations. Kernels may be coupled together to achieve different application goals. All kernels are required to supply a residual, which usually involves summing products of finite element shape functions.

Kernels may also provide diagonal and off-diagonal blocks of the (approximate) Jacobian matrix for the purpose of building certain preconditioners.

In order to further clarify the Kernel concept, we provide a simple example (single phase water pressure diffusion) kernel here. The diffusion of pressure written as $\nabla \cdot \left(\frac{k\rho_w}{\mu_w} \cdot \nabla p_w \right)$ equation, which contributes to the overall residual in the system is provided as an example. Figure 3 shows the actual codes of the pressure diffusion kernel. In this figure, `_test` is the test function evaluated at the quadrature point `_qp` and `_grad_phi` is the gradient of shape function evaluated at the quadrature point `_qp` (both provided by MOOSE), `_u` and `_grad_u` are the current solution variable and the gradient of the current solution variable this kernel operates on evaluated at the quadrature point `_qp`. `_permeability` is the intrinsic material permeability defined in material kernel that the physics kernels can access, `_dens_water` and `_visc_water` are the water phase fluid density and viscosity, respectively, as returned from the equation of state auxiliary Kernel. Every other term in the weak form of the general flow equation has similar kernel structure.

```
Real WaterMassFluxPressure_PT::computeQpResidual()
{
 _tau_water[qp] = _permeability[qp] * _dens_water / _visc_water;
 return _tau_water[_qp]*_grad_u[_qp] * _grad_test[_i][_qp];
}
```

```
Real WaterMassFluxPressure_PT::computeQpJacobian()
{
 _tau_water[qp] = _permeability[qp] * _dens_water / _visc_water;
 return _tau_water[_qp]*_grad_phi[_j][_qp] * _grad_test[_i][_qp];
}
```

Figure 3: Residual (left) and Jacobian (preconditioner, right) evaluations inside the pressure diffusion kernel for single phase flow of water.

Based upon the MOOSE framework, the FALCON code has developed a set of *"physics"* kernels handling the time derivatives, single- and two-phase flow equations, heat and energy transport, source-sink terms, geomechanics, as well as a set of *"Auxiliary"* and *"Material"* kernels for equations of state (EOS) and flow-transport-mechanical properties required for geothermal reservoir simulations. As shown and discussed in the sections that follow, these kernels all have modular, pluggable structure, and can be coupled in arbitrary ways depending on the type of problems of interest. It is also worth noting that the MOOSE framework provides a material kernel. Flow and transport properties such as porosity, permeability, and relative permeability can all be defined within this material kernel and can be accessed by the physics kernels during each residual evaluation. Furthermore, the material kernel has access to state variables if needed. This feature is particularly useful for hydrofracturing applications where fracturing significantly modifies the porosity and permeability of porous media.

4 Example Applications

4.1 Comparison with Analytical Solution

Our first example problem is to solve a simple one-dimensional heat conduction-convection problem using FALCON and compare the numerical solution with the analytical solution. In this particular example, only two equations, fluid flow and heat transport, are solved.

The analytical solution compared in this example is derived from the solution by Faust and Mercer [5], by omitting the heat exchange between confined aquifer and surrounding rock matrix. In order to obtain the analytical solution, the thermodynamic and transport properties, such as water density and viscosity are assigned as constants. Then the mass conservation equation reduced to a Laplacian equation of pressure (Equation 1), which gives a uniform velocity v_w along x-direction.

$$\tau \nabla^2 P + q_w^{'} = 0 \tag{1}$$

And the energy equation reads as:

$$K_m \frac{\partial^2 u}{\partial x^2} - v_w \rho_w c_w \frac{\partial u}{\partial x} = \rho_m c_m \frac{\partial u}{\partial t} \tag{2}$$

where $\rho_m c_m = \phi \rho_w c_w + (1-\phi)\rho_r c_r$. The c is specific heat capacity of water (subscripted with w) or rock (subscripted with r). And u is normalized temperature $u = \frac{T-T_0}{T_i - t_0}$, T_i and T_0 are the injection and initial temperature, respectively. K_m is the heat conductivity of wet rock.

The analytical solution for Equation 1 and 2 is given by Avdonin [1]:

$$u(\chi, \tau) = \frac{\chi}{(\pi\tau)^{1/2}} \int_0^1 exp\left[-(s\gamma(\tau)^{1/2} - \frac{\chi}{2s(\tau)^{1/2}})^2\right] \frac{ds}{s^2} \tag{3}$$

where $\chi = \frac{2x}{b}$,$\tau = \frac{4K_m t}{c_m \rho_m b^2}$, $\gamma = \frac{Q c_w \rho_w}{4K_m}$,Q is the injection rate, and b is the reservoir thickness (1-m in this example).

In FALCON simulations, the geometry used for this example is a 100 meter long rectangle, 1 meter in width, with a 1 meter grid resolution. The mesh consisted of 100 elements and 102 nodes. Table 1 summarizes the parameters used for this example. Initial conditions are set as pressure $P = 10MPa$, temperature $T = 200°C$, uniformly. The BC are set as: injection pressure $P_i = 10.5MPa$, temperature $T_i = 150°C$ at left side, and constant pressure $10MPa$, temperature $200°C$ are assigned at right side.

Figure 4 shows the comparison between numerical and analytical solutions after 5 years of simulated transport. It is clear that the numerical solution agrees well with the analytical

Table 1: Parameters used for the 1-dimensional convection-conduction problem numerical-analytical comparison.

Parameter	Value	Units
Porosity	0.20	-
Permeability	1×10^{-15}	m^2
Rock Density	2.5×10^3	kg/m^3
Rock Specific Heat	0.92×10^3	$J/kg\,°C$
Thermal Conductivity	1.5	$W/m\,°C$
Water Density	1×10^3	kg/m^3
Water Specific Heat	4.186×10^3	$J/kg\,°C$

solution. The small discrepancy is caused by the pressure and temperature dependent density and viscosity of water used in the FALCON simulations. The analytical solution assumes a constant fluid density and viscosity, which essentially decouples the the flow and transport problem.

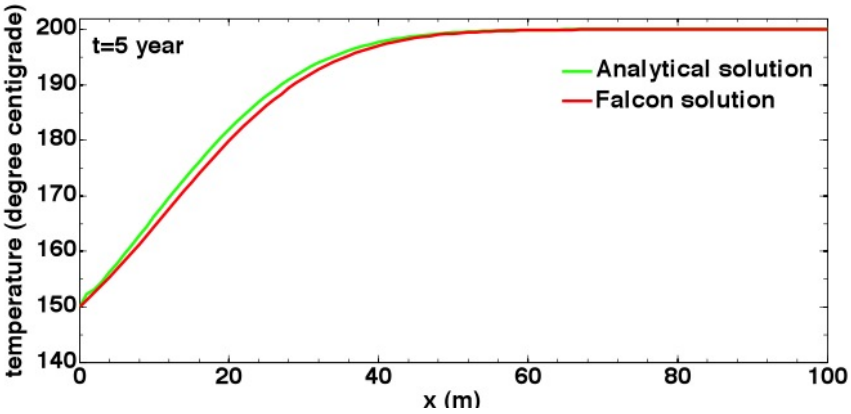

Figure 4: Comparison of the numerical and analytical solutions for 1-dimensional heat conduction-convection problem. Temperature profile calculated by FALCON and analytical solution at 5 years. The small discrepancy is caused by the pressure and temperature dependent density and viscosity of water used in the FALCON simulations. The analytical solution assumes a constant fluid density and viscosity, which essentially decouples the the flow and transport problem.

4.2 Thermal Stimulation of a Geothermal Reservoir

Management of fluid reinjection is of critical importance for maintaining geothermal reservoir performance. Reinjection has posed a problem for portions of the Hellisheidi Geothermal Field, southwest Iceland, where a number of wells are drilled into active faults. The Hellisheidi Geothermal Field is located in the southern part of the Hengill Area, an active volcanic system consisting of Mt. Hengill and fracture/fault zones to the north- and south-west (Smundsson, 1967; Franzson et al., 2005). Injection tests have resulted in swarms of small earthquakes and with the injectivity of the wells exhibiting a high dependence on temperature of the reinjected water. Strongly coupled thermo-hydro-mechanical effects on fractures in the fracture-governed reservoir likely explain the temperature dependent injectivity.

A number of injectivity tests have been conducted to support the development of the Hellisheidi Power Plant. For several of the wells, injection experiments were conducted using three types of water; 120°C untreated brine directly from the low-pressure boiler, a 90°C mixture of brine and condense water (7:3) from the turbines, and 15°C cold groundwater. These experiments were done in the three most promising wells in the Hsmli Reinjection Zone, HN-09, HN-12, and HN-16. The injectivity vs. T is plotted for all the wells in Figure 5. It should be mentioned here that the values for cold water in wells HN-12 and HN-16 are inaccurate. The wells are so permeable that the pressure changes in the pumping tests were not very clear.

The injection tests for estimating the injectivity were conducted as described below. Maximum flow of water at preferred temperature was injected into the well for several days. The wellhead pressure was monitored in order to estimate when the well had reached equilibrium. A pressure and temperature sensor was placed in the well at the depth of its main feed zone. The flow was lowered in three steps, each lasting for approximately 3 hours to allow the pressure to equilibrate to the new injection rate. Figure 6 is an example of pumping test results for the hot water injection into well HN-09. The pressure and temperature are plotted over the duration of the injection steps.

4.2.1 Model Setup

A radial structured mesh, with a radius of 250 meters, is being used to simulate the injection into well HN-09. The simulation domain is 100 meters thick, with the production zone begin represented as a 5-meter thick zone of fractured rock embedded in lower permeability (unfractured) reservoir rock. Figure 7 shows the simulation domain and the computational mesh.

Initial conditions being used in the simulations mimic those that exist in the reservoirs. The initial temperature distribution used in the simulation is shown in Figure 8, with the resulting water density, as calculated from the IAPWS-97 steam tables, shown on

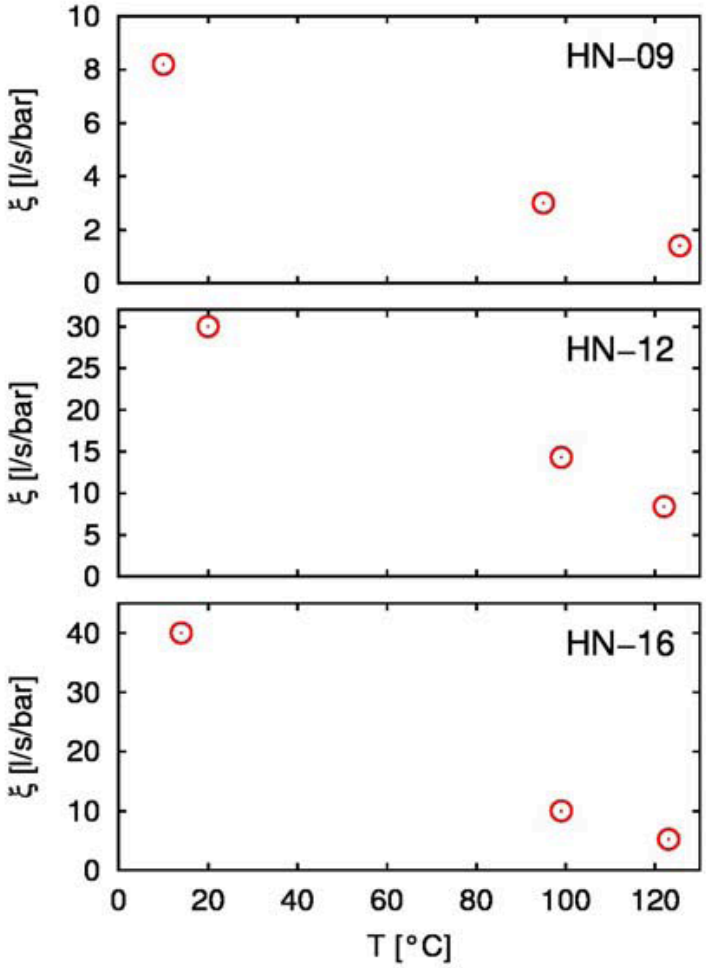

Figure 5: Injectivity at different values of temperature (T) in three wells in the Hsmli Reinjection Zone. The injectivity values for the lowest temperatures in wells HN-12 and HN-16 are not very accurate.

Figure 9. The temperature in the feed zone is approximately 264°C, with the temperature ranging from 263°C to 265°C. The water density in the reservoir ranged from approximately 772 to 776 kg/m^3 in the initial conditions.

The initial pressure in the reservoir was specified to a uniform 185 bars, and as the majority of the flow was expected to be primarily horizontal and limited to exist only within the thin fracture zone, the effects of gravity of the fluid flow and heat transport were neglected. This approach greatly simplified the specification of the boundary conditions needed for the simulations.

Feedback between the geomechanics and fluid flow are being implemented by revising the permeability of the feed zone by an effective fracture aperture, as calculated by the thermo-mechanical deformation of the mesh resulting from the injection of cold

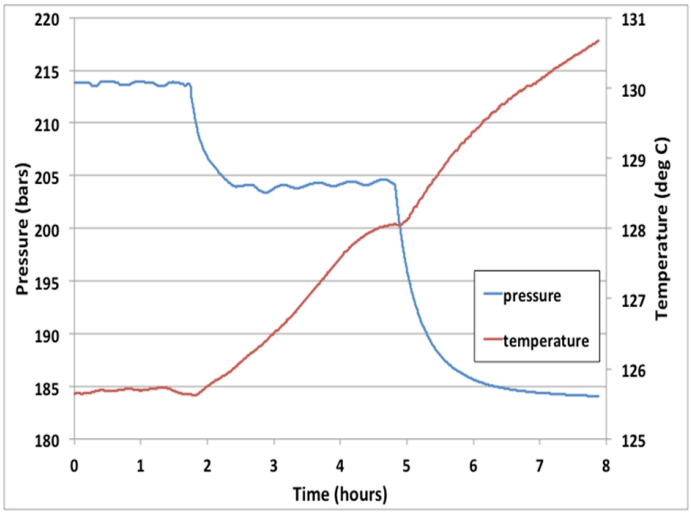

Figure 6: Injection test in well HN-09 using 120°C water. The pressure sensor is placed 30m above the bottom of the well showing the pressure and temperature over the duration of the test.

fluid into the initially hot reservoir. As the host reservoir rock thermally contracts, the effective permeability from the fractured feed zone increases using a cubic law approximation.

An initial modeling scenario, consisting of injecting approximately 30 l/s of 20°C pure water into the approximately 260°C reservoir, is currently underway. Preliminary simulation results are encouraging, where permeability increases on the order of 10X to 100X are predicted in the vicinity of well HN-09's feed zone. The reservoir matrix contraction in the feed zone near the injection well is predicted to approach 10^{-4} meters. Figure 10 shows the results of the geomechanical deformation in the vicinity of the injection well in the feed zone, along with the mesh that is adaptively refined by FALCON to capture the strong gradient in the temperature and resulting thermal deformation in the reservoir. Final results will be presented at the workshop.

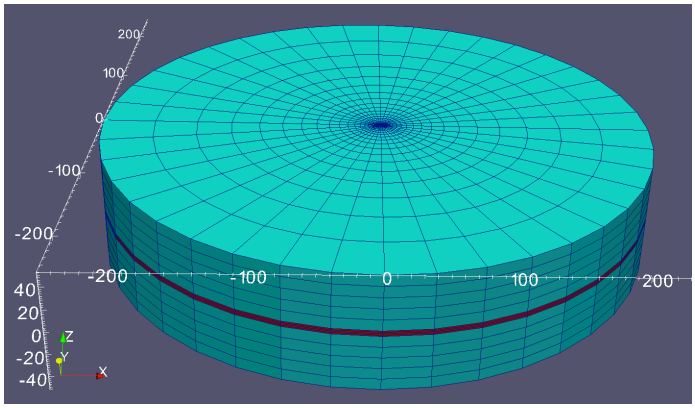

Figure 7: Computational domain used for the numerical simulations of injection into well HN-09. The red zone in the middle of the domain represents the fracture zone/fault system comprising the feed zone of the well.

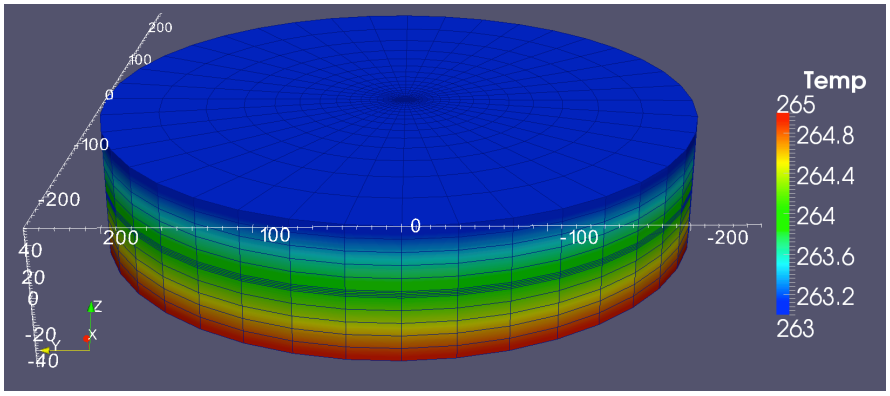

Figure 8: Initial temperature used for the simulations.

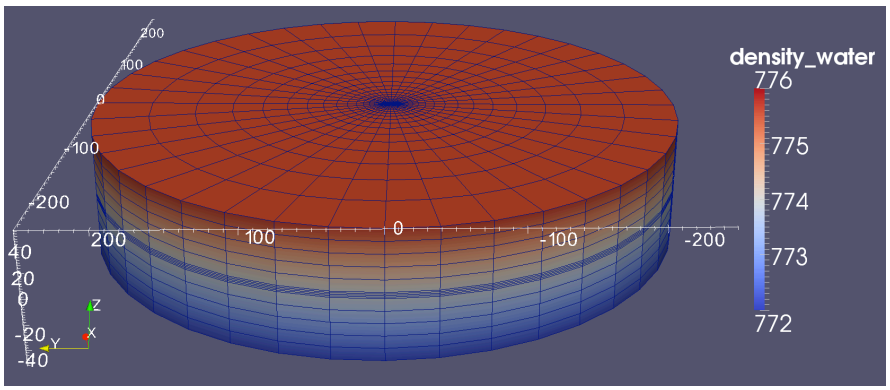

Figure 9: Initial water density distributions used for the simulations.

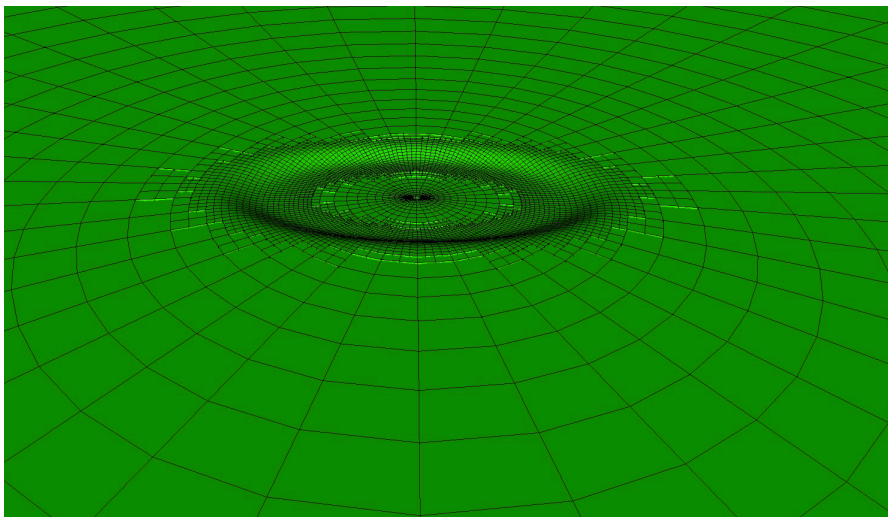

Figure 10: Predicted thermal contraction of the reservoir matrix in the feed zone in the vicinity of well HN-09. Note that the deformation is greatly exaggerated for illustration purposes.

Acknowledgement
The author would like to acknowledge travel support to the SIMS Conference provided by the International Energy Agency's Geothermal Implementing Agreement (IEA-GIA).

References

[1] N.A. Avdonin. Some formulas for calculating the temperature of a stratum subject to thermal injection. *Izvestiya Vysshikh Uchebnykh Zavedenii*, 7(4):37–41, 1964.

[2] Satish Balay, Kris Buschelman, Victor Eijkhout, William D. Gropp, Dinesh Kaushik, Matthew G. Knepley, Lois Curfman McInnes, Barry F. Smith, and Hong Zhang. PETSc users manual. Technical Report ANL-95/11 - Revision 2.1.5, Argonne National Laboratory, 2004.

[3] J. Carrayrou, P. Knabner J. Hoffmann, S. Krautle, C. de Dieuleveult, J. Erhel, J. van der Lee, V. Lagneau, K.U. Mayer, and K.T.B. MacQuarrie. Comparison of numerical methods for simulating strongly nonlinear and heterogeneous reactive transport problems-the momas benchmark case. *Computational Geosciences*, 14(3):483–502, 2010.

[4] R.D. Falgout and U.M. Yang. hypre: A library of high performance preconditioners. In *Computational Science-Iccs 2002*, Berlin, 2002. Springer-Verlag.

[5] C.R. Faust and J.W. Mercer. Geothermal reservoir simulation .1. Mathematcial-models for liquid-dominated and vapot-dominated hydrothermal systems. *Water Resources Research*, 15(1):23–30, 1979.

[6] D. Gaston, C. Newman, G. Hansen, and D. Lebrun-Grandié. MOOSE: A parallel computational framework for coupled systems of nonlinear equations. *Nuclear Engineering and Design*, 239:1768–1778, 2009.

[7] L. Guo, H. Huang, D. Gaston, C. Permann, D. Andrs, G. Redden, C. Lu, D. Fox, and Y. Fujita. A parallel fully-coupled fully-implicit solution to reactive transport in porous media using preconditioned jacobian-free newton-krylov method. *Journal of Computational Physics*, in review.

[8] G.E. Hammond, , A.J. Valocchi, and P.C. Lichtner. Application of jacobian-free newton-krylov with physics-based preconditioning to biogeochemical transport. *Advances in Water Resources*, 28(4):359–376, 2005.

[9] M. Heroux et al. Trilinos: an object-oriented software framework for the solution of large-scale, complex multi-physics engineering and scientific problems. http://trilinos.sandia.gov, 2008.

[10] B. S. Kirk, J. W. Peterson, R. H. Stogner, and G. F. Carey. libMesh: a C++ library for parallel adaptive mesh refinement/coarsening simulations. *Eng Comput-Germany*, 22(3-4):237–254, January 2006.

[11] D. Knoll, R. Park, and K. Smith. Application of the Jacobian-free Newton-Krylov method in computational reactor physics. In *American Nuclear Society 2009 International Conference on Advances in Mathematics, Computational Methods, and Reactor Physics*, Saratoga Springs, NY, May 3–7 2009.

[12] P. R. McHugh and D. A. Knoll. Inexact Newton's method solutions to the incompressible Navier-Stokes and energy equations using standard and matrix-free implementations. *AIAA J.*, 32:2394, 1994.

[13] C.W. Miller and L.V. Benson. Simulation of solute transport in a chemically reactive heterogeneous system - model development and application. *Water Resources Research*, 19(2):381–391, 1983.

[14] S. Molins, J. Carrera, C. Ayora, and M.W. Saaltink. A formulation for decoupling components in reactive transport problems. *Water Resources Research*, 40(10), 2004.

[15] J. Rutqvist, Y.S. Wu, C.F. Tsang, and G. Bodvarsson. A modeling approach for analysis of coupled multiphase fluid flow, heat transfer, and deformation in fractured porous rock. *Int. Journal of Rock Mechanics and Mining Sci.*, 39(4):429–442, JUN 2002.

[16] C.I. Steefel and K.T.B. MacQuarrie. Approaches to modeling of reactive transport in porous media. *Reviews in Mineralogy and Geochemistry*, 34:83–129, 1996.

[17] A.J. Valocchi, R.L. Street, and P.V. Roberts. Transport of ion-exchanging solutes in groundwater - chromatographic theory and field simulation. *Water Resources Research*, 17(5):1517–1527, 1981.

[18] W. Wagner, J.R. Cooper, A. Dittman, J. Kijima, H.-J. Kretzschmar, A. Kruse, R. Mares, K. Oguchi, H. Sato, I. Stocker, O. Sifner, Y. Takaishi, I. Tanishita, J. Trubenbach, and Th. Willkommen. The IAPWS Industrial Formulation 1997 for the Thermodynamic Properties of Water and Steam. *Trans. ASME*, 150(122):150–182, 1997.

[19] T. Xu, E. Sonnenthal, N. Spycher, and K. Pruess. TOUGHREACT - A simulation program for non-isothermal multiphase reactive geochemical transport in variably saturated geologic media: Applications to geothermal injectivity and CO2 geological sequestration. *Computers & Geosciences*, 32(2):145–165, 2006.

[20] G.T. Yeh, J. Sun, P.M. Jardine, W.D. Burgos, Y. Fang, M.-H. Li, and M.D. Siegel. HYDROGEOCHEM 5.0: A Coupled Model of Fluid Flow, Thermal Transport, and HYDROGEOCHEMical Transport through Saturated-Unsaturated Media: Version 5.0. Technical Report ORNL/TM-2004/107, Oak Ridge National Laboratory, Oak Ridge, TN, 2004.

[21] G.T. Yeh and V.S. Tripathi. A critical-evaluation of recent developments in hydrogeochemical transport models of reactive multichemical components. *Water Resources Research*, 25(1):93–108, 1989.

Optimisation of energy collection in a solar power plant

Esko K. Juuso *

* *Control Engineering Laboratory, Department of Process and Environmental Engineering, P.O. Box 4300, FI-90014 University of Oulu, Finland (e-mail: esko.juuso@ oulu.fi).*

Abstract: Solar power plants should collect any available thermal energy in a usable form at the desired temperature range, which improves the overall system efficiency and reduces the demands placed on auxiliary equipment. In addition to seasonal and daily cyclic variations, the intensity depends also on atmospheric conditions such as cloud cover, humidity, and air transparency. A fast start-up and efficient operation in varying cloudy conditions is important. Solar thermal power plants should provide thermal energy for use in an industrial process such as seawater desalination or electricity generation. Unnecessary shutdowns and start-ups of the collector field are both wasteful and time consuming. With fast and well damped controllers, the plant can be operated close to the design limits thereby improving the productivity of the plant. This study is based on tests done in Spain: the Acurex field supplies thermal energy in form of hot oil to an electricity generation system or a multi-effect desalination plant. The field consists of parabolic-trough collectors. Control is achieved by means of varying the flow pumped through the pipes in the field during the operation. Solar power plants can collect energy only when the irradiation is high enough. The nights and the heavy cloud periods need to come up with the storage. The demand may also vary during the daytime. The operation mode should be adapted to current operating conditions, weather forecasts and plans of the energy use. Different scenarios are compared with an intelligent dynamic simulator based on case specific linguistic equation models.

Keywords: Solar energy, intelligent control, nonlinear systems, adaptation, optimisation, linguistic equations, modelling, simulation

1. INTRODUCTION

Solar power plants should collect any available thermal energy in a usable form at the desired temperature range, which improves the overall system efficiency and reduces the demands placed on auxiliary equipment. In addition to seasonal and daily cyclic variations, the intensity depends also on atmospheric conditions such as cloud cover, humidity, and air transparency. A fast start-up and efficient operation in varying cloudy conditions is important. A solar collector field is a good test platform for control methodologies (Camacho et al., 1997; Juuso, 1999; Johansen and Storaa, 2002; Cirre et al., 2007; Limon et al., 2008; Roca et al., 2011; Ayala et al., 2011). The control strategies include basic feedforward and PID schemes, adaptive control, model-based predictive control, frequency domain and robust optimal control and fuzzy logic control.

Feedforward approaches based directly on the energy balance can use the measurements of solar irradiation and inlet temperature (Camacho et al., 1992). Lumped parameter models taking into account the sun position, the field geometry, the mirror reflectivity, the solar irradiation and the inlet oil temperature have been developed for a solar collector field (Camacho et al., 1997). A feedforward controller has been combined with different feedback controllers, even PID controllers operate for this purpose (Valenzuela and Balsa, 1998). The classical internal model control (IMC) can operate efficiently in varying time delay conditions (Farkas and Vajk, 2002). Genetic algorithms have also been used for multiobjective tuning (Bonilla et al., 2012).

Linguistic equations (LE) have been used in various industrial applications (Juuso, 1999, 2004). Modelling and control activities with the LE methodology started by the first controllers implemented in 1996 (Juuso et al., 1997) and the first dynamic models developed in 1999 (Juuso et al., 2000). The LE based dynamic simulator is an essential tool in fine–tuning of these controllers (Juuso, 2005). The LE controllers use model-based adaptation and feedforward features, which are aimed for preventing overheating, and the controller presented in (Juuso and Valenzuela, 2003) already took care of the actual setpoints of the temperature. The manual adjustment of the working point limit has improved the operation considerably.

Parameters of the LE controllers were first defined manually, and later tuned with neural networks and genetic algorithms. Genetic algorithms combined with simulation and model-based predictive control have further reduced temperature differences between collector loops (Juuso, 2006). Data analysis methods are based on generalised norms, which have been developed for condition monitor-

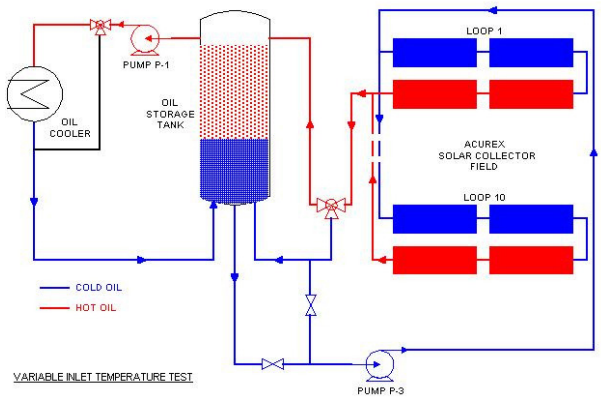

Fig. 1. Layout of the Acurex solar collector field.

ing (Juuso and Lahdelma, 2010), provide new data-driven tools for intelligent modelling (Juuso, 2010). A recursive version of the scaling approach was introduced in (Juuso, 2011).

New state indicators for detecting cloudy conditions and other oscillatory situations by analysing fluctuations of irradiation, temperature and oil flow (Juuso, 2012). The new indicators react well to the changing operating conditions and can be used in smart working point control.

This paper analyses the operation of new intelligent indicators introduced for adapting the LE controllers for start-up and operation in cloudy conditions and load disturbances. The analysis is based on recent experiments carried out in the *Acurex Solar Collectors Field of the Plataforma Solar de Almeria (PSA)* in Spain.

2. SOLAR COLLECTOR FIELD

The aim of solar thermal power plants is to provide thermal energy for use in an industrial process such as seawater desalination or electricity generation. Unnecessary shutdowns and start-ups of the collector field are both wasteful and time consuming. With fast and well damped controllers, the plant can be operated close to the design limits thereby improving the productivity of the plant (Juuso et al., 1998).

The *Acurex field* supplies thermal energy (1 MW_t) in form of hot oil to an electricity generation system or a Multi–Effect Desalination Plant. The field consists of parabolic–trough collectors. Control is achieved by means of varying the flow pumped through the pipes in the field (Fig. 1) during the operation. In addition to this, the collector field status must be monitored to prevent potentially hazardous situations, e.g. oil temperatures greater than 300 ^oC. The temperature increase in the field may rise up to 110 degrees. At the beginning of the daily operation, the oil is circulated in the field, and the flow is turned to the storage system (Fig. 1) when an appropriate outlet temperature is achieved. The valves are used only for open-close operation, and the overall flow F to the collector field is controlled by the pump. (Juuso et al., 1997)

The *energy balance* of the collector field can be represented by expression (Valenzuela and Balsa, 1998):

$$I_{eff} A_{eff} = (1 - \eta_p) F \rho c T_{diff}, \qquad (1)$$

where I_{eff} is effective irradiation (Wm^{-2}), A_{eff} effective collector area (m^2), η_p a general loss factor, F flow rate of the oil ($m^3 s^{-1}$), ρ oil density kgm^{-3}, c specific heat of oil ($Jkg^{-1}K^{-1}$) and T_{diff} temperature difference between the inlet and the outlet (^oC). The effective irradiation is the direct irradiation modified by taking into account the solar time, declination and azimuth.

3. MODELLING

The nonlinearities of the process is handled by nonlinear scaling of the variables. The parameters of the scaling functions are obtained by data analysis based on generalised norms and moments.

3.1 Scaling functions

The generalised norm is defined by

$$||^{\tau} M_j^p||_p = (M_j^p)^{1/p} = [\frac{1}{N} \sum_{i=1}^{N} (x_j)_i^p]^{1/p}, \qquad (2)$$

where the order of the moment $p \in R$ is non-zero, and N is the number of data values obtained in each sample time τ. The norm (2) calculated for variables x_j, $j = 1, \ldots, n$, have the same dimensions as the corresponding variables. The norm $||^{\tau} M_j^p||_p$ can be used as a central tendency value if all values $x_j > 0$, i.e. $||^{\tau} M_j^p||_p \in R$. This norm combines two trends: a strong increase caused by the power p and a decrease with the power $1/p$. (Lahdelma and Juuso, 2008, 2011).

The mean, the harmonic mean and the root mean square (rms) are special cases of (2), which represents the norms between the minimum and the maximum corresponding the orders $p = -\infty$ and $p = \infty$, respectively. The norm values increase with increasing order. When $p < 0$, all the signal values should be non-zero, i.e. $x \neq 0$. When the order $p \to 0$, we obtain from (2) the geometric mean. The computation of the generalised norms can be divided into the computation of equal sized sub-blocks, i.e. the norm for several samples can be obtained as the norm for the norms of individual samples. (Lahdelma and Juuso, 2008, 2011) The norm can be extended to variables including negative values (Juuso, 2011).

Scaling functions, also known as membership definitions, provide nonlinear mappings from the operation area of the (sub)system to the linguistic values represented inside a real-valued interval $[-2, 2]$, denoted as the linguistic range, see (Juuso, 2004). The membership definitions consist of two second order polynomials: one for negative values, $X \in [-2, 0)$, and one for non-negative values, $X \in [0, 2]$. The polynomials are configured with five parameters defined by (2) and the generalised skewness,

$$(\gamma_k^p)_j = \frac{1}{N \sigma_j^k} \sum_{i=1}^{N} [(x_j)_i - ||^{\tau} M_j^p||_p]^k. \qquad (3)$$

The standard deviation σ_j is the norm (2) with the order $p = 2$. The parameters of the scaling functions can be recursively updated with by including new samples in calculations. The number of samples K_s can be increasing or fixed with some forgetting or weighting (Juuso, 2011).

3.2 Working point model

The volumetric heat capacity increases very fast in the start-up stage but later remains almost constant because the normal operating temperature range is fairly narrow. This nonlinear effect is handled with the working point LE model

$$wp = a_1\tilde{I}_{eff} + a_2\tilde{T}_{diff} + a_3\tilde{T}_{amb} + a_4, \quad (4)$$

where $\tilde{I}_{eff}$, $\tilde{T}_{diff}$ and $\tilde{T}_{amb}$, which are obtained by nonlinear scaling of variables: efficient irradiation I_{eff}, temperature difference between the inlet and outlet, $T_{diff} = T_{out} - T_{in}$, and ambient temperature T_{amb}, correspondingly. The outlet temperature T_{out} is the maximum outlet temperature of the loops. The ambient temperature is usually not used. Interactions are defined by constant coefficients a_1, a_2, a_3 and a_4. Working point, wp, represents a fluctuation from the normal operation.

The working point variables already define the overall normal behaviour of the solar collector field, e.g. oscillatory behaviour is a problem when the temperature difference is higher than the normal. In the normal working point, $wp = 0$: the irradiation $\tilde{I}_{eff}$ and the temperature difference, $\tilde{T}_{diff}$, are on the same level. A high working point ($wp > 0$) means low $\tilde{T}_{diff}$ compared with the irradiation level $\tilde{I}_{eff}$. Correspondingly, a low working point ($wp < 0$) means high $\tilde{T}_{diff}$ compared to the irradiation level $\tilde{I}_{eff}$. The normal limit ($wp_{min} = 0$) reduces oscillations by using slightly lower setpoints during heavy cloudy periods. This is not sufficient when the irradiation is high between cloudy periods. Higher limits ($wp_{min} = 1$) shorten the oscillation periods after clouds more efficiently.

3.3 Dynamic LE model

Conventional mechanistic models do not work, since there are problems with oscillations and irradiation disturbances. In dynamic LE models, the new temperature difference $\tilde{T}_{diff}(t+\Delta t)$ between the inlet and outlet depends on the irradiation, oil flow and previous temperature difference:

$$\tilde{T}_{diff}(t + \Delta t) = a_1\tilde{T}_{diff}(t) + a_2\tilde{I}_{eff}(t) + a_3\tilde{F}(t) + a_4, \quad (5)$$

where coefficients a_1, a_2, a_3 and a_4 depend on operating conditions, i.e. each submodel has different coefficients. The membership definition of the outlet temperature does not depend on time; the bias term $a_4 = 0$. Model coefficients and the scaling functions for T_{diff}, I_{eff} and F are all model specific.

The fuzzy LE system with four operating areas is clearly the best overall model (Juuso, 2003, 2009): the simulator moves smoothly from start-up mode via low mode to normal mode and later visits shortly in high mode and low mode before returning to low mode in the afternoon. Even oscillatory conditions, including irradiation disturbances, are handled correctly. The dynamic LE simulator predicts well the average behaviour but requires improvements for predicting the maximum temperature since the process changes considerably during the first hour. For handling special situations, additional fuzzy models have been developed on the basis of the Fuzzy–ROSA method (Juuso et al., 2000).

4. INTELLIGENT LE CONTROL

The intelligent control system consists of a nonlinear linguistic equation (LE) controller with predefined adaptation models. For the solar collector field, the goal is to reach the nominal operating temperature $180 - 295\ ^oC$ and keep it in changing operating conditions (Juuso, 2011, 2012). The feedback controller is a PI-type LE controller with one manipulating variable, oil flow, and one controlled variable, the maximum outlet temperature of the loops. The controller provides a compact basis for advanced extensions. *High-level control* is aimed for manual activating, weighting and closing different actions.

4.1 Intelligent analysers

Intelligent analyzers are used for detecting changes in operating conditions to activate adaptation and model-based control and to provide indirect measurements for the high-level control. Several improvements were tested during a recent test campaign:

- The working point, which is obtained from the effective irradiation and the difference between the outlet and the inlet temperatures, is the basis of the adaptation procedures.
- The predictive braking indication is activated when a very large error is detected. A new solution was introduced to detecting the large error.
- The asymmetry detection was changed drastically: the calculation is now based on the changes of the corrected irradiation. The previous calculation based on the solar noon does not take into account actual irradiation changes.
- The new fluctuation indicators, which were introduced to detecting cloudiness and oscillations, are the main improvements aimed for practical use.
- The intelligent indicators of the fast changes of the temperatures (inlet, outlet and difference) were compared with the intelligent trend analysis, which was introduced. The trend analysis is based on the scaled variables which are also used in the controller. New and revised actions required updates of the parameters.

4.2 Advanced control

Adaptive LE control uses correction factors which are obtained from the working point value. The predictive braking and asymmetrical actions are activated when needed. Intelligent indicators introduce additional changes of control if needed. The test campaign clarified the events, which activate the special actions. Each action has a clear task in the overall control system.

Model-based control was earlier used for limiting the acceptable range of the temperature setpoint by setting a lower limit of the working point. The new fluctuation indicators are used for modifying the lower working point limit to react better to cloudiness and other disturbances. This overrides the manual limits if the operation conditions require that. This operated well in start-up and cloudy conditions. Oscillations are reduced efficiently in cloudy conditions and in the case of load disturbances. In heavy

cloudy conditions, the controller keeps the field ready to start full operation. Even a short sunny spell raised the temperatures to the operating range.

Intelligent trend analysis was performed for temperatures, irradiation and oil flow. These studies will be continued. The controller contains several parametric scaling functions for variables, errors, changes and corrections. The parameters were tuned before the test campaign by using previous test results. The parameters of the controller were updated for the revised actions. Offline tuning with the recursive approach will be done after the test campaign.

4.3 Optimisation

Energy collection depends on the oil flow, the temperature difference and the properties of the oil, see (1). High temperature differences are achieved by using low oil flow, and high flow leads to low temperature differences. The density decreases and the specific heat increases resulting a nonlinear increase of the term ρc (Fig. 2). In the start-up, the flow is limited by the high viscosity. (Juuso et al., 1998)

The highest energy collection in a time unit, i.e. the collected solar power, is achieved by selecting the optimal temperature difference, which depends on the irradiation and less on the ambient temperature. The optimisation is based on the oil properties and the inlet temperature, T_{in}. Then the working point (4), which is defined by the optimal T_{diff} and the irradiation, is used in the model-based control to adjust the setpoint.

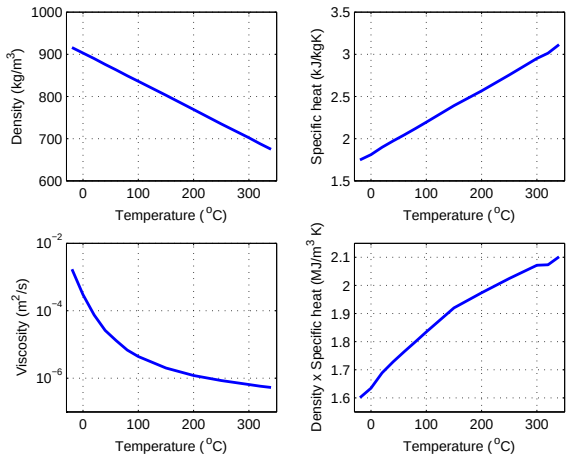

Fig. 2. Oil properties (Santotherm 55).

5. RESULTS

The new features of the controller was tested on a solar collector field at PSA in July 2012. The results are used in developing optimisation solutions for the energy collection.

5.1 Normal operation

On a clear day with high irradiation, the setpoint tracking was very fast: step changes from 15-25 degrees were achieved in 20-30 minutes with minimal oscillation. The working point adaptation was operating efficiently. The temperature was increased and decreased in spite of the irradiation changes. The working point limit activated the setpoint correction when the temperature difference exceeded the limit corresponding to the irradiation level. The oil flow changed smoothly: the fast changes were at the beginning of the step. Also the braking action was activated in these situations. Working point corrections and limiting the fast change were negligible.

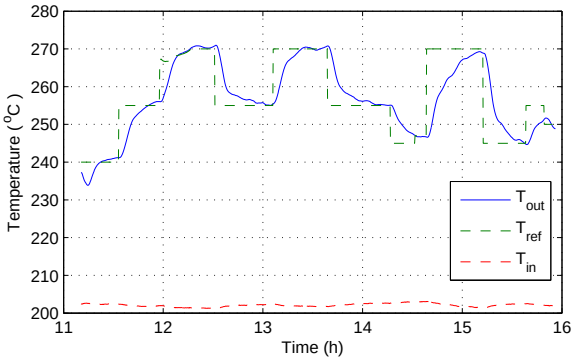

Fig. 3. Test results of the LE controller on a clear day.

On a fairly clear day with a lower and slightly varying irradiation, the setpoint correction was activated more often throughout the day. The temperature followed the setpoint well with smaller offsets. Working point corrections and limiting the fast change were negligible.

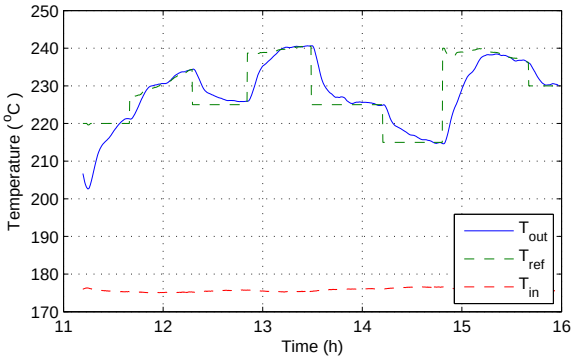

Fig. 4. Test results of the LE controller on a fairly clear day.

5.2 Cloudy conditions

Three cloudy periods occurred on the third day: a long period in the morning, a short light one close the solar noon and a short, but heavy, in the afternoon. The temporary setpoint correction operated well in these situations. In the first case, the temperature went down with 20 degrees but rose back during the short sunny spells, and finally, after the irradiation disturbances, high temperatures were achieved almost without oscillations with the gradually changing setpoint defined by the working point limit although the inlet temperature was simultaneously rising. The same approach operated well for the other two cloudy periods. The oil flow was changed smoothly also during these periods. The working point corrections were now very strong, but limiting the fast changes was hardly

needed. Strong braking was used in the beginning and in the recovery from the first cloudy period. There were problems with some loops during that day.

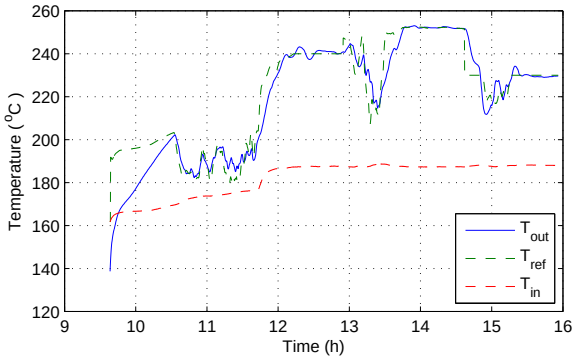

Fig. 5. Test results of the LE controller on a cloudy day.

The fourth day had two very different periods: the start was very bright and the irradiation was rising smoothly, but everything was changed just before the solar noon, and the heavy cloudy period continued the whole afternoon. The operation already started from low inlet temperature with the minimum flow. The whole start-up was very smooth despite the increasing irradiation and inlet temperature. The offset was removed when the new asymmetry correction of the controller. Also the small temperature increase, which was caused when a new loop was taken into use, was efficiently corrected. The working point corrections were activated only in the beginning, and limiting the fast change was negligible throughout this period.

The heavy clouds meant going back to the minimum flow, but also lower setpoints. The field was ready for normal operation and short sunny spells raised the temperature, but also the oil flow. The controller was ready to prevent a high overshoot, if the sky clears up. The field was in temperatures 160 - 210 ^oC for more than two hours although the loops were not tracking the sun all the time. The working point corrections were during this period very strong, but limiting the fast changes was hardly needed.

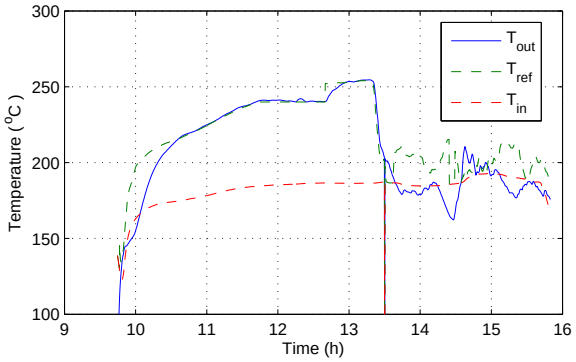

Fig. 6. Test results of the LE controller on a clear morning followed by heavy clouds.

5.3 Load disturbances

On the fifth day, the start-up followed the setpoint defined by the working point limit. In addition, there was an unintentional drop of 16.9 degrees in the inlet temperature. The disturbance lasted 20 minutes. The controller reacted by introducing a setpoint decrease of 19.8 degrees. The normal operation was retained in 50 minutes with only an overshoot of two degrees, but with some oscillations. The setpoint correction was too early and too large. The disturbance was repeated on the sixth day: maximum 13.5 degrees and 15 minutes. Now the setpoint was changed when the inlet temperature reached the minimum. The working point limit was changed to allow a higher setpoint in the recovery. The temperature drop was smaller (7.5 degrees) but the overshoot slightly higher (2.5 degrees). Also the recovery took less time (30 minutes). A third test was planned, but it was not possible to realize.

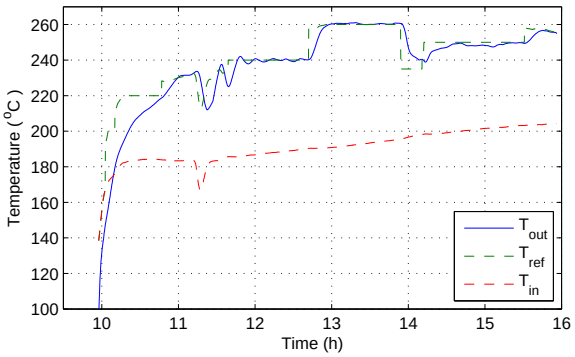

Fig. 7. Test results of the LE controller on a fairly clear day including a load disturbance.

5.4 Asymmetry correction

The new asymmetry correction was activated in several periods on the sixth day. There were good results on two previous days, but now the operation was better tuned for the afternoon as well. The setpoints were achieved in the range 0.5 degrees with hardly any offset. The change is considerable to the first days, when the outlet temperature exceeded the setpoint with 0.5-1 degrees, when the irradiation was increasing, and remained about 1.0 degrees lower when the irradiation decreased. Around the solar noon, the setpoint was achieved very accurately.

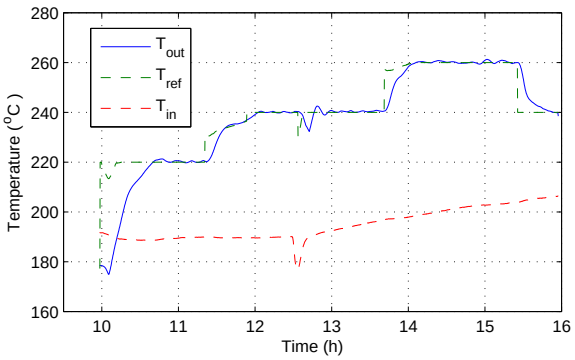

Fig. 8. Test results of the LE controller on a fairly clear day: asymmetry action.

5.5 Optimisation

The temperature increase in the collector field naturally depends on the irradiation, which is the highest close to the solar noon (Fig. 9). In this case, the inlet temperature is slightly increasing during the day (Fig. 7), which brought a possibility to use even higher outlet temperatures (Fig. 10). The temperatures increase with decreasing oil flow. A trade-off of the temperature and the flow is needed to achieve a good level for the collected power (Fig. 11). The working point (Fig. 12) is chosen from the high power range and used in the model-based control to choose or limit the setpoint.

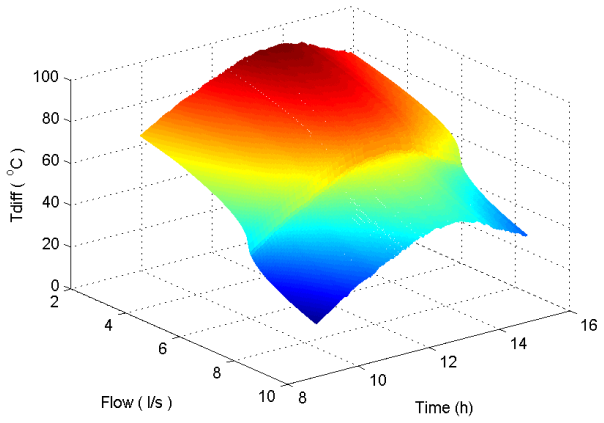

Fig. 9. Calculated temperature difference vs. oil flow on a fairly clear day.

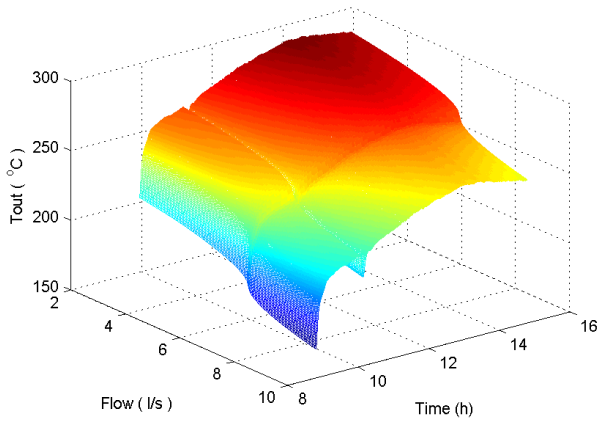

Fig. 10. Calculated outlet temperature vs. oil flow on a fairly clear day.

The power surface (Fig. 11) is highly nonlinear because of the nonlinear properties of the oil (Fig. 2). Disturbances of the inlet temperatures introduce similar fluctuation to the outlet temperature (Fig. 10). The acceptable range of the working point is limited: oscillation risks and high viscosity of the oil during the start-up must be taken into account. In the latest tests, the inlet temperatures are high already in the start-up, since the oil flow was not first circulated in the field. High irradiation periods would lead to too high outlet temperatures, if the oil flow is too low, but this is avoided by keeping the working point under two (Fig. 12).

The maximum collected power is achieved when the oil flow is close to 6 l/s. Another maximum area close to the upper limit of the oil flow is achieved around the solar noon on a clear day.

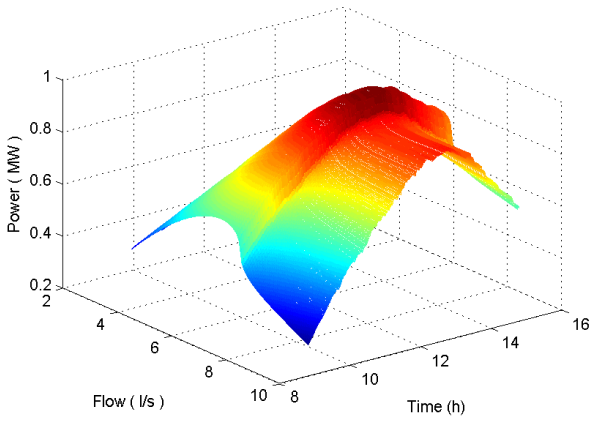

Fig. 11. Power vs. oil flow on a fairly clear day.

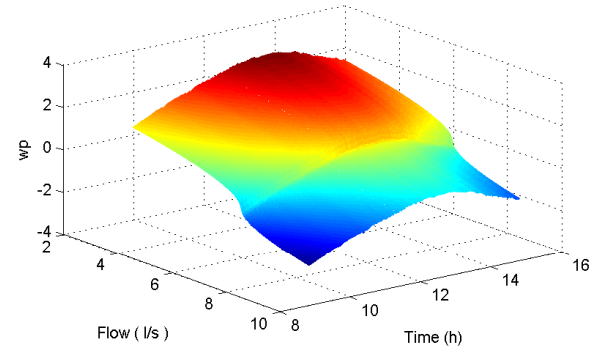

Fig. 12. Working point vs. oil flow on a fairly clear day.

6. CONCLUSION

The intelligent LE control system is based on predefined model-based adaptation techniques. The system activates special features when needed. Fast start-up, smooth operation and efficient energy collection is achieved even in variable operating condition. The new state indicators react well to the changing operating conditions and can be used in smart working point control to further improve the operation. The working point can be chosen in a way which improves the efficiency of the energy collection. A trade-off of the temperature and the flow is needed to achieve a good level for the collected power.

ACKNOWLEDGEMENTS

Experiments were carried out within the project "Intelligent control and optimisation of solar collection with linguistic equations (ICOSLE)" as a part of the project "Solar Facilities for the European Research Area (SFERA)" supported by the 7th Framework Programme of the EU (SFERA Grant Agreement 228296).

REFERENCES

Ayala, C.O., Roca, L., Guzman, J.L., Normey-Rico, J.E., Berenguel, M., and Yebra, L. (2011). Local model predictive controller in a solar desalination plant collector field. *Renewable Energy*, 36, 3001–3012.

Bonilla, J., , Yebra, L.J., Dormido, S., and Zarza, E. (2012). Parabolic-trough solar thermal power plant simulation scheme, multi-objective genetic algorithm calibration and validation. *Solar Energy*, 86, 531–540.

Camacho, E., Berenguel, M., and Rubio, F.R. (1997). *Adaptive Control of Solar Plants*. Springer, London.

Camacho, E., Rubio, F., and Hughes, F. (1992). Self-tuning control of a solar power plant with a distributed collector field. *IEEE System Control Magazine*, (April), 72–78.

Cirre, C.M., Berenguel, M., Valenzuela, L., and Camacho, E. (2007). Feedback linearization control for a distributed solar collector field. *Control engineering Practice*, 15, 1533–1544.

Farkas, I. and Vajk, I. (2002). Internal model-based controller for a solar plant. In *CD-ROM Preprints of the 15th Triennial World Congress*, 6 pp. IFAC.

Johansen, T.A. and Storaa, C. (2002). Energy-based control of a distributed solar collector field. *Automatica*, 38, 1191–1199.

Juuso, E. and Lahdelma, S. (2010). Intelligent scaling of features in fault diagnosis. In *Proceedings of the 7th International Conference on Condition Monitoring and Machinery Failure Prevention Technologies, 22-24 June, 2010, Stratford-upon-Avon, UK*, 15 pp. BINDT.

Juuso, E.K. (1999). Fuzzy control in process industry: The linguistic equation approach. In H.B. Verbruggen, H.J. Zimmermann, and R. Babuska (eds.), *Fuzzy Algorithms for Control, International Series in Intelligent Technologies*, 243–300. Kluwer, Boston.

Juuso, E.K. (2003). Intelligent dynamic simulation of a solar collector field. In *Simulation in Industry, 15th European Simulation Symposium ESS 2003*, 443–449. SCS, Gruner Druck, Erlangen, Germany.

Juuso, E.K. (2004). Integration of intelligent systems in development of smart adaptive systems. *International Journal of Approximate Reasoning*, 35, 307–337.

Juuso, E.K. (2005). Modelling and control of a solar thermal power plant. In *Proceedings of 16th Triennial World Congress, Prague, July 3-8, 2005*, 368–373. IFAC.

Juuso, E.K. (2006). Modelling and simulation in development and tuning of intelligent controllers. In *Proceedings of 5th Vienna Symposium on Mathematical Modelling, February 8-10, 2006, Vienna, Austria, Argesim Report 30*, 6–1 – 10. Argesim Verlag, Vienna. ISBN 3-901608-30-3.

Juuso, E.K. (2009). Dynamic simulation of solar collector fields in changing operating conditions. In *Proceedings of SIMS 50 - the 50th International Conference of Scandinavian Simulation Society, October 7-8, Fredericia, Denmark*, 341–348. DTU, Lungby, Denmark.

Juuso, E.K. (2010). Data-based development of hybrid models for biological wastewater treatment in pulp and paper industry. In *Proceedings of the 7th EUROSIM Congress on Modelling and Simulation, Prague, September 6-10, 2010*, 10 pp.

Juuso, E.K. (2011). Recursive tuning of intelligent controllers of solar collector fields in changing operating conditions. In *Proceedings of the 18th World Congress The International Federation of Automatic Control, Milano (Italy) August 28 - September 2, 2011*, 12282–12288. IFAC.

Juuso, E.K. (2012). Model-based adaptation of intelligent controllers of solar collector fields. In *Preprints of 7th Vienna Symposium on Mathematical Modelling, February 15-17, 2012, Vienna, Austria, Argesim Report S38*, 6 pp. Argesim, Vienna.

Juuso, E.K., Balsa, P., and Leiviskä, K. (1997). Linguistic Equation Controller Applied to a Solar Collectors Field. In *Proceedings of the European Control Conference - ECC'97, Brussels, July 1 - 4, 1997*, volume Volume 5, TH-E I4, paper 267 (CD-ROM), 6 pp.

Juuso, E.K., Balsa, P., and Valenzuela, L. (1998). Multilevel linguistic equation controller applied to a 1 MW solar power plant. In *Proceedings of the ACC'98, Philadelphia, PA, June 24–26, 1998*, volume 6, 3891–3895. ACC.

Juuso, E.K., Schauten, D., Slawinski, T., and Kiendl, H. (2000). Combination of linguistic equations and the fuzzy-rosa method in dynamic simulation of a solar collector field. In *Proceedings of TOOLMET 2000 Symposium - Tool Environments and Development Methods for Intelligent Systems, Oulu, April 13-14, 2000*, 63–77. Oulun yliopistopaino, Oulu.

Juuso, E.K. and Valenzuela, L. (2003). Adaptive intelligent control of a solar collector field. In *Proceedings of Eunite 2003 - European Symposium on Intelligent Technologies, Hybrid Systems and their implementation on Smart Adaptive Systems, July 10-11, 2003, Oulu, Finland*, 26–35. Wissenschaftsverlag Mainz, Aachen.

Lahdelma, S. and Juuso, E. (2008). Signal processing in vibration analysis. In *Proceedings of the Fifth International Conference on Condition Monitoring and Machinery Failure Prevention Technologies, 15-18 July 2008, Edinburgh, UK*, 867–878. BINDT.

Lahdelma, S. and Juuso, E. (2011). Signal processing and feature extraction by using real order derivatives and generalised norms. Part 1: Methodology. *The International Journal of Condition Monitoring*, 1(2), 46–53.

Limon, D., Alvarado, I., Alamo, T., Ruiz, M., and Camacho, E.F. (2008). Robust control of the distributed solar collector field ACUREX using MPC for tracking. In *Proceedings of 17th IFAC World Congress, Seoul, Korea*, volume 17, 958–963. IFAC. Http://www.ifac-papersonline.net/.

Roca, L., Guzman, J.L., Normey-Rico, J.E., Berenguel, M., and Yebra, L. (2011). Filtered smith predictor with feedback linearization and constraints handling applied to a solar collector field. *Solar Energy*, 85, 1056–1067.

Valenzuela, L. and Balsa, P. (1998). Series and parallel feedforward control schemes to regulate the operation of a solar collector field. In *Proceedings of the 2nd User Workshop Training and Mobility of Researchers Programme at Plataforma Solar de Almeria, November 10-11, 1998*, 19–24. Ciemat.

Scripting Modelica Models Using Python

Bernt Lie and Finn Haugen
Telemark University College, Porsgrunn, P.O. Box 203, N-3901 Porsgrunn, Norway
Corresponding author: Bernt.Lie@hit.no

September 13, 2012

Abstract

Modelica has evolved as a powerful language for encoding models of complex systems. In control engineering, it is of interest to be able to analyze dynamic models using scripting languages such as MATLAB and Python. This paper illustrates some analysis and design methods relevant in control engineering through scripting a Modelica model of an anaerobic digester model using Python, and discusses advantages and shortcomings of the Python+Modelica set-up.

1 Introduction

Modelica is a modern language for describing large scale, multidisciplinary dynamic systems (Fritzson, 2011), and models can be built from model libraries or the user can develop her own models or libraries using a text editor and connect the submodels either using a text editor or a visual tool. Several commercial tools exist, such as Dymola[1], MapleSim[2], Wolfram SystemModeler[3], etc. Free/research based tools also exist, e.g. OpenModelica[4] and JModelica.org[5]. More tools are described at `www.modelica.org`.

For most applications of models, further analysis and post processing is required, including e.g. model calibration, sensitivity studies, optimization of design and operation, model simplification, etc. Although Modelica is a rich language, the lack of tools for analysis has been a weakness of the language as compared e.g. to MATLAB, etc. Two commercial products are thus based on integrating Modelica with Computer Algebra Systems (MapleSim, Wolfram SystemModeler), while for other tools the analysis part has been more cumbersome (although Dymola includes possibilities for model calibration, an early but simple way of controlling models from MATLAB, etc.). A recent development has been the FMI standard[6], which promises to greatly simplify the possibility to script e.g. Modelica models from MATLAB or Python (FMI Toolbox for MATLAB[7]; PyFMI for Python[8]). Several Modelica tools now offer the opportunity to export models as FMUs (Functional Mock-up Units), whereupon PyFMI can be used to import the FMU into Python. Or the FMU can be directly generated from PyFMI. PyFMI is integrated into the JModelica.org[9] tool. More extensive integration with Python is under way for other (free) tools, too.

Python 2.7 with packages Matplotlib, NumPy, and SciPy offer many tools for analysis of models; a simple installation is EPD Free[10], but many other installations exist.

It is of interest to study whether the combination of (free software) releases of Modelica and Python can serve as useful tools for control analysis and design studies, and what limitations currently limit the spread of such a package. This paper gives an overview of basic possibilities for doing model based control studies by scripting Modelica models from Python. As a case study, a model of an anaerobic digester for converting cow manure to biogas is presented in Section 2. Section 3 presents various examples of systems and control analysis carried out by Python scripts using the model encoded in Modelica. Finally, the results are discussed and some conclusions are drawn in Section 4.

[1] `www.3ds.com/products/catia/portfolio/dymola`
[2] `www.maplesoft.com/products/maplesim`
[3] `www.wolfram.com/system-modeler`
[4] `www.openmodelica.org`
[5] `www.jmodelica.org`
[6] `www.fmi-standard.org`
[7] `www.modelon.com`
[8] `www.jmodelica.org/page/4924`
[9] `www.JModelica.org`
[10] `www.enthought.com`

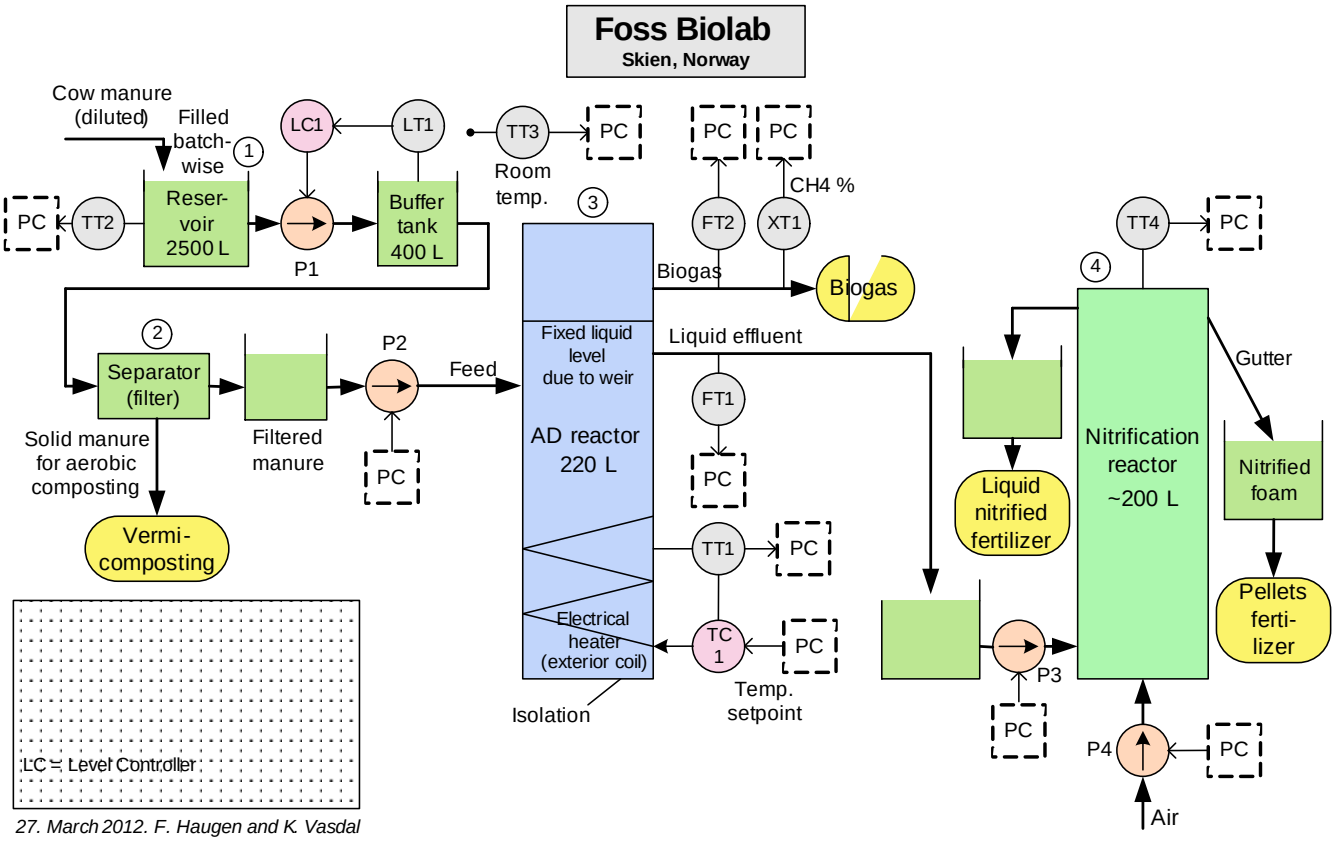

Figure 1: System for converting cow manure to biogas at Foss Biolab, Skien, Norway. Figure by F. Haugen and K. Vasdal.

2 Case study

2.1 Functional description

Figure 1 illustrates the animal waste conversion system at Foss Biolab in Skien, Norway, which converts cow manure into biogas utilizing Anaerobic Digestion (AD). In this case study, we consider the reactor only (blue box), where the *Feed* is described by a volumetric feed rate $\dot{V}_{\mathrm{f}}$ [L/ d] (control input) with a given concentration $\rho_{\mathrm{S_{vs,f}}}$ of volatile solids (disturbance).

The "liquid" level of the reactor is made constant by the use of a weir system, and it is possible to control the reactor temperature T accurately using electric heating (potential control input). The main product considered here, is the mass flow rate of methane out of the reactor, $m_{\mathrm{CH_4,x}}$ (controlled variable).

2.2 Model summary

A model of the reactor is presented in Haugen et al. (2012); in this paper, the same model is used but with a modified notation. The operation of the bio reactor is described by four states $j \in \left\{\rho_{\mathrm{S_{bvs}}}, \rho_{\mathrm{S_{vfa}}}, \rho_{\mathrm{X_a}}, \rho_{\mathrm{X_m}}\right\}$:

$$\frac{d}{dt}\rho_j = \frac{1}{\theta_j}\frac{\dot{V}_{\mathrm{f}}}{V}\left(\rho_{j,\mathrm{f}} - \rho_j\right) + R_j$$

where V is constant due to perfect level control, the residence time correction $\theta_{\mathrm{S}_j} = 1$ and θ_{X_j} may differ from 1, and furthermore:

$$\begin{aligned}
R_{\mathrm{S_{bvs}}} &= -Y_{\mathrm{S_{bvs}/X_a}} R_{\mathrm{a}} \\
R_{\mathrm{S_{vfa}}} &= Y_{\mathrm{S_{vfa}/X_a}} R_{\mathrm{a}} - Y_{\mathrm{S_{vfa}/X_m}} R_{\mathrm{m}} \\
R_{\mathrm{X_a}} &= R_{\mathrm{a}} - k_{\mathrm{a}}^{\mathrm{d}} \rho_{\mathrm{X_a}} \\
R_{\mathrm{X_m}} &= R_{\mathrm{m}} - k_{\mathrm{m}}^{\mathrm{d}} \rho_{\mathrm{X_m}}
\end{aligned}$$

Table 1: Nominal operational data for biogas reactor at Foss Biolab.

Quantity	Value	Unit	Comment
$\rho_{S_{bvs}}(0)$	5.81	g/L	Initially dissolved substrate biodegradable volatile solids
$\rho_{S_{vfa}}(0)$	1.13	g/L	Initially dissolved substrate volatile fatty acids
$\rho_{X_a}(0)$	1.32	g/L	Initial concentration of acetogenic bacteria
$\rho_{X_m}(0)$	0.39	g/L	Initial concentration of methanogenic bacteria
$\dot{V}_f$	50	L/ d	Volumetric feed flow of animal waste/manure
T	35	°C	Reactor temperature
$\rho_{S_{vs,f}}$	32.4	g/L	Feed concentration of volatile solids

Table 2: Nominal model parameters for biogas reactor at Foss Biolab.

Parameter	Value	Unit	Comment
V	250	L	Reactor volume
$\theta_{X_a} = \theta_{X_m}$	2.9	–	Correction of residence time for bacteria due to nonideal flow
Y_{S_{bvs}/X_a}	3.90	$\frac{\text{gbvs}}{\text{gX}_a}$	(Inverse) yield: consumption of bvs per growth of bacteria
Y_{S_{vfa}/X_a}	1.76	$\frac{\text{gvfa}}{\text{gX}_a}$	(Inverse) yield: production of vfa per growth of bacteria
Y_{S_{vfa}/X_m}	31.7	$\frac{\text{gvfa}}{\text{gX}_m}$	(Inverse) yield: consumption of vfa per growth of bacteria
Y_{CH_4/X_m}	26.3	$\frac{\text{gCH}_4}{\text{gX}_m}$	(Inverse) yield: production of methane per growth of bacteria
$K_{S_{bvs}}$	15.5	g/L	Half-velocity constant for bvs substrate
$K_{S_{vfa}}$	3.0	g/L	Half-velocity constant for vfa substrate
$\hat{\mu}_{35}$	0.326	d^{-1}	Maximal growth rate at $T = 35\,°\text{C}$,
$\alpha_{\hat{\mu}}$	0.013	$\frac{1}{°\text{C d}}$	Temperature sensitivity of maximal growth rate, valid $T \in [20, 60]$ °C
$k_a^d = k_m^d$	0.02	d^{-1}	Death rate constants for acetogenic and methanogenic bacteria
b_0	0.25	$\frac{\text{gbvs}}{\text{gvs}}$	Fraction biodegradable volatile solids in volatile solids feed
a_f	0.69	$\frac{\text{gvfa}}{\text{gbvs}}$	Fraction volatile fatty acids in biodegradable volatile solids feed

with

$$\begin{aligned} R_a &= \mu_a \rho_{X_a} \\ R_m &= \mu_m \rho_{X_m} \end{aligned}$$

and

$$\begin{aligned} \mu_a &= \frac{\hat{\mu}_a}{1 + K_{S_{bvs}} \frac{1}{\rho_{S_{bvs}}}} \\ \mu_m &= \frac{\hat{\mu}_m}{1 + K_{S_{vfa}} \frac{1}{\rho_{S_{vfa}}}} \\ \hat{\mu}_a &= \hat{\mu}_m = \hat{\mu}_{35} + \alpha_{\hat{\mu}} (T - 35), \text{ with units } °\text{C for } T \end{aligned}$$

The production (exit) rate of methane is given by

$$\begin{aligned} \dot{m}_{CH_4,x} &= R_{CH_4} V \\ R_{CH_4} &= Y_{CH_4/X_m} R_m. \end{aligned}$$

Feed concentrations of states are given as

$$\begin{aligned} \rho_{S_{bvs},f} &= b_0 \rho_{S_{vs},f} \\ \rho_{S_{vfa},f} &= a_f \rho_{S_{bvs},f}. \end{aligned}$$

Nominal operating conditions for the system are given in Table 1.
Model parameters are given in Table 2.

2.3 Systems and Control problems

A number of control problems are relevant for this system:

- simulation of the system for validation,
- study of model sensitivity wrt. uncertain parameters,
- tuning model parameters to fit the model to experimental data,
- state estimation for computing hidden model states,
- operation of control system,
- optimal control and model predictive control,
- etc.

Only a selected few of these problems are considered in the sequel.

3 Control relevant analysis

3.1 Basic Modelica description

The following Modelica encoding in file `adFoss.mo` describes the basic model:

```
model adFossModel
// Simulation of Anaerobic Digestion Reactor at Foss Biolab
  // Author:   Bernt Lie
  //           Telemark University College, Porsgrunn, Norway
  //           August 31, 2012
  //
  // Parameter values with type and descriptive text
  parameter Real V = 250 "reactor volume, L";
  parameter Real theta_X = 2.9 "residence time correction for bacteria,
                  dimensionless";
  parameter Real Y_Sbvs_Xa = 3.9 "Yield, g bvs/g acetogens";
  parameter Real Y_Svfa_Xa = 1.76 "Yield, g vfa/g acetogens";
  parameter Real Y_Svfa_Xm = 31.7 "Yield, g vfa/g methanogens";
  parameter Real Y_CH4_Xm = 26.3 "Yield, g methane/g methanogens";
  parameter Real K_Sbvs = 15.5 "Half-velocity constant for bvs, g/L";
  parameter Real K_Svfa = 3.0 "Half-velocity constant for vfa, g/L";
  parameter Real muhat_35 = 0.326 "Maximal growth rate at T=35 C, 1/d";
  parameter Real alpha_muhat = 0.013 "Temperature sensitivity of
                  max growth rate, 1/(C d)";
  parameter Real k_d = 0.02 "Death rate constants for bacteria, 1/d";
  parameter Real b0 = 0.25 "Fraction biodegradable volatile solids in
                  volatile solids feed, g bvs/g vs";
  parameter Real af = 0.69 "Fraction volatile fatty acids in bvs feed,
                  g vfa/g bvs";
  // Initial state parameters:
  parameter Real rhoSbvs0 = 5.81 "initial bvs substrate, g/L";
  parameter Real rhoSvfa0 = 1.13 "initial vfa, g/L";
  parameter Real rhoXa0 = 1.32 "initial acetogens, g/L";
  parameter Real rhoXm0 = 0.39 "initial methanogens, g/L";
  // Setting initial values for states:
  Real rhoSbvs(start = rhoSbvs0, fixed = true);
  Real rhoSvfa(start = rhoSvfa0, fixed = true);
  Real rhoXa(start = rhoXa0, fixed = true);
  Real rhoXm(start = rhoXm0, fixed = true);
  // Miscellaneous variables
  Real rhoSbvs_f "feed concentration of bvs, g/L";
  Real rhoSvfa_f "feed concentration of vfa, g/L";
  Real rhoXa_f "feed concentration of acetogens, g/L";
```

```
  Real rhoXm_f "feed concentration of methanogens, g/L";
  Real R_Sbvs "generation rate of Sbvs, g/(L*d)";
  Real R_Svfa "generation rate of Svfa, g/(L*d)";
  Real R_Xa "generation rate of Xa, g/(L*d)";
  Real R_Xm "generation rate of Xm, g/(L*d)";
  Real R_CH4 "generation rate of CH4, g/(L*d)";
  Real R_a "reaction rate acetogenesis, g/(L*d)";
  Real R_m "reaction rate methanogenesis, g/(L*d)";
  Real mu_a "growth rate acetogenesis, 1/d";
  Real mu_m "growth rate methanogenesis, 1/d";
  Real muhat_a "maximal growth rate acetogenesis, 1/d";
  Real muhat_m "maximal growth rate methanogenesis, 1/d";
  Real mdot_CH4x "mass flow methane production, g/d";
  // Defining input variables:
  input Real Vdot_f "volumetric feed flow -- control variable, L/d";
  input Real T "reactor temperature -- possible control input, C";
  input Real rhoSvs_f "feed volatile solids concentration -- disturbance, g/L";
equation
  // Differential equations
  der(rhoSbvs) = Vdot_f/V*(rhoSbvs_f - rhoSbvs) + R_Sbvs;
  der(rhoSvfa) = Vdot_f/V*(rhoSvfa_f - rhoSvfa) + R_Svfa;
  der(rhoXa) = Vdot_f/V/theta_X*(rhoXa_f - rhoXa) + R_Xa;
  der(rhoXm) = Vdot_f/V/theta_X*(rhoXm_f - rhoXm) + R_Xm;
  // Feed
  rhoSbvs_f = rhoSvs_f*b0;
  rhoSvfa_f = rhoSbvs_f*af;
  rhoXa_f = 0;
  rhoXm_f = 0;
  // Generation rates
  R_Sbvs = -Y_Sbvs_Xa*R_a;
  R_Svfa = Y_Svfa_Xa*R_a - Y_Svfa_Xm*R_m;
  R_Xa = R_a - k_d*rhoXa;
  R_Xm = R_m - k_d*rhoXm;
  R_a = mu_a*rhoXa;
  R_m = mu_m*rhoXm;
  mu_a = muhat_a/(1 + K_Sbvs/rhoSbvs);
  mu_m = muhat_m/(1 + K_Svfa/rhoSvfa);
  muhat_a = muhat_35 + alpha_muhat*(T-35);
  muhat_m = muhat_a;
  // Methane production
  mdot_CH4x = R_CH4*V;
  R_CH4 = Y_CH4_Xm*R_m;
 end adFossModel;
```

3.2 Basic Python script

The following Python script `adFossSim.py` provides basic simulation of the Anaerobic Digester reactor at Foss Biolab starting at the nominal operating point, and performing some step perturbations for the inputs:

```
#
# Python script for simulating Anaerobic Digester at Foss Biolab
#
# script:    adFossSim.py
# author:    Bernt Lie, Telemark University College, Porsgrunn, Norway
# location:  Telemark University College, Porsgrunn
# date:      August 31, 2012
```

```
# Importing modules

# matplotlib, numpy
import matplotlib.pyplot as plt
import numpy as np

# JModelica
from pymodelica import compile_fmu
from pyfmi import FMUModel

# Flattening, compiling and exporting model as fmu
adFoss_fmu = compile_fmu("adFossModel", "adFoss.mo")

# Importing fmu and linking it with solvers, etc.
adFoss = FMUModel(adFoss_fmu)

# Creating input data
t_fin = 100
adFoss_opdata = np.array([[0,50,35,32.4],[10,50,35,32.4],[10,45,35,32.4],
                          [30,45,35,32.4],[30,45,38,32.4],[60,45,38,32.4],
                          [60,45,38,40],[t_fin,45,38,40]])
adFoss_input = (["Vdot_f", "T", "rhoSvs_f"], adFoss_opdata)

# Carrying out simulation
adFoss_res = adFoss.simulate(final_time = t_fin, input = adFoss_input)

# Unpacking results
rhoSbvs = adFoss_res["rhoSbvs"]
rhoSvfa = adFoss_res["rhoSvfa"]
rhoXa = adFoss_res["rhoXa"]
rhoXm = adFoss_res["rhoXm"]
mdot_CH4x = adFoss_res["mdot_CH4x"]
Vdot_f = adFoss_res["Vdot_f"]
T = adFoss_res["T"]
rhoSvs_f = adFoss_res["rhoSvs_f"]
t = adFoss_res["time"]

# Setting up figure with plot of results
plt.figure(1)
plt.plot(t,rhoSbvs,"-r",t,rhoSvfa,"-g",t,rhoXa,"-k",t,rhoXm,"-b",linewidth=2)
plt.legend((r"$\rho_{S_{bvs}}$ [g/L]",r"$\rho_{S_{vfa}}$ [g/L]",
            r"$\rho_{X_a}$ [g/L]",r"$\rho_{X_m}$ [g/L]"),ncol=2,loc=0)
plt.title("Anaerobic Digestion at Foss Biolab")
plt.xlabel(r"time $t$ [d]")
plt.grid(True)

plt.figure(2)
plt.plot(t,mdot_CH4x,"-r",linewidth=2)
plt.title("Anaerobic Digestion at Foss Biolab")
plt.ylabel(r"$\dot{m}_{CH_4}$ [g/d]")
plt.xlabel(r"time $t$ [d]")
plt.grid(True)

plt.figure(3)
plt.plot(t,Vdot_f,"-r",t,T,"-g",t,rhoSvs_f,"-b",linewidth=2)
plt.axis(ymin=30,ymax=55)
plt.title("Anaerobic Digestion at Foss Biolab")
```

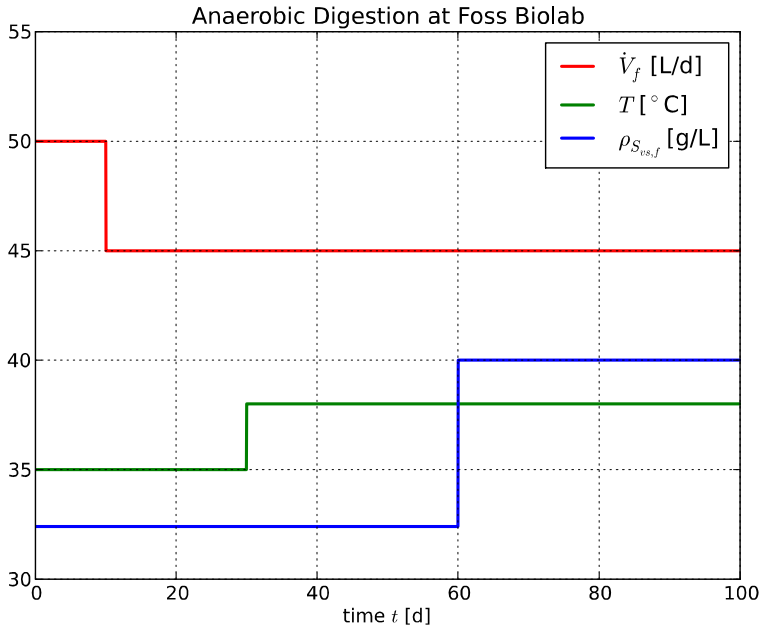

Figure 2: Nominal evolution of inputs at Foss Biolab, with perturbation.

```
plt.legend((r"$\dot{V}_f$ [L/d]",r"$T$ [${}^{\circ}$C]",
            r"$\rho_{S_{vs,f}}$ [g/L]"),loc=0)
plt.xlabel(r"time $t$ [d]")
plt.grid(True)

plt.show()
```

Running this Python script leads to the results in figs. 2 – 4:

3.3 Uncertainty analysis

Suppose the value of parameters b_0 and a_f are uncertain, but that we "know" they lie in intervals $b_0 \in 0.25 \times [0.9, 1.1]$ and $a_f \in 0.69 \times [0.9, 1.1]$. We can study the uncertainty of the model by running a number N_{MC} of Monte Carlo simulations were we draw values at random from these two ranges — e.g. assuming uniform distribution. The following modifications of the Python code will handle this problem, excerpt of script `adFossSimMC.py`:

```
#
# Python script for Monte Carlo study of Anaerobic Digester at Foss Biolab
#
# script:    adFossSimMC.py
# author:    Bernt Lie, Telemark University College, Porsgrunn, Norway
# location:  Telemark University College, Porsgrunn
# date:      August 31, 2012

# Importing modules

# matplotlib, numpy, random
import matplotlib.pyplot as plt
import numpy as np
import numpy.random as nr
```

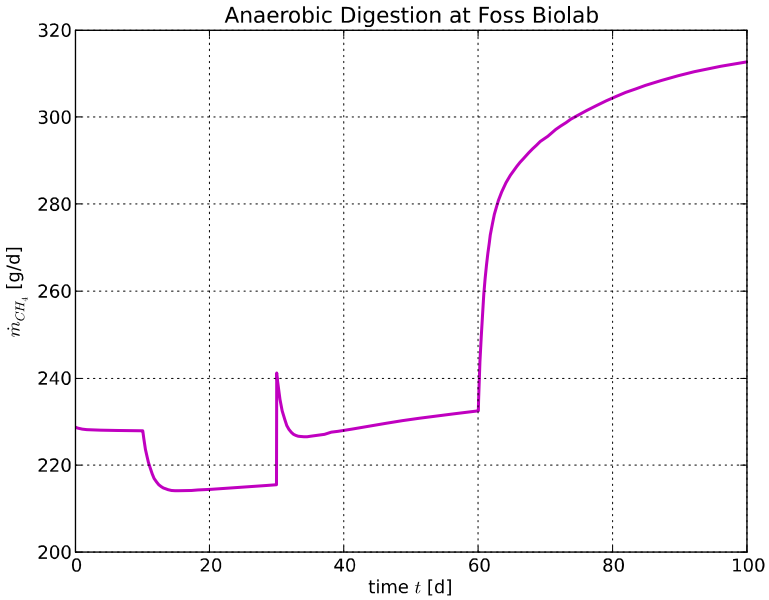

Figure 3: Nominal production of methane gas at Foss Biolab, with perturbation.

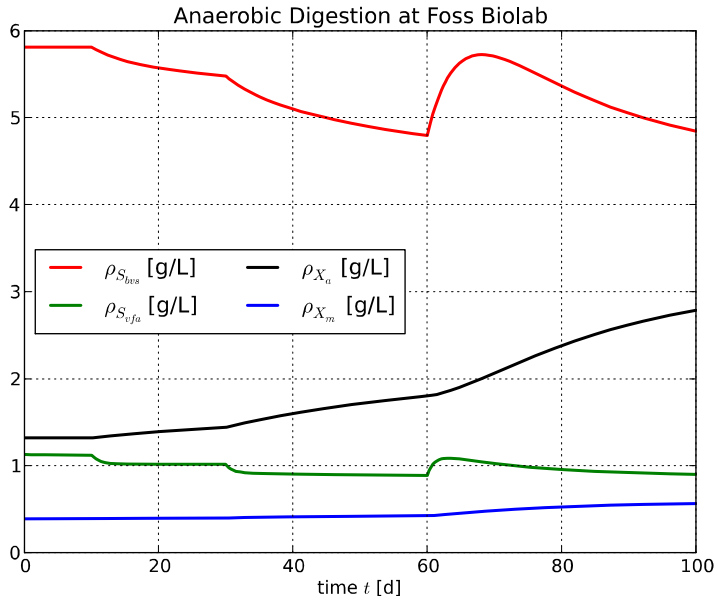

Figure 4: Nominal evolution of states at Foss Biolab, with perturbation.

```
...

# Carrying out simulation
adFoss_res = adFoss.simulate(final_time = t_fin, input = adFoss_input)

...

# Setting up figure with plot of results
plt.figure(1)
plt.plot(t,rhoSbvs,"-r",t,rhoSvfa,"-g",t,rhoXa,"-k",t,rhoXm,"-b",linewidth=2)
plt.legend((r"$\rho_{S_{bvs}}$ [g/L]",r"$\rho_{S_{vfa}}$ [g/L]",
            r"$\rho_{X_a}$ [g/L]",r"$\rho_{X_m}$ [g/L]"),ncol=2,loc=0)
plt.title("Anaerobic Digestion at Foss Biolab")
plt.xlabel(r"time $t$ [d]")
plt.grid(True)

...

# Monte Carlo simulations
Nmc = 20
b0nom = adFoss.get("b0")
afnom = adFoss.get("af")

for i in range(Nmc):
    b0 = b0nom*(1 + 0.1*(nr.rand()-0.5)*2)
    af = afnom*(1 + 0.1*(nr.rand()-0.5)*2)
    adFoss.set(["b0","af"],[b0,af])
    # Carrying out simulation
    adFoss_res = adFoss.simulate(final_time = t_fin, input = adFoss_input)

    # Unpacking results
    rhoSbvs = adFoss_res["rhoSbvs"]
    rhoSvfa = adFoss_res["rhoSvfa"]
    rhoXa = adFoss_res["rhoXa"]
    rhoXm = adFoss_res["rhoXm"]
    mdot_CH4x = adFoss_res["mdot_CH4x"]
    t = adFoss_res["time"]

    # Setting up figure with plot of results
    plt.figure(1)
    plt.plot(t,rhoSbvs,":r",t,rhoSvfa,":g",t,rhoXa,":k",t,rhoXm,":b",
             linewidth=1.5)

    plt.figure(2)
    plt.plot(t,mdot_CH4x,":m",linewidth=1.5)

plt.show()
```

The result are as shown in figs. 5 and 6.

3.4 Wash-out and recovery of reactor

Suppose that the reactor gets "washed out" by accidentally applying too high a feed rate $\dot{V}_{\mathrm{f}}$, e.g. $\dot{V}_{\mathrm{f}} = 120\mathrm{L}/\,\mathrm{d}$, while T and $\rho_{\mathrm{S_{vs,f}}}$ are as in Table 1. It is of interest to see whether the original production can be recovered. Figures 7 – 9 indicates the behavior over a period of more than 4 years (1500 d) of operation.

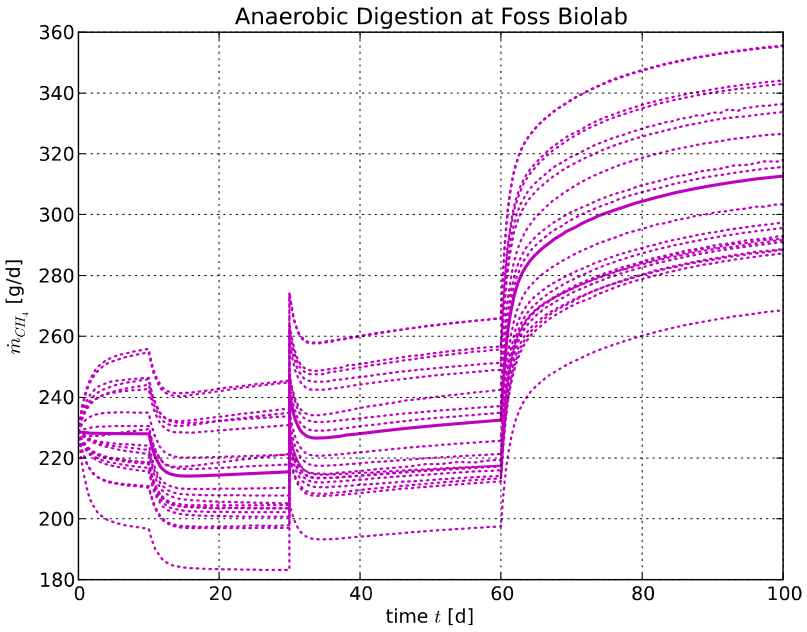

Figure 5: Monte Carlo study of methane production at Foss Biolab, with variation in b_0 and a_f.

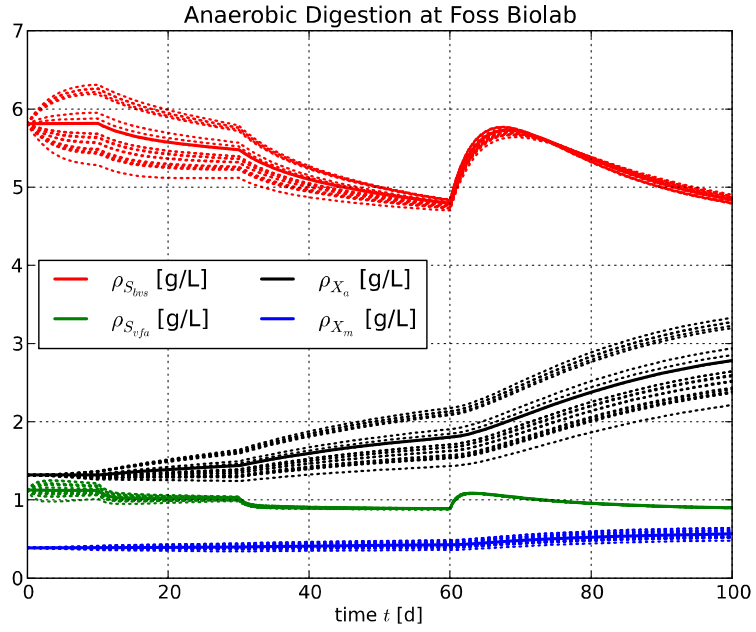

Figure 6: Monte Carlo study of evolution of states at Foss Biolab, with variation in b_0 and a_f.

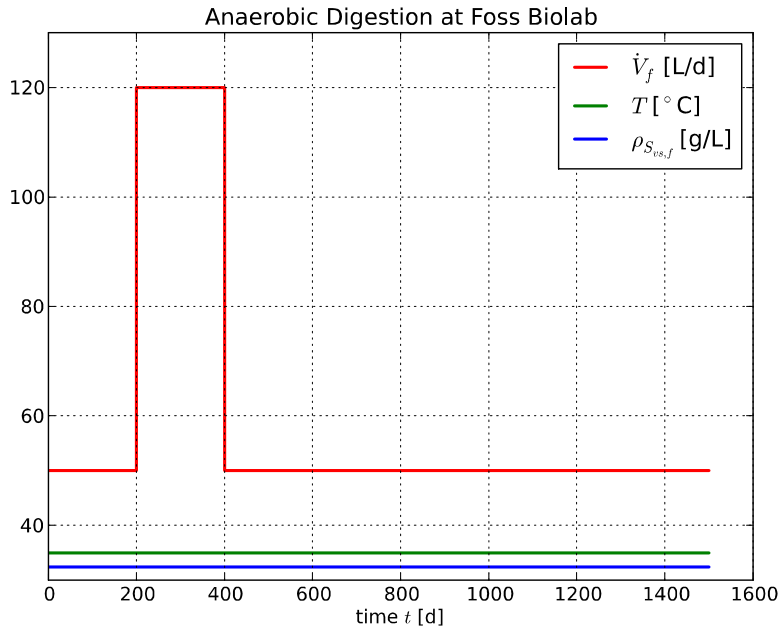

Figure 7: Evolution of inputs at Foss Biolab leading to wash-out/recovery.

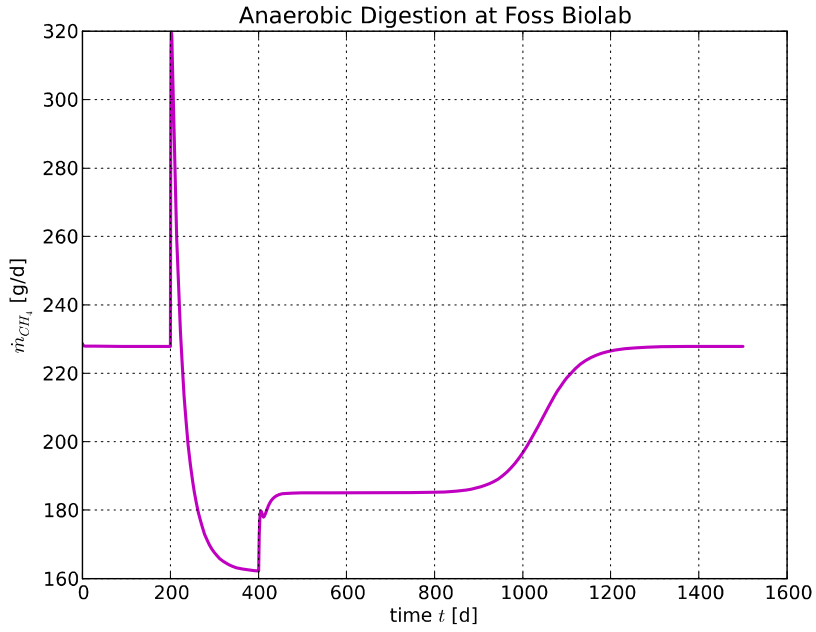

Figure 8: Production of methane gas at Foss Biolab during wash-out/recovery.

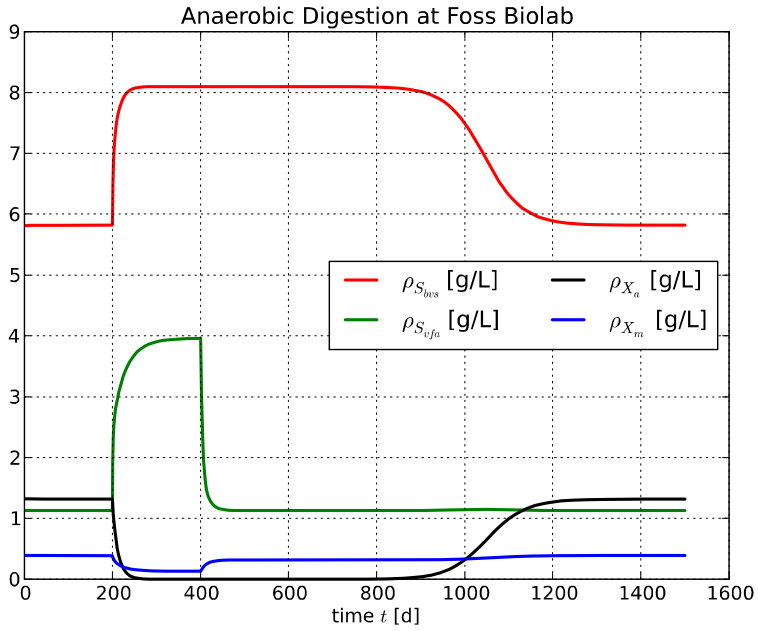

Figure 9: Evolution of states at Foss Biolab during wash-out/recovery.

As seen, although increasing $\dot{V}_{\mathrm{f}}$ initially leads to a significant increase in the methane production, the bacteria are washed out of the reactor leading to a dramatic fall in the methane production. Furthermore, it takes an inordinate long time to recover after a wash-out if the input is simply set back to the original flow rate. The steady state values at wash-out ($t = 400\,\mathrm{d}$) can be found to be

$$\begin{aligned}
\rho_{\mathrm{S_{bvs},wash-out}} &= 8.0999999985826001 \\
\rho_{\mathrm{S_{vfa},wash-out}} &= 3.96169944436781 \\
\rho_{\mathrm{X_a,wash-out}} &= 1.3193454767561001 \times 10^{-9} \\
\rho_{\mathrm{X_m,wash-out}} &= 0.13282069444970099
\end{aligned}$$

3.5 Optimal recovery of methane production

The accidental wash-out of bacteria is a serious problem in the operation of Anaerobic Digesters. It is thus of interest to see whether it is possible to recover the operation in an optimal way. We consider the possibility of recovering the operation in the 1100 d horizon spent to wash-out the bacteria, fig. 7 – 9. We thus seek to maximize the production of methane, but without using too much feed of animal waste. The following criterion is thus sought *maximized*:

$$J = \int_0^{T_{\mathrm{h}}} \left(\dot{m}_{\mathrm{CH_4,x}} - c_{\dot{\mathrm{V}}} \dot{V}_{\mathrm{f}} \right) dt$$

where $c_{\dot{\mathrm{V}}}$ is a cost parameter. We add the following constraints to make sure that the solution has physical meaning.

$$\begin{aligned}
\rho_{\mathrm{j}} &\geq 0 \\
\dot{m}_{\mathrm{CH_{4,x}}} &\geq 0 \\
\dot{V}_{\mathrm{f}} &\in [0, 120]\,\mathrm{L/\,d}.
\end{aligned}$$

We assume that the temperature T and the disturbance $\rho_{\mathrm{S_{vs,f}}}$ are as in Table 1.

To solve this problem, we use the Modelica extension class *optimization* in JModelica.org. In Modelica, the criterion function is *minimized*, so the criterion in Modelica needs to be $-J$ where J is as above. The essence of the Modelica code for this problem is as given below:

```
optimization adFossOpt(objective = J(finalTime), startTime=0, finalTime=T_h)
// Optimal recovery of Anaerobic Digestion Reactor at Foss Biolab
  // Author:   Bernt Lie
  //           Telemark University College, Porsgrunn, Norway
  //           September 2, 2012
  //
  // Instantiating model adf from class adFossModel
  adFossModel adf;
  // Additional parameters
  parameter Real T_h = 1100 "time horizon in optimization criterion, d";
  parameter Real cost_V = 1 "relative cost of animal waste";
  parameter Real Vdot_max = 120 "maximal allowed feed rate, L/d";
  parameter Real T_nom = 35 "nominal reactor temperature, C";
  parameter Real rhoSvs_f_nom = 32.4 "nominal feed concentration
                  of volatile solids, g/L";
  // Defining cost function
  Real J(start=0, fixed=true);
  // Defining input variable:
  input Real Vdot_f(free=true, min=0,max=Vdot_max) "max feed flow, L/d";
equation
  // Passing on inputs to model instance
  adf.Vdot_f = Vdot_f;
  adf.T = T_nom;
  adf.rhoSvs_f = rhoSvs_f_nom;
  // Computing cost function
  der(J) = - adf.mdot_CH4x + cost_V*Vdot_f;
constraint
  // Constraining states
  adf.rhoSbvs >= 0;
  adf.rhoSvfa >= 0;
  adf.rhoXa >= 0;
  adf.rhoXm >= 0;
  // Constraining methane production
  adf.mdot_CH4x >=0;
end adFossOpt;
```

With $c_{\dot{V}}$, the result is as in figs. 10 – 12. With $c_{\dot{V}}$, the result is highly oscillatoric time evolutions.

4 Discussion and Conclusions

Comparing Python to MATLAB for use in control studies reveals clear advantages and clear disadvantages for Python. Python is a free tool, and a rich programming language. However, there is (currently) no control toolbox for Python, the various packages and sub packages are not so well documented, and the quality of some tools are far from perfect. Yet, the combination of Python and Modelica/PyFMI offers ample opportunities for analysis of models and control studies. This paper illustrates this by showing how natural models can be encoded in Modelica, and how easy Modelica models can be accessed from Python using e.g. PyFMI. Furthermore, it is shown how natural and powerful Python is as a scripting language, e.g. for doing uncertainty/sensitivity analysis of dynamic models. Finally, a simple optimal control problem illustrates on-going research and development in extending the Modelica language using JModelica.org; similar extensions of the Modelica language are also studied in e.g. Bachmann et al. (2012). And yet, in this paper, only the most rudimentary use of Modelica and Python has been touched upon.

Currently, some key problems with the Python+Modelica combination are:

- There is no equivalent of MATLAB's Control Toolbox. This is such a shortcoming that many control engineers will not seriously consider the Python + Modelica combination. Some work at

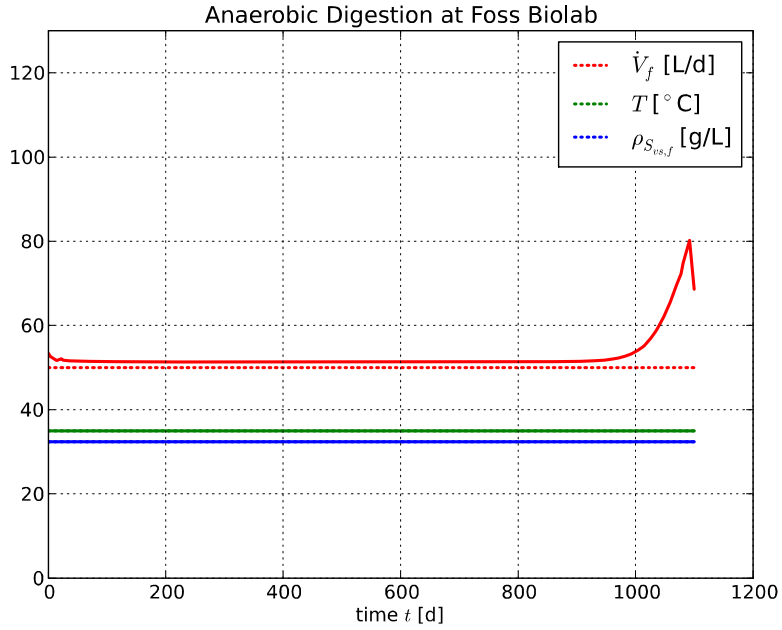

Figure 10: Evolution of optimal input $\dot{V}_f$ at Foss Biolab after wash-out (solid lines), with initial guess (dotted lines).

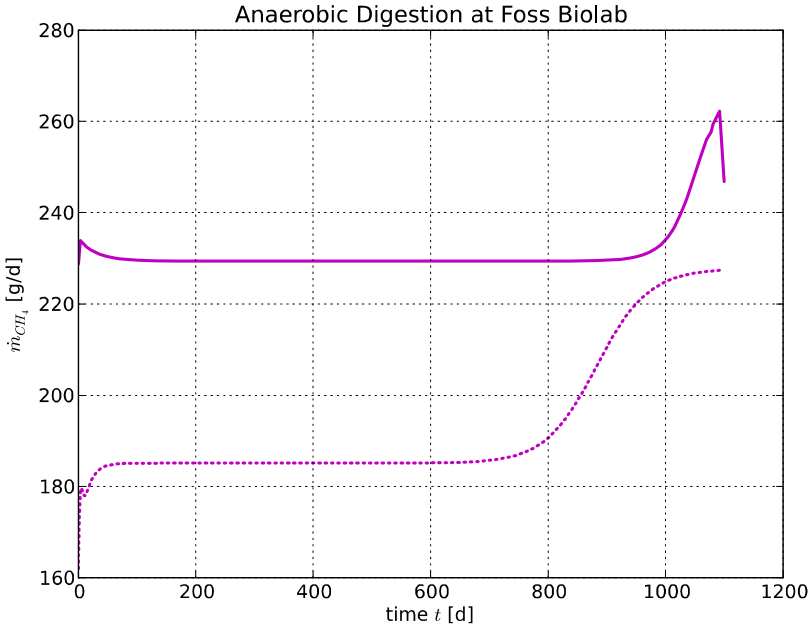

Figure 11: Evolution of optimally recovered methane production at Foss Biolab after wash-out (solid lines), with initial guess (dotted lines).

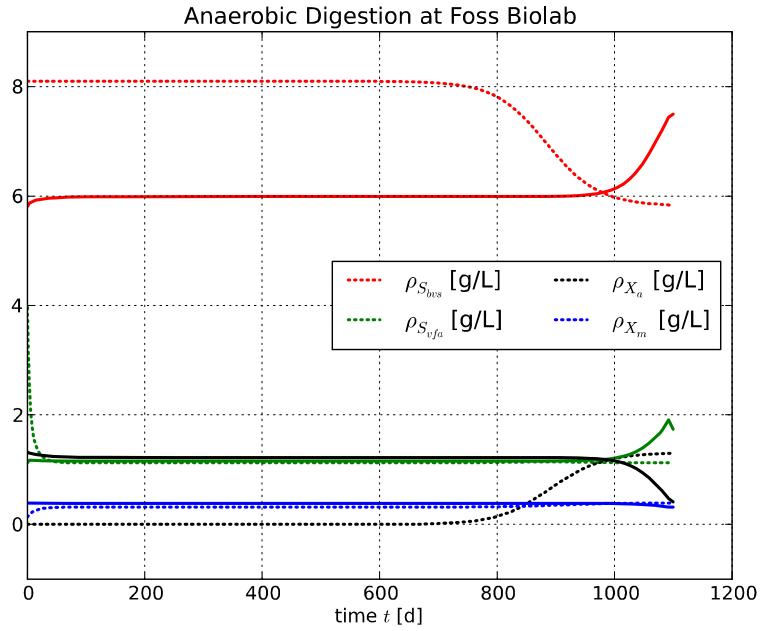

Figure 12: Evolution of optimally recovered states at Foss Biolab after wash-out (solid lines), with initial guess (dotted lines).

CalTech[11] aims to resolve this problem by developing a Python control toolbox, but there does not appear to be a clear timeline for such a toolbox. Within the Modelica groups, some on-going work addresses this by developing a [12] Linear Systems library within Modelica.

- Although there are a number of powerful (and free) optimization solvers, it is not trivial to integrate these into Python, and those which already have simple Python installers are often poorly documented and/or uses non-standard array packages. A minimal package should include LP, QP, NLP, and NLS solvers of high quality, and they should be equally simple to install in the main OS platforms.
- The FMI is a very positive initiative, and well suited to scripting using either Python or MATLAB. More work is needed in order to make FMI export from the various tools more standardized.
- The initiative of extending Modelica with optimization (and model calibration) possibilities is very interesting for the control society. It would be even more interesting if some standards evolve.

The evolution of alternatives to MATLAB + SIMULINK is very interesting, and Python + Modelica holds promise to be such a tool. There are advantages with commercial tools such as MATLAB + SIMULINK and similar tools for Modelica such as MapleSim and Wolfram SystemModeler, but in academia with limited resources for buying software, free software is of interest.

References

[1] Bachmann, B., Ochel, L., Ruge, V., Gebremedhin, M., Fritzson, P., Nezhadali, V., Eriksson, L., Sivertsson, M. (2012). "Parallel Multiple-Shooting and Collocation Optimization with OpenModelica". In *Proceedings of the 9th International Modelica Conference* (Modelica'2012), Munich, Germany, Sept.3-5, 2012.

[2] Fritzson, P. (2011). *Introduction to Modeling and Simulation of Technical and Physical Systems with Modelica®*. IEEE Press and Wiley, Hoboken, New Jersey.

[11] `http://sourceforge.net/apps/mediawiki/python-control/index.php?title=Main_Page`
[12] `https://modelica.org/libraries/Modelica_LinearSystems2`

[3] Haugen, F., Bakke, R., and Lie, B. "Mathematical Modelling for Planning Optimal Operation of a Biogas Reactor for Dairy Manure". *Presented at the IWA World Congress on Water, Climate and Energy (IWA-WCE)*, Dublin, 14 – 18. May 2012.

Modelling and analysis of offshore energy systems on North Sea oil and gas platforms

Tuong-Van Nguyen[a,*], Brian Elmegaard[a], Leonardo Pierobon[a], Fredrik Haglind[a], Peter Breuhaus[b]

[a] *Section of Thermal Energy, Department of Mechanical Engineering, Technical University of Denmark, Building 403, Nils Koppels Allé, 2800 Kongens Lyngby, Denmark*
[b] *Department of Energy, International Research Institute of Stavanger, Professor Olav Hanssens vei 15, 4021 Stavanger, Norway*

Abstract

Offshore processes are associated with significant energy consumption and large CO_2 emissions. Conventional North Sea oil and gas facilities include the following operations: crude oil separation, gas compression and purification, wastewater treatment, gas lifting, seawater injection, oil and gas export, and power generation. In this paper, a generic model of a North Sea oil and gas platform is described and the most thermodynamically inefficient processes are identified by performing an exergy analysis. Models and simulations are built and run with the tools Aspen Plus®, DNA and Aspen HYSYS®. Results reveal that the total exergy destruction of the system is particularly sensitive to the gas-to-oil ratio and amounts to 55-65 MW, while the total exergy losses amount to 15-20 MW. The gas compression train and the production manifold module are the most exergy-destructive operations of the oil and gas processing system, consuming 4-6 MW and 3-7 MW respectively, while the power generation system alone is responsible for 54-63 MW.

Keywords: Modelling, Energy Systems, Exergy Analysis, Oil and Gas platforms

1. Introduction

North Sea oil and gas platforms were responsible for about 26% of the total gross CO_2 emissions of Norway in 2011 [1]. It is generally assumed that the energy intensity and environmental impact of these offshore facilities will increase in the coming years, as a direct consequence of larger energy use to enhance hydrocarbon production [2, 3].

Concerns exist about the possible ways of evaluating and increasing the performance of these operations and thus reducing their environmental footprint. Exergy analysis is a method based on the 2^{nd} law of thermodynamics which has been widely used to characterise the efficiency of various industrial processes. Exergy is defined as the maximum theoretical useful work that can be extracted from any given system, in reference to a specific environment. Unlike energy, exergy can be destroyed; this enables locating and quantifying sources of thermodynamic irreversibilities. Exergy can also be interpreted as a quantification of primary energy and exergy destruction account thus for use of fuel throughout a process [4, 5].

Only a few studies have been conducted on the modelling and thermodynamic performance assessment of offshore platforms. Oliveira and Van Hombeeck [6] simulated a Brazilian petroleum plant with HYSIM and focused exclusively on the separation, compression and pumping modules. Their study showed that the most exergy-consuming steps were the petroleum heating operation taking place within the separation module, and the gas compression process. The separation step had the worst exergetic efficiency (22.2%) of the overall plant, which had by itself an exergetic efficiency of 9.7%. The authors suggested that the large exergy destruction taking place in the heating step was due to the high difference between the temperatures of the exhaust gases and of the petroleum, and that newer separation technologies could improve the thermodynamic performance of the platform.

Voldsund et al. [7, 8] simulated a specific North Sea offshore platform by using Aspen HYSYS®. The

*Principal corresponding author. Tel.: +4545254129
Email address: tungu@mek.dtu.dk (Tuong-Van Nguyen)

Nomenclature

Acronyms

DNA	Dynamic Network Analysis
NHV	Net Heating Value, kJ/kg
$NRTL$	Non-Random Two Liquid

Greek Letters

β	chemical exergy correction factor
η	efficiency

Latin Letters

$\bar{e}$	specific exergy (molar), J/mol
$\bar{R}$	ideal gas constant, J/(mol.K)
E	exergy, J
e	specific exergy (mass), J/kg
h	specific enthalpy (mass), J/kg
s	specific entropy (mass), J/(kg.K)
x	partial pressure
z	pollutant mass fraction

Subscripts and superscripts

*	relative
$_f$	fuel
$_p$	product
$_0$	dead state
$_{ch}$	chemical
$_d$	destruction
$_{kn}$	kinetic
$_k$	component
$_l$	loss
$_{ph}$	physical
$_{pt}$	potential

platform investigated in their study included separation, recompression and reinjection trains as well as fuel gas and export pumping systems. Results showed that the largest exergy destruction occurred in the gas re-injection trains (44.4%) and in the recompression process (17%). The authors reported an overall exergetic efficiency of 32% in the baseline case and suggested that the thermodynamic losses of the platform could be greatly reduced by avoiding anti-surge recycling and using more efficient compressors [8]. However, these previous studies considered specific inflow conditions and focused on the oil processing plant exclusively. The impacts of variations in production flows have not been thoroughly estimated and the utility systems for heat and power generation have not been assessed.

The present paper aims, on the one hand, to introduce models describing the full- and part-load behaviour of typical offshore platforms, which include the processing plant and the utility sub-systems. On the other hand, it attemps to assess the thermodynamic performance of the complete system and to quantify the effects of variations in the well-fluid composition. A generic process model of a North Sea oil platform is thus presented and analysed with respect to the 2^{nd} law of thermodynamics. In contrast to the previous works undertaken within this field, the production manifolds, the glycol dehydration and wastewater treatment processes, as well as the power generation systems with their part-load characteristics, are considered and analysed.

2. System description

Petroleum by itself is relatively dry and has a low content of light hydrocarbons, but is extracted along with gas and water. Offshore separation of these three phases is required to maximise the oil production and to minimise its gas and water content, for economical and process requirement issues. Crude oil is shipped onshore, while gas and water are either valorised or rejected into the environment. Factors such as the well-fluid thermo-physical properties, chemical composition, gas-to-oil (GOR) and water-to-oil (WOR) ratios, reservoir properties (e.g temperature, pressure, permeability) may strongly differ from one field to another, which implies that different technical considerations (e.g pressure and temperature levels) and technological choices (e.g number of trains, gas export, system configuration) apply for different cases. In addition, production flows vary significantly with time, affecting the plant performance [2].

However, although design differences exist amongst various North Sea oil platforms, it is worth noticing that gas purification and exportation, waste water treatment and seawater injection, have become the most preferred gas and water processing routes in this region [3]. Since the North Sea crude oil and natural gas are characterised by a low content of salt, hydrogen sulphide and carbon dioxide, neither desalting nor sweetening units are necessary. Typical offshore processing on North Sea oil platforms consists of 8 different sub-systems, namely:

- Production manifolds
- Crude oil separation
- Oil pumping and export
- Gas re-compression and purification
- Gas compression – lifting and exportation –
- Wastewater treatment
- Seawater injection
- Power generation

Hence, the generic platform model developed within this study includes the aforementioned processes and is based on the system configurations presented in the open literature for the crude oil processing [3, 9–12], for the gas treatment process [11–13], and for the water processing [14, 15]. A conceptual layout of the platform model, illustrating schematically material flows and interactions between the various parts of the plant, is shown in Figure 1. Internal system configurations, such as condensate recycling and anti-surge control, are not shown but are considered in the system modelling.

3. System modelling and simulation

3.1. System inputs

Crude oil contains a large inventory of multiple chemical compounds such as alkanes, alcenes and aromatics, ranging from light to heavy, branched to cyclic and saturated to unsaturated hydrocarbons. Complete compositional analyses are rarely carried out, which implies that the exact chemical composition of crude oil – nature of chemical compounds and amounts – is usually unknown. In general, crude oil is characterised by conducting a true boiling point (TBP) analysis: crude oil is separated into distillate fractions with different hydrocarbons composition and boiling points. The distribution of the boiling point range as a function of the fraction of crude oil distilled is called the true boiling point curve and gives an approximation of the crude oil properties and composition. Molecular weight, viscosity, specific density and gravity are measured for each distillate fraction, and thermal properties such as heating value and thermal conductivity are estimated by empirical correlations [9, 16].

Hence, it is not possible to define crude oil as an exact mixture of known components with known proportions. Crude oil is therefore represented by a group of known and hypothetical (also denominated pseudo-) components whose properties are created from the true boiling curve [9, 16]. In this study, crude oil is modelled as a mixture of 83 chemical compounds: CO_2, H_2O, O_2, N_2, Ar, H_2S, 47 hydrocarbons and 29 pseudo-components. Bulk properties of the crude oil mixture are given in Table 1.

Table 1: Crude oil properties

	Crude Oil
API	39.9
Specific gravity	0.826
Density (kg.m^{-3})	825.5
Light ends cut ($\%_{vol}$)	27.2

Gas may either be mixed with oil and enter the platform system through the same wells (associated gas) or be processed apart through specific wells (non-associated gas). In this paper, only associated gas was considered since it is the most encountered case in oil offshore processing, according to Bothamley et al. [3]. As seen in Table 2, North Sea natural gas has a low content of hydrogen sulphide and carbon dioxide, which justifies its appellation of sweet gas.

Table 2: Associated natural gas composition

Chemical Compound ($\%_{mol}$)	Natural Gas
N_2	4.37
CO_2	1.34
H_2S	0.2
CH_4	73.7
C_2H_6	6.10
C_3H_8	6.70
n-C_4H_{10}	2.48
i-C_4H_{10}	1.41
C_5+	3.70

Standard air, with a molar composition of 77.29% N_2, 20.75% O_2, 1.01% H_2O, 0.92% Ar and 0.03% CO_2, and standard seawater are processed in the offshore platform.

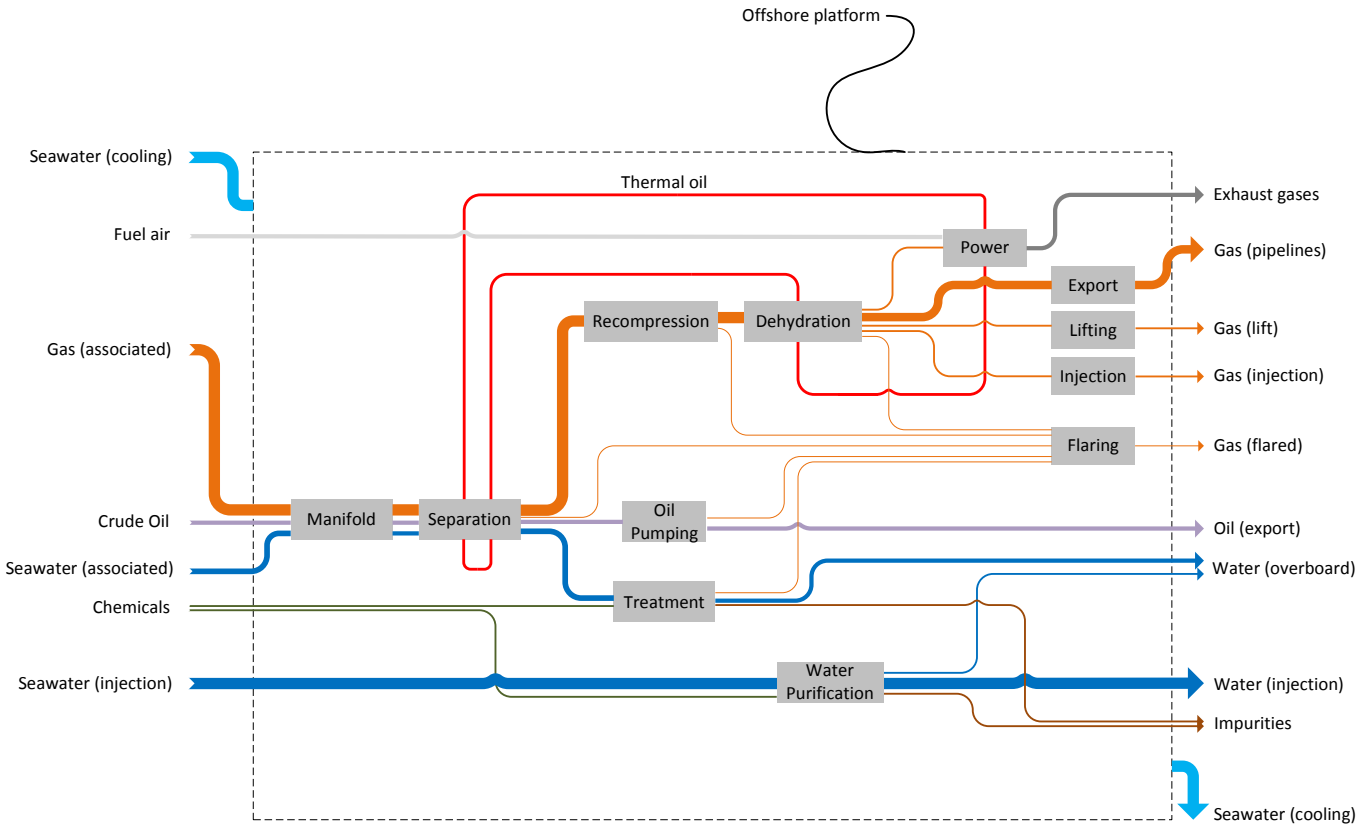

Figure 1: Conceptual layout of offshore processes on North Sea oil platforms

3.2. System sub-models

The overall platform system was divided into subsystems which were at first modelled separately and integrated afterwards in an overall model. The main aim of this system decomposition into sub-models was to investigate the steady-state behaviour of each process, to evaluate their thermodynamic performances and their sensitivity to operating parameters. Subsystems and corresponding mathematical models created within this study are described in the following sections. Unless something else is stated, operating parameters of each process model are fixed by the user and the models return the energy demand as well as the flow rates and compositions of the material streams. Modelling and simulation assumptions are presented in Table 3. Values in brackets [-] indicate several components of the specified type, each value corresponding to a particular component at a given location in the process.

Simulations based on case studies available in the open literature [6–8, 11, 12] were performed to validate the separation, gas re-compression and injection process models and showed a deviation smaller than 5%. The maximum difference is found in the prediction of the gas volumic flowrate at the outlet of the offshore platform system. Comparisons between manufacturer data and model predictions were conducted to validate the models developed for simulating the behaviour of the power generation units. For loads above 50%, which is the region of interest, the maximum relative error is found in the prediction of the gas turbine thermal efficiency and is around 3.7%.

3.2.1. Crude oil processing

Petroleum extracted through the several wells is transferred to the platform complex via a network of pipelines and a system of production manifolds. The individual well-streams are mixed and de-pressurised by choke boxes, which consist of valves and chokes, and fed afterwards into the separation train. Crude oil separation is promoted by gravity and takes place in four stages operating at four different pressure levels. The first three stages consist of three- and two-phase separators while the last stage comprises an electrostatic coalescer [3, 11, 12].

Pressure is decreased along the train by a series of throttling valves and the temperature of the separator feeds is increased by heat exchange with thermal oil

Table 3: General system specifications

Process	Component	Parameter	Unit	Value
Reservoir		Temperature	°C	71
		Pressure	MPa	7
Production Manifold	Throttle	Outlet pressure	MPa	[12,7]
	Mixer	Pressure drop	MPa	0.12
Separation	3-Phase Separator	Heat losses	MW	-
		Pressure level	MPa	[7,2.9,0.72]
		Pressure drop	bar	[0.5,0.3,0.05]
	Electrostatic coalescer	Heat losses	MW	-
		Pressure level	MPa	0.18
	Mixer	Pressure drop	bar	[0.05,0.02]
	Crude oil/glycol heat exchanger	Pressure drop	bar	[0.25,0.25]
		Temperature increase (cold side)	K	5
		Minimum temperature approach	K	10
Re-compression	Centrifugal compressor	Outlet pressure	MPa	[2.95,7]
		Isentropic efficiency	%	[64,67]
		Mechanical efficiency	%	[93,93]
	Gas/seawater heat exchanger	Outlet temperature	°C	[20,20,20]
		Pressure drop	bar	[0.25,0.1,0.025]
	Throttle	Outlet pressure	MPa	[2.93,0.75,0.18]
	Flash	Heat losses	MW	-
		Pressure drop	bar	[0.5,0.3,0.05]
Oil pumping	Pump	Outlet pressure	MPa	[0.545;3]
		Pump efficiency	%	[59,61]
		Driver efficiency	%	[90,90]
	Cooler	Outlet temperature	°C	15
		Pressure drop	bar	0.1
Waste water treatment	Throttle	Outlet pressure	MPa	0.12
	Cooler	Outlet temperature	°C	[25,15]
		Pressure drop	bar	[0.1,0.1]
	Hydro-cyclone	Separation Efficiency	%	97
	Skim vessel	Pressure level	bar	1.2
		Temperature level	°C	25
Glycol dehydration	Absorption column	Pressure level	MPa	7
		Temperature level	°C	31
		Minimum glycol-gas temperature approach	°C	18.5
	Flash drum	Temperature level	°C	37.8
	Throttle	Outlet pressure	bar	1.2
	Glycol/Thermal oil heat exchanger	Outlet temperature (cold side)	°C	165
		Pressure drop	bar	0.025
	Glycol/Seawater heat exchanger	Outlet temperature (hot side)		
		Pressure drop	bar	0.025
	Desorption column	Number of stages	-	5
		Stage efficiency	-	100%
		Condenser pressure	bar	1.2
		Condenser pressure drop	bar	0.2
		Condenser temperature	°C	98.9
		Reboiler pressure	bar	1.25
		Reboiler pressure drop	bar	0.2
		Reboiler temperature	°C	204.4
Waste heat recovery system		Temperature level (glycol side)	°C	[200,210,220]
Seawater injection system		Oxygen level	ppb	10
		Solids content	ppm	5

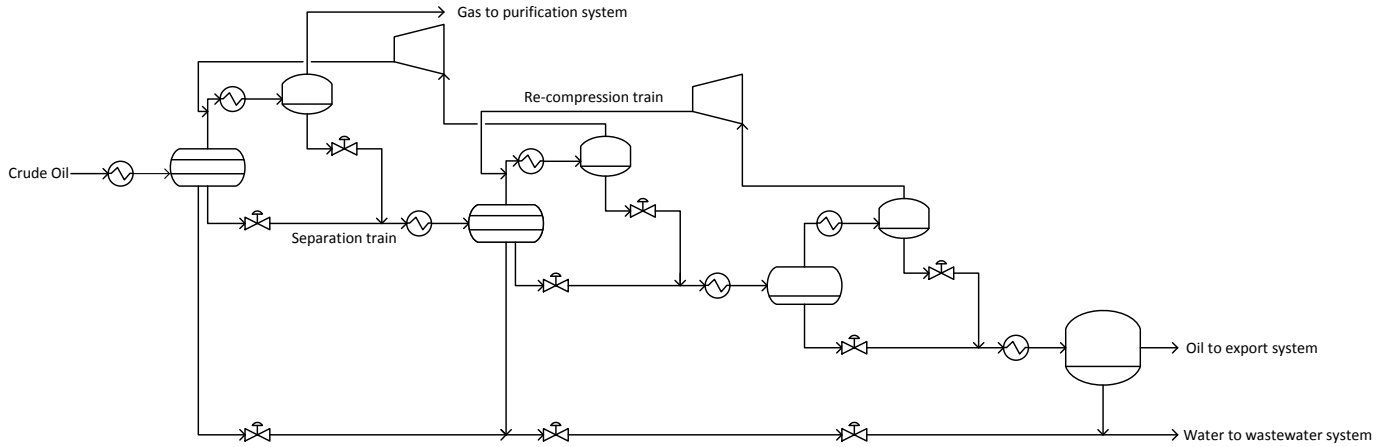

Figure 2: Flow sheet of the separation and gas re-compression train

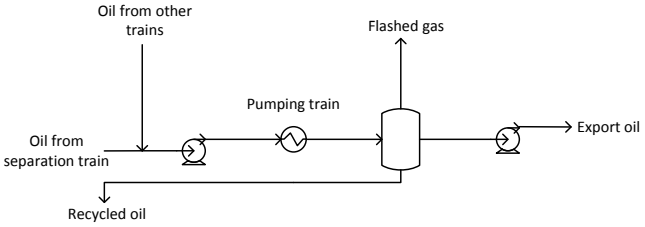

Figure 3: Flow sheet of the export pumping section

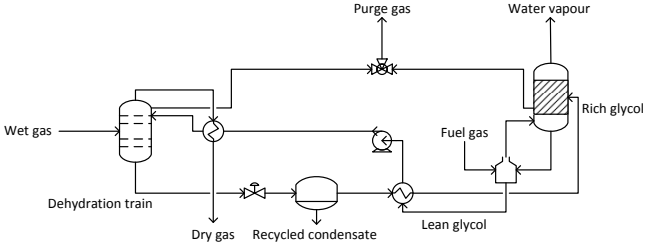

Figure 4: Flow sheet of the dehydration train

to increase the separation efficiency, as depicted in Figure 2. It is assumed that the gravity separators are continuously operated, that physical equilibrium is reached and that no liquid is entrained in the gas vapour phase. Power needed to sustain the electric field in the coalescer is neglected.

3.2.2. Gas re-compression

Product gas from the separators and recovered from the oil pumping train is led through the re-compression train. Temperature is decreased by seawater cooling and liquid droplets are separated and removed by scrubbing, resulting in a relatively dry gas which is then re-compressed. Condensate from the scrubbers is mixed with crude oil at the inlet of the separators, while pressurised gas is sent to the purification process. It is assumed that the gas re-compressors are run at a sufficient load, close to their design point, which avoids the need for recycling around these components to prevent surge issues.

3.2.3. Oil export and pumping

Oil from the separation train enters the export pumping system, shown in Figure 3, where it is mixed with oil and condensate removed in other steps of the plant. It is then cooled, pumped gradually, stored and exported to the coast via shipping.

3.2.4. Gas purification

In addition to the re-compression train, there are needs for a dehydration unit to prevent corrosion issues in gas pipelines, as illustrated in Figure 4, and for additional flash units to reduce the content of heavy hydrocarbons. Gas dehydration on offshore platforms is conventionally achieved by a glycol absorption/desorption system. Wet gas enters at the bottom of an absorption column, modelled as a packed absorber, and water is captured by liquid glycol by physical absorption. The glycol-water-natural gas mixture thereby enters a flash separator at an intermediate pressure to minimise the amount of natural gas entrained with the circulating glycol. It is then pre-heated to ease the water-glycol separation in the desorption column. A small fraction of dry natural gas is sent for stripping in order to increase the molar purity of glycol to 99.9%. Regenerated glycol is pumped to the absorber pressure and heated to ensure a minimum temperature difference of 20°C with the natural gas stream entering the system [12, 16, 17].

In contrast of the other process sub-models, in which operating parameters and inflows were set by the user or returned by other sub-models, and outflows derived by mass and energy balances, the gas dehydration sub-model calculates the optimal operating parameters (glycol and stripping gas flow rates, boilup and reflux ratios, heating demand) for a set of given constraints (water content, temperature level) on the outflows. The gas purification sub-model calculates the amount of circulating glycol required to reach a purity of 99.9% of natural gas at the outlet of the dehydration unit as well as the stripping gas flowrate.

3.2.5. Wastewater treatment

In the North Sea region, downstream cleaning of the produced water is essential for environmental and legislation reasons [18]: suspended particulates and dissolved hydrocarbons are removed by use of hydrocyclones. Wastewater flows then through a succession of throttles and enters a skimmer tank to recover oil traces before it is released to the environment.

3.2.6. Seawater injection

Seawater for re-injection must meet several quality requirements to avoid pipe corrosion and bacteria formation due to sediments, sulphides and oxygen compounds [19, 20]. It is processed in filtering units and deaeration towers before being pumped and injected into the petroleum reservoir. The seawater injection model calculates the chlorine and coagulants loading

required to decrease the concentration of oxygen and particulates to the desired level. It is at first assumed that the volume of water which should be injected into the reservoir is nearly constant. The impact of this assumption is evaluated later within this study by means of a sensitivity analysis.

3.2.7. Gas compression, lifting and exportation

A first fraction of the dry gas is used for lifting, which consists of injecting gas at high pressure into the reservoir via the oil wells to increase crude oil recovery. Lifting gas is cooled and scrubbed to further remove heavy hydrocarbons and to decrease the power requirements of the compressors. A second fraction of the dry gas is also cooled and compressed before being sent onshore through a network of subsea pipelines.

3.2.8. Power generation utility system

Electric power required at the different process modules is usually produced by gas turbines directly running on-site. They are selected considering the maximum expected power requirements over the offshore facility's life cycle. However, for reliability matters and in order to prevent unexpected plant shutdown, power generation is usually shared amongst multiple gas turbines running at part-load, which implies that their maximum thermal efficiency is not reached. In this study, the power utility system is modelled as two twin-spool gas turbines complemented by power turbines sharing equally the electrical power supply, with characteristics based on the SGT-500 engine developed by SIEMENS [21]. As shown in Figure 5, the gas turbine is connected to a waste heat recovery system: the thermal fluid is assumed to be a glycol/water mixture with a mass ratio of 40/60.

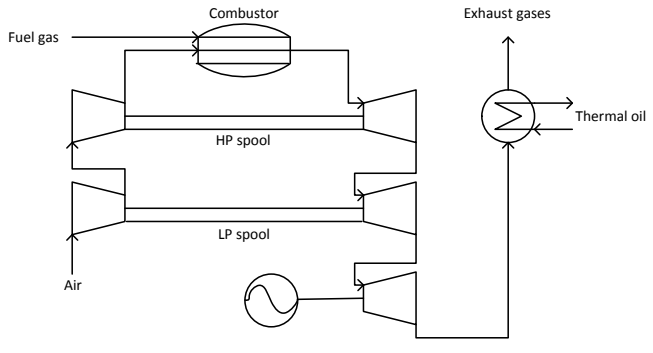

Figure 5: Flow sheet of the twin-spool gas turbine system

The developed power generation sub-model takes as input the electrical power demand from the other plant sections and derives the compressor and turbine off-load characteristics by application of a stage-stacking analysis [22–24]. Air and gas flows, operating conditions and isentropic efficiencies of the gas turbine components are calculated for the required load and are returned to the waste heat recovery sub-model.

3.2.9. Heating and cooling utility systems

Heating on-site is ensured by the waste heat recovery system connected to the gas turbines. In general, the highest temperature level of the platform is found at the reboiler of the desorption column [3]. The waste heat recovery sub-model is based on the heating demand from the platform processes. It is used to calculate the stack temperature of the exhaust flue gases of the power generation system, based on the assumption that the temperature of the thermal fluid is 200°C and 220°C at the inlet and outlet of the waste heat recovery system.

Cooling water is utilised to decrease the amount of heavy hydrocarbons entrained with natural gas and to prevent foaming and low loads in the separation system. This system sub-model is based on the cooling demand of the separation and gas processing trains, and returns the required flow rate of seawater used for cooling. The rejection temperature to the environment is constrained to a maximum of 25°C.

3.3. System simulation

3.3.1. Simulation basis

All processes, at the exception of the power generation and glycol dehydration processes, were simulated with Aspen Plus® version 7.2 [25]. Simulations of production manifolds, petroleum separation, oil pumping, gas re-compression, flaring and lifting were based on the Peng-Robinson equation of state, while simulations of the water purification and injection processes were based on the Non-Random Two Liquid (NRTL) model, usually more suited for electrolyte system modelling. Glycol dehydration was simulated with Aspen HYSYS® [26], using the glycol property package, claimed to predict more accurately the behaviour the tri-ethylene glycol-water mixture [17, 27]. Power generation was simulated by using the tool Dynamic Network Analysis (DNA), developed at the Technical University of Denmark [28].

3.3.2. Case studies and sensitivity analysis

Three cases have been investigated within this study, corresponding to the same platform – identical processes and operating conditions – but with different well-fluid compositions and loads. Specifications for each simulation are listed in Table 4. As emphasised by Svalheim et al. [2], production flows are strongly time-dependent. It is thus unlikely to find, for the same platform, three distinct situations with sensibly similar flow rates and sensibly different gas-to-oil (GOR) and water-to-oil (WOR) ratios. However, in order to provide a basis for comparison and to assess the impact of the gas and water contents of the well-fluid, each simulation case is defined on the same well-fluid molar flow rate.

Case 1, referred as the baseline case in the rest of this study, aims to represent a regular operation of an offshore platform, with oil, gas and water extracted along. Gas- and water-to-oil ratios have been chosen based on the production data of different oil platforms operating in the North Sea [29]. In the second case, the water-to-oil ratio is reduced by 50%, in order to describe the early life of an oil field, when only a small amount of water enters the platform system. Finally, the last case (Case 3) is featured by the same water-to-oil ratio as in the baseline case, but the gas molar fraction is increased by 33%, which corresponds to an intermediate situation in the lifespan of an oil field.

Table 4: Simulation specifications

Well-fluid properties		Case 1	Case 2	Case 3
Molar flow rate	(kmol/hr)	18446	18446	18446
Associated gas	%	48.60	50.71	64.80
Associated water	%	42.90	27.34	17.47
Crude oil	%	8.45	10.76	3.44
Gas-to-oil ratio	molar	5.75	4.71	18.85
Water-to-oil ratio	molar	5.08	2.54	5.08
Mass flow rate	(10^3 kg/hr)	618.3	696.5	490.8
Actual volume flow rate	(m^3/hr)	1484	1841	2079

Operating parameters such as seawater flow rate and gas export pressure differ from platform to platform depending on the physical properties of the oil field and on the pipeline network requirements. These design set-ups are varied one-at-a-time: default states set in the baseline cases and variation ranges in this parametric study are shown in Table 5.

Table 5: Sensitivity analysis parameters

Parameter	Unit	Default value	Variation range
Seawater injection flowrate	(Sm^3/hr)	1245.3	[900-2900]
Gas export pressure	(MPa)	17	[15-25]

4. Exergy analysis

4.1. Exergy balance

The concept of exergy derives from both the 1^{st} and 2^{nd} laws of thermodynamics and illustrates the potential of a system to bring change to its environment. Unlike energy, exergy is not conserved in non-ideal processes, which, in other words, means that the exergy entering a system is always larger than the exergy exiting it. The difference between the inlet $\dot{E}_i$ and outlet exergy $\dot{E}_o$ flow rates is called the exergy destruction rate $\dot{E}_d$, which indicates thus the locations and amplitudes of energy degradation [4]. The general exergy balance for a given system at steady-state can be expressed as follows:

$$\dot{E}_d = \sum \dot{E}_i - \sum \dot{E}_o \tag{1}$$

For a control volume at steady state, the exergy destruction rate becomes:

$$\dot{E}_d = \sum \left(1 - \frac{T_0}{T_j}\right) \dot{Q}_j - \dot{W}_{cv} + \sum \dot{m}_i e_i - \sum \dot{m}_e e_e \tag{2}$$

Where e and $\dot{m}$ are the specific exergy and mass flow rate of a material stream, respectively, and $\dot{Q}_j$ and $\dot{W}_{cv}$ the time rates of energy transfer by heat and work. The subscript 0 indicates the reference conditions, the subscripts i and e denote inlet and exit and the subscript j the boundary of the component of interest.

4.2. Exergy components

Alike enthalpy and entropy, exergy is an extensive property which can be defined for every stream of matter. The specific exergy of a material stream e is a function of its physical e_{ph}, chemical e_{ch}, kinetic e_{kn} and potential e_{pt} components and is defined as:

$$e = e_{ph} + e_{ch} + e_{kn} + e_{pt} \tag{3}$$

In this study, the kinetic and potential effects on the exergy associated with material streams are assumed negligible compared to the physical and chemical contributions. Physical exergy is related to temperature and pressure differences with the dead state, while chemical exergy is related to deviations in chemical composition with reference substances

present in the environment. The specific physical exergy per mass of a given stream e_{ph} can be calculated with the following formula:

$$e_{ph} = (h - h_0) - T_0(s - s_0) \quad (4)$$

Where h and s are the specific enthalpy and entropy of a stream of matter per unit-of-mass, respectively. By applying the Peng-Robinson and Non-Random-Two-Liquid thermodynamic equations of states, physical exergy values can be computed and deduced from the process simulations. Values of chemical exergy for pure substances are extracted from the reference models of Szargut and Morris [30, 31]. Chemical exergy of hypothetical components contained in crude oil is calculated with the following formula from Rivero [32] when their chemical composition is approximatively known:

$$E_{ch,i} = \beta NHV_i + \sum z_j E_{ch,j} \quad (5)$$

Where NHV_i stands for the Net Heating Value, z_j the mass fraction of metal impurities, $E_{ch,j}$ the corresponding chemical exergy and β the chemical exergy correction factor, expressed as:

$$\beta = 1.0401 + 0.1728\frac{z_{H_2}}{z_C} + 0.0432 z_{O_2} z_C + 0.2169 z_S z_C + (1 - 2.0628 z_{H_2} z_C) + 0.0428\frac{z_{N_2}}{z_C} \quad (6)$$

In the case that the chemical structure of an hypothetical component is unknown, the following relation is used, and gives, according to Rivero [32], less than 1% deviation:

$$E_{ch,i} = NHV_i \quad (7)$$

Finally, the specific chemical exergy of a mixture $\bar{e}_{ch,mix}$, on a molar basis, becomes:

$$\bar{e}_{ch,mix} = \sum x_k \bar{e}_{ch,k} + \bar{R} T_0 \sum x_k ln(x_k) \quad (8)$$

Where x_k is the partial pressure of the k gas and $\bar{R}$ the ideal gas constant.

4.3. Exergy efficiency

Applying an exergy balance on a specific process component k and calculating its exergy destruction rate $\dot{E}_{d,k}$, provides information on its thermodynamic inefficiencies. The exergy destruction rate of this component can then be related to the exergy destruction rate of the whole system $\dot{E}_d$ by calculating the exergy destruction ratio y^*_k, defined as:

$$y^*_k = \frac{\dot{E}_{d,k}}{\dot{E}_d} \quad (9)$$

Exergetic efficiency η_k for a sub-system k, which is a measure of its thermodynamic performance, can be defined by identifying fuel and product of interest. It should be emphasised that fuel and product exergies $\dot{E}_{f,k}$ and $\dot{E}_{p,k}$ of the sub-system of interest are not necessarily equal to its input $\dot{E}_{i,k}$ and output exergies $\dot{E}_{o,k}$.

$$\eta_k = \frac{\dot{E}_{p,k}}{\dot{E}_{f,k}} \quad (10)$$

Definitions of exergetic fuels and products for the components and sub-systems investigated within this study are extensively discussed in Bejan et al [4] and in Kotas [5].

5. Results

5.1. System simulation

This section introduces and discusses the results of the oil offshore platform modelling, which was described in detail in Section 3. Results of the process plant simulation are presented in Table 6, with flows expressed in standard cubic meters (Sm^3), which stands for volume measurements in standard conditions (temperature of 15°C and pressure of 1 atm). The power requirements of the offshore platform are shown in Table 7, with values expressed in MW.

Table 6: Processing plant simulation results - Outflow streams

System outputs		Case 1	Case 2	Case 3
Gas (export)	(10^3 Sm^3/hr)	166.4	213.4	279.4
Gas (lift)	(10^3 Sm^3/hr)	24.36	31.24	40.89
Water (overboard)	(Sm^3/hr)	123.3	90.00	50.41
Water (injected)	(Sm^3/hr)	1245	1245	1245
Oil (export)	(Sm^3/hr)	359.2	457.4	156.3

Results indicate that the power consumption of the offshore platform ranges from 18 to 23.5 MW and is strongly correlated to the energy demand of the gas lifting and exportation trains. In any case, this specific process is the major electricity consumer of the offshore plant and is responsible for 50% to 65% of the total power demand. This power consumption, both in absolute and specific terms, is larger in case 3 than in cases 1 and 2, as the power required to compress

Table 7: Processing plant simulation results – Power consumption (MW)

Power consumption	Case 1	Case 2	Case 3
Gas lifting and exportation	9.234	11.95	15.09
Seawater injection	6.973	6.973	6.973
Gas recompression	1.234	2.132	1.111
Oil pumping	0.530	0.674	0.230
Glycol dehydration	0.004	0.005	0.005
Wastewater treatment	-	-	-
Total (MW)	17.98	21.30	23.41
Total (MJ/Sm^3oil)	180.2	167.6	539.2
Total (MJ/Sm^3oil,eq)	117.7	109.2	176.8

the surplus of gas overcomes the decrease of power in the crude oil pumping and wastewater treatment sections. Additionally, gas compressors on offshore platforms are characterised by a relatively low isentropic efficiency and the use of anti-surge gas recycling has also an impact on the train power consumption.

Another important aspect of the power consumption profile of oil offshore platforms is the great demand associated with the seawater injection process, as a large amount of seawater must be pumped from atmospheric pressure to 11.5 MPa. This process demand accounts for 29% to 39% of the total power consumption and reaches nearly 7 MW. Seawater pumped for injection is not extracted through the same wells as oil and natural gas and does not enter the crude oil separation train. Conversely, oil, associated water and gas do thus not enter the water purification train, and variations in the well-fluid composition do therefore not directly affect the pumping work for seawater injection.

The third largest power demand of the offshore facility is the gas re-compression process, in which gaseous streams from the two- and three-phase separators are re-compressed to the original pressure level of 7 MPa. The electrical energy consumption of this system is larger by a factor two in the second case than in the first one, due to the larger fraction of crude oil and associated gas in the well-stream entering the separation train. Consequently, a greater amount of gas is recovered in the separation train and flows through the two booster compressors. However, although the associated gas flow rate is larger in case 3 than in case 2, the power demand of the re-compression train is much smaller, which suggests that most of the associated gas, rich in light-weight hydrocarbons, exits the separation train at the first separator and bypasses the booster compressors. In other words, the gas recompression power consumption is mostly dependent on the crude oil flow rate and composition, which contains medium-weight hydrocarbons such as propane and butane, more likely to vaporise in the second and third stages of the separation process.

In contrast, the variations of the associated water and oil flows in cases 2 and 3 have a limited impact on the process plant power consumption, because the oil pumping and water treatment processes have by themselves a low power demand. The power consumption of the dehydration unit is slightly higher in the case 3. As a result of a larger gas flow rate at the outlet of the recompression train, a greater amount of tri-ethylene must be processed to decrease the water content to the same purity level. However, as the main natural gas stream only flows through the absorption unit, electricity required by this process is only needed to compensate the pressure drops in the desorber column and to pump the liquid glycol from the desorber to the absorber pressure.

Table 8: Utility system simulation results – Characteristics (for 1 twin-spool turbine)

		Case 1	Case 2	Case 3
Air	Gas turbine inlet			
$\dot{m}$	(kg/s)	75.5	78.1	82.9
Gas	Combustion chamber inlet			
$\dot{m}$	(kg/s)	0.73	0.78	0.87
T	(°C)	15	15	15
p	(bar)	10.8	10.8	10.8
Flue Gases	Gas turbine outlet			
$\dot{m}$	(kg/s)	76.2	78.9	83.7
T	(°C)	316.1	324.6	330.6
p	(bar)	1.02	1.02	1.02
Flue Gases	Waste heat recovery outlet			
T	(°C)	266.9	277.6	286.3

5.2. Sensitivity analysis

The total power consumption of the oil and gas processing plant is, as seen in Table 7, strongly dependent on the power demands of the gas compression system and of the seawater injection process. Correlation between seawater volume and injection system power consumption is shown in Figure 6. Power consumption of the seawater injection train varies linearly with the volume of seawater to inject in the reservoir and increases by about 1 MW for each increment of 200 Sm^3/hr.

This result suggests that, as time goes on, since a larger seawater volume must be injected into the oil reservoir and a lower volume of gas is extracted, the power consumption of the water injection train may exceed the power demand of the gas compression process.

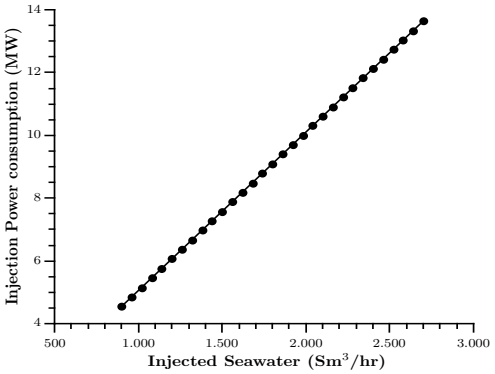

Figure 6: Effect of seawater injected volume on injection system power consumption

The gas export pressure is a parameter fixed by the requirements of the pipeline network system – since this value is subject to variations depending on the network and pipelines to which the offshore platform is connected, the effect of different pipeline constraints is illustrated in Figure 7. It is observed that the total compression train power consumption is clearly affected by the pressure level at which gas must be compressed. However, it is more likely that the operating pressure of the pipeline network system is between 18 and 22 MPa, which corresponds to a window of around 20% of the power demand of this process.

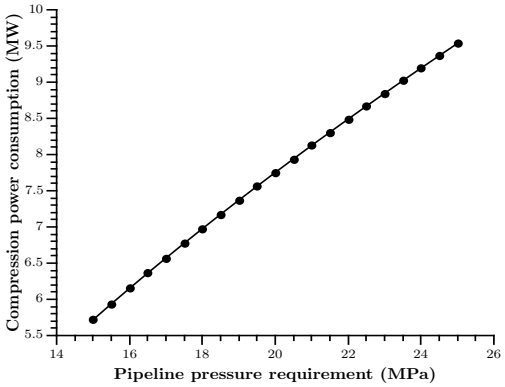

Figure 7: Effect of pipeline pressure requirement on compression train power consumption

5.3. Exergy analysis

In this study, an exergy analysis was undertaken based on dead state conditions of 5°C and 1 atmosphere. Exergy associated with each stream of matter present in the system is calculated and exergy destruction rates are examined for the three simulation cases. Based on the exergy analysis results calculated from the process simulation results, a simplified Grassmann diagram of the overall offshore platform system, which illustrates the input and output exergy flows for the baseline case, is shown in Figure 8.

Exergy is introduced in the form of raw materials (crude oil, associated gas and water, fuel air, seawater, chemicals) and exits in the form of valuable products (e.g crude oil and gas sent onshore) and waste streams (e.g wastewater and exhaust gases). The Grassmann diagram shows that the input and output exergies of this system are largely dominated by the exergy associated to the crude oil and gas streams, because of their high chemical exergy content. In the baseline case, the chemical exergy content of crude oil and gas are respectively 44.6 and 46.3 MJ/kg, and the exergies of these two materials are responsible for nearly 97% of the total exergy input. In comparison, the main contributors to exergy losses are material streams rejected to the environment without any practical use, such as flared gases, discharged seawater, wastewater and exhaust gases from the gas turbine systems, which represent in total less than 1%. Exergy associated with lifted gas and injected water is not considered as a loss, since these streams provide the benefit of increasing oil recovery. The exergy destruction rate accounts for about 1.3% of the total exergy input of the overall platform system: contributions of each sub-system are given in Table 9 for the three simulation cases and the distribution of the total exergy destruction over the various sub-systems is illustrated in Figure 9.

Results demonstrate that the total destroyed exergy on the overall offshore platform totals from 54.8 to 63.3 MW, with a share of 65-70% for the utility system (gas turbines and waste heat recovery) and 30-35% for the oil and gas processing system. This analysis shows that, although the production flows are significantly different from case to case, most of the total exergy destruction takes place within the power generation system, because of the large thermodynamic irreversibilities associated with chemical reactions occurring in the combustors.

When considering exclusively the oil and gas process plant, it is observed that the total exergy destruction of the latter is comprised between 15.5 and 19.1 MW. The exergy destruction within the production manifolds (3.05-7.18 MW) is particularly high, due to the pressure decrease from 16.5 to 7 MPa without generation of any useful product. Conversely, the exergy destruction within the gas compression and

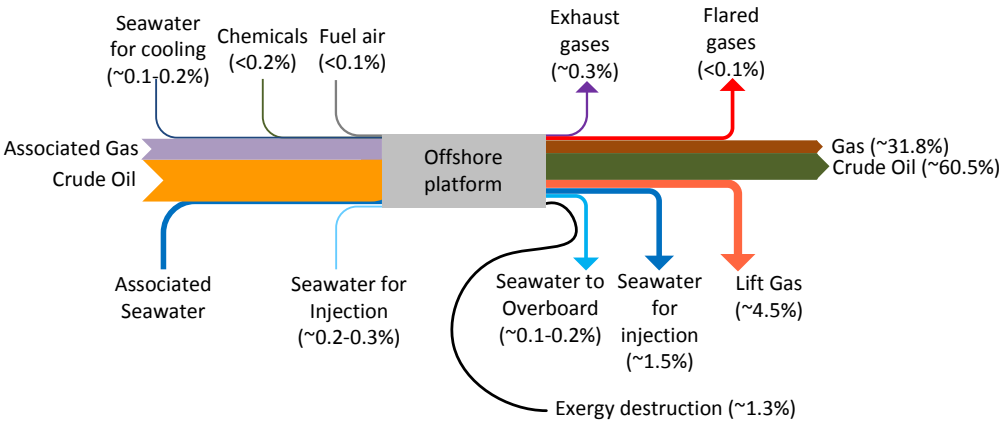

Figure 8: Grassmann diagram of the offshore oil and gas platform – Baseline Case

Table 9: Exergy destruction rates (MW) of the analysed simulation cases for an oil offshore platform

	Case 1	Case 2	Case 3
Production manifold	**4.61**	**3.05**	**7.18**
Separation	**2.22**	**2.83**	**1.39**
Heaters	0.95	1.12	0.72
Throttles	1.02	1.33	0.51
Separators	0.11	0.17	0.07
Mixers	0.14	0.21	0.09
Recompression	**2.31**	**2.13**	**2.09**
Coolers	1.36	1.15	1.39
Throttles	0.29	0.08	0.12
Compressors	0.42	0.66	0.35
Mixers	0.18	0.18	0.18
Flashes	0.06	0.06	0.06
Wastewater	**0.49**	**0.17**	**0.09**
Gas compression	**4.17**	**5.20**	**6.39**
Compressors	3.74	4.56	5.59
Coolers	0.39	0.60	0.76
Throttles	0.02	0.02	0.02
Mixers	0.02	0.02	0.02
Glycol dehydration	**0.01**	**0.01**	**0.01**
Oil pumping	**0.26**	**0.23**	**0.07**
Seawater	**1.92**	**1.92**	**1.92**
Processing plant	**16.0**	**15.5**	**19.1**
Waste heat recovery	**2.85**	**2.96**	**3.15**
Power generation	**36.0**	**39.0**	**41.0**
Compressors	3.18	3.51	3.76
Combustion chamber	28.0	30.4	32.0
Turbines	4.80	5.07	5.24
Utility plant	**38.8**	**42.0**	**44.2**
Offshore platform	**54.8**	**57.5**	**63.3**
Total (MJ/Sm^{3}oil)	**549**	**452**	**1458**
Total (MJ/Sm^{3}oil,eq)	**359**	**295**	**478**

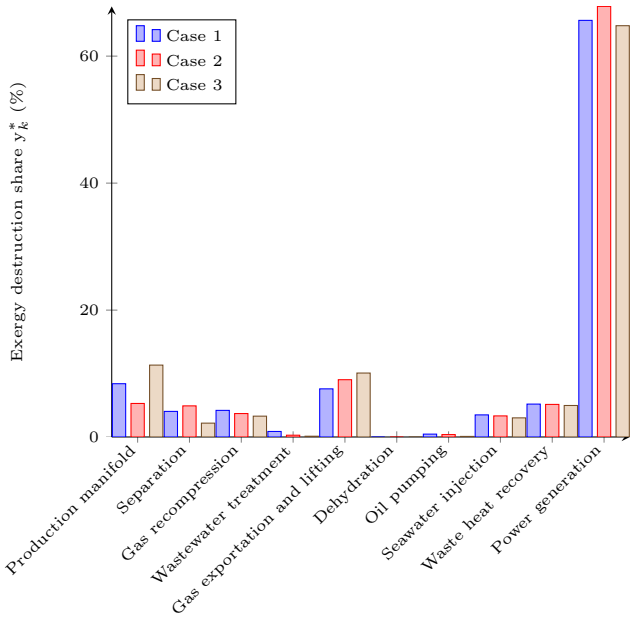

Figure 9: Exergy destruction share of the analysed simulation cases for an oil offshore platform

lifting process is in the same order of magnitude and is mainly due to the inefficiencies of the gas compressors (3.74-5.59 MW for the compressors alone).

The amount of exergy destruction is significantly greater in the case 3 than in the other cases, because of the higher content of gas in the well-fluid. This results in a larger flow rate to process in the production manifold and a higher volume of gas to compress to 15-20 MPa for exportation and lifting. Nearly equal exergy destruction takes place in the separation and re-compression steps, which is mainly due to the large inventory of mixers and recycles to enhance the hydrocarbon recovery. The smallest total exergy destruction of the process plant occurs in the case 2, where the crude oil fraction in the well-fluid is the largest and the water fraction the smallest of all studied cases. Although a larger flow rate is processed in the separation and pumping trains, which implies a higher amount of destroyed exergy in this sub-system, the exergy destruction in the production manifold is greatly reduced, which presents benefits at the scale of the overall processing plant.

Besides being responsible for large exergy destruction, the gas turbine system is also associated with large exergy losses, amounting from 15 to 18 MW, as shown in Table 10. The exergy losses are higher in the third case than in the two first ones because of the greater power demand of the process plant, which leads to a larger mass flow rate of flue gases and a higher stack temperature at the outlet of the waste heat recovery system.

Exergy losses associated with rejection of cooling water and wastewater overboard are comparatively small, since these streams are released at nearly atmospheric pressure and at a relatively close temperature to the ocean. Seemingly, exergy losses associated with flaring are negligible, since only gas ventilated from the glycol purification process is directly rejected into the environment without any valorisation. These losses increase with the amount of associated gas present in the well-fluid, as a larger gas flow rate leads to an increase in the amount of stripping gas required in the dehydration process, which is purged and discharged to the surroundings. The exergy losses in the investigated system total from 16.8 to 20.4 MW. About 90% of them is associated with rejection of high temperature exhaust gases to the environment. The remaining 10% is related to the exergy content of cooling and wastewater discharged overboard, as well as flared gases.

Table 10: Exergy losses (MW) of the analysed simulation cases for an oil offshore platform

	Case 1	Case 2	Case 3
Exhaust gases	15.5	17.3	18.7
Cooling water	1.1	1.4	1.3
Flared gases	0.21	0.25	0.33
Wastewater treatment	0.15	0.09	0.08
Total	16.8	19.0	20.4

Exergy efficiencies of the different sub-systems analysed in the baseline case are given in Table 11, with exergy rates expressed in MW. Since the production manifold, separation, and wastewater treatment consist mainly of throttles and mixers, the exergetic product is equal to null, which leads to the conclusion that the exergetic efficiency of these sub-processes is 0%.

Power generation and waste heat recovery are considered separately since they may be strongly dissimilar from platform to platform and since that they act as energy sources for the other processes. Exergy efficiency of this overall utility system is shown in Table 12, with exergy rates given in MW.

Table 11: Exergy efficiencies of the different process modules – Baseline Case

	Re-compression	Compression	Injection	Oil pumping
$\dot{E}_{d,k}$ (MW)	0.42	4.17	1.92	0.26
$\dot{E}_{f,k}$ (MW)	1.67	9.23	6.97	0.68
$\dot{E}_{p,k}$ (MW)	1.25	5.06	5.05	0.42
η_k(%)	74.8	54.8	72.4	61.7

Table 12: Exergy efficiency of the power generation and waste heat recovery system – Baseline Case

	Power Generation
$\dot{E}_{f,k}$ (MW)	85.7
$\dot{E}_{p,k}$ (MW)	26.4
η_k(%)	30.8

Results show that, apart from the production manifold and separation trains which are inherently exergetic-inefficient, the gas compression and the oil pumping sections have the lowest 2^{nd}-law efficiency. However, the oil pumping section has a much smaller power demand, for both low and high gas-to-oil ratios, than the gas compression train. For this reason, concentrating efforts on improving the gas compression train may be more cost- and exergy-effective. Moreover, a higher efficiency of the gas compression train would result in a lower power consumption, decreasing thus the amount of exergy destroyed in the gas turbine systems.

6. Discussion

Process simulation results are in accordance with the findings of Svalheim et al. [2], who stated that the largest power demand corresponds to the gas compression step and may rise with time, as the gas-to-oil ratio may increase at the beginning of the life span of an oil field. Moreover, since the amount of produced water increases in any case, using wastewater from the crude oil separation process has become one of the focus of several studies from literature [14, 15, 20]. It is nevertheless emphasised that the hydrocarbon content of the wastewater emulsion may result in plugging issues, and therefore further research and quality control of the treated water are necessary.

Despite the differences in terms of process configurations and well-fluid composition with the work of Voldsund et al. [7, 8], the application of exergy analysis reveals that, in general, for North Sea oil platforms, the compression-lifting process is, when the utility system and the production manifold are not considered, the most exergy-destructive step, with a calculated exergy destruction rate of 4 to 6 MW. The main discrepancy lies in the accounting of the exergy associated with overboard discharge of cooling water, which is considered as an exergy loss in this study, but assumed as an exergy destruction in their work, due to differences in the choice of the system boundaries. Similarly, the re-compression and separation steps rank as the second and third most exergy-destructive sections, while the exergy destruction taking place in the oil export pumping is negligible.

The work of Voldsund et al. [7, 8] suggests to focus on the gas compression train. Improving this part of the offshore platform system is indeed of particular importance, since a more efficient gas process would lead to a reduction of the power consumption, and to a lower exergy destruction in the oil processing plant and in the power generation system. However, it should be added that operating the gas turbines in part-load mode is a key issue, and that therefore a compromise on the peak efficiency for a higher part-load efficiency may be beneficial over the life span of the oil field.

Oliveira and Van Hombeeck [6], who investigated a Brazilian oil platform, also emphasised the large exergy demand and destruction associated with the gas compression step. However, the authors pointed out the importance of the crude oil heating operations taking place before the separation module. The considerable exergy consumption in the feed pre-heating is responsible for a furnace demand of about 25 MW exergy for a feed of 450 t/hr, which differs strongly from the findings of Voldsund et al. [7] and the present results. These discrepancies are mainly due to the temperature differences between the North Sea and the Brazilian feeds flowing out of the oil reservoir.

Oliveira and Van Hombeeck assumed feed characteristics of 7.4°C and 10.78 bars at the inlet of the separation train, whilst the well-fluid temperature is assumed here to 71°C at the inlet of the production manifold, which leads to a temperature of about 65°C at the inlet of the first-stage separator. These differences in results and conclusions suggest that oil offshore platforms located in different oil regions (North Sea, Gulf of Mexico, Brazilian Basin) may, with respect to exergy considerations, present highly different characteristics.

7. Conclusion

A generic North Sea offshore platform model was developed and presented, and predicts the material outflows and energy requirements under different sets of operating conditions and production flows. This overall model includes power generation, oil and gas processing, gas purification and seawater injection sub-models. The first sub-model was calibrated by use of published data from SIEMENS while the others were verified by comparison with open literature.

The performance of this integrated plant was assessed, based on the exergetic analysis method. Exergy is destroyed at a rate of 55-65 MW within the overall platform, with a share of 70-30% for the utility system (power generation and waste heat recovery) and the oil, gas and water processing, respectively. Exergy losses are also significant, amounting to about 17-20 MW, and are mostly due to the rejection of high-temperature exhaust gases from the cogeneration plant to the environment. However, the exergy destruction and loss rates represent only 0.5 to 1.5% of the total input exergy, due to the inherently large chemical exergy content of crude oil and natural gas.

Three simulation cases were investigated to analyse the effects of different gas-to-oil and water-to-oil ratios on the thermodynamic performance of this system, and to evaluate the exergy destruction share amongst the several system modules. The gas-to-oil ratio is the most important variable: a larger gas frac-

tion in the well-fluid stream causes a strong increase of the process plant power consumption and a larger exergy destruction in the production manifolds and gas compression trains.

Recovering more thermal exergy from the exhaust gases, improving the part-load efficiency of the gas turbine components and of the gas compression trains could significantly increase the thermodynamic performance of conventional oil and gas offshore platforms. Higher pressure levels in the separation train would lead to smaller exergy destruction rates in the manifold and re-compression trains, although this might result in a lower hydrocarbon recovery and conflict with the process constraints of other system sections.

Conventional exergy analysis does not allow evaluating interactions and cost flows between the system components and processes present on the whole offshore platform. Future work will address this issue by conducting an advanced exergy analysis, an exergoeconomic assessment and an evaluation of the uncertainties associated with the crude oil and gas compositions.

Acknowledgements

The authors gratefully acknowledge the funding from the Norwegian Research Council through the Petromaks programme, within the project 2034/E30 led by Teknova, and the technical support of Mari Voldsund from the Norwegian University of Science and Technology (NTNU, Trondheim).

References

[1] Sentralbyrå, S.. Lavere klimagassutslipp i 2011 (in Norwegian). 2011. URL http://www.ssb.no/klimagassn_en/.

[2] Svalheim, S., Directorate, N.P., King, D.C., Exploration, B.P.. Life of Field Energy Performance. In: Offshore Europe. July; Aberdeen: Society of Petroleum Engineers Inc.; 2003, p. 5.

[3] Bothamley, M., Campbell, J.M.. Offshore Processing Options for Oil Platforms. In: SPE Annual Technical Conference and Exhibition. Houston; 2004, p. 1–17. doi: 10.2118/90325-MS.

[4] Bejan, Adrian; Tsatsaronis, George; Moran, M.. Thermal Design and Optimization. John Wiley & Sons, Inc.; 1995.

[5] Kotas, T.J.. The Exergy Method of Thermal Plant Analysis. London: Butterworths; 1985.

[6] Oliveira Jr., S.D., Van Hombeeck, M.. Exergy Analysis of Petroleum Separation Processes in Offshore Platforms. Energy Conversion and Management 1997;38(15-17):1577–1584.

[7] Voldsund, M., Ståle, I., Røsjorde, A., He, W., Kjelstrup, S.. Exergy Analysis of the Oil and Gas Separation Processes on a North Sea Oil Platform. In: Proceedings of ECOS 2010 - The 23rd International Conference on Efficiency, Cost, Optimization, Simulation and Environmental Impact of Energy Systems. Lausanne; 2010, p. 303–310.

[8] Voldsund, M., He, W., Røsjorde, A., Ertesvåg, I.S., Kjelstrup, S.. Evaluation of the Oil and Gas Processing at a Real Production day on a North Sea Oil Platform Using Exergy Analysis. In: Proceedings of ECOS 2012 - The 25th International Conference on Efficiency, Cost, Optimization, Simulation and Environmental Impact of Energy Systems. 2012, p. 260–274.

[9] Jones, D.S.J.. An introduction to crude oil and its processing. In: Handbook of Petroleum Processing; chap. 1. Springer; 2006, p. 1–45.

[10] Baker, R.O.N.. Oil and Natural Gas : Offshore Operations. 2004.

[11] Manning, F.S., Thompson, R.E.. OILFIELD PROCESSING OF PETROLEUM. Tulsa: PennWell Books; 1991.

[12] Plisga, W.C.L.G.J.. Standard Handbook of Petroleum & Natural Gas Engineering. Gulf Professional Publishing; second ed.; 2004. ISBN 0750677856.

[13] H. K., Abdel-Aal; M. A., Fahim; Mohamed, A.. Overview of Gas Field Processing. In: Petroleum and Gas Field Processing; chap. 10. New York: Marcel Dekker, Inc.; 2003, p. 1–6.

[14] H. K., Abdel-Aal, M. A., Fahim; Mohamed, A.. Produced Water Treatment. In: Petroleum and Gas Field Processing; chap. 9. Gulf Professional Publishing; 2003, p. 1–31.

[15] Vik, Eilan Arctander; Dinning, A.J.. Produced Water Re-Injection The Potential to Become an Improved Oil Recovery Method. Tech. Rep.; Aquatem A/S; Oslo; 2009.

[16] Abdel-Aal, H. K.; Aggour, Mohamed; Fahim, M.A.. Composition and Characteristics of Crude Petroleum - A brief review. In: Petroleum and Gas Field Processing; chap. 2. New York: Marcel Dekker, Inc.; 2003, p. 42–52.

[17] Ryba, A.. Optimization of Natural Gas Dehydration. Ph.D. thesis; AGH University of Science and Technology; 2005.

[18] Awal, M.R., Herd, B.L., Engineering, P.. Extent of Environmental Impact of Petroleum. In: Environmentally Conscious Petroleum Engineering; chap. 2. 2009, p. 12–15.

[19] Puntervold, T., Austad, T.. Injection of seawater and mixtures with produced water into North Sea chalk formation: Impact on wettability, scale formation and rock mechanics caused by fluid-rock interaction. In: Proceedings of SPE/EAGE Reservoir Characterization and Simulation Conference. Society of Petroleum Engineers; 2007, p. 1–12.

[20] Patton, C.C.. Injection-Water quality. Journal of Petroleum Technology 1990;42(10):1238–1240.

[21] SIEMENS, . SGT-500 Industrial Gas Turbine. Tech. Rep.; Siemens Industrial Turbomachinery AB; Finnspong; 2011.

[22] Song, T. W.; Kim, T. S.; Kim, J. H.; Ro, S.T.. Performance prediction of axial flow compressors using stage characteristics and simultaneous calculation of interstage parameters. In: Proceedings of the Institution of Mechanical Engineers. Institution of Mechanical Engineers; 2001, p. 89–98.

[23] Muir, D.E., Saravanamuttoo, H.I.H., Marshall, D.J.. Health Monitoring of Variable Geometry Gas Turbines for the Canadian Navy. Transactions of the ASME 1989;111(April):244–250.
[24] Spina, P.R.. Gas Turbine performance prediction by using generalized performance curves of compressor and turbine stages. In: Proceedings of the ASME Turbo Expo 2002. 2002, p. 1073–1082.
[25] Technology, A.. Aspen Plus - Modelling Petroleum Processes. Moutain View: Aspen Technology, Inc.; 1999.
[26] Technology, A.. Hysys 2004.2 Simulation Basis. Cambridge: Aspen Technology, Inc.; 2004.
[27] Dimian, A.C.. Integrated Design and Simulation of Chemical Processes. Amsterdam: Elsevier B.V.; first ed.; 2003. ISBN 0444829962.
[28] Elmegaard, B., Houbak, N.. DNA A General Energy System Simulation Tool. In: Proceedings of SIMS 2005 - 46th Conference on Simulation and Modeling. Trondheim: Tapir Academic Press; 2005, p. 1–10.
[29] Directorate, N.P.. Fact Pages. 2012. URL http://factpages.npd.no/factpages/.
[30] Szargut, J.. Chemical exergies of the elements. Applied Energy 1989;32(4):269–286.
[31] Morris, D.R., Szargut, J.. Standard chemical exergy of some elements and compounds on the planet earth. Energy 1986;11(8):733–755.
[32] Rivero, R., Rendon, C., Monroy, L., Group, E., Mexicano, I.. The Exergy of Crude Oil Mixtures and Petroleum Fractions: Calculation and Application. International Journal of Applied Thermodynamics 1999;2(3):115–123.

SIMS 53rd conference
Reykjavik, Iceland, October 3-5 2012

Optimizing the design of hydropower stations

Jonas Elíasson and Guðmundur Ludvigsson

Abstract

State of the art: Local optimization is common knowledge but leads to difficult calculations and time consuming search for an optimum. Global optimization is difficult in spreadsheets or matlab software but becomes easy in a software using Genetic Algorithms. An Objective Function is built by finding the net present value of the future income from energy sales and subtracting the financial and running costs. The basic equations are studied; different objectives, resource utilization policies and environmental considerations are discussed with respect to their influence on the result. In the final phase a Genetic Algorithm routine search out an optimum and this is demonstrated on a case study example.

Introduction

Local optimization of individual structures such as tunnel diameters is common knowledge in design of hydropower stations. The calculations are very difficult however. The search for an optimum is also very time consuming.

Global optimization is very difficult, even fully computerized in spreadsheets or matlab programs. The software application HYDRA overcomes this difficulty by using Genetic Algorithms.

The HYDRA software produced by Univ. of Icel. in cooperation with NPCI and Tech. Univ. of Vienna. In the reference list the 5 first references discuss this application. In this lecture is focusses on the special principles that are the working mechanism of this application and also shows a case study.

One principle used, is the mathematical maximization of an objective function is (Eliasson *et al* 1997):

$$\max f(x_1, x_2,\ldots,x_n) \quad a_i \le x_i \le b_i \text{ for } i = 1 \text{ to } n \qquad (1)$$

$$g_j(x_1,x_2,\ldots,x_n) \le c_j \quad \text{for } \forall\ j \qquad (2)$$

In this chapter the principle of optimal profit is introduced as our objective, so $f(x_1,x_2,\ldots,x_n)$ is the profit, depending on the vector $(x_1,x_2,\ldots,x_n)$, that stores all the necessary variables needed to compute the power production and investment costs. This leads to a method that in fact includes many of the conventional local optimization methods used so far, and can yield the same results.

By assuming an infinite energy demand and a fixed energy price, k_e, the present value of the revenue of energy sale becomes (Eliasson & Ludvigsson 1996):

$$NPV = T - G = k_e \cdot E \cdot \left(\frac{1-(1+r)^{-N}}{r}\right) - C \cdot v \cdot \left(\frac{1-(1+r)^{-N}}{r}\right) - C \qquad (3)$$

Where T is total income, G gross expenses, r is the interest rate, N is the lifetime of the investment, C is the project investment, ν is the annual operation and maintenance cost, k_e is the unit price of energy, and E is the annual energy capacity of the hydrostation.

As all costs and revenues are included in the objective function, the optimization can be considered global. Inserting NPV for $f(x_1, x_2,\ldots,x_n)$ in (2) gives:

$$dNPV = \sum_{i=1}^{n} \frac{\partial NPV}{\partial x_i} dx_i = 0 \Rightarrow \frac{\partial NPV}{\partial x_i} = 0 \text{ for all } i = 1 \text{ to } n \qquad (4)$$

The optimization that Mosonyi (1991), and since then other authors, presents for tunnels, may be deduced from (4). This is local optimization. Often, variable costs of other project items than the conduit itself are not taken into account, which results in a larger tunnel diameter than the optimal one.

Example 1: Local optimization of x_1, the diameter of a headrace tunnel

$$\frac{\partial NPV}{\partial x_i}=0 \qquad NPV = k_e \cdot E \cdot \left(\frac{1-(1+r)^{-N}}{r} \right) - C \cdot v \cdot \left(\frac{1-(1+r)^{-N}}{r} \right) - C$$

Speculations on how long the economic lifetime N should we and what the interest rate r and the annual maintenance cost ν should be is outside our topic so we put N very large (40 – 60 years), v < r < 10 % and get:

$$NPV = \frac{k_e}{r} \cdot E \cdot -C \cdot \frac{v \cdot +r}{r} \Rightarrow \left(k_e \cdot E \cdot -C \cdot \left(v \cdot +r\right)\right)\frac{1}{r} = \left(k_e \cdot E \cdot -C \cdot a\right)\frac{1}{r}$$

The tunnel diameter x_1 only affect the energy losses in the E term and the construction costs of the tunnel itself in the C term. We differentiate partially with respect to x_1:

$$\frac{\partial NPV}{\partial x_i}=0 \Rightarrow k_e \frac{dE}{dx_1} = a \frac{dC}{dx_1}$$

We take x_1 to be the diameter of the tunnel. Now E depends on $A = \pi x_1^2$, the tunnel area, as smaller tunnel diameter means greater flow resistance and less energy output. We also take $C = k_3 A L$ where L is the tunnel length, k_3 the tunnel construction cost per cubic meter so construction costs decrease with decreasing tunnel diameter. Somewhere there must be an optimum.

Choosing Chezy's formula to represent the flow resistance will result in the following formula

$$A = \left(\frac{T_k \cdot k_e}{k_3 \cdot a} \cdot \frac{2{,}5 \cdot e \cdot \gamma \cdot Q_v^{\,3}}{C_e^{\,2} \cdot \mu} \right)^{2/7}$$

Where C_e is Chezy's coefficient of flow resistance, e is efficiency of power station, γ is unit weight of water and μ is the ratio of hydraulic radius over square root of A, it is 0,25 – 0,28 for most tunnel cross-sections.

What have we got here? It is one of many forms of the formula for optimal size of a headrace tunnel cross section in a hydroelectric power plant. Now several questions arise. First: is the formula explicit and ready to use ? Answer is no, k_3 and C_e depend slightly on x_1 (tunnel diameter) so at least we have to use some iteration. Second: are there limitations to the validity? Answer is yes, we have used simplifying assumptions to get through a very complicated part of the calculations, which is the relationship between flow resistance and annual energy production, for details we must refer to Eliasson 1997. Third: is the formula generally valid accepting the limitations and possible iterations? Answer is no, there is a cost item not included in the formula, which is the size of powerhouse and mechanical equipment.

The conclusion of this example is that even using complicated methods, local optimization can only produce implicit formulas of limited validity. Counterexamples do exist, but they are few and uninteresting.

Different objectives

The result of example 1 brings us back to the global problem of eq. (3). We may ask the question if the principle of profit optimization is really global enough, can it possibly include important objectives such as environmental consideration and the reasonable demand for cheap electricity for public utilities? Can these considerations be included in a profit maximizing objective function?

Environmental considerations have two sides, first there is the resource utilization principle, second the principle of nature conservation. These two sides will be discussed in examples 2 and 3.

Example 2: The principle of long-term marginal costs
In the first case we don't want the utilization of a certain amount of resource to spoil the resource. This can happen in harnessing hydroelectric energy. We never utilize 100 % of a resource, there is always something left, and what is left is usually uneconomical to use. Diminishing energy resources of the world have as consequence rising prices, energy resources that are uneconomical to harness today, maybe economical tomorrow. But it is usually uneconomical to enlarge old power plants, so considerable hydroelectric energy may go lost in the future if we build only small power plants today.
The principle of long-term marginal cost has been applied in Norway and Iceland. In short it says that a resource shall be utilized until the marginal cost, J kr/kwh, matches the long-term price for other (fossil) energy.
In order to understand this design principle imagine that we plan a power station with annual energy output E. Then we plan a little bit bigger power station with annual energy output E + dE. Assuming that our plan is the most economical way to achieve the enlargement dE, the principle of long term marginal cost tells us that the power station is big enough not spoil the resource if:

$$dC/dE = J$$

Then the size of the power station is right. If our dC/dE < J we have to try a bigger station, if dC/dE > J we have to make it smaller. How can this be included in our objective function eq. 3? ?
Differentiating eq. 3 with respect to E and putting the result equal to zero as in eq. (4) results in:

$$\frac{d}{dE}(k_e \cdot E - C(1+\nu))\left(\frac{1-(1+r)^{-N}}{r}\right) = 0 \Rightarrow k_e = \frac{dC}{dE}(1+\nu) = J(1+\nu)$$

Which shows that for the optimum of the objective function, k_e is equal to the marginal cost of energy instead of the power sales price. By simply replacing the power sales price with the long-term marginal cost (augmented for operation and maintenance) we change the objective from profit maximization to resource utilization. The conclusion of example 2 is that selecting the k_e different from the power sales price the objective function is changed from profit maximization to another objective, e.g. marginal cost design.

Example 3: Nature conservation.
Second class, or the second site, of environmental considerations is that the development must not harm the environment, the values of nature have to be conserved.
Total conservation is simple; law (conservation act) protects the project site and the project suspended. Several sites are protected this way in almost every country in the world. The respective area is usually made a national monument.
Partial conservation can be made in a number of ways. The most common is restrictions on land use (such as borrow pits and fill areas), restrictions on storage volumes in reservoirs or minimum (or maximum) flows in rivers and many other things. Such restrictions either enters the cost function directly through their influence on unit prices or as restriction on the vector $(x_1,x_2,\ldots,x_n)$ in eq. (2) and through that they become a natural element in the optimization

process. E.g. if we are supposed not to let the water level in a storage reservoir not exceed a certain elevation H, and suppose the storage volume V(H) in this reservoir is $x_2 = V$, then we have

$$x_2 < V_{max}(H)$$

As a natural restriction in the optimization.
Usually there are various environmental obligations involved in the permit the developer must obtain prior to construction of the power plant. This may involve various cost items that are not functions of the vector $(x_1,x_2,\ldots,x_n)$ but independent of it and can therefore not be included in the optimization in the way we just did with the reservoir elevation. This may be items to protect and research wildlife or fish habitats or create public access to scenic areas. These cost items do not affect the optimization as such as they drop out in the differentiation in eq. (4), but they affect the resulting profit and may turn it negative and thus render the project unfeasible for the developer. In the case of marginal costs, they can keep the average cost above the marginal cost and thus rule the project out. In such a way environmental obligations can serve the same purpose as total conservation.
In short, including environmental obligations that protect the nature in the optimization eqs (1) – (4) is usually not a problem.

Global optimisation

The global optimization problem cannot be solved analytically, the nonlinear constraints eq. 2 rule this possibility out completely. Therefore the program HYDRA has been developed to solve the global optimization problem. It does so using genetic algorithms, but it belongs to the class of methods called evolutionary methods (Goldberg 1989). One does not have to understand how genetic algorithms work, it is sufficient to know that the method seeks out the optimum by giving the vector $\{ x_i \}$ a definite values, calculating C and comparing the results. This sounds as both impractical and time consuming, but the genetic algorithm seeks out the optimum and finds it with astonishing speed (Eliasson et al 1997[1], 1997[2], 1998 and 1999).

Example 4: Global optimization of simple powerplant
A simple example, shown in figure 1 (Eliasson et al 1997[1]). Eqs. 1 – 4 are derived by direct mathematical analysis and solved. To do so it was necessary to build special approximation formula for the powerhouse and other construction elements shown in fig 1. The mathematical solution is compared to the findings of the HYDRA program in table 1, NPV, for different number of individuals P, generations G and mutation probability μ. It is necessary to explain the parameters P, G and μ shortly.
The computer stores $\{x_i\}$ vectors as P individual strings in the memory. Profit is calculated for all of them and the best performing (highest profit) individuals selected, these are the "parents". By special mixing of the elements of the best vectors a new set of P individuals is formed, this set is a new generation the "children". Now the process is repeated G times. To prevent the process to get stuck in a local maxima brand new children, unrelated to the parents are formed randomly, the mutation probability μ decides how often this happens. When the process stops after G generations the optimum should be found.

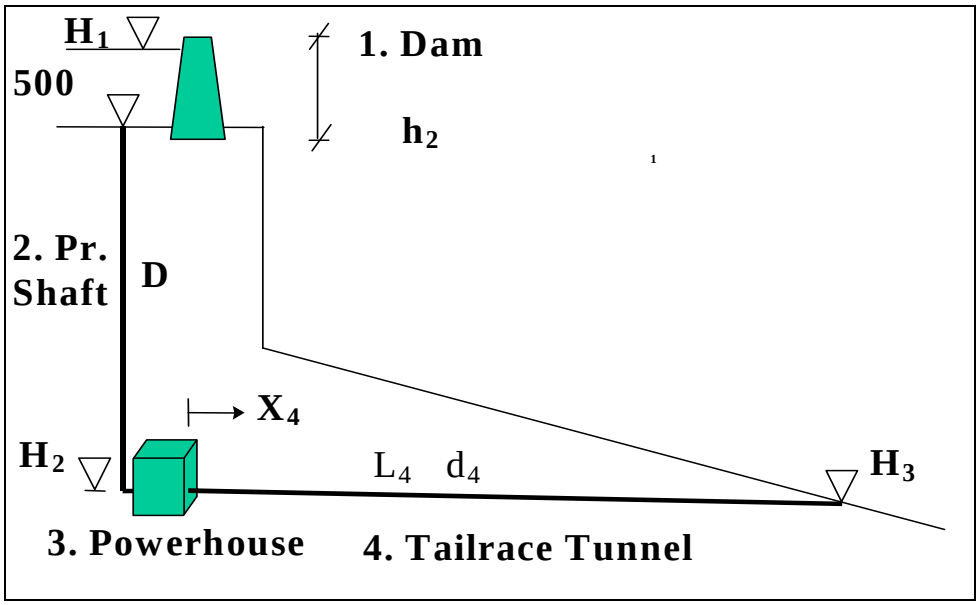

Fig. 1 Simple hydropower plant(Eliasson *et al* 1997[1]).

Table 1. Mathematical solution (bold) compared to optimisation results,

P		50	50	50	50	50	20	20
G		100	100	100	100	100	200	200
μ		0.001	0.005	0.01	0.025	0.05	0.025	0.05
D	**4,0**	4.0	4.0	4.0	3.9	4.0	4.0	3.9
H_1	**543,0**	543	543	543	543	543	543	543
H_2	**48,2**	44	49	49	48	42	50	44
H_3	**44,9**	39	46	46	45	37	46	39
NPV	**28594**	28580	28594	28594	28590	28569	28593	28576
dNPV	-	-14	0	0	-4	-25	-1	-18

The trick in this computation is to select P, G and μ so the optimum is truly found, without spending excessive computertime by selecting P, G and μ too high.
When the results of the optimization are compared with the mathematical solution, it is obvious that the runs where the P, G and μ parameters are optimally tuned reach results very close to the true optimum.

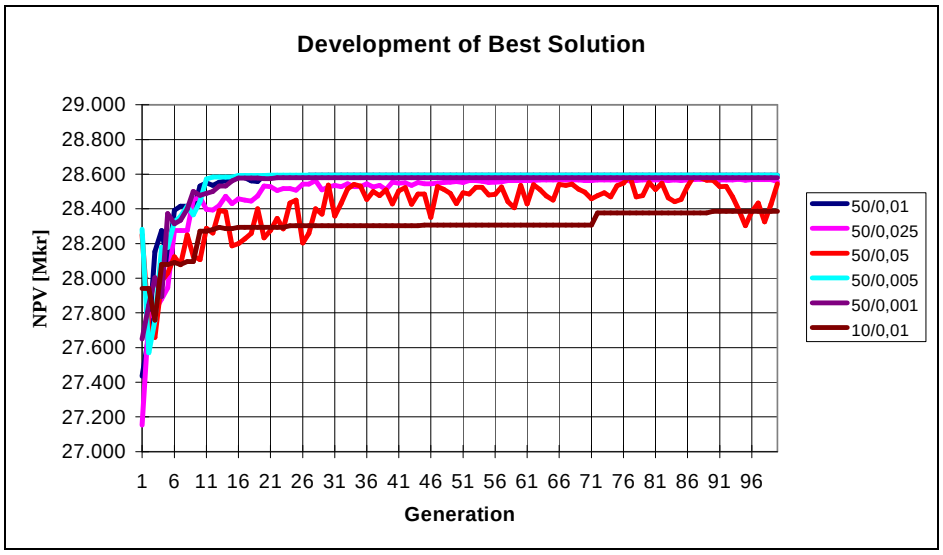

Figure 2. Development of solution for the different parameters in table 1
Eliasson *et al* 1997[1]

The result of the conventional local optimization method is also calculated and it gives an optimum diameter, D, of 4.5 m, which is a 0.5 m difference in the diameter between methods. The conclusion of example 3 is that genetic algorithm is a suitable tool for finding the optimal plant arrangement.

The HYDRA software is a shell that contains program objects that calculate the NPV of all construction elements (Eliasson *et al* 1997[2]). Points that have geographical coordinates connect them and these can be included in the optimization if necessary. Thus tunnel lengths and position of powerhouses can be found, see e.g. the tailrace tunnel in fig. 1 example 3. Here L_4 is optimized.

Experience shows that running times are in the vicinity of 2-4 minutes for very complicated hydropower plants, depending on the size of population and number of generations. G = 2P seems to be a suitable rule and in most cases P = 30 is enough. The suitable m is highly dependent upon P see fig. 1 example 3.

HYDRA has performed very well on very complicated project planning tasks (Eliasson *et al* 1998, Eliasson *et al* 1999[1] and Eliasson *et al* 1999[2]). Fig 3 shows the object diagram in Eliasson *et al* 1999. It is a good example of the complexity that can be handled by the program.

In the beginning all the objects in HYDRA used approximation formulas to calculate the NPV of their respective construction elements. Today cost estimates based on quantities and locally adjusted unit prices for concrete, dam fills, tunnel-driving etc. are used. An exception from this is the powerhouse but here the old formula is still in use. The guidelines for a more advanced powerhouse object have been given in chapter 5 in Eliasson *et al* 1999[1], and this important contribution is by professors Matthias, H. – B. and G., Doujak of Technical University of Vienna. G., Doujak, further elaborates the subject in chapter 4 in Eliasson et al 19992, this time.

To find the profit E has to be calculated. This has to be the expected power output of the station. This calculation has to be performed for each individual in each generation. This is

done by using the load factors derived in (Eliasson 2000). The load factors have to be putted into HYDRA in the beginning of each run. The method to find them is very complicated and will not be repeated here.

Global optimization results, theoretical remarks

Some information is included in the optimization in an implicit manner and has to be extracted by means of theoretical considerations. Lets take a few examples.

In theory, we search for maximum profit in the optimization. We have not considered the average cost of power per kwh the utility can offer the customers. We have only considered a fixed market price but a utility may want to offer cheaper electricity to its customers. What can be done?

Example 5: Average power cost and opportunity cost
For the utility the average power cost is

$$k_0 = \frac{G_a}{E} = \frac{G_a}{T_a / k_e} \cong k_e \frac{G}{T} \Rightarrow k_0 = k_e \frac{G}{G + \kappa H}$$

Here G_a and T_a are annual values in contrast to the NPV's G and T. The factor κ is to take care of that the ratio of annual values is not exactly the same as the ratio of NPV´s. A common value of κ is between 0.9 and 1.1
If we make a series of optimizations for lower and lower sales price k, the profit H will tend to zero and in that limit we get:

$k_o = ke$

Or the average power cost is equal to the unit energy sales price. This is called the break-even price or the opportunity cost price. It is the lowest unit price one can offer for a commodity without loosing money.

Case studies

Skagafjordur Iceland
The scheme is described in (Eliasson *et al* 1998). It consists of a storage reservoir (Austurbugur Storage = AS) and one or two powerhouses downstream. The reservoir is considered to release a fixed discharge to the powerhouse turbines. The discharge is calculated from the project capacity, a load factor of 0.816 is used. Economical benefits are calculated from power sales and surplus capacity that can act as a spinning reserve according to (prices in US dollars):

Primary power	0.03	$/kWh
Spinning reserve	7.14	$/kW/a

The investment cost includes various owner's costs as % of construction costs:

Camp and Mobilisation	6,2 %
Contingencies	20 %
Supervision and Engineering	12,66 %
Preliminary Investigation Cost	2,33 %
Other Owner's Cost	4,18 %
Interest During Construction	17,83 %

Table 2 Various owner's costs

Annual operation and maintenance is 0,8% of the project investment. The interest rate in NPV calculation is 6% and project economic lifetime 40 years.

Eventual use of thermal reserves has the following tariff:

Thermal reserve power	0.06	$ /kWh
Standby thermal reserve	17.14	$/kW/a

The main results of the optimisation compared to Fljotsdalsvirkjun are as follows:

Project	I.c.[1]	Power	Inv.c.[2]	B.e.p.[3]	C.cost[4]	Po.cost	A.stor. (AS)	
	Mw	Gwh/a	M$	$/kwh	M$/Mw	$/kwh/a	m.a.s.l	M m^3
Merkigilsvirkjun	176	1.259	355	0.021	2.01	0.286	708	282
SV / Villinganes	123	879	283	0.024	2.30	0.314	709	179
Giljamúli	103	735	237	0.024	2.30	0.329	704,5	215
Fossárvirkjun	92	655	245	0.028	2.65	0.371	705	223
Fljotsdalsvirkjun	*176*	*1.259*	*328*	*0.019*	*1.86*	*0.257*		

[1]Installed capacity [2]Investment costs [3]Break even price [4]Capacity cost

Table 3 Comparison of project economies

Notice in table 3, that each arrangement gives a different maximum elevation of the Austurbugur storage (AS), which clearly shows that the optimal size of the storage is very much dependent on other parts of the scheme.

Following answers to the principal questions concerning the project were given:

How much power can be economically exploited in the region?

Merkigilsvirkjun gives 176 MW installed capacity with anticipated production of 1259 Gwh/a. This is about 60 % of the technically harnessable potential in the area.

The locations and the dimensions of main construction items.

Main features are a headrace tunnel 46 km long and 4.9 m wide, and a pressure shaft 366 m deep and 2.7 m wide.

What is the construction cost of the respective power stations.

The construction costs are 2.0 – 2.3 M$/Mw, a very competitive price.

How does the economy of individual projects compare to Fljotsdalsvirkjun. Skagafjoerdur hydro is 10 – 20% more expensive than the Fljotsdalur project.

What further field investigations will be necessary

This is as follows:

- More information is needed on the effect of rhyolite on tunnelling conditions.
- Unmapped spots on Nyjabaejarfjall and west of the junction of the Austari Joekulsa river and the Vestari Joekulsa river need to be mapped.
- Streams flowing from the Nyjabaejarfjall area to Austari Joekulsa have to be gauged and their discharge estimated.
- Environmental investigations need to be started as soon as possible.

The last point is because this hydropower potential is indeed very attractive so eventual adverse effects of the exploitation on the environment have to be uncovered as quickly as possible.

It is remarkable that the most economical project is the Merkigilsvirkjun project. From this we can draw the inference that field investigations in the Merkigilsvirkjun area, that is in the eastern part of the Skagafjoerdur catchment, have to be given high priority.

Fljotsdalur

This example is taken from (Eliasson *et al* 1997 and 1999[1] and 1999[2]).

Table 4. Premliminary optimisation 1997

Description		PPR_1	PPR_2	O_{1150}	O_∞
Reservoir level	m.a.s.l.	664.5	668.5	665.1	667.6
Headrace tunnel dia.	m	5.0	5.0	4.3	4.8
Pressure shaft dia.	m	2.9	2.9	2.6	2.7
Power	MW	213	239	211	233
Energy	GWh/a	1159	1300	1150	1278
Investment	BIKR	21.16	22.91	19.92	21.96
Profit	BIKR	10.90	13.44	12.28	13.86
ΔProfit/ΔInvestment	% / %	0/0	+23/+8	+13/-6	+27/+4

Optimised dimensions are bold faced. 60 BIKR ≅ 1 billion $ in 1997

The O_{1150} optimisation seeks a slightly higher dam (increased discharge to the plant) to compensate for increased power losses in narrower conduits.

The O_∞ optimisation results in a significantly higher dam compared to the PPR_1. The explanation is that in the project planning report, the size of the power plant and the size of reservoir is selected on basis of a power market scenario at the expected construction time of the plant, but the optimisation assumes infinite demand. The solution is however not far from the PPR_2 arrangement.

The global optimisation O_{1150}, leads to a 0,7 m narrower headrace tunnel compared to the PPR. Local optimisation, considering only variable cost of the headrace, leads to the same result as in the PPR (5 m). The power capacity reduction due to increased headlosses, is compensated with a slightly larger reservoir (increased discharge).

The O_∞ optimisation results in a slightly smaller headrace diameter compared to the PPR. It is quite natural when compared to O_{1150}, that this optimisation seeks a larger tunnel, because there are no market restrictions.

The same logic can be used to explain the difference in the pressure shaft diameter. There is, however, a problem with the maximum velocity in the shaft. In both optimisations the diameter breaks the design criteria that the maximum velocity should be below 8 m/s. For both O_{1150} and O_∞, the minimum diameter that satisfies this constraint should be selected by the user, in both cases close to d = 2,8 m, depending on design discharge. This has a minor economical significance in this case, but is however a good example of how dependent constraints $g(x, y) \geq 0$ have to be considered in the future development. The way to handle this is to develop and add a penalty function, $\Phi(x)$, to the construction cost of the pressure tunnel type object (and other objects where necessary), that 'penalizes' the tunnel if it's water velocity exceeds the allowed value but is otherwise zero. This prevents the Genetic Algorithm from breaking this constraint.

The O_∞ optimisation results in a larger energy output than in the PPR_1. This is natural, as this optimisation assumes plant stage, which means no market restrictions and no extra benefit for the system. The extra benefit is that interactions between Fljótsdalur Power Plant and the existing power system produces substantial extra energy (estimated 250 GWh/a firm energy in the PPR) through better utilisation of the water resources.

The project investment is 6% lower in optimisation O_{1150} compared to the PPR_1, resulting in a 13% higher profit, which is a significant improvement. The optimisation O_∞ on the other hand leads to a 4% higher investment and a 27% higher profit. When it is kept in mind that the

PPR_1 plans a future raising of the dam to reservoir level 668,5 m.a.s.l (Fljótsdalur Engineering Joint Venture 1991), the result of O_∞ is very close to the PPR_2 version.
In order to ensure the best possible result in the global optimisation the cost estimation of the whole scheme is completely revised. The VOS construction cost functions are removed and replaced with new cost functions, specially prepared by the engineering consultants (Helgason, pers. comm.).
Now similar runs as for the Plant Stage are performed. The results are presented in table 5.

Table 6. Tabulation of significant data and net profit of the investment
(optimised dimensions are bold faced). 60 BIKR ≅ 1 billion $

Description		PPR_1	PPR_2	O_{1150}	O_∞
Reservoir level	m.a.s.l.	664.5	668.5	665.1	669.6
Headrace tunnel dia.	m	5.0	5.0	4.3	5.3
Pressure shaft dia.	m	2.9	2.9	2.6	2.8
Power	MW	212	239	210	242
Energy	GWh/a	1159	1300	1149	1325
Investment	BIKR	22.78	24.40	22.18	24.91
Profit	BIKR	9.36	11.78	9.72	11.97
ΔProfit/ΔInvestment	% / %	0/0	+26/+7	+4/-3	+28/+9

The O_{1150} optimisation leads to a similar arrangements as the plant stage optimisation. The O_∞ however shows significant changes. This is because the new cost formulas do not represent the true variation of the costs except in a narrow region around the PPR_1 values. Therefore the results of the O_∞ optimisation are hardly applicable. However a comparison of the columns O_∞ in Tables 4 and 5, shows how important it is that the cost formulas in the optimisation are accurate. It may therefore be concluded that it is worth the effort for the consultants, to take the time and trouble to have the cost formulas in Hydra improved with formulas specially designed by themselves, in order to improve the accuracy of optimisations performed.
The economical result is of course dominated by the overall increase in the construction cost, compared to the plant stage, which leads to a considerable decrease in the profit, probably meaning considerable decrease in the profit margin of venture capital.

References

Eliasson, J., Jensson, P. and Ludvigsson, G.; *Opimal design of Hydropower plants; in Hydropower 97*, Broch, Lysne, Flatabo and Helland-Hansen (eds), Balkema, Rotterdam.; 1997.

Eliasson, J., Jensson, P. and Ludvigsson, G.; *Software to optimise of Hydropower Plants Design*; Daniel J. Mahony (ed) WATERPOWER'97 Proceedings of the International Conference on Hydropower, Georgia World Congress Center Atlanta, Georgia Aug. 5 – 8. 1997 pp. 1673 - 1683, ASCE N.Y. 1; 1997.

Eliasson, J., Jensson, P., Ludvigsson, G., Tomasson H. & Bjarnason H.; *A proposal to exploit optimally the hydropower potential of Skagafjoerdur Iceland*; Hydrovision '98, Reno, Nevada USA; 1998.

Eliasson, J., Ludvigsson, G., Doujak, E., Ólsen, A. and Matthias, H. – B.*; A proposal to exploit optimally the hydropower of Fljotsdalur Iceland*, Waterpower 99 Conference, Las Vegas, Nevada, USA, July 7 – 9, 1999[1], (Published by ASCE on a CD-ROM ISBN 0-7844-0440-2)

Eliasson, J., Ludvigsson, G., Doujak,; *Global Optimisation of Hydropower Plants;* International Hydropower & Dams Conference: Hydropower into the next century, Gmunden, Austria 18-20 October 1999[2]

Eliasson, J., *Load factors of hydropower plants and its importance in planning and design.* 11th seminar on hydropower plants Nov. 15 – 17 2000, Tech. Univ. Vienna (Accepted for presentation Aug. 2000)

Goldberg, D. E. (1989). *Genetic Algorithms in Search Optimization & Machine Learning.* Addison-Wesley.

Mosonyi, E. (1991). *High-Head Power Plants Volume Two/A & Two/B. Akadémiai Kiadó*, Budapest.

ACAUSAL MODELING AND SIMULATION OF THE STANDALONE SOLAR POWER SYSTEMS AS HYBRID DAEs

Arash M. Dizqah*[1], Krishna Busawon[1] and Peter Fritzson[2]

[1]School of Computing, Engineering and Information Sciences , Northumbria University, NE1 8ST Newcastle Upon Tyne, UK

[2]PELAB Programming Environment Lab, Dep. Computer Science , Linköping University, SE-581 83 Linköping, Sweden

***Abstract*—Due to the presence of algebraic constraints as well as existing of different modes of operation, a standalone solar power system consisting of photovoltaic arrays, battery bank, electrical load, and a converter is becoming a complex system that can no longer be modeled using the conventional block diagram approach. While the block diagram approach is based on causal interactions between a chain of the ordinary differential equations (ODE), a more appropriate acausal approach solves a flat model of the system consisting of hybrid differential algebraic equations (HDAE). In effect, this paper proposes a nonlinear HDAE-based model of a standalone solar power system. The proposed model is presented using the Modelica language that allows object-oriented and acausal modeling of the multi-mode systems. Next, a general purpose solver is employed to simulate the system. The results of the simulation shows proper match with the information available in the components datasheet. It is shown that the simulation provides a sufficiently accurate prediction of all the system behaviors, which is vital for any model-based controller, including mode transitions.**

***Index Terms*—hybrid DAE; photovoltaic (PV); battery; boost-type DC-DC converter; Modelica; acausal modeling; standalone solar power.**

I. INTRODUCTION

ADVANCES in photovoltaic (PV) technologies during the last decade have increased the share of the solar energy in the growing electricity market. The PV modules are nonlinear and complex still very popular components since they are easy to install and operate. A conventional solar power system employs an array of PV modules as a generator to supply DC, AC, or mixed electrical load demands. It consists of a converter that normally boosts up the generated DC voltage to match the load characteristics. This converter is equipped with a maximum power point tracker (MPPT) to harvest the maximum available power. The system may optionally consist of an inverter for being connected to AC loads or the grid. Moreover, it consists of a battery bank to overcome the power fluctuation that is the result of the uncertainty in the solar irradiance. The battery also provides a constant voltage bus, which is essential for the MPPT algorithm. Although the voltage changes with regard to the amount of the current as well as the state of the charge (SOC) of the battery, it can be assumed constant during the time that the MPPT calculates the operating point. Figure 1 illustrates the topology of the standalone solar power system selected in this study.

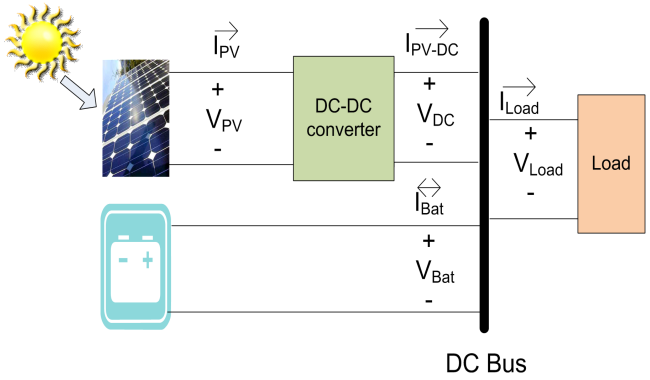

Fig. 1. HRES topology in this study.

In order to study the behavior of the solar power system as well as to design model-based controllers, it is essential to model and simulate the system accurately. However, there are two major challenges, namely, the algebraic constraints introduced by the PV module and the battery, and the multi-mode operation of the battery. Altas and Sharaf [1] used the simplification techniques introduced by Buresch [2] as well as and simulate the solar power system consisting of a PV module. Since the Simulink basic components, which provide classical block diagram simulation approach, does not support algebraic states, they introduced a weak dynamic as a short transport delay to their model. Villalva, Gazoli and Filho [3] proposed two simulation scenarios based on equivalent electrical circuits, to simulate the PV module. The proposed scenarios in [3] employ the SimPowerSystems that is one of the Simulink toolboxes for acausal simulation to overcome the algebraic loop introduced by the PV module. The acausal simulation needs the system to be modeled as differential algebraic equations (DAE). Petcut and Dragomir [4] introduced a first-order differential equation associated to the original algebraic equation of the PV module.

*Corresponding author. Email address: arash.moradinegade@northumbria.ac.uk

associated to the original algebraic equation of the PV module.

They proved that the equilibrium point of this differential equation and the solution of the algebraic equation are exactly the same. Introducing this differential equation, they modeled and simulated a PV module with Simulink basic components. Carrero, Amador, and Arnaltes [5] simply fed back the output current of the PV module that introduces algebraic loop. Guasch and Silvestre [6] proposed a comprehensive model for lead-acid batteries along with an equivalent electrical circuit appropriate for simulation. However, their model needs an acausal approach to be simulated because of proposed algebraic loops. Moreover, they introduced a linear interpolation to simulate the mode transition period without considering it as a multi-mode (or in general hybrid) system. Tremblay and Dessaint [7] employed the Simulink SimPowerSystems toolbox to propose an acausal simulation of the lead-acid battery.

Due to the presence of algebraic constraints, the standalone solar power system cannot be decomposed into a chain of blocks with causal interaction and it requires being simulated employing an acausal approach [8]. Moreover, the different modes of operation introduced by battery cause discontinuity points in overall system mathematical model and classify it as an hybrid system [9]. In this paper, a mathematical model of the standalone solar power system is proposed as HDAEs. The Modelica is employed to create an acausal model of the system and the developed model is solved using a general purpose solver. The results of the simulation have been compared with information available in the PV and the battery datasheets provided by the manufacturers that indicate good accuracy.

An outline of the paper is as follows: In the next section, the mathematical models of the system components are presented. Section 3 provides the employed simulation method as well as an overview of the developed Modelica model. The results and their validations are discussed in Section 4. Finally, Section 5 presents a conclusion of the study.

II. SOLAR POWER SYSTEM MATHEMATICAL MODEL

A. PV module and PV array

A PV cell is a P-N junction that is typically modeled with an equivalent electrical circuit [10]. Fig. 2 illustrates a single-diode equivalent electrical circuit of a PV cell, which is also applicable to model a PV module. The PV module consists of several PV cells connected together in series. A PV array, which is a combination of several photovoltaic modules in series and parallel arrangement, can be modeled with the same circuit, too. There are six electrical parameters in this model, namely, the stray capacity C that can be neglected, the ideality factor of the diode n_D, the photocurrent I_{ph}, the reverse saturation current of the diode I_0, the series resistor R_s, and the shunt resistor R_{sh}. While the series resistor R_s is the sum of structural resistances, the shunt resistor R_{sh} represents the leakage current [11]. There are prior researches to estimate the electrical parameters from the PV module information available in datasheet [3], [11], [12]. Through this study, it is assumed that the equivalent electrical circuit of the PV module has already been identified using one of these methods. In Fig.

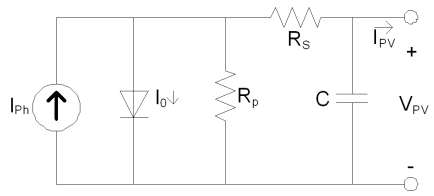

Fig. 2. The single-diode equivalent electrical circuit of a PV module.

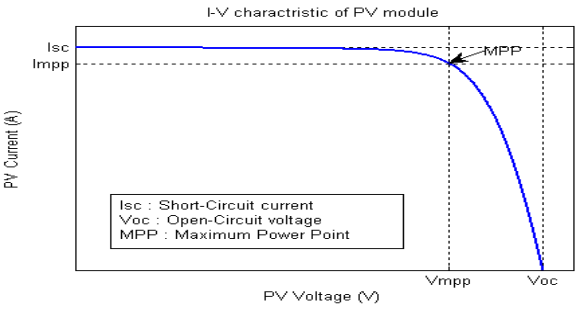

Fig. 3. The $I-V$ curve of the PV module for the STC.

2, applying the Kirchhoff current law (KCL) to the junction point of these two resistors gives the characteristic equation of the PV module, which is a nonlinear transcendental equation, as follows:

$$I_{pv} = I_{ph} - I_0 \left\{ exp(\frac{V_{pv} + R_s I_{pv}}{n_d N_s} \frac{q}{K T_c}) - 1 \right\} - \frac{V_{pv} + R_s I_{pv}}{R_{sh}}. \quad (1)$$

where V_{pv} and I_{pv} are, respectively, the output voltage and current of the PV module and all other symbols are defined as follows:

q	The electron charge (1.6021810^-19)
K	The Boltzman constant (1.3806610^-23)
N_s	The number of the PV cells in series as the PV module (-)
T_c	The current amount of the PV cell temperature (K)

The photocurrent I_{ph} and the reverse saturation current of the diode I_0 are calculated with (2) and (3) based on available parameters in the datasheets and the estimated electrical parameters [3], [13]. The performance of different PV modules are measured at a standard test condition (STC), which is defined as follows:

- The cell temperature of $25C$
- The Global solar irradiance of $1000(W/m^2)$
- Air Mass of 1.5

Fig. 3 shows the PV current-voltage $(I-V)$ curve indicating the maximum power point (MPP). The MPP varies due to changes in operating conditions (i.e. the solar irradiance and the cell temperature) and requires being followed by a MPPT algorithm.

$$I_{sc} = \left(\frac{R_s + R_{sh}}{R_{sh}} I_{sc,stc} + k_I \left(T_c - T_{c,stc} \right) \right) \frac{S}{S_{stc}}. \quad (2)$$

$$I_0 = \frac{I_{sc,stc} + k_I\,(T_c - T_{c,stc})}{\exp(\frac{V_{oc,stc} + k_V\,(T_c - T_{c,stc})}{n_d N_s}\frac{q}{KT_c}) - 1}. \quad (3)$$

where:

$I_{sc,stc}$	The short-circuit current of the PV module at the STC (A)
k_I	The temperature coefficient of the short-circuit current (A/C)
k_V	The temperature coefficient of the open-circuit voltage (V/C)
S	The current amount of the solar irradiance (W/m)
S_{stc}	The amount of the solar irradiance for the STC (W/m)
$T_{c,stc}$	The amount of the cell temperature at the STC (K)
$V_{oc,stc}$	The open-circuit voltage of the PV module at the STC (V)

The PV array of the solar power system introduces an algebraic nonlinear constraints between V_{PV} and I_{PV}, i.e., none of these variables are among degrees of freedom and the former is an algebraic state.

B. Boost-Type DC-DC converter

The boost-type DC-DC converter is one of the converter options which is implemented based on the switching-mode circuit technology containing at least one energy storage and two semiconductor switches. However, in the ideal case a single-pole double-throw switch can be used. Figure 4 illustrates the electrical circuit for a boost-type DC-DC converter with an ideal switch.

Middlebrook and Cuk [14] proposed a state-space averaging approach to model the boost-type DC-DC converter. They suggested two i_L and v_C states for the continuous conduction mode (CCM) in which the instantaneous inductor current is always greater than zero. According to the proposed approach there is a state-space system for the converter at each state of the switch and the overall state-space model is the weighted average of these two models. The weighting factor is switching duty-cycle (D) as the only manipulating control signal. The switching duty-cycle is the duration of time that the circuit remains in each state. Equations (4) and (5) provide the average model of the boost-type DC-DC converter using ideal switch and diode.

$$\begin{bmatrix} \dot{i_L}(t) \\ \dot{v_C}(t) \end{bmatrix} = \begin{bmatrix} -\frac{R_L}{L} - \frac{R_C(1-D)}{L(1+\frac{R_C}{R})} & -\frac{1-D}{L(1+\frac{R_C}{R})} \\ \frac{1-D}{C(1+\frac{R_C}{R})} & -\frac{1}{RC(1+\frac{R_C}{R})} \end{bmatrix} \times \begin{bmatrix} i_L(t) \\ v_C(t) \end{bmatrix} + \begin{bmatrix} \frac{1}{L} \\ 0 \end{bmatrix} V_{in}(t). \quad (4)$$

$$V_{out}(t) = \begin{bmatrix} \frac{R_C(1-D)}{1+\frac{R_C}{R}} & \frac{1}{1+\frac{R_C}{R}} \end{bmatrix} \begin{bmatrix} i_L(t) \\ v_C(t) \end{bmatrix}. \quad (5)$$

C. Lead-acid battery

There are different types of batteries applicable for backup/storage of the solar power system. The authors in [15] [16] presented a comprehensive reviews and comparisons of different battery technologies for the renewable energy applications. The battery introduces an algebraic constraint between

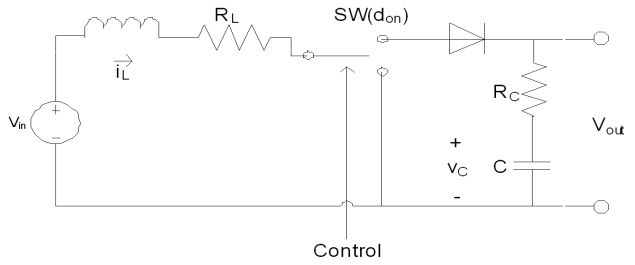

Fig. 4. The electrical circuit of the boost-type DC-DC converter with an ideal switch.

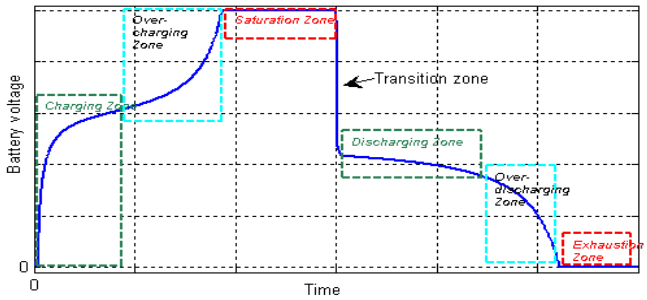

Fig. 5. Different working zones of the lead-acid batteries.

V_{bat} and I_{bat} where the former is an algebraic state. Fig. 5 illustrates a complete operating cycle of the battery starting from the charging zone up to completely being discharged, i.e., the exhaustion zone [6]. In Fig. 5, it can be seen that the battery is a multi-mode component introducing discontinuity to the system. Tremblay and Dessaint [7] proposed an equivalent electrical circuit (Fig. 6) as well as the following hybrid mathematical presenting two modes of operation, namely, charging, and discharging:

$$V_{bat} = \begin{cases} V_0 - RI_{bat} + V_{exp} - \frac{P_1 C_{max}}{C_{max} - charge} charge - \frac{P_1 C_{max}}{charge + 0.1 C_{max}} I_{bat} & \text{mode=charging,} \\ V_0 - RI_{bat} + V_{exp} + \frac{P_1 C_{max}}{charge - C_{max}} charge + \frac{P_1 C_{max}}{charge - C_{max}} I_{bat} & \text{mode=discharging.} \end{cases} \quad (6)$$

$$mode = \begin{cases} charging & I_{bat} \le 0, \\ discharging & I_{bat} > 0. \end{cases} \quad (7)$$

$$\frac{dcharge}{dt}(t) = \quad (8)$$

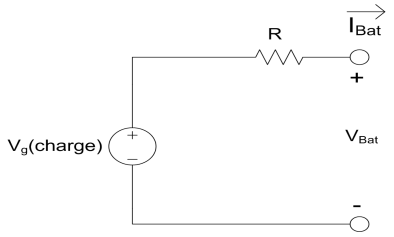

Fig. 6. The equivalent electrical circuit for the lead-acid battery.

$$\frac{\mathrm{d}V_{exp}}{\mathrm{d}t}(t) = \begin{cases} \frac{P_2}{3600}|I_{bat}|(P_3 - V_{exp}) & \text{mode=charging,} \\ -\frac{P_2}{3600}|I_{bat}|V_{exp} & \text{mode=discharging.} \end{cases} \quad (9)$$

where V_{bat} and I_{bat} are the voltage and the current of the battery, respectively. The parameters P_1-P_3 are the experimental parameters requires being identified for each type of the battery and V_{exp} (V) models the exponential behavior of the battery voltage during the mode transition period. While the current direction varies instantaneously, the voltage of the battery changes with an exponential factor after the mode transition. The C_{max} is the maximum amount of the battery capacity (Ah), R is the internal resistor of the battery (Ω), $charge$ (Ah) is the actual battery capacity, and V_0 is the battery constant voltage (V).

III. SIMULATION

According to the block diagram approach for modeling and simulation, the system is decomposed into distinguished blocks with causal interactions. In a sequential procedure starting from the first block through all others, the simulator calculates output values with respect to the inputs and then feeds the outputs to the next block as their input variables. Although it is a straightforward approach, it still suffers from several drawbacks. In order to decompose a system into a chain of causal interacting blocks, the system must have just the differential states coupled with algebraic equations to calculate the outputs. In other words, it must be a system of ordinary differential equations (ODE) and any algebraic equation has to calculate only an algebraic variable that is a degree of freedom. However, most of the electrical and mechanical systems introduce algebraic states. An algebraic state is a state of the system which is restricted with an algebraic equation. Any system consisting of algebraic states, which are modeled with DAEs rather than ODEs, requires being simulated employing an acausal approach.

Despite a causal model which expresses an algorithm to calculate the variables, the acausal modeling is a declarative approach in which individual parts of the model are directly described as equations that are in general HDAEs. An HDAE represents both continuous-time (either differential or algebraic) and discrete-time behaviors [9]. Although there are general purpose numerical HDAE solvers such as tools in [17],[18],[19], the acausal modeling still needs to be described with a programming language. Modelica [20], which is an object-oriented and equation-based language providing the capability to model the hybrid systems [21], is an option to describe complex systems using an acausal approach. Among a number of available implementations of the Modelica compiler, the OpenModelica platform [22] has been selected for this study chiefly because it supports more features of the Modelica language comparing with the others. The platform translates the Modelica descriptions into a flat model in the form of HDAEs, then generates C or XML code from the flat model. The compiled model is simulated using the integrated DASSL that is a general purpose HDAE solver [19].

TABLE I
THE FIRST PLANE OF THE MODELICA CODES MODELING THE SOLAR POWER SYSTEM.

```
model HRES_SolarSystem
  Modelica.Blocks.Sources.Constant Sx(k = 300.0);
  Modelica.Blocks.Sources.Constant Tx(k = 298.15);
  Modelica.Electrical.Analog.Basic.Ground ground;
  HRES.PVArray pvarray(Npvp = 10);
  Modelica.Blocks.Sources.TimeTable DutyCycle(table = [...]);
  Modelica.Blocks.Sources.Step ramp(startTime = 5, offset = 10,
height = -6);
  Modelica.Electrical.Analog.Basic.VariableResistor load;
  HRES.BoostConverter converter(Rl = 0.001, Rc = 0.3, L = 0.0005,
C = 0.005);
  HRES.LeadAcidBattery battery1;
  HRES.LeadAcidBattery battery2;
  HRES.LeadAcidBattery battery3;
  HRES.LeadAcidBattery battery4;
equation
  connect(Tx.y,pvarray.Tx);
  connect(Sx.y,pvarray.Sx);
  connect(pvarray.n,ground.p);
  connect(pvarray.p,converter.p1);
  connect(converter.n1,ground.p);
  connect(converter.n2,ground.p);
  connect(DutyCycle.y,converter.D);
  connect(converter.p2,load.p);
  connect(ramp.y,load.R);
  connect(load.n,ground.p);
  connect(converter.p2,battery1.p);
  connect(battery1.n,battery2.p);
  connect(battery2.n,battery3.p);
  connect(battery3.n,battery4.p);
  connect(battery4.n,ground.p);
end HRES_SolarSystem;
```

Table I shows the first plane of the developed Modelica codes that models the standalone solar power system. From Table I, it can be seen that the proposed model consists of a PV array connected to a resistive load through a converter. A battery bank including four lead-acid batteries is employed to prevent power fluctuations. All these components are also modeled as separate classes of the Modelica language. For instance, Table II summaries such a model for the lead-acid battery and its multi-mode operation.

TABLE II
A SUMMARY OF THE LEAD-ACID BATTERY MODELICA CLASS.

```
class LeadAcidBattery
  ...
equation
  chargeState = if noEvent(ibat ≤ 0) then true else false;
  der(charge) = 1/3600 * ibat;
  der(Vexp) = if chargeState then
    P2/3600 * abs(i) * (P3 − Vexp)
    else −(P2 * abs(i))/3600 * Vexp;
  when change(chargeState) and pre(chargeState) then
    tmp = if not chargeState then
      pre(vbat) − V0 − R * pre(ibat)−
      (P6 * Cmax)/(Cmax − pre(charge)) * pre(charge)−
      (P6 * Cmax)/(pre(charge) + 0.1 * Cmax) * pre(ibat)
      else 0;
    reinit(Vexp, tmp);
  end when;
  soc = 1 − charge/Cmax;
  vbat = if chargeState then
    V0 − R*ibat − (P1*Cmax)/(Cmax − charge)*charge−
    (P1 * Cmax)/(charge + 0.1 * Cmax) * ibat + Vexp
    else V0−R*ibat−(P1*Cmax)/(Cmax−charge)*charge−
    (P1 * Cmax)/(Cmax − charge) * ibat + Vexp;
end LeadAcidBattery;
```

IV. RESULTS, VALIDATION, AND DISCUSSION

The proposed model is used to simulate a solar power system consisting of an array of the Kyocera KC200GT PV modules [23] and a bank of the Panasonic LC-R127R2PG lead-acid batteries [24]. The authors in [3] and [7], respectively, presented the identified electrical parameters of the PV module and the lead-acid battery that are used in this study.

Fig. 7 shows the simulated current-voltage ($I-V$) and power-voltage ($P-V$) curves of the KC200GT PV module at the STC condition.It is observed that the proposed model predicts the curve very close to the empirical data provided by the manufacturer (the circle markers). The simulated MPP is in the same position of the experimental point as well.

Fig. 8 illustrates the simulation results of the LC-R127R2PG lead-acid battery [24] for a full cycle as in Fig. 5 that is a cycle of charging, over-charging, saturation, discharging, over-discharging, and exhaustion zones. While the battery is being charged for 100 minutes, it is discharged afterward. It also indicates that after 25 minutes it enters into the over-charging zone. Discharging with the current of $7.2A$ in average, it takes around 35 minutes for the battery, which matches with the information available in datasheet [24], to reach the cut-off voltage that is around $10.2V$.

The solar power system is simulated using the proposed model for the following scenario:

- Simulation duration is 10 minutes.
- The solar irradiance is $1000W/m^2$ and the cell temperature is $25°C$.
- The PV array consists of 10 connected KC200GT PV modules. The load demand suddenly increases to more than the

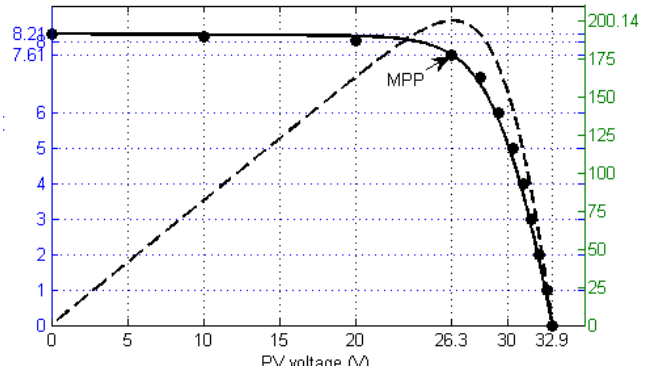

Fig. 7. The simulated current-voltage curve of the KC200GT PV module at the STC.

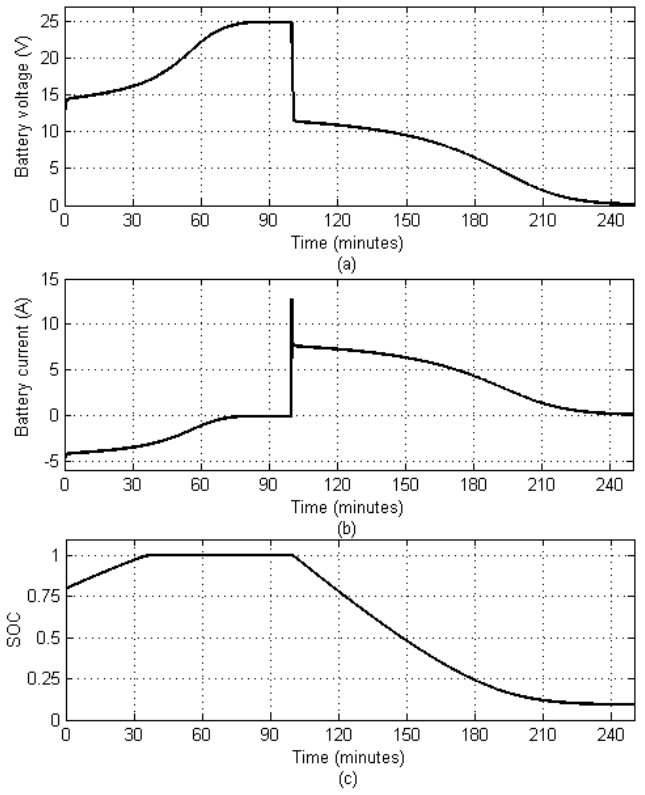

Fig. 8. The simulated (a) battery voltage, (b) battery current, and (c) the SOC of the battery.

modules in parallel arrangement.
- The battery bank consists of 4 connected LC-R127R2PG lead-acid batteries in series arrangement.
- The manipulating control signal changes according to a stepwise pattern.
- The load demand suddenly increases at t = 5.
- After 6 minutes the generated power by the PV array declines.

In Fig. 9, it can be seen that the battery absorbs excess energy when there is and provides the deficit energy when the PV module cannot provide adequate energy. For the first 5 minutes, the generated power is more than load demand and the battery, which absorbs the excess energy, is in charging

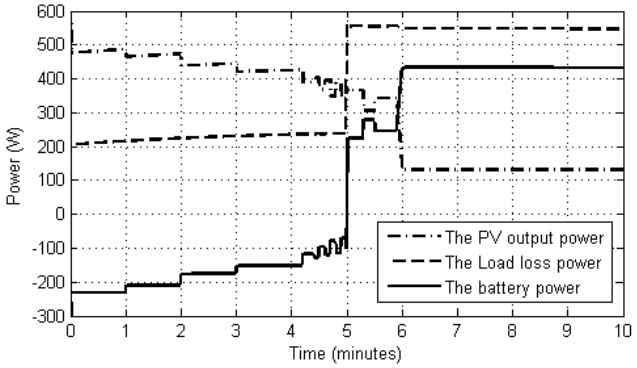

Fig. 9. The simulated battery, load, and PV powers.

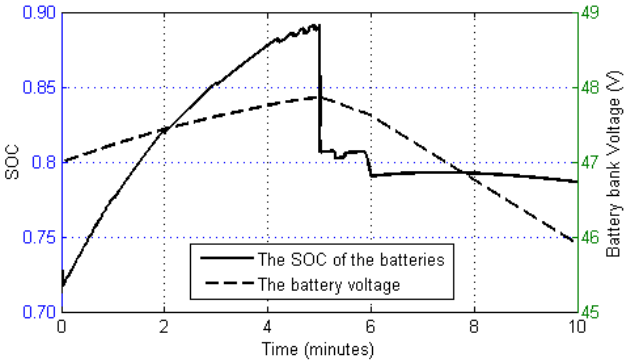

Fig. 10. The simulated SOC and the voltage of battery bank.

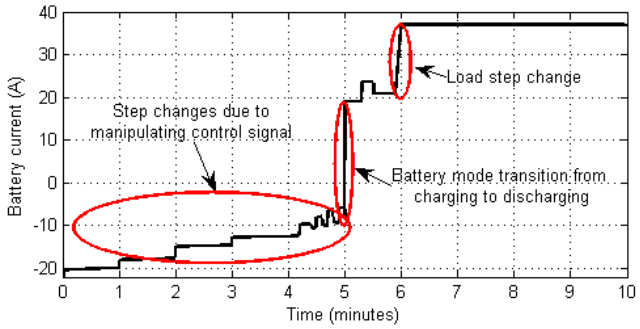

Fig. 11. The simulated battery current.

generated power at $t = 5$ minutes that switches the state of the battery, which now provides the deficit energy, to the discharging mode. At $t = 6$ minutes the battery provides more power because the generated power by the PV array declines even less due to manipulating of the control signal. Fig. 9 illustrates a power loss of around 10% in the DC-DC converter, which is the difference of the power generated by the PV array and the sum of the load and the battery powers, chiefly because of the internal resistance of the coil.

Fig. 10 illustrates the details of battery bank. It is observed that during the period of charging of the battery bank ($time < 5$ minutes), the voltage and the SOC of the battery bank increase continuously. However, the voltage of the battery suddenly falls at $t = 5$ minutes to the nominal value by the transition from charging mode to discharging mode. There is another step change at $t = 6$ minutes as the result of decreasing the generated power by the PV array (Fig. 9). The SOC also declines moderately after $t = 5$ minutes since the battery is being discharged.

Finally, Fig. 11 depicts the variation of the battery bank current during the simulation period. While it is less than zero, which means the battery bank is in charging mode, before the $time = 5$ minutes, it suddenly becomes greater than zero after entering in the discharging mode. The small step changes are due to variation in the control signal causing changes in the harvested energy from the PV array. A load demand increase at $t = 6$ minutes causes a sharp climb of the battery bank current that matches the power variation in Fig. 9.

V. CONCLUSION

This paper proposes an acausal model, which is based on the HDAE, to simulate the solar power system. The proposed model presents the nonlinear algebraic constraints, which are introduced by the PV array and the battery, as DAEs. Moreover, it models different modes of the battery operation as a hybrid system. The Modelica language is employed to describe the system as an acausal model organized as separate Modelica classes for different components. The OpenModelica environment as an integrated modeling and simulation Modelica tool-set is used to simulate the system with the DASSL general purpose integrator. The PV array and the lead-acid battery bank are separately simulated and validated with information available in datasheets that show very good accuracy. The whole solar power system is also simulated and discussed thoroughly indicating accurate prediction of all the system behaviors including mode transitions. The highest level Modelica codes as well as a summary of the battery Modelica class are presented.

VI. ACKNOWLEDGMENT

The authors would like to thank the Synchron Technology Ltd. company for their partial financial support of this research.

REFERENCES

[1] I. H. Altas, and A. M. Sharaf. A photovoltaic array simulation model for matlab-simulink GUI environment. In *Proc. Intl. Conf. Clean Elect. Power (ICCEP)*, pages 341–345, 2007.

[2] M. Buresch. *Photovoltaic Energy Systems Design and Installation*. McGraw-Hill, New York, 1983.

[3] M. G. Villalva, J. R. Gazoli, and E. R. Filho. Comprehensive approach to modeling and simulation of photovoltaic arrays. *IEEE Transactions on Power Electronics*, 24:1198–1208, 2009.

[4] F. M. Petcut, and T. L. Dragomir. Solar cell parameter identification using genetic algorithms. *Journal of Control Engineering and Applied Informatics*, 12:30–37, 2010.

[5] C. Carrero, J. Amador, and S. Arnaltes. A single procedure for helping PV designers to select silicon PV

modules and evaluate the loss resistances. *Journal of Renewable Energy*, 32:2579–2589, 2007.

[6] D. Guasch, and S. Silvestre. Dynamic battery model for photovoltaic applications. *Progress in Photovoltaics: Research and Applications*, 11:193–206, 2003.

[7] O. Tremblay ,and L. Dessaint. Experimental validation of a battery dynamic model for ev applications. *World Electric Vehicle Journal*, 3:10–15, 2009.

[8] M. Najafi,and R. Nikoukhah. Modeling and simulation of differential equations in scicos. In The Modelica Association, editor, *Modelica Conference*, 2006.

[9] H. Lundvall, P. Fritzson, and B. Bachmann. Event handling in the openmodelica compiler and runtime system. In *the 46th Conference on Simulation and Modeling (SIMS 2005)*, Trondheim, Norway, 2005.

[10] M. K. Deshmukh, and S. S. Deshmukh. Modelling of hybrid renewable energy system. *Renewable And Sustainable Energy Reviews*, 12:235–249, 2008.

[11] J. J. Soon, and K. S. Low. Photovoltaic model identification using particle swarm optimization with inverse barrier constraints. *IEEE Transactions on Power Electronics*, 27:3975–3983, 2012.

[12] K. Ishaque, Z. Salam, and H. Taheri. Simple, fast and accurate two-diode model for photovoltaic modules. *Journal of Solar Energy Materials and Solar Cells*, 95:586–594, 2011.

[13] Q. Kou, S. A. Klein, and W. A. Beckman. A method for estimating the long-term performance of direct-coupled PV pumping systems. *Journal of Solar Energy*, 64:33–40, 1998.

[14] R. D. Middledbrook,and S. Cuk. A general unified approach to modelling switching-converter power stages. In *Proc. of IEEE Power Electronics Specialist conference*, 1976.

[15] M. Beaudin, H. Zareipour, A. Schellenberglabe, and W. Rosehart. Energy storage for mitigating the variability of renewable electricity sources: An updated review. *Energy for Sustainable Development*, 14:302–314, 2010.

[16] K. C. Divya, and J. Ostergaard. Battery energy storage technology for power systems an overview. *Electric Power Systems Research*, 79:511–520, 2009.

[17] SUNDIALS. Suite of nonlinear and differential/algebraic equation solver. https://computation.llnl.gov/casc/sundials/.

[18] DAETS. Defferential-algebraic equations by taylor series. www.cas.mcmaster.ca/ nedialk/dates/.

[19] DASSL. Defferential algebraic system solver. www.cs.ucsb.edu/ cse/.

[20] Modelica. Modelica association. www.modelica.org.

[21] P. Fritzson. *Introduction to modelling and Simulation of Technical and Physical Systems with Modelica*. John Wiley & Sons, New York, 2011.

[22] OpenModelica. Open-source modelica-based modeling and simulation env. www.openmodelica.org.

[23] Kyocera. KC200GT, high efficiency multicrystal photovoltaic module. www.kyocerasolar.com/assets/001/5195.pdf, 2012.

[24] Panasonic. LC-R127R2PG, panasonic batteries. www.farnell.com/datasheets/1624915.pdf.

Design of new hydroelectric power projects in Iceland

The design of new hydroelectric projects at Landsvirkjun is aided by simulation of their operation. New projects can, however, change the optimal operation of existing reservoirs and hydroelectric stations. For that reason simulations always include the total existing power system plus the project being studied. Landsvirkjun uses it proprietary simulation model LpSim based on a well known two step process of water value calculation and simulation of operation as described in Lindqvist 1962.

LpSim uses a two step process to simulate the operation of the power system. First a dynamic programming algorithm is used for water value calculation. The water value is the price of water formulated as a function of reservoir volume and time. The water value defines the strategy used for releasing water from the reservoirs. The second step is the simulation of system operation for a period of N years with time resolution down to one day. Simulated values are; releases from reservoirs, generation in hydro, geothermal and thermal power stations, transmission on a simplified DC transmission system and delivery of energy to customers. Stochastic nature of inflows is accounted for by simulating the operation several times for different inflow scenarios.

Now let's formulate the simulation as the function f that returns the net income I (revenue from energy sales minus the cost of thermal operation/purchased energy from other players) and the minimum reservoir level r_l. The input to the model is a set of inflow scenarios F, the system description S, the load L and simulation period T

$$I = f(F, S, L, T)$$

For a given set of flow scenarios and a given system the net income is maximized by scaling the load.

$$L^* = arg \max_L f(F, S, L, T)$$

With the constraint that reservoir levels in the simulations must be higher than a given minimum

$$r_l \geq r_{min}$$

The load L^* that maximizes the net income is defined as the maximum load for system S, noted as L_S^*.

Now the tool needed to describe how Landsvirkjun uses it's simulation software for design have been defined.

For a new hydroelectric station, or any other part of the system for that matter, its effect on the maximum load can be used as a measure of increase in income created by the investment.

For a hydroelectric station s under consideration the following optimization problems can be solved:

$$L_S^* = arg\max_L f(F, S, L, T) \quad \text{(A)}$$

$$L_{S+s}^* = arg\max_L f(F, S+s, L, T) \quad \text{(B)}$$

The difference between (A) and (B) defines the energy that can be sold from the total system because of investment in hydroelectric station s. This difference is called the energy capacity of s defined as:

$$E_s = L_{S-s}^* - L_S^*$$

When taking a decision on installed capacity of the station s, the energy capacity of the station can be calculated as a function of installed capacity p

$$E_s(p) = L_{S-s(p)}^* - L_S^*$$

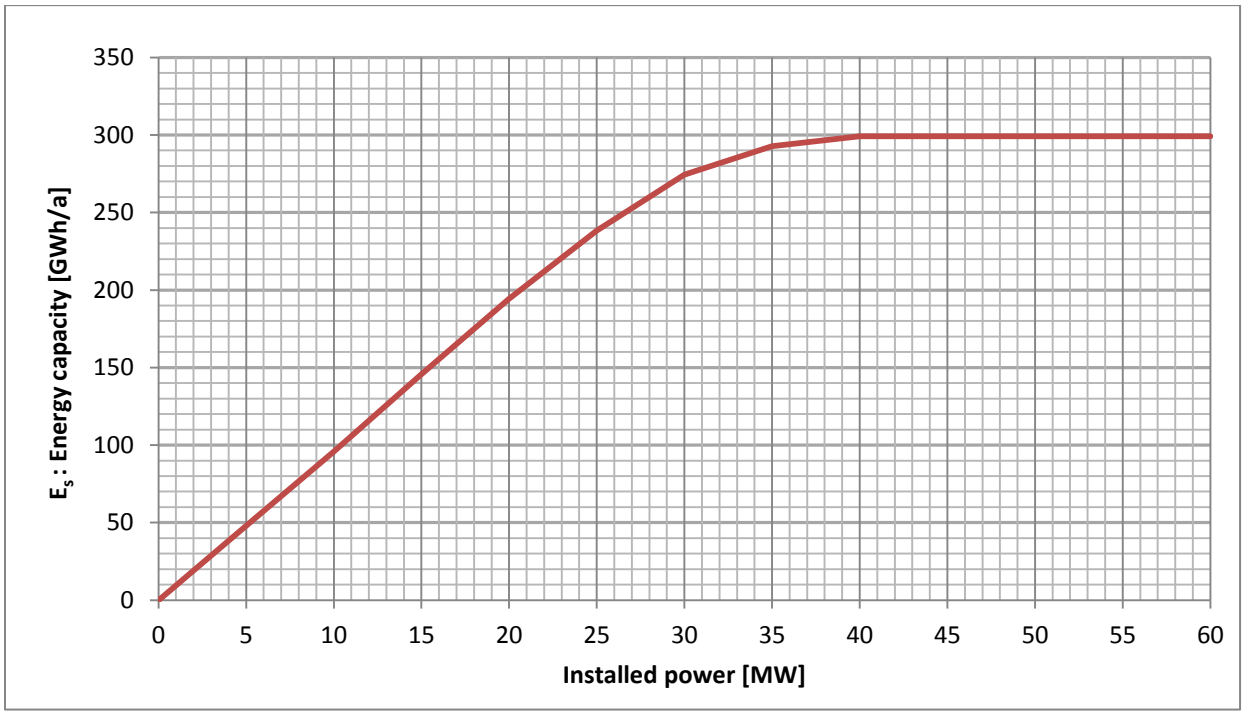

Figures 1 : An example of the energy capacity function $E_s(p)$ as a function of installed power for a single hydroelectric power station. Adding more than 40 MW does not increase the systems capability to serve higher load.

Different design attributes of system objects, such as reservoir size or transmission capacity, can be estimated using the same method.

As the whole system is always simulated, the energy capacity of a power project can be higher than its energy production. When hydroelectric power stations in different drainage basins are connected, the synergic effect can be considerable. This was, for instance, the case when Karahnjukar HEP in East Iceland was built. Estimating the energy capacity of that project as a stand-alone underestimated the energy capacity by 20%.

References

Lindquist, J. 1962. "Operation of a hydrothermal electric system: A multistage decision process", AIEE Journal (April 1962).

Skuli Johannsson & Elias B Eliasson, “Simulation Model of the Hydro-Thermal Power System in Iceland” , www.veldi.is (June 2002)

Proceedings of SIMS 2012, the 53rd Scandinavian Simulation and Modelling Society Conference
Reykjavik, Iceland, 4–6 October 2012

Temperature Condition Modelling for well IDDP-1 in Krafla, N-Iceland

Gudni Axelsson[1),3)], Sigrídur Sif Gylfadóttir[1)] and Thorsteinn Egilson[2)]

1) Iceland GeoSurvey (ÍSOR), Grensásvegur 9, IS-108 Reykjavík, Iceland
2) Iceland GeoSurvey (ÍSOR), Rangárvellir 3, IS-602 Akureyri, Iceland
3) University of Iceland, Saemundargötu 6, IS-101 Reykjavík, Iceland
Corresponding author e-mail: *gax@isor.is*

Abstract

The transient temperature conditions near the bottom of well IDDP-1 in Krafla, which was drilled into a magma intrusion, have been simulated by some simple models addressing: (i) evolution of temperature conditions at the magma intrusion, (ii) cooling of a permeable layer above the magma due to drilling circulation losses, (iii) reheating of the permeable layer after drilling and (iv) temperature evolution during discharge testing in 2010. The modelling is quite speculative because of limited data constraints, but results indicate that the temperature conditions and evolution can be explained by the models used. The possibility that the magma was emplaced during the Krafla volcanic episode 25 – 35 years ago can neither be confirmed nor refuted, but if the intrusion is so old a thickness of at least 50 – 100 m is required. The effective thickness of the permeable layer and its equilibrium temperature, are estimated to be about 45 m and 390 – 400°C, respectively. No direct contact with the magma is needed to explain the superheated (up to 380°C) steam discharged by well IDDP-1. The situation near the bottom of the well clearly warrants further study, both through more complex modelling and with further data-constraints.

1. Introduction

This paper presents the results of modelling work performed to help understanding temperature conditions at the bottom of the IDDP-well in Krafla, which have been an issue of much interest and speculation. This involves both modelling of temperature conditions, and the temperature evolution, around the magma encountered as well as modelling of temperature changes near well-bottom during heating-up after drilling and during discharge testing of the well. Issues like the age and size of the magma intrusion, the slow warming-up of the well near well-bottom after drilling (in view of the presence of the magma) as well as the constantly increasing temperature of the super-heated steam discharged by the well, during most of the discharge period, have been of particular interest. The modelling was done through a series of simple modelling exercises, which can be linked together in a sort of unified picture, rather than through the development of a complex numerical model. For more details see Axelsson (2010) and Axelsson *et al.* (2012).

Well IDDP-1 was drilled within the Krafla caldera, at a location where the depth to an inferred magma chamber was estimated to be about 4.5 km on the basis of MT/TEM resistivity surveying. Pre-drilling was done in 2008 while the main drilling phase started in March 2009. Drilling progressed normally to about 2 km depth but then severe drilling problems started occurring. The well was side-tracked twice but a depth greater than 2104 m couldn't be reached. It slowly became clear that this was because of an unexpected magma intrusion. The well was completed by inserting a slotted liner extending from 1950 to 2080 m

depth. A 10 – 20 m volcanic glass plug (quenched magma) at the bottom of the well isolates it from the magma. The drilling operation was terminated on July 7th and the drill-rig prepared for mobilization. Cooling of the well through water circulation was continued up to August 11th 2009. Fridleifsson *et al.* (2010a) and Elders and Fridleifsson (2010) present the overall status of the IDDP-project while Hólmgeirsson *et al.* (2010) and Fridleifsson *et al.* (2010b) describe the drilling of well IDDP-1.

After the completion of the drilling operation the well was allowed to heat up until March 2010, when the first attempt at discharge testing the well was made. Continuous discharge testing started during the middle of May the same year, however, continuing for more than three months. During both of these phases a comprehensive program of data collection was in effect, including regular temperature- and pressure-logging during the heating-up period and well-head parameter monitoring during the discharge test. This paper is based on data available in late 2010. In late summer 2011 testing of well IDDP-1 started again, providing additional data.

2. The modelling problem

A simplified sketch of well IDDP-1, and the relative location of the magma intrusion and main permeable layer near the bottom of the well, as modelled in this study, is shown in Fig. 1. The figure also shows the different aspects modelled. It should be noted that both the magma intrusion and the permeable layer are assumed to be extensive layers of constant thickness, not necessarily horizontal. This conforms to the fact that most such intrusions are either kind of dikes or sills. A magma intrusion of some other shape can't be ruled out, however, which adds uncertainty to the modelling. The possibility that the magma encountered is simply the top of the Krafla magma chamber may be ruled out on the basis of data on the location of the chamber, in particular MT/TEM resistivity data and data on natural seismicity (Mortensen *et al.*, 2009).

The modelling discussed here focuses on the aspects/items listed below. Note that more relevant information for each of these is presented in the following chapter, which presents the methodology and results of modelling each aspect/item.

(i) Temperature conditions inside and around the magma intrusion and how they may have evolved since emplacement of the magma. Here the main unknowns are the time of emplacement, which may have been during the Krafla volcanic episode in 1975 – 1984 or perhaps later, and the thickness of the intrusion. Other unknowns are the temperature of the magma at the time of emplacement and its present temperature. A further uncertainty arises because the rhyolitic magma of the intrusion does not have a simple melting point temperature, but solidifies over a temperature-range controlled by the solidification of the different minerals of the magma. Finally, the temperature conditions above the magma intrusion may have evolved both through simple heat conduction and heat carried by convection.

(ii) Cooling of the permeable layer above the magma intrusion due to the circulation losses occurring during the IDDP-1 drilling operation and up to August 11, 2009. This permeable layer is assumed to correspond to the series of feed-zones associated with circulation losses between 2040 and 2075 m. Even though the loss-zones may mostly be associated with discrete fractures they are simulated by an equivalent permeable layer of a fixed thickness in this study. This reservoir layer is assumed to be separated

from the magma by an approximately 30 – 50 m thick non-permeable layer (yellow layer in Fig. 1).

(iii) Reheating of the permeable layer during the time the well was closed after August 11, 2009 (i.e. the temperature recovery of the layer as observed through repeated temperature logs). This is basically by heat flow from the rocks above and below the layer, which can be considered to be relatively unaffected by the cooling of the permeable layer.

(iv) Temperature evolution of the permeable layer during discharge of the well, based on well-head measurements during discharge testing of the well in 2010. This actually involves a complex process of boiling in the layer, because of the dramatic pressure drop during the discharge of the well, and later superheating of the steam generated. Modelling this process accurately was beyond the scope of this study so a much more simplistic approach was taken.

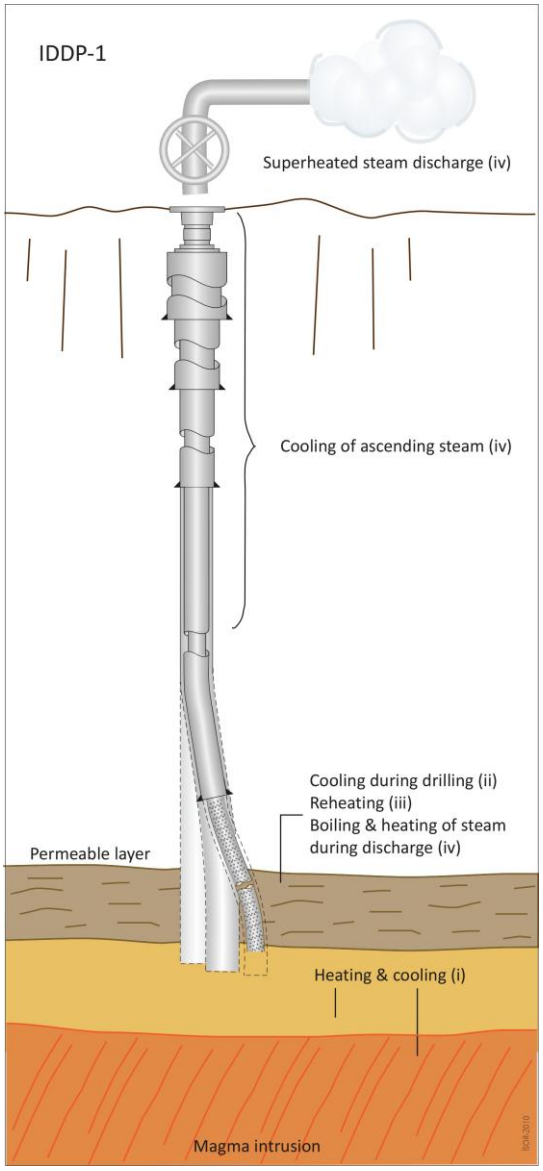

Figure 1. *A simplified sketch of the setup and different aspects considered in the simple temperature condition modelling for well IDDP-1. Markings ((i) – (iv)) refer to items in the list above. Figure not to scale.*

The purpose of the modelling was to try to understand, and explain, the overall temperature evolution, at least approximately, through the modelling exercises. The main data available to constrain the modelling are (for more details see Axelsson, 2010) data on the lithology of layers and structures intersected by the well, some preliminary results of petrological studies of samples derived from the magma (glass samples) and the surrounding rocks, data on circulation loss zones during drilling of the deepest part of the well, temperature and pressure logs measured during the wells' temperature recovery from August 2009 to March 2010 (figures 2 and 3) and discharge test data collected during the wells' main testing phase from May through August 2010. Apart from the first few days of testing the well discharged dry steam. Well-head pressure and steam temperature (Fig. 4) were measured and enthalpy estimated on basis of these two parameters. Because of the extremely high temperature most of the measurements are considered rather uncertain, however. The steam flow-rate is believed to have been in the range of 25 – 35 kg/s.

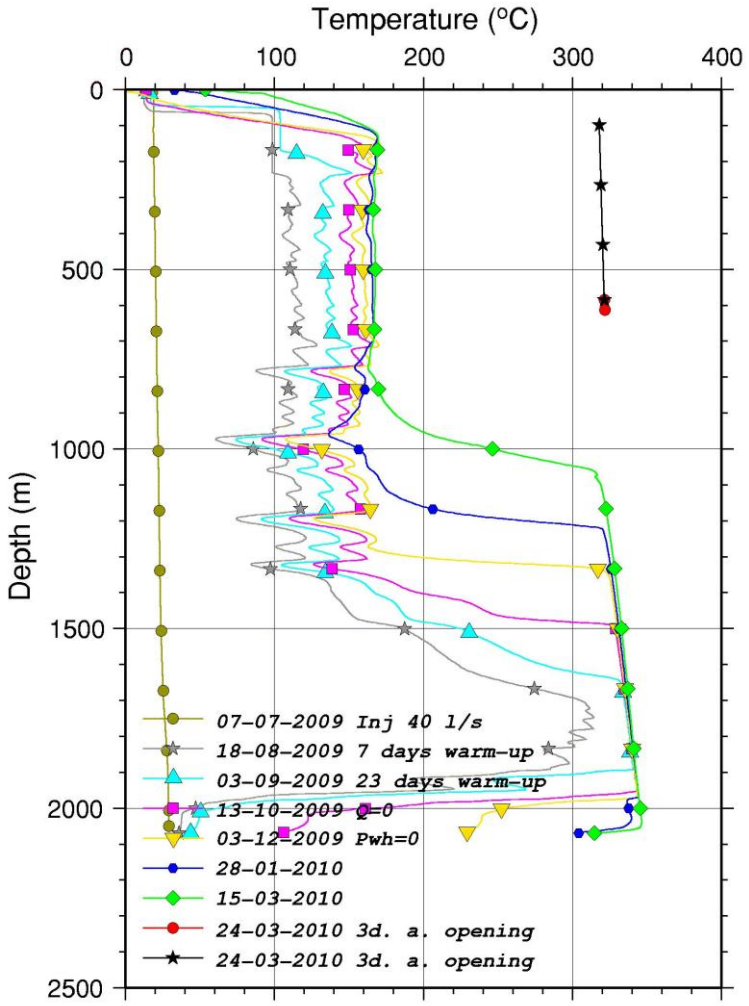

Figure 2. *Temperature logs measured during heating up of well IDDP-1 after drilling (data from the ÍSOR-database).*

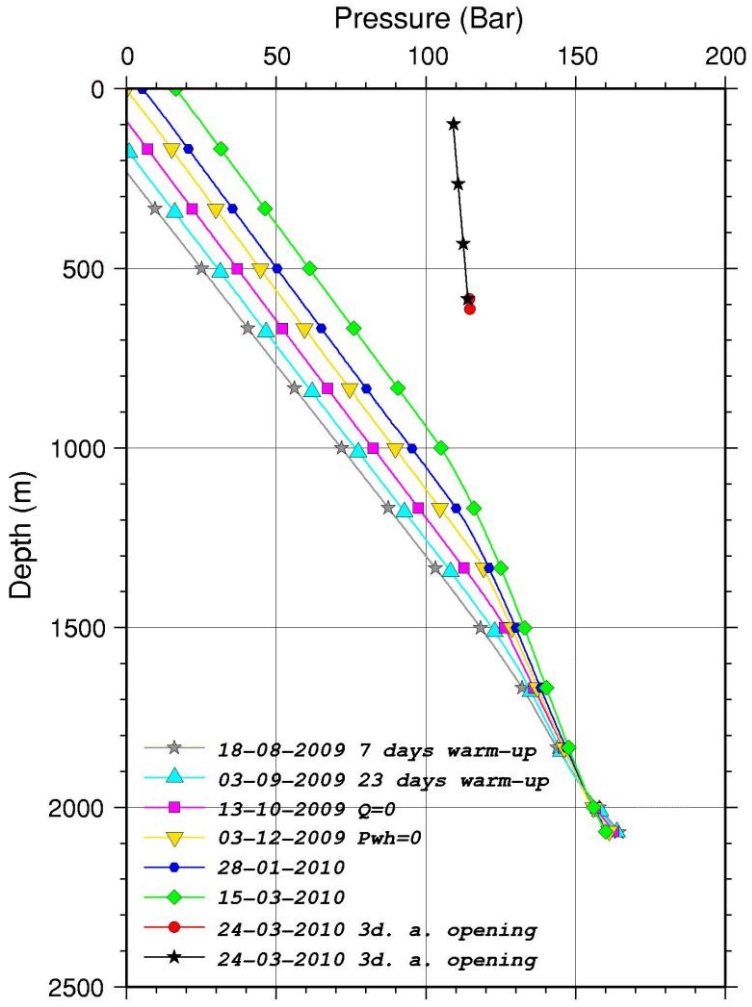

Figure 3. *Pressure logs measured during heating up of well IDDP-1 after drilling (data from the ÍSOR-database).*

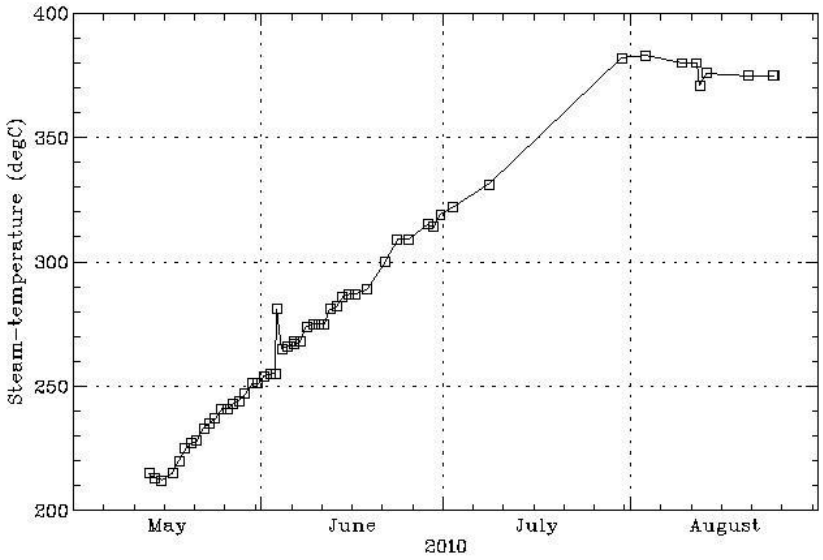

Figure 4. *Steam temperature at well-head during discharge testing of well IDDP-1 (data from the Landsvirkjun database).*

3. Simple Temperature Condition Modelling

The table below presents some of the main parameters and properties used in the modelling study presented here, along with the symbols used and numerical values assumed for them. Note that some of the parameters are estimated through the modelling study. It should be noted that the thermal properties of the magma and rock involved here are not accurately known; hence the values in the table should only be considered as approximate values.

Table 1. Parameters, symbols, properties and constants used in the simple model calculations.

Parameter	Value	Comment
Magma layer thickness, H	Unknown	
Initial (liquidus) magma temperature, T_i	~950°C	See (a) above (chapter 2)
Solidus temperature of magma, T_s	~700°C	See (a) above (chapter 2)
Present magma temperature	~850-900°C	See (a) above (chapter 2)
Initial host rock temperature, T_0	~340°C	Approximate
Latent heat of melting of magma, L_m	400,000 J/kg	Approximate
Thermal conductivity of rhyolite magma, k_m	2.0 J/m°Cs	Bagdassarov and Dingwell (1994)
Density of rhyolite magma, ρ_m	2300 kg/m^3	Bagdassarov and Dingwell (1994)
Heat capacity of rhyolite/granophyre, β_r	800 J/kg°C	Approximate
Density of solid rhyolite/granophyre, ρ_r	2700 kg/m^3	Approximate
Thermal conductivity of solid rhyolite/granophyre, k_r	1.5 J/m°Cs	Approximate
Thickness of permeable layer, h	> 35 m	See also chapter 3.3; Fig. 1
Distance separating permeable layer and magma	~30-50m	See Fig. 1
Average porosity of permeable layer, φ	0.1	Approximate
Density of liquid water in permeable layer, ρ_w	700-1000 kg/m^3	
Heat capacity of liquid water, β_w	4200 J/kg°C	
Heat capacity of 300-400°C steam, β_w	~2300 J/kg°C	At ~25 bar-g
Temp. of perm. layer before drilling, T_p	380-400°C	This analysis
Temp. of perm. layer after drilling, T_0	~25°C	Fig. 3
Density of basaltic rock, ρ_b	2900 kg/m^3	Stacey (1977)
Thermal conductivity of basalt, k_b	2.5 J/m°Cs	Stacey (1977)
Heat capacity of basalt, β_b	700 J/kg°C	Stacey (1977)

3.1 Magma Intrusion Temperature Conditions

Two models were set up to try to model the temperature evolution of the magma intrusion and its' surroundings (item (i) above), neither of which captures accurately the essence of the evolution. They should, however, provide fairly good approximations, which should aid in

understanding the issue. It should be noted that the magma in the intrusion may have originated through secondary melting of an older solid intrusion (i.e. granophyre) having come into contact with hot basaltic magma, sometime after the Krafla volcanic episode. Another model (model B) involves a magma-layer of constant thickness emplaced at a temperature well above the magmas' solidus temperature (Table 1), such that the layer doesn't solidify appreciably during the time period being considered.

One model assumes the magma has a single liquidus/solidus-temperature (not a temperature range) and that it starts solidifying right after intrusion, (model A). This model involves a magma-layer of constant thickness emplaced at a temperature near the magmas' solidus point (assumed to be approximately 850°C). The magma layer solidifies both from above and below while heating up the surrounding rock. Turcotte and Schubert (1982) present a mathematical solution for this model. The results of the modelling (Axelsson, 2010) can't be used to rule out the possibility that the magma was intruded as long ago as 30 years, since temperatures 40 – 50 m above the original magma boundary would only have risen to ~400°C (estimated temperature of permeable layer). It should be kept in mind that model A has the draw-back of assuming a single liquidus/solidus-temperature. In addition it assumes that the magma in the intrusion (sill) remains stationary as it solidifies in a symmetric manner from both above and below. It seems possible that the magma does solidify from the bottom up through a sort of convective process during which material solidifying near the top, sinks to the bottom, and liquid magma rises to the top.

Figure 5, which also presents results of calculations with model A, shows the estimated minimum thickness of such a layer, if it were still to be molten at the centre of the layer, as a function of time. In spite of the drawbacks of model A Fig. 5 should provide an approximate estimate of the minimum initial thickness of the magma intrusion as a function of age, if it were to still remain molten inside. For an age of 35 years a minimum thickness of 40 m would be required.

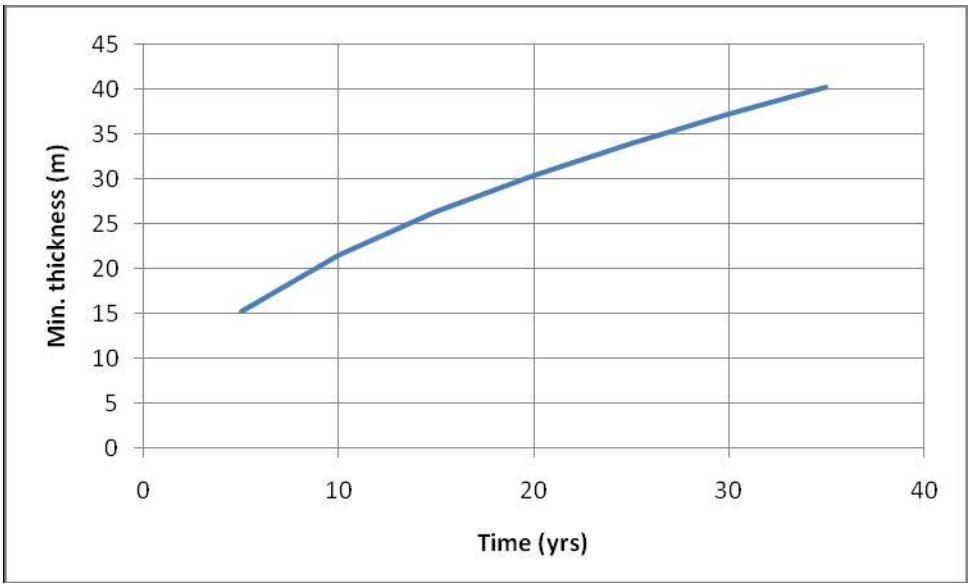

Figure 5. *Minimum thickness of the magma layer of model A, if it were still to be molten at its centre, as a function of time since its emplacement. Note that 25 – 35 years have passed since the last Krafla volcanic episode.*

Another model assumes the magma is so hot at intrusion that it doesn't solidify significantly during the time elapsed since the intrusion (model B). A solution to the associated mathematical problem can be found in Carslaw and Jaeger (1959). This situation may possibly be closer to the actual situation encountered at the bottom of the IDDP-well, since preliminary petrological results indicate that the magma, which is believed to be rhyolitic in nature, may have been as hot as 950°C or more at the time of emplacement while its' solidus temperature may only be about 700°C (Table 1). The estimated temperature conditions inside and above such a magma intrusion are shown in figures 6 and 7, at different times after emplacement, for different intrusion thickness (50 and 100 m, respectively).

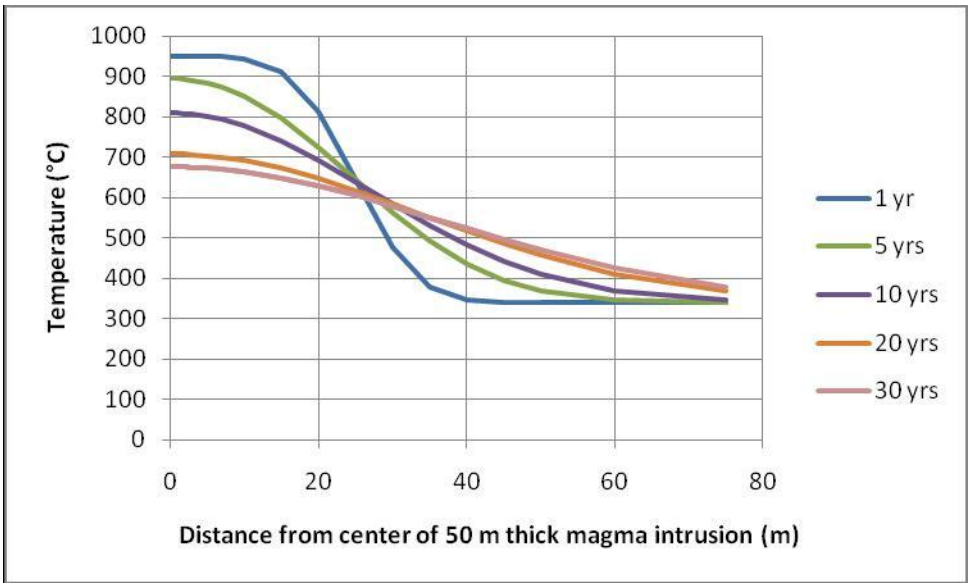

Figure 6. *Temperature conditions inside and above a 50 m thick intrusion emplaced at a temperature of 950°C in 350°C hot host rock (magma intrusion model B). Different curves apply to different times of emplacement.*

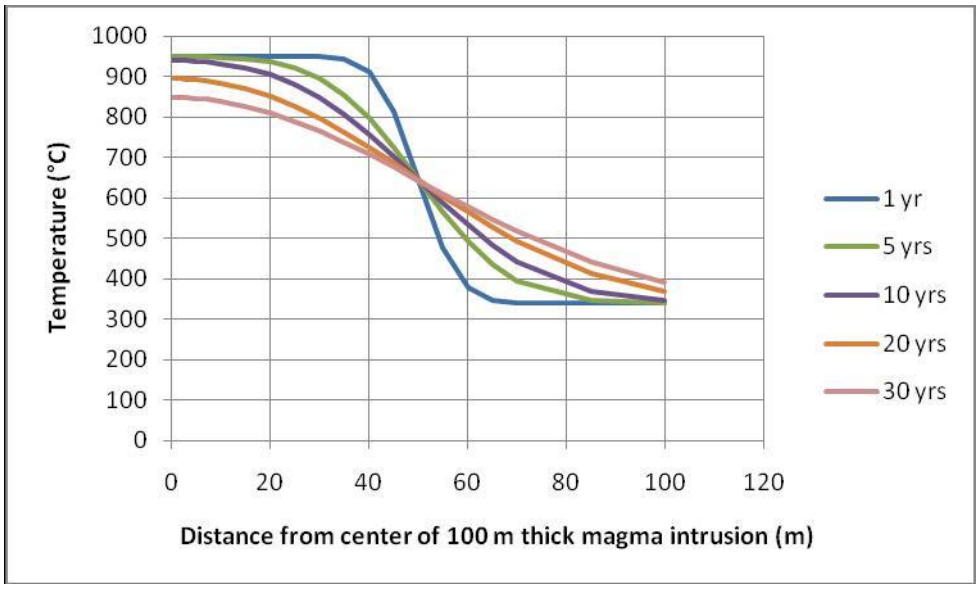

Figure 7. *Same as Fig. 6 except that intrusion is here assumed 100 m thick.*

This model is considered more realistic than model A, as already mentioned. It also conforms better with the idea of non-stationary/convective solidification of the magma mentioned above. But again the results can't be used to rule out completely the possibility that the magma was intruded during the Krafla volcanic episode. The figures predict somewhat higher temperature 30 m above the intrusion than the present temperature of about 400°C (see later), but the difference is really not any greater than the uncertainty in the model calculations. The slightly higher temperature may also indicate more efficient heat transfer in the permeable layer than by heat conduction alone, i.e. by the advection of water and steam, or even by superheated steam.

Model B can also help constrain the possible thickness of the magma intrusion. Fig. 6 shows that if the intrusion (sill) is only 50 m in thickness, its internal temperature would be way below its estimated temperature at present (Table 1) as well as being below the solidus temperature. In the case of 100 m thickness (Fig. 7) the internal temperature would still be approximately high enough.

The idea behind the thermal modelling with models A and B was to help determine whether the magma emplacement occurred during the last Krafla volcanic episode, 25 – 35 years ago, and also to help estimate how thick the intrusion could be. The main conclusion is that this can neither be confirmed nor refuted. The results from model B, however, seem to indicate that to maintain the present high internal temperature the intrusion needs to be relatively thicker than the minimum thickness indicated by model A, or at least 50 – 100 m. To rephrase this conclusion one could say that if such a thickness is considered unlikely, emplacement 25 – 35 years ago would also be unlikely. A final point worth mentioning is that both models demonstrate the extremely slow heating above the intrusion due to heat conduction alone.

3.2 Cooling due to Drilling Circulation Losses

The next item to consider (item (ii), see Chapter 2 above) is the cooling of the permeable layer between about 2040 and 2075 m depth, where most of the circulation losses occurred in the granophyric rocks near the bottom of the well. This is done by first assuming uniform cooling of a layer of constant thickness (35 m) and estimating how far into the formation the effect of the 4.5 months of circulation losses (at 30 l/s on the average) spread, i.e. up to what radial distance a cooling-front may have reached. The calculations were based on a model set up by Böðvarsson (1972), in which porous-media heat advection is assumed (heat conduction neglected because of short time-scale). Figure 8 presents the estimated cold-front radius as a function of the thickness of the permeable layer (see Table 1 for relevant properties). For the estimated thickness of 35 m the radial distance is estimated to be 76 m. Hence the estimated cooled volume equals 630,000 m^3. It should be mentioned that this approach involves a slight discrepancy because it assumes that the permeable layer is saturated with liquid water. In fact the layer is likely to have been saturated with superheated steam (see Section 3.4) instead.

This model is somewhat inaccurate as it neglects cooling of the impermeable rock above and below the layer, an inaccuracy which is not highly significant, however. It can be estimated roughly by estimating the thickness of a so-called boundary layer cooled by heat conduction from the hot impermeable rock on the outside into the permeable layer (see e.g. Turcotte and Schubert, 1982). It gives the approximate distance into the impermeable rock where the

temperature has dropped by 90%. Thus we estimate the cooled boundary layer of the impermeable rock to be about 5 m thick, on the average, on each side of the permeable layer. Thus the cooled layer effective thickness is estimated to equal approximately 45 m.

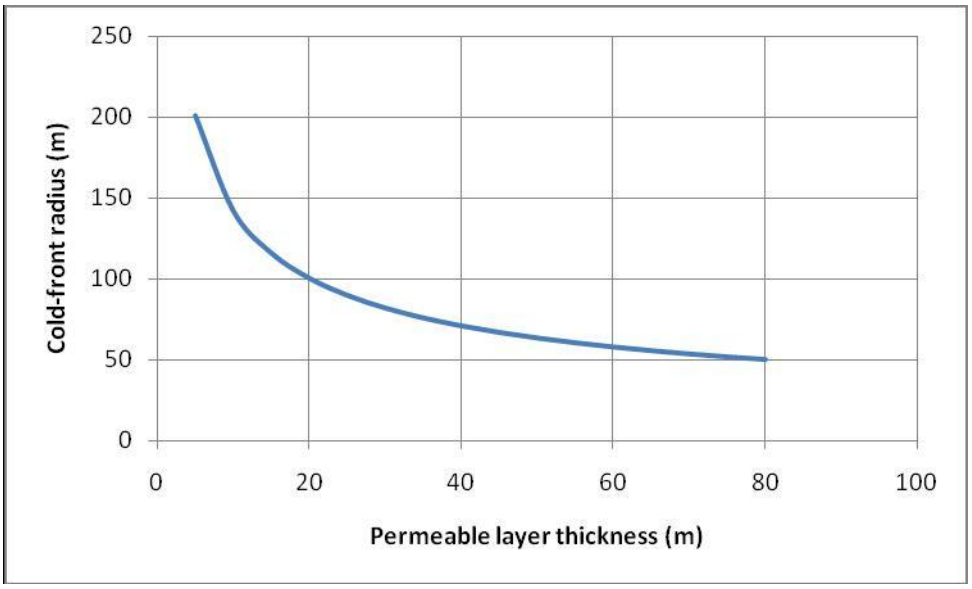

Figure 8. *Estimated radial distance to the cooling-front in the permeable layer, as a function of layer thickness, after 4.5 months of average 30 l/s circulation losses.*

3.3 Reheating after Drilling

The third item on the modelling list (item (iii), see Chapter 2) is the heating of the cooled layer during the thermal recovery of the well after drilling, as observed through temperature logging (Fig. 2). This is done by deriving a mathematical solution to the heat diffusion equation for an initially cold layer, of constant thickness, in otherwise hot rock (Axelsson, 2010). Applying the Laplace-transform method comes in handy here, but the solution can also be found in Carslaw and Jaeger (1959).

During this modelling phase the layer thickness and the undisturbed temperature of the permeable layer were adjusted until a satisfactory match between the observed data and model calculations was obtained. The results are presented in Fig. 9, which shows a very good correspondence between observed and modelled values. Note that the model assumes a 45 m thick "cooled layer", which corresponds very well with the results of Section 3.2, i.e. the fact that most of the circulation losses occurred between 2040 and 2075 m depth, approximately. To that 35 m thickness ~10 m can be added because of the 5 m cooled boundary layers on either side of the permeable layer.

3.4 Temperature Evolution during Discharge Testing

The fourth and final item on the modelling list (item (iv), see Chapter 2) is the heating up of the steam discharged by the well during the ~3.5 months of discharge testing. It should be noted that only some basic calculations have been done yet for this item, more complex modelling was beyond the scope of the present study, as already mentioned. This part of the modelling is principally based on the temperature- and pressure-log data available (figures 2 and 3) and data on the temperature of the steam discharged during the discharge testing of

well IDDP-1 (Fig. 4). Table 2 summarizes the main physical parameters of the well during three stages of the discharge test.

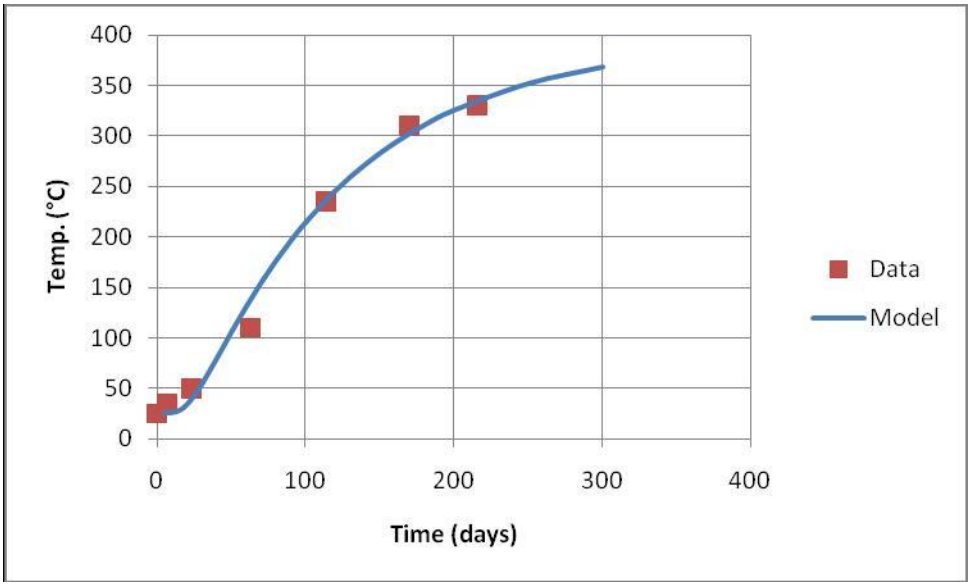

Figure 9. *Thermal recovery of well IDDP-1 after drilling, both observed (Fig. 2, at ~2070 m depth)) and simulated by a model of a cooled 45 m thick layer in a hot rock-mass (390°C). The calculated temperature is that in the centre of the layer. The 45 m layer thickness and 390°C yield the closest match between observed and calculated temperatures.*

Table 2. *Approximate physical parameters down-hole, and at well-head, for well IDDP-1 during different stages of the wells' discharge test. Down-hole conditions during discharge based on an estimated 10°C drop in steam temperature while flowing up the well (see later). The symbols T, p and h stand for temperature, pressure and enthalpy, respectively.*

	Location	T (°C)	p (bar-g)	h (kJ/kg)	Comment
At end of heating period	down-hole	345	160	1630	liquid near boiling
First days of discharge	down-hole well-head	220 210	~23 ~19	2800 2796	wet steam
At end of discharge	down-hole well-head	390 380	~26 ~22	3217 3201	superheated steam

It is clear that when the discharge test starts the feed-zones of the well between 2000 and 2100 m depth where approximately at boiling conditions. When the pressure in the well at the feed-zones drops, perhaps as low as to 20-30 bar, the feed-zones soon start yielding dry steam, and a boiling front starts propagating into the formation away from the well. At first the temperature of the steam is close to the boiling temperature at ~20 bar-g, but once the boiling/dry-steam front has propagated some distance from the well the steam flowing towards the well is heated by the rock, which is likely to be more than 150°C hotter than the steam. Thus the steam becomes superheated as it flows towards the well, and as the boiling/ dry-steam front propagates further away from the well the superheated steam picks up more heat from the rock.

Further away from the well, beyond the radius of influence of circulation loss cooling, the reservoir fluid is most likely steam at 160 bar-g and about 390°C. This would be superheated steam at an enthalpy of about 2900 kJ/kg. No direct contact with the magma is needed to explain the continuous heating of the steam up to the last month of the discharge test.

Another thing to keep in mind is that the 4.5 months of circulation losses may correspond to approximately the same mass of water as produced during the 3.5 month discharge test (less accurately known). Thus the water discharged towards the end of the discharge test may still have been mostly circulation water lost into the permeable layer. This contention may be assessed by studying the chemical composition of steam-samples collected during the discharge test. Any remaining circulation water should all have been converted to steam in-situ by now. It should be kept in mind, however, that the model proposed here may involve an oversimplification since some of the circulation water may have percolated (sunk due to gravity) to depths greater than that of the permeable layer and would, therefore, not have been recovered during the discharge.

The temperature of the steam appears to level off at about 380°C towards the end of the discharge test (Fig. 4). This is believed to indicate that the steam entering the well at this stage had reached the temperature of the formation at the feed-zone depth, when entering the well. To try to assess the inflow temperature, the cooling of the steam as it flows up the upper part of the well, which is colder than the steam, needs to be estimated. This can be done on the basis of a solution presented by Carslaw and Jaeger (1959), which equates the decline in the energy content of the ascending steam with heat-flow into the surrounding formation (Axelsson, 2010). Assuming that the steam is about 200°C hotter than the formation around the well in the top 1300 – 1500 m a cooling of the steam of the order of 15°C (±5°C) at the end of the discharge test is obtained. Thus the formation temperature appears to be close to 390 – 400°C, in good agreement with the results of modelling the heating up of the permeable layer (Section 3.3).

5. Conclusions

This paper has described the results of a series of simple modelling exercises involving the transient temperature conditions near the bottom of well IDDP-1. The modelling was broken up into the following phases:

(i) Evolution of temperature conditions inside, and around, the magma intrusion since its emplacement.
(ii) Cooling of a permeable layer above the magma due to circulation losses during drilling.
(iii) Reheating of the permeable layer after drilling.
(iv) Temperature evolution of the permeable layer, and the wells discharge, during discharge testing of the well in 2010.

It should be emphasised that the modelling is quite speculative, mostly because of limited data constraints, but the results indicate that the temperature conditions at the bottom of the IDDP well and the temperature evolution during drilling, temperature recovery and discharge can be explained by the model(s) proposed here. The main results are the following:

(1) The possibility that the magma was emplaced during the Krafla volcanic episode 25 – 35 years ago can neither be confirmed nor refuted. If the intrusion is of that age a

thickness of at least 50 – 100 m would be required for the present high temperature to be possible, as well as a kind of "convective" solidification from below.

(2) The parameters best constrained through the modelling are considered to be the effective thickness of the permeable layer and its undisturbed temperature, about 45 m and 390 – 400°C, respectively, based on the re-heating of the layer and discharge test data.

(3) The superheated (up to 380°C) steam discharged during the output test of well IDDP-1 in 2010 is considered to have been mostly circulation water heated by the 390 – 400°C rocks of the permeable layer. No direct contact with the magma is needed to explain the high temperature obtained.

The situation near the bottom of well IDDP-1 clearly warrants further study, both because the modelling presented here was relatively simple and because further data-constraints would be highly important. More complex modelling could be applied, e.g. to model the discharge test data. Further data constraint may also be provided by additional petrological studies and chemical analyses of steam samples collected during the wells discharge.

The question whether well IDDP-1 can maintain the energy output (~15 MW_e), achieved during the 2010 discharge test, in the long-term, can unfortunately not be answered on basis of available data and the present modelling results. This boils down to whether "far-field" recharge into the permeable layer will be sufficient and whether large enough heat-exchange volumes and surfaces are available to heat the recharge (most likely at 340°C) to 390 – 400°C. This needs considerable further study as well as further discharge testing of the well with accurate monitoring of relevant flow parameters. It may be mentioned that carefully executed reinjection in the vicinity of the well may be the solution if the "far-field" recharge turns out not to be sufficient. This would in essence constitute a kind of EGS-operational scheme.

The work presented here was based on data available towards the end of 2010. A second flow test of the IDDP-well was started in May 2011. It started out with two brief test episodes in May and August while in late September 2011 continuous discharge testing, under restricted flow-conditions, started. This last testing phase was on-going up to the summer of 2012, apart from some brief interludes for maintenance and other activity.

The monitoring data from the second discharge test was not taken into account in the modelling study discussed here as it was collected after the completion of the study. The results of the test can be compared with the modelling results, however, in particular the results of Section 3.4. During the present discharge phase (starting late September 2011) the steam flow has been restricted to make the testing more easily manageable and has varied between 6 and 12 kg/s at a well-head pressure of about 140 bar. Surprisingly the temperature of the steam has now been drastically higher than during the first test, or between 400 and 450°C.

This high temperature of the steam discharged contradicts the results of Section 3.4, with two possible explanations coming to mind: (a) That some changes have occurred in conditions in the productive layer intersected by the well above the magma intrusion since 2010, perhaps more direct access to the thermal energy of the intrusion. (b) That the simple model used here doesn't catch the nature of the heat transfer in the permeable layer accurately enough. This reveals that the situation needs further study, including more accurate modelling, which is beyond the scope of the present study. It may be mentioned that a Horner analysis

of the temperature recovery after drilling (Fig. 11) indicates an equilibrium temperature as high as 500°C. The lower limit of the equilibrium temperature indicated by the Horner-method is close to 400°C, however, reflecting the uncertainty in the analysis.

Acknowledgements

Landsvirkjun, The National Power Company of Iceland, is acknowledged for financing the modelling study presented above and for allowing publication of the data presented.

Bibliography

Axelsson, G., 2010: Temperature condition modelling for well IDDP-1. Landsvirkjun/Iceland GeoSurvey report LV-2010/119 / ÍSOR-2010/051, 27 pp.

Axelsson, G., Th. Egilson, S.S. Gylfadóttir, 2012: Modelling of temperature conditions near the bottom of well IDDP-1 in Krafla, N-Iceland. Submitted to *Geothermics*.

Bagdassarov, N.S. and D.B. Dingwell, 1994: Thermal properties of vesicular rhyolite. *Journal Volc. Geotherm. Res.*, **60**, 179–191.

Bödvarsson, G., 1972. Thermal problems in the siting of reinjection wells. *Geothermics*, **1**, 63-66.

Carslaw, H.W. and J.C. Jaeger, 1959. *Conduction of Heat in Solids*. Second Edition, Claredon Press, Oxford, 403 pp.

Elders, W.A. and G.Ó. Fridleifsson, 2010. The science program of the Iceland Deep Drilling Project (IDDP): A study of supercritical geothermal resources. *Proceedings World Geothermal Congress 2010*, Bali, Indonesia, 25-29 April, 9 pp.

Fridleifsson, G.Ó., A. Albertsson and W.A. Elders, 2010a. Iceland Deep Drilling Project (IDDP) – 10 years later – Still an opportunity for international collaboration. *Proceedings World Geothermal Congress 2010*, Bali, Indonesia, 25-29 April, 5 pp.

Fridleifsson, G.Ó., B. Pálsson, B. Stefánsson, A. Albertsson, E. Gunnlaugsson, J. Ketilsson, R. Lamarche and P.E. Andersen, 2010b. Iceland Deep Drilling Project. The first IDDP drill hole drilled and completed in 2009. *Proceedings World Geothermal Congress 2010*, Bali, Indonesia, 25-29 April, 4 pp.

Hólmgeirsson, S., Á. Gudmundsson, B. Pálsson, H.Á. Bóasson, K. Ingason and S. Thórhallsson, 2010. Drilling operations of the first Iceland deep drilling well (IDDP). *Proceedings World Geothermal Congress 2010*, Bali, Indonesia, 25-29 April, 10 pp.

Mortensen, A.K., Á. Gudmundsson, B. Steingrímsson, F. Sigmundsson, G. Axelsson, H. Ármannsson, H. Björnsson, K. Ágústsson, K. Saemundsson, M. Ólafsson, R. Karlsdóttir, S. Halldórsdóttir and T. Hauksson, 2009. Jarðhitakerfið í Kröflu – Samantekt rannsókna á jarðhitakerfin og endurskoðað hugmyndalíkan (The Krafla geothermal system – compilation of research findings and revised conceptual model). Iceland GeoSurvey, report ÍSOR-2009/057 (in Icelandic), 209 pp + 2 maps.

Stacey, F.D., 1977. *Physics of the Earth*. John Wiley & Sons, New York, 414 pp.

Turcotte, D.L. and G. Schubert, 1982. *Geodynamics. Applications of Continuum Physics to Geological Problems*. John Wiley & Sons, New York, 450 pp.

Condition monitoring of an epicyclic gearbox at a water power station

Jussi Immonen[*], Sulo Lahdelma[*], Esko Juuso[**]

[*]*Mechatronics and Machine Diagnostics Laboratory, Department of Mechanical Engineering, P.O.Box 4200, FI-90014 University of Oulu, Finland (e-mail: {jussi.immonen|sulo.lahdelma}(at)oulu.fi).*

[**]*University of Oulu, Control Engineering Laboratory, P.O.Box 4300, FIN-90014 University of Oulu, Finland (e-mail: esko.juuso(at)oulu.fi).*

Abstract: Epicyclic gearing or planetary gearing is a gear system that consists of one or more outer gears, or planet gears, revolving around a central, or sun gear. Typically, the planet gears are mounted on a movable arm or carrier, which itself may rotate relative to the sun gear. It is challenging to monitor epicyclic gearboxes, due to their complex structure consisting of many rolling elements. A complex structure and versatile components also result in a long stoppage if a failure occurs. Therefore, it is important to detect incipient faults at an early stage. In this paper, vibration analysis is used for the condition monitoring of an epicyclic gearbox at a water power station. There is a distinct difference between vibration quantities: vibration velocity responds very well to vibrations with frequencies less than 1000 Hz; an even better response is obtained when using acceleration and its higher derivatives, which also provide more information on higher frequencies. Because of the quite high rotational speed of the output, vibration velocity is not good enough for the condition monitoring of the gear in question. Acceleration and its higher order derivatives should be used in order to obtain better responsiveness to changes in the condition of the gearbox. Complex models based on mechanisms are needed in order to calculate the vibration components in the frequency range and to identify the possible faulty components. There was also one vibration component in the gear the source of which could not be discovered with certainty.

Keywords: Condition monitoring; diagnostic; higher order derivatives; epicyclic gearbox.

1. INTRODUCTION

Gear trains are used to transmit motion between shafts. They are critical components in industry and therefore their condition monitoring must be in order, particularly with large gears that can have months of delivery time. The aim of this paper was to develop the current condition monitoring of a two stage epicyclic gearbox at a water power station in order to detect faults at an earlier stage. The previous gearbox suffered a sudden breakdown despite continuous condition monitoring. The breakage was due to the second stage planet gear breaking into half. There were also other faults in the gears, namely impact traces and wearing on the ring gears.

Water power plants are used as an adjusting energy source and thus the load of the gear varies during usage even though the rotation speed stays constant. Depending on energy needs, there are also frequent starts and stops, which stress machines. The condition monitoring of a variable loaded planetary gear, such as that used in a bucket wheel excavator and wind turbines, has been under active investigation (Villa et al., 2012; Bartelmus and Zimroz, 2009a, 2009b; Vicuña, 2010; Hameed et al., 2009; Barszcz and Randall, 2009; Combet and Zimroz, 2009). There are also studies of the modelling of epicyclic gears (Ambarisha and Parker, 2007; Bartelmus et al., 2012). The models based on mechanisms are very detailed.

Different methods for fault detection in epicyclic gears have been investigated. Feng and Zuo (2012) used a common spectral analysis to detect faulty gears in a two stage planetary gearbox. Eltabach et al. (2012) investigated the condition monitoring of a planetary gear in a lifting crane. They suggested using parameters extracted from spectrum, demodulation or cyclostationary analysis to diagnose a fault more accurately. Blunt and Keller used new methods to detect a fatigue crack in the planet gear carrier of a helicopter transmission. The methods worked well under test-cell conditions but failed in low-torque on-aircraft conditions (Blunt and Keller, 2006). Rzeszucinski et al. (2012) presented a new condition indicator based on the amplitude of a probability density function to monitor the health of epicyclic transmissions in helicopters. Wu et al. (2012) studied the characterisation of gear faults in a variable rotating speed using Hilbert-Huang Transform (HHT), and

Heyns et al. (2012) used HHT to compute an envelope of a residual signal er to obtain a discrepancy signal. McFadden (1991) has developed a technique for calculating the time domain averages of the individual planet gears and sun gear.

2. EPICYCLIC GEARBOX

The gearbox under study was a two stage epicyclic gearbox that transforms the water turbine's 87.2 rpm to 750 rpm for the generator. The first stage, i.e. the low speed side, is in the planetary mode and the second stage, i.e. the high speed side, is in the star mode. The structure of the gearbox is presented in Figure 1: the middle section, consisting of a sun gear in the 1st stage and a ring gear in the 2nd stage ring gear, is a floating installation. The gear toothing is double helical.

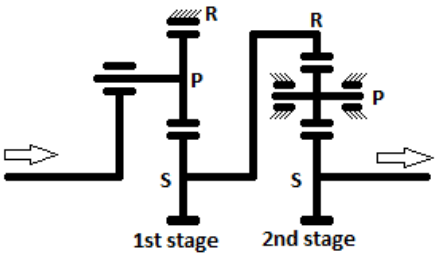

Figure 1. Structure of the two stage epicyclic gearbox.

Epicyclic gears are complex structures. Therefore, it is difficult to calculate their vibration frequencies, and some mistakes in calculations are present in literature (Klein, 2000; Taylor, 2000). In this study, the gear frequencies were calculated with the help of papers (Vicuña, 2010; Mäkikyrö, 2006).

Epicyclic gears can have three different modes on the basis of which the component is fixed, with the exception of a differential gear, in which all the parts are in motion and which therefore needs two drives. The three modes of epicyclic gears are *planetary (pl)*, *star (st)* and *solar (so)*. Table 1 shows these modes in a reduction gear. To calculate failure frequencies, one must first calculate the rotating frequencies of the shafts.

Rotating frequencies for the gear types shown in Table 1 are indicated in Table 2, where f_C is the rotating frequency of a carrier, f_P is the rotating frequency of a planet gear, f_R is the rotating frequency of a ring gear, f_S is the rotating frequency of a sun gear, z_P the number of teeth in a planet gear, z_R the number of teeth in the ring gear and z_S the number of teeth in the sun gear.

The general solution for gear mesh frequency in epicyclic gears is

$$f_m = |f_R - f_C| z_R . \qquad (1)$$

A cracked or broken sun gear tooth causes an impact every time a planet gear passes over it.

Table 1. Different types of epicyclic gears.

	fixed component	**driving / driven shaft in reduction gear**
planetary (pl)	*ring gear*	*sun / carrier*
solar (so)	*sun gear*	*ring / carrier*
star (st)	*carrier*	*sun / ring*

Table 2. Rotating frequencies of three types of epicyclic gears.

	fixed component	**driving shaft**	f_{output}	f_P
planetary (pl)	$f_R = 0$	f_S	$f_C = \frac{z_S}{z_S + z_R} f_S$	$\frac{-z_S(z_R - z_P)}{z_P(z_S + z_R)} f_S$
solar(so)	$f_S = 0$	f_R	$f_C = \frac{z_R}{z_S + z_R} f_R$	$\frac{z_R(z_S + z_P)}{z_P(z_S + z_R)} f_R$
star (st)	$f_C = 0$	f_S	$f_R = \frac{-z_S}{z_R} f_S$	$\frac{-z_S}{z_P} f_S$

Therefore, the broken sun gear tooth frequency is:

$$f_{fS} = y|f_S - f_C|, \qquad (2)$$

where *y* is the number of planet gears.

By inserting values from Table 2 to the above formulas, frequencies are obtained for the three modes of epicyclic gears. A cracked or broken planet gear tooth meshes with both the sun and the ring gear and

therefore a broken tooth is in contact with other teeth twice per revolution. The frequencies for broken planet gear are

$$f_{fP}^{pl} = 2\frac{z_S z_R}{z_P(z_S + z_R)}|f_S|, \quad (3)$$

$$f_{fP}^{so} = 2\frac{z_S z_R}{z_P(z_S + z_R)}|f_R|, \quad (4)$$

$$f_{fP}^{st} = 2\frac{z_S}{z_P}|f_S|. \quad (5)$$

For ring gear, a cracked or broken tooth gives the following frequencies:

$$f_{fR}^{pl} = y|f_C| = y\frac{z_S}{z_S + z_R}|f_S|, \quad (6)$$

$$f_{fR}^{so} = y\frac{z_R}{z_S + z_R}|f_R|, \quad (7)$$

$$f_{fR}^{st} = y|f_R| = y\frac{z_S}{z_R}|f_S|. \quad (8)$$

The frequencies for the gearbox under study are shown in Table 3.

The impacts caused by a cracked or broken tooth are usually detected with the help of time synchronous averaging or an envelope spectrum. For a single planet gear, however, these methods may not be sufficient, because the vibrations caused by a broken tooth may be hidden under other meshing vibrations. For this, a short signal sample is taken every time a planet gear passes by the vibration sensor. The waveform signal samples are then put in order by taking into account the rotation sequences and averaged. (McFadden, 1991)

Table 3. Gear's rotating frequencies and number of teeth.

	Teeth	**Hz**
1st stage (planetary)		1.45
Gear mesh frequency		132.24
Planet rotation		4.9
Sun gear	35	22.67
Planet gears	27 x 6	9.8
Ring gear	91	8.72
2nd stage (star)		12.5
Gear mesh frequency		450
Planet rotation		18
Sun gear	36	75
Planet gears	25 x 6	36
Ring gear	86	31.4

3. SIGNAL PROCESSING

The weighted l_p norm,

$$\left\|x^{(\alpha)}\right\|_{p,\frac{1}{N}} = \left(\frac{1}{N}\sum_{i=1}^{N}\left|x_i^{(\alpha)}\right|^p\right)^{\frac{1}{p}} = \left(\frac{1}{N}\right)^{\frac{1}{p}}\left\|x^{(\alpha)}\right\|_p, \quad (9)$$

where all the weight factors are equal to $\frac{1}{N}$, has been proved to be an efficient indicator in condition monitoring (Lahdelma and Juuso, 2011a, 2011b; Lahdelma et al., 2010; Lahdelma and Laurila, 2012).

The measurements were performed with the SKF Microlog Consultant CMXA 48 data collector with SKF CMSS 2111 accelerometers. Sensors were attached to the gearbox with magnets. The upper cutoff frequency of the measurements was 20 kHz for one sensor, 15 kHz for two sensors and 10 kHz for four sensors. At the time of the measurements, generator power was 7.8 – 8.0 MW and water flow in the turbine 143 - 146 m^3/s. Each measurement lasted about 15 seconds. Both the ends of the gearbox were measured in the horizontal and vertical direction. The measurements were analysed by means of the SKF Analysis and Reporting Module program. The turbine rotated at a constant speed of 87.2 rpm.

4. RESULTS

It should be noted that the gearbox under study was a new one, and no measurements from the broken gearbox are presented. Vertical acceleration signals from both the ends of the gear are shown in Figure 2. The levels of the vibrations in the 1st stage are low and no signs of impacts are present. The vibration levels in the 2nd stage are three times higher than in the 1st stage but still very low considering the size of the gear

Figures 3 and 4 show measured amplitude or peak spectra from both the stages of the gearbox in the vertical direction. In both the spectra, the dominating

frequency components are at 450 Hz and its multiples and sidebands. This is the gear mesh frequency of the 2nd stage. A common time-domain feature is a peak value obtained as the absolute maximum values of the signal in a chosen sample. The calculated peak values differ in some cases slightly from the actual peaks seen in Figures 3 and 4 because of the frequency resolution of the visualisation program.

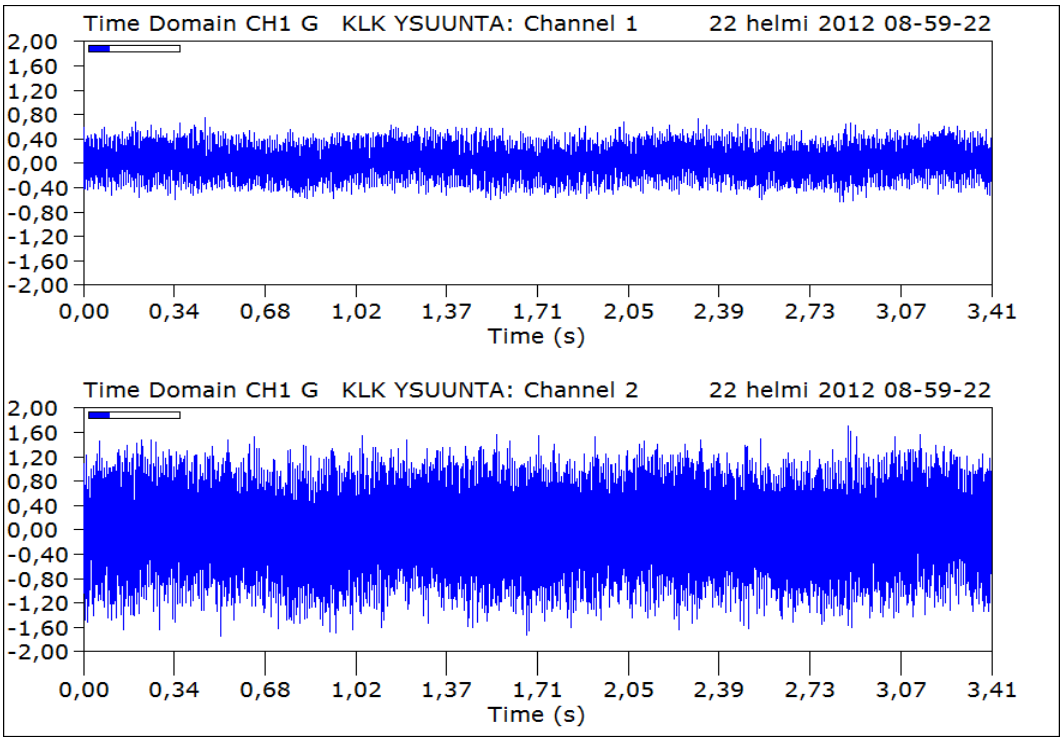

Figure 2. Acceleration signals (g) of the gearbox measured in the vertical direction: channel 1 is the 1st stage and channel 2 the 2nd stage, g=9.80665 m/s^2.

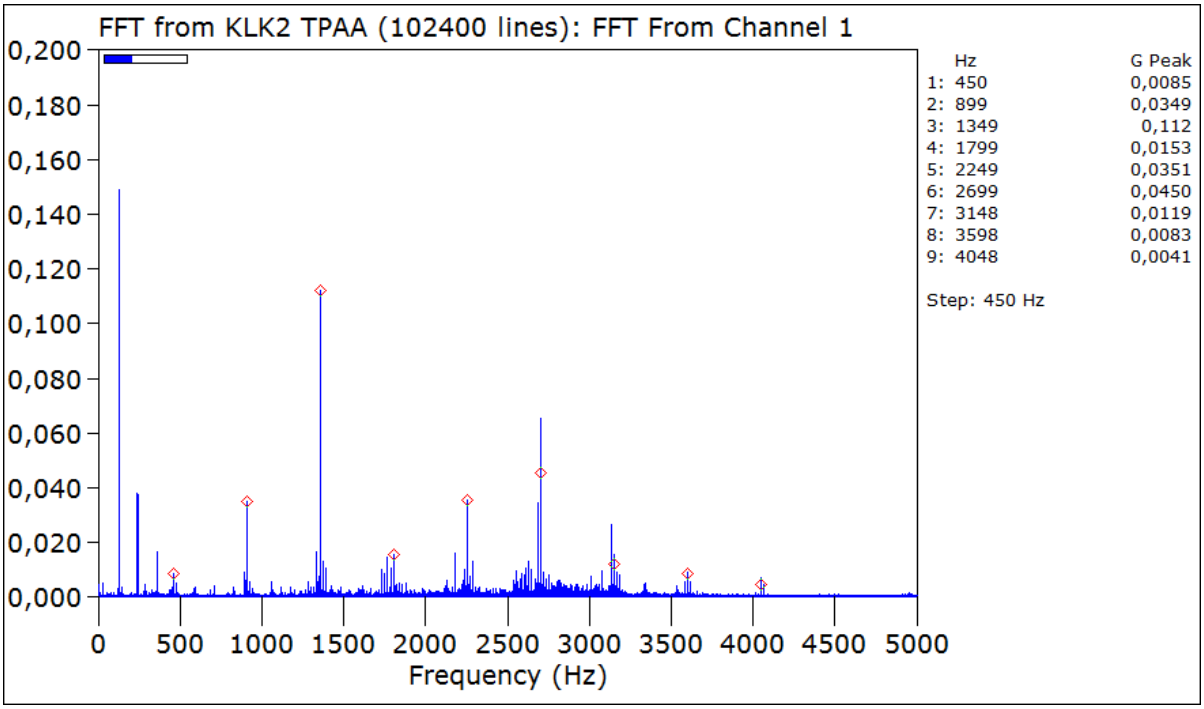

Figure 3. a_{peak} (g) spectrum from the 1st stage, g=9.80665 m/s^2: the peak value of the gear mesh frequency (450 Hz) and its multiples are denoted by ◊ .

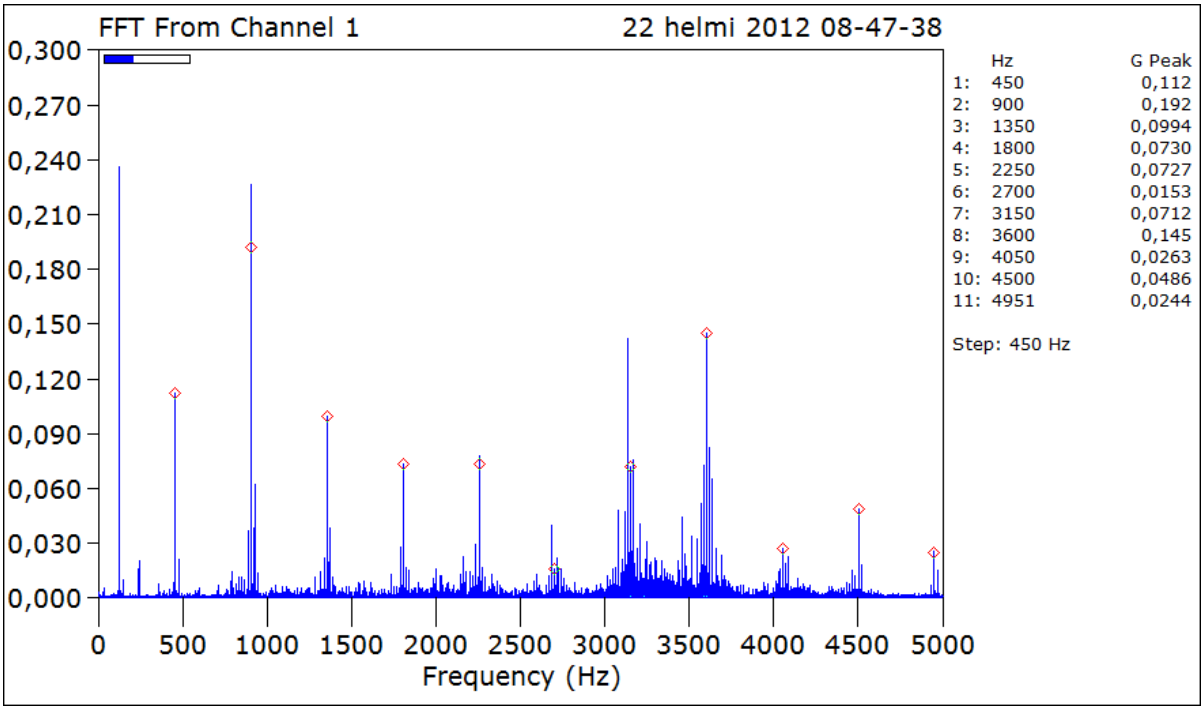

Figure 4. a_{peak} **(g) spectrum from the 2nd stage, g=9.80665 m/s^2: the peak value of the gear mesh frequency (450 Hz) and its multiples are denoted by ◊.**

The sidebands of the 2nd stage gear mesh frequency are 18 Hz apart, which is the same as the rotating frequency of the planets in that stage. There is a strong component at the frequency of 119 Hz, whose second multiple also is visible. This requires further studies since the source is not easy to discover unambiguously.

The 1st stage gear mesh frequency 132 Hz is not visible in the spectrum shown in Figure 3, which is due to the gearbox structure where all the planet gears are in different phases of the mesh. The phase difference is

$$\frac{z_R}{y} = \frac{91}{6} = 15.1667\,, \qquad (10)$$

where z_R is the number of teeth in ring gear and y is the number of planet gears.

The phase difference between planet gears is $\frac{1}{6}2\pi$ and it is evenly distributed in the range [0, 2π]. Therefore, opposite planet gears are in opposite phases and annul each other's vibrations.

The condition monitoring of the gearbox was conducted earlier by monitoring the root-mean-square velocity (v_{rms}) trend in the frequency range 0 - 1000 Hz and by analysing regularly recorded vibration signals. Figure 5 shows the v_{rms} spectrum and Figure 6 the $\dddot{x}_{peak}$ spectrum from the 2nd stage in the frequency range 0 - 10 kHz in the horizontal direction. They clearly show that v_{rms} alone is not sufficient to monitor this type of gear.

The gear faults can be indicated early with acceleration and its higher derivatives. The velocity emphasises lower frequencies. The higher multiples of the gear mesh frequency are not seen, since all the velocity components in the higher frequencies are negligible (Fig. 5). Acceleration and its higher derivatives within the range 0 - 10 kHz provide substantially more information particularly from the multiples of the gear mesh frequency and their sidebands, see Figures 3, 4 and 6. The higher frequency range also shows possible friction-induced vibration.

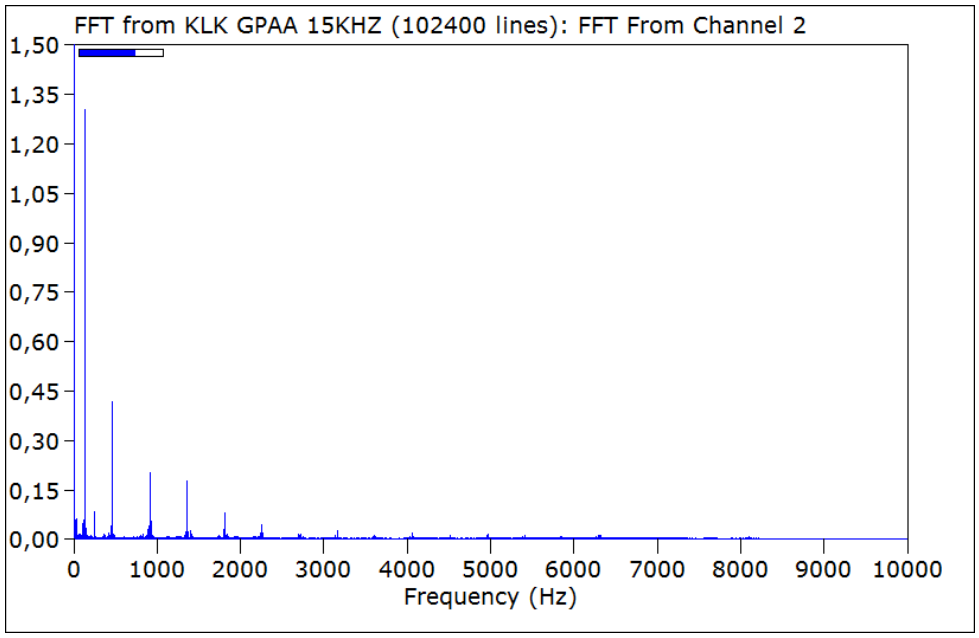

Figure 5. v_{rms} **(mm/s) spectrum from the 2nd stage in the horizontal direction.**

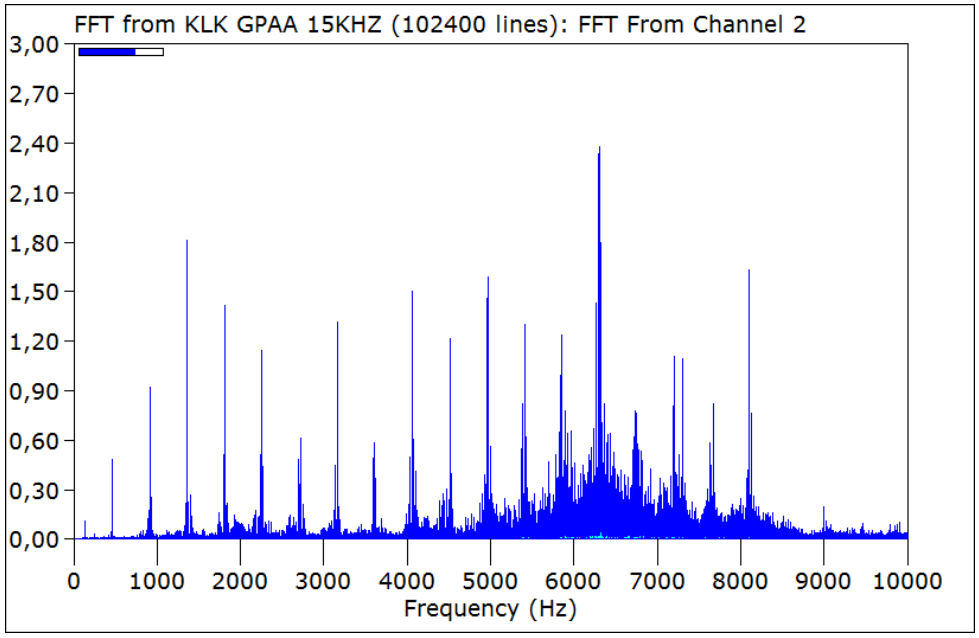

Figure 6. $\ddot{x}_{peak}$ **(kg/s) spectrum from the 2nd stage in the horizontal direction, g=9.80665 m/s^2.**

5. CONCLUSIONS

Vibration velocity responded very well to the vibrations with frequencies less than 1000 Hz. However, an even better response was obtained by acceleration and its higher derivatives, which also produced more information on higher frequencies. Considering the quite high rotational speed of the 2nd stage, it can be concluded that vibration velocity is not sufficient for monitoring the condition of the gearbox in question. Acceleration and its higher order derivatives should also be used in order to obtain better responsiveness for changes in the condition of the gearbox. Future work will include studies of the usability of the weighted l_p norm and real order derivatives $x^{(\alpha)}$ in the condition monitoring of an epicyclic gearbox.

ACKNOWLEDGEMENTS

This work was done as a part of the project “Integrated condition-based control and maintenance (ICBCOM)”. The funding of the TEKES (the Finnish Funding Agency for Technology and Innovation) and Kemijoki Oy is acknowledged.

REFERENCES

Ambarisha, V. K. and Parker, R. G. (2007). Nonlinear dynamics of planetary gears using analytical and finite element models. *Journal of Sound and Vibration*, 302 (3), 577-595.

Bartelmus, W., Chaari, F., Zimroz, R., Barszcz, T. and Haddar, M. (2012). Modeling of transmission used in wind turbines. In *The Ninth International Conference on Condition Monitoring and Machinery Failure Prevention Technologies*.

Bartelmus, W. and Zimroz, R. (2009a). Vibration condition monitoring of planetary gearbox under varying external load. *Mechanical Systems and Signal Processing*, 23, 246-257.

Bartelmus, W. and Zimroz, R. (2009b). A new feature for monitoring the condition of gearboxes in non-stationary operating conditions. *Mechanical Systems and Signal Processing*, 23, 1528-1534.

Barszcz, T. and Randall, R. B. (2009). Application of spectral kurtosis for detection of a tooth crack in the planetary gear of a wind turbine. *Mechanical Systems and Signal Processing*, 23, 1352-1365.

Blunt, D. M. and Keller, J. A. (2006). Detection of a fatigue crack in a UH60A planet gear carrier using vibration analysis. *Mechanical Systems and Signal Processing*, 20, 2095-2111.

Combet, F. and Zimroz, R. (2009). A new method for the estimation of the instantaneous speed relative fluctuation in a vibration signal based on the short time scale transform. *Mechanical Systems and Signal Processing*, 23, 1382-1397.

Eltabach, M., Jung, T. and Sieg-Zieba, S. (2012). Vibration analysis for gears damage detection in lifting cranes. In *The Ninth International Conference on Condition Monitoring and Machinery Failure Prevention Technologies*.

Feng, Z. and Zuo, M. J. (2012). Vibration signal models for fault diagnosis of planetary gearboxes. *Journal of Sound and Vibration*, 331 (22), 4919-4939.

Hameed, Z., Hong, Y. S., Cho, Y. M., Ahn, S. H. and Song, C. K. (2009). Condition monitoring and fault detection of wind turbines and related algorithms: A review. *Renewable and Sustainable Energy Reviews*, 13, 1-39.

Heyns, T., Heyns, P. S. and Zimroz, R. (2012). Combining discrepancy analysis with sensorless signal resampling for condition monitoring of rotating machines under fluctuating operations. In *The Ninth International Conference on Condition Monitoring and Machinery Failure Prevention Technologies*.

Klein, U. (2000). *Schwingungsdiagnostische Beurteilung von Maschinen und Anlagen*, 2. edition, Verlag Stahleisen GmbH, Düsseldorf.

Lahdelma, S. and Juuso, E. (2011a). Signal processing and feature extraction by using real order derivatives and generalised norms. Part 1: Methodology. *International Journal of Condition Monitoring*, 1 (2), 46-53.

Lahdelma, S. and Juuso, E. (2011b). Signal processing and feature extraction by using real order derivatives and generalised norms. Part 2: Applications. *International Journal of Condition Monitoring*, 1 (2), 54-66.

Lahdelma, S., Juuso, E. and Strackeljan, J. (2010). Using Condition Indices and Generalised Norms for Complex Fault Detection. In *Aachener Kolloquium für Instandhaltung, Diagnose und Anlagenüberwachung (AKIDA) Aachen, Germany 17.-18 November 2010*, 255-270, Verlag R Zillekens Germany.

Lahdelma, S. and Laurila, J. (2012). Detecting misalignment of a claw clutch using vibration measurements. In *The Ninth International Conference on Condition Monitoring and Machine Failure Prevention Technologies.*

McFadden, P. D. (1991). A Technique for Calculating the Time Domain Averages of the Vibration of the Individual Planet Gears and the Sun Gear in an Epicyclic Gearbox. *Journal of Sound and Vibration*, 144(1), 163-172.

Mäkikyrö A (2006) *Condition monitoring of the planetary gears of the tension leveling line*, Master's thesis, University of Oulu, Faculty of Technology, Department of Mechanical Engineering. (In Finnish)

Rzeszucinski, P. J., Sinha, J. K., Edwards, R., Starr, A. and Allen, B. (2012). A novel condition indicator gearbox diagnosis: amplitude of probability density function (APDF). In *The Ninth International Conference on Condition Monitoring and Machinery Failure Prevention Technologies*.

Taylor, J. I. (2000) *The Gear Analysis Handbook*, VCI Publishing, USA.

Vicuña, C. M. (2010). *Contributions to the analysis of vibrations and acoustic emissions for the condition monitoring of epicyclic gearboxes*, Doctor Thesis, Aachener Schriften zur Rohstoff- und Entsorgungstechnik des Instituts für Maschinentechnik der Rohstoff-industrie, Verlag R. Zillekens, Aachen.

Villa, L. F., Reñones, A., Perán, J. R. and Miguel, L. J. (2012). Statistical fault diagnosis based on vibration analysis for gear test-bench under non-stationary conditions of speed and load. *Mechanical Systems and Signal Processing*, 29, 436-446.

Wu, T. Y., Chen, J. C. and Wang, C. C. (2012). Characterization of gear faults in variable rotating speed using Hilbert-Huang Transform and instantaneous dimensionless frequency normalization. *Mechanical Systems and Signal Processing*, 30, 103-122.

Input Variable Selection in Modelling of Desulphurization Efficiency

Riku-Pekka Nikula, Esko Juuso, Kauko Leiviskä

Control Engineering Laboratory, P.O.Box 4300, FI-90014 University of Oulu, Finland
(e-mail: riku-pekka.nikula@oulu.fi.)

Abstract: Several methods are applied to find the input variables with predictive power to the degree of desulphurization modelling. The methods are applied on the data from a desulphurization plant processing flue gases coming from a coal-fired power plant. In non-linear and complex industrial processes, the nature of the relationships between the variables may be vague and a functional model based on a physical interpretation of the process may be difficult to define. Data-driven statistical modelling approaches are, therefore, reasonable alternatives. However, such models may become corrupted due to the inclusion of uninformative, weakly informative or redundant variables. Linear correlation coefficients, principal component analysis and regression, partial least squares regression, mutual information based algorithms and the general regression neural network are tested in the selection of the informative variables. The results obtained are relevant to desulphurization plant monitoring development.

Keywords: artificial neural networks, desulphurization plant, input variable selection, machine learning, modelling, process monitoring

1. INTRODUCTION

In model development, the preliminary assumption is that one or several candidate variables are capable of describing some of the output behaviour. The input variable selection task is common to the development of all statistical models. It depends on the discovery of relationships within the available data. In the case of parametric, or semi-parametric empirical models, the difficulty of the input variable selection task is somewhat alleviated by the a priori assumption of the functional form of the model, which is based on some physical interpretation of the underlying system or process being modelled (May et al. 2011). Although such a model is theoretically the most accurate, it may be difficult to develop. Data-driven statistical modelling approaches do not have an assumption regarding the model structure. Instead, the model is developed after the variable selection or the variables are selected simultaneously during the model training.

Several aspects impact on the formation of an optimal input set. First of all, d potential inputs form 2^d-1 input subsets. The testing of all the subset combinations with a large d requires efficient algorithms. Including more inputs in a model increases the computational burden of the model. This is further exacerbated in time series studies, in which appropriate lags must be chosen. As the lag of input time series increases, so does the number of inputs to the model and consequently the memory requirement of the model increases. According to 'the curse of dimensionality' by Bellman (1961), the linear increase in the dimensionality of the model results in the total volume of the modelling problem domain increasing exponentially. Moreover, understanding complex models is more difficult than understanding simple models that give comparable results. Inclusion of redundant and irrelevant input variables worsens the training of the models – especially artificial neural networks (ANNs). Redundant variables increase the number of local minima in the error function that is projected over the parameter space of the model (Bowden et al. 2005; May et al. 2011). Irrelevant variables add noise into the model inducing misconvergence and poor model accuracy. The most important characteristic of the input set is the inclusion of predictive power. In conclusion, the optimal input variable set has the fewest input variables needed to describe the behaviour of the output, with minimum redundancy and without uninformative variables.

Using analytical methods to define an optimal input set evidently has advantages. However, a unifying theoretical framework is lacking (May et al. 2011). The approaches are diverse, but can be broadly classified into three main classes: wrappers, filters and embedded methods (Guyon and Elisseeff, 2003). Wrappers approach the task as part of the optimisation of model architecture. The optimisation searches through the input combinations and selects the set which yields the optimal generalisation performance of the trained learning machine. Embedded methods perform variable selection in the process of training and are usually specific to given learning machines. Filters distinctly separate the variable selection task from the specific learning machine. Filters use statistical analysis techniques to measure the relevance of individual, or combinations of, input variables. The approach provides a generic selection of variables, not tuned for the specific learning machine. The approach can be also used as a pre-processing step to reduce space dimensionality and overcome overfitting. Sophisticated

wrappers and embedded methods improve predictor performance compared with simple variable ranking methods, but the improvements are not always significant (Guyon and Elisseeff, 2003). Wrappers and filters require a criterion or test to determine the influence of the selected input variable or variables and a strategy for searching among the combinations of candidate variables (May et al. 2011).

In this study, data from the desulphurization plant of a coal-fired power plant is analysed. Process systems generally contain varying degrees of non-linearity. Consequently, the presumption is that the process model should be non-linear although linear parts could be involved in the plant behaviour. Because of this, Artificial Neural Networks (ANNs) which are capable of modelling non-linear relationships give a good premise for modelling. ANN architectures can be built with arbitrary flexibility and can be successfully trained using any combination of the input variables which are good predictors. The model-free input variable selection approach – implying the filters – is considered here. The linear relationships of the candidate variables to the response variable – degree of desulphurization – are analysed with cross-correlations and partial correlation. Dimensionality reduction is performed by forming the linear combinations of the original variables by using Principal Component Analysis (PCA) and Partial Least Squares (PLS) regression. To get a grasp of the non-linear relationships among the variables, Mutual Information (MI) based criteria are used. In addition to all the original variables, the selections produced by correlation analyses are used as inputs to PCA and PLS regression; the selections from correlation analyses and the input scores produced by PCA and PLS regression are used as inputs to the evaluation of the mutual information based criteria. To obtain a generalized impression of the performance of all the formed input variable sets, General Regression Neural Networks (GRNNs) are trained. This type of neural network is chosen, because it can be designed very quickly. PLS regression models are tested for comparison. The next Section explains the used methods and the process being analysed. The main results are presented and discussed thereafter.

2. METHODS AND MATERIALS

2.1 Linear and Non-linear Filters

Filter algorithms typically measure relevance and optimality criteria that are used to discover the important input variables. Incremental search strategies tend to dominate the filter approaches, because the relevance measure is typically bivariate statistic of the candidate-output relationship. Each of the relationships is evaluated. Currently, two broad classes of filters have been considered: those based on linear correlation; and those based on information theoretic measures, such as mutual information (May et al., 2011).

Input variable ranking based on the Pearson correlation is one of the most widely used methods. The candidate variables are sorted by the order of decreasing correlation and the selection is based on greedy selection of the first k variables, or upon all variables having correlation significantly different from zero. The method is classed as a maximum relevance filter and only the interactions between each candidate and the output is considered. The Pearson correlation, R_{xy}, is defined by

$$R_{xy} = \frac{\sum_{i=1}^{n}(x_i - \bar{x})(y_i - \bar{y})}{\sqrt{\sum_{i=1}^{n}(x_i - \bar{x})^2 \sum_{i=1}^{n}(y_i - \bar{y})^2}} \quad (1)$$

where x_i, y_i $\bar{x}$, $\bar{y}$ and n are the candidate variable, the target variable, the corresponding mean values and the total number of observations, respectively. In (1), the numerator is simply the sample covariance; and two terms in the denominator are the square root of the sample variances.

If the candidate variables are themselves correlated, redundancy is an important issue. In such a case, the correlation ranking approach is likely to select too many variables, since many candidates will each provide the same information regarding the target variable. Given three variables x, y and z, the partial correlation measures the correlation between x and y after the relationship between y and z has been discounted. The partial correlation $R_{xy \cdot z}$ can be determined from the Pearson correlation using

$$R_{xy \cdot z} = \frac{R_{xy} - R_{xz}R_{yz}}{\sqrt{\left(1 - R_{xz}^2\right)\left(1 - R_{yz}^2\right)}}. \quad (2)$$

The limitations of linear correlation analysis have created interest in alternative statistical measures of dependence, which are more adept at identifying and quantifying dependence that may be chaotic or non-linear; and which may therefore be more suitable for the development of ANN models (May et al. 2011). Mutual information is a measure of dependence that is based on information theory and the notion of Shannon's (1948) entropy, and is determined by the equation

$$I(x;y) = \iint p(x,y) \log \frac{p(x,y)}{p(x)p(y)} dxdy, \quad (3)$$

where $p(x)$ and $p(y)$ are the marginal probability density functions of x and y, respectively; and $p(x,y)$ is the joint (bivariate) density. $I(x;y)$ denotes the mutual information, which is a measure of dependence between the density of the variable x and the density of the target y. Mutual information measures the quantity of information about a variable y that is provided by a second variable x. The advantage of mutual information over linear correlation is that it is based solely on probability distributions within the data and is therefore an arbitrary measure, which makes no assumption regarding the structure of the dependence between variables (May et al., 2011). The difficulty is that the densities $p(x)$, $p(y)$ and $p(x,y)$ are all unknown and hard to estimate from data. The case of

continuous variables is the hardest. One can consider quantizing the variables or approximating their densities with a non-parametric method such as Parzen windows (Guyon and Elisseeff, 2003).

In feature selection literature, there are several filters using a variety of heuristic criteria based on mutual information. Current best practice has been to hand-design the criteria, augmenting the individual feature relevance with various penalties to manage the feature redundancy (Brown, 2009). Brown (2009) offers a descriptive "top-down" framework, showing that several heuristic criteria in the literature can be expressed in a common functional form

$$J = I(x_n; y) - \beta \sum_{k=1}^{n-1} I(x_n; x_k) + \gamma \sum_{k=1}^{n-1} I(x_n; x_k \mid y), \quad (4)$$

where β and γ are configurable parameters varying in [0,1].Variable x_n is the n^{th} variable being evaluated; x_k represents the already selected variables; and y is the target variable. The first term $I(x_n;y)$ ensures feature relevance (mutual information); the second term with the parameter β penalises high correlations (redundancy) between variable itself and the existing variables; the third term with the parameter γ depends on the class conditional probabilities. Brown (2009) has identified 12 separate criteria that can be described within this framework; four of them are tested in this study. Mutual Information based Feature Selection (MIFS) criterion by Battiti (1994) includes the relevance and redundancy but omits the conditional term. Maximum-Relevance Minimum-Redundancy (MRMR) criterion by Peng et al. (2005) takes the mean of the redundancy term, but omits the conditional term. Joint Mutual Information (JMI) criterion by Yang and Moody (1999) has all the three terms and can be defined by (5). Conditional Mutual Information Maximization (CMIM) by Fleuret (2004) can be defined by (6):

$$J_{jmi} = I(x_n; y) - \frac{1}{n-1} \sum_{k=1}^{n-1} \left[I(x_n; x_k) - I(x_n; x_k \mid y) \right], \quad (5)$$

$$J_{cmim} = I(x_n; y) - \max_k \left[I(x_n; x_k) - I(x_n; x_k \mid y) \right]. \quad (6)$$

2.2 Principal Component Analysis and Regression

Principal component analysis (PCA) is a commonly adopted technique for reducing the dimensionality of a dataset X. PCA achieves dimensionality reduction by expressing the d variables ($x_1,...,x_d$) as k feature vectors named principal components (PCs). Mathematically, PCA relies on an eigenvector decomposition of the covariance or correlation matrix of the process variables. PCA is scale-dependent, and therefore, it is conventional to adjust the variables to zero mean and unit variance. PCA decomposes the data matrix X as the sum of the outer product vectors t_i and p_i plus a residual matrix E (Wise and Gallagher, 1996):

$$X = t_1 p_1^T + t_2 p_2^T + ... + t_k p_k^T + E \ . \quad (7)$$

The t_i vectors are known as scores and contain information on how the samples relate to each other. The scores form an orthogonal set ($t_i^T t_j = 0$ for $i \neq j$). The p_i vectors are known as loadings and p_i are eigenvectors of the covariance matrix. The t_i, p_i pairs are arranged in descending order according to the associated eigenvalue λ_i. The first pair captures the largest amount of variation in the data that is possible to capture with a linear factor. Each subsequent pair captures the greatest possible amount of variance remaining at that step. Usually, it is not practical to compute all the k eigenvectors, since most of the variability in the data is typically captured in the first few PCs. A common selection method is to choose all the PCs whose eigenvalues exceed some threshold λ_0, or generate a plot of the cumulative eigenvalue as a function of the number of PCs so that the desired amount of variance is explained (May et al. 2011).

Alternatively, Principal Component Regression (PCR) can be used to select the PCs. Then, multiple linear regression models are built based on response variables Y and varying number of PCs explaining X. Selection of the components can be done by choosing the PCs that optimize the predictive ability of the model (Wise and Gallagher, 1996). Typically, the available data is divided into training and validation sets. The residual error of prediction on the validation samples is determined as a function of the number of PCs. In k-fold cross-validation, the original set is randomly partitioned in k subsamples. Thus, in *10*-fold cross-validation 90 % of the data is used to train the model and 10 % is used in validation. Each subsample is used exactly once as the validation data.

2.3 Partial Least Squares Regression

Partial Least Squares (PLS) regression extracts latent variables that explain the variation in the predictor variables X and the variation in X which is the most predictive of the response variables Y. In other words, PLS attempts to find factors that are correlated with Y while describing a large amount of the variation in X. As a point of comparison, in PCR the components solely explain the variance in X. As in PCA, the latent vectors or scores (t_1, t_2...) are orthogonal. The selection of components can be done like in PCA and PCR. In addition to choosing the components that explain the most variance in X, the components that explain the most variance in Y can be chosen. See Geladi and Kowalski (1986) for more detailed information on PLS regression.

2.4 General Regression Neural Networks

Developed by Specht (1991), the general regression neural network (GRNN) is a supervised feedforward artificial neural network. It uses a nonparametric estimate for the probability density function of the data. Non-linear relationships between inputs and output can be modelled with a GRNN. The network architecture is fixed which means that multiple models do not need to be trained to optimise the network

architecture. It has only a single parameter, the kernel bandwidth, which needs to be learned during training. The parameter is named 'spread' hence. Training is much faster than with other artificial neural networks, such as Multi-Layer Perceptrons (MLPs) trained using the backpropagation algorithm. The GRNN uses memory based (lazy) learning, and therefore it has an increased memory requirement to store the training data and a greater computational requirement when querying the network than an MLP. Further information about the method can be found in Specht (1991).

2.5 Performance Criteria

Three criteria are adopted for assessing the models developed. The popular measure of predictive performance is the mean squared error (*MSE*). Another statistical error measure is the mean absolute error (*MAE*). Goodness-of-fit can be evaluated with the coefficient of determination (r^2). The drawback of these criteria is that the best result does not necessarily mean an optimal model. Models with large number of input variables tend to be biased as a result of overfitting. In (8), (9), and (10), y_j , $\bar{y}$, $\hat{y}_j$, $\tilde{y}$, and n are the observed value, the mean of the observed value, the corresponding predicted value, the mean predicted value and the total number of observations, respectively. The criteria are expressed as:

$$MSE = \frac{1}{n}\sum_{j=1}^{n}(y_j - \hat{y}_j)^2 , \tag{8}$$

$$MAE = \frac{1}{n}\sum_{j=1}^{n}\left|y_j - \hat{y}_j\right| , \tag{9}$$

$$r^2 = \frac{\sum_{j=1}^{n}\left(y_j - \bar{y}\right)\left(\hat{y}_j - \tilde{y}\right)}{\sqrt{\sum_{j=1}^{n}\left(y_j - \bar{y}\right)^2 \sum_{j=1}^{n}\left(\hat{y}_j - \tilde{y}\right)^2}} . \tag{10}$$

2.6 Desulphurization Process and the Data

The coal-fired Salmisaari power plant consists of two main units for energy production and a desulphurization plant, which processes the flue gases from both main units. Boiler 1 is a combined heat and power plant with the capacity of 160 MW_{el} and 300 MW_{th} and boiler 7 is a heat unit with the capacity of 180 MW_{th}. The efficiency of nearly 90 % is reached in combined heat and power generation.

The desulphurization plant consists of two parallel reactors which process the flue gases. Fig. 1 demonstrates the principle of operation. Flue gases from the furnace of the steam boiler of the power plant arrive at the electrostatic precipitator ('preliminary separator') which separates fly ash. Flue gases without any solid particles come to the reactor from above and are mixed with lime sludge using compressed air. The particles of sludge and sulphur dioxide molecules are partly mixed in the reactor and reaction products fall at the bottom of the silo. Reaction continues in bag filters, in which gases flow through textile tube and 99.7 % of solid particles remain on its walls. Purified gases go via the fans into the chimney and out in the air. Middle product accumulating at the bottom of the reactor is used to produce sludge, and necessary amount of end product from below the filter is added to it. Together with water, these form the base of sludge. Lime is added in the form of lime milk to achieve the desired level of desulphurization. The amount of sludge pumped into the reactor is controlled so that all water in sludge evaporates and flue gas going to the filter is dry. The method is called half-dry, because the chemical reaction occurs partly in the wet, partly in the dry state. The outgoing end product is used for earth works such as filling ditches, strengthening man-made hills or under the dumping areas.

The variable y for the degree of desulphurization is formed from the similarly standardized SO_2 concentration measurements from the flue gas before (SO_2^{in}) and after (SO_2^{out}) the desulphurization plant. Therefore, the equation $y = 1 - SO_2^{out} / SO_2^{in}$ was considered proper for this study. Table 1 shows some characteristics of the used data. One hour average data is used. Data sets A and B represent the typical operation of the plant; data sets C and D represent a campaign during which higher than the typical degree of desulphurization was used. The set E is a combination of A, B and D. 1686 hours were removed from the set due to memory overflows during the training of GRNNs with the full length data. Thus, the final length of E was 3000 hours. The term 'std' is standard deviation. The candidates for a model input set include 66 variables. The variables that are presented in Section 3 are described in Table 2. The set included some computational variables. With y and other computational variables, it has to be noticed that the uncertainty of measurement is cumulative. The values produced by the computations are less accurate than the single original measurement values. However, the measurement uncertainty is not considered in this study any further. Equations for x_{57}, x_{58}, x_{64}, and x_{65} are presented in (11), (12), (13), and (14):

$$x_{57} = \frac{x_1 \cdot x_3}{\frac{\sqrt{x_6}}{\sqrt{x_6}+\sqrt{x7}} \cdot x_{60} \cdot x_8} , \tag{11}$$

$$x_{58} = \frac{x_2 \cdot x_3}{\frac{\sqrt{x_7}}{\sqrt{x_6}+\sqrt{x7}} \cdot x_{60} \cdot x_8} , \tag{12}$$

$$x_{64} = \frac{(x_1 + x_2)\cdot x_3}{x_{52} + x_{53}} , \tag{13}$$

$$x_{65} = x_8 / x_{14} . \tag{14}$$

Table 1. Description of the used data

set	year/month	length	degree of desulph. (%)			
		(hours)	mean	std	max	min
A	2009/12 - 2010/5	2801	69.2	6.1	91.9	32.0
B	2009/10-12	1401	71.5	7.6	91.6	51.0
C	2012/1-3	969	81.4	4.0	92.1	67.4
D	2012/3	484	87.2	2.1	96.0	80.0
E	(part of A)+B+D	3000	74.9	8.2	96.0	51.0

Table 2. Candidate variables

variable	***explanation***
x_1	sludge volume flow to reactor 1
x_2	sludge volume flow to reactor 2
x_3	sludge density in feeding tank
x_6	pressure over reactor 1 inlet duct
x_7	pressure over reactor 2 inlet duct
x_8	SO_2 emission measurement before desulphurization plant
x_9	Power plant power output
x_{11}	H_2O in B chimney
x_{14}	feeding tank level
x_{16}	mixing water volume flow
x_{17}	mixing tank density
x_{20}	O_2 after electrostatic precipitator 1
x_{22}	flue gas temperature before desulphurization plant
x_{23}	flue gas pressure before desulphurization plant fan
x_{24}	flue gas pressure after desulphurization plant fan
x_{27}	circulating dust silo level
x_{28}	raw water volume flow to feeding tank
x_{32}	NO_x in B chimney
x_{33}	NO_x into A chimney
x_{36}	pressure difference over reactor 1
x_{37}	pressure difference over reactor 2
x_{38}	pressure difference over bag filters 1
x_{42}	O_2 in boiler 1 flue gas
x_{44}	CO_2 in boiler 1 flue gas
x_{45}	pressure after electrostatic precipitator from unit 7
x_{52}	SO_2 mass flow from unit 1
x_{53}	SO_2 mass flow from unit 7
x_{57}	'ratio of sludge and SO_2 into reactor 1'
x_{58}	'ratio of sludge and SO_2 into reactor 2'
x_{59}	'sum of sludge mass flows to reactors 1 and 2'
x_{60}	'sum of flue gas flows from units 1 and 7'
x_{62}	flue gas temperature out of reactor 2
x_{63}	SO_2 mass flow to desulphurization plant
x_{64}	'ratio of sludge flow and SO_2 mass flow'
x_{65}	'ratio of SO_2 before desulph. plant and feeding tank level'

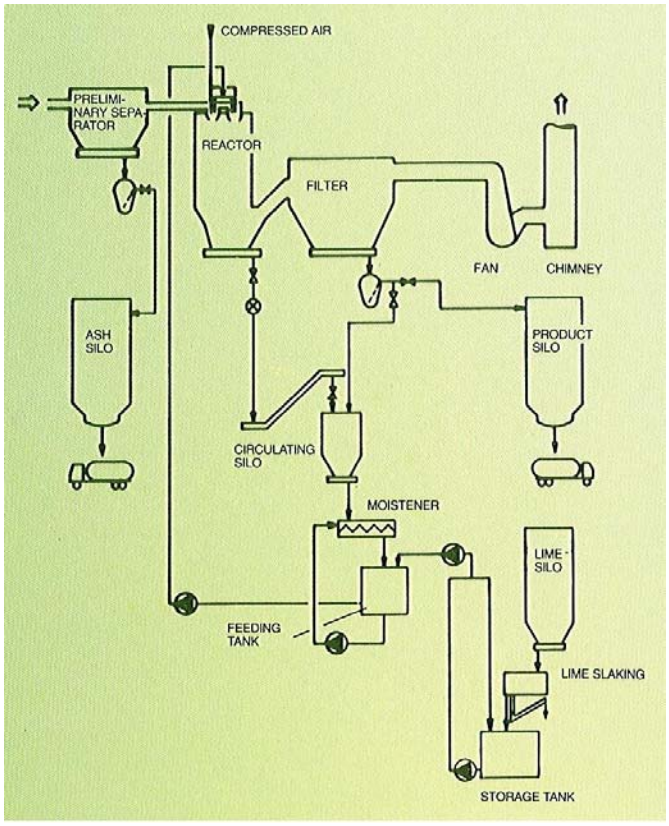

Fig. 1. The desulphurization plant with half-dry method (Helsinki Energy Board, 1980s).

3. RESULTS

In this Section, the mentioned methods are applied to the Salmisaari data. All the studies were performed using Matlab (version 7.12) software (Mathworks Inc., Natick, MA, USA, 2011). All the methods were applied on data normalized to zero mean and unit variance. The main results are presented and discussed.

3.1 Correlations

Correlation coefficients were studied with data sets A and C. Only the coefficients to the response variable y were studied. Cross-correlations were used to find the 24 hour lags. Data was normalized so that auto-correlations at zero-lag were identically 1.0. The results with zero-lag correspond to the output of (1). Data was modified with logarithm of the absolute value, square, inverse, and square root of the absolute value. To define strong correlations two limits were made: Limit I was $|R_{xy}|>2/\sqrt{d}$, and limit II was $|R_{xy}| > 0.5$. The parameter d is the number of candidates. Table 3 shows the variables, of which correlations were larger than the limit II. The column with the title 'zero-lag' indicates the correlation without any modifications or lag. The column with the title 'the largest' indicates the largest correlations using the modified data. The column 'modification' shows the lag in hours and the method used to modify the data.

Forty-nine variables measured up to the limit I with the set A, whereas the corresponding number was 43 with the set C. The variables that measured up to the limit I were tested with partial correlation in such a way that z included all the other variables that measured up to the limit I except the variable being tested. Using partial correlation, only a single variable x_{63} measured up to the limit I. The partial correlation $R_{x_{63}y\cdot z}$ was -0.333 with the set A, and -0.602 with the set C.

Table 3. The largest absolute correlations

set A	zero-lag	the largest	modification
x_8	0.617	0.617	0
x_{11}	-0.640	-0.643	-1, $log(\|x\|)$
x_{17}	-0.572	-0.572	0
x_{27}	0.543	0.584	-14, x^2
x_{33}	0.611	0.614	-3, x^2
x_{44}	-0.711	0.720	0, x^{-1}
x_{45}	-0.280	-0.690	-13, $log(\|x\|)$
x_{63}	-0.598	-0.619	-1, x^2
x_{65}	0.610	0.610	0
set C	**zero-lag**	**the largest**	**modification**
x_{16}	-0.376	-0.511	-1, x^2
x_{20}	-0.444	0.505	-23, x^{-1}
x_{23}	0.479	-0.502	-2, x^2
x_{44}	-0.571	-0.724	-11, $log(\|x\|)$
x_{52}	-0.819	-0.825	0, x^2
x_{53}	-0.637	-0.637	0
x_{62}	-0.505	0.506	-21, x^{-1}
x_{63}	-0.816	-0.816	0
x_{64}	0.639	-0.783	0, x^{-1}

3.2 Principal Component Analysis and Partial Least Squares Regression

All the variables and only the variables that measured up to the correlation limits I and II were fed to PCA and PLS regression. PCA produced the same number of principal component scores which was the number of input variables. To reduce the dimensionality, the components were chosen based on the variance that they explain from the total variance of the input space. The variance of the components that explain most were summed up until the set criterion was measured up. In this study, the first limit was 80 %, the second was 95 %, and the third was 99 %. Table 4 shows the number of components explaining the defined variance using different data sets. On the sets A and B correlation selections from the set A were used, and on the sets C and D the selections from C were used. The percentage of variance explained in y was considered with PLS regression. The same limits were used and results are shown in Table 4.

An alternative way to determine the proper amount of components was to develop regression models to the prediction of the response y. The models were built with data sets A, B, C, and D so that the amount of components varied from one to thirty. All the variables and only the variables that measured up to the correlation limit I were used. The models were validated with *10*-fold cross-validation. The mean squared error performance was evaluated based on the difference between estimated $\hat{y}$ and actual y. The results from principal component regression validation are shown in Fig. 2. The y axis values correspond to the mean observed.

Table 4. The number of components explaining the defined variance in *X* with PCA (left) and *y* with PLS regression (right)

variance limit	A	B	C	D	variables
80	8|3	8|4	11|4	8|5	all
95	19|9	18|8	24|8	20|7	all
99	29|28	28|22	35|13	29|15	all
80	4|2	6|2	6|3	5|3	cor. limit I
95	13|5	14|4	15|6	13|6	cor. limit I
99	23|14	22|12	25|11	20|18	cor. limit I
80	4|1	4|2	3|1	3|2	cor. limit II
95	6|2	7|2	6|2	6|5	cor. limit II
99	8|3	8|3	8|4	7|6	cor. limit II

The linear regression models performed relatively well taking into consideration the weak linear relationships of the variables to the response variable. *MSE* decreases as the number of components increases with some exceptions. *MSE* was below 0.43 using five components with all the data sets. Apart from the set D, *MSE* was below 0.28 with eight components. With sets A and B the standard deviations of *MSE* were low and decreasing as the number of components increased. The set C had the lowest standard deviation of MSEs with four to five components. Inclusion of components seemed to increase the standard deviation. The set D had lower than 0.1 standard deviations the first time with 16 components. The results show that using a large number of components will generally do a good job in fitting the current observed data. On the other hand, it is a strategy that can lead to overfitting and can give an overly optimistic estimate for the expected error. Fig. 2 indicates that achieving a quite constant *MSE* level needs three to seven components, which can be interpreted as a proper amount of input components for a principal component regression model.

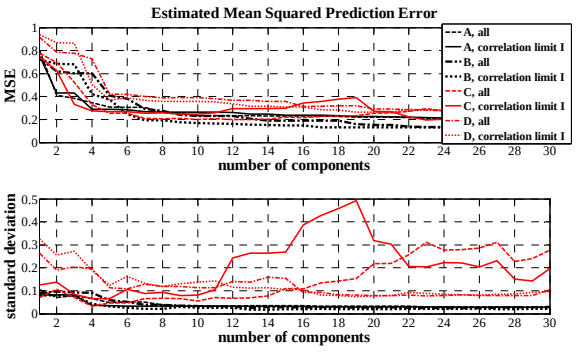

Fig. 2. Principal component regression validation results.

Fig. 3 shows corresponding results for PLS regression. The *MSE* reaches a relatively low level when the model has three or four components, and the level stays quite constant when

the amount of components is increased. Also the standard deviation of MSE was quite constant after the fourth component apart from the C set. In general, the performance of PLS regression was somewhat better than PC regression using a small number of components. The results indicate that a proper amount of components for a PLS regression model is slightly smaller than for a PC regression model.

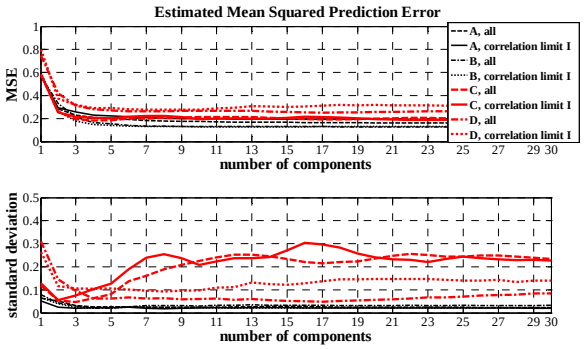

Fig. 3. Partial least squares regression validation results.

3.3 Mutual Information Based Criteria

All the variables, PCA scores, and PLS regression input scores together with the response variable were analysed with the mutual information based criteria using data sets A, B, C, and D. PCA and PLS regression scores were done using all the candidates. The procedure greedily chose the variable with the largest incremental gain until the chosen number of variables was reached. The number of the input variables to be selected was chosen to be 20 variables. The continuous variables were quantized for the mutual information calculations. The data of each variable were quantized in the first case to 10 bins and in another case to 100 bins so that the bin limits were quantiles with a regular interval. In MIFS, the heuristic weighting β was chosen to be 0, 0.5, and 1 in different tests. When β = 0, the method is reduced into mutual information ranking. In conclusion, 3·4·2·6=144 input sets were created. Because of limited space, Table 5 shows only the largest mutual information of ten first variables chosen from sets A and C together with the set B (10 bins), which eventually led to the most promising modelling result.

Table 5 shows that the quantization has a large effect on the result. With all the tested criteria, the first selected variable was always the same on the same data set, but could differ based on the quantization as Table 5 indicates with C. The subsequent variables varied based on the criteria used. This arises from the varying emphasis the different criteria have on the redundancy and conditional terms of (4). Obviously, the varying operational states of the different sets have an influence in the varying selections of input variables. The same is seen in correlation rankings, see Table 3.

Table 5. The largest mutual information using sets A, C, and B

set A		set C		set B
10 bins	100 bins	10 bins	100 bins	10 bins
x_{44},0.6773	x_{44}, 2.4090	x_{52},0.9652	x_{65},3.5723	x_{63},0.6883
x_{45},0.6194	x_{8}, 2.3962	x_{64}, 0.9198	x_{8},3.5400	x_{45},0.5371
x_{11},0.5062	x_{65}, 2.3961	x_{63}, 0.8950	x_{59},3.5145	x_{32},0.5012
x_{65},0.4758	x_{45}, 2.3339	x_{53}, 0.7426	x_{64},3.5134	x_{64},0.4798
x_{8},0.4703	x_{11}, 2.3314	x_{44},0.6950	x_{57},3.5018	x_{22},0.4500
x_{33},0.4481	x_{7}, 2.3111	x_{65},0.4806	x_{58},3.5013	x_{44},0.4317
x_{17},0.4285	x_{36}, 2.3033	x_{8},0.4520	x_{9},3.4994	x_{53},0.3935
x_{42},0.4210	x_{37}, 2.2976	x_{24},0.4336	x_{62},3.4990	x_{52}, 0.3879
x_{63},0.4038	x_{52}, 2.2929	x_{42},0.4206	x_{24},3.4916	x_{23},0.3716
x_{27},0.3916	x_{62},2.2799	x_{28},0.4193	x_{38},3.4909	x_{65},0.3690

3.4 Evaluation of the Selected Inputs in Modelling

Evaluation of the chosen sets was done with a heuristic trial-and-error approach by building GRNNs with different input sets. In GRNNs, spread values 0.1, 0.5, 1, 2, and 10 were tested, but an optimal value for the spread value was not searched for. To test GRNNs, there were three cases. In the first case, the network was trained with the set A and the performance was tested with the set B. In the second case, the network was trained with the set C and tested with the set D. In the third case, the sets A, B, and D formed the training set E and the set C was the test set. The number of components from PCA and PLS regression were chosen based on the variance limits discussed earlier. Only the number of components defined with the sets A and C were used. Considering correlation, PCA, and PLS regression sets, the selected sets formed from the analysis of A were used to train GRNNs on A set and E set. Similarly, sets formed from the analysis of C were used to train GRNNs on C set and E set. Mutual information criteria based selections were tested with all the 20 selected variables and with only ten variables which were chosen first by each criterion. All of these selections were used on each training set A, C, and E. Sets formed based on linear correlations included zero lagged variables without any modifications. GRNNs were trained with every input variable set, spread value, and training set (A, C, and E) separately. Therefore, the number of trained GRNNs was 2·5·2 + 4·5 + 9·5·2 +18·5 + 9·5·2 + 18·5 + 144·5·3 + 144·5·3 = 4720.

The model prediction performance on the test sets was monitored with mean squared error, mean absolute error, and the coefficient of determination. Table 6 shows the best results of the GRNN performance on the test sets with the input sets formed with the different methods. From the test sets B and D only the better result is shown. The best result at the last row of Table 6 was achieved with MIFS (β = 0) from the analysis of the set B. All the presented mutual information criteria based results in Table 6 were reached with data quantized into ten bins.

The best performing neural networks were obtained with input sets that were formed by mutual information based criteria using data quantized into ten bins. Obviously, the quantization into 100 bins was not a proper method. Mutual information criteria based sets performed better with ten than twenty variables indicating that the amount of input variables is highly important part of the selection. A neural network with PLS regression input scores as inputs performed poorly. Variables chosen by the linear correlation produced slightly better performing models than the models with PCA scores as inputs.

Table 6. General regression neural network prediction performance without validation

method	*MSE*	*MAE*	r^2	*spread*	*test set*
correlation	0.54	0.58	0.46	1	B
PCA	0.54	0.59	0.46	1	B
PLS regression	0.72	0.63	0.28	0.1	D
MI-based (20 var.)	0.42	0.49	0.58	1	B
MI-based (10 var.)	0.36	0.46	0.64	1	B
correlation	0.44	0.51	0.56	1	C
PCA	0.52	0.54	0.48	1	C
PLS regression	0.92	0.76	0.07	0.1	C
MI-based (20 var.)	0.36	0.48	0.64	1	C
MI-based (10 var.)	0.30	0.41	0.70	1	C

The performance of the best performing GRNN was compared with PLS regression models, which were built with the same input set. Also the linear correlation sets were tested in PLS regression models for the sake of comparison. In PLS regression models, one to nine latent variables (components) were tested. Training and test sets were composed from the set E, which was randomly partitioned into ten subsamples of the same size; validation set was the set C. *10*-fold cross-validation was performed to validate the results. Table 7 summarises the performance of the models. The values correspond to the mean observed. The corresponding variability is indicated by the standard deviations, which are the values in parentheses. The presented results are chosen so that the validation *MSE* is as small as possible. The PLS regression model with the correlation limit I set in Table 7 has two latent variables; the model with MI-based set has three latent variables. Fig. 4 shows the normalized degree of desulphurization and the predictions by the GRNN and PLS regression models on the validation period C. The predictions do not follow all the peaks or slower changes in the degree of desulphurization; the predictions have some harsh errors as well. Some of these parts are marked by red ellipses in Fig. 4. The general level of the degree of desulphurization can be found promisingly well.

Table 7. *10*-fold cross-validation *MSE*

model	*training*	*test*	*validation*
PLSR (correlation set)	0.2518(0.0033)	0.2574(0.0413)	0.2652(0.0022)
PLSR (MI-based set)	0.2862(0.0027)	0.2888(0.0279)	0.2707(0.0023)
GRNN (MI-based set)	0.2217(0.0023)	0.2468(0.0276)	0.3009(0.0051)

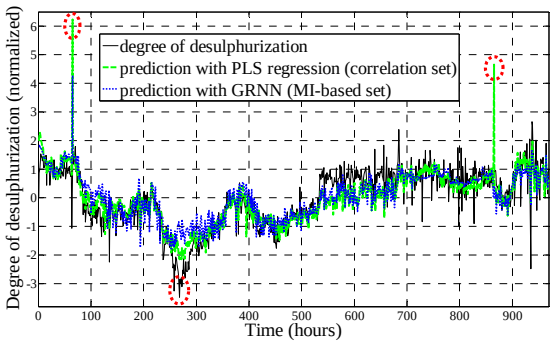

Fig. 4. The degree of desulphurization predicted by PLS regression and GRNN models during the validation period.

4. DISCUSSION

The results indicate that variable selection based on mutual information criteria is the most valid approach from the tested approaches in the considered context. The optimal way to quantize the process variables for the approach needs further research. The fact that industrial processes often involve non-linear behaviour came up in the study. Variables or components chosen by linear methods gave worse non-linear predictions. On the other hand, the linear PLS regression models performed slightly better than the non-linear GRNN model considering the prediction error in validation. However, the GRNN was not optimised by searching for the optimal number of input variables and the optimal value of the kernel bandwidth of the network. The development of the model for the desulphurization benefits from the lags discovered by cross-correlation, because the dynamics of the process need to be taken into consideration.

The use of score vectors from PCA or PLS regression in a neural network was the least promising approach in this study. However, Mohamad-Saleh and Hoyle (2008) use PCA successfully for the elimination of correlated information in the input data of a Multi-Layer Perceptron neural network. Linker (2005) use PCA scores as inputs to a sigmoid feedforward neural network. Lennox et al. (2001) also report the use of PCA and PCR in addition to cross-correlation in analysis of input and output variables for dynamic process models. Li et al. (2007) use PLS regression input and output scores combined with a Radial Basis Function neural network. To compare, only input scores were used as inputs to GRNN in this study.

There are several potential methods not studied here. The use of another mutual information based algorithm, Partial Mutual Information (PMI), for input selection of GRNNs is reported in May et al. (2008) and Bowden et al. (2005). The use of Self-Organizing Maps solely or combined with other methods is reported by (Similä and Laine 2005; Bowden et al. 2005). Laurinen and Röning (2005) report the use of a Bayesian network and expert information in the selection of inputs to a feedforward neural network. The assistance from a

process expert is generally reported being valuable in input variable selection (Simula and Alhoniemi, 1999; Lennox et al. 2001; Laurinen and Röning, 2005).

Guyon and Elisseeff (2003) recommend selecting variables in two ways. Firstly, variables should be ranked using a correlation coefficient or mutual information, and secondly, a nested subset selection method performing forward or backward selection or multiplicative updates should be used. This study is in agreement with that. Considering the GRNN, the sets selected with mutual information based criteria performed the best. However, a good model is achieved by fine tuning, where the use of a wrapper or an embedded method seems inviting.

ACKNOWLEDGEMENTS

This research was done as a part of the Measurement, Monitoring and Environmental Assessment (MMEA) programme managed by Cleen Ltd. The authors would like to thank the Finnish Funding Agency for Technology and Innovation (Tekes) for financial support. Helsinki Energy and the personnel are gratefully acknowledged for their contribution.

REFERENCES

Battiti, R. (1994). Using mutual information for selecting features in supervised neural net learning. *IEEE Trans. Neural Networks,* volume 5 (4), 537-550.

Bellman, R. (1961). *Adaptive control processes: a guided tour,* Princeton university press, New Jersey.

Bowden, G. J., Dandy, G. C., and Maier, H. R. (2005). Input determination for neural network models in water resources applications. Part 1 – background and methodology. *Journal of Hydrology,* volume 301 (1-4), 75-92.

Brown, G. (2009). A new perspective for information theoretic feature selection. *Proceedings of the twelfth international conference on artificial intelligence and statistic,* volume 5, 49-56.

Fleuret, F. (2004). Fast binary feature selection with conditional mutual information. *The Journal of Machine Learning Research,* volume 5, 1531-1555.

Geladi, P., and Kowalski, B. R. (1986). Partial least squares regression: a tutorial. *Analytica Chimica Acta,* volume 185, 1-17.

Guyon, I., and Elisseeff, A. (2003). An introduction to variable and feature selection. *The Journal of Machine Learning Research,* volume 3, 1157-1182.

Helsinki Energy Board (1980s). An official brochure of the Salmisaari desulphurization plant.

Laurinen, P., and Röning, J. (2005). An adaptive neural network model for predicting the post roughing mill temperature of steel slabs in the reheating furnace. *Journal of Materials Processing Technology,* volume 168 (3), 423-430.

Lennox, B., Montague, G. A., Frith, A. M., Gent, C., and Bevan, V. (2001). Industrial application of neural networks – an investigation. *Journal of Process Control,* volume 11, 497-507.

Li, R., Meng, G., Gao, N., and Xie, H. (2007). Combined use of partial least-squares regression and neural network for residual life estimation of large generator stator insulation. *Measurement Science and Technology*, volume 18 (7). 2074-2082.

Linker, R. (2005). Spectrum analysis by recursively pruned extended auto-associative neural network. *Journal of Chemometrics*, volume 19, 492-499.

May, R. J., Dandy, G. C., Maier, H. R., and Nixon, J.B. (2008). Application of partial mutual information variable selection to ANN forecasting of water quality in water distribution systems. *Environmental Modeling and Software,* volume 23 (10-11), 1289-1299.

May, R., Dandy, G., and Maier, H. (2011). Review of input variable selection methods for artificial neural networks, In Kenji Suzuki (Ed.), *Artificial neural networks - methodological advances and biomedical applications,* 19-44. InTech.

Mohamad-Saleh, J., and Hoyle, B. S. (2008). Improved neural network performance using principal component analysis. *Int. Journal of the Computer, the Internet and Management*, volume 16 (2), 1-8.

Peng, H., Long, F., and Ding, C. (2005). Feature selection based on mutual information: criteria of max-dependency, max-relevance, and min-redundancy. *IEEE Transactions on Pattern Analysis and Machine Intelligence,* volume 27 (8), 1226-1238.

Shannon, C. E. (1948). A Mathematical theory of communication. *Bell System Technical Journal,* volume 27, 379-423, 623-656.

Similä, T., and Laine, S. (2005). Visual approach to supervised variable selection by self-organizing map. *International Journal of Neural Systems,* volume 15 (1&2), 101-110.

Simula, O., and Alhoniemi, E. (1999). SOM based analysis of pulping process data. *Proceedings of international work-conference on artificial and natural neural networks (IWANN '99),* volume II, 567-577.

Specht, D., F., (1991). A General regression neural network. *IEEE Transactions on Neural Networks*, volume 2 (6), 568-576.

Wise, B.M., and Gallagher, N.B. (1996). The process chemometrics approach to process monitoring and fault detection. *Journal of Process Control,* volume 6 (6), 329-348.

Yang, H., and Moody, J. (1999). Data visualization and feature selection: new algorithms for nongaussian data. *Advances in Neural Information Processing Systems,* volume 12.

COST AND EFFECTIVENESS OF GEOTHERMAL DRILLING

Bjorn Mar Sveinbjornsson and **Sverrir Thorhallsson**[1]
[1]Iceland GeoSurvey (ÍSOR),
Grensásvegur 9, 108 Reykjavík,
ICELAND
bms.isor@gmail.com, sverrir.thorhallsson@isor.is

ABSTRACT

For geothermal power projects about 40-50% of the total investment cost lies in drilling of the production and reinjection wells and the steam supply system to the plant. Current geothermal project costs for conventional flash-steam plants are about 4,000 USD per kilowatt (kW) of power. Roughly half of the well cost comes from materials and infrastructure and the other half is from the rental of rigs and services (day rates). Drilling of each hole to 2,000-2,500 m may take anywhere from 32 to 60 days. The cost of wells does thus critically depend on the effectiveness of drilling, that is to say the number of working days. The paper describes an analysis of the drilling performance of 77 high-temperature geothermal production and reinjection wells in the Hengill geothermal area in Iceland drilled from 2001 to 2011, and assesses the statistical level of risk. The study compares workdays in drilling holes of two different casing programmes, and two trajectories of vertical or directional drilling. The production casing was either of a regular diameter of 244.5 mm (9⅝") or a large diameter of 339.7 mm (13⅜"). The workdays were normalized to a reference well of four sections, Section 0 of initial drilling to 90 m, Section 1 to 300 m, Section 2 to 800 m, and Section 3 to 2,235 m depth (Figure 3). The workdays used to drill each of the sections of the hole were broken down and analysed for seven different activities. The average and standard deviation for each of the four well sections was calculated and the findings used for the model calculations. For large diameter holes an average of 45 days was required, but 47 days for holes of the regular programme. No difference was found for vertical or directional trajectories.

The Monte Carlo method was applied to obtain a statistical estimate of the number of workdays and the cost of a reference hole to 2,235 m with large casings and directionally drilled. The cost estimate is based on assumed prices for services and material, but not on the actual cost which was not made available for the study for commercial reasons. The actual drilling contract for Hellisheiði was based on meter rates (not day rates) and sharing of the risk when problems are encountered. The cost figures presented in this study reflect what the cost may be, but not the contract. The estimated cost was found to be $4,318,000 with a standard deviation σ of $451,000. The cost lies with 95% confidence between $3,517,000 and $5,262,000. About 31% of the holes encountered drilling problems which led to higher drilling costs. The additional cost due to drilling problems was estimated on the basis of workdays that were required to solve the problem beyond the average number of workdays required in the respective section. In most cases the difficulties were due to a loss of circulation or collapsing geological formations where the drill string got stuck. The additional cost due to these problems was though low in most cases. It exceeded 1 σ in 23% of the 77 drilled holes, 2 σ in 13% and 3 σ in only 8%. The majority of holes were thus drilled according to the original schedule, demonstrating that the perceived high risk of drilling such holes is less than commonly thought.

The Injectivity ((kg/s)/MPa) is determined at the end of drilling by logging the pressure response to different rates of pumping water onto the well. These results are compared to the final well output obtained later by flow testing. Such estimates of future production are valuable for deciding

whether to drill deeper, drill a sidetrack or to apply well stimulation before moving the drilling rig off the well. The average generating capacity amounted to ~5.7 MW of electricity per well, but surprisingly there was not a significant difference in the mass flow output that could be related to the trajectory nor the well diameter.

1. INTRODUCTION

After successful development of the Nesjavellir Field in the Hengill Geothermal Area (commissioned 1990, generating 120 MW_e of electricity and 300 MW_t of hot water), Reykjavík Energy decided to explore other prospects in the area. In the years 2001–2011 the company drilled 55 exploratory and production wells as well as 17 reinjection wells in the Hengill Area, and 5 make-up wells in the Nesjavellir Field. The Hellisheiði Geothermal Plant, about 20 km east of Reykjavík, was commissioned in four stages 2006-2011. It generates 303 MW_e of electricity and 133 MW_t of hot water for district heating. This intensive drilling period in the same geothermal area provided a unique source of data to obtain statistical estimates of the cost and effectiveness of geothermal drilling. A first attempt to analyse this data was undertaken by Sveinbjornsson (2010). The following paper reports the main topics of that reference, with emphasis on the frequency of problems which lead to excessive additional cost. The number of working days to complete each of four depth sections of the well was analysed and the time broken down to show how much was spent on drilling, tripping, casing, cementing, logging, repair etc. The results were then grouped according to which well design was used and technology applied. Cost calculations in this study are based on assumed prevailing prices for services and material, as the real cost was not made available. The drilling was done by Iceland Drilling Co. (Jarðboranir ehf) after international tendering, where the cost is based on performance, i.e. price per meter of hole drilled, and unit costs for material. In the case of problems the cost is shared, and then day rates come into play. The majority of the wells were drilled with modern drilling rigs, up to four at the same time, all-hydraulic with a top-drive and the large ones with automatic pipe handling. The time breakdown in this study was worked out from the geological daily reports prepared by Iceland GeoSurvey (ÍSOR) as the daily reports of the rigs are confidential.

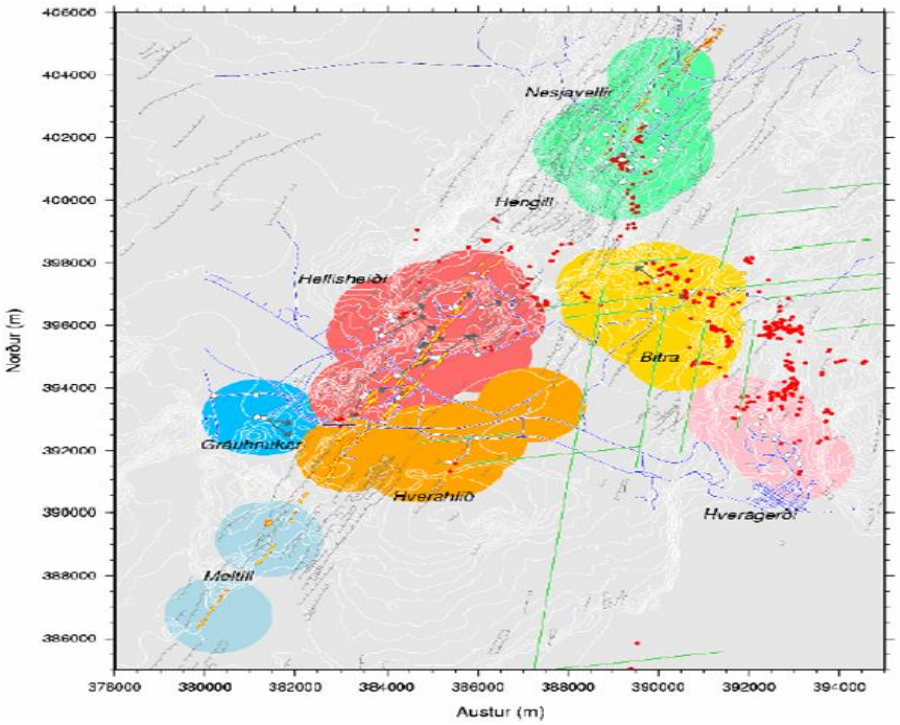

Fig. 1. Prospective fields in Hengill Geothermal Area. Figure from Reykjavik Energy. The Nesjavellir Field is green. Most of the wells drilled in the years 2001–2011 were in the Hellisheidi, Grauhnukar and Hverahlid Fields. Location of those wells and the formation temperature at depth are shown in Fig. 2.

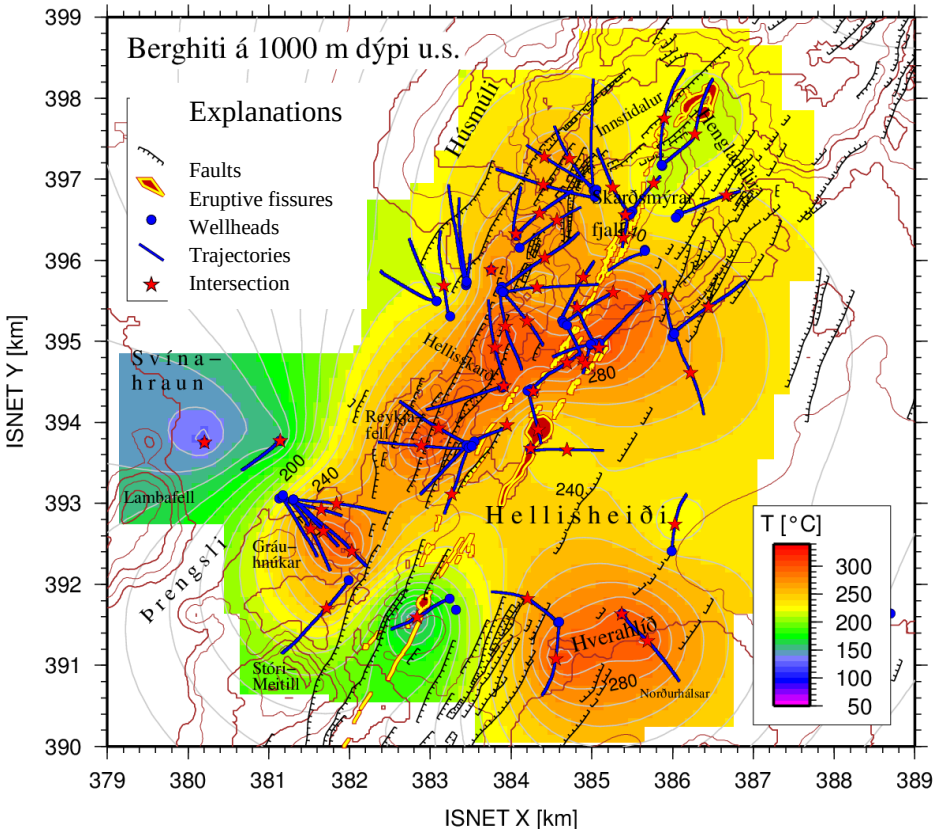

Fig. 2. Formation temperature in the southern half of Hengill Area at 1,000 m below sea level. Blue dots and lines indicate wellheads and trajectories of directional wells. A red star on the trajectory indicates where the well reaches the depth of the map. Figure from Gunnarsson, Reykjavik Energy (2012).

2. DRILLING IN THE HENGILL AREA

A recent description of the conceptual model of the Hengill geothermal system was given by Franzson et al. (2010). Fig. 1 shows the drill fields of the Hengill Area. Most of the wells analysed were drilled in the fields of Hellisheidi, Grauhnukar and Hverahlid (Fig. 2).

Two types of casing designs for high temperature wells were used in the Hengill Area. The wells were either drilled vertical or directional. The most common type is that of a directional well with a "large diameter" casing program. The initial drilling (Section 0) is by a small rig with a 26" bit down to 90 m for a 22½" surface casing, followed by Section 1 drilled by a larger rig with a 21" bit to 300 m for the 18⅝" anchor casing. Inclined drilling starts with a kick-off point (KOP) in Section 2, where the inclination is gradually built up by 2.5–3.0° per 30 m. The section is drilled with a 17½" bit to 800 m for 13⅜" production casing. The open hole in Section 3 is drilled with a 12¼" bit to a depth of 1,800 to 3,300 m for 9⅝" slotted production liner. The other design is narrower and called the "regular diameter" casing program. The sections are the same but the diameters 18⅝" of the surface casing, 13⅜" anchor casing, 9⅝" production casing, and 7" slotted production liner. Fig. 3 shows the design of a vertical well of regular diameter and a directional well of large diameter.

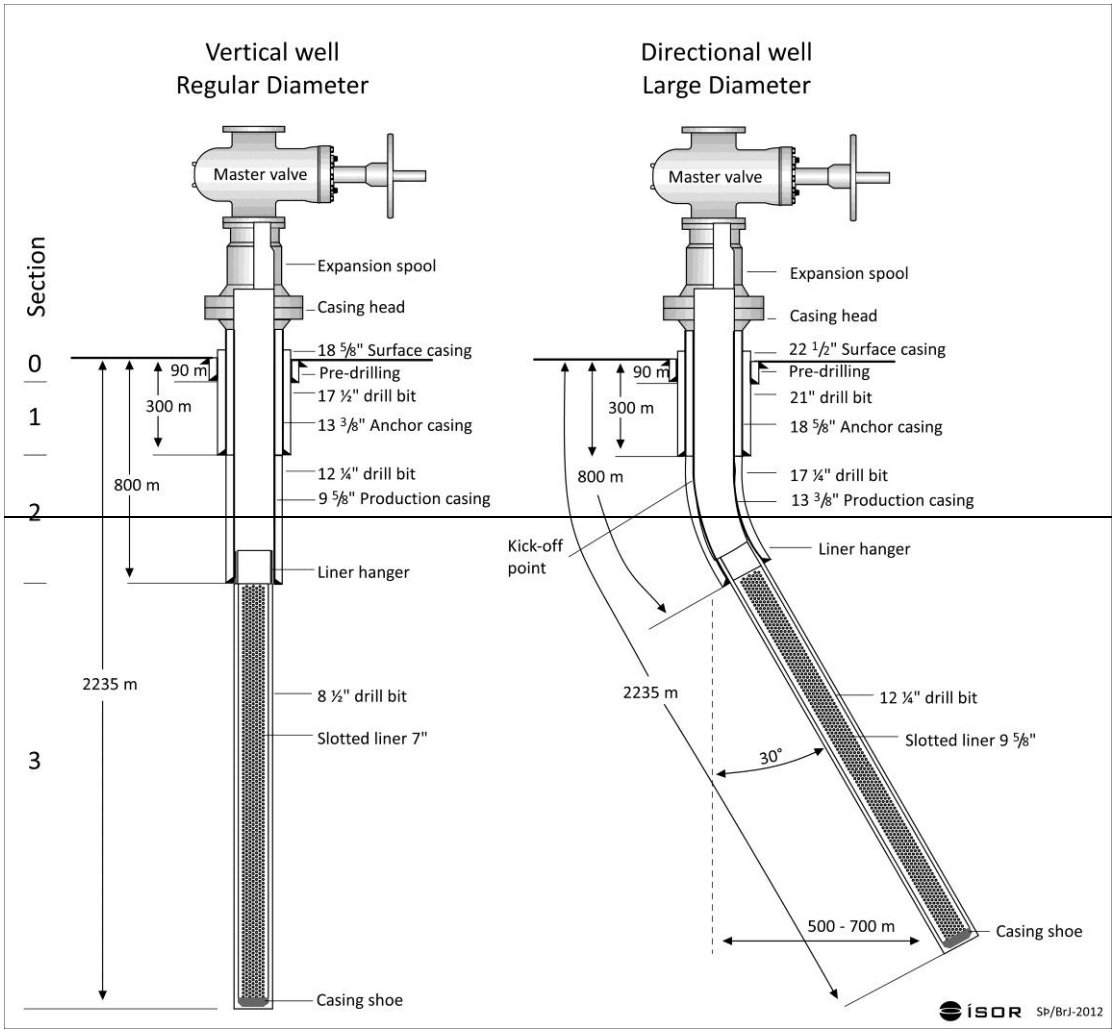

Fig. 3. Design of a vertical well of regular diameter and a directional well of large diameter. The well is divided into four sections, numbered 0-3, according to the depth interval drilled. The figure shows the depth intervals, on the left, for the reference well. The same section numbers are used in the tables.

Fig. 4. A drilling rig on site at Hellisheiði (200 t hook load capacity). Photo Jarðboranir.

Seven drill rigs were used in the drilling. Two small rigs with a hook-load capacity of 50 tons were used in the initial drilling (pre-drilling) to 90 m depth. An intermediate rig (100 t) was used mostly for the shallower sections and four larger rigs (179–300 t) were used in all sections, but preferably in the deepest ones.

The initial drilling was performed with air hammer and foam or tricone bits with tungsten carbide inserts, using mud and water as circulation fluids. Rotary drilling techniques with tricone bits were applied in Section 1 from 90–300 m. depth, but in Section 2 from 300–800 m depth a mud motor was used to rotate the bit and a MWD (Measurement While Drilling) tool inserted in the drill string to monitor direction (Azimuth) and inclination of the well. In Section 3 below the 800 m production casing until total depth no mud was used but drilling was carried out with only water as long as there were no circulation losses, but in most wells then switched over to aerated water by compressed air for pressure balance.

3. TIME ANALYSIS OF DRILLING DATA

To compare the drilling time for different wells, the respective numbers of workdays were normalized for a reference well of that design and the average depth of the group which was 2,235 m. The frequency distribution of workdays for each section is asymmetric with the most frequent value lower than the average. An example of this distribution is presented in figure 5 for the workdays in drilling Section 3 from 800-2,235 m in 46 large diameter directional wells. The data is best fitted by a Beta-PERT distribution, defined by the lowest, most likely and the highest value observed.

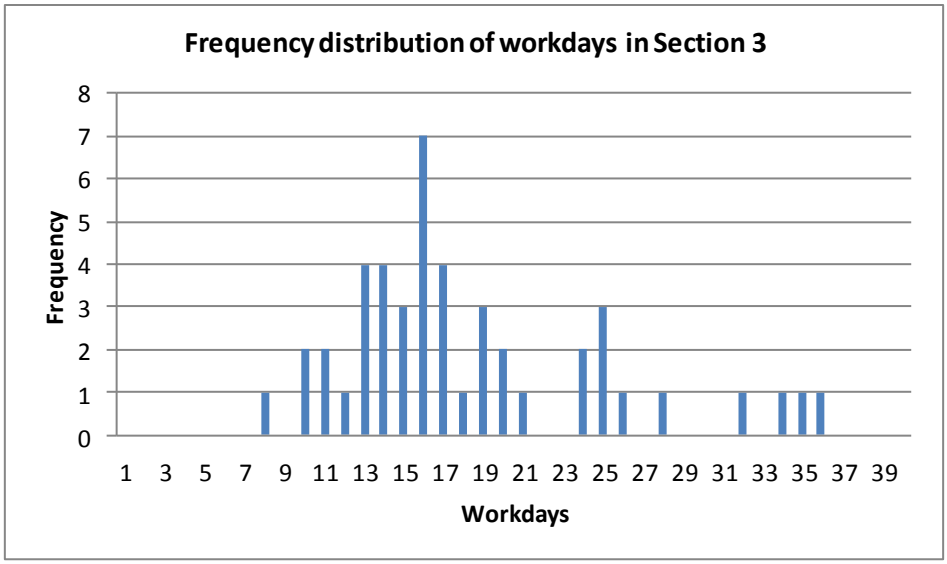

Fig. 5. Frequency distribution of normalized workdays in drilling Section 3 from 800-2,235 m in 46 large diameter directional wells. The data is asymmetric and best fitted by a Beta-PERT distribution.

Table 1. shows the lowest, most likely and highest values of normalized workdays in drilling the four sections of directional large diameter wells. Average and standard deviation are calculated for the respective Beta-PERT distribution.

Wells			Workdays total			Beta-PERT		
Section	Drilled	Number	Lowest	Most likely	Highest	Average	St. deviation	
	(m)	of wells				(days)	(σ)	(%)
0	0-90	38	3	4	14	5.5	1.8	33
1	90-300	44	4	8.5	29	11.2	4.2	37
2	300-800	46	6	9	20	10.3	2.3	23
3	800-2,235	46	8	16	36	18.0	4.7	26
Total	**2,235**					**45.0**	**6.9**	

Table 1. Normalized workdays for large diameter reference wells.

The number of wells varies as fewer reports were available on the sections of initial drilling and drilling for the anchor casing than the sections of drilling for the production casing and the productive open hole. Figure 6 below shows the distribution of the resulting reference class for the total of workdays in drilling of large diameter wells. The input to the simulation is from Table 1. With 95% confidence the workdays lie between 32.1 and 60.1 days. The average for the empirical data of the total is 45.0 days.

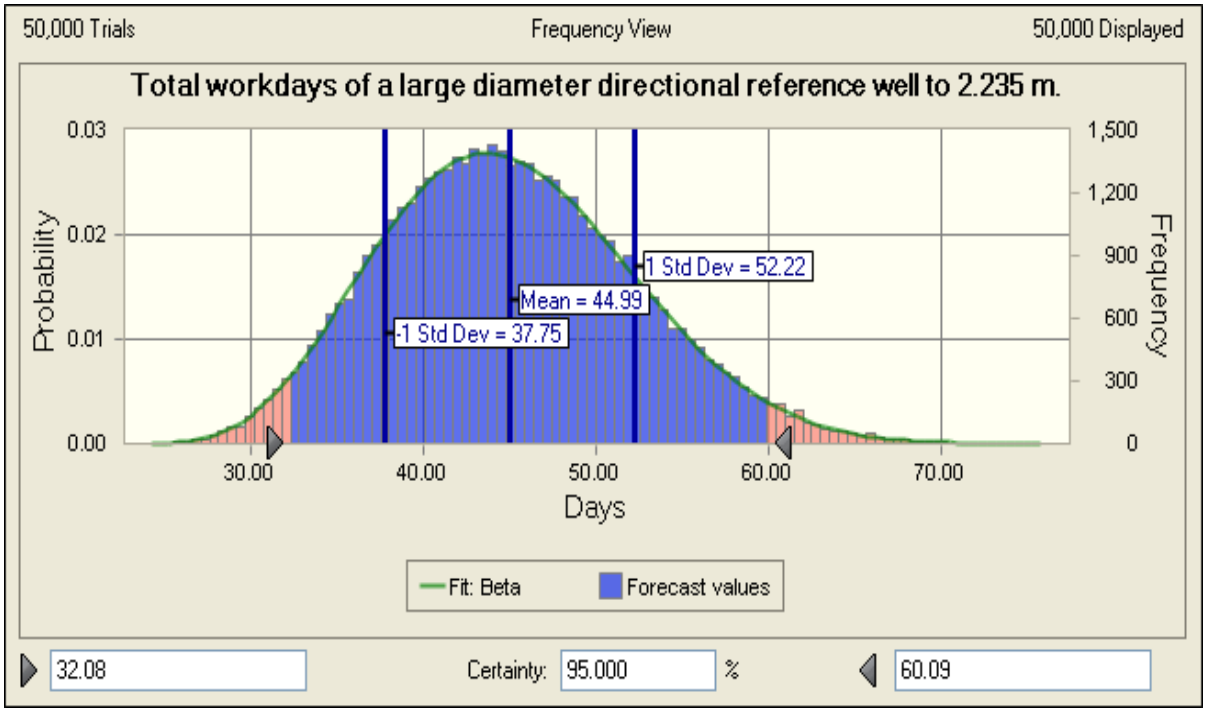

Fig. 6. Distribution of total workdays of a large diameter directional reference well to 2,235 m, from Monte Carlo simulation.

The workdays were also analysed for each section of drilling and the time used for different activities such as actual drilling, running and cementing casing, delays due to drilling problems, logging, installation of wellhead (BOPES), repairs of equipment, and other reasons for delays. The results of that analysis are shown in Table 2.

Holes			Workdays	Percentage in different activities						
Section	Drilled	Number	Average	Drilling	Casing	Probl.	Logging	Compl.	Repairs	Other
	(m)	(n)	(d)	(%)	(%)	(%)	(%)	(%)	(%)	(%)
0	0-90	38	5,5	47,0	28,1	9,5	0,0	11,0	1,7	2,7
1	90-300	44	11,2	36,6	26,3	10,0	9,9	12,5	2,9	1,7
2	300-800	46	10,3	46,6	21,7	5,1	11,2	11,0	3,9	0,6
3	800-2,235	46	18,0	54,4	5,8	11,1	15,8	7,5	4,8	0,6

Table 2. Percentages of total workdays used in different activities of drilling a directional, large diameter reference well.

Besides the analysis for the reference well of the directional “large diameter” type it is of interest to compare the number of workdays for directional and vertical wells of the “regular” program which have casing diameters of 18⅝" surface, 13⅜" anchor, 9⅝" production casing and a 7" slotted liner. The results are shown in Tables 3 and 4. The number of wells varies according to the number of each type drilled and the availability of reports. The average and the standard deviation are calculated assuming a Beta-PERT distribution for the workdays. The total workdays for the large diameter directional wells are 45.0 days compared to 45.8 days for much fewer vertical wells.

Workdays for large diameter wells
Depth 0-300 m

Diameter (")	Number of wells	Workday average (d)	St. Dev. (s)
Section 0: 0-90 m			
26	38	5.5	1.8
Section 1: 90-300 m			
21	44	11.2	4.2

Directional
Depth 300-2,235 m

Diameter (")	Number of wells	Workday average (d)	St. Dev. (s)
Section 2: 300-800 m			
17½	46	10.3	2.3
Section 3: 800-2.235 m			
12¼	46	18.0	4.7
Total workdays			
		45.0	6.9

Vertical
Depth 300-2,235 m

Diameter (")	Number of wells	Workday average (d)	St. Dev. (s)
Section 2: 300-800 m			
17½	5	9.8	0.8
Section 3: 800-2.235 m			
12¼	7	19.3	3.7
Total workdays			
		45.8	5.9

Table 3. Workdays for large diameter directional and vertical wells. The first two sections to 300 m are drilled vertical and then the rest of the well, Section 2 and 3, are either drilled directional or vertical.

Workdays for regular diameter wells
Depth 0-300 m

Diameter (")	Number of wells	Workday average (d)	St. Dev. (s)
Section 0: 0-90 m			
21	25	5.8	2.2
Section 1: 90-300 m			
17½	25	8.3	2.0

Directional
Depth 300-2,235 m

Diameter (")	Number of wells	Workday average (d)	St. Dev. (s)
Section 2: 300-800 m			
12¼	17	10.7	2.0
Section 3: 800-2.235 m			
8½	17	18.7	3.0
Total workdays			
		43.5	4.7

Vertical
Depth 300-2,235 m

Diameter (")	Number of wells	Workday average (d)	St. Dev. (s)
Section 2: 300-800 m			
12¼	6	12.2	2.8
Section 3: 800-2.235 m			
8½	5	22.0	6.3
Total workdays			
		48.3	7.5

Table 4. Workdays for regular diameter directional and vertical wells.

The directional regular diameter wells take 43.5 days on average but fewer vertical wells 48.3 days. Considering the numbers in each group and the respective standard deviations the difference in total workdays is not significant. It is of interest to note that for directional wells the average for 17 narrower program wells is 43.5 days compared to 45.0 days for 46 wells of the large diameter program.

4. COST ANALYSIS

The cost structure in this paper is such that there is a day rate for the drilling rig and crew and also for the many services engaged such as for cementing, directional drilling, drilling mud, logging etc. These daily costs vary according to the technology requirements of the equipment, geographic area, and prevailing market conditions. The unit material costs on the other hand reflect the commodity prices for steel, cement, fuel oil etc. and their overall cost is therefore more predictable as the usage quantity can be calculated. On top of this the remoteness of the site and proximity to supplies and services affect these costs. A small drill rig is used for Section 0 to 90 m (initial drilling), but the Sections 1, 2 and 3 are drilled by a larger rig.
The estimated cost of drilling the reference well of the large diameter program was calculated on the basis of the number of workdays required for each section of the drilling, using a weighted average of the day rates for different activities. A breakdown of cost for different sections is shown in Table 5.

Item of cost	Time		Material		Total	
	($)	(%)	($)	(%)	($)	(%)
Site and moving in of rigs					490,000	11.3
Section 0: 0-90 m	219,048	69.2	97,648	30.8	316,696	7.3
Section 1: 90-300 m	634,031	79.5	163,417	20.5	797,448	18.5
Section 2: 300-800 m	633,154	60.7	410,379	39.3	1,043,533	24.2
Section 3: 800-2,235 m	1,202,106	72.0	468,628	28.0	1,670,734	38.7
					4,318,411	*100*

Table 5. Breakdown of cost for a large diameter directional reference well to 2,235 m.

5. VARIANCE IN THE TOTAL COST

To obtain an estimate of the variance in total cost Monte Carlo simulations were carried out using probability distributions for the uncertainties in the number of workdays, the unit costs of material, and day rates for the drilling rigs. Figure 7 shows the distribution for the total cost of the reference well of the large diameter directional program. Note that here the cost of the drill site, cellar and water supply, as well as the cost of moving rigs in, are included. The average obtained for the simulation is $4,317,588, compared to the total cost of $4,318,410 obtained in Table 5. The standard deviation was found to be $451,229. The cost lies with 95% confidence within the limits $3,517,000 and $5,262,000. Sensitivity analysis shows that the number of workdays causes most of the uncertainty, 58.4% in Section 3, 28.3% in Section 1, and 11% in Section 2. Graphs for accumulated probability indicate that in 30% cases the cost exceeds $4,541,000 and in 30% cases the cost will be lower than $4,055,000.

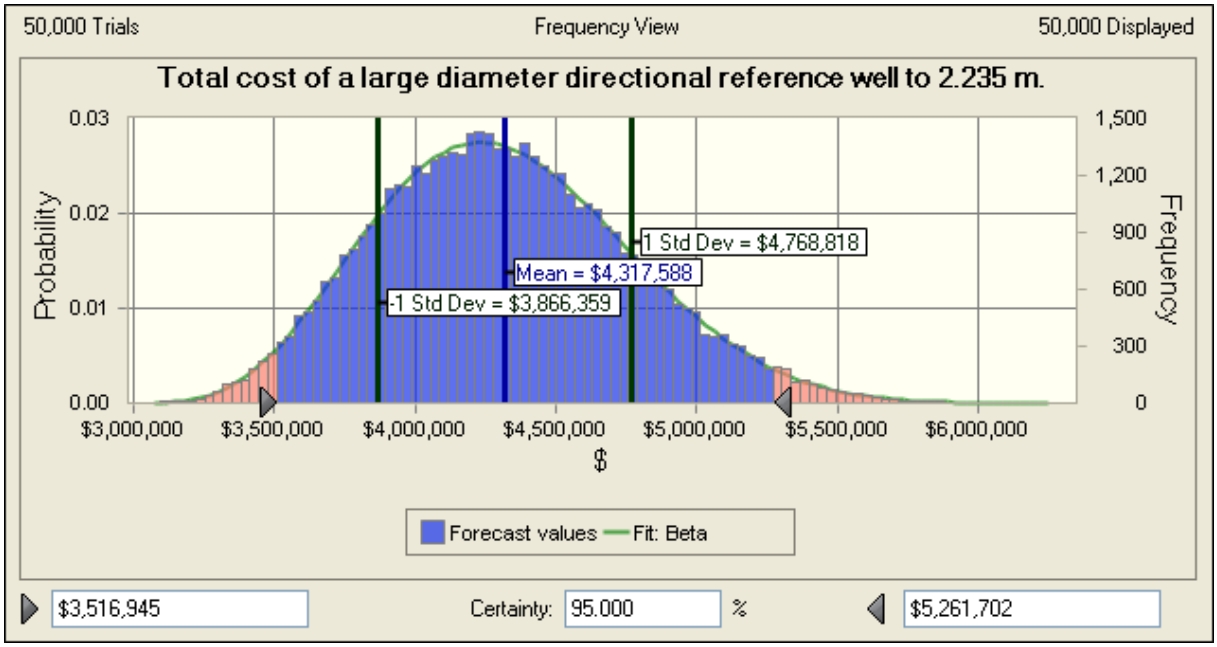

Fig. 7. Total cost of the large diameter directional reference well to 2,235 m.

6. DRILLING PROBLEMS

Although most wells were drilled according to the original schedule, some wells encountered difficulties resulting in workdays exceeding considerably the average for the respective activity. The drilling reports were examined to find the cause of the excess workdays. Most common were problems due to loss of circulation or collapsing geological formations where the rig got stuck. The time analysis identified such problems in 24 wells or 31% of the 77 wells drilled. The additional cost was though low in most cases.

Problems due to geological formations were the primary cause of problems in 18 of the 24 wells. They led to other problems such as difficulties in running the casing in 3 wells and excessive cement loss into the formation. In 5 wells the rig got stuck and had to cut the drill string by explosives, loosing the bottom hole assembly, collars and part of the drill pipes in the well. This occurred twice in one well. Four wells were sidetracked due to a stuck drill string and 2 because of a wrong direction. Two wells were abandoned because of collapse and a stuck drill string. Repairs of top drive of drill rigs were necessary in drilling 4 wells, sometimes due to excessive strain in attempts to free a stuck string. In 2 wells the section of initial drilling had to be divided into two steps due to overpressure in shallow boiling aquifers.

The additional cost due to drilling problems was estimated on the basis of workdays that were required to solve the problem beyond the average number of workdays required in the respective section. Also taken into account was the cost of cement, bentonite and other supplies in excess of what is accounted for in a reference well. Sections that were abandoned by sidetracking were counted as additional cost in workdays and material used. Thirdly the cost of lost equipment and drill string in the hole that could not be recovered, was counted as lost in hole charge. Figure 7 shows the cost above the average, for the 24 problem wells.

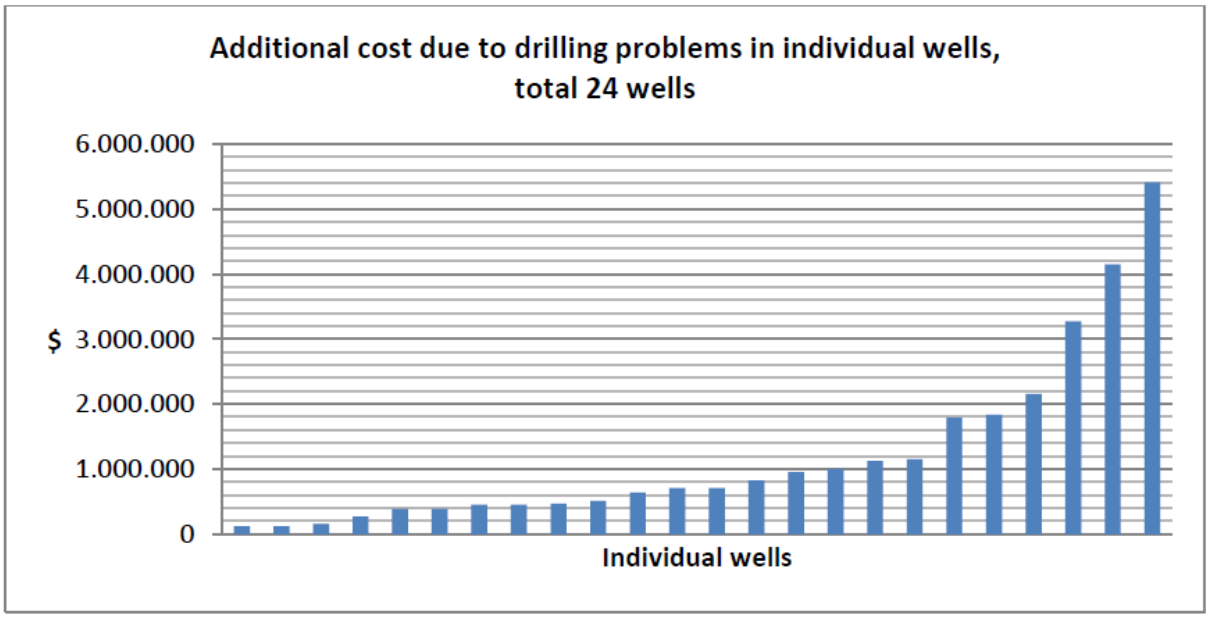

Fig. 7. Additional cost due to drilling problems in individual wells, total 24 wells.

Considering the standard deviation σ of $450,000 for the reference well, 18 of the wells have an additional cost less than 3 σ.
To obtain a view in terms of the σ the additional cost was divided by the σ and the frequency calculated as percentage of the total wells drilled. Fig. 8 shows the result.

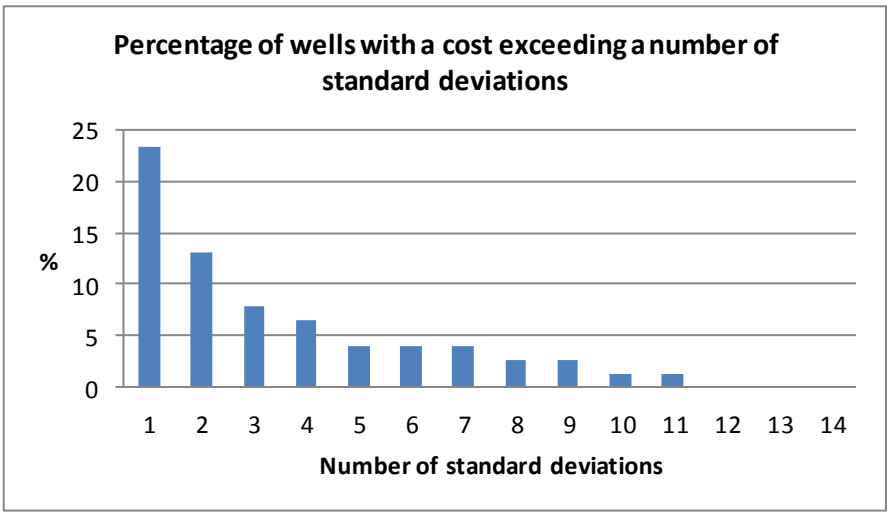

Fig. 8. Percentage of the total of drilled wells with additional cost due to drilling problems larger than a multiple of the standard deviation σ of the reference well.

For 77 wells drilled the additional cost was larger than one σ in 18 wells or about 23%. It exceeded 2 σ in 10 wells or 13% and 3 σ in 6 wells or nearly 8% of the total. This distribution can be of aid in estimating additional risk due to such problems on top of the risk included in the statistical distribution of the reference well.

7. POWER OUTPUT OF WELLS

The overall economics of a geothermal power project is strongly influenced by the power output per well, or how much can be reinjected, which is also considered in evaluating the drilling effectiveness. Table 6 shows the power output per drilled geothermal production well and per productive well in the Hellisheiði Field of the Hengill Area. It is of interest to note that the difference between the regular and large diameter wells appears insignificant.

Diameter	Drilled production wells	Productive wells	Power per drilled well (MW_e)	Power per productive well (MW_e)
Large diameter	38	33	5.8	6.7
Regular diameter	15	13	5.7	6.6
Total	*53*	*46*	*5.8*	*6.7*

Table 6. Power output of drilled production wells in megawatts (MW_e) of electricity that can be generated.

The data bank could be used for other comparisons such as vertical vs. directional wells, drilling with water only or managed pressure drilling by aerating the water. Only 7 of the large diameter and 5 of the regular diameter wells in the Hengill Area were however drilled vertical. A comparison with vertical wells is therefore not reliable.

For success metrics, comparisons were made between the Injectivity at the end of drilling and the confirmed total mass flow of the well. The Injectivity ((kg/s)/MPa) is determined at the end of drilling by logging the pressure response to different rates of pumping water onto the well, each step lasting a few hours. It serves as the first indicator of the well productivity. Fig. 9 shows a log/log-graph of total mass flow (kg/s) of wells at 8 bar-g drawn against Injectivity (kg/MPa*s). The range of mass flow lies between 10-100 kg/s and the Injectivity between 20-350 (kg/MPa*s). The figure clearly indicates a linear relation but the data points are scattered due to different enthalpy of the mass flow which depends on the temperature of the major feedpoint of each well.

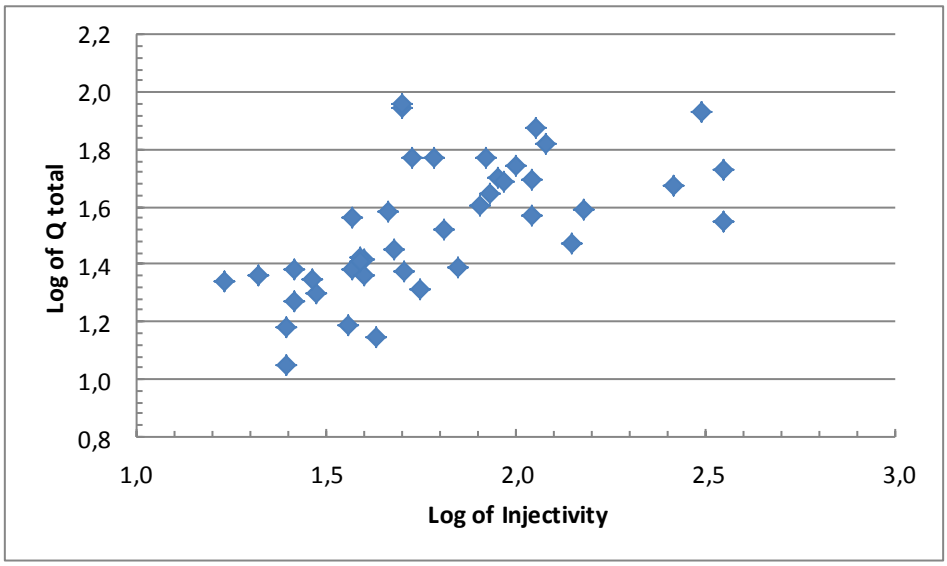

*Fig. 9. A log/log graph of total mass flow (kg/s) of wells at 8 bar-g drawn against Injectivity (kg/MPa*s).*

The results indicate that to obtain reliable predictions of yield on the basis of the Injectivity one must also consider reservoir conditions and enthalpy of the expected discharge. Such predictions would be valuable for decisions, whether to deepen a well or redrill the last section as a sidetrack or “fork”.

8. CONCLUSIONS

The results of this analysis of cost and effectiveness of geothermal drilling clearly indicate that the the perceived high risk in this kind of drilling is less than commonly thought. The standard deviation of the total cost of a well is about 10% of the average cost. Only 6 wells, or 8% of the total 77 wells drilled, had costs exceeding 3 standard deviations. The risk lies mainly in the nature of the geological formation, problems due to loss of circulation or collapsing walls where the rig gets stuck.
No significant difference was found in the time required to drill holes of the wider 13⅜" production casing or the regular narrower casing of 9⅝" diameter. No difference either was found in the time used to drill vertical or inclined directional holes. The difference in power output between the regular and large diameter wells also appears insignificant.

9. ACKNOWLEDGEMENTS

We thank Reykjavik Energy (Orkuveita Reykjavíkur) for permission to use the drilling data from the Hengill Area. Reykjavik Energy and National Energy Authority (Orkustofnun) gave financial support to undertake this work.

REFERENCES

Franzson, H., Gunnlaugsson, E., Árnason, K., Sæmundsson, K., Steingrímsson, B., and Harðarson, B.S., 2010: *The Hengill Geothermal System, Conceptual Model and Thermal Evolution.* Proceedings World Geothermal Congress, Bali, Indonesia, 25–29 April 2010, 9 pp.

Sveinbjornsson, B.M., 2010: *Cost and risk in drilling high temperature wells in the Hengill field.* MSc thesis, Reykjavik University, 62 pp. + appendices.

Thorhallsson, S. and Sveinbjornsson, B.M., 2012: *Geothermal drilling cost and drilling effectiveness.* Proceedings of a "*Short Course on Geothermal Development and Geothermal Wells*", organized by UNU-GTP and LaGeo, in Santa Tecla, El Salvador, March 11-17, 2012.

Proceedings of SIMS 2012, the 53rd Scandinavian Simulation and Modelling Society Conference
Reykjavik, Iceland, 4–6 October 2012

Modelling Sustainable Geothermal Energy Utilization

Gudni Axelsson

Iceland GeoSurvey (ÍSOR), Grensásvegur 9, IS-108
and University of Iceland, Saemundargötu 6, IS-101
Reykjavík, ICELAND
Corresponding author e-mail: *gax@isor.is*

Abstract

Sustainable development involves meeting the needs of the present without compromising the ability of future generations to meet their needs. The Earth's enormous geothermal resources have the potential to contribute significantly to sustainable energy use worldwide and to help mitigate climate change. Experience from the use of geothermal systems world-wide, lasting several decades, demonstrates that by maintaining production below a certain limit the systems reach a balance between net energy discharge and recharge that may be maintained for a long time. Therefore, a sustainability time-scale of 100 to 300 years has been proposed. Modelling studies furthermore indicate that the effect of heavy utilization is often reversible on a time-scale comparable to the period of utilization. The long production histories that are available for geothermal systems worldwide provide the most valuable data available for studying sustainable management of geothermal resources, and reservoir modelling is the most powerful tool available for this purpose. Long utilization experiences from e.g. Iceland, New Zealand, El Salvador, Kenya and China are reviewed and sustainability modelling studies for a few geothermal systems in these countries presented.

1. Introduction

Geothermal resources are distributed throughout the Earth's crust with the greatest energy concentration associated with hydrothermal systems in volcanic regions at crustal plate boundaries. Yet exploitable geothermal resources may be found in most countries, either as warm ground-water in sedimentary formations or in deep circulation systems in crystalline rocks. Shallow thermal energy suitable for ground-source heat-pump utilization is available world-wide and attempts are underway at developing enhanced geothermal systems (EGS) in places where limited permeability precludes natural hydrothermal activity. The potential of the Earth's geothermal resources is enormous when compared to its use today and to the future energy needs of mankind and even though geothermal energy utilization has been growing rapidly in recent years it is still miniscule compared with the Earth's potential. There is, therefore, ample space for accelerated use of geothermal resources worldwide in the near future.

Sustainable development has been receiving ever increasing attention and emphasis world-wide and it's become clear that some kind of sustainable development is essential for the future of mankind, both because of the Earth's limited resources and for environmental reasons. The Earth's geothermal resources have in fact the potential to contribute significantly to sustainable energy use worldwide and to help mitigate climate change. Two main issues are of principal significance when sustainable geothermal utilization is being considered; (1) the question whether geothermal resources can be used in some kind of sustainable

manner at all and (2) the issue of defining an appropriate time-scale. The first issue can only be addressed on the basis of comprehensive knowledge on the geothermal system in question; both on its inherent nature and on its production capacity. Modelling plays a key role in assimilating that knowledge.

The energy production potential of geothermal systems, in particular hydrothermal systems, is predominantly determined by pressure decline due to production (Axelsson, 2008). This is because there are technical limits to how great a pressure decline in a well can be for it to remain productive. The production potential is also determined by the available energy content of the system, i.e. by temperature or enthalpy and size. The pressure decline is determined by the rate of production, on one hand, and the nature and characteristics (size, permeability, boundary conditions, etc.) of the geothermal system, on the other hand. Natural geothermal reservoirs can most often be classified as either ***open*** or ***closed***, with drastically different long-term behaviour, depending on their boundary conditions.

Pressure declines continuously with time, at constant production, in closed systems or ones with small recharge (relative to the production). In such systems the production potential is limited by lack of water rather than lack of thermal energy. Pressure stabilizes in contrast in open systems because recharge eventually equilibrates with the mass extraction. The recharge may be both hot deep recharge and colder shallow recharge. The latter will eventually cause reservoir temperature to decline and production wells to cool down. In such systems the production potential is limited by the reservoir energy content (temperature and size) as the energy stored in the reservoir rocks will heat up the colder recharge as long as it is available/accessible. The situation is somewhat different for EGS-systems and sedimentary systems utilized through production-reinjection doublets and heat-exchangers with 100% reinjection. Then the production potential is predominantly controlled by the energy content of the systems involved. But permeability, and therefore pressure variations, are also of controlling significant in such situations.

Experience from the use of geothermal systems worldwide, lasting several decades (long utilization histories), clearly indicate that geothermal systems can be utilized for several decades without significant decline in output due to the fact that they often appear to attain a sort of semi-equilibrium in physical conditions during long-term energy-extraction. In other cases physical changes in geothermal systems are so slow that their output is not affected for decades. Various modelling methods, applicable to geothermal systems, are the principal tools available to study the possible sustainable utilization of geothermal resources and modelling studies have, in fact, extended the case histories to 1 or 2 centuries. Such modelling studies are the subject matter of this paper.

Sustainable geothermal utilization has been discussed to some degree in recent years, often without a clear vision of what the term "sustainable" entails. A general and logical definition has been missing. In addition, the terms *renewable* and *sustainable* are often confused. The former should refer to the nature of a resource, while the latter should refer to how it is used. A considerable amount of literature dealing with the issue has been published during the last decade, with Axelsson (2010) providing information on several relevant references. The reader is, furthermore, referred to a recent special issue of the international journal *Geothermics* (Mongillo and Axelsson, 2010). The following chapter is devoted to a review of several aspects of the issue of sustainable geothermal energy utilization.

2. Sustainable Geothermal Utilization

The definition of the term ***sustainable development***, most often referred to today, is a definition stemming from the so called Brundtland report (World Commission on Environment and Development, 1987):

> *Humanity has the ability to make development sustainable to ensure that it meets the needs of the present without compromising the ability of future generations to meet their own needs.*

This is a very general definition, which is nonetheless being increasingly used to analyse most aspects of human endeavours and progress. Sustainable development, of course, includes meeting the energy-needs of mankind and geothermal resources can certainly play a role in sustainable energy development, in particular since it is recognized that they should be classified among the renewable energy sources.

Two main issues are of principal significance when geothermal sustainability is being discussed and evaluated. These are (1) the question whether geothermal resources can be used in some kind of sustainable manner at all and (2) the issue of defining an appropriate time-scale. Long utilization histories, such as those discussed later, clearly indicate that geothermal systems can be utilized for several decades without significant decline in output due to the fact that they often appear to attain a sort of semi-equilibrium in physical conditions during long-term energy-extraction. Modelling studies have, consequently, extended the periods to 1 or 2 centuries, as already mentioned.

The second issue is the time-scale. It is clear that the short time-scale of 25-30 years usually used for assessing the economic feasibility of geothermal projects is too short to reflect the essence of the Bruntland definition, even though economic considerations are an essential part of sustainability. It is furthermore self-evident that a time-scale with a geological connotation, such as of the order of millions of years, is much too long. This is because at such a time scale the sustainable potential of a geothermal system would only equal the natural flow through the system. Therefore an Icelandic working group proposed a time-scale of the order of 100 – 300 years as appropriate (Axelsson *et al.*, 2001). Others have proposed time scales of the order of 50 – 100 years. Fig. 1, presented by the working group, is intended to capture the essence of its definition of sustainable production, for the time scale proposed by the group, i.e. if production is below a certain level (E_0) it can be maintained while production above the limit can't be maintained and has to be reduced before the period chosen has ended.

It is important to keep in mind, however, that sustainable geothermal utilization not only involves maintaining production from each individual geothermal system. This is because sustainable development should incorporate all aspects of human needs and activity. It is also important to keep in mind that sustainable development does, in addition, not only involve preserving the environment, as sometimes assumed. In fact, sustainable utilization involves an integrated economic, social and environmental development. Therefore geothermal production can e.g. to some extent be excessive (greater than the sustainable level) for a certain period if outweighed by improved social and/or economic conditions.

It is difficult to establish the sustainable production level, E_0, for a given geothermal system. This is because the production capacity of geothermal systems is usually very poorly known during exploration and the initial utilization step, as is well known. Even when considerable

production experience has been acquired estimating accurately the production capacity, and hence the sustainable production level, can be challenging.

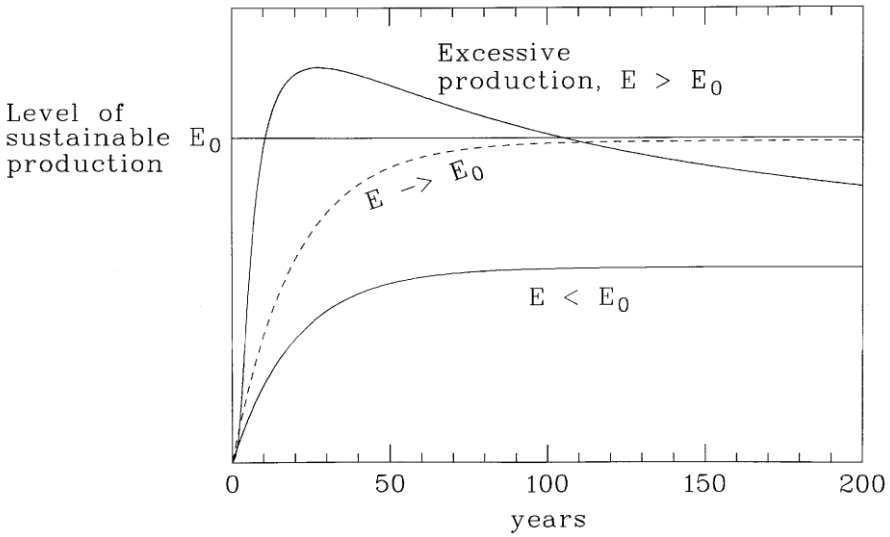

Figure 1. *A schematic graph showing the essence of the definition of sustainable production presented by Axelsson* et al. *(2001). Production below the sustainable limit* $\mathbf{E_0}$ *can be maintained for the whole period being assessed, while greater production can't be maintained.*

In spite of this downside one should bear in mind that the sustainable production level of a particular geothermal resource can be expected to increase over time with increasing knowledge on the resource, i.e. through continuous exploration and monitoring. In addition it can be expected to increase additionally through technological advances, e.g. in exploration methods, drilling technology and utilization efficiency.

When appraising the more general sustainable geothermal utilization an evaluation shouldn't necessarily focus on a single geothermal system. Either the combined overall production from several systems controlled by a single power company can be considered or several systems in a certain geographical region, even whole countries. Therefore, individual geothermal systems can e.g. be used in a cyclic manner, through which one system is rested while another is produced at a rate considerably greater than $\boldsymbol{E_0}$, and vice versa. This idea is based on an expected reclamation (recovery) of most geothermal systems when utilization is stopped, on a time-scale comparable to that of the utilization (Axelsson, 2010). The recovery expectation is both based on experience and results of numerical modelling.

This bring us to the possible production modes for individual geothermal systems, which can be incorporated in a more general sustainable geothermal utilization scheme, shown in Fig. 2. Mode (3) is cyclic and would require the utilization of another geothermal system, or other systems, when the primary one is being rested. Mode (4) is a variation of mode (3) in which utilization at a reduced rate is envisioned during the resting period instead of a complete stop.

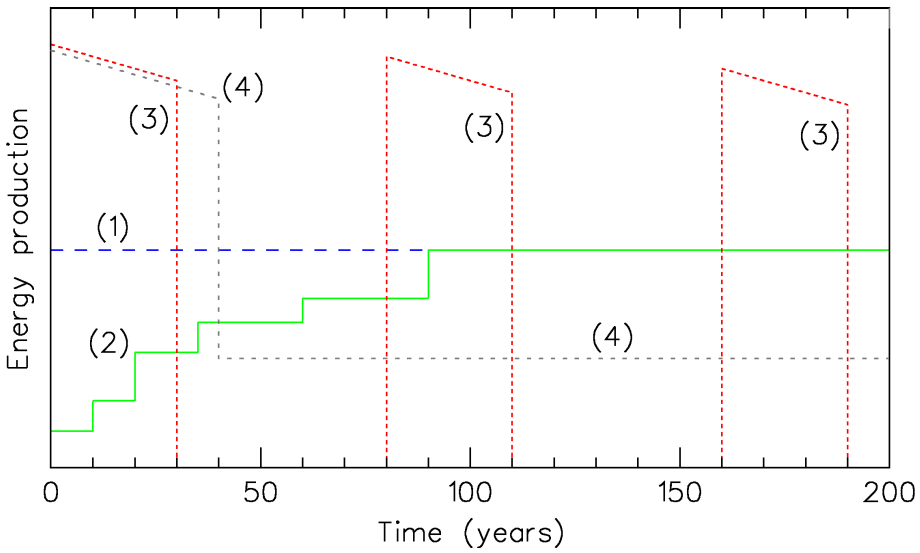

Figure 2. *Different production modes for geothermal systems which can be incorporated into sustainable geothermal utilization scheme (based on Axelsson, 2010).*

3. Sustainability Modelling

3.1 The Basis – Long Case Histories

A number of geothermal systems worldwide have been utilized for several decades. These provide the most important information on the response of geothermal systems to long-term production, and on the nature of the systems, if a comprehensive monitoring program has been in operation in the field. Such information provides the basis of understanding the issue of sustainable geothermal utilization, as well as the basis of sustainability modelling. Axelsson (2010) lists a number of well-known examples of systems that have been in use for 30 or more years. A number of low-temperature (< 150°C) geothermal systems in Iceland have been used for even longer than three decades; their production histories are presented in Axelsson *et al.* (2010a).

Most of the case histories referred to above have shown it is possible to produce geothermal energy in such a manner that a previously unexploited geothermal system reaches a new equilibrium, and this new state may be maintained for a long time. Pressure decline during production in geothermal systems can cause the recharge to the system to increase approximately in proportion to the rate at which mass is extracted. The new equilibrium is achieved when the increased recharge balances the discharge. Experience has also demonstrated that when reinjection is applied, cold-front breakthrough can be averted and thermal decline managed for decades.

One of the best examples of long-term utilization is the low-temperature Laugarnes geothermal systems in Reykjavík, Iceland, where a semi-equilibrium has been maintained the last four decades indicating that the inflow, or recharge, to the systems is now about tenfold (assuming the artesian flow to approximately equal the recharge) what it was before production started. In other cases geothermal production has been excessive and it has not been possible to maintain it in the long-term. The utilization of the vapour-dominated Geysers geothermal system in California is a well-known example of excessive production. For a few years, the installed electric generation potential corresponded to more than 2000

MW_e, which has since been reduced by more than half because of pressure decline in the system due to insufficient fluid recharge (Goyal and Conant, 2010).

Another low-temperature long-term utilization example is worth mentioning, or the sedimentary geothermal resources in the Paris Basin. Sedimentary geothermal resources are, quite different from volcanic or convective tectonic systems because of how extensive in area they are. The Paris Basin hosts a vast geothermal resource associated with the Dogger limestone formation, which stretches over 15,000 km^2 (Lopez *et al.*, 2010). The Dogger resource is mainly used for space heating through a doublet scheme, consisting of a closed loop with one production well and one reinjection well. Utilisation of the Dogger geothermal reservoir started in 1969 and following the two oil crises more than fifty geothermal plants had been constructed in the Paris Basin. Some of the doublets have been abandoned, mostly due to economic reasons, at least temporarily. Today some doublets are being revitalized and new ones are being drilled. The production and reinjection wells of the Paris doublets are usually separated by a distance of about 1,000 m to minimise the danger of cooling due to the reinjection. Experience, lasting 3 – 4 decades, has shown that no significant cooling has yet taken place in any of the Paris production wells. This is in spite of various modelling studies, which have indicated that the doublets should start to cool down after 2 decades or so (Lopez *et al.*, 2010).

Axelsson (2010), furthermore, lists several high-temperature, volcanic type geothermal systems with long utilization case histories that should provide important data to base sustainability modelling on. These include:

- Ahuachapan, El Salvador, used since 1976
- Cerro Prieto, Mexico, used since 1973
- Larderello, Italy, used since the 1950s
- Krafla, Iceland, used since 1976
- Svartsengi, Iceland, used since 1976
- Olkaria, Kenya, used since 1981
- Matsukawa, Japan, used since 1966
- Palinpinion, Philippines, used since 1983
- Tiwi, Philippines, used since 1979
- Wairakei, New Zealand, used since 1958

3.2 Long-term Sustainability Modelling

Modelling studies, which are performed on the basis of available data on the structure and production response of geothermal systems, or simulation studies, are the most powerful tools to estimate the sustainable potential (i.e. E_0) of the systems (Axelsson, 2010). They can also be used to assess what will be the most appropriate mode of utilization in the future and to evaluate the effect of different utilization methods, such as reinjection. It is possible to use either complex numerical models, or simpler models such as lumped parameter models, for such modelling studies (Axelsson *et al.*, 2005). The former models can be much more accurate and they can both simulate the main features in the structure and nature of geothermal systems and their response to production. Yet lumped parameter models are very powerful for simulating pressure changes, which are in fact the changes which are the main controlling factor for the responses of geothermal systems.

The basis of reliable modelling studies is accurate and extensive data, including data on the geological structure of a system, its physical state and not least its response to production. The last mentioned information is most important when the sustainable potential of a geothermal system is being assessed and if the assessment is to be reliable the response data must extend over a few years at least, or even a few decades, as the model predictions must extend far into the future.

The sustainable potential of geothermal systems, that have still not been harnessed, can only be assessed very roughly. This is because in such situations the response data mentioned above is not available. It is, however, possible to base a rough assessment on available ideas on the size of a geothermal system and temperature conditions as well as knowledge on comparable systems. This is often done by using the so-called volumetric assessment method with the Monte Carlo method (Axelsson, 2008).

Axelsson (2010) presents the results of modelling studies for three geothermal systems that were performed to assess their sustainable production potential, or to provide answers to questions related to this issue. Two of these are the Hamar geothermal system in Svarfadar-dalur in north Iceland, which is used for space heating and other direct uses in the town of Dalvík and in the surrounding region, and the Beijing Urban geothermal system below the city of Beijing in China, which is used for heating and other direct uses in the city.

The Hamar geothermal system has been used since 1969, and during the last few years the average yearly production has been about 30 l/s of 65°C water. A lumped parameter model, as well as an energy content model, were used for the Hamar modelling study (see figures 3 to 5). The results of the calculations show the sustainable production potential of the system is probably a little bit more than the present production, i.e. about 40 l/s average production (see water-level predictions until the year 2170 in Fig. 4). It appears, however, that the sustainable energy production potential of the Hamar system is controlled by energy content and the limited size of the thermal water system, rather than by pressure decline, as can be seen from Fig. 5.

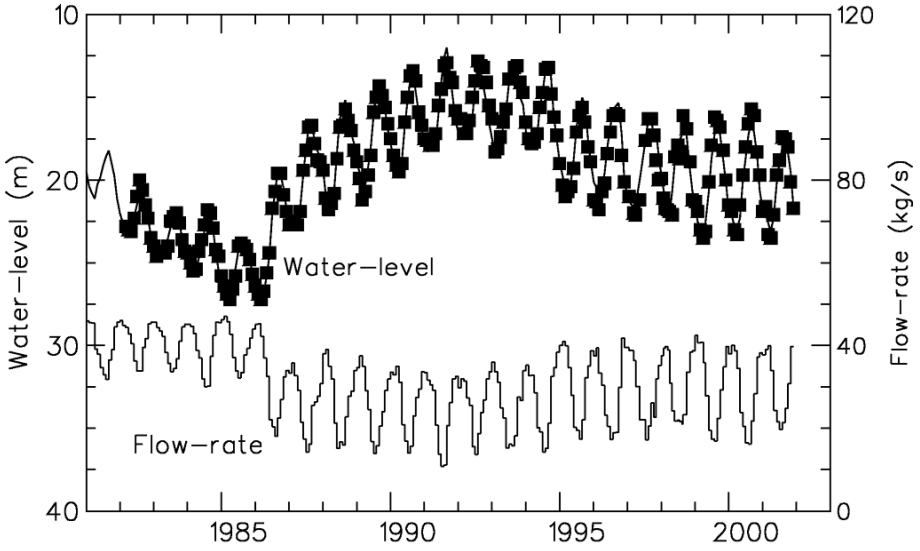

Figure 3. *Production history of the Hamar geothermal system in N-Iceland. The water-level history was simulated by a lumped-parameter model (squares = measured data, line = simulated data). From Axelsson (2010).*

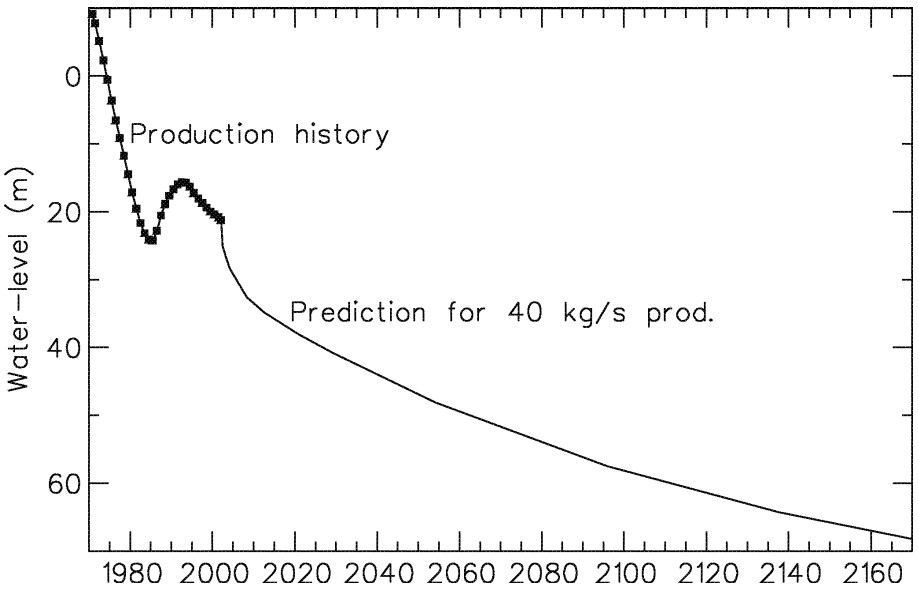

Figure 4. *Predicted water-level changes in the Hamar geothermal system for a 200-year production history (figure shows annual average values). From Axelsson (2010).*

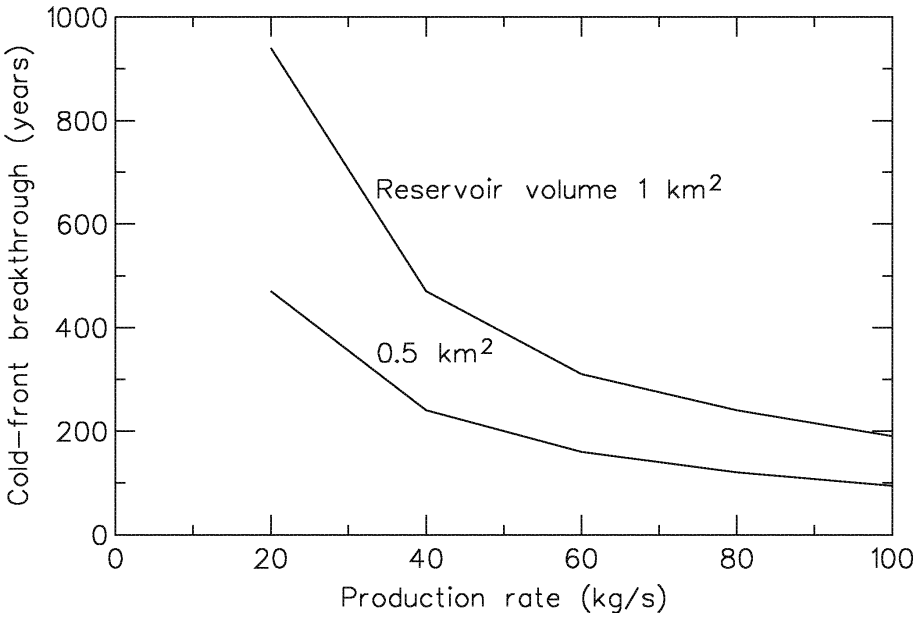

Figure 5. *Estimated cold-front breakthrough times for the Hamar geothermal system based on the model of Bödvarsson (1972). From Axelsson (2010).*

The Beijing Urban geothermal system is embedded in permeable sedimentary layers (carbonate rocks) at 1 – 4 km depth below Beijing and has been used since the 1970s (Liu *et al.*, 2002). The average yearly production from the system has been a little over 100 l/s of 40 to 90 °C water (mainly used during the four coldest months of the year). The response of the geothermal system to this production and predictions by a lumped parameter model (see figures 6 and 7) show the production potential of the Beijing Urban system is constrained by limited water recharge to the system, but not energy content.

The model calculations for the Beijing Urban system demonstrate the sustainable potential of the system is less than 100 l/s average yearly production. However, this depends on how much water-level drawdown will be acceptable in 100 to 200 years. Through a revision of the

mode of utilization, which would involve reinjection of a large proportion of the water extracted, the sustainable potential could be as much as 200 l/s average yearly production. That would be a 100% increase of the production maintained from the system until now. Simple energy balance calculations show that more than sufficient thermal energy is in place in the system if the reinjection-production system is managed efficiently, as in the Paris Basin.

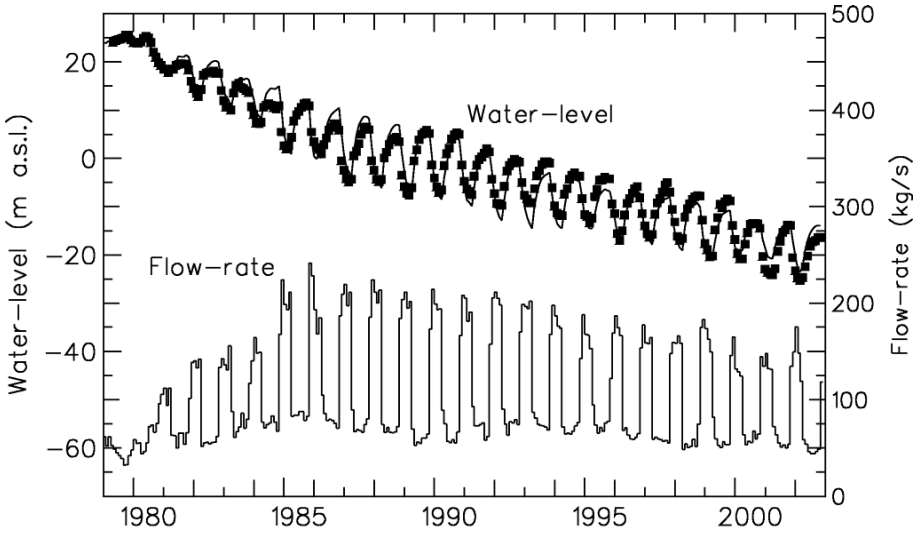

Figure 6. *The production history of the Urban geothermal field in Beijing with the water-level history simulated by a lumped-parameter model (squares = measured data, line = simulated data). From Axelsson (2010).*

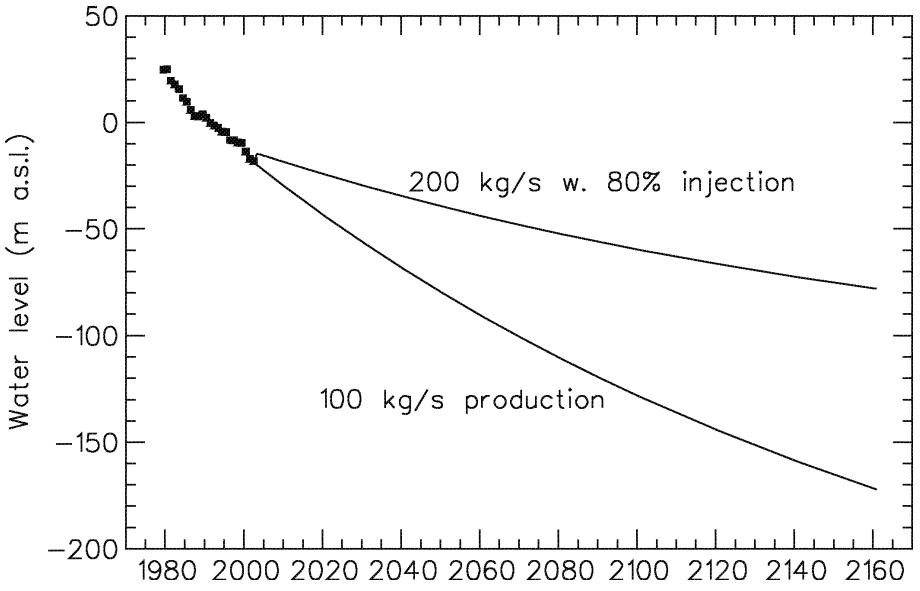

Figure 7. *Predicted water-level changes in the Urban geothermal field in Beijing for a 200-year production history (figure shows annual average values). From Axelsson (2010).*

Nesjavellir is one of the high-temperature geothermal areas in the Hengill volcanic region in southwest Iceland. It has been in use since 1990, at first for direct heating and later for cogeneration of electricity and heat. Today, the generating capacity of the Nesjavellir power plant is 120 MW_e electrical power and 300 MW_{th} thermal power. A 3D numerical simulation model, as well as a lumped parameter model, have been set up for the Nesjavellir system.

The present numerical model is actually a part of a much larger and more complex numerical model of the whole Hengill-region and surroundings (Björnsson *et al.*, 2003). The results of calculations by these models have demonstrated the present rate of utilization is not sustainable; that is, the present production cannot be maintained for the next 100 to 300 years (Fig. 8). The model calculations indicate, however, the effects of the present intense production should mostly be reversible. Figure 9 shows the reservoir pressure should recover over approximately the same time scale as the period of intense production. The thermal cooling effects, which are rather limited in amplitude and not as well determined (poorly constrained in the model because no cooling has been observed yet) as the pressure effects, appear to last much longer according to the numerical model. Therefore, it should be possible to utilize the Nesjavellir system, in the long term, according to production modes (3) or (4), described above (Fig. 2).

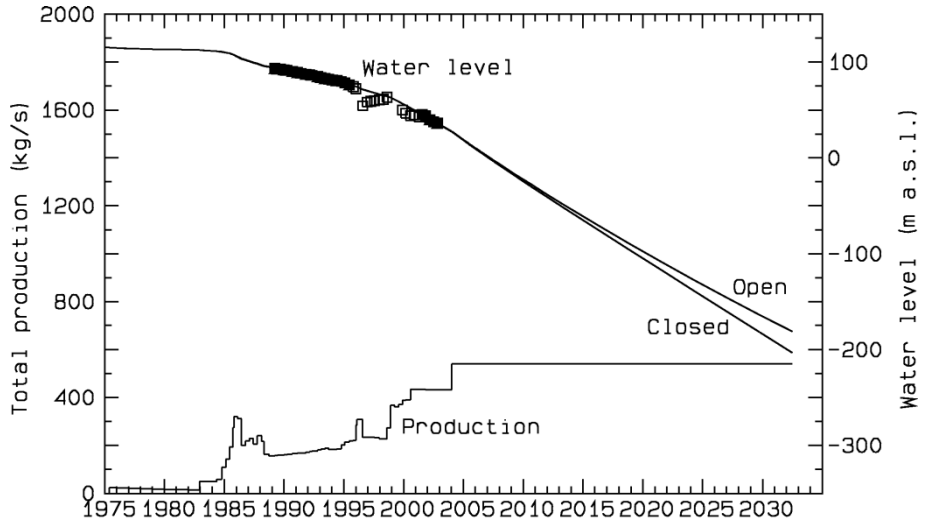

Figure 8. *Pressure decline data (measured as water level) from an observation well at Nesjavellir simulated by a lumped parameter model and pressure decline predictions, calculated using an open (optimistic) and a closed (pessimistic) model, for a 120 MWe future production scenario (Axelsson, 2010). The total mass extraction from the field is also shown (no injection into main reservoir).*

Another two modelling studies, which are in fact sustainability modelling studies, have been carried out for the Ahuachapan high-temperature geothermal system in El Salvador and the Wairakei high-temperature geothermal system in New Zealand. The main results of these two studies are reviewed below. Both systems constitute examples of systems having quite long and well documented production and response histories. The Ahuachapan study focussed on the long term management of the geothermal system, based on monitoring data collected since its utilization started in 1976 (Monterrosa and Montalvo, 2010). Figure 10 shows simulated and predicted pressure changes in the Ahuachapan geothermal system up to 2075 assuming production at full power plant capacity of 95 MW_e (gross). The figure shows a modest decline in reservoir pressure. The decline may require future modification of power plant conditions, such as some lowering of turbine inlet pressure, however (Monterrosa and Montalvo, 2010).

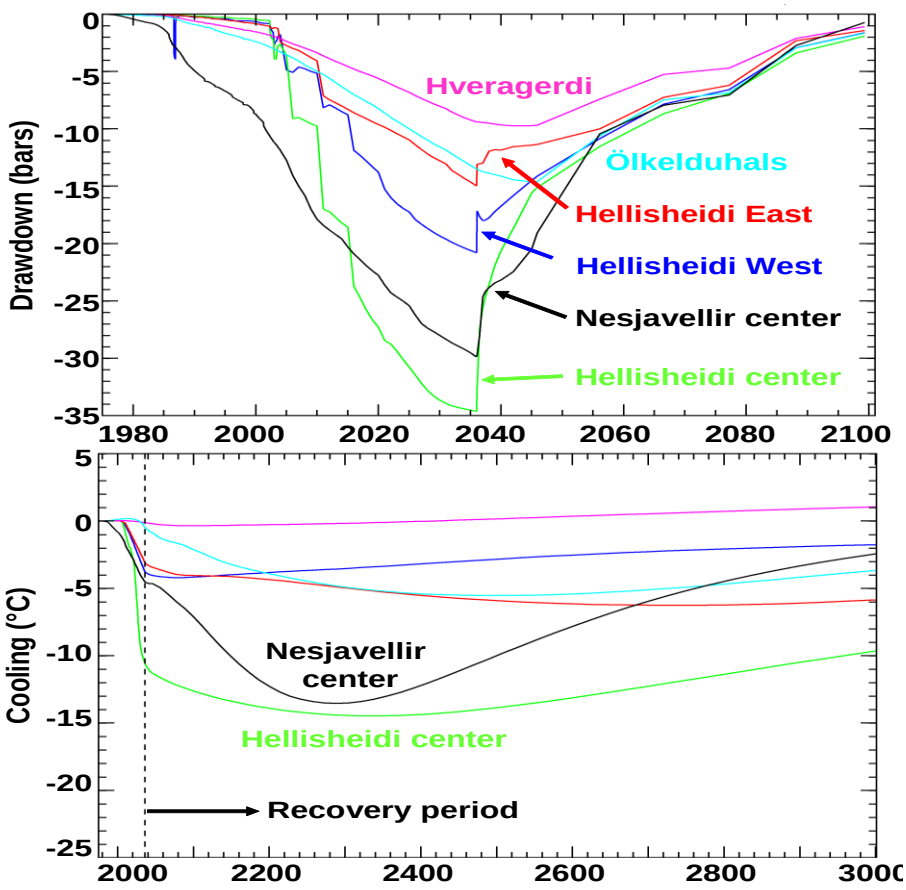

Figure 9: *Calculated changes in reservoir pressure and temperature in different parts of the Hengill area, including the central part of the Nesjavellir geothermal reservoir, during a 30-year period of intense production, and for the following recovery (production stopped in 2036). Predicted temperature changes are not well constrained because no cooling has been observed as of 2010. Figure from Axelsson* et al. *(2010b); see also Björnsson* et al. *(2003).*

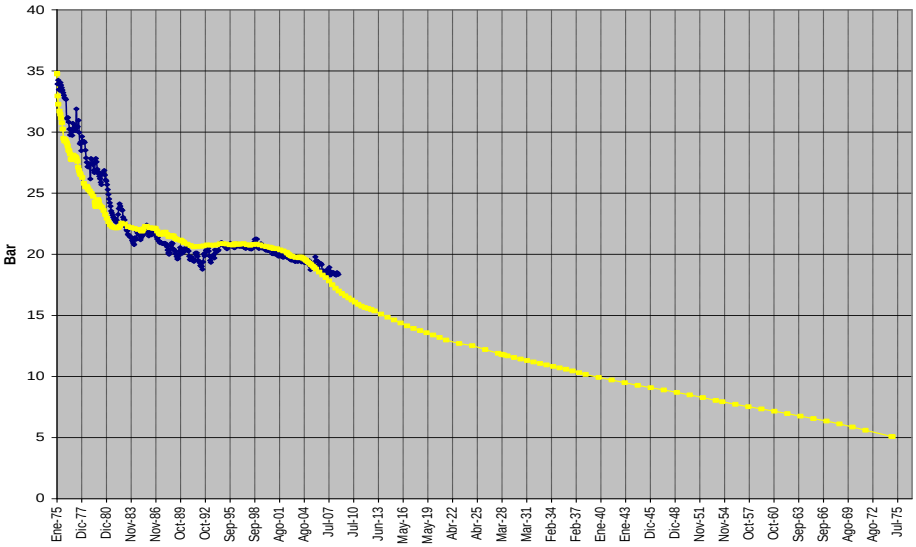

Figure 10: *Predicted pressure changes in the Ahuachapan geothermal system in El Salvador up to 2075, for a future scenario of 95 MWe constant production. Figure from Axelsson* et al. *(2010b); see also Monterrosa and Montalvo (2010).*

The Wairakei system in New Zealand has been utilized since 1958 and recently the electricity generation has corresponded to an average electrical generation of 170 MW_e. The sustainability modelling study for Wairakei focussed on predicting the systems response for another 50 years or so as well as predicting the recovery of the system once energy production will be stopped, after about 100 years of utilization (O'Sullivan *et al.*, 2010; see also O'Sullivan and Mannington, 2005). An example of the results of the study is shown in Fig. 11, which shows on one hand the pressure response of the system and on the other its temperature evolution. As in the case of Nesjavellir presented above, the pressure recovers very rapidly while temperature conditions evolve much more slowly.

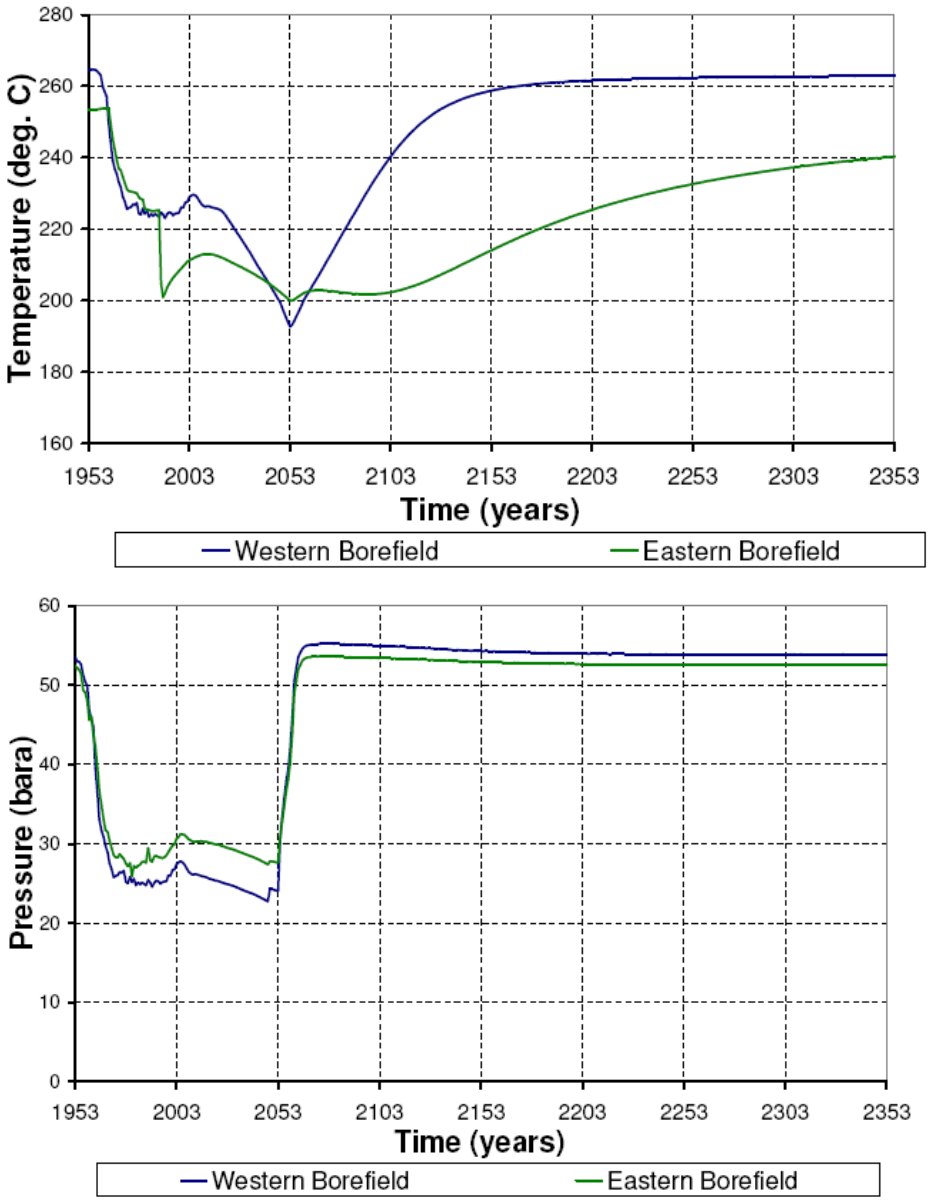

Figure 11: *Predicted pressure and temperature recovery in the Wairakei geothermal system in New Zealand following 100 years of production. Figure from Axelsson* et al. *(2010b); see also O'Sullivan and Mannington (2005) and O'Sullivan* et al. *(2010).*

Finally it may be mentioned that Rybach *et al.* (2000) and Ungemach *et al.* (2005) have performed sustainability modelling studies for ground source heat pump applications and

the doublet operations in the Paris Basin, respectively. Reviewing those studies is beyond the scope of this paper. Axelsson (2010) also presents the results of a simple sustainability modelling study for the Olkaria-I sector of the Olkaria high-temperature, volcanic geothermal system in Kenya.

4. Conclusions

It is argued that geothermal resources can be utilized in a sustainable manner if a time-scale of the order of 100 – 300 years is assumed. This paper has discussed the issue of sustainability modelling and presented several examples of such work, focussing on this long time-scale. The modelling examples either focus on long-term predictions or the recovery of geothermal systems following periods of heavy utilization. The sustainable energy production potential of a geothermal resource is either controlled by the reservoir pressure decline caused by production or by the energy content of the system in question, both depending on the nature of the resource in question. Case histories of numerous geothermal systems world-wide, which have been utilized for several decades, provide the most important data for sustainability and renewability research, including sustainability modelling.

As the possible role of geothermal energy utilization in sustainable development receives increasing attention and sustainability research is stepped up, international collaboration on issues related to sustainable geothermal utilization has been increasing. Collaboration through the International Energy Agency's (IEA) Geothermal Implementing Agreement (GIA) has e.g. been significant. A specific task of the GIA has in recent years focussed on collecting information, identifying research needs, facilitating international collaboration on the issue through workshops and meetings, as well as facilitating the publication of scientific papers and reports on geothermal sustainability studies and research (Axelsson *et al*., 2010b).

Several research issues, which have been identified through the IEA-GIA sustainability work, need to be studied in conjunction with sustainability research and modelling. Some of these are listed below (from Axelsson, 2010; see also Rybach and Mongillo, 2006):

(1) What factors are most significant in controlling long-term reservoir behaviour and capacity? These include: size, permeability, boundary conditions, natural recharge, reinjection, etc.
(2) How significant and far-reaching are long-term production pressure drawdown and reinjection cooling effects? In particular, how significant is interference between adjacent geothermal areas?
(3) Which are the optimum strategies for the different modes of production presented above, such as continuous and periodic production and reinjection scenarios in different cases?
(4) How rapidly and effectively do geothermal systems recover during breaks after periods of excessive production?
(5) What is the reliability of long-term (~100 years) predictions of reservoir production response using various methods (stored heat, simple analytical models, complex 3D models, etc.)?
(6) What information should be collected at pre-exploitation and early development stages to significantly reduce uncertainties in long-term resource sustainability assessments?

Bibliography

Axelsson, G., 2010: Sustainable geothermal utilization – Case histories, definitions, research issues and modelling. *Geothermics*, in press, 31 pp.

Axelsson, G., 2008: Production capacity of geothermal systems. *Proceedings of the Workshop for Decision Makers on the Direct Heating Use of Geothermal Resources in Asia,* Tianjin, China, May 2008, 14 pp.

Axelsson, G., Th. Jónasson, M. Ólafsson and Á. Ragnarsson, 2010a: Successful Utilization of Low-Temperature Geothermal Resources in Iceland for District Heating for 80 Years. *Proceedings World Geothermal Congress 2010*, Bali, Indonesia, April 2010, 10 pp.

Axelsson, G., C. Bromley, M. Mongillo and L. Rybach, 2010b: The sustainability task of the International Energy Agency's Geothermal Implementing Agreement. *Proceedings of the World Geothermal Congress 2010*, Bali, Indonesia, April 2010, 8 pp.

Axelsson G., G. Björnsson and J. Quijano, 2005: Reliability of lumped parameter modelling of pressure changes in geothermal reservoirs. *Proceedings of the World Geothermal Congress 2005*, Antalya, Turkey, April, 8 pp.

Axelsson, G., Á. Gudmundsson, B. Steingrímsson, G. Pálmason, H. Ármannsson, H. Tulinus, Ó.G. Flóvenz, S. Björnsson and V. Stefánsson, 2001: Sustainable production of geothermal energy: suggested definition. *IGA-News*, Quarterly No. 43, January-March 2001, 1-2.

Björnsson, G., Hjartarson, A., Bodvarsson, G.S., Steingrímsson, B., 2003: Development of a 3-D geothermal reservoir model for the greater Hengill volcano in SW-Iceland. *Proceedings of the TOUGH Symposium 2003*, *Berkeley, CA, USA*, 12 pp.

Bödvarsson, G., 1972: Thermal problems in the siting of reinjection wells. *Geothermics*, **1**, 63-66.

Goyal, K.P., and T.T. Conant, 2010: Performance history of The Geysers steam field, California, USA. *Geothermics*, **39**, 321–328.

Liu, J., X. Pan, Y. Yang, Z. Liu, X. Wang, L. Zhang and W. Xu, 2002: Potential assessment of the Urban geothermal field, Beijing, China. *Proceedings of the International Symposium on Geothermal and the 2008 Olympics in Beijing*, Beijing, October, 211-217.

Lopez, S., V. Hamm, M. Le Brun, L. Schaper, F. Boissier, C. Cotiche and E. Giuglaris, 2010: 40 years of Dogger aquifer management in Ile-de-France, Paris Basin, France. *Geothermics*, in press.

Mongillo, M.A., and Axelsson, A. (guest editors), 2010: Special issue on sustainable geothermal utilization. *Geothermics*, *39,* 279–402.

Monterrosa, M. and F. Montalvo, 2010: Sustainability analysis of the Ahuachapan geothermal field – Management and modelling. *Geothermics*, *39,* 370–381.

O'Sullivan, M. and W. Mannington, 2005: Renewability of the Wairakei-Tauhara geothermal resource. *Proceedings of the World Geothermal Congress 2005*, Antalya, Turkey, April 2005, 8 pp.

O'Sullivan, M., Yeh, A., and Mannington, W., 2010: Renewability of geothermal resources. *Geothermics*, *39,* 314–320.

Rybach, L., and M. Mongillo, 2006: Geothermal sustainability – A review with identified research needs. *Geothermal Resources Council Transactions*, **30**, 1083–1090.

Rybach, L., T. Megel and W.J. Eugster, 2000: At what scale are geothermal resources renewable? *Proceedings of the World Geothermal Congress 2000*, Kyushu-Tohoku, Japan, May-June 2000, 867-872.

Ungemach, P., M. Antics and M. Papachristou, 2005: Sustainable geothermal reservoir management. *Proceedings of the World Geothermal Congress 2005*, Antalya, Turkey, April 2005, 12 pp.

World Commission on Environment and Development, 1987: *Our Common Future*. Oxford University Press, Oxford, 400 pp.

Optimal and sustainable use of the Dogger aquifer geothermal resource: long-term management and new technologies

S. Lopez[1*], V. Hamm[1], O. Goyeneche[1]

1: BRGM, 3, avenue C. Guillemin, 45060 Orléans CEDEX 2.

*presenter: s.lopez@brgm.fr, +33.(0)2.38.64.39.38

Abstract

Geothermal energy has been supplying heat to district networks in the Paris Basin for more than 40 years. In this densely urbanized area, the main target of all exploration and exploitation projects has been the Dogger aquifer (1500-2000 m deep). Initial difficulties, due to corrosion and scaling related problems, have been overcome in the mid-1980s and, since then, operations have been providing heat daily to more than 150,000 dwellings. Operating facilities use the “doublet” technology which consists of a loop with one production well and one injection well. Consequently, injection of the cooled brines leads to the progressive exhaustion of the resource at the local doublet scale. Most of the research effort has been focused on quantifying the temporal evolution of the cooling, and to forecast the lifetimes of doublets and the occurrence of the “thermal breakthrough”.

Yet, with the need for carbon free energy sources there has been a revival of geothermal energy development in France: many projects are presently being considered and new operations have already been carried out. In this context, it appears that the aquifer geothermal resource has to be managed and modeled as a whole. For this purpose, BRGM maintains an up-to-date hydraulic and thermal model of the aquifer which can help policy makers to improve regulatory framework and which can support stake holders to carry out new operations. Moreover, because of potential conflicts of use which are emerging in densely exploited areas, a fine understanding of reservoir behavior is needed and new technological solutions must be developed: exploration and exploitation of underlying or overlying aquifers, seasonal heat storage...

Historical perspective

40 years of geothermal exploitation of The Dogger aquifer

The Paris basin is the largest onshore sedimentary basin in France. It occupies a vast part of Northern France (110,000km^2) and extends northward to Belgium and below the English Channel. Its origin is linked to a period of rifting in Permo-Triassic times. The central part of the Basin, where the subsidence was the greatest, is filled with about 3000 m of sediments (Guillocheau *et al.*, 2000; Delmas *et al.*, 2002).

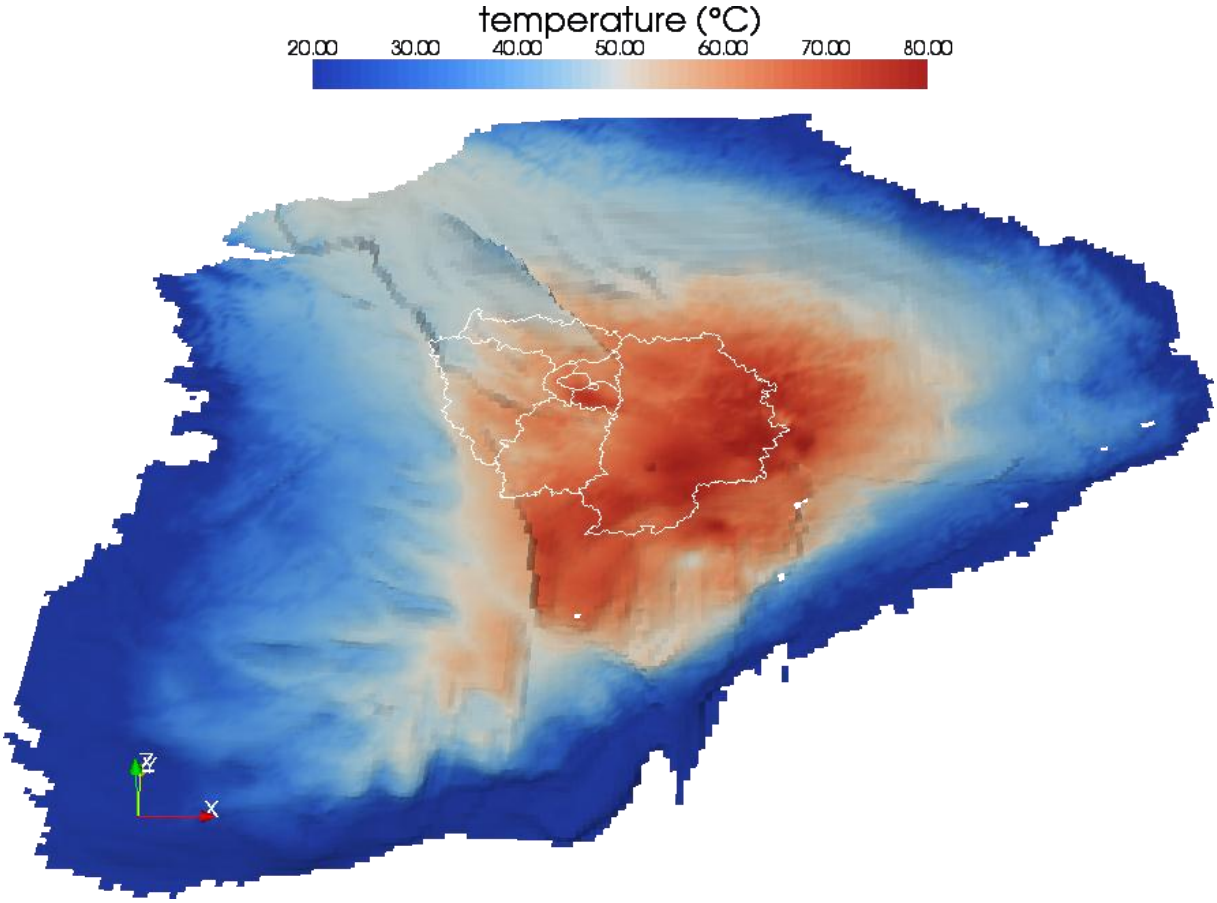

Figure 1 : 3D view of the top of the Dogger aquifer and associated temperatures (white wirelines highlight the Ile de France region with Paris at its center)

Among the four main lithostratigraphic units exhibiting aquifer properties in the basin, the mid-Jurassic (Dogger) carbonate rocks were identified as the most promising geothermal development target below the urbanized Paris area (Ungemach *et al.*, 2005). Several oil-bearing reservoirs were also identified in this geological unit some of which correspond to the target layers for geothermal exploitation. In its slow circulation through the basin, the fluid reaches depths of 2000m where it acquires its geothermal potential with good transmissivities and temperature that can reach 80°C in the deepest areas.

The geothermal development of French sedimentary basins started in the early-1970s (Lemale and Pivin, 1987; Demange *et al.*, 1995; Laplaige *et al.*, 2005; Lopez *et al.*, 2010). In the Paris basin, the main target has been the Dogger aquifer whose development was favored by three main technical and economic factors:

- The presence of a productive hot reservoir, located at a reasonable depth, whose characteristics (temperature and transmissivities) were suitable for the supply of district heating networks (cf. temperature map on figure 1).
- The existence of an important potential heat market, with densely populated areas, suitable for low-temperature energy production: the Paris area with more than 10 million inhabitants.
- Availability of public policy incentives and insurance policies that favored the development of new energy sources.

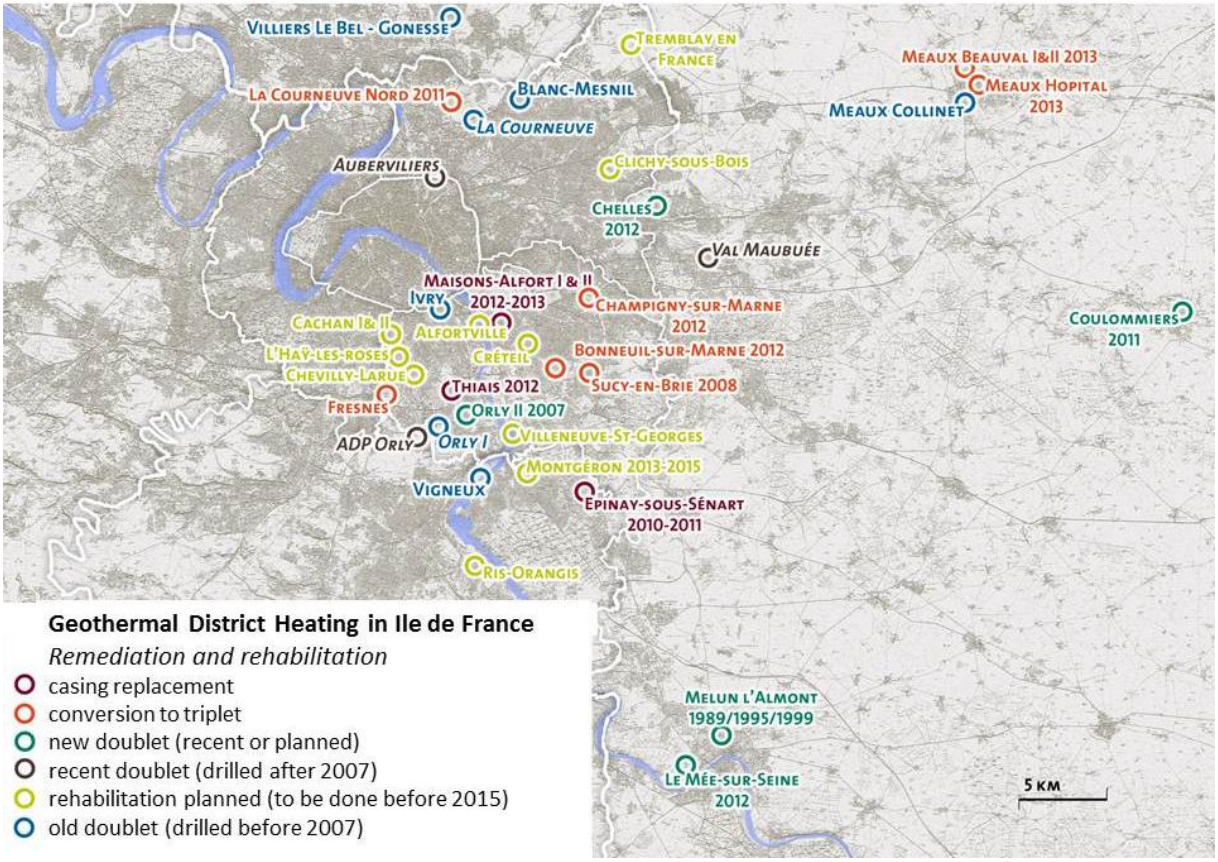

Figure 2 : Remediation and/or rehabilitation of deep geothermal wells in the Paris area (Ile de France region) (map by C. Chery/BRGM)

The first successful operation targeting the Dogger aquifer was drilled at Melun l'Almont in 1969, more than 40 years ago (cf. location map on figure 2). It is still active today, providing space heating for 5000 houses, after the replacement of the first two wells. Nevertheless, the growth in exploitation of the Dogger geothermal potential has not been steady instead and has rather been reflecting the French technical and economic context. A large number of operations were planned and completed in the aftermath of the 1973 and 1979 oil crises, when governmental policies supported energy conservation and the development of alternative sources of energy. The drilling of new doublets was especially favored by the development of an insurance policy that covered geological hazard (e.g., poor flow rate), as well as long term behavior and exploitation of the doublet (i.e., decrease in the temperature of the produced brine).

The 1986 drop in fossil energy prices impeded new operations and initiated a period marked by very little activity. Forty-two wells were abandoned for technical (corrosion or scaling) or economic

reasons (low profitability of geothermal operations compared with fossil energies, drop in interest rates that penalized older loans used to finance geothermal operations). The vast majority of abandoned operations lie in the northwest part of the Basin, which is the area of lowest geothermal fluid temperature ranging from 55 to 65°C (figure 1).

Then, during the 90s and until the middle of the years 2000, drilling activities in the Paris basin were reduced to the replacement of damaged wells or the development of existing facilities (Laplaige *et al.*, 2005). Tough there has been a boost in geothermal activity at the turn of the century, over half of the existing district heating networks with a geothermal supply in the Paris region (17 out of 29) were equipped with gas cogeneration plants. This choice had significant impacts on existing geothermal loops. The resulting reduction of the average exploitation flow rate induced an increase of corrosion and scaling related problems. These damaged several well casings that had to be replaced. In 2005, the average rate of geothermal energy use for the group of 29 heat networks was around 60%, compared to 72% for the previous situation when there were no cogeneration facilities (Laplaige *et al.*, 2005).

As a consequence of the growing needs for producing heat in a less polluting way and with a lower carbon footprint, it's been a few years now that old wells are progressively being replaced, several new geothermal doublets have been drilled and many other operations are planned (figure 2). By the beginning of 2012, there were more than 120 deep geothermal wells exploiting the Dogger aquifer in the Paris basin. Moreover, some areas are becoming so densely exploited that potential resource exploitation conflicts are emerging and new challenges concern mainly the sustainable exploitation of the aquifer as a whole.

Exploitation characteristics

Nearly all geothermal operations exploiting the Dogger aquifer use the "doublet" technology consisting of a closed loop with one production well and one injection well. The wells target productive layers which lie between 1500 and 2000 m deep. They are usually completed with an open hole through a reservoir thickness ranging from 100 to 150m of carbonate deposits. By the end of the 1970s, the routine acquisition of well logs, especially flowmeter logs, revealed the high vertical and lateral variability in the hydrological characteristics of the aquifer. There can be from 3 to 20 individual productive layers in the formation with a cumulative thickness (*net pay*) of only 10% of the total aquifer thickness. On average, this net total productive thickness is of the order of 20 m, with 10–15 high permeability (2–20 Darcy) layers. A single productive layer may represent as much as 80% of the total flow rate (Lemale, 2009).

Formation temperatures at the top of the productive layers are generally between 55°C and 80°C (figure 1). The mean temperature gradient between the surface and the formation is 3.5 ◦C/100 m. Minimum temperatures are found at 1650m below surface, northeast of Paris, where average thermal gradients are as low as 2.75 ◦C/100 m. This zone corresponds to a cold anomaly area that can be explained by regional cold water flows coming from the upper parts of the aquifer. Some authors proposed that this cold area could be linked to circulations induced by the historical intensive exploitation of overlying aquifers for drinkable water, since the middle of the 19th century (Burrus, 1997). Maximum gradients of 4.1°C/100m are recorded southeast of Paris.

The salinity of exploited brines ranges from 6.4 mg/l to 35 mg/l. At basin scale, salinity increases from the southeast, where the reservoir outcrops (0.5 g/l), to the deepest area where it reaches 35 g/l.

These salinity variations influence the brine density and viscosity and hence the aquifer-scale fluid flow (Menjoz and Lambert, 1991), but these variations have a negligible effect at the scale of geothermal doublet exploitation.

Facies and diagenetic porosity reduction patterns are complex. The original porosity and permeability properties are strongly influenced by contemporaneous dissolution events related to high frequency sea level fluctuations. Fracture porosity is often present (Delmas *et al.*, 2002). Investigations showed a direct relation between the porosity and the sedimentary environment, particularly where the sandy sediments with matrix porosity were deposited (Rojas.J. *et al.*, 1989).

The doublet technology has several advantages:

- There are no environmental impacts as the cooled geothermal brine is fully reinjected, and prohibitive costs of chemical processing of geothermal brines for surface disposal are avoided.
- Production flow rate is maintained whereas a single well exploitation would have progressively reduced the reservoir pressure, eventually affecting pumping conditions.
- Thanks to the pressure interference the exploitation pressures are stabilized and the area impacted by pressure variation is limited: an exploitation domain can be legally defined by the authorities, thus allowing the setup of an efficient strategy for the optimal management of the aquifer.

From the doublet scale to regional scale management

Cold water breakthrough is an inevitable consequence of the doublet approach. The practical lifetime of a geothermal project can be defined as the time for the produced fluid temperature to decline to a level that exploitation is no longer beneficial. During the 1980s, when most of the doublets were drilled, numerical modeling studies based on rather pessimistic assumptions estimated the average lifetime of geothermal doublets to be 20–25 years. Most of the doublets have now been exploited for more than 20 years, and, so far, no thermal decline has been observed in any but one of the geothermal loops and one more may be suspected on another operation.

Although the practical lifetime is longer than had been expected, uncertainty still remains about when and how much the temperature will decline. Since the beginning of geothermal exploitation in the Paris Basin, the resource has been exploited without any real attempt to optimally manage the Dogger resource. Now, as the predicted thermal breakthrough time of some doublets is approaching, the non-sustainable character of individual geothermal projects has become a matter of concern for many stakeholders. Consequently, there is a urgent need to define guidelines to be followed for the development of new doublets in order to properly manage and optimize the exploitation of the resource. This is especially true in districts where the doublet density is already high or where the density of surface heating networks would make future intense exploitation probable.

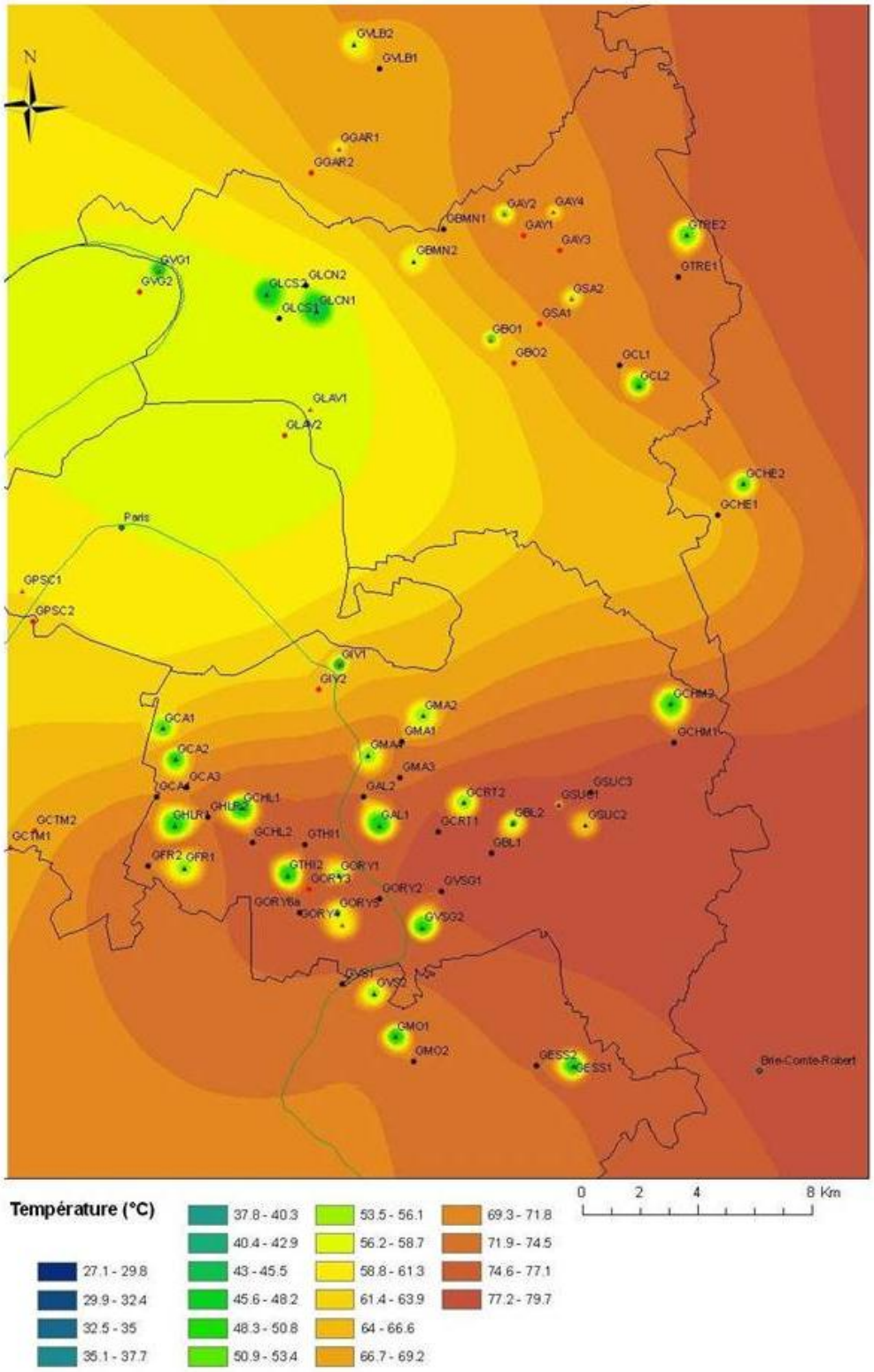

Figure 3: Temperature of the resource in densely exploited areas (Hamm *et al.*, 2010)

A long term project devoted to Dogger aquifer management has been started in 2007. This project is run cooperatively by ADEME (French Environment and Energy Management Agency), BRGM, and the Ile de- France Regional Council. As of today, out of the 35 pairs currently operating in the Paris

region, 27 are located in Val-de-Marne and Seine-Saint-Denis areas. Since 2009, a regional model of the geothermal resource and of the impact of its exploitation has been developed with the objectives (figure 3) :

- to better understand the extension of the cooled zones and to optimize the forthcoming operations (rehabilitation or location of new wells, doublets or any other technology),
- to be able to predict the production temperature evolution of existing producing wells.

Modeling works have been constrained using the “Dogger database” which was created in 2001. For all operations, this database contains all historical data since 1969 concerning drilling, workovers, plant equipment, aquifer characteristics, operating histories (flow rate, injection temperature and pressure, etc.) and monitoring data. The regional model is regularly updated and new data from the Dogger exploitation are integrated via the database.

Finally, in very densely exploited areas, sophisticated completion schemes and well architectures such as horizontal or multi-lateral wells may be an interesting option if they become economically affordable (Ungemach *et al.*, 2011; Hamm and Lopez, 2012).

Sensitivity analysis of reservoir models

Until today, only one case of temperature decline has been observed among all the exploited geothermal doublet of the Paris basin. This very slight decline has been very satisfactorily reproduced by several modeling teams (figure 4). Nevertheless, the temperature of the produced brine temperature is far from being stable and the amplitude of the observed fluctuations is still greater than the amplitude of the temperature decline. First, the reliability of the measurements introduces uncertainties. Measurements are performed on the geothermal loop at the surface, and therefore depend on the working conditions of the loops (mainly flow rate) and heat losses through the casing between the reservoir and the well head. Besides, the precision of the instruments does not permit systematic measurement of small variations. Finally, the numerical forecasts are often made assuming periods of constant production rate with constant injection temperatures, whereas production flow rates may also fluctuate as well as injection temperatures which depend on weather conditions.

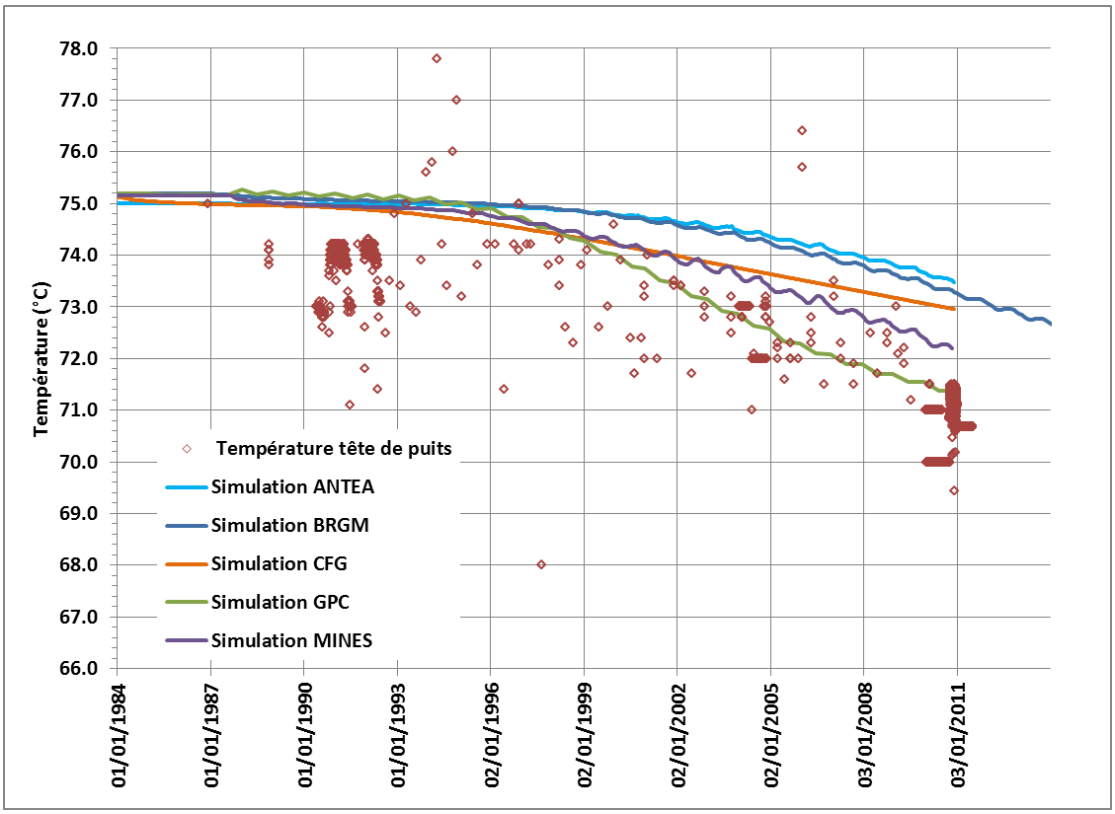

Figure 4: Downhole reservoir temperature (color lines) compared with the observed well head brine temperature (red circles) on the Alfortville operation.
Simulation results were obtained by different modeling teams (Hamm et al., 2011)
There is a 1 to 2 °C difference between reservoir and well head temperature which is due to heat losses along the casing.

Nevertheless, it is worth noting that regional modeling predicts thermal decline on another operation though it is not observed yet. It is very likely that such discrepancies between model predictions and observations are linked to the very scarce data available for reservoir characterization. This scarcity introduces a great deal of uncertainty in the modeling results. Indeed, data points are separated by the distance between the production and the injection wells inside the reservoir which is often greater than 1km. Consequently, accurate identification and correlation of productive layers or estimation of the true productive thickness remain very difficult tasks. This is all the more important because these parameters are among the most important in controlling the time of the thermal breakthrough, and hence the overall lifetime of the doublet (Menjoz, 1990).

As only the beginning of a single temperature decline has been observed among the nearly 40 operating doublets of the Paris basin, numerical modeling remains the best way to forecast the thermal breakthrough, and to provide a basis for devising a sustainable strategy for the development of the Dogger aquifer (see also see also:Ungemach *et al.*, 2007; Ungemach, 2008). Modeling studies can be performed at different scales, ranging from the full regional scale, i.e., the entire Paris Basin, to the smaller scale of a pair of neighboring doublets or even a single doublet. Accurate numerical modeling of heat or chemical transport requires spatial and temporal discretization designed to avoid numerical dispersion or instabilities. Thus, horizontal mesh must be fine around wells, as must be vertical mesh near the boundaries between the reservoir and adjacent layers to correctly reproduce heat exchanges. Selection of the modeling scale and of the physical processes to be investigated is often the result of a trade-off between the accuracy required to answer a particular question and the available computing power.

The conceptual model of the aquifer will have a great influence on the modeling results. As the productive levels of the aquifer cannot be individually correlated, they are generally grouped into distinctive facies units whose lateral continuity is assumed according to geological knowledge. It is often considered that the Dogger aquifer is correctly represented with three productive layers, each corresponding to one of the geological units : Comblanchian, Oolitic, and Cyclical (Rojas.J. *et al.*, 1989; Lopez *et al.*, 2010). Yet, it has also been proved very efficient to divide the total productive thickness (net pay) into two identical layers with the same properties and an impervious inter-strata layer between them that accounts for the thermal capacitive effects (heat store) of all impervious layers (Antics *et al.*, 2005; Hamm *et al.*, 2011).

In the early 80s, modeling predictions of the thermal breakthrough that were made were rather pessimistic. The reason of this was that they were only considering the total productive thickness as one productive layer and were neglecting impervious interstrata. Figure 5 shows the difference between such an *old-fashioned* conceptual models and a three productive layer model with impervious confining layers. If the doublet's practical lifetime is defined on the assumption that a 3°C temperature drop is economically acceptable, simulation S1, which is the *old-fashioned* one, predicts a practical lifetime of 17 years, whereas simulation S3, the simulation with three productive layers yield a practical lifetime of 62 years.

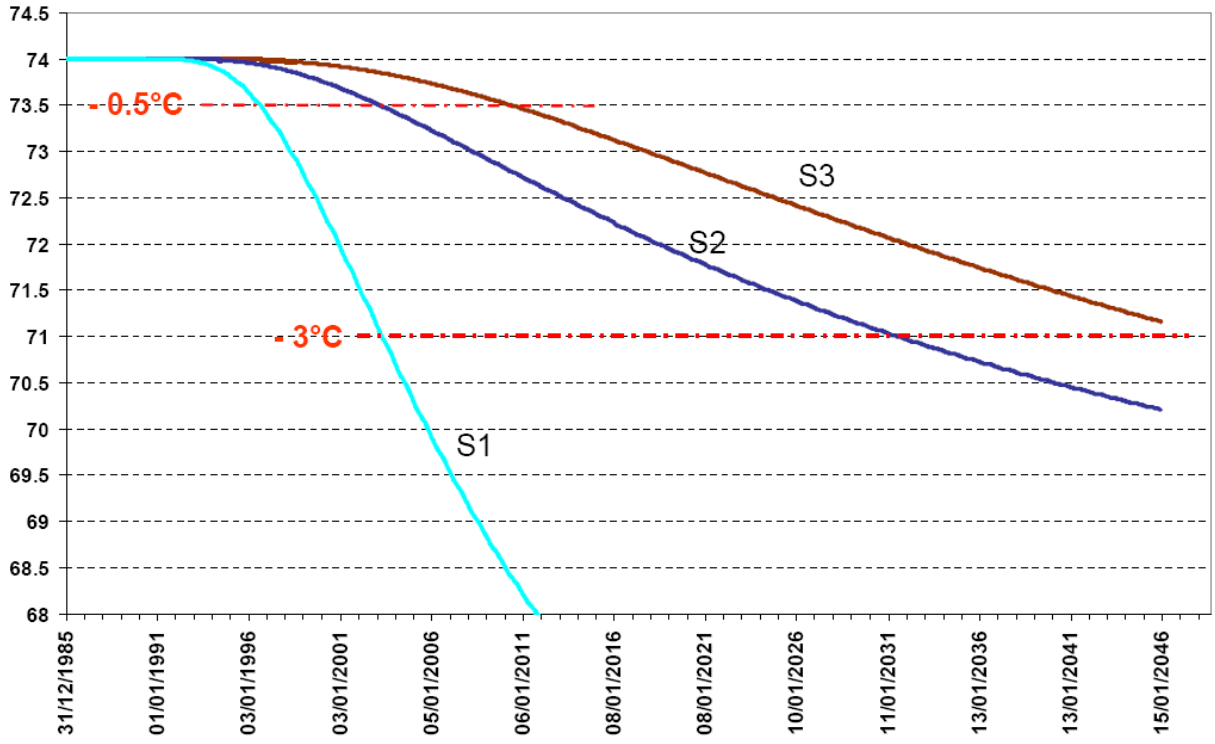

Figure 5: Production temperature decline at the production well of an isolated geothermal doublet for different conceptual model of the Dogger aquifer. (Lopez *et al.*, 2010)
S1 – one productive layer only, S2 – one productive layer and impervious but conductive confining layers, S3 – three productive layers and impervious but conductive confining layers and inter-strata. Initial reservoir temperature is 74°C.

To perform a sensitivity analysis of parameters influencing the thermal breakthrough, a reference case was defined for a geothermal doublet in the Dogger aquifer. Then several simulations were run varying these parameters inside realistic ranges. Parameters that were considered were the

thicknesses of the impervious strata layer, the vertical structure of the reservoir (number of productive layers), difference in transmissivity of the productive layers, thermal properties rock (thermal conductivity, heat capacity, dispersivity), operating parameters (flow rate, injection temperature) and the distance between the production and the injection wells inside the reservoir. The histogram in figure 6 summarizes the results of the sensitivity analysis and shows the impact of the several parameters on the thermal breakthrough time and the amplitude of the temperature decline.

The most important parameters, controlling both the thermal breakthrough time (early recycling of cooled brine) and the amplitude of the thermal decline are: flow rate, injection temperatre, the distance between wells and the thickness of the impervious inter-strata (conductive heat store). Consequently, these parameters must be introduced into the simulation models as accurately as possible : any uncertainty on these input parameters will induce a significant uncertainty on the final results. Whereas the distance between wells can be estimated from the drilling reports with a reasonable degree of confidence, the correct reproduction of the history of exploitation flow rates and injection temperatures is much less guaranteed. Indeed, it depends greatly on the efficiency and correctness of the Dogger database and the careful and repeated recollection of all operational data which represents a large amount of data. Thus, in order to achieve a sustainable management of the aquifer geothermal resource, improving models needs a precise monitoring of geothermal operations and a rigorous and full storage of all corresponding data. This point is especially important because of the gradual nature of the temperature decline and the very small amplitude of the changes that are to be modeled, in comparison with background noises (figure 6).

Less influent parameters are the thermal properties of the rock, the distribution of transmissivities between productive layers and, to an even lesser extent, the vertical structure of the conceptual model. The impact of the vertical structure of the reservoir is indeed limited to the immediate vicinity of the injection well, where convective effects are predominant. Away from this zone of relatively high velocities, diffusion processes tend to homogenize the reservoir temperatures and smooth the temperature front corresponding to the cooled brine injection. Consequently, a two layers structure of the "sandwich" type is then largely enough to correctly predict the thermal behavior of the producing well.

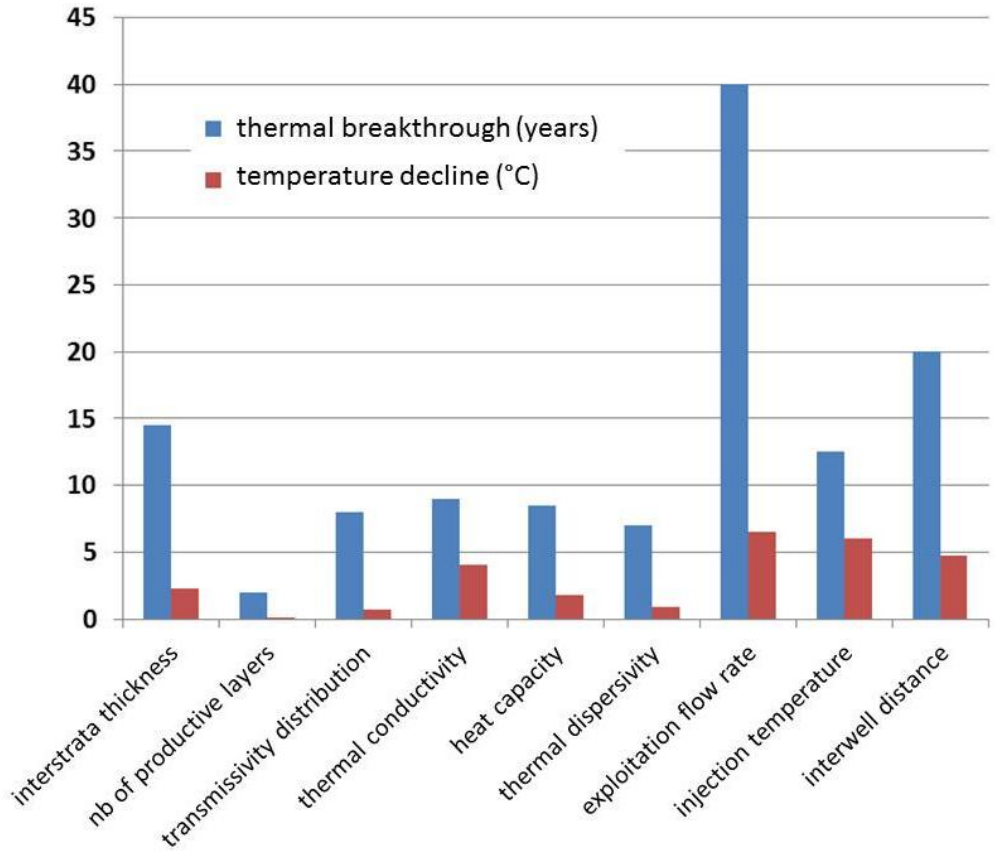

Figure 6 : Maximum impact on breakthrough time and production temperature decline for nine key parameters of numerical models. (Hamm *et al.*, 2011)

It is also worth noting that an inter-comparison study involving 5 French modeling teams coming from different organizations has been organized to benchmark their modeling tools and compare their modeling practices (figure 4 and Hamm *et al.*, 2011).

New developments

Rehabilitation of old operations

As the geothermal wells are getting older, and as many of them suffered corrosion and scaling related problems, the need for their rehabilitation is becoming more and more important. The most frequent rehabilitation scheme is the conversion of a doublet into a triplet by drilling a new well from the old doublet platform which becomes the producer and the two old wells that are used for injection. In terms of determining the new well location, each case is site specific and depends on neighboring installations, aquifer properties, well diameters, and the like. Nevertheless, several theoretical studies were performed on an isolated doublet to quantify the impact of the possible rehabilitation schemes on the practical lifetime of the operation.

Figure 7 shows the production temperatures corresponding to different rehabilitation schemes of a 30 years old isolated geothermal doublet. The “usual” triplet conversion is compared with the drilling of a brand new doublet from the old platform and a two steps operation consisting in first drilling a

new production well to operate a triplet for ten years and then drilling another well to have a new doublet. According to simulation results, this second approach does not seem to be too prejudicial in terms of temperature decline and may be a way to spread drilling costs over two distinct periods.

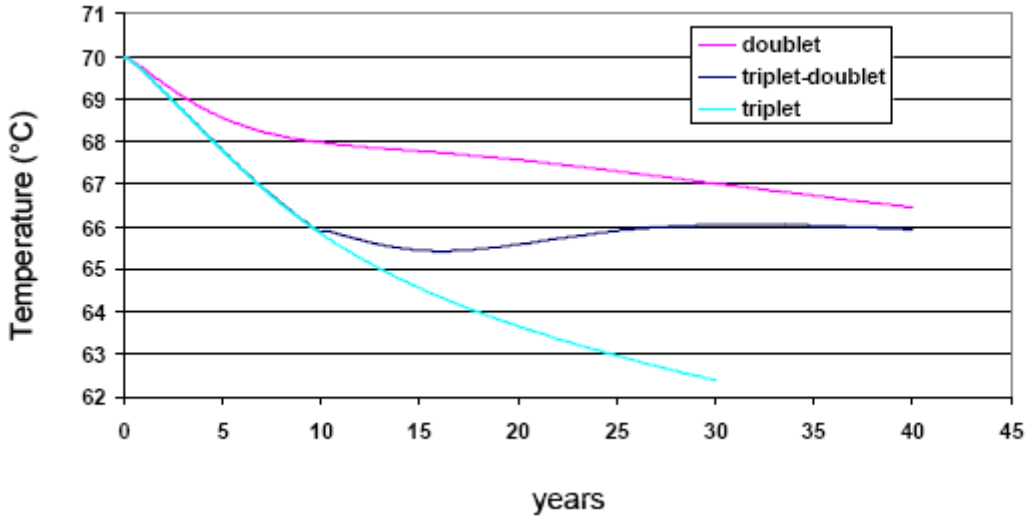

Figure 7 : Production temperatures corresponding to different rehabilitation schemes of a 30 years old isolated geothermal doublet. (Le Brun *et al.*, 2009; Le Brun *et al.*, 2011)
Initial reservoir temperature is 70°C.

Targeting new resources

Below the Dogger aquifer, some Triassic sandstones units have good reservoir properties and may constitute attractive geothermal targets for district heating (cf. temperature map in figure 8). Unsuccessful attempts at their geothermal exploitation were made in the early 80s: these deep layers proved hotter but much less productive than the overlying Dogger aquifer. Moreover, for the only operation where they have been exploited until now, there were injection related problems with the injectivity index being lower than the productivity index: throughout the one year of operation, one third of the produced flow rate was not being reinjected into the reservoir but disposed into a neighboring river.

To avoid these critical reinjection problems, a possible option would be to produce the hot brines from the Triassic aquifers but inject the cooled brines into the Dogger aquifer. Nevertheless, this solution might trigger geochemical reactions that may impact negatively the properties of the Dogger aquifer, notably its porosity (Castillo *et al.*, 2011).

An alternative option to develop the geothermal potential of these deep aquifers is to resort to more sophisticated, but still rather expensive, well architectures. Indeed, simulation works show that in these clastic environments, horizontal wells are particularly well adapted with higher injectivity or productivity index and a more gradual temperature decline at the production well. Moreover, when drilling horizontal wells perpendicular to the high conductive paths, the production fluid temperature may still not be affected by the cold injection after 30 years of geothermal exploitation (Hamm and Lopez, 2012). If these modeling results are confirmed at a production stage, it would be a promising breakthrough for further developments in geothermal well design.

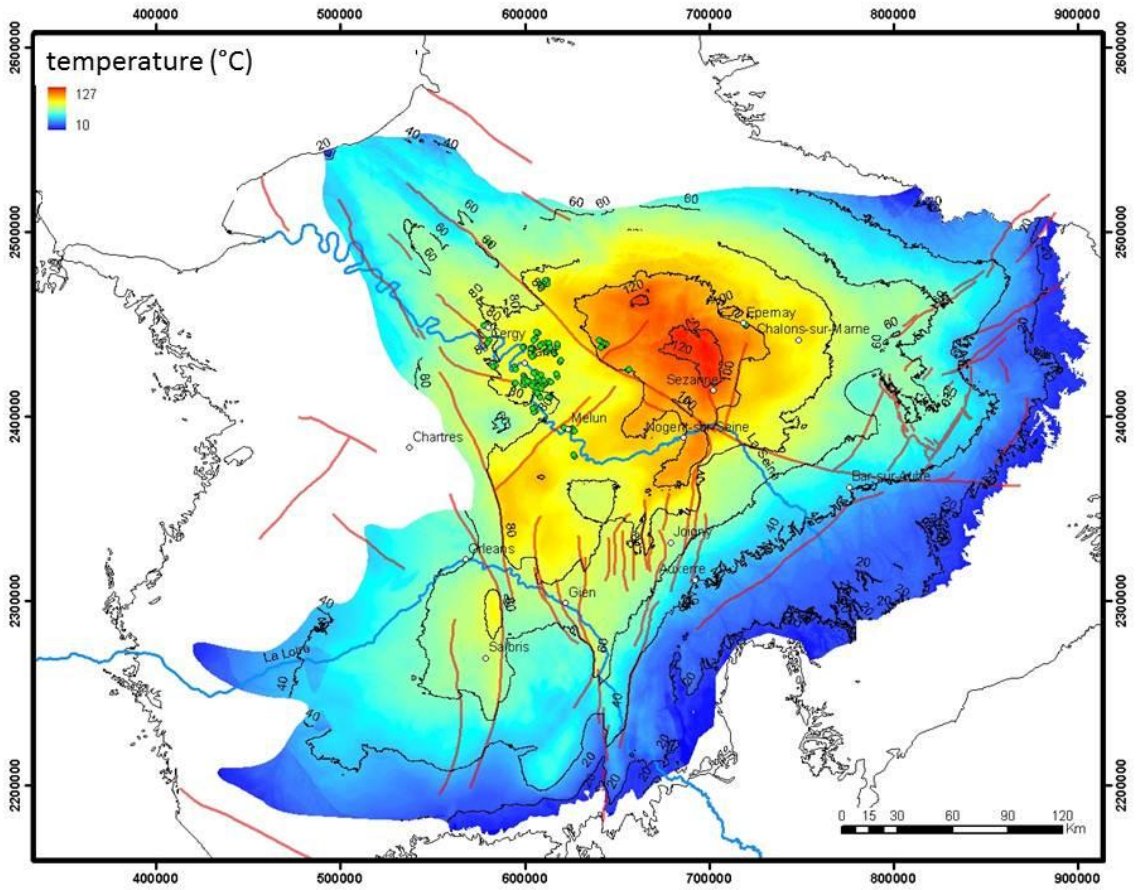

Figure 8: Estimation of the temperature at the top of the Donnemarie sandstones
Donnemarie sandstones are the deepest aquifer units of the Triassic series of the Paris basin (Bouchot *et al.*, 2008)

Deep Aquifer Heat Storage

Demand for heat is characterized by considerable fluctuations over time. Although there are short period variations in demand (mornings, weekends, etc.), variations in the weather in temperate zones impose a highly seasonal pattern. The thermal power requirement in winter is therefore an order of magnitude greater than in summer, which mainly consists in the household demand for hot water. This pattern of temporal variation requires a heat production capacity that is far greater than the average annual power requirement.

Since most of the energy sources used to meet the seasonal peaks are of fossil origin, they make a significant contribution to CO_2 emissions. In addition, some of the energy inevitably produced by various processes may not be needed in the summer and, if it is not collected, will be wasted. In this context, current industrial processes such as incineration of waste and also possible future major solar thermal or thermodynamic systems come to mind. The storage of thermal energy overcomes the temporal mismatch between production and consumption, thereby making it possible to reduce the baseload power capacity and the use of more polluting sources. The economic and environmental advantages of storage will depend on the cost of the storage system and the nature and price of the energy stored relative to the savings provided when the energy is retrieved. The aim therefore is to store “decarbonized” energy that is in excess or has low environmental impact when it is available in the summer and to retrieve it in the winter, so as to avoid use of fossil energies.

In the very long term, seasonal storage of waste heat in the Dogger aquifer could become a way to smooth energy demand during winter peak production periods, and possibly restore the initial aquifer temperatures. Storage in aquifers is especially suited to urban environments as it uses a minimum of surface area. For open loop storage in deep aquifers, the high cost of the drilling required to reach the targeted geological levels makes this solution incompatible with single-occupancy dwellings. Conversely, it is particularly appropriate to district heating systems and provides a geothermal solution that is complementary to conventional heat-mining systems.

This is so because, given their centralized production, heating networks make it possible to envisage large scale and high power storage during periods of low demand. They also allow better control of polluting emissions and development of use of renewable sources and/or waste energy that are difficult to access or to use: deep geothermal energy and also biomass or waste incineration. Seasonal storage of this energy in aquifers makes it possible to increase the annual amount of energy supplied to networks from renewable sources, with a corresponding reduction in wintertime recourse to fossil fuels.

Experience gained from the geothermal exploitation of the Paris Basin suggests the key issues regarding seasonal Aquifer Thermal Energy Storage in the Dogger aquifer are likely to be the high temperature of the stored brine and the cyclical reversal of injection and production wells.

The high temperature of the injected brine, hotter than the aquifer natural state, may produce undesirable chemical reactions. According to preliminary geochemical modeling Dogger brines should not be heated above 105°C to avoid scaling related problems and formation damage (Castillo and Azaroual, 2010).

Concerning the reversal of the production/ injection cycles, no long-term experience is available for the Dogger aquifer, but lessons from the recent deep Neubrandenburg aquifer thermal energy storage project illustrate that final heat consumption and the return temperature in the heating network (i.e., surface installations) are of greater concern than fluctuations that might be related to the deep reservoir (Kabus *et al.*, 2009; Réveillère *et al.*, submitted).

Finally, an interesting point is that selecting a storage temperature so that the initial reservoir temperature is the arithmetic average of the cold injection temperature and the hot storage temperature will make that the energy coming from conventional heat mining will exactly compensate the heat losses due to the injection of hot brines into a warm aquifer (figure 9). Thus, depending on the number and type of wells, several technological configurations may be imagined that are combinations of use of conventional geothermal technology and heat storage.

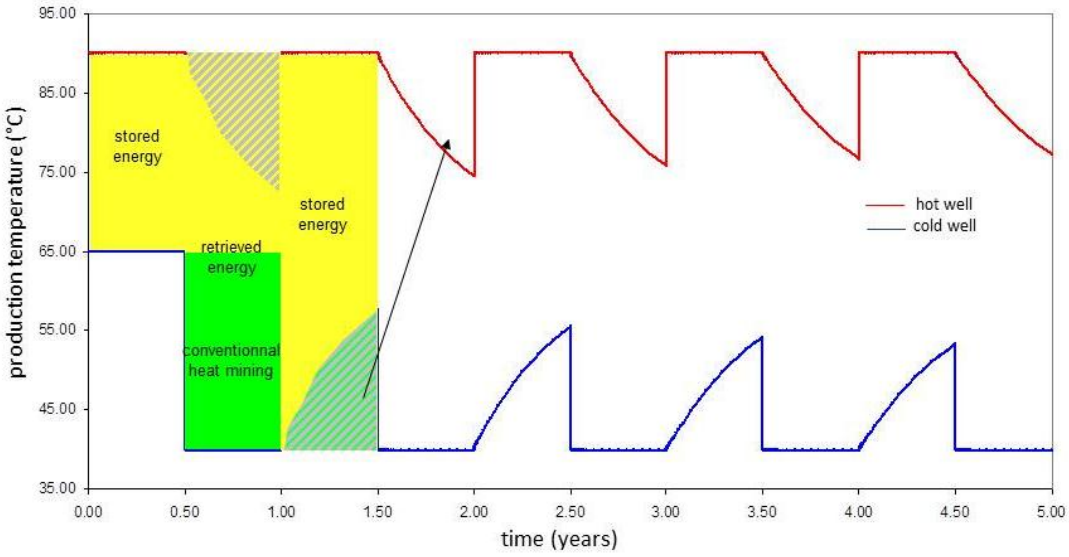

Figure 9: Stored and retrieved energy during seasonal cycles
Initial reservoir temperature is 65°C, heat is stored at 90°C during the summer and cooled brines are injected at 40°C during the winter.

Acknowledgments

All the works concerning the conventional geothermal exploitation of the Paris basin aquifers are co-funded by BRGM and the French Environment and Energy Management Agency (ADEME). The works regarding the possibilities for deep aquifer heat storage in the Dogger aquifer has been co-funded by the ANR Stock-E program and the partners of the Geostocal project (CFG Services, CPCU, EIVP, IFPEN, Mines Paristech, Paris-Est Marne la Vallée University).

The first author would also like to acknowledge travel support to the SIMS Conference provided by the International Energy Agency's Geothermal Implementing Agreement (IEA-GIA).

Antics M., Papachristou M., Ungemach P. (2005) - Sustainable heat mining. A reservoir engineering approach. *Proceedings of the 30th Workshop on Geothermal Reservoir Engineering,* January 31-February 2, 2005, Stanford University, Stanford, California.

Bouchot V., Bialkowski A., Lopez S., Ossi A., Chiles J., Garibaldi C., Jorand C. (2008) - Evaluation du potentiel géothermique des réservoirs clastiques du Trias du Bassin de Paris. BRGM. (technical report RP-56463-FR).

Burrus J. (1997) - Contribution à l'étude du fonctionnement des systèmes pétroliers : apports d'une modélisation bi-dimensionnelle. Thèse de doctorat,Ecole des Mines de Paris.

Castillo C., Azaroual M. (2010) - Reactive transport simulations of geochemical processes induced by ATES operations in the Dogger aquifer (Paris Basin). *38th IAH Congress,* September 12-17, 2010, Krakow, Poland.

Castillo C., Kervévan C., Jacquemet N., Hamm V., Bouchot V., Sanjuan B. (2011) - Assessing the Geochemical Impact of Injection of Cooled Triassic Brines into the Dogger Aquifer (Paris Basin, France): a 2D Reactive Transport Modeling Study. *36th Workshop on Geothermal*

Reservoir Engineering, January 31 - February 2, 2011, Stanford University, Stanford, California.

Delmas J., Houel P., Vially R. (2002) - Paris Basin petroleum potential. IFP.

Demange J., Jaudin F., Lemale J., Menjoz A. (1995) - The Use of Low-Enthalpy Geothermal Energy in France. *World Geothermal Congress,*

Guillocheau F., Robin C., Allemand P., Bourquin S., Brault N., Dromart G., Friedenberg R., Garcia J., Gaulier J., Gaumet F., Grosdoy B., Hanot F., Le Strat P., Mettraux M., Nalpas T., Prijac C., Rigollet C., Serrano O., Grandjean G. (2000) - Meso-Cenozoic geodynamic evolution of the Paris Basin: 3D stratigraphic constraints. *Geodinamica Acta*, 13, 4 p. 189-245.

Hamm V., Le Brun M., Castillo C., Ausseur J., Borozdina O., Cordier E., Gille A., Goblet P., Ungemach P. (2011) - Gestion de la ressource géothermique du Dogger de la région Ile-de-France – Année 2011. Rapport intermédiaire. BRGM. (technical report RP-60399-FR).

Hamm V., Lopez S. (2012) - Impact of Fluvial Sedimentary Heterogeneities on Heat Transfer at a Geothermal Doublet Scale. *Proceedings of the 37th Stanford Geothermal Workshop,* January 30 - February 1, 2012, Stanford, California, U.S.A.

Hamm V., Castillo C., Le Brun M., Goyeneche O., Lopez S., Ignatiadis I., Azaroual M., Malon J. (2010) - Mise en oeuvre de la gestion de la ressource géothermique du Dogger de la région Ile-de-France dans le cadre du dispositif d'acquisition et de stockage des données. BRGM. (technical report BRGM/RP-58834-FR).

Kabus F., Wolfgramm M., Seibt A., Richlak U., Beuster H. (2009) - Aquifer Thermal Energy Storage In Neubrandenburg - Monitoring Throughout Three Years Of Regular Operation. *Effstock 2009, Thermal Energy Storage for Efficiency and Sutainability,* June 1417, 2009, Stockholm, Sweden.

Laplaige P., Lemale J., Decottegnie S., Desplan A., Goyeneche O., Delobelle G. (2005) - Geothermal Resources in France - Current Situation and Prospects. *World Geothermal Congress,* 2005, Antalya, Turkey.

Le Brun M., Hamm V., Lopez S., Ungemach P., Antics M., Ausseur J., Cordier E., Giuglaris E., Goblet P., Lalos P. (2011) - Hydraulic and Thermal Impact Modelling at the Scale of Geothermal Heating Doublets in the Paris Basin, France. *Proceedings of the 36thWorkshop on Geothermal Reservoir Engineer,* January 31 - February 2, 2011, Stanford, California, U.S.A.

Le Brun M., Hamm V., Lopez S. (2009) - Modélisation de l'impact thermique et hydraulique sur l'exploitation de l'aquifère du Dogger pour différents scénarios de réhabilitation d'un doublet géothermique type. Rapport intermédiaire. BRGM. (technical report BRGM/RP-57779-FR).

Lemale J. (2009) - La géothermie. Paris, France : Technique et Ingénierie, Dunod/Le Moniteur. 307 p.

Lemale J., Pivin M. (1987) - La filière géothermique, premier bilan. Paris, France : Agence Francçaise pour la Maitrise de l'Energie (AFME). 80 p.

Lopez S., Hamm V., Le Brun M., Schaper L., Boissier F., Cotiche C., Giuglaris E. (2010) - 40 years of Dogger Aquifer management in Ile-de-France, Paris Basin, France; Sustainable utilization of geothermal energy. *Geothermics*, 39, 4 p. 339-356.

Menjoz A., Lambert M. (1991) - Hydrodynamique des aquifères profonds et incidence des effets de densité. *Hydrogéologie*, 4 p. 311-320.

Réveillère A., Hamm V., Cordier E., Goblet P., Lesueur H. (submitted) - Supplying district heating networks through Aquifer Thermal Energy Storage: integrated energetic and economic model. Application in the Paris basin. *Geothermics*

Rojas.J., Giot D., Le Nindre Y., Criaud A., Fouillac C., Brach M., Menjoz A., Martin J. C., Lambert M. (1989) - Caracterisation et modelisation du reservoir geothermique du dogger. Bassin parisien, france. Rapport final. BRGM. (technical report RR-30169-FR).

Ungemach P., Antics M., Lalos P., Borozdina O., Foulquier L., Papachristou M. (2011) - Geomodelling and well architecture, key issues to sustainable reservoir development. *Proceedings of the 37th Workshop on Geothermal Reservoir Engineering,* January 30 – February 1, 2011, Stanford, California.

Ungemach P. (2008) - Geothermal Reservoir Management Technology and Problem Areas. *Petroleum Engineering Summer School,* Inter-University Centre, Dubrovnik, Croatia.

Ungemach P., Antics M., Papachristou M. (2005) - Sustainable Geothermal Reservoir Management. *World Geothermal Congress,* 2005, Antalya, Turkey.

Ungemach P., Papachristou M., Antics M. (2007) - Renewability Versus Sustainability. A Reservoir Management Approach. *European Geothermal Conference,* 2007, Unterhaching, Germany.

SUSTAINABILITY ANALISYS OF THE BERLIN GEOTHERMAL FIELD, EL SALVADOR.

Manuel Monterrosa, Lageo El Salvador

ABSTRACT

Over the past 20 years, the Berlin geothermal field has been in commercial operation through step wise development, at the moment the installed capacity is 109.2 MW. The total mass extracted ranges 870 kg/s which are delivered by 14 producer wells with average discharge enthalpy of 1300 kJ/kg and average steam flow rate of 20 kg/s. At the field, there are hot brine injection (180 and 140 °C) which is performed using 19 injection wells and cold injection (ambient temperature) with the operation of one well. A high pressure pumping station is also used manly when the gravity injection is going down. During the long term exploitation 18 bar of pressure drawdown was observed into the field and perhaps the main process observed in producer wells is boiling and there are no evidence of cooling due to injection.

Since long term exploitation began sustainable development was a very important commitment for LaGeo, during the first stages of exploitation the field management, monitoring technics and numerical modeling were soon implemented. LaGeo as part of its corporative sustainable policy is focused to define the sustainable energy level and performance indicators; all of them are also part of concession contract granted by SIGET (electricity energy regulator entity) in year 2000.

Preliminary results indicate the sustainable energy level of the Berlin resource is higher than the actual installed capacity, and there are defined at least 5 performance indicators which are: energy efficiency utilization, resource life, recovery time, subsidence, power plant performance, in this paper is discussed just 3 of them the another one are under analisys.

INTRODUCTION

Over the past 10 years, LaGeo is working to develop a sustainability protocol which is part of its corporative sustainable policy and to complete with the regulatory framework of the national electricity law and the concession contract granted by the regulatory agency Superintendencia General de Energía y Telecomunicaciones SIGET. The main scope of the protocol is to calculate the sustainable energy level Eo for each exploited geothermal resource. The general methodology is based in the work presented by Axelsson and the working group at ISOR (Axelsson 2001) and in order to define specific performance indicators we utilize the work of Bjarnadottir (Bjarnadottir2010) where specific indicators were suggested.

In this paper, we are presenting the main aspects of the protocol and how is being implemented at the Berlin geothermal field

SUSTANABILITY PROTOCOL

Sustainable geothermal utilization has received ever increasing attention over the decade, but the discussion has suffered from a lack of a clear definition of what it involves and from a lack of relevant policies. The word "sustainable" has in addition become quite fashionable and several authors have used it at will. A considerable amount of literature dealing with the issue has been published during the last decade.

Axelsson propose for the term "sustainable production", for each geothermal system, and for each mode of production, there exists a certain level of maximum energy production, Eo, below which it will be possible to maintain constant energy production from the system for a very long time 100-300 years (Axelsson, 2004). If the production rate is greater than Eo it cannot be maintained for this length of time. Geothermal energy production below, or equal to Eo is termed "sustainable production" while production greater than Eo is termed excessive production.

It is difficult to establish the sustainable production level Eo for a given geothermal system. This is because the production capacity of the geothermal systems is usually poorly known during exploration and the initial utilization step, as is well known. Even when considerable production experience has been acquired estimating accurately the production capacity, and hence the sustainable production, can be challenging.

In another hand, the sustainable production level of a particular geothermal resource can be expected to increase over time with increasing knowledge on the resource, i.e. through continuous exploration and monitoring. In addition it can be expected to increase through technological advances, e.g. in exploration methods, drilling technology and utilization efficiency.

Regarding with the performance indicators which serve as a gauge on how well a system is working; they also help what direction to take if there is a problem to address. In the case of geothermal sustainability indicators should be able to measure the degree of sustainability of a given operation, the progress towards sustainability and/or whether it looks like sustainable production o utilization can be maintained as proposed.

The sustainability protocol proposed by LaGeo is as follow:

1- Assess of the sustainable level Eo using volumetric stored heat assessment as was presented by Mufler & Cataldi and other authors (Mufler and Cataldi 1978, Bjorsson 2007 and Sarmiento 2007)) which should be assess using Monte Carlo method and 50 years of commercial utilization. The level of sustainable or

excessive production will be estimated together with the evolution of the indicators, due to can't be established a priori at this early stage.

2- Establish at least the follow indicators
    a. Utilization efficiency using the exergy of the whole system (field-power plant) and it should be compared with similar resource utilization.
    b. Productive lifetime is the time that the resource can sustain the present level of production which is dependent of the change on physical condition of the fluid in the resource mainly pressure drawdown and temperature changes. The lifetime is measured by numerical modeling taking into the account the present installed capacity hence total mass extraction and running the model for 50 years and to verify if it is possible to maintain certain level of steam delivered to the power plant.
    c. Recovery time or reclamation time which is the time it takes the resource in terms of pressure and temperature to recover from exploitation. It is not expected that the pressure and temperature will recover in the same timescale due to pressure and temperature diffusion behave hence the pressure will recover faster than the temperature. The recovery time is estimated through numerical modeling putting in zero the mass extraction node and running in order to recover the reservoir.
    d. Change in dissolved chemicals which are affecting by pressure and temperature change and also by inflow of injection or other cold fluids.
    e. Ground subsidence which may be a result of geothermal fluids withdrawal during the energy production. Subsidence is dependent of the pressure drawdown and geological rocks formation above the reservoir and usually is measured in specific sites by high accuracy topographic level meter.
    f. Primary energy efficiency which measure how much primary energy extracted is converted to electricity.
    g. Power plant performance indicator: Load and capacity, availability, parasitic load, vacuum pressure at the condenser and Non Condensable Gases.

THE BERLIN GEOTHERMAL FIELD

The Berlin geothermal field is located 110 km towards to the East of the El Salvador country where the Tecapa volcanic complex is located. The field went to commercial operation in 1992 with 2x5 MW back pressure units. Later on during 1999 went on line 2x28 MW condensing type units, 2006 went 1x44 MW and finally in 2007 went on line the 9.2 MW binary bottoming unit to complete the 109.2 MW present installed capacity.

The Figure 1 shows the well and power plant location

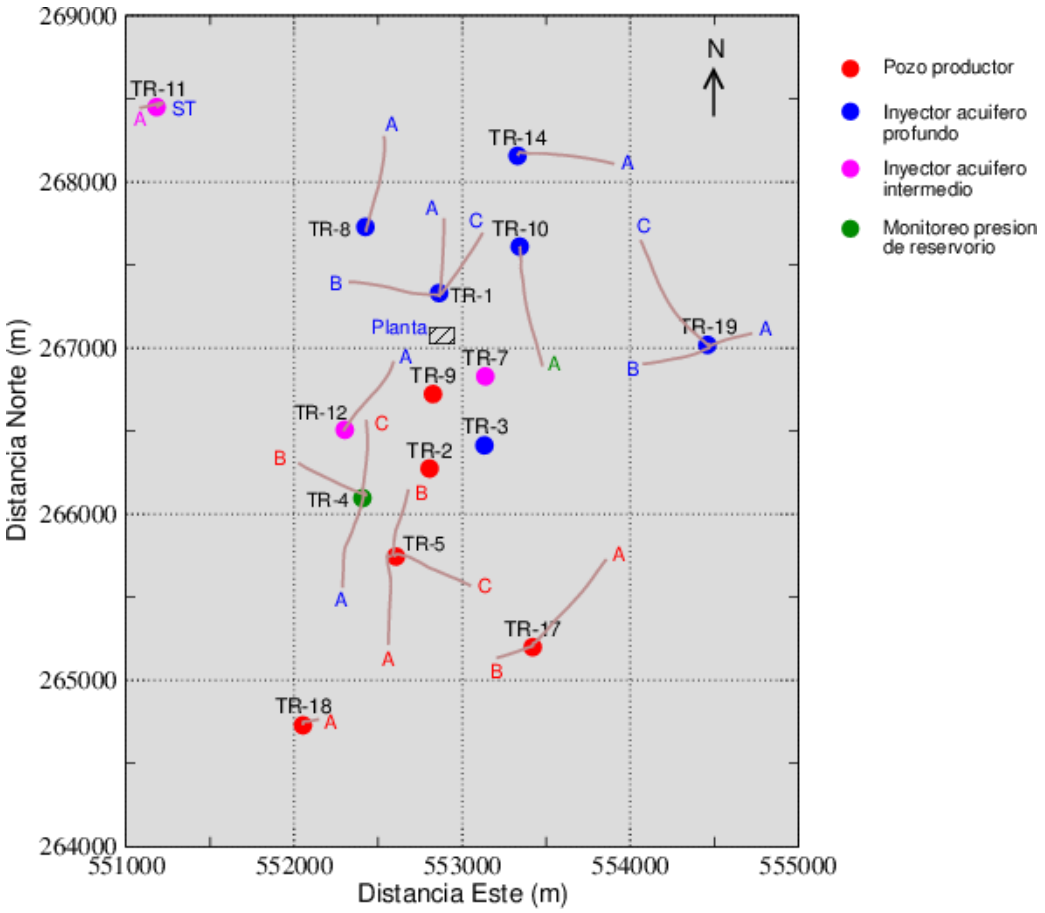

Figure 1, The well location at the Berlin geothermal field

At present, 38 wells were drilling at the Berlin field, 14 of them are producers and 20 injectors (4 are abandoned). The Figure 2 presents the total mass extracted which ranges 870 kg/s, the steam delivered to the power plant is approximately 220 kg/s and the injected brine is 650 kg/s which is partially injected using high pressure pumping system located al TR-1 site.

The total pressure drawdown is approximately 18 bar however over the last 12 years is being reduced to less 10 bar, the discharging enthalpy is fairly constant in most of producer wells and no evidence of cooling due to injection has been observed into the field however some boiling is perhaps the main process affecting the reservoir.

Some aspects affecting the sustainable production are related to calcite in well TR-18, steam cap declining at southern part of the steam field, high concentration of NCG at TR-18A and silica plugging at injection wells and pipe line in special those connected to binary unit. As part of field maintenance there are undertaken several activities to reduce the impact in this issues

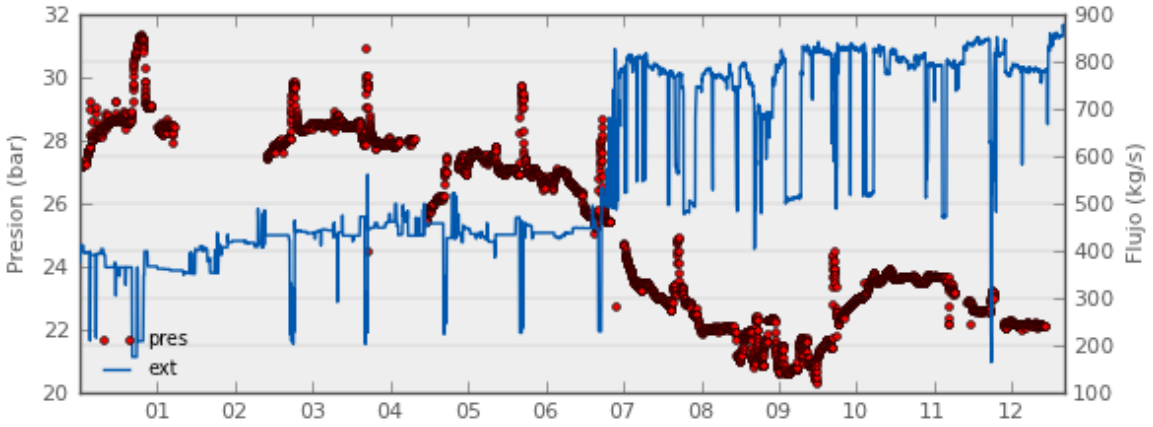

Figure 2: Pressure and mass extraction at the Berlin field

SUSTAINABILITY ANALISYS.

According with the methodology describe before, the first parameter to be calculated is the level of sustainable production Eo which was did by volumetric "stored heat" and Monte Carlo probabilistic estimation performed with Cristal Ball. The main parameters for the calculations are presented in the Table 1.

Table 1: Volumetric estimation for the Berlin field

	Parametros de entrada	Simbolo	Unidades	Distribucion	Probado Minimo	Probable Most likely	Posible
1	Porosidad	Φ	%	Triangular	20	15	5
2	Area del recurso	A	km2	Triangular	5.5	14.2	40
3	Espesor	H	m	Triangular	2100	2500	3138
4	Densidad roca	σ	kg/m3	Constante	2600		
5	Capacidad calorifica roca	Cr	kJ/kgoC	Constante	0.85		
6	Temperatura reservorio	Tr	oC	Triangular	260	290	300
7	Temperatura referencia	Ts	oC	Constante	40		
8	Densidad agua a condicion de reservorio	σ	kg/m3	Constante	900		
9	Entalpia agua a condicion de reservorio	hr	kJ/kg	Triangular	1100	1200	1350
10	Entalpia a temperatura referencia o sumidero	hs	kJ/kg	Constante	167.7		
11	Factor de recuperacion	Fr	%	Constante	20		
12	Eficiencia conversion	η	%	Constante	11		
13	Periodo de vida	T	Años	Constante	50		
14	Factor de planta	Lf	%	Constante	95		
15	Factor de conversion						

The results indicate the level of sustainable production Eo for the Berlin geothermal field could be between 235-240 MW over a period of 50 years of commercial operation and considering the percentile 90% as shown in Figure 3

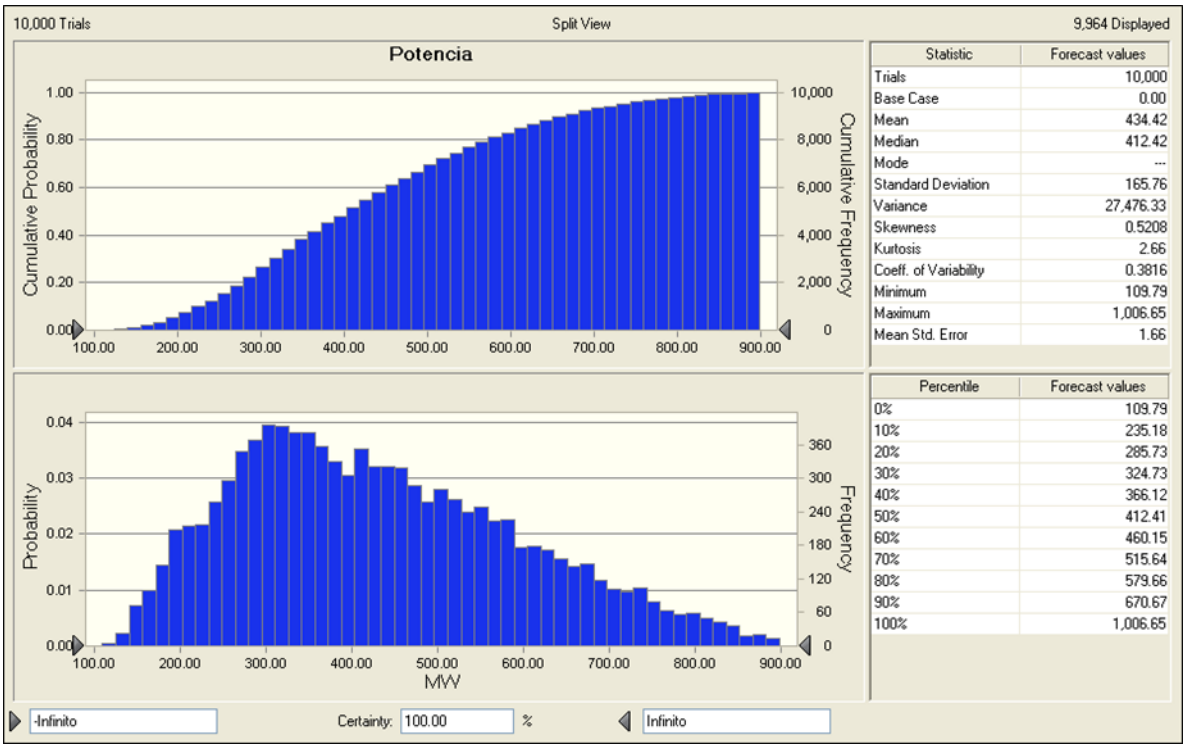

Figure 3. Estimation of sustainable energy production at the Berlin field

The present installed capacity at the field is 109 MW and the level of sustainable energy production is 235 MW therefore the operational level could be considered as sustainable.

The first performance indicator presented in this work is the Utilization Efficiency estimated by exergy. The Figure 4 presents a bench marking over 20 geothermal power plant efficiency around the world, as observed the Berlin plant is over the average.

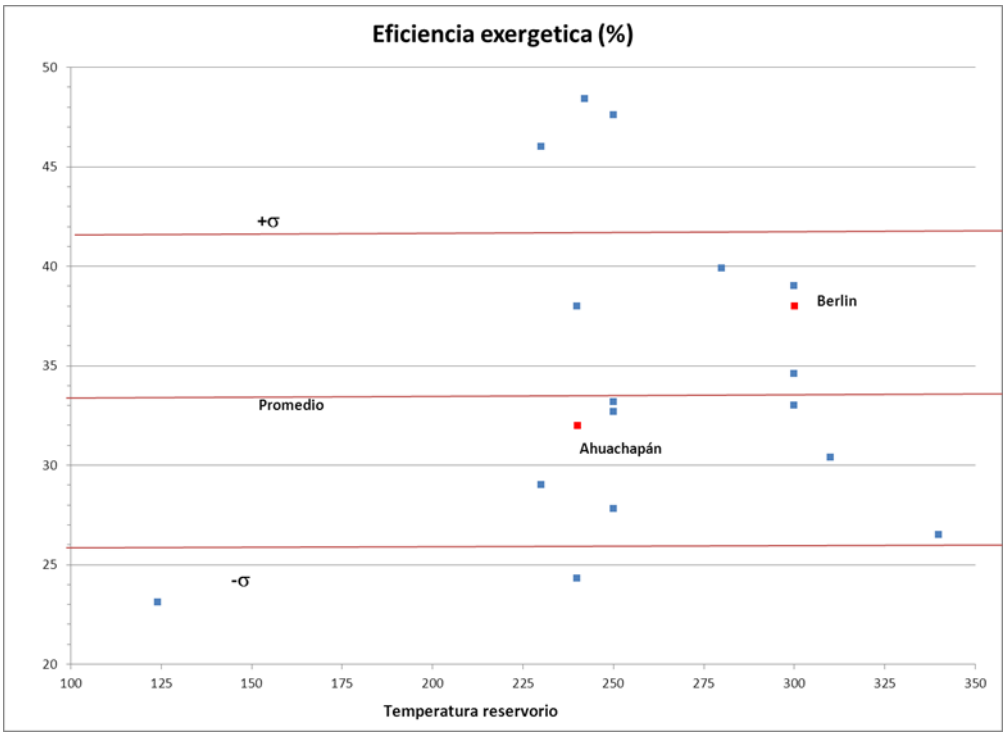

Figure 4: Exergy efficiency of power plants around the world

The second and third indicators are based in numerical modeling which is a powerful tool to estimate the Productive Lifetime and the Recovery Time: Firstly a good enough calibrated model must be available, the standard code used by LaGEO is TOUGHII and iTOUGHII which are running in Linux operative system, beside this, the natural state and production models are also utilized during the adjusting process and finally is utilized a coupled model (wellflow model coupled with reservoir models).

For the Productive Lifetime indicators the resource is considered as source of steam delivered to power plants without any make up wells therefore it is steam declining the main issue to be considered, for this reason the well flow model is considering with constant well head pressure (as being utilized at present time). The mass delivered by the wells is decreasing until a practical limit could reach. The limit is the steam required to operate at least one unit 28 MW (50 kg/s steam which mean 200 kg/s total mass at 0.25 dryness).

The results are shown in Figure 5, the mass flow rate is declining around 2.5 kg/s/year thus the simulation suggests it is possible to operate the geothermal field for at least 50 years with at least one power unit, considering this condition as productive lifetime.

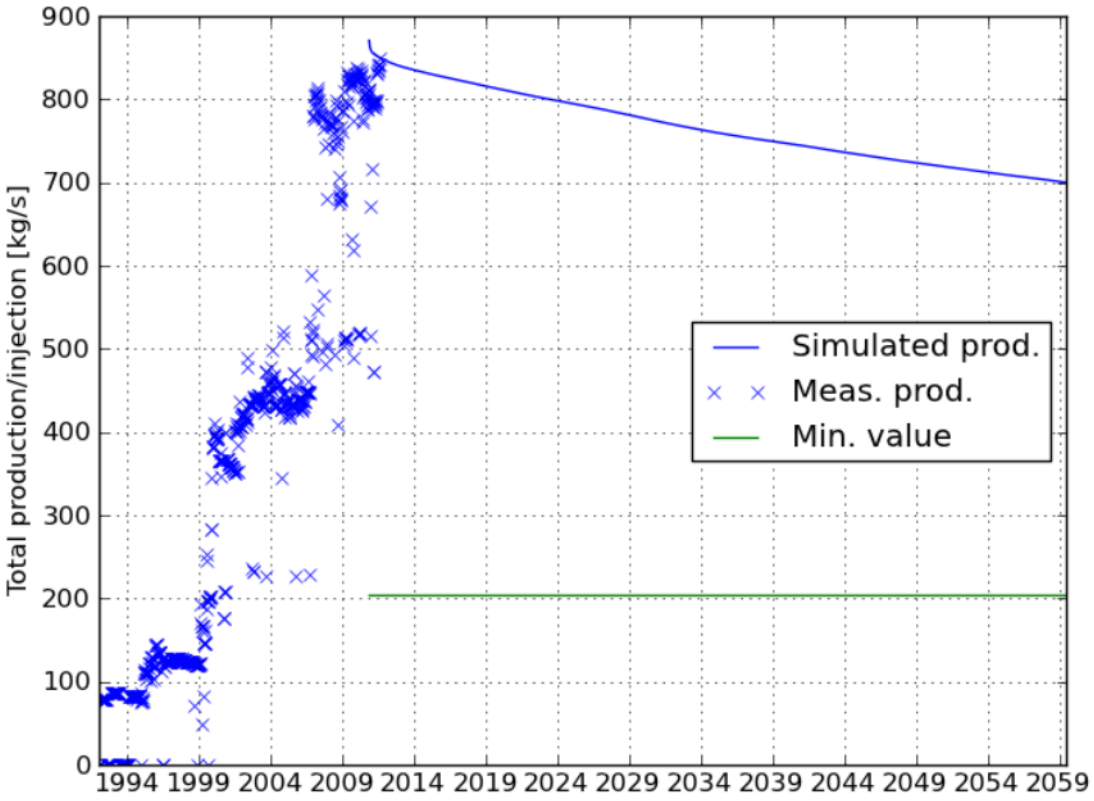

Figure 5. Productive life time Indicator of the Berlin Geothermal Field

In order to estimate the Recovery time indicator, in the numerical model, the sinks and source nodes are eliminated (mass=zero) therefore no mass and energy are delivered or injected after the thermal and hydraulic recovery began. The results are shown in the Figure 6, as observed the pressure at monitoring well is suddenly increasing until reach similar initial pressure after 33 years of recovery, therefore the utilization of the geothermal resource is recovered in short term period however it is not the case of temperature which will require more time.

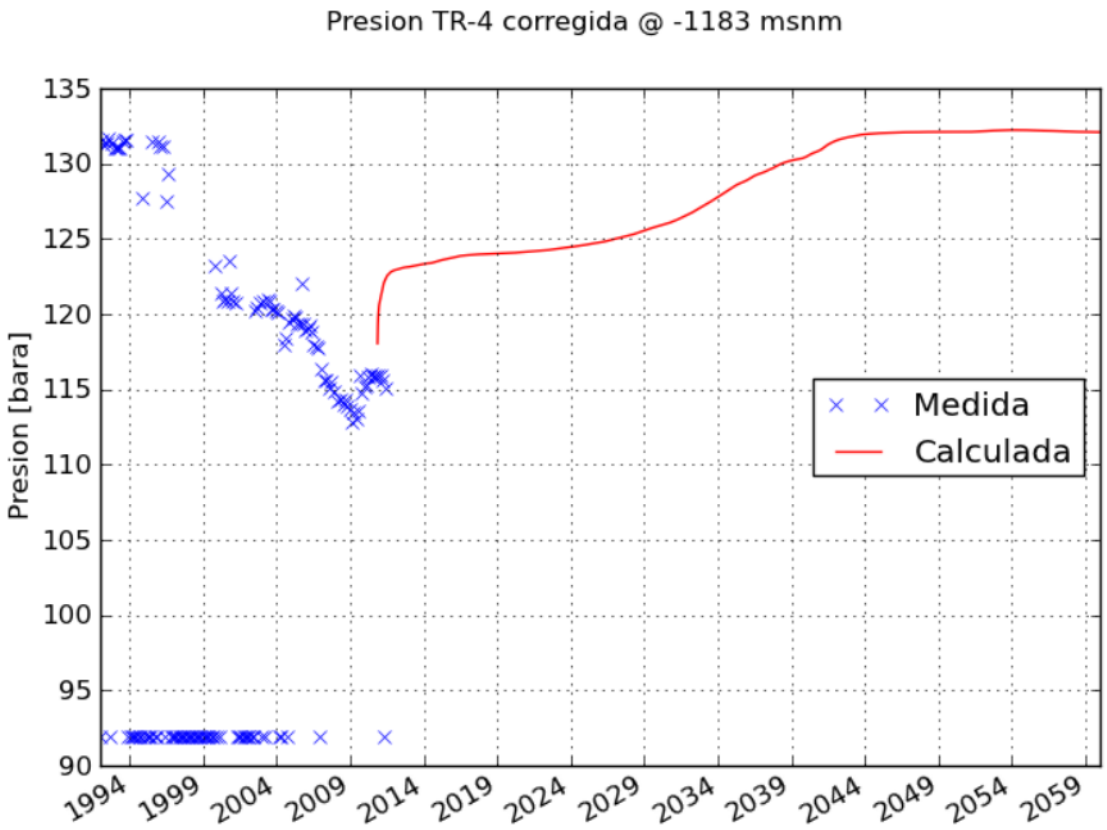

CONCLUSIONS

1- The Berlin geothermal field is being in commercial operation for at least 20 years during this period no evidence of irreversible conditions has been observed to the whole productive field. Spite of LaGeo is focused to develop a more complete sustainable utilization to guarantee a stable condition for at least 50 years of operation.

2- The preliminary results indicate it is possible to do an analysis on the sustainability for the Berlin Geothermal field which suggests the utilization of the resource is doing in a sustainable way.

3- The numerical modeling is being utilized as powerful tools to estimate the sustainable operation indicators.

Acknowledgement

The author would like to acknowledge travel support to the SIMS Conference provided by the International Energy Agency's Geothermal Implementing Agreement (IEA-GIA).

REFERENCES

Axelsson, Gudmudsson, Palmasson, Steimgrimsson, 2001. Sustainable production of geothermal energy, suggested definition, IGA News, Quaterly No.43.

Axelsson, Bjornsson, Stefansson, 2004. Sustainable utilization of geothermal resource for 100-300 years. Proceeding of twenty ninth workshop on reservoir engineering, Stanford University.

Bjarnadottir, R, 2010. Sustainability evaluation of geothermal system in Iceland- Indicators for sustainable production, MSc thesis, Scholl of Engineering and Natural Science , University of Iceland.

Muffler P, Cataldi R., 1978. Method for regional assessment of geothermal resource. Geothermics vol 7, Pergamon Press Ltd

Bjornsson G, Sarmiento Z. 2007. Geothermal resource assessment- Volumetric reserves estimation and numerical modeling. UNU GTP Short course on Geothermal development in Central America

Sarmiento Z., Steimgrimsson B. 2007. Computer programme for resource assessment and risk evaluation using Monte Carlo simulation. UNU GTP Short course on Geothermal development in Central America

Towards A Parallel Distributed Equation-Based Simulation Environment

Robert Braun[1] and Petter Krus[1]

Linköping University, Division of Fluid and Mechatronic Systems, SE-58183 Linkping, Sweden

Abstract. Distributed solvers provide several benefits, such as linear scalability and good numerical robustness. By separating components with transmission line elements, simulations can be run in parallel on multi-core processors. At the same time, equation-based modelling offers an intuitive way of writing models. This paper presents an algorithm for generating distributed models from Modelica code using bilinear transform. This also enables hard limitations on variables and their derivatives. The generated Jacobian is linearised and solved using LU-decomposition. The algorithm is implemented in the Hopsan simulation tool. Equations are transformed and differentiated by using the SymPy package for symbolic mathematics. An example model is created and verified against a reference model. Simulation results are similar, but the equation-based model is four to five times slower. Further optimisation of the algorithm is thus required. The future aim is to develop a distributed simulation environment with integrated support for equation-based modelling.

Keywords: model generation, equation-based modelling, distributed solvers, symbolic expressions, numerical solvers

1 Introduction

As products are becoming more complex, the importance of large-scale and multi-disciplinary system simulation is constantly increasing. The use of new powerful product development methods, such as numerical optimization, real-time simulations and hardware-in-the-loop has greatly increased the need for high-performance simulations.

State-of-the-art environments in modern system simulations use equation-based object-oriented (EOO) modelling together with centralized solver algorithms. The equation-based approach offers a very intuitive way for users to write models. Centralized solvers, however, suffer from poor scalability, which means that execution time grows more than linearly with the model size, and are naturally difficult to parallelise for multi-core processors. There are also difficulties in splitting up models for co-simulation or hardware-in-the-loop simulations. Furthermore, fault tracing in an erroneous model is often difficult.

This paper proposes the use of distributed solvers in combination with equation based modelling. Having one small Jacobian matrix for each sub-component

offers nearly-linear scalability. Figure 1 shows an overview of the basic idea. With the use of transmission line element modelling, components can be numerically isolated from one another. This guarantees numerical stability and makes models inherently parallel, and thereby suitable for taking advantage of multi-core processors [1]. Distributed solver simulations can also be seen as a sort of natural co-simulation, making them very suitable for interaction between different simulation tools. A possible drawback with the transmission line element method is that wave propagation phenomena are affected by the size of the time step. If wave propagation is of importance, fixed-size time steps are therefore to be preferred. Experiments using variable time steps with distributed solvers was performed by [2], but the gains was found to be very small. On the other hand, the use of distributed solvers makes it possible to use smaller time steps in certain parts of the model, where a higher resolution is required. Time steps can thus be varied in model space rather than in time space.

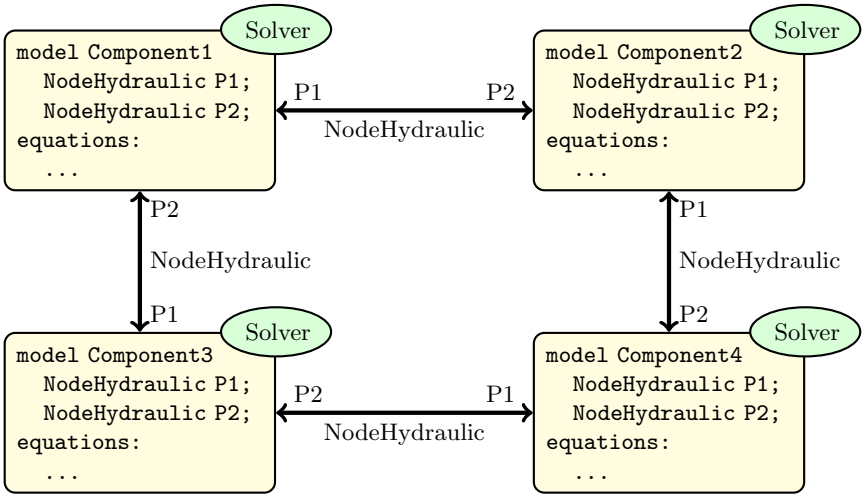

Fig. 1. This paper proposes the use of equation-based modelling in a distributed solver environment. Distributed solvers can provide linear scalability, good numerical properties and natural parallelism.

Distributed simulation environments exist, but they lack built-in support for equation-based modelling. The Hopsan simulation package described in this paper uses pre-compiled libraries written in plain C++ code. Previous attempts to introduce equation-based modelling manually using Mathematica have been successful [3]. This has in turn been used to generate models from Modelica by transforming them to Mathematica syntax [4]. It does, however, require the use of external proprietary tools which cannot be embedded in the simulation tool. Experiments have also been made by going the other way around and intro-

ducing transmission line element models in existing Modelica tools [5][6]. The advantage of implementing equation-based modelling in an existing distributed environment is that already existing features, such as connectors, delays, utility functions and parallel algorithms, can be used directly.

An alternative solution could be to import equation-based models from the Functional Mock-up Interface (FMI), an open standard for interfacing between simulation environments. This is currently being implemented in the Hopsan simulation tool [7]. It is, however, a more cumbersome and likely slower solution, more suitable for importing large models already created in another simulation tool.

2 Transmission Line Element Method

Distributed solvers provide great advantages for performance and numerical properties [8]. Splitting up a model does, however, introduce time delays between sub-models, which affects the mathematical correctness. It is therefore desirable to use a modelling approach where these delays can be physically motivated. This is possible because of the fact that information propagation never happens infinitely fast in a physical system. One such approach is the transmission line element method (TLM). Most physical system models can be rearranged to consist of resistive and capacitive subcomponents. With TLM modelling, each capacitive component in the model is replaced by a transmission line element with a characteristic impedance. The method is related to the method of characteristics [9] and to transmission line modelling as described in [10].

In fluid power systems the capacitive components are represented by pipes (or volumes). These would equal springs in mechanical systems or capacitors in electrical systems. Consider a pipe with time delay ΔT, see figure 2. Each side has two state variables, pressure (p) and flow (q).

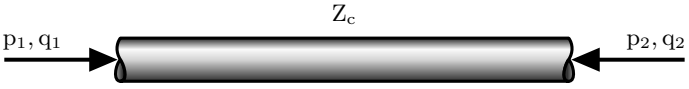

Fig. 2. Transmission line elements are used to numerically isolate different parts of a model from each other. Each part can then be solved independently from the rest of the model.

At a given time t the pressure at one end of the pipe is a function of the characteristic impedance Z_c, the flow at this end at time t, and the flow and pressure at the other end at time $t - \Delta T$, see equations 1 and 2. This can be derived from the four-pole equation [11].

$$p_1(t) = Z_c[q_1(t) + q_2(t - \Delta T)] + p_2(t - \Delta T) \tag{1}$$

$$p_2(t) = Z_c[q_2(t) + q_1(t - \Delta T)] + p_1(t - \Delta T) \tag{2}$$

For simplicity, these equations can be decoupled by introducing a wave variable (c), representing the information travelling from one end to the other at time ΔT:

$$c_1(t) = Z_c q_2(t - \Delta T) + p_2(t - \Delta T) \tag{3}$$

$$c_2(t) = Z_c q_1(t - \Delta T) + p_1(t - \Delta T) \tag{4}$$

This yields the decoupled transmission line equations. These are used as boundary equations in the resistive components:

$$p_1(t) = Z_c q_1(t) + c_1(t) \tag{5}$$

$$p_2(t) = Z_c q_2(t) + c_2(t) \tag{6}$$

In a hydraulic system model, this is implemented by letting the capacitive components calculate c and Z_c from pressure and flow. The resistive components then read c and Zc, apply the boundary equations to calculate pressures, and then in turn use the pressures to calculate flows.

3 Model Generation Algorithm

To solve an equation system, it is necessary to generate a symbolic Jacobian matrix, together with vectors of state variables and system equations. The first step is to parse a Modelica file, containing a model object with connectors, algorithms, equations, variables and parameters. Connectors are hard-typed and the actual connection must be handled by the target simulation environment. Variable limitations specified by the user must also be taken into account. There are two important criteria for the equation system to be solvable. First, the number of equations must equal the number of variables. Second, the resulting Jacobian matrix must not be singular. Verifying the first condition is obviously trivial. Solving the dynamic parts of the system can be done by using the trapezoidal rule, see equation 7. A more effective way of using this is to use bilinear transform, see equation 8. This transforms the equations from continuous to discrete-time by replacing all Laplace operators with a function of the delay operator (z), see figure 4.

$$x(t + h) = x(t) + \frac{1}{2}h(x(t) + x(h + t)) \tag{7}$$

$$F_d(z) = F_a(s)\Big|_{s=\frac{2}{T}\frac{z-1}{z+1}} = F_a\left(\frac{2}{T}\frac{z-1}{z+1}\right) \tag{8}$$

An important aspect in models of non-linear systems is variable limitations. Certain variables are for physical reasons not allowed to be smaller than or larger than specified limits. It is often also necessary to explicitly set the derivatives of the variable to zero when exceeding the limits. In a fixed-step environment with distributed solvers it is not practical to rely on event handling for restarting the solvers when a variable exceeds its limitation. Instead, all limitations must be inserted directly into the transformed equations. Two special functions are used to specify limitations, `VarLimit()` and `VarDerLimit()`, which limit only the variable, or the variable together with the derivative, respectively. In the current implementation, the call to the limitation function must be written directly after the equation(s) defining the variable (and derivative) to be limited. It would be desirable that these equations can be identified automatically by the parser, but for time reasons this has not been included in this paper.

The use of bilinear transform makes it possible to explicitly factor out a given variable from an equation. This allows limit functions to be inserted around the remaining part of the equation. First consider equation 9. This equation gives a relationship between a position x and an external force f. First, the position variable is factored out symbolically as in equation 10. Finally, a `limit()` function is inserted around the remaining part of the equation, effectively limiting the variable x, see equation 11.

$$\mathrm{F}_1(x, f) = 0 \tag{9}$$

$$x - \mathrm{F}_1(f) = 0 \tag{10}$$

$$x - \mathrm{limit}(\mathrm{F}_1(f), x_{min}, x_{max}) = 0 \tag{11}$$

The limitation of derivatives are performed in a similar way. Equation 12 defines the velocity v as a function of the position and the force. The velocity variable is factored out (equation 13), and a function called `dxLimit()` is inserted before the remaining part of the equation (14). This function returns one if the position variable is within limits, otherwise zero. The limitation functions `limit()` and `dxLimit()` are shown in figure 3. The derivative of `limit()` is `dxLimit()`, and the derivative of `dxLimit()` is zero.

$$\mathrm{F}_2(v, x, f) = 0 \tag{12}$$

$$v - \mathrm{F}_2(x, f) = 0 \tag{13}$$

$$v - \mathrm{dxLimit}(x, x_{min}, x_{max})\mathrm{F}_2(x, f) = 0 \tag{14}$$

It is important that the generated equations are simplified as much as possible. Having longer equations than necessary means that the generated code will take longer to evaluate each time step, resulting in a slower model. Furthermore, it is important that equations are simplified in the correct way. It is for example

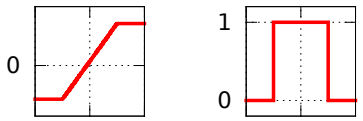

(a) limit() (b) dxLimit()

Fig. 3. Two limitation functions can be inserted into the transformed equations, one that limits a variable, and one that limits the derivative of a variable.

desirable that all delay operators are factored together. Having too many delayed variables will otherwise become a bottleneck. Too many power operators, including square roots, will likely also reduce performance.

The next step is to generate a Jacobian matrix. This is done by analytically differentiating each equation with respect to each state variable. As a consequence of the fact that users are allowed to write equations in arbitrary order, it is possible that the Jacobian matrix will become singular. When solving an equation system in matrix form, however, inverting the Jacobian matrix will be inevitable. A singular matrix thus makes the system unsolvable and must be avoided. One way to guarantee this is to ensure that no element on the diagonal are zero. This can be achieved by ensuring all diagonal elements are constants. With this method, the matrix will always be invertible regardless of the working point. This is possible for most physical equation systems. A weaker requirement is that all diagonal elements must at least be analytically different from zero. In this case, the Jacobian may become singular, but only for certain values of the state variables.

Once a non-singular Jacobian has been generated, any fixed-step numerical solver can be used. In this paper, an iterative Newton-Rhapson solver is used, see equation 15. In most cases one iteration is sufficient, but more iterations may be required in models with strong non-linearities.

$$x_{k+1} = x_k(t) - J_k(t)^{-1} G(x_k(t)) \tag{15}$$

Inverting the Jacobian matrix each time step is a time-consuming solution. A more efficient method is to use LU-decomposition, a matrix form of Gaussian elimination [12]. The Jacobian is first decomposed to a product of an upper matrix, which only has elements above the diagonal, and one lower that only has elements on or below the diagonal: $Jx = b \Leftrightarrow LUx = b$. Then the system $Ly = b$ is solved for y, which in turn is used to solve $Ux = y$ for x. This algorithm can also easily be re-written for parallel execution [13]. In this paper, parallelism was, however, implemented in model space rather than using parallel algorithms.

The full procedure for generating and simulating equation-based models are shown in figure 4.

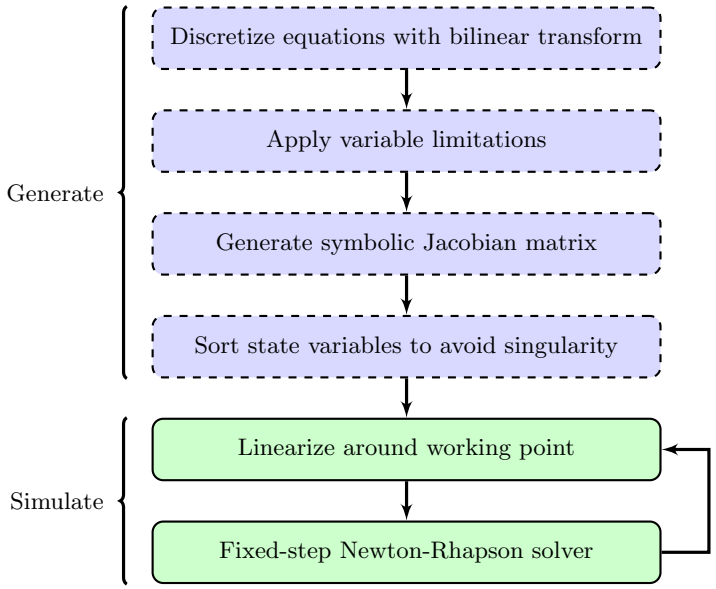

Fig. 4. Bilinear transform is used to convert equations to discrete form. This makes it possible to apply variable limitations before generating the symbolic Jacobian. Equations are solved using distributed fixed-step solvers.

4 Implementation

The algorithm described in this paper was implemented in Hopsan, a cross-platform distributed simulation environment developed at Linköping University [14][7]. The application is fully object-oriented and uses pre-compiled component libraries. No compilation is thus required during runtime. The simulation core is separated from the graphical interface, making it suitable for both desktop and embedded applications [15]. It has built-in support for multi-threaded simulations, which uses the time independences introduced by the transmission line element method [1].

Converting equations to plain code requires symbolic computations. SymPy is a free Python library for symbolic computations, providing objects for symbols, functions and expressions. It is capable of all necessary operations such as replacing symbols, simplifications, factorization and differentiation [16][17]. The choice fell on SymPy mainly due to the fact that Hopsan has a built-in Python console, making a Python library ideal for early experimenting.

Due to the use of distributed solvers, only a subset of the Modelica language can be used. Most importantly, all connectors are hard-coded to match the Hopsan node types. An example of a hydraulic node connector is shown in listing 1.1. This is necessary because all connections are handled by the simulation core. Custom connectors are, therefore, not allowed. Other Modelica

features that contradict the distributed modelling approach, such as the `inner` and `outer` keywords, are also not allowed. Another reduction is imposed by the use of fixed-step solvers. This practically eliminates the need for event handling, which is thus not supported. Sub-classing and functions are also not supported, although this could easily be implemented in the future. Algorithm sections are allowed, but only once before and once after the equation section in each model. Nested algorithm sections are not allowed due to the limitation of only one Jacobian matrix in each component. There are, however, no technical difficulties in introducing this in the future. The standard Modelica library contains many built-in intrinsic mathematical functions [18], most of which are supported. A list of supported functions are shown in table 4.

sin	atan2	exp	div
cos	sinh	log	rem
tan	cosh	log10	mod
asin	tanh	sign	floor
acos	abs	integer	ceil
atan	sqrt	der	

Table 1. These Modelica functions are supported by the implementation of the model generation algorithm.

```
connector NodeHydraulic "Hydraulic Node"
   Real      p "Pressure";
   Real      q "Flow";
   Real      c "Wave Variable";
   Real      Zc "Characteristic Impedance";
end NodeHydraulic;
```

Listing 1.1. Connectors must be hard-typed to match the Hopsan node types. This code shows a hydraulic node connector in Modelica syntax.

Equations can either be written directly in the graphical interface in Hopsan or loaded from an external Modelica file. The generator utility function parses the equation, verifies the syntax and the number of unknowns and replaces any reserved words with temporary strings.

Lists with all equations, variables, state variables and parameters are created. These are in turn used to define symbols, functions and expressions in SymPy. The equations are transformed to discrete form. After this, the variable limits are applied using the `factor()` and `subs()` SymPy functions for factorization and variable substitution. The Jacobian matrix is created by differentiating the equations using the `diff()` SymPy function. The equations are then returned to Hopsan and translated from Python to C++ syntax. Unit delays in the equations are replaced by Hopsan delay methods ($z^{-n}x = \text{mDelay}(x, n)$). All integer

variables are also converted to decimal numbers to ensure precision and avoid phenomena such as "$1/2 = 0$".

The next step is to ensure that the resulting Jacobian matrix is not singular. This is performed by a bubble-sort algorithm that attempts to arrange system equations so that they include their corresponding state variable. If this fails, the generation is aborted because the system is not solvable. The performance of this sorting could be improved by a more sophisticated algorithm, but this was not considered necessary as the required time was very small compared to the rest of the process. If everything was successful, the Jacobian is converted to C++ source code together with a fixed step Newton-Rhapson using LU-decomposition, which is in turn compiled to a Hopsan component. The symbolic Jacobian is also displayed in a dialogue to the user.

5 Example: Hydraulic Pressure Relief Valve

As a demonstration of the method, a model of a hydraulic pressure relief valve is presented. This problem is interesting because it contains several difficult modelling phenomena, such as second order dynamics, variable limitations and a non-linear flow function. A relief valve consists of a cone attached to a spring. When pressure on the high-pressure side overcomes the pre-tension of the spring, the cone will move, allowing oil to flow to the low-pressure side, see figure 5.

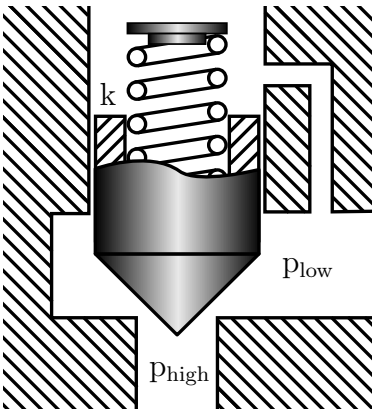

Fig. 5. A pressure relief valve consists of a spring-loaded cone. It will open when the force from the high-pressure side exceeds the pre-load of the spring.

The cone is modelled as an inertia with damping and end of stroke limitations. It is subjected to a spring force, a spring pre-load and the forces from the low and high oil pressure, see equation 16. The flow is a function of the square root

of the pressure difference. Square roots, however, are undefined for numbers that are smaller than or equal to zero. For this reason, a sign function is used. An overlapping is also introduced to avoid the non-linearity at zero, see equation 17. Normally, a model of a hydraulic valve should take cavitation (zero pressure) into account. For time and space reasons, this has been left out in this example.

$$M_v\ddot{x}_v + B_v\dot{x}_v + k_e x_v = (p_1 - p_2 - p_{ref})A_v \tag{16}$$

$$q = C_q A\sqrt{\frac{2}{\rho}(p_1 - p_2)} \tag{17}$$

The Modelica code is shown in listing 1.2. An annotation is added that tells Hopsan that this is a Q-type component (see section 2). Two hydraulic connectors and two signal connectors are then added; the latter are used to show cone position and cone velocity for debugging purposes. Parameters are specified in standard Modelica syntax with type, name, unit, default value and description. Four local variables are also used. These are assigned in the algorithm section, before the equations. Moving explicit expressions from equations to algorithms like this can greatly improve simulation performance. In the equation section, the `Variable2Limits` function is written among the other equations. The two equations above must define the variable and the derivative to be limited. The limit equation will not be included in the system equations later on; it will be removed once the limitation is applied. The resulting Jacobian matrix and system equations are shown in equation 18.

$$\begin{bmatrix} 1 & 0 & 0 & 0 & \mathrm{f}(p_1,p_2) & \mathrm{f}(p_1,p_2) \\ \mathrm{f}(p_1,p_2,x_v) & 1 & 0 & 0 & \mathrm{f}(x_v) & \mathrm{f}(x_v) \\ \mathrm{f}(p_1,p_2) & 0 & 1 & 0 & \mathrm{f}(p_1,p_2,x_v) & \mathrm{f}(p_1,p_2,x_v) \\ 0 & 0 & 1 & 1 & 0 & 0 \\ 0 & 0 & 0 & -Z_{c1} & 1 & 0 \\ 0 & 0 & -Z_{c1} & 0 & 0 & 1 \end{bmatrix} \begin{bmatrix} x_v \\ d_{xv} \\ q_2 \\ q_1 \\ p_1 \\ p_2 \end{bmatrix} = \begin{bmatrix} \mathrm{f}(p_1,p_2,q_2,x_v) \\ \mathrm{f}(d_{xv},p_1,p_2,x_v) \\ \mathrm{f}(d_{xv},x_v) \\ \mathrm{f}(q_1,q_2) \\ \mathrm{f}(p_1,q_1) \\ \mathrm{f}(p_2,q_2) \end{bmatrix} \tag{18}$$

The example model was verified against an existing model of a relief valve written in plain code. For this, an example model consisting of a volume provided with constant flow, connected to a pressure relief valve and an orifice was used, see figure 6. The size of the orifice is reduced by a step function after 0.3 seconds to test the dynamics of the relief valve. All components in the test system model were created from Modelica equations and compared to a reference system model where all components were written in plain code. The resulting pressure in the volume in the two models are shown in figures 7 and 8.

Simulation performance was investigated by running 10^6 iterations and measuring simulation time. The model generated from Modelica had an average of 2379 ms while the reference model was notably faster, with an average of 454 ms. Enabling the multi-core support in Hopsan on a dual-core computer reduced simulation time for the generated model to 1696 ms. The reference model

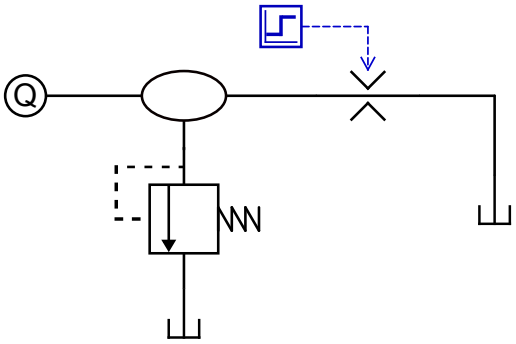

Fig. 6. A system model consisting of a pressure relief valve connected to a volume with a flow source and an outlet orifice was used for validation.

performed less well with parallel simulations, due to overhead time costs. Comparing the smallest average time for both models, the Modelica model was 4.535 times slower than the reference model. A fair comparison with another simulation tool is not possible because Hopsan is the only tool with support for TLM with correct time delays. In the test run, only one iteration was used in the solvers. This was sufficient to give accurate results when using the same time step as the reference model.

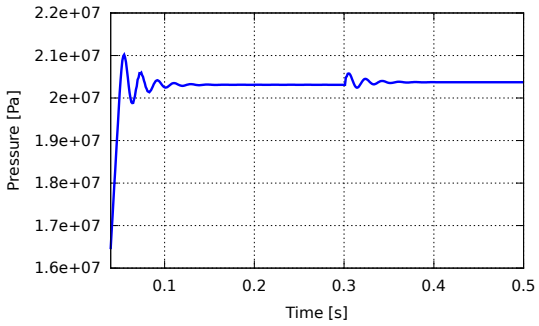

Fig. 7. When the pressure relief valve reaches its reference value it will have some oscillations due to the mass-spring dynamics and a disturbance after .3 seconds.

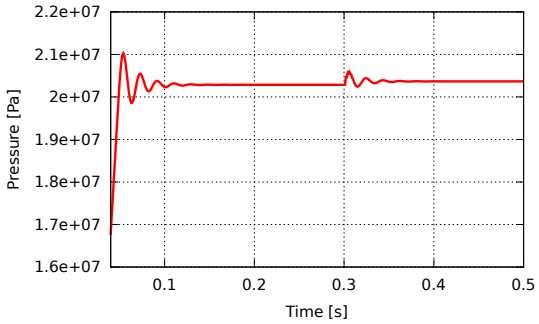

Fig. 8. The generated model show no differences in simulation results compared to the reference model.

```
model MyPressureReliefValve "My Hydraulic Pressure Relief Valve"
  annotation(hopsanCqsType = "Q");

  NodeHydraulic P1, P2;
  NodeSignalOut xv, dxv;

  parameter Real rho(unit="kg/m^3")=870 "Oil Density";
  parameter Real visc(unit=Ns/m^2"")=0.03 "Dynamic Viscosity";
  parameter Real Dv(unit="m")=0.03 "Spool Diameter";
  parameter Real Bv(unit="N/(m*s)")=0.03 "Damping Coefficient";
  parameter Real Mv(unit="kg")=0.03 "Spool Mass";
  parameter Real Xvmax(unit="m")=0.03 "Maximum Spool Displacement";
  parameter Real Cq(unit="-")=0.67 "Pressure-Flow Coefficient";
  parameter Real phi(unit="rad")=0.01 "Stream Angle";
  parameter Real ks(unit="N/m")=100 "Spring Constant";
  parameter Real p0(unit="Pa")=1e5 "Pressure For Turbulent Flow";
  parameter Real pref(unit="Pa")=2e7 "Reference Opening Pressure";

  Real Av "Valve Cross Section Area";
  Real w "Area Gradient";
  Real kf "Flow Force Spring Constant";
  Real ke "Total Effective Spring Constant";

algorithm
  Av := 3.1415*Dv**2/4;
  w  := 3.1415*Dv*sin(phi);
  kf := 2*Cq*w*cos(phi)*(p1-p2);
  ke := ks+kf;

equation
  Mv*der(der(xv.out))+Bv*der(xv.out)+ke*xv.out = (P1.p-P2.p-pref)*Av;
  Mv*der(dxv.out)+Bv*dxv.out+ke*xv.out = (P1.p-P2.p-pref)*Av;
  VarDerLimit(xv.out, dxv.out, 0, Xvmax);
  P2.q = xv.out*Cq*w*sqrt(2/rho)*(sqrt(p0+abs(P1.p-P2.p))-sqrt(p0))*sign(P1.p-P2.p);
  P1.q = -P2.q;
  P1.p = P1.c+P1.Zc*P1.q;
  P2.p = P2.c+P2.Zc*P2.q;

end MyPressureReliefValve;
```

Listing 1.2. A hydraulic pressure relief valve was modelled in Modelica. A special variable limitation function was introduced.

6 Conclusions

A distributed solver approach provides good numerical properties and is suitable for running parallel simulations. This paper presents a method for generating components for a distributed solver simulation tool using the Modelica language. A solution for efficiently implementing variable limitations, including their derivatives, is also described. Finally, the method is demonstrated by generating a dynamic model and comparing it to a reference model written in plain C++ code.

Results show that the method is applicable. Experimental results show no fundamental differences in simulation results compared to a reference model. The generated model is, however, substantially slower than the reference model. This was expected since equation-based models require the solvers to do more work than in a manually coded model, where equations to a large extent can be solved beforehand. Optimizing simulation performance further is, however, still desirable, especially if models are to be used in real-time applications. Possible speed-ups could be achieved from performing the LU decomposition analytically before generating the components, instead of numerically each time step. Further simplification of the equations may also be possible, as well as optimizing the generated code and the solver.

The model generation in itself was quite slow, due to the use of a Python package. Some symbolic operations in SymPy are also not implemented for special cases, and therefore not fully reliable. A great improvement would be to use a C++ library for symbolic computations instead. Using the Modelica parser and rewriting it for distributed solvers could also be an option.

One of the most important advantages of using equation-based modeling with distributed solvers is scalability. The time required for solving an equation system numerically increases super-linearly to the number of equations, making centralized solvers slow for large models. With distributed modeling, the equation system is naturally decomposed into one small system for each component, which can greatly reduce simulation time.

7 Acknowledgements

This work was supported by ProViking research school and the Swedish Foundation for Strategic Research (SSF).

References

[1] R. Braun, P. Nordin, B. Eriksson, and P. Krus. High Performance System Simulation Using Multiple Processor Cores. In *The Twelfth Scandinavian International Conference On Fluid Power*, Tampere, Finland, May 2011.

[2] A. Jansson, P. Krus, and J-O Palmberg. Variable time step size applied to simulation of fluid power systems using transmission line elements. In *Fifth Bath International Fluid Power Workshop*, Bath, England, 1992.

[3] Petter Krus. An automated approach for creating component and subsystem models for simulation of distributed systems. In *Proceeedings of the Nineth Bath International Fluid Power Workshop*, Bath, England, 1996.

[4] B. Johansson and P. Krus. Modelica in a Distributed Environment Using Transmission Line Modelling. In *Modelica 2000 Workshop*, Lund, Sweden, October 2000.

[5] Kaj Nystrm and Peter Fritzson. Parallel Simulation with Transmission Lines in Modelica. In *5th International Modelica Conference*, Vienna, Austria, September 2006.

[6] M. Sjölund, R. Braun, P. Fritzson, and P. Krus. Towards Efficient Distributed Simulation in Modelica using Transmission Line Modeling. In *3rd International Workshop on Equation-Based Object-Oriented Languages and Tools*, Oslo, Norway, October 2010.

[7] http://www.iei.liu.se/flumes/system-simulation/hopsanng/, February 2012.

[8] P. Krus. Robust System Modelling Using Bi-lateral Delay Lines. In *Proceedings of the 2nd Conference on Modeling and Simulation for Safety and Security*, Linköping, Sweden, 2005.

[9] Air Force Aero Propulsion Laboratory. Aircraft hydraulic system dynamic analysis. Technical report, Air Force Aero Propulsion Laboratory, 1977.

[10] P.B. Johns and M.A. O'Brian. Use of the transmission line modelling (T.L.M) method to solve nonlinear lumped networks. *The Radio And Electronic Engineer*, 50(1/2):59–70, 1980.

[11] D.M. Auslander. Distributed system simulation with bilateral delay-line models. *Journal of Basic Engineering*, pages 195–200, June 1968.

[12] Petter Krus. Robust Modelling Using Bi-Lateral Delay Lines for High Speed Simulation of Complex Systems. In *DINAME 2011 : 14th International Symposium on Dynamic Problems in Mechanics*, 2011. Invited conference contribution.

[13] M. Vlach. Lu decomposition and forward-backward substitution of recursive bordered block diagonal matrices. *Electronic Circuits and Systems, IEE Proceedings G*, 132(1):24 –31, february 1985.

[14] M. Axin, R. Braun, A. Dell'Amico, B. Eriksson, P. Nordin, K. Pettersson, I. Staack, and P. Krus. Next Generation Simulation Software Using Transmission Line Elements. In *Fluid Power and Motion Control*, Bath, England, October 2010.

[15] B. Eriksson, P. Nordin, and P. Krus. Hopsan NG, A C++ Implementation Using The TLM Simulation Technique. In *The 51st Conference On Simulation And Modelling*, Oulu, Finland, 2010.

[16] David Joyner, Ondřej Čertík, Aaron Meurer, and Brian E. Granger. Open source computer algebra systems: Sympy. *ACM Commun. Comput. Algebra*, 45(3/4):225–234, January 2012.

[17] SymPy Development Team. Sympy. http://sympy.org/, February 2012.

[18] Peter Fritzson. *Principles of Object-Oriented Modeling and Simulation with Modelica 2.1*. Wiley-IEEE Computer Society Pr, 2006.

Available online at www.sciencedirect.com
ScienceDirect
SIMS 00 (2012) 1–21
SIMS 2012
www.elsevier.com/locate/procedia

A homogeneous two-phase flow model of an evaporator with internally rifled tubes☆

Axel Ohrt Johansen[a,b], Brian Elmegaard[b]

[a]DONG Energy - Thermal Power, Kraftværksvej 53, Dk-7000, Fredericia, Denmark
[b]Technical University of Denmark, Nils Koppels Allé, Building 403, DK-2800 Kgs. Lyngby, Denmark

Abstract

In this article a numerical model for solving a transient one dimensional compressible homogeneous two phase model is developed. It is based on a homogeneous model for predominantly one-dimensional flows in a vertical pipe element with internal rifles. The homogeneous model is based on the assumption of both hydraulic- and thermal equilibrium. The consequences and aspects will briefly be discussed in that context. The homogeneous flow model consists of three hyperbolic fluid conservation equations; continuity, momentum and energy and the pipe wall is modelled as a one dimensional heat balance equation. The models can be reformulated in the four in-dependant parameters p(pressure), h(enthalpy) u(velocity) and T_w(wall temperature). Constitutive relations for the thermodynamic properties are limited to water/steam and is given by the IAPWS 97 standard. Wall friction and heat transfer coefficients are based on the Blasius friction model for rifled boiler tubes and the correlation by Jirous respectively. The numerical method for solving the homogeneous fluid equations is presented and the method is based on a fifth order Central WENO scheme, with simplified weight functions. Good convergence rate is established and the model is able to describe the entire evaporation process from sub-cooled water to super-heated steam at the outlet.

1. Introduction/motivation

Along with the liberalization of electricity markets in Northern Europe and Denmark, there is an increasing need to quickly regulate the large central power plants to cover the current supply of electricity and district heating. Much focus has been put in optimizing the individual power plants, so they can meet the requirements to stabilize the power supply and district heat production, caused by the stochastic nature of wind farms. Electricity generation based on wind has primacy in terms of production and the central power plants have to fill the gap between producing and consuming power. In periods of very high wind generation, the central power plants are thus forced to run down into low load and maintain a contingency in case the wind unexpectedly fails to come. In these situations, there may still be a need for district heating production, why we might consider turbine bypass in the steam power plants and directly produce district heating from the boiler at moderate pressure.

Keywords: Two phase flow, Vertical evaporator, Dynamic load, Internal Rifled Boiler Tubes, Central WENO, Hyperbolic balance laws.

☆Modelled by a fifth order Central WENO scheme for solving hyperbolic balance laws.

Email address: axejo@dongenergy.dk (Axel Ohrt Johansen)

Operating flexibility is therefore of great importance for the business economics of the plants and also a prerequisite for a stable electrical system. No matter how strong focus is put on this operational flexibility, power plants, however, will always be subject to technical limitations - e.g. boiler dynamics, coal mill dynamics, flame stability and material constraints. The power plants' ability to stabilize the electrical system can be increased substantially if we get a better understanding of the thermodynamic and flow changes, which occur in the evaporation process. Siemens has spent years developing a new evaporator concept, in brief; it has developed an evaporator with vertical boiler tubes lined with internal rifles. The system is called the SLMF principle (Siemens Low Mass Flux), see [1], which can be used for very specific evaporator systems. One of the advantages of using SLMF is that the boiler's primary operating area (Benson minimum) can be moved from the traditional 35-40% load. In new constructions this transition point is to around 20% load. In this way we avoid the very expensive and time consuming Benson transition, when an installation must adapt to the free electricity market and drive down the load. There is very little literature on the subject and there is a modest material relating to the mathematical description of heat transfer and pressure drop in rifled boiler tubes. Back in 1985 Harald Griem, [1] wrote on the subject, and both KEMA and Siemens have performed considerable experimental work that is considered company secrets. Other authors who have dealt with the topic experimentally are [2], [3], [4] and [5]. They have developed consistent algebraic expressions for frictional pressure drop and heat transfer in internally rifled boiler tubes. A Weighted Essentially non-oscillatory (WENO) solver code is implemented in c++ under MicroSoft Visual Studio 2008, and the solver is validated in [6]. The water/steam table is based on a fast bi-linear interpolation scheme, where the lookup table are based on the IAPWS97 standard, which is implemented in FORTRAN 90. The lookup table is described in [7].

2. Evaporation in steam power boilers

A power plant boiler works as a heat exchanger. On one side the fuel is burned and the product of combustion is a hot gas exchanging radiant heat to the water on the other side of the heat exchanger. The boiler is traditionally built as a tower, inside the hot gas is produced and the walls of the boiler are made of pipes welded together, in these pipes the water flows.

The heat flux is approximately 200-400 kW/m^2 in the lower sections of the boiler and is represented as radiation. At the upper part of the tower, the radiation is still dominating, but it is also necessary to take convective heat transfer into account. At the bottom section, where the radiation from gas to the pipe wall is dominating, the heat transfer on the outside is so massive that it is no longer setting the restriction for the optimal heat transfer. Instead, the limit is set by the heat transfer rate from the pipe-wall to the water inside the pipe.

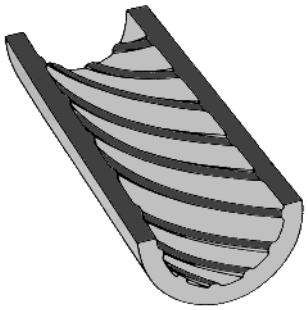

Fig. 1. Center cutting of an internal rifled boiler tube

One parameter that determines the heat transfer rate on the inside of the pipe is the fluid velocity near the inner pipe wall. If the velocity can be increased without increasing the net mass flux through the boiler, the heat transfer rate can be increased. With that assumption it is possible to build a more compact boiler,

by taking into account the specific type of combustion processes (Coal, Gas Wood pellets ect.). Internally rifled boiler tubes (IRBT) are an attempt to speed up the velocity at the wall and keep the vertical tube of a boiler construction. The mass flux through the IRBT are usually in the range of 1000 kg/m^2s and is less than the half as is seen in traditional Benson boiler panel walls, with a moderate pipe inclination.

In addition to the increase in heat transfer, the IRBTs are characterised by an excellent performance concerning two phase flow. The swirl is very good for separation of liquid from gas. The centrifugal force will increase the rate of light fluid to the centre of the pipe and force the heavy fluid components to near the wall, which will improve the cooling of the pipe and thereby increase the heat transfer and decrease the wall temperature of the pipe. Additionally the IRBT have the following advantages: The rifles will enlarge the surface of convective heat transfer, increasing the turbulent intensity in the boundary layer and increase the relative velocity between the wall and core fluid by rotational flow.

The advantages of the IRBT have a price. The pressure loss is higher than in the traditional boiler tubes, but it can be used in a constructive way. When super critical boilers operate at part load, stability problems can occur. The problem is usually solved by building individual pressure loss at each pipe inlet section. Thus the increased pressure loss in the IRBT can be utilized to replace the traditional built in pressure loss and thereby not increase the pumping power

3. Methods

Although the assumptions of thermodynamic equilibrium are often made in two-phase flow models, the phases rarely find themselves at thermal equilibrium. Some degree of thermal non-equilibrium arises in practically all situations and specially in dynamic situations, thermal non equilibrium must always be present so that heat and mass transfer can take place. Thermodynamic equilibrium does exist between a liquid and its vapour separated by a flat interface e.g., water and steam in a closed vessel. In the classical case of stationary vapour / bubble in large amount of liquid, the vapour and liquid temperatures are equal. However, due to the effect of surface tension, even in this equilibrium situation, the system temperature must be slightly above the saturation temperature corresponding to the pressure of the liquid. It is only in the case of the flat interface, that both phases can be exactly at saturation. Thus, the absence of hydraulic and thermal equilibrium is the rule rather than the exception in multi phase flows. In this chapter we outline a homogeneous dynamic flow model, based on the two layer flow model outlined in [8].

3.1. Thermo-Hydraulic model

The homogeneous model is based on the assumption of both hydraulic and thermal equilibrium and consists of three conservation equations, which can be reformulated in the three in-dependant variables ρ(density), $\dot{m}$(mass flow) and E(internal energy), where the dependant variables z (axial position in the pipe) $\in [0\ ,..., l_z]$ and t(time) $\in [0\ ,..., \infty[$. The pipe length is l_z. For the massflow given by: $\dot{m} = \bar{\rho} u A$ we find:

Continuity equation:

$$\frac{\partial}{\partial t}\left(\bar{\rho}A\right) + \frac{\partial}{\partial z}\left(\dot{m}\right) = 0 \tag{1}$$

where $A{=}\pi r_i^2$ is the cross section area of the pipe and r_i is the inner radius of the pipe. The mixture density is given by $\bar{\rho}$.

Momentum equation:

$$\frac{1}{A}\frac{\partial}{\partial t}\left(\dot{m}\right) + \frac{1}{A}\frac{\partial}{\partial z}\left(\dot{m}u\right) = -\frac{\partial \bar{p}}{\partial z} - \bar{\rho} g \cos\left(\theta\right) - F_w - F_s \tag{2}$$

where the mixture fluid velocity is given by u, g is the gravity and θ is the angle of pipe inclination measured from the vertical direction. The mixture pressure is given as $\bar{p}$ and the shear forces due to wall friction is given by: $F_w{=}\frac{S_w}{A}\tau_w$ and τ_w is given by (6) and S_w is the perimeter. The turbulent Reynolds stresses in the mixing fluid is given by $F_s = \frac{S_w}{A}\tau_s$.

Energy equation:

$$\frac{\partial}{\partial t}\left(\bar{\rho}A\bar{h} + \frac{1}{2}\bar{\rho}Au^2 - pA\right) + \frac{\partial}{\partial z}\left(\dot{m}\bar{h} + \dot{m}\frac{1}{2}u^2\right) = S_w q_e^{''} - \dot{m} g \cos\left(\theta\right) \tag{3}$$

Here the mixture enthalpy is given as $\bar{h}$. Equation (3) can be reformulated by use of the definition of the total specific convected energy: $\bar{e} = \bar{h} + 1/2u^2 + gz\cos\left(\theta\right)$ and by using the continuity equation to eliminate the gravitational terms on the left side, we find:

$$\frac{\partial}{\partial t}\left(A(\bar{\rho}\bar{e} - \bar{p})\right) + \frac{\partial}{\partial z}\left(\dot{m}\bar{e}\right) = q_e^{''} S_w - \dot{m} g \cos\left(\theta\right) \tag{4}$$

where $q_e^{''}$ represents the heat flux per unit surface area through the inner wall and S_w is the perimeter of the heated domain. The internal energy E is given as: $E{=}(\bar{\rho}\bar{e} - \bar{p}) \cdot A$, which is measured in [J/m].

3.2. Hydraulic closure laws

Closure laws in relation to the momentum equation is presented here. The axial shear stress is modelled by for example the Van Driest mixing length theory, see [9]:

$$\begin{aligned}\tau_s &= -\frac{\partial}{\partial z}\left(\rho \bar{u'v'}\right) \\ &\approx l^2 \bar{\rho} \frac{\partial u^2}{\partial z^2}\end{aligned} \tag{5}$$

and is used as an damping in the solution domain where we experienced transients initiated by large gradients in the density (compressibility). This is only applied for a restricted domain where the steam quality $x \in$ [-0.02,0.02]. The corresponding wall shear stress is given by

$$\begin{aligned}\tau_w &= f_w \bar{\rho} \frac{u \cdot |u|}{2} \\ &= f_w \frac{G \cdot |G|}{2\bar{\rho}}\end{aligned} \tag{6}$$

The term f_w is the dimensionless friction coefficient based on the single phase frictional coefficient in heated rifled tubes: $f_w = \frac{a}{Re^b} + c$. In table (1) we propose coefficients given by [1], for different rifled profiles. In [3] the same formulation of f_w is used and the author has for specific rifled pipes reported an absolute relative error less than 6.3 %.

Table 1. Algebraic relations of f_w for different profiles. [1]

type	RR6	RR5	RR4	RR2
a	1702	0.56	16.26	1.65
b	1.18	0.32	0.71	0.44
c	0.032	0.01309	0.01509	0.02344

In the two-phase region the friction factor is adjusted according to a two-phase multiplier, formulated by [10]. In that case f_w is based on fluid properties for saturated liquid. The model that is based on [10] calculates the two phase multiplier as:

$$\phi^2 = 1 + B \cdot x \cdot \left(\frac{\rho_l}{\rho_f} - 1\right) \tag{7}$$

Where the coefficient B is:

$$B = 1.58 - 0.47\frac{p}{p_c} - 0.11 \cdot \left(\frac{p}{p_c}\right)^2 \tag{8}$$

Note that the critical pressure (p_c) is 221.2 [bar] for water/steam. B is adjustment as: B = B - (B - 1)·(10· x - 9). The correlation of (7) is compared to the well known and more computation intensive model of Friedel and is illustrated in figure (2).

3.3. Pipe Wall Model

The heat transfer processes from a combustion process (radiation and convection) to the water and steam circuit in a power plant, is using the pipe wall as the transfer median, to transport the energy from the furnace to the cooling media, in this case water / steam flowing in the panel wall. The solution of problems involving heat conduction in solids can, in principle, be reduced to the solution of a single differential equation, by Fourier's law. The equation can be derived by making a thermal energy balance on a differential volume element in the solid. A volume element for the case of conduction only in the z-direction is illustrated in figure (3).

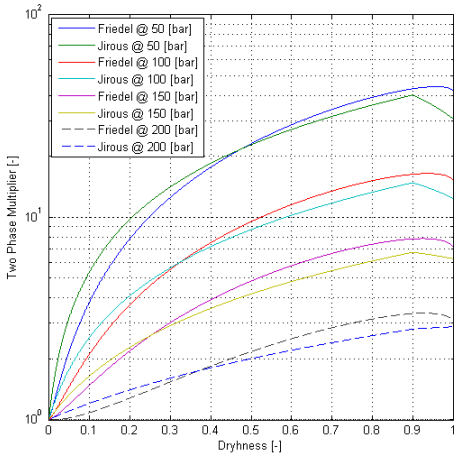

Fig. 2. Comparison of two-phase-multipliers of Jirous and Friedel.

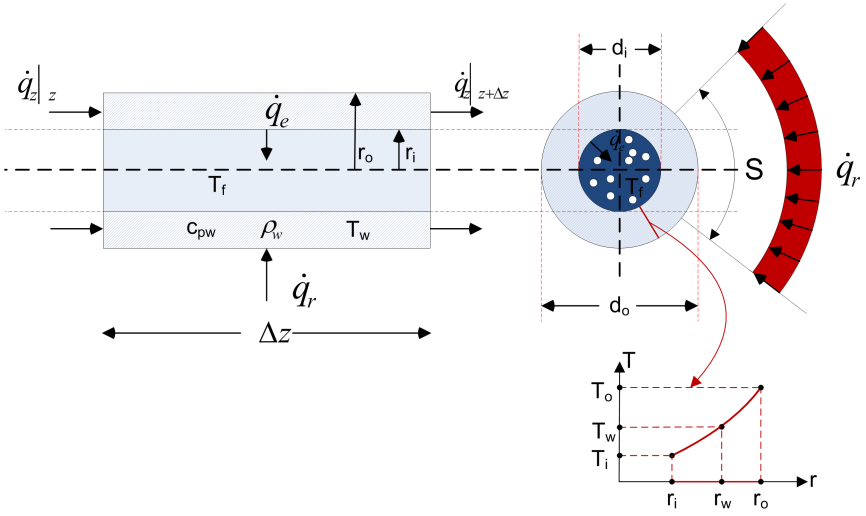

Fig. 3. Energy transfer and heat flow terms on a slice of a pipe wall element.

The balance equation becomes:

$$\frac{\partial T_w}{\partial t} = \alpha \frac{\partial^2 T_w}{\partial z^2} + \frac{\dot{q}_r}{\rho_w C_{pw}} \frac{S}{A_c} - \frac{\dot{q}_e}{\rho_w C_{pw}} \frac{d_i \pi}{A_c}, \quad z \in [0, l_z] \wedge t \geq 0 \tag{9}$$

where C_{pw} and ρ_w are the heat capacity and the density of the pipe wall and $A_c = \pi(r_o^2 - r_i^2)$ is the cross section area of the pipe wall. T_w is the mean wall temperature forced by the heat fluxes $\dot{q}_r$ and $\dot{q}_e$ expressing the heat flux from the furnace and the heat flux to the cooling fluid respectively.

Hence we can summarize the *system of balance laws* (SBL), given by (1), (2), (4) and (9), into a compact vector notation, given by:

$$\frac{\partial \Phi(z,t)}{\partial t} + \frac{\partial f(\Phi(z,t))}{\partial z} = \mathbf{g}(\Phi(z,t)) + \mathbf{h}(\frac{\partial \Phi}{\partial z}, \Phi(z,t)), \quad \Phi \in R^m, m = 4, \quad t \geq 0 \wedge \quad z \in \Omega \tag{10}$$

where the dependent variable Φ and the flux vector $\mathbf{f}$ are given as

$$\Phi = \begin{pmatrix} \bar{\rho}A \\ \dot{m} \\ E \\ T_w \end{pmatrix}, \quad f(\Phi) = \begin{pmatrix} \dot{m} \\ \frac{\dot{m}^2}{\bar{\rho}A} + pA \\ \frac{(E+pA)\dot{m}}{\bar{\rho}A} \\ 0 \end{pmatrix}$$

and the source and diffusion vectors are given as:

$$\mathbf{g}(\Phi) = \begin{pmatrix} 0 \\ p\frac{\partial A}{\partial z} - \bar{\rho}gA\cos\theta - \sqrt{\frac{\pi}{A}}f_w\frac{\dot{m}|\dot{m}|}{\bar{\rho}A} \\ S_w q_w'' - \dot{m}g\cos(\theta) \\ \alpha\frac{\partial^2 T_w}{\partial z^2} + \frac{\dot{q}_r}{\rho_w C_{pw}}\frac{S}{A_c} - \frac{\dot{q}_e}{\rho_w C_{pw}}\frac{d_i\pi}{A_c} \end{pmatrix} \text{ and } \mathbf{h}(\Phi) = \begin{pmatrix} 0 \\ \frac{l^2 S_w}{\bar{\rho}A^3}\frac{\partial \dot{m}^2}{\partial z^2} \\ 0 \\ \alpha\frac{\partial^2 T_w}{\partial z^2} \end{pmatrix}$$

Here the dependent variables are $\bar{\rho}$, $\dot{m}$, E and T_w meaning the fluid density, mass flow, total energy of the conserved fluid and wall mean temperature respectively. The pressure can be determined iteratively by water steam tables: p=$p(E,\rho)$. The source term $\mathbf{g}$ consists of both source/sink terms and the diffusion term $\mathbf{h}$ includes contributions from the mixing length eddy viscosity (5), working as a damping term in the vicinity of x=0, and the thermal diffusion in the pipe wall as well.

3.4. Constitutive relations for the heat pipe model

For isotropic materials, we introduce the thermal diffusivity given by: $\alpha = \frac{k_w}{\rho_w C_{pw}}$ given in $[m^2/s]$, which in a sense is a measure of thermal inertia and expresses how fast heat diffuses through a piece of solid. For a typical panel wall, the thermal diffusivity is approximately $1.98 \cdot 10^{-6}$ $[m^2/\mathrm{s}]$ at $200°C$, see [11]. The radiation from the furnace to the pipe surface is given by the heat flux $\dot{q}_r$. The heat flux $\dot{q}_e$ represents the convective heat transfer between the pipe wall inner surface and the flowing fluid in the pipe, and is given as: $\dot{q}_e$=$h_t(T_w - T_f)$, where h_t is the convective heat transfer coefficient and $T_w - T_f$ is the driving temperature difference, which is positive for boiling. For isotropic materials (pipe wall), we have expressions for specific heat capacity C_{pw}, heat conductivity k_w and density ρ_w as function of temperature in Kelvin from [11] and [12].

A simple, fast and robust model of the heat transfer in film boiling, is given by [13]. The heat transfer coefficient h_{fb} is given as

$$h_{fb} = c_f \dot{q}_r^{\,0.673} \quad [W/m^2K] \tag{11}$$

where the coefficient c_f is given by the below expression, which is a function of the saturation temperature (T_s), measured in $[^oC]$

$$c_f = \frac{0.06136}{\left[1 - (\frac{T_s}{378.64})^{0.0025}\right]^{0.73}} \tag{12}$$

The single phase laminar heat transfer coefficient (h_s) is calculated from

$$\begin{aligned} Nu_s &= \frac{h_s d_i}{k_f} \\ &= 4.36 \end{aligned} \tag{13}$$

and is valid for $L/d_i > 50$ and $\frac{d_i G}{\mu} < 2000$. For turbulent single phase flow and $\frac{d_i G}{\mu} > 10{,}000$ we use

$$\begin{aligned} Nu_s &= \frac{h_s d_i}{k_f} \\ &= 0.023\left(\frac{d_i G}{\mu_l}\right)^{0.8}\left(\frac{c_p \mu_f}{k_f}\right)^{1/3} \end{aligned} \tag{14}$$

The total heat transfer coefficient is given by (15), and consists of two contributions; one from the convective heat transfer boundary layer associated to the flowing fluid inside the heat pipe and one that relates to conduction through the pipe wall material.

$$h = \frac{1}{\frac{1}{h_c} + \frac{r_i}{k_w} \cdot \ln(r_w/r_i)} \tag{15}$$

where h_c is expressing the heat transfer coefficient due to the thermal boundary on the inner side of the pipe wall and r_w is defined by $T_w = T_r(r_w)$. Since we use the calculated average wall tube temperature as driver in the calculation of the total heat transport to the fluid, we must know r_w.

Due to the knowledge of radial conduction in the pipe, we use a simple analytical wall temperature profile, for estimating the inner wall temperature, expressed by the averaged wall temperature (T_w), based on the heat transfer through the isotropic pipe wall to the flowing fluid. Let $T_r(r)$ represent the radial temperature distribution by

$$\begin{aligned} T_r(r) &= \frac{T_i - T_o}{\ln(\frac{r_i}{r_o})} \ln(\frac{r}{r_o}) + T_o \\ &= a_0 \ln(\frac{r}{r_o}) + T_o \end{aligned} \tag{16}$$

where r is the pipe radius with suffix (i=inner) and (o=outer). This temperature profile for radial isotropic pipes, is the steady state solution to the 1D Fourier's law of heat transfer. Hence, for small values of the thermal diffusivity, the averaged wall temperature can reasonable be estimated by:

$$\begin{aligned} T_w &= \frac{1}{A_c} \int_{r_i}^{r_o} 2\pi r \cdot T_r(r) dr \\ &= \frac{2\pi}{A_c} \left[a_0 \left[x^2 \ln(x)/2 - x^2/4 \right]_{r_i}^{r_o} - a_0 \ln(r_o) \left[x^2/2 \right]_{r_i}^{r_o} \right] + T_o \cdot \left[x^2/2 \right]_{r_0}^{r_1} \\ &= a_1 \cdot T_i + (1 - a_1) \cdot T_o \end{aligned} \tag{17}$$

where a_1 is given by

$$a_1 = \frac{r_i^2}{r_i^2 - r_o^2} - \frac{1}{2ln(r_i/r_o)} \tag{18}$$

Hence the entire heat transfer can be estimated for the temperature range in between the wall mean temperature (T_w) and the fluid mixture temperature (T_f), which is assumed homogeneous and well mixed with a temperature boundary layer represented by h_c. The one dimensional pipe wall model does only consists of axial heat transfer term, and have no spatial resolution in the radial dimension.
The inner wall temperature can be determined by use of the equation for pure conduction through the pipe:

$$\dot{q}_r S = \frac{2\pi k_w}{\ln(r_o/r_i)}(T_o - T_i) = \frac{2\pi k_w}{\ln(r_w/r_i)}(T_w - T_i). \tag{19}$$

Hence we find T_i by insertion (17) in (19):

$$T_i = T_w + \frac{q_r S \ln(\frac{r_o}{r_i})(1 - a_1)}{2\pi k_w} \tag{20}$$

and hence r_w in (15) can be determined from (17) and (20) and we find

$$h = \frac{1}{\frac{1}{h_c} + \frac{r_i(a_1 - 1)}{k_w} \cdot \ln(r_i/r_o)} \tag{21}$$

where h_c is smoothed in-between h_s and h_{fb} depending of the dryness of the fluid. Additionally h_c is adjusted on the basis of a smoothing between laminar and turbulent single phase flow as well as for two-phase

flow. The smoothing function is based on a third order function and the associated slopes are determined numerically. Note that the heat flux is positive for $T_i > T_f$. Using the model parameters from table (2) we find a_1=0.423 and the temperature fall above the thermal boundary is: T_o-T_i=27.9 [^oC], which gives a temperature gradient in the pipe wall of dT/dr= 3930 [$^oC/m$] for a heat flux of q_e=100 [kW/m^2]. The heat conduction in the material is the most significant barrier for an effectively cooling of the tube wall.

3.5. Auxiliary relations

The Water / Steam library IAPWS 97 by [14] is used as a general equation of state, to derive thermodynamic properties of water and steam. In some relations we need a relationship for the pressure as function of density and enthalpy: p=p(ρ,$\bar{h}$). This can be done by a Newton Rapson solver. To improve the computational speed, we recommended to use a look up table within at least 200000 nodes, based on bilinear interpolation, see [7]. Here we create a look up table to ensure water/steam properties within an accuracy below 0.3% as an absolute maximum, due to [7]. Note that the density is smoothed in the vicinity of the saturation line of water to avoid heavy gradients and discontinuities.

3.6. Boundary conditions

It is convenient to use boundary conditions to the model which are physically measurable. Therefore, the following properties are used as boundary conditions; velocity (u), pressure (p) and enthalpy (h). This allows us to rewrite the boundary conditions to those properties, which are described by Φ, see (10). The Dirichlet boundary conditions are given by (22) and the corresponding Neumann boundary conditions are obtained by applying the chain rule for differensation of complex functions, and are given by (23).

$$\text{Dirichlet BC}: \begin{cases} \rho A \\ \rho A u \\ \rho A(h + \frac{u^2}{2} + gz\cos(\theta)) - pA \\ \rho T_w \end{cases} \tag{22}$$

where θ is the angle of the pipe inclination with respect to the horizontal.

$$\text{Neumann BC}: \begin{cases} A\frac{\partial \rho}{\partial z} + \rho\frac{\partial A}{\partial z} \\ uA\frac{\partial \rho}{\partial z} + \rho u\frac{\partial A}{\partial z} + \rho A\frac{\partial u}{\partial z} \\ \frac{\partial(\rho A)}{\partial z}\left[h + \frac{u^2}{2} + gz\cos(\theta)\right] + \rho A\left[\frac{\partial h}{\partial z} + u\frac{\partial u}{\partial z} + g\cos(\theta)\right] - A\frac{\partial p}{\partial z} - p\frac{\partial A}{\partial z} \\ \frac{\partial T_w}{\partial z} \end{cases} \tag{23}$$

3.7. Numerical Solution of Hyperbolic Transport Equation

Let us consider a hyperbolic *system of balance laws* (SBL) formulated on a compact vector notation, given by (10), where Φ is the unknown m-dimensional vector function, $\mathbf{f}(\Phi)$ the flux vector, $\mathbf{g}(\Phi)$ a continuous source vector function on the right hand side (RHS), with z as the single spatial coordinate and t the temporal coordinate, Ω is partitioned in n_z non-overlapping cells: $\Omega = \cup_{i=1}^{n_z} I_i \in [0, l_z]$, where l_z is a physically length scale in the spatial direction. This system covers the general transport and diffusion equations used in many physical aspects and gas dynamics as well. The SBL system is subjected to the initial condition:

$$\Phi(z, 0) = \Phi_0(z) \tag{24}$$

and the below boundary conditions given by:

Dirichlet boundaries:

$$\Phi(z = 0, t) = \Phi_A(t) \text{ and } \Phi(z = l_z, t) = \Phi_B(t) \tag{25}$$

and

Neumann boundaries:

$$\frac{\partial \Phi(z = 0, t)}{\partial z} = \frac{\partial \Phi_A(t)}{\partial z} \text{ and } \frac{\partial \Phi(z = l_z, t)}{\partial z} = \frac{\partial \Phi_B(t)}{\partial z} \tag{26}$$

The above boundary conditions can be given by a combination of each type of boundaries. The Dirichlet condition is only specified, if we have ingoing flow conditions at the boundaries.

The development of a general numerical scheme for solving *PDE*'s may serve as universal finite-difference method, for solving non-linear convection-diffusion equations in the sense that they are not tied to the specific eigenstructure of a problem, and hence can be implemented in a straightforward manner as black-box solvers for general conservation laws and related equations, governing the spontaneous evolution of large gradient phenomena. The developed non-staggered grid is suitable for the modelling of transport of mass, momentum and energy and is illustrated in figure (4),where the cell $I_j = \left[z_{j-1/2}, z_{j+1/2}\right]$ has a cell width Δz and Δt the time step.

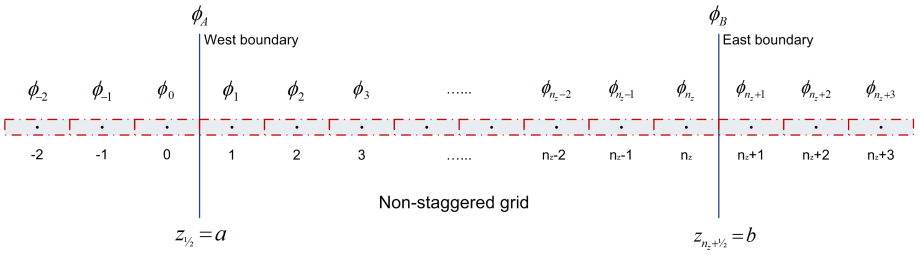

Fig. 4. The computational grid [0,l_z] is extended to a set of ghost points for specifying boundary conditions.

In this section, we review the central fifth order WENO schemes in one spatial dimension, developed by [15] with uses modified weight functions outlined by [16]. We recall the construction of the non-staggered central scheme for conservation laws. The starting point for the construction of the semi-discrete central-upwind scheme for (10) can be written in the following form:

$$\frac{d\Phi_j(t)}{dt} = -\frac{1}{\Delta z}\left[F_{j+1/2} - F_{j-1/2}\right] + S_j(\Phi). \tag{27}$$

where the numerical fluxes $F_{j+1/2}$ are given by

$$F_{j+1/2} = \frac{a^+_{j+1/2} f(\Phi^-_{j+1/2}) - a^-_{j+1/2} f(\Phi^+_{j+1/2})}{a^+_{j+1/2} - a^-_{j+1/2}} + \frac{a^+_{j+1/2} a^-_{j+1/2}}{a^+_{j+1/2} - a^-_{j+1/2}}\left[\Phi^+_{j+1/2} - \Phi^-_{j+1/2}\right]. \tag{28}$$

Notice that the accuracy of this scheme is determined by the accuracy of the reconstruction of Φ and the ODE solver. In this chapter the numerical solutions of (27) is advanced in time by mean of third order TVD Runge-Kutta method described by [17]. The local speeds of propagation can be estimated by

$$a^+_{j+1/2} = \max\left\{\lambda_N\left(\frac{\partial f(\Phi^-_{j+1/2})}{\partial\Phi}\right), \lambda_N\left(\frac{\partial f(\Phi^+_{j+1/2})}{\partial\Phi}\right), 0\right\}, \tag{29}$$
$$a^-_{j+1/2} = \min\left\{\lambda_1\left(\frac{\partial f(\Phi^-_{j+1/2})}{\partial\Phi}\right), \lambda_1\left(\frac{\partial f(\Phi^+_{j+1/2})}{\partial\Phi}\right), 0\right\}.$$

with $\lambda_1 < ... \lambda_N$ being the eigenvalues of the Jacobian given by $\mathbf{J}=\frac{\partial f(\Phi(z,t))}{\partial\Phi}$. Here, $\Phi^+_{j+1/2}=p_{j+1}(z_{j+1/2})$, and $\Phi^-_{j+1/2}=p_j(z_{j+1/2})$ are the corresponding right and left values of the piecewise polynomial interpolant $\{p_j(z)\}$ at the cell interface $z=z_{j+1/2}$.

To derive an **e**ssentially **n**on-**o**scillatory reconstruction (ENO), we need to define three supplementary polynomials ($\tilde{\Phi}_1$, $\tilde{\Phi}_2$, $\tilde{\Phi}_3$), approximating $\Phi(z)$ with a lower accuracy on I_i. Thus, we define the polynomial of second-order accuracy, $\tilde{\Phi}_1(z)$, on the reduced stencil S_1: (I_{i-2}, I_{i-1}, I_i), $\tilde{\Phi}_2(z)$ is defined on the stencil S_2: (I_{i-1}, I_i, I_{i+1}), whereas $\tilde{\Phi}_3(z)$ is defined on the stencil S_3: (I_i, I_{i+1}, I_{i+2}). Now, we have to invert a 3×3 linear system for the unknown coefficients $\{a_j\}$, $j \in \{0, ..., 2\}$, defining $\tilde{\Phi}_1, \tilde{\Phi}_2, \tilde{\Phi}_3$. Once again, the constants determining the interpolation are pre-computed and stored before solving the PDEs. When the grid is uniform, the values of the coefficients for $\tilde{\Phi}_1, \tilde{\Phi}_2$ and $\tilde{\Phi}_3$ can be explicitly formulated. It is left to the reader to read [15] or [6] for further details about determining the coefficients in the reconstructed polynomials. To implement a specific solution technique, we extend the principle of the central WENO interpolation defined in [18]. First, we construct an ENO interpolant as a convex combination of polynomials that are based on different discrete stencils. Specifically, we define in the discrete cell I_i:

$$\tilde{\Phi}^i(z) \equiv \sum_j w_j \times \tilde{\Phi}_j(z), \quad \sum_j w_j = 1 \quad \text{for} \quad w_j \geq 0 \ \text{ for} j \in \{1, .., 4\}, \tag{30}$$

and $\tilde{\Phi}_1$, $\tilde{\Phi}_2$ and $\tilde{\Phi}_3$ are the previously defined polynomials. $\tilde{\Phi}_4$ is the second-order polynomial defined on the central stencil S_5: $(I_{i-2}, I_{i-1}, I_i, I_{i+1}, I_{i+2})$ and is calculated such that the convex combination in (30), will be fifth-order accurate in smooth regions. Therefore, it must verify:

$$\tilde{\Phi}_{opt}(z) = \sum_j C_j \times \tilde{\Phi}_j(z) \ \ \forall z \in I_i, \quad \sum_j C_j = 1 \quad \text{for} \quad C_j \geq 0 \ \text{ for } j \in \{1, .., 4\}, \tag{31}$$

The calculation of $\tilde{\Phi}^+_{i+1/2}$,$\tilde{\Phi}^-_{i+1/2}$ produces the following simplified result:

$$\begin{aligned}\tilde{\Phi}^+_{i+1/2} =& \left(-\frac{7}{120}w_4 - \frac{1}{6}w_1\right)\bar{\Phi}_{i-2} + \left(\frac{1}{3}w_2 + \frac{5}{6}w_1 + \frac{21}{40}w_4\right)\bar{\Phi}_{i-1} \\ &+ \left(\frac{5}{6}w_2 + \frac{1}{3}w_1 + \frac{11}{6}w_3 + \frac{73}{120}w_4\right)\bar{\Phi}_i + \left(-\frac{1}{6}w_2 - \frac{7}{6}w_3 - \frac{7}{120}w_4\right)\bar{\Phi}_{i+1} + \left(\frac{1}{3}w_3 - \frac{1}{60}w_4\right)\bar{\Phi}_{i+2}\end{aligned} \tag{32}$$

$$\begin{aligned}\tilde{\Phi}^-_{i+1/2} =& \left(-\frac{1}{60}w_4 + \frac{1}{3}w_1\right)\bar{\Phi}_{i-2} + \left(-\frac{1}{6}w_2 - \frac{7}{6}w_1 - \frac{7}{120}w_4\right)\bar{\Phi}_{i-1} \\ &+ \left(\frac{5}{6}w_2 + \frac{1}{3}w_3 + \frac{11}{6}w_1 + \frac{73}{120}w_4\right)\bar{\Phi}_i + \left(\frac{1}{3}w_2 - \frac{5}{6}w_3 + \frac{21}{40}w_4\right)\bar{\Phi}_{i+1} + \left(-\frac{1}{6}w_3 - \frac{7}{120}w_4\right)\bar{\Phi}_{i+2}\end{aligned} \tag{33}$$

To calculate the weights w_j, j$\in \{1, 2, 3, 4\}$, we review another technique to improve the classical smoothness indicators to obtain weights that satisfy the sufficient conditions for optimal order of accuracy. It is well known from [15], that the original WENO is fifth order accurate for smooth parts of the solution domain

except near sharp fronts and shocks. The idea here is taken from [16] and uses the hole five point stencil S_5 to define a new smoothness indicator of higher order than the classical smoothness indicator IS_i. The general form of indicators of smoothness are defined in [18]:

$$IS_j^i = a_1^2 \Delta z^2 + \frac{13}{3} a_2^2 \Delta z^4 + O(\Delta z^6), \quad j \in \{1, 2, 3\}. \tag{34}$$

and the form of IS_4^i is given by [15]:

$$IS_4^i = a_1^2 \Delta z^2 + \left[\frac{13}{3} a_2^2 + \frac{1}{2} a_1 a_3 \right] \Delta z^4 + O(\Delta z^6). \tag{35}$$

where a_0 and a_1 can be determined by solving the coefficients to reconstructed polynomial $\tilde{\Phi}_4$ on S_5. For estimating the weights w_k, k $\in \{1, 2, 3, 4\}$, we proceed as follows: Define

$$IS_k^* = \frac{IS_k + \epsilon}{IS_k + \epsilon + \tau_5} \tag{36}$$

where IS_k, k $\in \{1, 2, 3\}$ are given by (34), IS_4 given by (35) and $\tau_5 = |IS_1 - IS_3|$. The constant ϵ is a small number. In some articles $\epsilon \approx$ from $1 \cdot 10^{-2}$ to $1 \cdot 10^{-6}$, see [18]. Here we use much smaller values of ϵ for the mapped and improved schemes in order to force this parameter to play only its original role of not allowing vanishing denominators at the weight definitions. The weights w_k are defined as:

$$w_k = \frac{\alpha_k^*}{\sum_{l=1}^4 \alpha_l^*}, \quad \alpha_k^* = \frac{C_k}{IS_k^*}, \quad k \in \{1, 2, 3, 4\} \tag{37}$$

The constants C_j represent ideal weights for (30). As already noted in [18], the freedom in selecting these constants has no influence on the properties of the numerical stencil; any symmetric choice in (31), provides the desired accuracy for $\tilde{\Phi}_{opt}$. In what follows, we make the choice as in [15]:

$$C_1 = C_3 = 1/8, C_2 = 1/4 \text{ and } C_4 = 1/2. \tag{38}$$

3.7.1. Convection-Diffusion equations

Let us again consider the general System of Conservation Laws (SCL), given by equation (10), where the source term g is replaced by a dissipative flux:

$$\frac{\partial \Phi(z,t)}{\partial t} + \frac{\partial f(\Phi(z,t))}{\partial z} = \frac{\partial}{\partial z} \left(g(\Phi(z,t), \frac{\partial \Phi}{\partial z}) \right), \quad t \geq 0, \quad z \in \Omega \tag{39}$$

The gradient of g is formulated on the compressed form: $g(\Phi, \frac{\partial \Phi}{\partial z})_z$ as a nonlinear function $\neq$ zero. This term can degenerate (39) to a strongly parabolic equation, admitting non smooth solutions. To solve it numerically is a highly challenging problem. Our fifth-order semi-discrete scheme, (27)-(28), can be applied to (10) in a straightforward manner, since we can treat the hyperbolic and the parabolic parts of (39) simultaneously. This results in the following conservative scheme:

$$\frac{d\Phi_j(t)}{dt} = -\frac{1}{\Delta z} \left[F_{j+1/2} - F_{j-1/2} \right] + G_j(\Phi, t). \tag{40}$$

Here $F_{j+1/2}$ is our numerical convection flux, given by equation (28) and G_j is a high-order approximation to the diffusion flux $g(\Phi, \frac{\partial \Phi}{\partial z})_z$. Similar to the case of the second-order semi-discrete scheme of [19], operator splitting is not necessary for the diffusion term. By using a forth order central differencing scheme, outlined by [20], we can apply our fifth-order semi-discrete scheme, given by (27) and (28), to the parabolic equation (10), where $g(\Phi, \frac{\partial \Phi}{\partial z})_z$ is a function of ϕ and its derivative in space (diffusion). The diffusion term can be expressed by a high-order approximation:

$$G_j(t) = \frac{1}{12\Delta z} \left[-G(\Phi_{j+2}, (\Phi_z)_{j+2}) + 8 \cdot G(\Phi_{j+1}, (\Phi_z)_{j+1}) - 8 \cdot G(\Phi_{j-1}, (\Phi_z)_{j-1}) + G(\Phi_{j-2}, (\Phi_z)_{j-2}) \right] \tag{41}$$

where

$$
\begin{aligned}
(\Phi_z)_{j+2} &= \frac{1}{12\Delta z}\Big[25\Phi_{j+2} - 48\Phi_{j+1} + 36\Phi_j - 16\Phi_{j-1} + 3\Phi_{j-2}\Big], \\
(\Phi_z)_{j+1} &= \frac{1}{12\Delta z}\Big[3\Phi_{j+2} + 10\Phi_{j+1} - 18\Phi_j + 6\Phi_{j-1} - \Phi_{j-2}\Big], \\
(\Phi_z)_{j-1} &= \frac{1}{12\Delta z}\Big[\Phi_{j+2} - 6\Phi_{j+1} + 18\Phi_j - 10\Phi_{j-1} - 3\Phi_{j-2}\Big] \quad \text{and} \\
(\Phi_z)_{j-2} &= \frac{1}{12\Delta z}\Big[-3\Phi_{j+2} + 16\Phi_{j+1} - 36\Phi_j + 48\Phi_{j-1} - 25\Phi_{j-2}\Big]
\end{aligned} \tag{42}
$$

and Φ_j are the point-values of the reconstructed polynomials.

3.7.2. Source Term

Next, let us consider the general SCL given by (10) and restrict our analysis to the source term of the form: $g(\Phi, t)$ as a continuous source vector function $\neq$ zero. By integrating system (10) over a finite space-time control volume $I_i, \Delta t$ one obtains a finite volume formulation for the system of balance laws, which usually takes the form

$$
\Phi(z,t)_j^{n+1} = \Phi(z,t)_j^n - \frac{\Delta t}{\Delta z}\left(f_{j+1/2} - f_{j-1/2}\right) + \Delta t g(z,t)_j, \quad t \geq 0, \quad z \in \Omega \tag{43}
$$

The integration of (10) in space and time gives rise to a temporal integral of the flux across the element boundaries $f_{j+1/2}$ and to a space-time integral g_i of the source term inside I_i. In practice, one must replace the integrals of the flux and the source in (43) by some suitable approximations, that is to say one must choose a concrete numerical scheme. For SBL a numerical source must be chosen. Here, not only the three classical properties are required, but some additional properties are needed for the global numerical scheme: It should be well-balanced, i.e. able to preserve steady states numerically. It should be robust also on coarse grids if the source term is stiff.

3.7.3. Boundary conditions for Non-staggered grid

For a system of m equations we need a total of m boundary conditions. Typically some conditions must be prescribed at the inlet boundary (z=a) and some times at the outlet boundary (z=b). How many are required at each boundary depends on the number of eigenvalues of the Jacobian $\mathbf{A}$ that are positive and negative, respectively and whether the information is marching in or out for the boundaries.

By extending the computational domain to include a few additional cells on either end of the solution domain, called ghost cells, whose values are set at the beginning of each time step in some manner that depends on the boundary condition. In figure (4) is illustrated a grid with three ghost cells at each boundary. The idea behind the ghost point approach is to express the value of the solution at control points outside the computational domain in terms of the values inside the domain plus the specified boundary condition. This allows the boundary condition to be imposed by a simple modification of the internal coefficients using the coefficients of the fictitious external point. This can result in a weak imposition of the boundary condition, where the boundary flux not exactly agree with the boundary condition. By establishing a Taylor expansion around the boundary a or (b), we can express a relationship between the ghost points outside the solution domain and grid points inside the domain. For further details see [6].

3.7.4. Time discretization

The semi-discrete ODE given by (27) is a time dependent system, which can be solved by a TVD Runge-Kutta method presented by [17]. The optimal third order TVD Runge-Kutta method is given by

$$
\begin{aligned}
\Phi_j^{(1)} &= \Phi_j^n + \Delta t L(\Phi_j^n), \\
\Phi_j^{(2)} &= \frac{3}{4}\Phi_j^n + \frac{1}{4}\Phi_j^{(1)} + \frac{1}{4}\Delta t L(\Phi_j^{(1)}), \\
\Phi_j^{n+1} &= \frac{1}{3}\Phi_j^n + \frac{2}{3}\Phi_j^{(2)} + \frac{2}{3}\Delta t L(\Phi_j^{(2)}), \quad \text{for } j \in [1, n_z].
\end{aligned} \tag{44}
$$

The stability condition for the above schemes is

$$CFL = \max\left(u_j^n \frac{\Delta t}{\Delta z}\right) \leq 1, \tag{45}$$

where CFL stands for the *Courant-Friedrichs-Lewy* condition and u_j^n is the maximum propagation speed in cell I_j at time level n.

4. Results

In this section we setup and solve a homogeneous boiler tube model for two cases; one without IRBT and one with Siemens RR5 pipes. The governing equations are defined by the system of balance laws given by equation (10) including the pipe wall model given by equation (9) for the solution domain given by $\Omega \in [0,l_z]$.

4.1. Numerical setup

Three Dirichlet boundary conditions are applied for the hydraulic case and two Neumann boundaries are applied for the pipe wall model, given as zero gradients in the wall temperature at each pipe end (No heat loss). The intention is to model an evaporator, which can induce oscillations initiated by the compressibility, which arise as a result of a phase shift in the lower part of the evaporator. Therefore, we apply a constant downstream Dirichlet pressure boundary condition, that is corresponding to a stiff system, without any pressure absorption effects in the down stream turbine system due to compressibility. An analogy to this is a geyser, where there is a constant surface pressure and an intense heat absorption in the bottom region, whereby an oscillating pressure wave is initiated due to the compressibility of the fluid, caused by intense heat from the underground. Additionally we force the model with both a constant enthalpy and mass flux located on the upstream boundary, supplied by a constant heat flux along the entire heat pipe. The numerical scheme is the fifth order WENO scheme outlined in chapter (3.7) and consists of 400 computational points with CFL number of 0.8. The numerical scheme is tested for consistency and stability with respect to both a scalar- and a system of hyperbolic equations and has been successfully compared to analytical results from the literature as well as other published results. This work is outlined in [7].

The model is soft started in two steps, at t=0 [s] is the pure hydraulic model soft started during 4 seconds, without heat flux. After 10 seconds the heat flux is build-up during four seconds. This is done to avoid heavy shock waves moving forward and back in the entire solution domain. If the soft start period is reduced to only 1 second, heavy pressure oscillations occur. The soft start model is based on a third order theory [21], which gives a C^2 continuous sequence, which means zero gradients of the first derivative at both ends of the soft start period. The model data are listed below in table (2). The dynamic start-up process can be seen in figure (6), where the density is given in $[kg/m^3]$, pressure in [bar], Temperature in $[^oC]$, enthalpy in [kJ/kg] and mixture velocity in [m/s].

4.2. Model consistency

The model consists of 400 differential elements, thus ensuring a smooth continuous solution. By reducing the number of computational cells to only 50 elements, one would observe a more intensive standing wave at the entrance of two-phase region, which is due to intensive heating of the differential cell in the vicinity of the boiling zone, where we have an intensive negative slope in the density as function of the enthalpy, hence the density change becomes so violent that a pressure wave is established to ensure momentum balance. Using a CFL number higher than 1.0 is leading to instabilities due to the semi implicit scheme.

4.3. Simulation results - without IRBT

In figure (5) we illustrate the output results for each 25 sec. of simulation, referring to the solution of the full-scale evaporator at Skærkækværket unit 3 (SKV3) in Fredericia (Denmark), without IRBT. Here we have a tower boiler which consists of 4x56 parallel boiler tubes representing an entire mass flow of 90 [kg/s] flowing in 193.5 meter long heat pipes with an inclination of 12 degree. A steady state solution is obtained after approximately 250 seconds, and is depicted in figure (6) together with the initial conditions. The entire pressure drop and heat uptake fit (± 5 %) with steady state experiments performed at (SKV3). The simulation results shows how the state of the fluid gradually moves from the inlet condition, in the form of subcooled water, to the two phase zone, in which the boiling is starting, and finally reaches the super heating zone, where the dry steam is superheated to approximately 360 $[^oC]$. The pressure drop is fixed downstream in the form of a Dirichlet boundary condition, corresponding to measured pressure level from (SKV3). The Pressure distribution along the evaporator reflects different pressure loss models, the pressure

Table 2. Geometrical and numerical specifications. Data in parentheses are referring to simulation without IRBT.

Parameter	Value	Unit	Parameter	Value	Unit
Gravity (g)	9.81	[m/s^2]	Spatial start position	0.000	[m]
Spatial end position (L)	38.25 (193.40)	[m]	Inner diameter of pipe (d_i)	23.8	[mm]
Outer diameter of pipe (d_o)	38.0	[mm]	Heat conductivity in wall (k_w)	10.139	[w/mK]
Wall density (ρ_w)	7850.0	[kg/m^3]	Specific heat capacity of pipe wall (Cp_w)	527.21	[J/kg/K]
Heat flux ($\dot{q}_e$)	100.000	[W/m^2]	Wall roughness (λ)	1.0E-6	[m]
Initial Enthalpy - Inlet	1187.6988	[kJ/kg]	Initial Enthalpy - Outlet	1187.6988	[kJ/kg]
Initial Pressure - Inlet	92.3762	[Bar]	Initial Pressure - Outlet	92.3762	[Bar]
Initial Velocity - Inlet	0.0	[m/s]	Initial Velocity - Outlet	0.0	[m/s]
Pressure BC (Dirichlet - Outlet)	92.3762	[Bar]	Enthalpy BC (Dirichlet - Inlet)	1187.6988	[kJ/kg]
Velocity BC (Dirichlet - Inlet)	0.200(1.1711)	[m/s]	Simulation time	200.0	[s]
Output frequency	0.1	[s]	CFL number	0.80	[-]
Number of computational grids (N_p)	400	[-]	Riffle type	RR5 1.5994(No rifels)	[-]

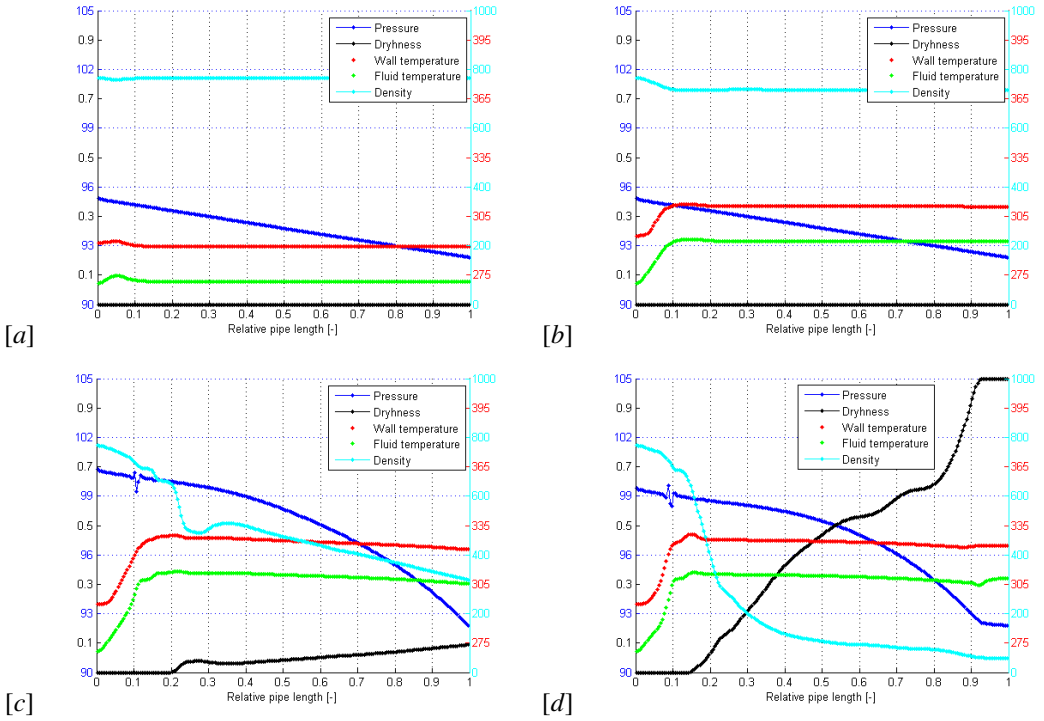

Fig. 5. Solution of SKV3 evaporator model without IRBT after (a):25, (b):50, (c):75 and (d):100 sec.

gradient of single and two-phase regions respectively. The pressure drop in the two-phase region involves the two phase multiplier, outlined in (7), which multiplies the pressure gradient with up to 16 times relative to the pressure gradient for saturated water. The inlet velocity is specified as an upstream Dirichlet boundary condition, and is soft started by use of the before mentioned smooth function, having a soft start period of four seconds. The super heated steam leaves the down stream boundary at steady state flow condition with a speed of app. 24 [m/s]. This ensures a smooth hydraulic flow condition of a cold evaporator. After words the heating is build up smoothly, applied by the same smoothing technique, so that undesirable thermal shock phenomena is reduced to a minimum. A standing pressure wave in the front of the boiling zone of the fluid is created by the very intense negative slope in the fluid density at the entrence to the two phase region. This

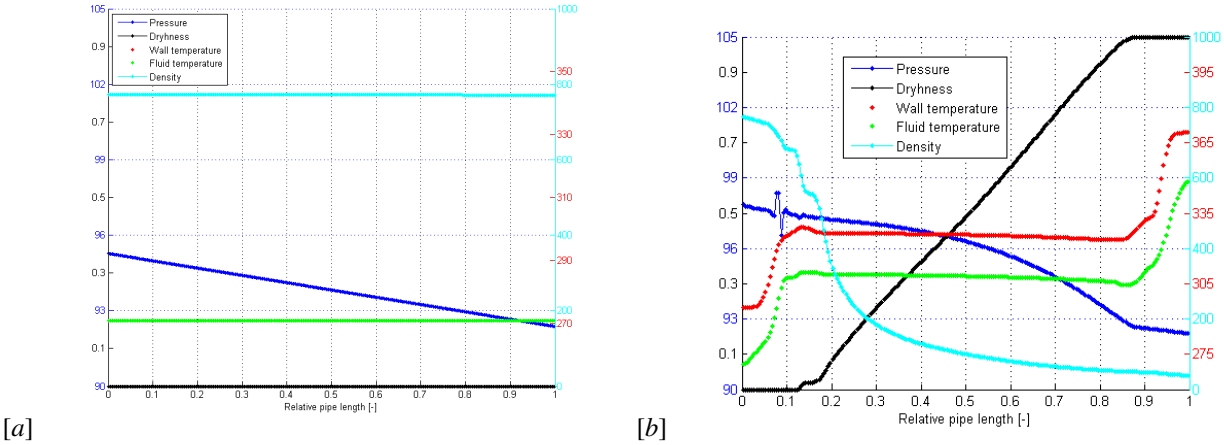

Fig. 6. Initial (a) and steady state solution (b) of SKV3 evaporator model without IRBT.

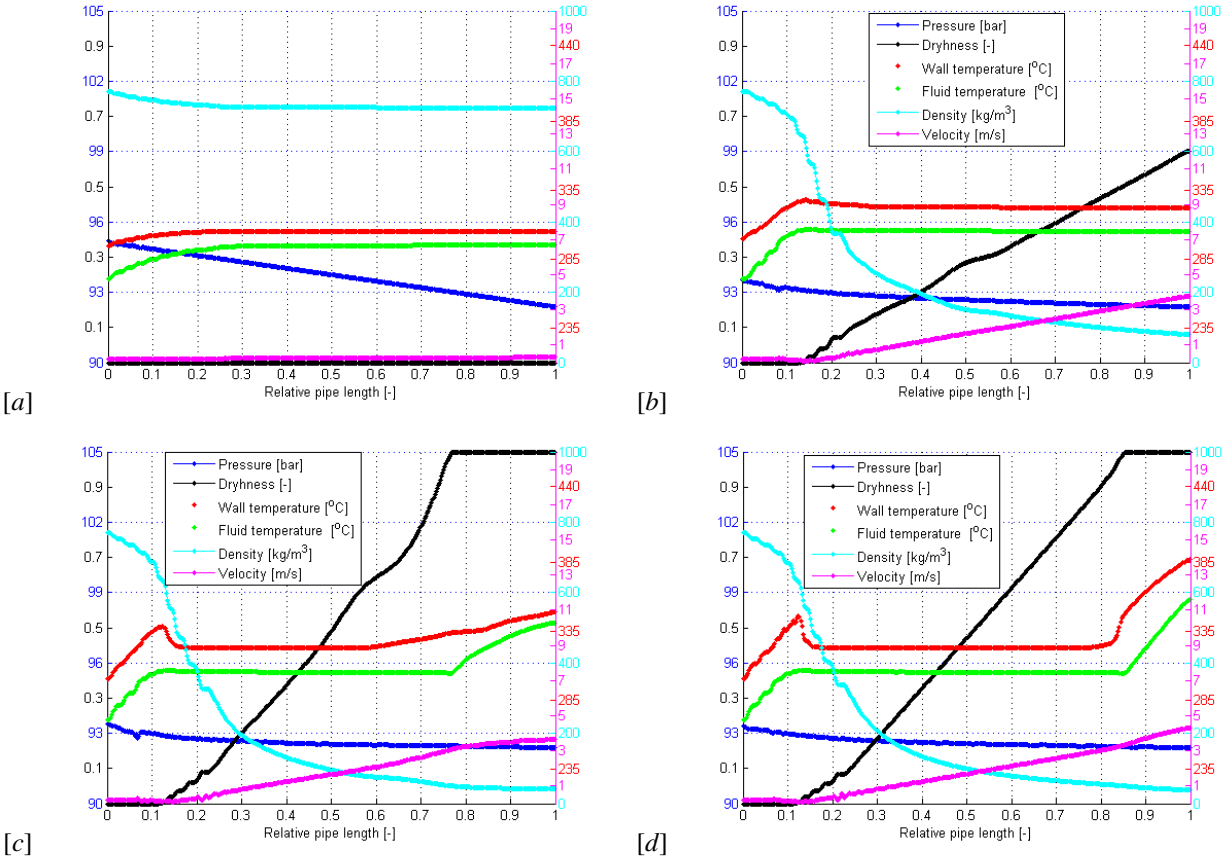

Fig. 7. Solution of Modified SKV3 vertical evaporator model with SLMF after (a):50, (b):100, (c):150 and (d):200 [s].

pressure-drop oscillations could occur, when there exists large upstream compressibility in the flow boiling system, see ([22], [23]). This phenomenon is increased in a vertical evaporator where the heating phase has

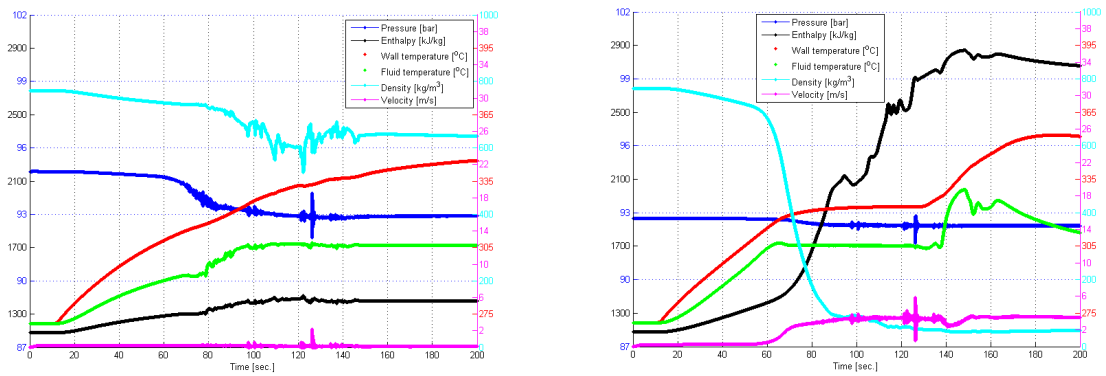

Fig. 8. Modified SKV3 vertical evaporator model with IRBT at station A(left) and B(right).

a heavy column of liquid to be transported out of the solutions area, which can initiate stability problems. This phenomenon occurs at low operating pressure in the evaporator or low firing, ie. heating the bottom of the evaporator. The dryness line in figure (5) expresses the mass based percentage of the steam flowing in the evaporator tube, not surprisingly, this process linearly corresponding to a constant heat flux along the tube.

Pressure-drop oscillations can be characterised as a secondary phenomenon of dynamic instability, which is triggered by a static instability phenomenon. Pressure-drop oscillations occur in systems having a compressible volume upstream of, or within, the heated section. Pressure-drop oscillations have been studied in considerable details by Maulbetsch [24] and Griffith [25], for sub cooled boiling of water, and by Stenning et al. [26], [27], for bulk boiling of freon-11. Maulbetsch and Griffith found that the instability was associated with operation on the negative sloping portion of the pressure-drop - flow curve.

4.4. Simulation results - with IRBT

By converting the SKV3 boiler to a system equipped by RR5 internal rifled boiler tubes (IRBT), this will normally lead to a complete redesign of both the furnace- and the evaporator system, but in this fictive case we use the same heat transfer area, despite the fact, that the IRBT considerably improve the heat transfer in the boiling zone. In this new setup, the length of the boiler tubes are reduced from 193.5 [m] to 38.25 [m] and the number of parallel tubes are increased from the original 4 x 56 to 4 x 270 parallel tubes. We have proved used a very low mass flux (corresponding to approx. 10% load), specifically to analyze the effects of the wall temperature distribution. It should be emphasized that this simulation event is a fictional setup and is rather a calculation example of what can happen in an evaporator tubes, if near zero flow momentarily occurs.

The vertical IRBT leads to an decrease in the mass flux, which is illustrated in (7) for instant pictures of 100, 150, 175 and 200 [s] of simulation. The wall temperature are varying in time and reach a peak while the flow locally is approaching zero, caused by local pressure oscillations initiated by the compressibility at the entrance of the two phase region. The bad cooling caused by near zero flow can have disastrous consequences for the pipe material and may ultimately lead to a meltdown of the evaporator tube. In practice, this is avoided by increasing the circulation through the evaporator. The pressure drop through the evaporator tube is unrealistically low, due to the very low mass flux (105 [kg/m^2s]). Normally, the mass flux of IRBT is approx. 1200 [kg/m^2s] at 100% load. In figure (8) is listed timeseries of the thermo hydraulic data at two stations located at A(z=$\frac{1}{8}l_z$) and B(z=$\frac{7}{8}l_z$). The thermo hydraulic conditions in station A is situated in the subcooled region while the station B is situated in the super heated region. Both stations are affected by the compressibility effect, initiated in the entrance to the boiling zone. Pressure waves are approaching up- and down stream due to the eigenvalues of the hyperbolic governing equations (λ_1=c, λ_2=u+c and λ_3=u-

c) where λ_i, i=1,3 is the eigenvalues and c is the local speed of sound for the two phase mixture. In the downstream station B we can also see minor slugs of enthalpy for t=100 [s], which also is referring to the compresibility phenomena.

4.5. Model consistency

The model consists of 400 differential elements, thus ensuring a smooth continuous solution. By reducing the number of computational cells to only 50 elements, one would observe a more intensive standing wave at the entrance of two-phase region, which is due to intensive heating of the differential cell in the vicinity of the boiling zone, where we have an intensive negative slope in the density as function of the enthalpy, hence the density change becomes so violent that a pressure wave is established to ensure momentum balance. Using a CFL number higher than 1.0 is leading to instabilities due to the semi implicit scheme.

4.6. Discussion

The two simulation cases shows two very different thermo hydraulic conditions. The simulation of (SKV3) without IRBT is verified against steady state measurements and the pressure drop and heat uptake fits quite well (± 5 %). The case of IRBT does not reach a steady state condition after 200 [s] and is illustrating an absolute worst case of boiler layout. It is interesting to see that it is possible to initiate local temperature spikes in an evaporator tubes - even before the boiling region - caused by the compressibility phenomena. The above results show that the numerical model is able to simulate the pressure drop and heat transfer in evaporator tubes (with and without IRBT), in both a time and spatial resolution. However, despite the extremely large in-linearities in the fluid density, and the hyperbolic nature of the governing equations, the model is capable to calculate a dynamic response over the saturation zones in the evaporator. Under normal conditions, the sub-cooled section of the evaporator will be separated from the two-phase section, to ensure numerical stability, but by use of the WENO technique, this can be handled in one setup. It is unfortunately not possible to compare the numerical calculations with measured data, since the IRBT evaporator model is a hypothetical example, but the boundary data are taken from measurements from SKV3.

It is interesting to see how the tube wall temperature may be increased, as a result of poor heat transfer due to the low flow rate in the subcooled section of the evaporator. Further downstream, where the flow speed increases, progressively better heat transfer are observed and a more homogeneous axial temperature distribution all the way down to the superheated section, where the material temperature rises again.

Similarly, we can observe that there are several different models of the wall friction into play, which is revealed by considering the slope of the pressure downstream in figure (7). The pressure gradient is ultimately the greatest in the two-phase region, due two-phase multiplier. we see also that the pressure gradient for superheated steam also, not surprisingly, are larger than sub-cooled liquid.

The Central WENO schemes are designed for problems with piecewise smooth solutions containing discontinuities. The Central WENO scheme has been successful in the above applications, especially for solving the pressure distribution down streams an evaporator. The inlet conditions is sub cooled water and the out flow is superheated steam. Minor pressure waves are initiated in the transition zones to the two phase region (x=0), because of the compressibility of the fluid. The pressure oscillations generated in the entrance to the boiling zone is controlled by the shear stresses in the momentum equation (0.01 $[m^2/s]$, which smooth the oscillations due to diffusion of momentum. The model is very time consuming in solving the system, because the total energy is determined iteratively as well as the density is a function of pressure and enthalpy. The model is stable as long as the CFL number is less than one and the speed of sound is below the highest calculated speed of sound in the fluid domain, determined at each time step. We can conclude that the solution procedure is non-oscillatory in the sense of satisfying the total-variation diminishing property in the one-dimensional space. No numerical wiggles are observed in the hyperbolic models and smooth solutions are observed in the continuous zones of the flow regimes.

4.7. Conclusion

In this article we have solved the dynamic flow equations and associated wall model for a boiler tube, by use of a fifth order WENO scheme. Simulations with and without a model of the inner rifling of the boiler tube has been carried out. The calculations include the entire evaporation process from sub-cooled water to super-heated steam, which includes a massive change in fluid density downstream. The simulations show that there is a very large pressure drop across the boiler tube without rifling, while the tube with rifling has a significantly lower pressure drop, due to the lower mass flux, although the relative pressure drop in the rifle tube is significantly higher compared to the smooth boiler tube. We also see that the mass flux in IRBT for design reasons are significantly lower. The model handles perfect the pressure oscillations occurring in the two phase region, as a result of the increased compressibility of the fluid. This instability generates minor enthalpy slugs downstream in the calculations. In the IRBT simulations we experience very low mass flux just before the entrance to the two-phase region, which locally gives a very poor cooling of tube wall and rising wall temperature. We can generally conclude that WENO scheme both numerically and in terms of stability is well suited to solve such an complicated hyperbolic system of PDE's with respect to the transformed independent solution parameters.

5.

References

[1] H. Griem, Untersuchung zur thermohydraulik innenberippter verdampferohre., PhD thesis, Technische Universitat Munchen, Lehrstuhl fur Termische Kraftanlagen. (1).
[2] J. Pan, D. Yang, Z. Dong, T. Zhu, Q. Bi, Experimental investigation on heat transfer characteristics of low mass flux rifled tube upward flow., International Journal of Heat and Mass Transfer. 54 (2011) 2952–2961.
[3] D. Yang, J. Pan, C. Zhou, X. Zhu, Q. Bi, T. Chen, Experimental investigation on heat transfer and frictional characteristics of vertical upward rifled tube in supercritical cfb boiler., Experimental Thermal and Fluid Science. 35 (2011) 291–300.
[4] X. Zhu, Q. Bi, Q. Su, D. Yang, J. Wang, G. Wu, S. Yu, Self-compensating characteristic of steam-water mixture at low mass velocity in vertical upward parallel internally ribbed tubes., Applied Thermal Engineering. 30 (2010) 2370–2377.
[5] X. Fan, S. Wu, Heat transfer and frictional characteristics of rifled tube in a 1000 mw supercritical lignite-fired boiler., School of Energy Science and Engineering, Harbin Institute of Technology, China. 1 (2010) 1–5.
[6] A. O. Johansen, E. B., J. N. Sørensen, Implementation and test of a fifth order central weno scheme for solving hyperbolic balance laws., Applied Thermal Engineering ,1-25. (1).
[7] A. O. Johansen, E. B., Implementation scheme for water steam properties., Applied Thermal Engineering ,1-25. (1).
[8] S. M. Ghiaasiaan, Two-Phase Flow, Boiling, and Condensation in Conventional and Miniature Systems, 1st Edition, Cambridge University Press, Georgia Institute of Technology, 2008.
[9] E. V. Driest, On turbulent flow near a wall., Journal of the Aeronautical Sciences. 23 (1956) 1007–1011.
[10] F. Jirous, Analytische methode der berechnung des naturumlaufes bei dampferzugern, VGB Heft 5 (1978) 366–372.
[11] P. D. Bentz, R. Prasad, Kuldeep, Thermal performance of fire resistive materials i. characterization with respect to thermal performance models., NIST, Building and Fire research Laboratory, Gaithersburg. (MD 20899-8615).
[12] M. Rohrenwerke, Rohre aus warmfesten und hochwarmfesten Stahlen Werkstoffblatter., 1st Edition, MannesMann Rohrenwerke, 1988.
[13] F. Brandt, FDBR-FACHBUCHREIHE - warmeubertragung in Dampferzeugern und Warmeaustauschern., band 2 Edition, Vulkan-Verlag, Essen., 1985.
[14] W. Wagner, H.-J. Kretzschmar, International Steam Tables - Properties of Water and Steam Based on the Industrial Formulation IAPWS-IF97, 2nd Edition, Springer, Berlin Heidelberg, 2008.
[15] G. Capdeville, A central weno scheme for solving hyperbolic conservation laws on non-uniform meshes., J. Comp. Phys.,2977-3014. (227).
[16] M. Castro, B. Costa, W. S. Don, High order weighted essentially non-oscillatory weno-z schemes for hyperbolic conservation laws., Journal of Computational Physics 230 ,1766-1792.
[17] S. Gotlieb, C. Shu, Total variation diminishing runge-kutta schemes., Math. Comp., 73-85 (67).
[18] D. Levy, G. Pupo, G. Russo, Compact central weno schemes for multidimensional conservation., SIAM J. Sci. Comput. ,656-672. (22).
[19] A. Kurganov, E. Tadmor, New high-resolution central schemes for nonlinear conservation laws and convection-diffusion equations., J. Comput. Phys. ,241-282. (160).
[20] A. Kurganov, D. Levy, A third-order semidiscrete central scheme for conservation laws and convection-diffusion equations., SIAM J. Sci. Comp. No.4 ,1461-1488. (22).
[21] C. C. Richter, Proposal of New Object-Oriented Equation-Based Model Libraries for Thermodynamic Systems., 1st Edition, Von der Fakultat fur Maschinenbau, der Technischen Universitat Carolo-Wilhelmina zu Braunschweig., 2008.
[22] A. Bergles, e. a. J.H. Lienhard, Boiling and evaporation in small diameter channels., Heat Transf. Eng. 24 (2003) 18–40.
[23] S. Kakac, B. Bon., A review of two-phase flow dynamic instabilities in tube boiling system., Int. J Heat Mass Transfer. 51 (2008) 399–433.
[24] J.S.Maulbetsch, P.Griffith, A Study of System-Induced Instabilities in Forced-Convection Flows With Subcooled Boiling., 1st Edition, no. 5382-35, NIT Engineering Projects Lab Report, 1965.
[25] J.S.Maulbetsch, P.Griffith, Prediction of the onset of System-Induced Instabilities in Subcooled Boiling., 1st Edition, no. 799-825, EURATOM Report, Proc. Symp. on Two-phase flow dynamics at Eindhoven, 1967.
[26] A.H.Stenning, T.N.Veziroglu, Flow Oscillations Modes in Forced Convection Boiling., 1st Edition, no. 301-316, Heat Transfer and Fluid Mech. Inst., Stanford Univ. Press., 1965.
[27] T. A.H.Stenning, G.M.Callahan, Pressure-Drop Oscillations in Forced Convection Flow with Boiling., 1st Edition, no. 405-427, EURATOM Report, Proc. Symp. on Twophase flow dynamics., 1967.

Hydro Power Systems: Scripting Modelica® Models for Operational Studies in Education

Telemark University College
Faculty of Technology
Porsgrunn, Norway

Dietmar Winkler* Bernt Lie†

Abstract

Telemark University College is offering a master degree program called "Systems and Control Engineering". Most students of that program have a background in either electrical, mechanical, control engineering or a combination of those. Since Norway covers about 99% of its electrical energy demand using hydro-electric power plants it is natural to also educate master students in the subject of hydro power systems.

About three years ago the Telemark University Colleges started a cooperation with the Norwegian power company "Skagerak Energi" in order to offer real-life projects for students and to establish a new teaching course for second year master students called "Modelling and Simulation of Hydro Power Systems". That course teaches the students the basic principles of hydro-electric power generation starting the prediction of precipitation "down" to the distribution of electrical power in the grid with other loads and consumers connected to it.

This paper presents the teaching approach we have taken so far and our evaluations of open-source tools to be used within the "Modelling and Simulation of Hydro Power Systems" course. The evaluations were also focused on possibilities of scripting model simulations.

*Dietmar.Winkler@hit.no
†Bernt.Lie@hit.no

1 Teaching hydro power systems

1.1 Overview

Teaching hydro power systems gives one the great opportunity to deliver combined knowledge of at least three major engineering domains:

- Mechanical engineering
- Electrical engineering
- Control engineering

In detail the course deals with:

- Formulation of mathematical models across different physical domains (e.g., mechanical, electrical, hydrological).
- Introduction to the object-oriented modelling language Modelica.
- Development of a simple hydro power plant model which can be extended to more complex and accurate models.

- The benefit of using object orientation when implementing such models, with special emphasis on how the model can be gradually extended.

We use the modelling language Modelica[1] which was especially designed for models which contain components from different physical domains. The benefit of using Modelica in teaching are for example:

openness Students can look at the exact equation based mathematical description of physical systems

multi-domain nature In Modelica it is possible to connect the different domains (e.g., electrical, mechanical, control) within one model in order to get close representation of the real physical system.

object-orientation Enhancing models in a "top-down" manner is very simple. This means students can start working on simple models and increase the level of detail later on.

1.2 Using modelling and simulation in projects

After having learnt about the mathematical and physical theory of hydro power systems, students can now apply that knowledge in working on operational studies. Those studies consist normally of real-life problems which need to be solved. In the past our students have for example worked on "Modelling and Optimisation of Deviation in Hydro Power Production"[1] and "Stability Analysis of AGC in the Norwegian Energy System"[2]. In the latter example it was especially important to use scripting and optimisation tools.

[1] Modelica® is a registered trademark of the Modelica Association `https://modelica.org`

2 Modelling tool chain used so far

2.1 The modelling language Modelica

Modelica® is a unified object-oriented language for systems modelling. It is developed by the *Modelica Association*[2] which was founded in 1996 and consists of members from industry, university and rersearch organisations.
The *Modelica Association* also develops the free and open-source *Modelica Standard Library*(MSL)[3] which is currently at version 3.2 and consist of 1280 non-trival models and 910 functions. The MSL makes it possible to generate models of complex systems in a simple and quick manner.
Since Modelica is especially suitable for multi-domain modelling and also because of the transparency of its models we decided to base our "Modelling and Simulation of Hydro Power Systems" course on this powerful modelling language.

2.2 The modelling tools

In the course so far, we were using the commercial modelling tool *Dymola*[4]. There are several reasons for this. One is that our students are mainly engineering students with little programming background. Since our hydro power systems course should mainly concentrate on the modelling and simulation tasks and not so much on the programming side we needed something that the students are comfortable working with and can learn within a reasonable short period of time. Basically this means that we needed a Modelica tool that allows to edit models graphically in a drag-and-drop manner rather than doing textual programming.
Another reason was that for the course we also liked to demonstrate the real power of Modelica with detailed models of a complete hydro

[2] `http://www.modelica.org`
[3] `https://modelica.org/libraries/Modelica`
[4] `http://www.dymola.com`

power system. For this task we came across the `HydroPowerLibrary`[5] which includes such complex models and easy to use examples.

2.3 Example from the `HydroPowerLibrary`

A typical example that the students model in the end of the course is a complete hydro power system as depicted in Fig. 1 consisting of:

- Reservoir
- Waterway
- Turbine with turbine regulator
- Generator
- Power grid

With such a model one can investigate the process of synchronising a generator that is driven by water turbine to the grid and then look at the power balance.
There are a lot of interesting aspects that the students can look into. E.g.,

- How aggressive should the turbine controller be?
- when can the electrical connection between the electrical generator and the electrical grid be made?
- what happens when it comes sudenly to a load change on the electrical grid?

And those are just some of the many scenarios that one can simulate with this model. One thing all of the different simulation scenarios have in common though is that one would like to automate the simulations with variations of some parameters, i.e., doing parameter sweeps.

[5]The `HydroPowerLibrary` is developed by Modelon, see `http://www.modelon.com`

2.4 Drawbacks of the commercial tools

Especially the automation of several simulations is something where *Dymola* was kind of weak or cumbersom to use. Also at this point the engineering students begin to see why it might be necessary and more convenient to be able to use a scripting language.
One of the most powerful scripting languages is *Python*[6]. Unfortunately, the tool *Dymola* provides neither a convenient to use own scripting language nor does it provide a direct interface for Python. That is why we started to look at alternatives.
Another drawback, we as an academic institution see, is that students should be learning to use tools that they will also be able to use after they finished their degree at our university college. This might be a kind of moral aspect but a valid one none-the-less since many of our students come from countries where they basically can not afford to buy a licence (even when working at a company). It is also important for the students to be able to reproduce the results of their project and study work without restrictions after they have left higher education.

3 Going Open-Source in Modelling and Simulation

Using Modelica® as an open modelling language is only the first step. We now looked into open-source tools that allows us to create the models in a convenient way, execute the simulation and do post-processing and optimisation.
The most advanced open-source Modelica modelling and simulation tools are currently *OpenModelica*[7] and *JModelica.org*[8].
First we looked at *OpenModelica* which already provides a graphical editor called “OMEdit”. Unfortunately that editor did not appear to be all that stable at the time of writing so we concentrated more on the script interface. Here

[6]`http://www.python.org`
[7]`http://openmodelica.org`
[8]`http://jmodelica.org`

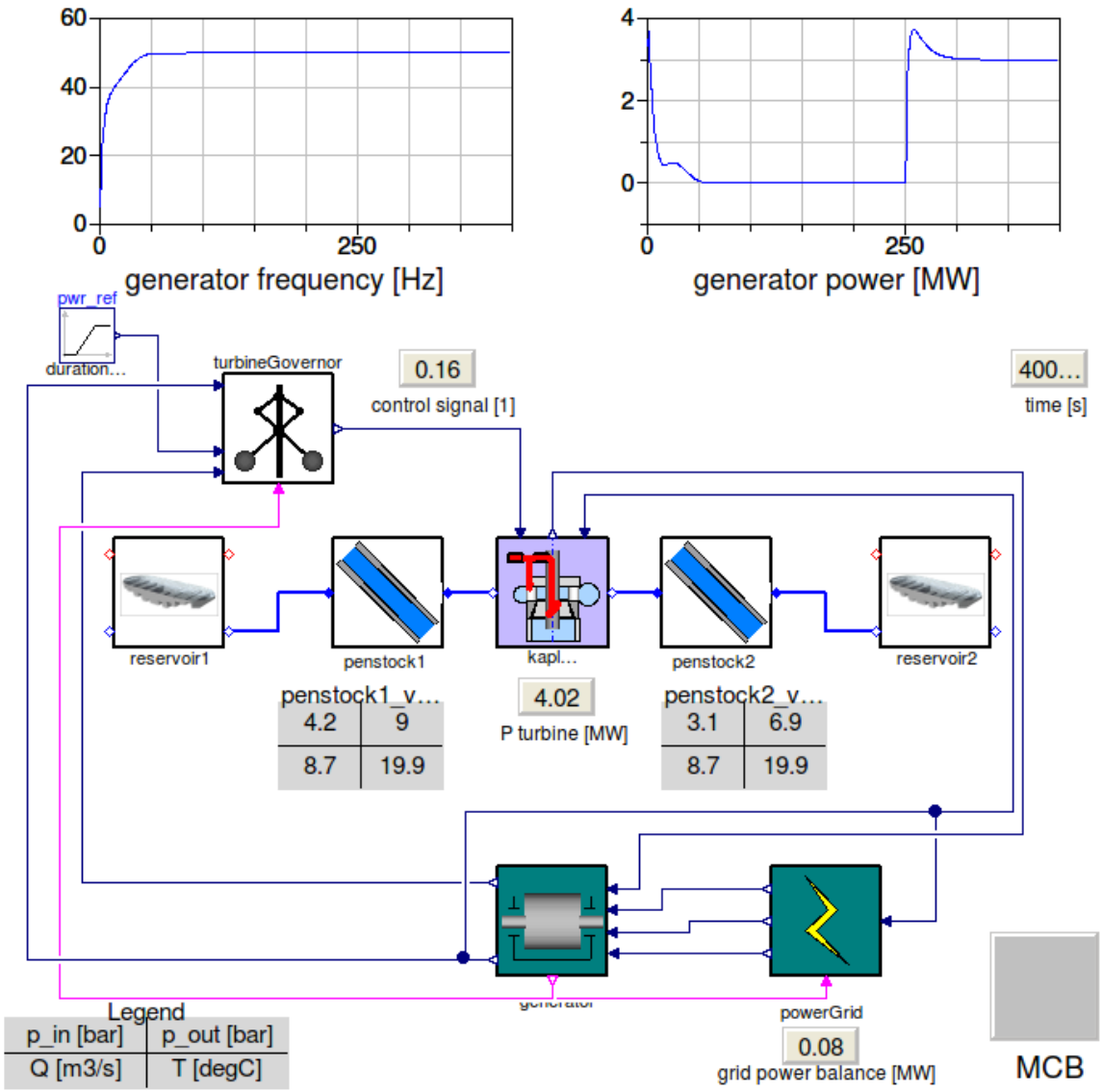

Figure 1: Screenshot from a `HydroPowerLibrary` example modelled in Dymola

OpenModelica provides the possibility to use *MetaModelica*, a special language that was developed not just for scripting but also programming the compiler itself[3]. As of version 1.8.1, *OpenModelica* also provides a beta version of Python Scripting.

JModelica.org is heavily reliant on Python and the whole simulation routine is controlled by using Python. Also does *JModelica.org* use the FMI standard [4] that offers the possibility to use exported models from other simulation tools. Thus we decided to start testing *JModelica.org* at first and wait with *OpenModelica* until the Python interface has become more mature.

Though not yet feature complete when it comes to the Modelica Language Specification[5] both tools are already powerful enough to simulate hydro power systems. However the remaining part of the paper shall present the experiences we made with *JModelica.org*.

3.1 Simplifying the models

The first thing we tried was exporting a `HydroPowerLibrary` model as a FMU and then later importing this into *JModelica.org*. Unfortunately this was not possible and we concluded this was possibly caused by either a non-standard export on the one side or a not fully implemented import functionality on the other

side.
However we continued with loading a simple `HydroPowerLibrary` model directly. Again this failed because of lacking support of certain functions used in the `HydroPowerLibrary` model. In the end we decided to build a very simplified model that represents the functionality of a hydro power system consisting of a turbine and generator equivalent that is controlled by a turbine controller and is that then synchronised with the grid.
The `SimpleSystem` is depicted in Fig. 2.
The idea for this model is that one can look at the turbine and generator unit as torque source `hpTorque` that is used to accelerate their inertia `hpInertia`. The before an electrical generator can be connected with the electrical grid it needs to be synchronised. The process of synchronisation consists for several prerequisites:

- Same direction of rotation
- Same voltage level
- Same frequency

Now the simple model can only be used to simulate the frequency difference and the direction of rotation, i.e., the run-up of the generator. But this is actually sufficient for quite a lot of case studies.
When we only look at the active power balance then we can think of the electrical grid as a large inertia `gridInteria`. If the generated power and the load power are in balance then the grid inertia rotating at a constant frequency of $50\,Hz$. Any electrical load can be represented via the `loadTorque` that can be calculated by:

$$T_{el} = \frac{P_{el}}{\omega^*}$$

where T_{el} stands for the electrial torque, P_{el} for the electrical power and ω^* for the specific rotational velocity[9] The last central component in the `SimpleSystem` is the synchronisation switch which is represented by a mechanical clutch `SyncSwitch` which closes when the frequencies of the generator and the grid are near enough. In this case we are starting to close the "switch" when the frequencies are within $1\,Hz$ of each other.

[9]Ddepending on the number of poles in an electrical generator the angular velocity can vary and needs to be taken into account when calculating the rotatonal energy.

3.2 Simulation with *JModelica.org*

The simplified system from Fig. 2 could almost be loaded into *JModelica.org*. The only thing that we needed to fix was that *JModelica.org* did not cope with some of the more advanced initialisation options used in the clutch model but not actually needed in our case.
Error messages that we needed to fix were:

```
The binding expression of the
variable initType does not match
the declared type of the variable
```

and

```
String variables are not supported
```

The simple solution was to simply remove those parts from the models used from the *Modelica Standard Library*. This is best achieved by doing as so called "save total" of the model and then manipulating the used models there.
The following script will then generate a successful simulation of the `SimpleSystem` in *JModelica.org*:

```
# Import the function for compilation
# of models and the FMUModel class
from pymodelica import compile_fmu
from pyfmi import FMUModel
# Import the plotting library
import matplotlib.pyplot as plt

# Define model file name and class name
mofile = 'SimpleSystemTotal.mo'
model_name = 'SimpleSystem'

# Compile model
fmu_name = compile_fmu(model_name,mofile)

# Load model
grid = FMUModel(fmu_name)
```

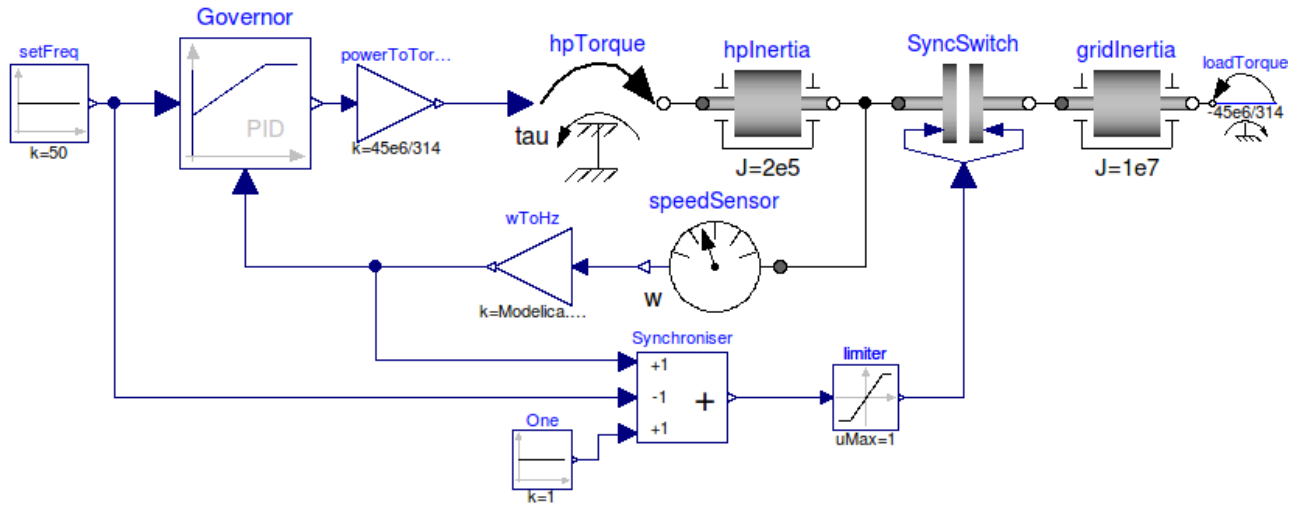

Figure 2: Screenshot of a simple system

```
# Simulate the model
res = grid.simulate(final_time=600)
f_gen = res['wToHz.y']
f_grid = res['gridInertia.w']
t  = res['time']

# Generating the Plot
plt.figure(1)
plt.title('Synchronising a generator')
plt.ylabel('Frequency [Hz]')
plt.xlabel('Time [s]')
plt.plot(t, f_gen, t, f_grid)
plt.grid()
plt.show()
```

and the resulting plot can be seen in Fig.3

3.3 Scripting and Optimisation

Now that we can run a simulation an extension for doing a parameter sweep can be easily achieved. It follows a variant of the previous simulation script only this time we run several simulations after each other in order to see the effect of having different hydro plant powers available (in the range of $40\,MW \ldots 140\,MW$):

```
# Import the function for compilation
# of models and the FMUModel class
from pymodelica import compile_fmu
from pyfmi import FMUModel

# Import the plotting library
import matplotlib.pyplot as plt
# Import numpy
import numpy as np

# Define model file name and class name
mofile = 'SimpleSystemTotal.mo'
model_name = 'SimpleSystem'

# Compile model
fmu_name = compile_fmu(model_name,mofile)

# Load model
grid = FMUModel(fmu_name)

# Define initial conditions
p_var = 10
p_min = 40e6
p_max = 140e6

turbine_gain = np.linspace(p_min,p_max,p_var)/
               (2*np.math.pi*50)

# Setup of plot
plt.figure(1)
plt.hold(True)
plt.title('Synchronising a generator')
plt.ylabel('Frequency [Hz]')
plt.xlabel('Time [s]')

# Running the different simulations
```

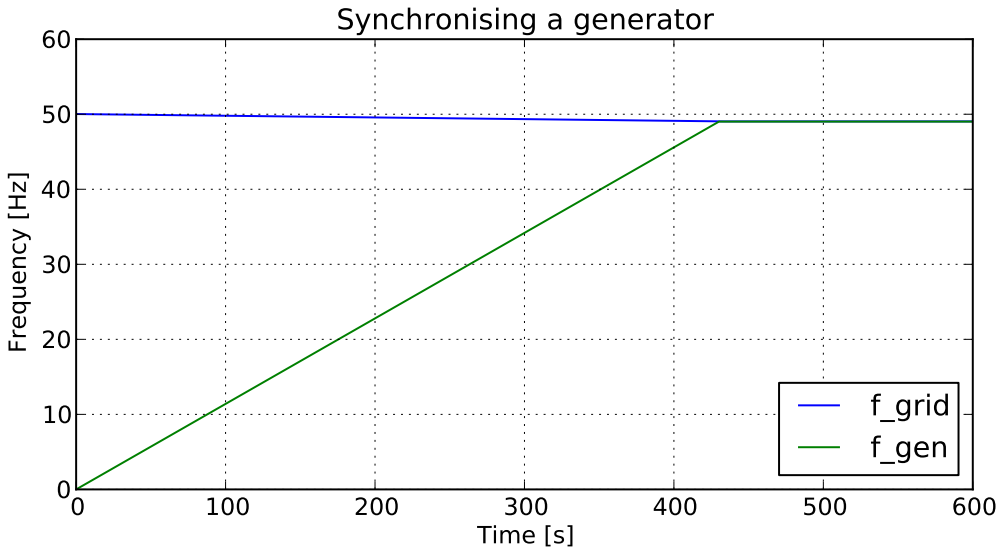

Figure 3: Simulation result from *JModelica.org*

```
for i in range(p_var):
   # Set initial conditions in model
   grid.set('turbineGain',turbine_gain[i])
   # Simulate
   res = grid.simulate(final_time=600)
   # Get Simulation result
    f_gen = res['wToHz.y']
    f_grid = res['gridInertia.w']/
             (2*np.math.pi)
    t  = res['time']
    plt.plot(t, f_gen, t, f_grid)
plt.grid()
plt.show()
```

Using thise code we will get a plot like shown in Fig. 4 where the different rising graphs represent the frequencies of the accelerated turbine-generator unit. For example can one see that the starting power of $P_{gen} = 40W$ is in this case not enough to bring back the grid frequency to $50Hz$.

4 Conclusion

Our study has shown that is possible to simulate Hydro Power Systems with open-source tools that also allow for convenient scripting. However the there is still room for improvement both, on the compiler side in order to support more Modelica models, especially from the Modelica Standard Library. The other thing that is actually still lacking (but in development) in *JModelica.org* is a graphical editor. Without such a tool it will be hard to convince engineering students of the benefits and possibilities of Modelica and its rich modelling potentials.

The scripting itself is thanks to Python very easy and quick to learn and the produced plots are thanks to `Matplotlib` also more advanced as what *Dymola* would be able to produce.

To be honest, the open-source tools are not quite mature enough to allow us to completely switch our courses away from the commercial solutions we are currently using. But at least for student projects (i.e., where students can invest more time and energy) those offer a very interesting alternative and we are definitely continuing the evaluation as the tools keep improving all the time.

References

[1] D. Winkler, H. M. Thoresen, I. Andreassen, M. A. S. Perera, and B. R. Sharefi, "Modelling and Optimisation of Deviation in Hydro Power Production," in *Proceedings of the 8th International Modelica Conference*, vol. 1, (Dresden, Germany), Modelica Association, Modelica Association

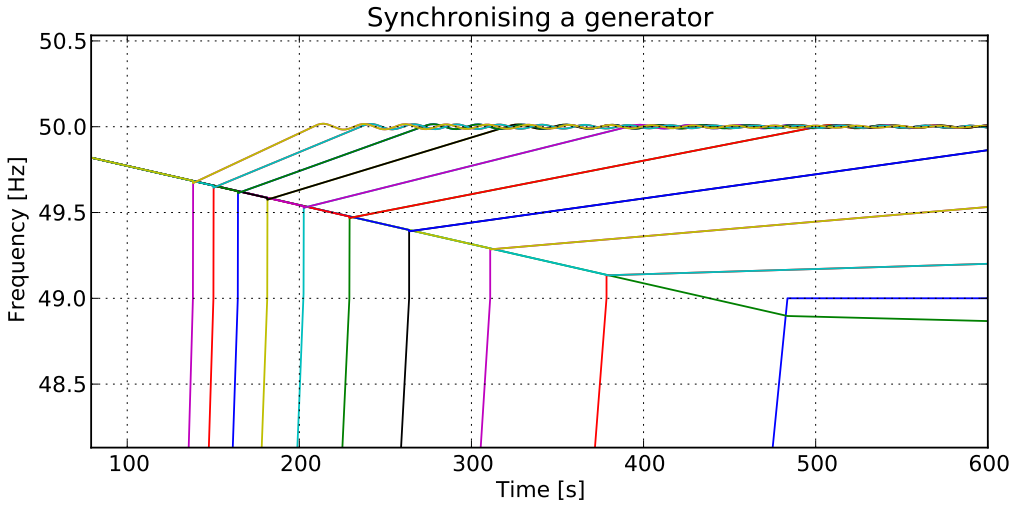

Figure 4: Simulation result of a simulation sweep with varying $P_{gen} = [40 \ldots 140]\,MW$

and Technische Universität Dresden, 20th - 22rd March 2011. ISBN: 978-91-7393-096-3 Linköping Electronic Conference Proceedings ISSN (print):1650-3686 ISSN (online):1650-3740.

[2] I. Andreassen and D. Winkler, "Stability Analysis of AGC in the Norwegian Energy System," in *Proceedings of 'The 52nd Scandinavian Conference on Simulation and Modeling (SIMS 2011)'* (S. o. S. D. o. S. Dahlquist, Erik (MÏardalen University and T. (MERO), eds.), (Västerås, Sweden), pp. 133–143, Scandinavian Simulation Society, Mälardalen University, 29th - 30th September 2011. ISBN: 978-91-977493-7-4.

[3] A. Pop and P. Fritzson, "Metamodelica: A unified equation-based semantical and mathematical modeling language," in *Modular Programming Languages* (D. Lightfoot and C. Szyperski, eds.), vol. 4228 of *Lecture Notes in Computer Science*, pp. 211–229, Springer Berlin / Heidelberg, 2006. 10.1007/11860990_14.

[4] M. . A. M. . B. C. . C. C. . E. H. . J. A. . M. J. . M. M. . N. T. . N. D. . O. H. . P. J.-V. . W. S. Blochwitz, T. ; Otter, "The functional mockup interface for tool independent exchange of simulation models," in *Proceedings of the 8th International Modelica Conference, March 20th-22nd, Technical Univeristy, Dresden, Germany*, Linköping Electronic Conference Proceedings, pp. 105–114, Linköping University Electronic Press, Linköpings universitet, March 2011.

[5] Modelica Association, *Modelica®– A Unified Object-Oriented Language for Physical Systems Modeling – Language Specification*, version 3.3 ed., 5th September 2012.

Modeling Fluid and Energy Flow in Liquid Dominated Hydrothermal Systems

Larus Thorvaldsson
Halldor Palsson

October 2, 2012

Abstract

A new modeling approach of fluid flow in geothermal reservoirs is presented in the paper. Two models are presented, one which is applicable for groundwater hydrology and another more complex for hydrothermal systems. The performance of the groundwater model is then compared with the well known Theis solution.

Both problems are formulated and solved by using a highly customizable set of C++ libraries and tools, collectively named OpenFOAM, along with polynomial interpolation for the physical properties of water as functions of temperature.

Preliminary results from a more general modeling work on hydrothermal systems are presented in simple case studies, showing the basic abilites of the programming platform to solve problems for flow in porous media. It is concluded that the modeling framework is both flexible and efficient, and an added benefit is that it is under constant improvement by a large group of developers and incorporates cutting edge technologies in numerical analysis for mathematical modeling.

1 Introduction

Using numerical methods to solve non-linear partial differential equations (PDE) first became feasible in the late 1960's with the advent of digital computers. These methods were first applied to problems involving groundwater as well as oil and gas reservoirs, while the modelling of geothermal reservoirs lagged behind [1]. This was mostly due to the fact that the modelling of geothermal reservoirs is considerably more complicated where the equations are typically of the advection-diffusion type, describing conservation of mass, momentum and thermal energy. These equations are furthermore coupled with each other and are frequently non-linear, which adds considerably to the complexity of their solutions.

The earliest efforts to apply numerical models to geothermal reservoirs were made in the early 1970's, while the usefulness of numerical modelling did not begin to gain acceptance by the geothermal industry until after the 1980 Code Comparison Study [2]. Since that study was performed, the experiences gained in carrying out site-specific studies as well as generic reservoir modelling studies have led to a constant improvement in the capabilities of numerical reservoir models.

Over the last 20 years computer modeling of geothermal reservoirs using finite volume methods has become a standard practice. The most common approach is to apply the TOUGH2 code, developed by the Earth Sciences Division of Lawrence Berkeley National Laboratory in the 1980's. TOUGH2 is a general numerical simulation code for multi-dimensional coupled fluid and heat flows of multiphase multicomponent fluid mixtures in porous and fractured media [3].

An alternative modeling work is presented here, based on OpenFOAM, which is a library of highly efficient codes developed for the solution of general PDE's. The object orientation and operator overloading of C++ has enabled the developers of OpenFOAM to build a framework for computational fluid dynamics that enables modelers to work at a very high level of abstraction [4]. This makes it possible to manipulate the set of partial differential equations that describe the problem and customize the solver itself for each class of cases that needs to be solved. This is the main motivation for using OpenFOAM, as an alternative to currently existing models, such as TOUGH2.

2 Methods and Materials

In this section the governing equations for two phase flow in porous media are presented in the form they are implemented in a numerical model. This involves the equations themselves, fluid properties, boundary conditions and then the programming implementation itself.

2.1 Solver for groundwater systems

Implementation of new models in OpenFOAM is in most cases relatively simple. Low level operations regarding individual computational cells or the solution of linear systems do not need to be addressed in most cases, and the programming framework is designed with customization in mind.

As an example of this, one can take the basic equation that describes hydraulic head in a homogenous aquifer over time

$$\frac{\partial p}{\partial t} = \frac{T}{S}\nabla^2 p \tag{1}$$

where T is the transmissivity and S is the storativity of the aquifer.

This equation can easily be implemented in OpenFOAM by the following lines

```
fvm::ddt(p) - fvm::laplacian(T/S, p)
```

where the transmissivity and storativity have been defined. Nevertheless more coding is needed, such as defining the variables as field functions, but the developer does not need to become familiar with the inner workings of the numerics. A good example are the functions `fvm::ddt` and `fvm::laplacian` shown above, which will automatically result in a construction of a linear system for an implicit solution of an unsteady diffusion equation.

In order to verify the solver, it is possible to compare it with the well known similarity solution to equation 1 that Theis gave in 1935 for a homogenous confined aquifer [5]. By using the similarity transform

$$u = \frac{r^2 S}{4Tt} \tag{2}$$

where r is the radial distance from the well and t is time, Theis showed that the drawdown s could be expressed in terms of the well function W such that

$$s = \frac{Q}{4\pi T} W(u). \tag{3}$$

Here Q is the volumetric extraction of water from the well and W is the well function, which is known as the exponential integral outside of hydrogeology literature and is defined as

$$E_1(u) = W(u) = -\gamma - \ln u + \sum_{k=1}^{\infty} \frac{(-1)^{k+1} u^k}{k \cdot k!} \tag{4}$$

where $\gamma \approx 0.57721$ is the Euler-Mascheroni constant.

Since an analytical solution exists for this case it is ideal for testing purposes of the code. However there are some differences that should be addressed, for example the well has to have some finite surface area, in order to define the boundary conditions of the aquifer, and the size of the aquifer has to be finite.

2.2 Solver for a hydrothermal system

In order to model two phase flow in porous media it must be assumed that mass and energy are conserved. The continuity equation describes mass conservation and is given such that

$$\frac{\partial}{\partial t}(\rho) + \nabla \cdot (\rho \vec{u}) = 0$$

where ρ is the average density of the phases and $\vec{u}$ is the superficial velocity. This eqation is solved for every time step in order to ensure continuity.

The solver then applies a PIMPLE pressure-velocity corrector loop, where SIMPLE and PISO algorithms have been merged for a more robust pressure-velocity coupling. This makes it possible to solve stiff differential equations by coupling a SIMPLE outer corrector loop with a PISO inner corrector loop, while also achieving more stability for larger time-steps compared to PISO [6].

In this case the problem at hand involves laminar flow, where inertial forces are negligable Darcy's law can be applied to the velocity equation, giving

$$\frac{\partial}{\partial t}(\rho \vec{u}) + \frac{\mu}{\kappa} \vec{u} = 0 \tag{5}$$

instead of the full Navier-Stokes equations.

The energy equation is then given as

$$\frac{\partial}{\partial t}(\rho h) + \nabla \cdot (\rho \vec{u} h) = \nabla \cdot (\alpha \nabla h) \tag{6}$$

where h is the enthalpy of the water and alpha is the effective thermal diffusivity of the water. Note that the porosity is disregarded here, but without the loss of generality.

The physical properties of density ρ, viscosity μ and heat capacity c_p are all assumed to be seventh degree polynomial fuctions of temperature, such that

$$f(T) = \sum_{i=0}^{7} a_i T^i \tag{7}$$

where f is the physical property and a_i are the respective coefficients given in Table 1.

Table 1: Coefficients for physical properties

	$\rho(T)$	$\mu(T)$	$c_p(T)$
a_0	-4.844433993781387e+04	27.732508110282716	1.869467009204107e+06
a_1	1.004443612129644e+03	-0.578169744144130	-3.863103544592875e+04
a_2	-8.796904074130724	0.005172930468241	3.434316124950962e+02
a_3	0.043005953646541	-2.573544345985454e-05	-1.698437537901375
a_4	-1.265747239408929e-04	7.686291653398755e-08	0.005045265306273
a_5	2.240156150413993e-07	-1.377781528721409e-10	-9.000139889194412e-06
a_6	-2.205980438513678e-10	1.372177963166062e-13	8.925534508747834e-09
a_7	9.319510246689768e-14	-5.856417743042797e-17	-3.795296368702309e-12

3 Results

3.1 Groundwater system

A one dimensional axi-symmetric mesh was generated for simulating groundwater flow around a well where water was being extracted. The mesh was divided into 100 cells.

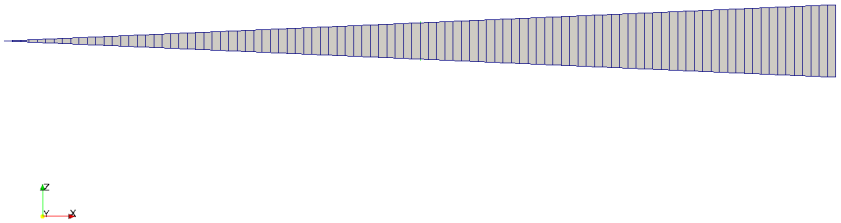

Figure 1: A top-down view of the axi-symmetrical one-dimensional mesh.

The mesh can be seen in Figure 1, its radius extends to 1 km, but the well is assumed to have a radius of 10 cm.

Figure 2 shows the numerical solution and the Theis solution at time $t = 10^5$. It can be seen that there is good agreement between the solution, despite the approximations in the numerical solution, such as the aquifer only extending to a finite radius from the well, and the requirement on the well to have some finite surface area.

Figure 3 shows the relative difference between the two solutions. It can be seen that they agree very well, where the maximum difference between the two

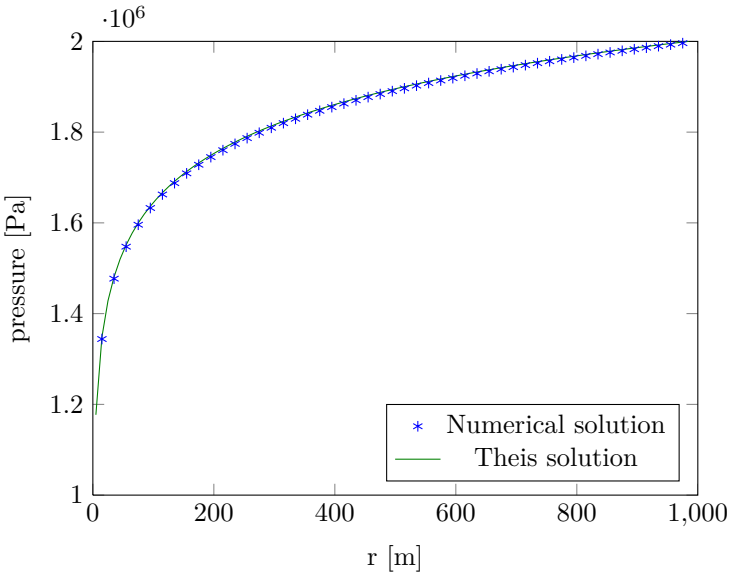

Figure 2: A comparison of the Theis solution and the numerical solution for a confined aquifer up to 1 km radius

is below 0.35%.

3.2 Natural convection in a ideal reservoir

The case study for hydrothermal systems is more complex than the previous one. The problem is modeled as two dimensional geothermal system, with constant temperature at its roots and at its surface. The system is assumed to have homogenous permeability of $\kappa = 10^{-10}$ and a temperture of 280 K at the bottom and 380 K at the top.

Figure 4 shows the temperature distribution in the reservoir resulting from the temperature difference between the roots of the system and the top. The figure shows irregular behaviour of upwards flowing regions and downwards flowing regions. This is even indicated more clearly if the velocity vectors are considered where hot plumes rise from the bottom to the top and drop again once they are cooled.

Figure 5 shows the density distribution, which drives the flow. Since it is a function of temperature it follows figure 4 closely. Lighter hotter plumes can be seen rising, while colder denser plumes fall back down.

4 Discussion

This paper illustrates the applicability of the OpenFOAM platform to take on current problems in geothermal reservoir modeling as well as flow in porous media in general. Because of the structure of the OpenFOAM libraries, the partial differential equations which describe the problems and the models themselves can be implemented in a consistent manner with minimal work.

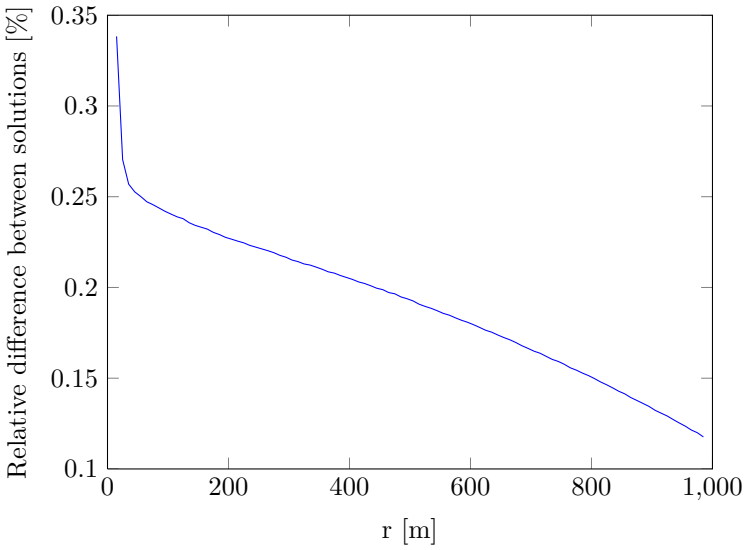

Figure 3: The relatice difference between the Theis solution and the numerical solution up to 1 km radius

However this work is still in progress, so there are many factors still unaccounted for. The hydrothermal model is for example not compressible, which makes it lack some features of the groundwater model. The next step in the project is to combine those two models, where the physical properties are also functions of pressure by applying a thermodynamic formulation such as IAPWS-IF97.

Currently the main focus of the research is to include phase changes in the model and account for a two phase mixture within some regions of the reservoir. The main challenge in this work is to ensure a stable solution despite the discontinuities in physical properties that arise as a result of phase changes. This has still not been resolved adequately and some instabilities are seen in two phase solutions, hence no results are shown here for such computations.

Despite those current issues, it can be proposed that the OpenFOAM platform is very promising for geothermal reservoir modeling. However, such further research and modeling work will always require comparison work, especially with well known and mature reservoir models.

On a whole, this approach in modeling geothermal reservoirs has several advantages over present methods. Since the libraries are highly customizable, wellbore-reservoir interaction can for example be modeled in a flexible way and adjusted to represent known data from measurements. Furthermore, standards such as IAPWS-IF97 for fluid properties can be implemented directly into the code, giving a more accurate description of hyrdothermal systems.

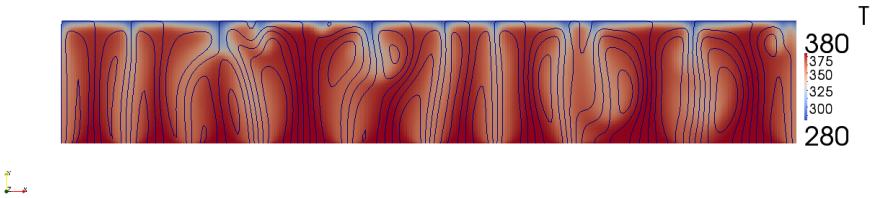

Figure 4: The temperature distribution and streamlines of a hydrothermal system

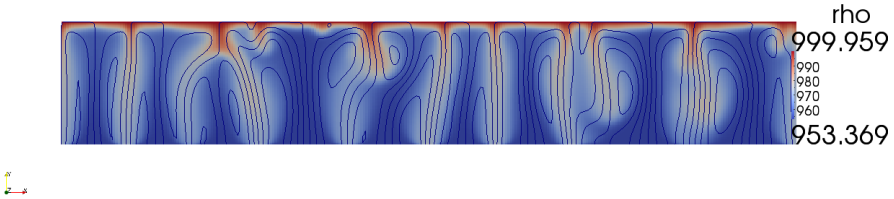

Figure 5: The density distribution and streamlines of a hydrothermal system

References

[1] Michael J. O'Sullivan. State of the art of geothermal reservoir simulation. *Geothermics*, 30(4):395–429, August 2001.

[2] Stanford Geothermal Program. Proceedings of the Special Panel on Geothermal Model Intercomparison Study. In *Report SGP-TR-42*, Stanford, CA, 1980.

[3] Karsten Pruess. TOUGH2 — A General Purpose Numerical Simulator for Multiphase Fluid and Heat Flow. Technical Report May, Lawrence Berkeley Laboratory, Berkeley, California, 1991.

[4] H G Weller, G Tabor, Hrvoje Jasak, and C Fureby. A tensorial approach to computational continuum mechanics using object-oriented techniques. *Computers in Physics*, 12(6), 1998.

[5] CV Theis. The relation between the lowering of the piezometric surface and the rate and duration of discharge of a well using groundwater storage. *Transactions - American Geophysical Union*, 16:519–524, 1935.

[6] Miguel a. Rodrigues, Luis Padrela, Vitor Geraldes, José Santos, Henrique a. Matos, and Edmundo Gomes Azevedo. Theophylline polymorphs by atomization of supercritical antisolvent induced suspensions. *The Journal of Supercritical Fluids*, 58(2):303–312, September 2011.

Longterm hydro and geothermal reservoir operation

In order to find the optimal way to model a hydro dominated system one needs to avoid unnecessary spillage of water. The operation cost of thermal plants is in accordance with used fuels while the source of energy for geothermal plants is free and for short time considerations unlimited supply. Hydro plants on the other hand also have a free source of energy but limited supply. To avoid unnecessary spillage Lindqvist (1962) essentially proposed a method to give value to the water stored in a reservoir in order to find optimal ways for the operation of power systems. This water value method is used in Landsvirkjun proprietary long term reservoir simulation software named LpSim but has been developed futher. LpSim simulates the system operation iteratively in a two step process.

First a dynamic programming algorithm is used for water value calculation. The water value is the price of water formulated as a function of reservoir volume and time. The water value defines the strategy used for releasing water from the reservoirs. The second step is the simulation of system operation for a period of N years with time resolution down to one day. Simulated values are; releases from reservoirs, generation in hydro, geothermal and thermal power stations, transmission on a simplified DC transmission system and delivery of energy to customers. Stochastic nature of inflows is accounted for by simulating the operation several times for different inflow scenarios.

One of the main drawbacks of using dynamic programming for water value calculation is it's sensitivity to dimensions often called ,,the curse of dimensionality". To avoid this problem a simplified version of the power system is used in water value calculation often containing only one equivalent reservoir.

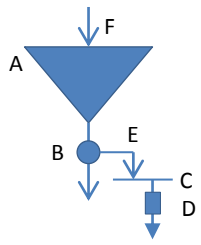

Figure 1 : Simplified system used in water value calculation. A. Reservoir, B. Generator, C. Bus, D. Load,E. Transmission line.

A widely known method for addressing this simplified problem is to combine all reservoir volumes and power plants into one and then the inflow into the equivalent reservoir becomes the sum of inflow into individual reservoirs in the original system. By doing this the characteristics of the inflow into the equivalent reservoir become the mix of inflow characteristics into individual reservoirs. However, since the original inflow characteristics are essential to the operation of the whole system this mixture of characteristics can potentially become a bad approximation.

To avoid this problem, LpSim constructs three equivalent reservoirs, each having a sum of inflows that have similar characteristics and belong to the same subsystem. The water value for each subsystem is then calculated. This way the main inflow characteristics can be preserved and mapping the watervalue onto the true system can be done in a simple way.

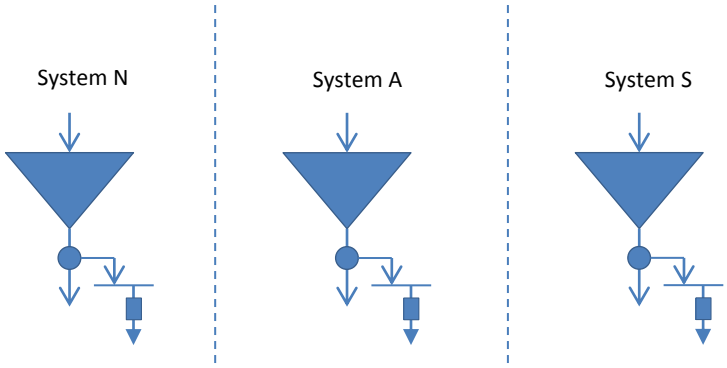

This method has the drawback that the load for each subsystem is not known as this method does not take into account the transmission of energy between subsystems using the transmission system.

To solve this problem Landsvirkjun has developed a simple iterative process.

1. The water value for the system is calculated by combining all reservoirs and hydroelectric stations into a three reservoir equivalent system
2. The water value is applied to all reservoirs not accounting for different inflow characteristics

3. The operation of the original system is simulated with week long timesteps. Comparing the cost of hydroelectrinc generation to thermal using the water value.
4. Now a second water value calculation is prepared by splitting the system into subsystems. The load for each system is the local load plus the exported energy to other subsystems minus the import from other subsystems as it was simulated in the first simulation phase (3). This way the method accounts for transmission possibilities between the subsystems.
5. Based on new water values the operation of the original system is simulated again.
6. Step 4 is repeated if the last simulation resulted in better operation than the last simulation.

The heuristic approach described here has been tested extensively on Landsvirkjuns system and outperforms the original method (step 1 to 3) when system load is high. That is sufficient for Landsvirkjun a hight load is essential in many practical studies. The water value converges under normal conditions after three calculation steps (1 and 4) but the convergence must constantly be monitored.

Typical reduction is cost of thermal production and power purchases is in the range of 20-40%.

References

Lindquist, J. 1962. "Operation of a hydrothermal electric system: A multistage decision process", AIEE Journal (April 1962).

Skuli Johannsson, Elias B Eliasson, "Simulation Model of the Hydro-Thermal Power System in Iceland", www.veldi.is (2002)

PROCEEDINGS, 53rd SIMS Conference on Simulation and Modeling
The National Energy Authority (NEA), Reykjavik, Iceland, October 3 - 6, 2012

A COUPLED WELLBORE-RESERVOIR SIMULATOR UTILIZING MEASURED WELLHEAD CONDITIONS

Halldora Gudmundsdottir, Magnus Thor Jonsson and Halldor Palsson

University of Iceland
Hjardarhagi 2-6
Reykjavik, 107, Iceland
e-mail: halldorag@gmail.com

ABSTRACT

The main objective in this study is to develop a coupled wellbore-reservoir simulator to allow for more integrated modeling and to use wellhead conditions to a greater extent than has been done so far by defining them as main inputs to the coupled model. The program TOUGH2 is used to simulate the behavior of a reservoir while a new model, FloWell, is designed to simulate two phase flow in a wellbore. Finally, a detailed numerical model of the Reykjanes geothermal field in Iceland is constructed, including the coupled FloWell-TOUGH2 model.

FloWell produced simulations in good agreement with pressure logs from wells at Reykjanes and Svartsengi geothermal fields. An inverse estimation with iTOUGH2 was effective in finding new permeabilities for the Reykjanes reservoir, providing a reasonable match for the natural state of the reservoir as well as the observed pressure drawdown. Predicting the response of Reykjanes reservoir in 2012-2027, for a production to maintain 150 MW_e power generation with 77.8 kg/s injection, caused the mass being removed at a higher rate than physically possible. Increasing the injection to 220 kg/s resulted in a steady decline in pressure and after 15 years of simulation a total of 18 bar drawdown in pressure was detected in the reservoir and 12 bar at the boundaries.

NOMENCLATURE

A	cross sectional area [m^2]
d	diameter [m]
f	friction factor
Fr	Froude number
g	acceleration due to gravity [m/s^2]
G	mass velocity [kg/m^2s]
h	enthalpy [J/kg]
$\dot{m}$	mass flow [kg/s]
k	permeability [mD]
p	pressure [Pa]
$\dot{Q}$	heat loss [W/m]
PI	productivity index
Re	Reynolds number
S	slip ratio
u	velocity [m/s]
We	Weber number
x	steam quality
z	axial coordinate
Φ	friction correction factor
σ	surface tension [N/m]
α	void fraction
ρ	density [kg/m^3]
μ	dynamic viscosity [Pa/s]
ε	roughness [m]

Subscripts

l	liquid phase
g	gas or vapor phase

INTRODUCTION

With growing world population and increasing environmental concerns, the demand for renewable energy and sustainable use of resources is steadily rising. Excessive exploitation of geothermal resources is often pursued, resulting in cooling of rocks, reduced production capacity and finally depletion of geothermal reservoirs. Mathematical models are therefore one of the most fundamental tools in geothermal resource management for they can be used to extract information on conditions of geothermal systems, predict reservoir's behavior and estimate production potential (Axelsson, 2003).

Most reservoirs are monitored by descending equipment to measure pressures and temperatures in wells. From these measurements the drawdown in pressure in a reservoir can be estimated. This is a time consuming and expensive process which usually involves a production stop in producing geothermal wells. On the other hand, well conditions are observed constantly by measuring instruments

accessible at the top of wells. From the information gathered at the wellheads much can be learned about the behavior of wells and consequently the reservoir behavior. Therefore, a method for simulating the response of geothermal systems to exploitation, such as the drawdown in pressure, by easily obtained wellhead parameters is very desirable.

The main objective in this study is to create a practical tool to evaluate the state of geothermal reservoirs and well performances using measured wellhead conditions and inverse analysis. This is to be done by coupling a wellbore simulator to a reservoir simulator with the measured conditions as main inputs. For this purpose the program TOUGH2 is used to simulate the multi phase flow in a reservoir while a new wellbore simulator, FloWell, is designed to simulate the behavior of wells. The inverse analysis, performed with the program iTOUGH2, enables continuous evaluation of chosen parameters in both FloWell and TOUGH2 and the measured wellhead conditions provide up to date data to model the current situation in the geothermal system.

In addition to coupling FloWell to TOUGH2 the wellbore simulator FloWell is validated with pressure logs from the Reykjanes and Svartsengi geothermal fields in Iceland. Finally, a detailed numerical model of the Reykjanes geothermal field including the coupled FloWell-TOUGH2 model is constructed and used in several forecasting scenarios where different reservoir management options are examined.

THE PHYSICAL MODEL FLOWELL

Following sections describe the mathematical approaches behind the wellbore simulator FloWell. The expressions of the governing equations for single and two phase flow proposed by Pálsson (2011) are used in this study.

Single phase flow

The continuity equation derives from conservation of mass and can be written as

(1)

The energy equation contains a kinetic energy part, gravitational potential energy part and thermal energy part. The equation can be written as

(2)

The momentum equation contains inertia, pressure changes, hydrostatic pressure and head loss part. The relation is written as follows

(3)

where f is the friction factor and d is the pipe diameter. Possible relations for the friction factor are the Blasius equation for smooth pipes

(4)

and the Swamee-Jain relation, where the effect of pipe roughness is included;

(5)

The Reynolds number used for the evaluation of the friction factor is defined as

(6)

Two phase flow

In two phase flow the flow consist of liquid and vapor states. Assuming constant pipe diameter, using the void fraction definition and introducing the uniform velocity u instead of the actual velocities, the continuity equation becomes

(7)

Similar to single phase flow, the energy equation can be written as

(1)

By using the mass fraction x, the uniform velocity u and the partial derivatives the energy equation can be expressed on the form

(2)

where γ is defined as

(3)

The momentum equation for two phase flow can be written as

(4)

where Φ^2 is the frictional correction factor for pressure loss in two phase flow and η is defined as

(5)

Since u is based on a fluid with liquid properties, the friction factor is evaluated based on

(6)

Friction correction factor

Various relations exist for the friction correction factor Φ^2. Here, two relations will be presented, the Friedel and Beattie approximations. The Friedel correction factor is defined as

(7)

where

(8)

(9)

(10)

(11)

(12)

(13)

The ρ_x is the homogenous density based on steam quality. The Bettie correction factor is much simpler, and can be calculated by a single equation (García-Valladares et al., 2006)

(14)

Void fraction definition

One of the critical unknown parameter in predicting pressure behavior in a wellbore is the void fraction, which is the space occupied by gas or vapor. Countless void fraction correlations have been created and it can often turn out to be a difficult task choosing the appropriate correlation.

The homogeneous model is the most simplified. The two phases, liquid and vapor, are considered as homogeneous mixture, thereby traveling at the same velocity. Another approach is to assume that the phases are separated into two streams that flow with different velocities. The modified homogeneous model introduces the slip ratio, *S*, which is the ratio between the flow velocities at given cross section. The model can be written as

(15)

In the homogenous model it is assumed that the slip ratio is equal to one. Other models extend the simple homogenous flow model by using other derived relations as the slip ratio. Zivi (1964) proposed that the slip ratio was only dependent on the density ratio of the phases;

(16)

Chisholm (1973) arrived at the following correlation for the slip ratio

(17)

One of the more complex void fraction based on slip ratio is the one introduced by Premoli et al. (1970). Their slip ratio is defined as

(18)

where

(19)

(20)

(21)

(22)

(23)

The Lockhart-Martinelli correlation (1949) is often chosen due to its simplicity. In this model, the relationship between void fraction, steam quality, density and viscosity is derived as

(24)

Rouhani and Axelsson (1970) proposed a void fraction computed by a semi-empirical equation given as

(25)

ρ_g ρ_g ρ_l

This model is more extensive than previous model, where it takes into account the effects of cross sectional are of the pipe, mass flow rate of the mixture, surface tension and gravitation.

THE MODEL TOUGH2

TOUGH2 is a general numerical simulator for non-isothermal multi phase flow in porous and fractured media. TOUGH2 calculates the thermodynamic conditions present in a predefined geothermal reservoir by integrating basic mass and energy balance equations for a given domain. The mass and energy equations are discretized in space based on an integral finite difference method. To obtain numerical stability required for multi phase flow calculations the time is discretized as a first order finite difference in a fully implicit manner. This results in a set of coupled nonlinear equations which are solved by employing Newton-Raphson iteration. TOUGH2 accounts for sinks and sources in calculations and the generation rates can be time dependent or independent. Furthermore, it can be assumed that wells operate on deliverability against fixed bottomhole pressures and productivity indices (Pruess, 1999).

THE MODEL ITOUGH2

Inverse problems often lead to difficult optimization routines with no straightforward solution. Therefore, no general method is at hand to solve all inverse problems. The most common formulation is based on system identification techniques and least-squares fitting of parameterized models to measured data. In brief, inverse modeling consists of estimating model parameters from measurements of system response at discrete points in time and space.

A number of mathematical models and data processing techniques can be used in solution of an inverse problem. A basic simulation package called iTOUGH2 is frequently used. iTOUGH2 is a computer program for parameter estimation and sensitivity and uncertainty analysis. The program contains various minimization algorithms to find the minimum of the objective function which is the difference between model results and measured data. The basic procedure in iTOUGH2 is to continuously compare the calculated output from TOUGH2 to measure data while changing the value of selected input parameters. If a change in an input parameter results in reduction of the objective function, the program has found a better estimation for the parameter. In this study the Levenberg-Marquardt minimization algorithm is used to evaluate the objective function.

iTOUGH2 is usually run in combination with TOUGH2, a forward simulator for non-isothermal multiphase flow in porous and fractured media, but can also be linked to non-TOUGH2 models. In that way the iTOUGH2 can be used as an inverse analyzing tool for models such as the wellbore simulator FloWell (Finsterle, 2007).

To be able to link non-TOUGH2 models with iTOUGH2, a protocol called PEST has been implemented in iTOUGH2. The protocol enables interaction between the non-TOUGH2 model and iTOUGH2 through a clear and simple communication format (Finsterle, 2010).

THE BASIC ARCHITECTURE OF FLOWELL

For this study, a numerical wellbore simulator has been developed and named FloWell. The simulator is built around eq. (1)-(32) defined in the chapter The *Physical Model of FloWell* and MATLAB is used as a programming language.

To perform a simulation with FloWell the following input parameters are needed:

- Inner diameter and depth of a well
- Roughness of the pipe walls in a well
- Total mass flow rate at the wellhead
- Enthalpy of the working fluid
- Bottomhole pressure or wellhead pressure

Features and assumptions

The wellbore simulator is capable of:

- Modeling liquid, two phase and superheated steam flows
- Allowing users to choose between various friction, friction correction factor and void fraction correlations
- Performing wellbore simulations from the bottomhole to wellhead section, or from the wellhead to the bottom of the well
- Providing simulated results, such as pressure and temperature distribution as well as steam quality, friction, velocity, enthalpy and void fraction at each dept increment
- Providing graphical plots of simulated pressure and temperature profiles

Some general assumptions have been made in the development of the simulator. It is assumed that:

- The flow is steady and one dimensional
- Multiple changes of the wellbore geometry, such as diameters and roughness, do not occur
- Simulations will be restricted to wells with single feedzones
- The fluid is pure water
- Phases are in thermodynamic equilibrium
- Fluid properties remain constant within a step
- The presence of non-condensable gases and dissolved solids is ignored

The simulator solves the continuity, energy and momentum equations up or down the well using numerical integration. The *ode23* function built in MATLAB is used to evaluate the differential equations. The depth interval is adjusted by the integration function and at each depth node the function produces velocity, pressure and enthalpy values.

VALIDATION OF FLOWELL

Validation is usually achieved through model calibration, that is comparing results from the simulation to actual system behavior. To validate FloWell, data, provided by the Icelandic company HS Orka, from wells at two geothermal fields, Reykjanes and Svartsengi, in the Reykjanes peninsula is used.

FloWell offers a considerably wide selection of empirical correlations for two phase calculations. Which correlation performs best is a question many

scientists and researches struggle to answer. More often than not, there is no one right answer to this question as it can prove to be difficult to find one correlation to simulate the diverse characteristics found in geothermal wells.

Utilizing the features iTOUGH2 has to offer, a measure of how each void fraction correlation performs in simulating the pressure and temperature profiles in a well can be found. Since FloWell is a non-TOUGH2 model, an inverse run with iTOUGH2-PEST is initialized to calculate an objective function. The function describes how a simulation with FloWell fits measured data, in this case data points from pressure logs. If, for example, the objective function calculated using the void fraction correlation by Rouhani-Axelsson is lower than the one found with the Homogenous correlation, the Rouhani-Axelsson correlation is more likely to simulate the expected behavior of the well.

The objective function is calculated for each well and for all void fraction correlations. The calculated objective functions are compared within each well and the correlation which yields the lowest objective function is identified. With that, a ranking of the correlations can be established for each well. These individual rankings can be summarized to find an overall ranking for the wells. Several feedzones are present in a well but since FloWell is a single feedzone simulator the most reliable simulations would be the ones that only reach the bottom of the production casing. Simulating further down the well is also an option but it may invite unreliable predictions

The results from the void fraction comparison show that the model by Chisholm most often yields results closest to measured data. The model by Premoli et al. is the one that is most often in second place, the model by Rouhani-Axelsson is most often in third place and the model by Lockhart-Martinelli is most often in fourth place. The model by Zivi is the one that produces the worst predictions, placing most often in the last two places. To further summarize the results the correlation by Rouhani-Axelsson ranks most often in the top three while the model by Zivi ranks most often the lower three as before.

To better understand how FloWell performs, visual results are of great help. Wells RN-11, RN-12, RN-21, RN-24 and SV-21 have similar characteristics. They are vertical wells with low enthalpy fluid and steam fraction between 9-13% at the wellhead. Simulations for wells RN-12 and SV-21 can be seen in Fig. 2 and 3. For these simulations the Blasius equation and the model by Friedel are used to calculate the friction factor and friction correction factor.

Figure 1: Simulations for well RN-12 with FloWell.

Figure 2: Simulations for well SV-21 with FloWell.

For well RN-12 the Rouhani-Axelsson and the Chisholm void fraction correlations perform the best. For well SV-21 the Homogenous correlation shows simulations closest to the measured data. The Homogenous correlation usually yields adequate simulations for wells with a low steam fraction, for it assumes that the phases travel at the same velocity. This is the case in well SV-21, the steam fraction in the well is between 9-10%, while the steam fraction in well RN-12 is little over 13%.

Since FloWell is also capable of starting at the bottom of a well and calculating up, it is interesting to see a simulation up the well versus down the well. Simulations up well SV-21 are presented in Fig. 4. Comparing Fig. 3 and 4 it can be seen that considerable difference is between simulating up the well and down the well. Despite this difference, the homogenous correlation still performs best and the model by Zivi the worst. From this discussion the question which option is more accurate arises. As it is easier to measure wellhead parameters than downhole ones, wellhead conditions are constantly

being monitored and noted. From that alone it may be concluded that simulating down the well is more accurate but if carefully measured parameters exist at the top and at the bottom it may prove difficult to favor one over the other

Figure 4: Simulations for well SV-21 starting at the bottom and simulating up.

FloWell manages to simulate the behavior of geothermal wells to some extent but no correlation simulates the exact pressure profile in a well. It is intriguing to use inverse analysis with iTOUGH2-PEST to improve parameters in the void fraction correlations so simulations with FloWell better fit measured data. Using the Homogenous model in Eq. (22) to calculate the void fraction in well RN-11, FloWell yields a simulation that is not very close to the known pressure profile. It is assumed that the slip ratio is equal to one in the Homogenous correlation. If inverse analysis is applied to well RN-11 and the slip ratio evaluated, several iterations with iTOUGH2-PEST result in a new value for the slip ratio, *S=1.68*. Using this value instead of one in the Homogenous correlation, almost a perfect match to the measured data is obtained with FloWell as seen in Fig. 5.

Figure 5: Simulations for well RN-11 with the original Homogenous model (blue) and with improved slip ratio (green).

THE COUPLED FLOWELL-TOUGH2 MODEL

In addition to designing a coupled wellbore-reservoir model, an inverse analysis with continually measured wellhead parameters as observations is applied to the coupled model to improve the model design and keep it up to date. For the model calibration the inverse analysis program iTOUGH2 is used. Usually, the emphasis is on calibrating the reservoir model TOUGH2, but the method suggested here is to apply an inverse analysis on the wellbore simulator as well. This is to be done in an iterative manner where measured wellhead conditions are used to calibrate the reservoir model to find estimates for the bottomhole pressures in wells. These bottomhole pressures are then used to calibrate the wellbore simulator. This iteration process is explained in detail in following paragraphs.

One of the main focuses in this study is to utilize the measured wellhead parameters to a greater extent than has been done so far, by using them as an input to the coupled model and to calibrate the model with an inverse analysis. As new wellhead parameters are measured they are imported into the coupled model and an iterative inverse analysis process is initiated. This results in continuous improvements being made to the model design in the reservoir simulator and in the wellbore simulator.

The basic methodology behind the coupled model is illustrated in Fig. 6. The parameters that are measured or estimated at the wellhead, the mass flow rate, enthalpy and pressure, are the input to the wellbore simulator FloWell. FloWell calculates the bottomhole pressures in the wells using available empirical correlations. To couple FloWell to TOUGH2 the bottomhole pressures are inserted into the input file for TOUGH2. An inverse analysis by iTOUGH2 on the reservoir model returns new values for the bottomhole pressures in the wells. Lastly, these new values are used in a second inverse analysis performed on the wellbore simulator by iTOUGH2-PEST to obtain a new estimate on parameters in void fraction correlations. From this point, the whole process is repeated where FloWell calculates new bottomhole pressures with the improved void fraction correlation. This iteration is continued until a stopping criteria has been met.

Although the basic ideology seems simple enough, the total coupling and calibration process is considerably more complicated as illustrated in Fig. 7. The model design is best explained by taking a regular power plant with several producing wells that has been operated for i+1 years as an example. Historical data about the rate of production and the

pressure drawdown in the reservoir is available, as well as continually measured data at the top of the wells

Figure 6: The basic ideology for the coupled FloWell-TOUGH2 model.

Figure 7: The detailed model design for the coupled FloWell-TOUGH2 model.

In the first step a conceptual model is constructed for the reservoir in question. Before simulating the response of the reservoir to production the natural state of the reservoir is obtained by using a reasonable value for the permeability (k_{guess}) until a steady state has been reached. Supposing that historical data describing the pressure drawdown in the reservoir exists for year 1 to year i the data can be used to calibrate the model in order to obtain a fairly good estimate for permeability (k_{new}) of the rock structure in the reservoir.

In step 2 it is assumed that measured wellhead conditions, mass flow rates ($\dot{m}_t$), enthalpies (h) and pressures (P_t), are available for every month of the year i+1. These parameters are used as inputs into FloWell, which calculates the bottomhole pressures (P_b) in producing wells in the reservoir.

Desirably, the next move would be to insert the calculated bottomhole pressures and the measured mass flow rates at the wellheads directly into the TOUGH2 model. However, TOUGH2 does not offer an option in which a mass flow rate and a bottomhole pressure for a well can both be used as inputs.

In the model design presented here, the DELV type is used to couple FloWell with TOUGH2. In step 3, the calculated bottomhole pressures from FloWell are entered to the reservoir model that has been arranged for year i+1 and guess values assigned to the productivity indices (PI) of the wells. By using mass flow rates as observations to calibrate the TOUGH2 model and to find new estimates for the productivity indices that suite the bottomhole pressure and mass flow rate for each well, the flow rates have now been linked to the coupled model. This calibration has to be performed in twelve timesteps where each timestep represents one month. In total the timesteps add up to one year, year i+1 in production. The reason for this is that TOUGH2 does not allow the user to define time-dependant bottomhole pressures, the pressures have to be fixed throughout the simulation.

As it is custom to denote only one productivity index for a well an average is taken of the twelve values obtained above (PI_{ave}). The average values of the productivity indices, one average value for each well, are now inserted into the TOUGH2 model instead of the guess values and a forward run in twelve timesteps executed as before. After each run, pressures in the elements where wells are defined (P_e) are extracted from the output report from TOUGH2, along with mass flow rates ($\dot{m}_{new}$).

At this stage, the variable K (which is dependent on the density and viscosity of the fluid and the relative permeability) can be calculated with following equation as described by Pruess (1999);

In step 4 a new estimate for the permeability that describes year i+1 is found with iTOUGH2. Similarly to step 1, the MASS option in TOUGH2 is used and values for mass flow rates observed at the wellheads inserted into time-dependent tables. Since forward runs with MASS should not differ much from runs with DELV, the element pressures found in step 3 are

used as observations for the inverse analysis in step 4. The inverse analysis results in permeability that yields element pressures that are close to the ones used as observations. These new element pressures can then be used along with correct mass flow rates ($\dot{m}_t$), the productivity indices and the variable K found in step 3 to achieve new bottomhole pressures ($P_{b,new}$) with Eq. (33).

The final step involves the calibration of FloWell with iTOUGH2-PEST. The new bottomhole pressures calculated in step 4 are used as observations in the inverse analysis and the parameters chosen for evaluation are variables in void fraction correlations. When the void fraction has been manipulated so bottomhole pressures match the ones from step 4 the first iteration has been completed. This new void fraction is inserted into FloWell and the procedure repeated until a stopping criteria has been reached.

A CASE STUDY OF REYKJANES GEOTHERMAL FIELD

Reykjanes Conceptual Model

The Reykjanes peninsula, situated at the south-western end of Iceland, is an onshore continuation of the Mid-Atlantic Ridge. The general topography of the Reykjanes peninsula has been shaped by sub- and postglacial fissure eruptions that created the northeast trending hyaloclastite ridges and crater rows. No central geothermal volcanoes have been developed in Reykjanes so the heat sources for the high temperature fields in the peninsula are a dyke swarms (Friðleifsson et al., 2009).

From resistivity measurements reaching down to 1000 km it is believed that the geothermal system at Reykjanes covers about 10 km^2 in area. Interpretations of satellite pictures indicate however that the geothermal system becomes considerably more extensive with depth, where large parts of the system may lie beneath the ocean floor far south of the Reykjanes Peninsula (Friðleifsson et al., 2009).

The Reykjanes power plant began producing 100 MW_e in May 2006 with two 50 MW_e twin steam turbines with sea cooled condensers. HS Orka plans to expand the power production by 50 MW_e in coming years as well as increase injection to support the pressure in the reservoir (HS Orka, 2009).

Little is known about the pressure change in the Reykjanes reservoir before power production started in the area but the data available indicates that the drawdown in pressure was hardly more than 2 to 3 bar prior to production (Hjartarson and Júlíusson, 2007). During the first months of production, steep decline in pressure was detected which continued until spring 2007. In total, from beginning of year 2006, the pressure drawdown in the center of the reservoir (RN-12) had reached the maximum of 36 bar while at the boundaries (RN-16) the drawdown is much less or 21 bar. This goes hand in hand with the magnitude of mass being extracted from the reservoir (HS Orka, 2011).

Numerical Model

The numerical model can be broken down into four main parts:

i. A natural state model defining the Reykjanes geothermal reservoir prior to any production from the area.
ii. A reservoir model to simulate the production history ranging from the year 1977 to the year 2010 in Reykjanes along with calibration of the model against measured pressure drawdown in the reservoir over the production period.
iii. A coupled wellbore-reservoir model where wellhead measurements in 2011 are used to calibrate both the wellbore and the reservoir model.
iv. A forecasting model using the results from parts i-iii where different scenarios are simulated to predict the reservoir's response the next 15 years.

The mesh design is based on the conceptual model of Reykjanes geothermal field. Fig. 8 shows the overall mesh used. The mesh covers 10x10 km area and consists of 2064 elements where 344 elements are defined inactive. The numerical model of Reykjanes geothermal field consists of 12 layers, each with 172 elements and a thickness of 300 m. The horizontal mesh remains the same for each layer. Fig. 9 displays the innermost core of the mesh along with placements of wells at Reykjanes geothermal field. The rock types for the Reykjanes geothermal field can be seen in Fig 10. Layers A and L have the rock type names CAPR1 and BASE1 for the cap and base rock and the boundary of the Reykjanes geothermal field SIDE1. For the surroundings and the center of the reservoir rock type names ROCK1-5 have been assigned.

The initial conditions of the reservoir are set by a temperature gradient of 100°C/km with a corresponding hydrostatic pressure gradient. For simplicity and to facilitate calculations in the inverse program iTOUGH2 by reducing number of unknowns, the permeability in x and y direction in this model is assumed to be the same.

Table 1: Physical properties

Physical properties	*Values*
Rock density	
Thermal conductivity	
Heat capacity	
Porosity	10%

exploitation sta

others.

1977 to 2010. This pa

Reykjanes reservoir th measured pressure dr -12 and RN-16 as observations.

The parameter estimat 2

the objecti ecreased to 94% of the initial value.
wells RN-12 and RN-
the permeability Fig. 11 and 12.

ite accurately. The model

the boun

Figure 8

Table 2
the p - and z-direction [mD].

	SIDE 1	*1+2*	*ROCK 3+4*	*ROCK 5*
xy (guess)	2.00	20.00	20.00	100.00
z (guess)	0.010	1.00	1.00	200.00
xy (estimate)	0.41	4.48	6.04	97.48
z (estimate)	0.0097	1.66	0.97	117.77

Figure 9
placements of wells a

Figure 30
model.

Numerical Results

For the natural state t

100.000 years and

Figure 11: Sim
drawdown in well RN-12.

Figure 12: Simulated pressure drawdown vs. measured drawdown in well RN-16.

For the coupled model calculated bottomhole pressures are inserted to the reservoir model along with guess values ($3.0 \cdot 10^{-12}$ m^3) for the productivity indices of the wells. The reservoir model is then calibrated using observed mass flow rates and enthalpies at the wellheads, yielding new estimates of the productivity indices in all wells for the year 2011. Along with the productivity indices, the permeability of ROCK5 in xy- and z-direction is calibrated. Only the permeability of the center of the reservoir is considered in order to minimize the number of unknowns since the total process is very computational expensive. The parameter, shown in red in Eq. (32) in the Rouhani-Axelsson void fraction correlation is chosen for the inverse estimation with iTOUGH2-PEST to improve the model design in FloWell.

It takes approximately five iterations for the average of the productivity indices in the reservoir model and the void fraction in the wellbore model to reach equilibrium. The iteration process yields productivity indices in the range of $0.300\text{-}2.267 \cdot 10^{-12}$ m^3 for wells in consideration and an estimation of 0.111-0.122 for the parameter in the Rouhani-Axelsson void fraction correlation. For the permeability it takes around eight iterations to reach steady state. Minor changes are observed for the permeability of ROCK5, especially for the permeability in xy-direction. This is not unexpected since the simulation time only spans one year.

The purpose of designing a reservoir model is to use it to predict the future response of the reservoir to different production scenarios. In this study, four different production scenarios were modeled for the Reykjanes geothermal field. All scenarios involved simulations up to the year 2027.

- **Scenario 1**: Maintaining the same total production and injection rates as in the year 2011.
- **Scenario 2**: Maintaining the same total production rate as in the year 2011 and increasing the injection rate to 30% of the total extracted mass.
- **Scenario** 3: Increasing the production capacity of the power plant by 50 MW_e and maintaining the injection rate as in the year 2011.
- **Scenario 4**: Increasing the production capacity of the power plant by 50 MW_e and the injection rate to 30% of the total extracted mass.

In the forecasting model the forward simulator TOUGH2 is used. FloWell is excluded in this part but the permeability distribution found in the historical and the coupled FloWell-TOUGH2 models is used for the predictions.

Predictions of pressure drawdown in the center of the Reykjanes reservoir (well RN-12) and at the boundaries (well RN-16) are illustrated in Fig. 13 and 14. Scenarios are distinguished by colors where dotted lines represent cases with increased injection.

The figures show that in scenario 1 the pressure drawdown decelerates and the pressure in the reservoir is close to achieving equilibrium with just a total of 3-4 bar decline in pressure for the prediction period. By increasing the injection, the pressure in the reservoir starts to rise again as displayed for scenario 2. In scenario 3 the power generation is boosted up to 150 MW_e with almost no injection taking place. Approaching five years of simulation a decline of 18 bar in the reservoir and 12 bar at the boundaries is observed. After five years of simulation a convergence failure is encountered in TOUGH2 indicating that mass is being removed at a higher rate than physically possible. When adding considerably to the injection in scenario 3 less decline is detected and after 15 years of simulation the total drawdown in pressure is equal to the total drawdown after 5 years in scenario 3.

Fig. 15 shows the development of the average enthalpy for the years 1977 to 2027. From the figure it can be concluded that the greater the production is from the reservoir, the greater the average enthalpy of the geothermal fluid becomes. Increasing the production causes the pressure to drop to a greater extent. As the pressure drops, boiling starts in shallow feedzones in the wellbores and the enthalpy increases. However, the injection in scenarios 2 and 4

supports the pressure in the reservoir and hinders boiling to occur, which yields lower enthalpy.

Figure 13: Pressure drawdown in well RN-12 in the forecasting scenarios.

Figure 14: Pressure drawdown in well RN-16 in the forecasting scenarios.

Figure 15: The average enthalpy development in wells in Reykjanes in the forecasting scenarios.

As noted above, scenario 3 causes convergence failure in TOUGH2. Increasing the production rates of the wells and keeping them constant throughout the simulation displays that the recharge to the reservoir cannot keep up with the rate of extraction. This also indicates that existing wells at Reykjanes may not support increased production from the reservoir and new wells covering larger area must be drilled. It should be mentioned that calculations of production rates needed for power generation of 150 MW_e are based on the state of the geothermal fluid observed in 2011. However, increased production causes the pressure to drop and boiling to start in the reservoir, yielding geothermal fluids with higher enthalpy. More steam can be obtained from fluids with higher enthalpy than the ones with lower enthalpy so the total mass of geothermal fluid needed for power production diminishes. Therefore, the pressure drop due to increased production will eventually result in less mass extraction from the reservoir. From this discussion it can be assumed that scenarios 3 and 4 display the worst-case scenario of increased production from the reservoir and that this increased production may even sustain greater power generation than 150 MW_e.

CONCLUSIONS AND FUTURE WORK

The focus of this work was to develop a model that can simulate the flow in a geothermal reservoir as well as the flow in a production well in a coupled manner using measured wellhead conditions as main inputs. The program TOUGH2 was used to simulate the behavior of a reservoir while a new model was designed to simulate two phase flow in a wellbore.

The validation of FloWell displayed that in most wells the simulations were in good agreement with pressure logs from wells at Reykjanes and Svartsengi geothermal fields. Furthermore, a comparison was made between available void fraction correlations in FloWell, resulting in the Rouhani-Axelsson correlation fitting the data best in most cases while the Zivi correlation produced the worst fit. Despite these results it is difficult to favor one correlation over the others, to reach conclusive results more extensive data must be examined.

A detailed numerical model of the Reykjanes geothermal field in Iceland including the coupled wellbore-reservoir model was constructed. An acceptable pressure distribution for the natural state was obtained in most wells. The exploitation and pressure drawdown history of the Reykjanes reservoir was used to find new estimates for the permeability in xy-direction and z-direction in the rock types SIDE1 and ROCK1-5. The new estimates yielded an excellent fit to the pressure data, but since the rock structure of Reykjanes was only roughly divided into sections it cannot be stated that these estimates reflect the actual permeability distribution.

Measured wellhead conditions for each month of the year 2011 were used to couple the numerical model to FloWell. The coupling procedure was carried out in an iterative manner where the model design in FloWell and in the numerical model was improved by calibration with iTOUGH2. The parameters improved were the productivity indices of the wells, a variable in the Rouhani-Axelsson void fraction correlation and the permeability in the center of the reservoir.

The calibrated numerical model was used in forecasting scenarios to predict the reservoir's response to future exploitation. Four scenarios were considered where the production rates of the wells were either kept constant as observed in 2011 or increased to maintain a 150 MW_e power production, with an increase in injection or not. Increasing the production the pressure dropped in the reservoir and the average enthalpy of the geothermal fluid in the reservoir increased. Seeing as the production rates were fixed throughout the simulations in the scenarios it can be assumed that they can sustain even greater power generation than 150 MW_e.

In the future, several improvements could be made to the wellbore simulator FloWell, the coupled FloWell-TOUGH2 model and the numerical model of Reykjanes. The option of multiple feedzones in a well as well as diverse changes of a wellbore geometry could be incorporated into FloWell. For the coupled FloWell-TOUGH2 model and the numerical model of Reykjanes it would be advisable to increase the simulation time when more measured wellhead data becomes available. Lastly, the modeling approach introduced in this study should be applied to other geothermal systems with as accurate data as possible to improve its performance and hopefully extend its application field.

ACKNOWLEDGEMENTS

The authors wish to thank the Geothermal Research Group (GEORG) for the financial support during the research presented in the paper.

REFERENCES

Axelsson, G. (2003). Sustainable Management of Geothermal Resources. *Proceedings*, the International Geothermal Conference, Reykjavik, Iceland.

Chisholm, D. (1973). Pressure gradients due to friction during the flow of evaporating two-phase mixtures in smooth tubes and channels. *International Journal of Heat and Mass Transfer*, 16:347–358.

Finsterle, Stefan (2007). "iTOUGH2 User's Guide", Lawrence Berkeley National Laboratory, Berkeley, USA.

Finsterle, Stefan (2010), "iTOUGH2 Universal Optimization Using the PEST Protocol, User's Guide", Lawrence Berkeley National Laboratory, Berkeley, USA.

Friðleifsson, G. Ó, Sigurðsson, Ó., Albertsson, A., Þórólfsson, G. and Blöndal, Á. (2009). "Sjálfbærni jarðhitans á Reykjanesi", HS Orka, Reykjanesbær, Iceland.

Hjartarson, A. and Júlíusson, E. (2007) "Reiknilíkan af jarðhitakerfinu á Reykjanesi og spar um viðbrögð þess við 100 MW rafmagnsframleiðslu". ÍSOR, Reykjavík, Iceland.

HS Orka. (2011). "Financial Statements 2011". HS Orka, Reykjanesbær, Iceland.

Lockhart, R.W. and Martinelli, R.C. (1949). "Proposed Correlation of Data for Isothermal Two-Phase, Two Component Flow in Pipes", *Chemical Engineering Progress Symposium Series,* 45: 39-48.

Pálsson, H. (2011), "Simulation of two phase flow in a geothermal well", Lecture notes in the course VÉL203F Geothermal Systems at the University of Iceland.

Premoli, A., Francesco, D., Prima, A. (1970). An empirical correlation for evaluating two-phase mixture density under adiabatic conditions. *In European Two-Phase Flow Group Meeting*, Milan, Italy.

Pruess, K., Oldenburg, C. and Modidis G. (1999). "TOUGH2 User's Guide, Version 2.0", Lawrence Berkeley National Laboratory, Berkeley, USA

Rouhani Z. and Axelsson G. (1970). "Calculations of volume void fraction in the subcooled and quality region", *Int J Heat Mass Transfer*, 13:383-93.

Zivi, S.M.. (1964). Estimation of steady state steam void fraction by means of the principle of minimum entropy production. The *ASME Journal Heat Transfer* 86:247–252.

COMPARISON OPEN MODELICA - DYMOLA FOR POWER PLANT SIMULATION

Elena Tomas Aparicio, Erik Dahlquist and Hailong Li, School of Sustainable development of society and technology, Mälardalen University, Vasteras, Sweden

Peter Fritzson, Per Östlund, Programming Environment Laboratory (PELAB), Linkoping University, Linköping, Sweden

ABSTRACT

In this paper a comparison is made between OpenModelica and Dymola for a simulation model of a power boiler. The similarities and differences are presented. Dymola has the advantage of having a more elaborate user interface and solver, but the OpenModelica user interface and solver has improved very much during last few years. The advantage of OpenModelica is that anyone can use the models without having to pay high license fees, something that is of significant interest when installations are made in industries. In many ways a combination of the two is advisable, where Dymola can be used for application developments and later OpenModelica can be used in the actual installations. It has been seen in this application for a CFB boiler that it is easy to use the same model in both environments without any modifications. Still, the solver for Open Modelica is not as powerful as for Dymola, which may be a problem for on-line applications for larger models, while no problem for small models.

1.INTRODUCTION AND LITERATURE REVIEW

Energy conversion system models are usually complex models which require a high structured programming language. Generally dynamic models are preferred in order to reach a deeper understanding of the process. Many studies have pointed out Modelica as a straightforward object oriented language developed for modeling of large physical systems (Fritzson, 2004), (Modelica Association, 2007). Dymola is an engineering simulation tool using Modelica language (Mattsson et al, 1998). OpenModelica is an alternative tool based on open source code. Both Dymola and OpenModelica include several Modelica libraries (MSL – the Modelica Standard Library) from Modelica Association in their distributions (Otter and Elmqvist, 2001). There are also Modelica libraries for e.g. power plants (Casella and Leva, 2005) and other energy conversion systems (Salogni and Colonna, 2010). In Casella et al. (2007) a dynamic model of a biomass-fired-power-plant is presented. Jansson et al (2008), Järvensivu (2001), Hauge et al (2005), Mercangöz and Doyle (2006) and Dhak et al (2004) have shown how model based control can be implemented and Karlsson et al (2009) how models can be adapted to compensate for fouling. Sandberg et al. have modeled the actual fouling. Mälardalen University has developed their own Modelica models for pulp and paper industry and power plant applications, as well as for gasification. There is also commercial equation-based modeling and simulation software similar to Modelica used for process industry. This is named gPROMS and was developed by Imperial College in London under leadership of professor Costas Pantelides. Model structure is similar, but at least some years ago there were only two solvers available for gPROMS. Thesehave a varying time step depending on how fast the dynamics of the process is. OpenModelica and Dymola have solvers for both varying time step and fixed time step. Dymola have additional functions compared to Open Modellica, but Open Modellica is adding new functions continually as well.

2. METHODOLOGY:

A semi-dynamic on-line application of the proposed simulation approach has been used in the simulation of a CFB boiler at Mälarenergi in Västerås as well as at Korsnäs pulp mill in Gävle in tests during 2010 - 2011. Here the connection between the DCS and the simulation model was established with Simulink.Modelica models were used after compilation allowing better control of the signal processing between simulation and the process database. The project at Mälarenergi was financed by Värmeforsk (and power companies) and the project at Korsnäs by KKS (and Korsnäs and ABB).

The CFB boiler model developed by Mälardalen University (MDH) includes the combustion section, the water/steam system and the exhaust gas train. The model is validated towards real plant data and is capable to successfully predict operation performance. A more detailed description of this model can be found in Sandberg et al. (2011).

During 2010 and 2011 the model was used on-line at Mälarenergi AB for diagnostic purposes. The plant is a combined heat and power plant (CHP). Boiler 5 has been modeled. This is a 180 MW_{th} biomass fired CFB boiler.

The components of the Modelica/Dymola model can be seen in Figure 1. The components are as follows: 1. Air flow to boiler, 2. Fuel flow and composition, 3. Boiler/reactor, 4. Ash flow, 5. Air flow to Intrex, 6. Intrex – fluid bed/G-valve where solids come down from cyclone and is heat exchanged towards steam, 7. Cyclone separator where larger particles are separated but also gas cooled, 8. The heat exchanger in the walls of the cyclone where gas is cooled towards steam, 9- 11. Steam heating, gas cooling heat exchangers, 12. Economizers where feed water is heated (and evaporated), 13. Air pre-heating, 14. Exhaust gas flow and composition, 15. Air flow to pre-heater, 16. Feed water flow, 17-18. Steam flow and temperature/pressure to turbine, 19. Electric power produced, 20-22. Feed water injection to heat exchangers. There are three mass inventories in the model: (i) gas in the boiler including the bed material, fuel etc.; (ii) bed material and gas in the so called Intrex, a bubbling bed below the cyclones where separated sand is fluidized and cooled in two super heaters before the sand is re-entering the CFB boiler; (iii) the steam system with water and steam.

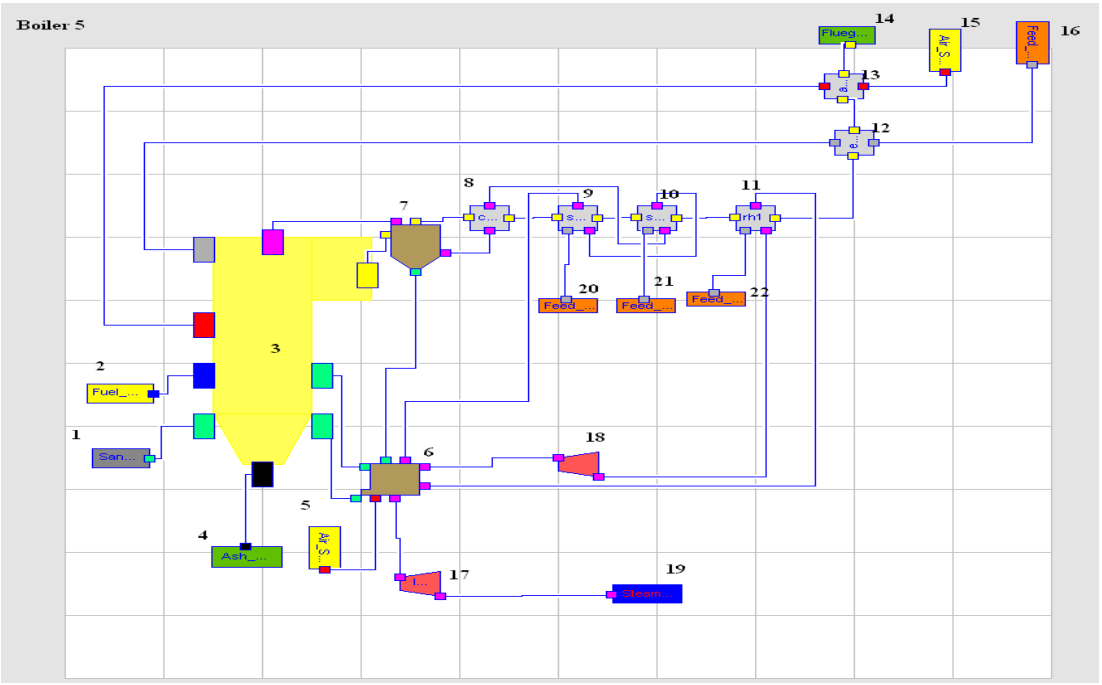

Figure 1. View of the CFB boiler in Dymola interface. Showing boiler 5 at Mälarenergi CHP plant.

Temperature, gas composition and flow rates are measured all the way through the boiler and exhaust gas train and in the steam system. These measurements are then compared to the values predicted from the simulation using the same input data. This includes fuel flow, fuel composition, air flow and feed water flow to the steam drum. Unfortunately the fuel composition has not been able to measure; if moisture content varies the impact will be significant. Measurment of moisture and higher heating value (HHV) of the fuel we want to include in the future research. Use of NIR (near infrared) measurement on-line is a tool we develop together with Bestwood. On-line measurement of moisture is already installed at Eskilstuna CHP, but the development of models for HHV is still ongoing at our lab in Västerås.

The equations used are primarily stoichiometric calculations of how the biomass is converted through combustion, giving adiabatic temperature and cooling through heat transfer and through transport of material from the boiler combustion zone. The mass in the bed inventory as a function of time is given from:

$$\partial m_{\text{inventory}} / \partial t = \sum m_{\text{i,in}} - \sum m_{\text{i,out}} \quad (1)$$

where $m_{i,in}$, is the mass input flow of each single component of the composition vector i= (C,H,O,N,CO_2,H_2O,NO_2,ash) and $m_{i,out}$, is the corresponding output flow. The change in concentration of each component is given by c_i in the bed inventory:

$$\partial c_i/\partial t = \left(\sum (c_i \cdot m_j)_{in} - \sum (c_i \cdot m_k)_{out}\right) / m_{inv.} \quad (2)$$

where j runs through all incoming flows and k all outgoing flows of the inventories. Except the bed inventory we also have one inventory for the Intrex and one for the steam system. The steam system has only water and steam components, while the Intrex has the same components as the bed. The temperature $T_{inventory}$ in the inventory is calculated from the energy balance:

$$\partial T_{inventory}/\partial t = \left(\begin{array}{l} \left(\left(\sum T_j \cdot cp_i \cdot c_i \cdot m_{j_{in}}\right) - \left(\sum T_j \cdot k \cdot cp_i \cdot c_i \cdot m_{k_{out}}\right)\right) + \\ \left(\Delta H - U \cdot A \cdot (T_{inventory} - T_{outside})\right) \end{array} \right) / \left(m_{inventory} \cdot \left(\sum c_i \cdot cp_i\right)\right) \quad (3)$$

Here ΔH (enthalpy) is the energy released during combustion and U is the overall heat transfer coefficient, A is the heat exchanger area and $T_{outside}$ the temperature at the other side of the heat exchanger surface (steam temperature vs. exhaust gas temperature), cp_i is the heat capacity for each component i. The correlations describing the change in each single component is also included in the model. Carbon, C, in the biomass is combusted to CO_2, and the hydrogen is forming H_2O. Oxygen, O, in the fuel is used for the combustion aside of the oxygen in the air. N, in the fuel is assumed oxidized to NO_2 partly, as a function of oxygen surplus and temperature. Separation of sand is performed in cyclones and cooling in heat exchangers with gas to gas, gas to steam or gas to water transfer. We have not included inventories in the heat exchangers as the residence time is very short.

The combustion/gasification processes are modeled as an extension of eq (2):

$$\partial c_i/\partial t = \left(\left(\sum (c_i \cdot m_j)_{in} - k \cdot [c_i]^a\right) - \sum (c_i \cdot m_k)_{out}\right) / m_{inv.} \quad (4)$$

where k is a reaction constant and a an exponent giving the non-linearity of the conversion. For components being removed c_i is decreasing while for those being created c_i is increasing

So far we have primarily been running the models as semi-steady state, but we want to include the full dynamics as this has a significant importance for both the diagnostics and the model based control, especially to meet varying moisture and HHV of the fuel.

3. MODEL VALIDATION AND RESULTS

The boiler simulation model has been verified towards process data. In Table 1 a comparison between measured and predicted data from the simulation for full load and partial load is presented. We have just included these situations for average load conditions to give a picture of how the model has been tuned towards process data. It should be noticed that the measurements in the boiler are not "the truth". In reality the temperature at different positions in the boiler varies a lot. We thus have tuned the model towards reasonable averages measured in the on-line positions at different positions in the boiler. The absolute value though may vary many hundred degrees between the wall and the center of the boiler at the same elevation, according to measurements we have made but not published yet.

Table 1 Measured process data (DCS) compared to predictions made with the simulation data

Part load (July 5, 2011) at 6.2 kg/s fuel, 30.1 kg/s air flow and 24 kg/s feed water flow			
Variables	DCS	Prediction	Error%
Steam temperature after HPSH2 (°C)	434	439	1.0
Fluegas temperature after cyclone (°C)	550	566	2.9

Fluegas temperature before cyclone (°C)	551	576	4.6
Steam temperature after cyclone (°C)	366	353	-3.6
Full load (September 2011) 16.5 kg/s fuel, 79.8 kg/s air, 48.8 kg/s feed water			
Steam temperature after High Pressure Super Heater 2 (°C)	494	488	-1.2
Bed temperature (°C)	833	879	5.2
Fluegas temperature before cyclone (°C)	758	757	0
Steam temperature after cyclone (°C)	385	379	-1.5

As can be seen the absolute error varies between 0 and 5 %. With the proposed approach with a new methodology for adaptation of models to process data we will improve the accuracy significantly. This includes correlating the on-line measurements to manual measurements of the temperature profile at specified positions.

In figure 2 below we can see how the difference between different sensors in the boiler at the same elevation varies in time over fibe hours. As can be seen they change level simultaneously, but the absolute value varies with approximately 40 ^{o}C in this case.

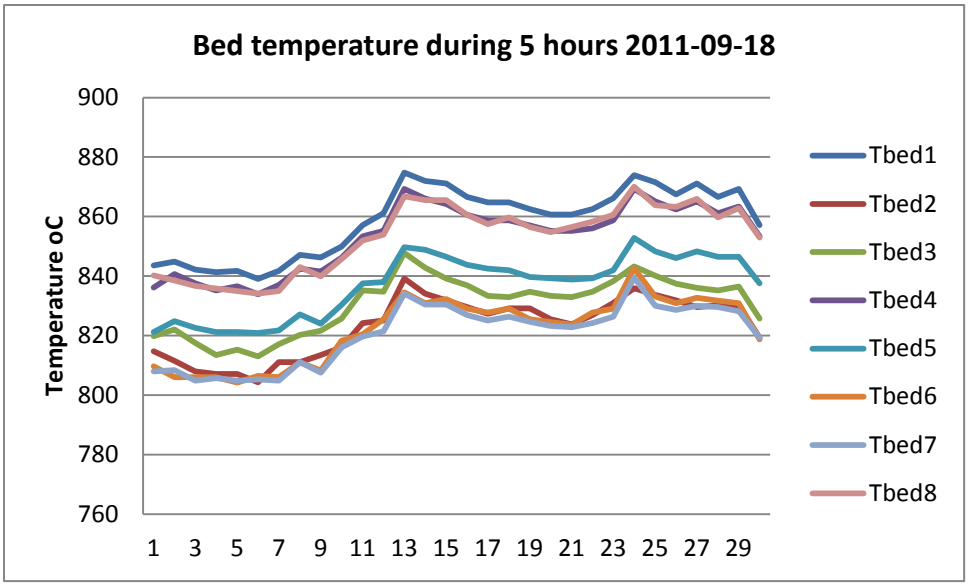

Figure 2. Bed temperature at the same elevation for eight meters.

For our purpose of using the model for diagnostics, decision support, maintenance on demand and model based control still it is the variations we want to measure and not primarily the absolute values of temperature etc. Then it is OK just to have reasonable data to fit the mass and energy balances.

4. COMPARISON OF DYMOLA AND OPENMODELICA FROM A USER PERSPECTIVE

OpenModelica and Dymola, as well as gPROMS all are equation-based and object oriented and all have simultaneous solver approach. OpenModelica and Dymola as well as some other vendors support the Modelica model standard, whereas gPROMS has its own model format. You configure the complete simulation problem as a big equation system, which is solved simultaneously. In reality the equation system is split into smaller systems automatically, to get faster convergence , but it is a big difference compared to the earlier simulation systems with sequential solvers. With the simultaneous solver we can really correlate different sensor along the process to each other, which gives us the possibility to get better diagnostics.

A key task is then to formulate equations covering all modeling tasks, where the number of equations and variables must be the same for each sub-model. This can seem like a simple task- just do it. In reality still it is not self- evident what is a variable or a parameter and thus it may be complicated to know “where you are”. We have noticed that it is even stricter with this in OpenModelica than in Dymola. A major problem thus for the model developer is to both get the right number of variables and equations, as well as to know that it is actually the RIGHT equations we have formulated. Sometimes you can note that you really would need one extra equation, but it is definitely not clear which you can take away instead! A preliminary (not released) version of OpenModelica contains a debugging tool that is addressing many of these problems, explaining which equations give rise to selected computed variables, and providing on-line interactive stepping, breakpoints, browsing of variable values, etc. (Pop et al, 2012). See also OpenModelica on-line simulation (Asghar et al, 2011).

Because of the structure with simultaneous equation solver it is very difficult to do debugging. In principle you can work in a structured way so that you make a smaller system and then connect several smaller systems to one big one. This is in principle simple, but in practice not that easy. This is especially tricky when you want to use simulations on line, and start developing a steady state model with fixed values as input. When you then connect dynamic input signals it may be quite tricky to really get the simulator to work, as the number of variables and equations suddenly are incorrect. At MDH we have been using a link to process data bases making Modelica models as compiled objects into Simulink/Matlab. When you then debug the actual Modelica model and all is working, it may still be tough to get the compiled model to work when you make the linking to the on-line signals. It thus would be interesting in the future to have some kind of automatic function between on-line use and off-line use, where you just run with constants or simple general functions to generate input to the simulations.

Concerning the transfer between Dymola and OpenModelica we have noticed that the new version of OpenModelica actually can directly convert a Modelica Dymola model into one that can be simulated in OpenModelica and reverse. Still, where we see a warning in Dymola it may be a real fault in Open Modelica, as this has stricter definitions of what is accepted, more in accordance with the Modelica language standard. This is both good and bad, but is definitely a problem as you have even more difficulty to debug them in Dymola. A

recommendation thus would be to have less strict rules for this, so that you have a chance to compile and test-run your code, before you do changes in the code. In future versions of Open Modellica there will be a warning instead, to make it easier to debug.

Concerning accuracy we have not seen any difference between OM and Dymola, but sometimes the solutions have taken longer time with OM. As the solvers for OM are developed continuously we hope this will be less in the future, but it is of course a “moving target”.

An example of results from the on-line application of simulation towards measured process data is seen in the figure 3 below.

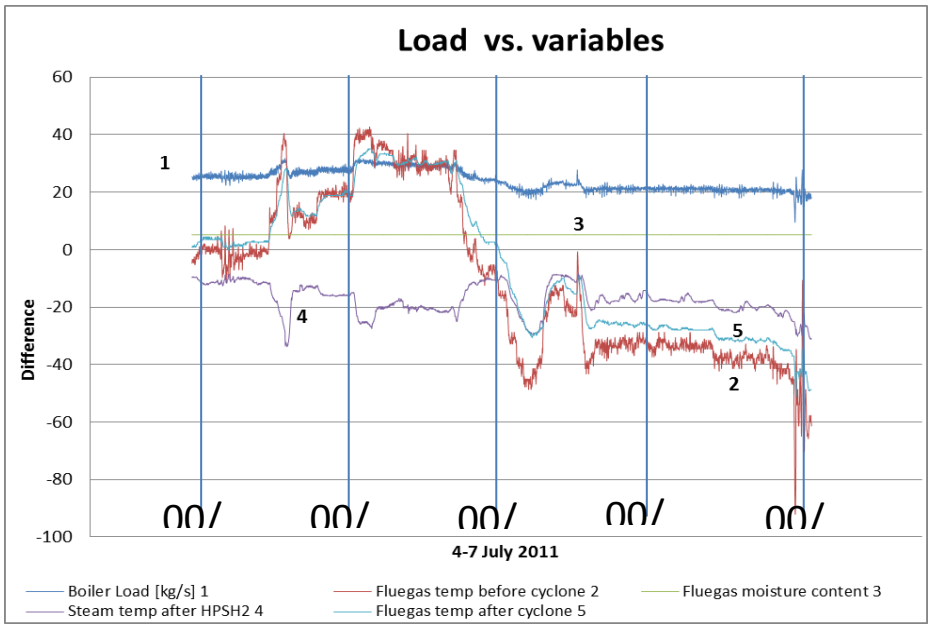

Figure 3. Difference between simulated and measured data for five variables in boiler 5 July 4-7 2011.

Here we can see that the load (curve 1) was going down after approximately July 5. We can see that the temperature predicted by the model first goes up in the flue gas compared to the measured temperature before the cyclone as well as after the cyclone, but as the load is lowered this swings to the opposite. The flue gas moisture signal (3) is constant all the time, and the variations are so small that it can be questioned if the sensor is giving correct values. The steam temperature in the corresponding heat exchanger High Pressure Super Heater 2 (HPSH2 , curve 4) is moving in the opposite direction during the first two days, but is following the same direction during the last two days. It is not obvious what the reason is, but may be related to fouling of the heat exchangers during the first two days with a reduced heat transfer rate as a result, while the heat transfer is better during the last two days. Still, this is not verified. The difference in fluegas temperature after cyclone (5) is first increasing, but later decreasing again. We believe it is due to temporarily combustion in the cyclone, which should not take place under normal conditions.

We also have sent the differences to a Bayesian Net, where different faults can be seen visually. An example of this is seen in the figure 4 below.

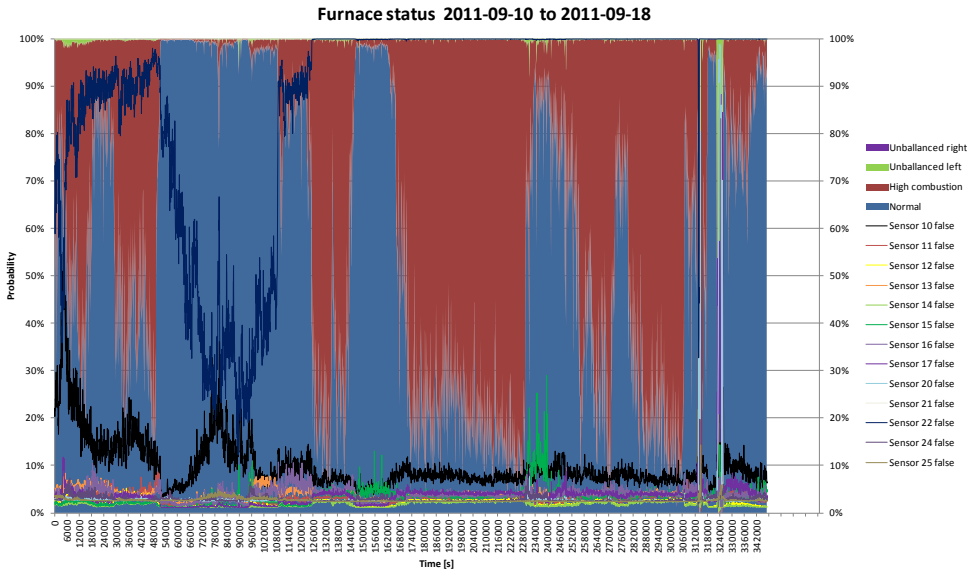

Figure 4. Bayesian Net of differences between simulated and measured data from Boiler 5 during the period September 10 to September 18, 2011,

Figure 4 indicates problems with high combustion, feeding problems of fuel on right (violet) and left (green) side, and also deviation between predicted and measured values for temperature meters in the bed above the feed at the left respectively right side of the bed. Variables to the right: Unbalance right, unbalanced left, high combustion, 6 temperature sensors in the bed, 7 temperature sensors above the bed.

5. DISCUSSION AND CONCLUSIONS

From the tests we have performed at Mälarenergy AB with on-line simulation combined with process data measurements we can conclude that a number of different type of faults have been possible to determine. The combination with BN, Bayesian Nets, is a feasible approach as experiences of different kind can be combined to generate a good decision support for process operators. Still, it will take time to make the system automatically adaptive with new experiences, although the goal will be to reach this. It is principally possible to develop a model in e.g. Dymola and then convert it into an Open Modelica model just by opening it in this environment, or the reverse. This is advantageous as it then is possible to make use of the advantages in the two platforms. This is very positive for the users of Modelica language. It is thus possible to use new functions developed in one of the platforms also for models developed in the other.

ACKNOWLEDGMENTS

We would like to thank Mälarenergi for support in the work and Swedish Energy Agency, Värmeforsk and the Knowledge Foundation for financial support.

REFERENCES

Asghar A., Tariq S, Torabzadeh-Tari M, Fritzson P, Pop A., Sjölund M., Vasaiely P., and Schamai W. An Open Source Modelica Graphic Editor Integrated with Electronic Notebooks and Interactive Simulation. In Proceedings of the 8th International Modelica Conference (Modelica'2011), Dresden, Germany, March.20-22, 2011.

Avelin A, Jansson J, Dotzauer E., Dahlquist E.: (2009). Use of combined Physical and Statistical Models for On-line Applications in the Pulp and Paper Industry. Mathematical and Computer Modeling of Dynamical Systems: Methods, Tools and Applications in Engineering and Related Sciences, 1744-5051, 15-5, 425–434.

Casella, F. and Leva, A. (2005).Object-Oriented Modelling & Simulation of Power Plants with Modelica. Proceedings of the 44th IEEE Conference on Decision and Control, and the European Control Conference. Seville, Spain, December 12-15, 2005.

Casella, F., van Putten, H. and Colonna, P. (2007). Dynamic simulation of a biomass-fired steam power plant: a comparison between causal and a-causal modular modelling. Proceedings of the IMECE '07, International Mechanical Engineering Congress and Exhibition, No. IMECE2007-41091, ASME, Seattle,WA, 2007.

Casella, F. and Colonna P. (2012). Dynamic modeling of IGCC. Applied Thermal Engineering, 35, 91-111.

Chen S-C, Berggren J. ad Zehnpfund A.: Multivariable CD control applications, ipw 10/2008, 6p.

Chen S-C: Two dimensional web property variation modeling and control. US Patent 5,893,055. Apr 6, 1999.

Ciarapica, F.E., Giacchetta, G. (2006). Managing the condition-based maintenance of a combined-cycle power plant: An approach using soft computing techniques. Journal of Loss Prevention in the Process Industries, 19, 316–325.

Dahlquist E., Widarsson B. and Tomás-Aparicio E.: Demand-based maintenance and operators support based on process models. Project report P08-815. ISSN 1653-1248. Dec 2011.

Dhak Janice, Dahlquist Erik, Holmström Kenneth, Ruiz Jean CTP,Grenoble,France, Belle Juergen, Goedsche Frank,.: Developing a generic method for paper mill optimization, Control Systems, Quebec city, Canada, June 14-17, 2004

Donoso-Bravo A., Mailier J., Martin C., Rodriguez J., Aceves-Lara C.A. and Vande Wouwer A. (2011) Model selection, identification and validation in anaerobic digestion: A review. Water research, 45, 347-5364.

Fritzson, P. Principles of Object Oriented Modeling and Simulation with Modelica 2.1, 940 pages, ISBN 0-471-471631, Wiley-IEEE Press. January 2004.

Modelica Association. (2007). Modelica – A unified Object-Oriented Language for Physical Systems Modeling, Language Specification Version 3.0, www.modelica.org.

Hauge, T. A., Slora, R. & Lie, B. (2005). "Application and roll-out of infinite horizon MPC employing a nonlinear mechanistic model to paper machines". Journal of Process Control 15(2), 201-213

Jansson J., Grobler F. and Dahlquist E.: Modelbased control and optimization of continuous digester. TAPPSA Journal, July 2008, p 26- 33

Javed, F., Arshad, N., Wallin, F., Vassileva, I., Dahlquist, E., 2010. Engineering Optimization Models at Runtime for Dynamically Adaptive Systems. 2010 15th IEEE International Conference on Engineering of Complex Computer Systems (ICECCS), art. no. 5628607, pp. 253 – 254, 22-26 March, 2010, Oxford, UK, ISBN 978-1-4244-6638-2

Järvensivu M., Saari K. and Jämsä-Jounela S.-L., Intelligent control system of an industrial lime kiln process, Control Engineering Practice, Vol. 9, 589-606. 2001.

Karlsson, Christer P.; Avelin, Anders; and Dahlquist, Erik (2009) "New Methods for Adaptation to Degeneration in Process Models for Process Industries," Chemical Product and Process Modeling: Vol. 4 : Iss. 1, Article 25. DOI: 10.2202/1934-2659.1127. Available at: http://www.bepress.com/cppm/vol4/iss1/25

Lübken M., Wichern M., Schlattmann M., Gronauer A. and Horn H. (2007). Modelling the energy balance of an anaerobic digester fed with cattle manure and renewable energy crops. Water Research, 41, 4085–4096.

Mattsson, S.E., Elmqvist, H.and Otter, M. (1998). Physical system modeling with Modelica. Control Engineering Practice, 6 (4), 501–510.

Mercangöz Mehmet, Doyle Francis J., University of California, Santa Barbara, USA Plantwide optimization of a pulp mill process, Control Systems 2006 ,Tampere, Finland, June 6-8, 2006

Otter, M. and Elmquist, H. (2001). Modelica – Language, Library, Tools, Workshop and EU-Project RealSim.

Pop, A, Sjölund M , Asghar A, Fritzson P, Casella F. Static and Dynamic Debugging of Modelica Models. In Proceedings of the 8th International Modelica Conference (Modelica'2012), Munich, Germany, Sept.3-5, 2012.

Sandberg J., Bel Fdhila R., Dahlquist E. and Avelin A. (2011). Dynamic simulation of fouling in a circulating fluidized biomass fired boiler. Applied Energy, 88, 1813–1824.

Salogni, A. and Colonna, P. (2010). Modeling of solid oxide fuel cells for dynamic simulations of integrated systems. Applied Thermal Engineering, 30, 464-477.

Thorin E., Johan Lindmark; Erik Dahlquist; Eva Nordlander; Eva Nordlander; Jan Kastensson, Niklas Leksell. Performance Optimization of the Växtkraft Biogas Production Plant. Applied Energy. Accepted paper 6 March, 2012.

Vassileva, I., Wallin, F., Dahlquist, E.: Analytical comparison between electricity consumption and behavioral characteristics of Swedish households in rented apartments . Applied Energy 90 (1), pp. 182-188,2012.

Vassileva I. and Dahlquist E.: Economical savings through lowering energy consumption in rented apartments. a case study in Västerås area. Journal of numerical and applied mathematics, vol 1(90), 2008, pp 234-245

Venkatasubramanian V, Rengaswamy R, Yin K, Kavuri S N. (2003a). A review of process fault detection and diagnosis Part I: Quantitative model-based methods. Computers and Chemical Engineering, 27, 293-311.

Venkatasubramanian V, Rengaswamy R, Yin K, Kavuri S N. (2003b). A review of process fault detection and diagnosis: Part II: Qualitative models and search strategies. Computers and Chemical Engineering 27, 313-326.

Venkatasubramanian V, Rengaswamy R, Yin K, Kavuri S N. (2003c). A review of process fault detection and diagnosis: Part III: Process history based methods. Computers and Chemical Engineering, 27, 327-346.

Widarsson, B. and Dotzauer, E. (2008). Bayesian Networks-based early-warning for leakage in recovery boilers. Applied Thermal Engineering, 28-7, 750-764.

Widén J, M. Lundh, I. Vassileva, E. Dahlquist, K. Ellegård and E. Wäckelgård (2009) Constructing load profiles for household electricity and hot water from time-use data – modeling approach and validation. Energy and Buildings. Energy and Buildings 41: 753–768

Development of a multi-level approach to model and optimise the Kalina Split Cycle for marine diesel engines

Ulrik Larsen, Tuong-Van Nguyen, Fredrik Haglind*

Section of Thermal Energy, Department of Mechanical Engineering, Technical University of Denmark, Building 403, Nils Koppels Allé, 2800 Kongens Lyngby, Denmark

Abstract

In the marine sector there is a strong motivation for increasing the propulsion system energy efficiency, mainly because of increasing fuel prices and stricter upcoming emission regulations. The Kalina cycle, based on a mixture of ammonia and water as working fluid, exhibits higher conversion efficiencies than conventional power cycles and could be suitable for this purpose. The Split Cycle technique provides a method to further increase the thermal efficiency, by reducing the thermodynamic losses in the heat recovery system. This is achieved by having two separate streams of different ammonia concentrations entering and leaving a first evaporator stage before being mixed at the inlet of a second evaporator stage. It seems that modelling efforts showing the advantages of the Split Cycle have not been presented in the literature yet. Thus, a thermodynamic model of the Split Cycle is introduced in this work. Modelling and optimisation of the rather complex cycle requires approaching the problem at different system levels. This paper investigates tools and methods suitable for demonstrating the feasibility and advantages of the Split Cycle. The integrated model developed and presented in this paper combines three sub-models all using the NIST REFPROP equations of state: a separator and mixing subsystem model to handle the inherent constraints of the Split Cycle, a component-based model to optimise the heat exchanger operating conditions, and a process model to investigate the complete thermodynamic cycle. Results suggest a 9% net power output increase and 7% higher thermal efficiency compared to the baseline case.

Keywords: Kalina Split Cycle, Multi-Level Modelling, Process Integration, Waste Heat Recovery

1. Introduction

The International Maritime Organisation, under the United Nations organisation, is expected to adopt an energy efficiency design index (EEDI) for ships in 2013. For this reason and because of increasing fuel prices, this sector is in need of technologies that could further improve the efficiency of propulsion systems [1].

In this context, growing attention is paid to waste heat recovery power cycles, with the Kalina Cycle among those. Named from its inventor Alexander Kalina in 1983 [2], this thermodynamic cycle is using a mixture of water and ammonia as working fluid.

It was intended for waste heat recovery in three main fields of application: geothermics at temperatures from 100-200°C [3–10], integrated combustion engine heat recovery mainly at temperatures around 300°C [11–15] and for gas turbines at even higher temperatures [16–20]. A well-documented and tested Kalina cy-

*Principal corresponding author. Tel.: +4545254113
Email address: frh@mek.dtu.dk (Fredrik Haglind)

Nomenclature

Acronyms

EEDI	Energy Efficiency Design Index
EOS	Equation of State
IP	Intermediate Pressure
NIST	National Institute of Standards and Technologies
SC	Split Cycle
TRF	Tillner-Roth and Friend

Greek Symbols

Δ	Difference between to states

Symbols

$\dot{m}$	Mass flow rate
H	Non-specific enthalpy
h	Specific enthalpy
p	Pressure
Q	Vapour quality
S	Mass flow rate splitting fraction
T	Temperature
x	Ammonia fraction by mass
y	Ammonia fraction by mole

Subscripts

b	Boiling point
c	Composite stream
d	Dew point
e	Exhaust gas
f	Separator feed stream
i	Inlet stream
l	Lean ammonia concentration
L	Liquid fraction
o	Outlet stream
r	Rich ammonia concentration
V	Vapour fraction
w	Working fluid

cle pilot plant converting heat at relatively high temperatures (450-550°C), from a gas furnace is the Canoga plant (USA)[4, 21–23].

In 1985 Kalina filed a petition for a US patent [24] on the Split Cycle, which is an alternative configuration of the Kalina process. In that petition the process is described only qualitatively and no model proving the comparative advantages seems to have been published since. The focus of this paper is therefore to present a thermodynamic model and an optimisation methodology of the Kalina Split Cycle process (SC).

In the conventional Kalina cycle, heat exchange in the heat recovery system only takes place between two streams: the heat source (e.g exhaust gases from a gas turbine) and the heat sink (ammonia-water mixture working fluid). The specific feature of the SC is that two cold streams of different ammonia concentrations run through a preheater and a first evaporator stage. The two streams are then mixed before entering a second evaporator and a superheater.

The higher complexity of this process introduces additional degrees of freedom and unknowns at different system levels. There is therefore a need for a multi-level approach which addresses these modelling and optimisation challenges.

The approach and models developed to evaluate a Kalina SC are presented in the following. The thermodynamic performance of the modified heat recovery system is assessed in comparison with a baseline case, which is a conventional Kalina cycle based on exhaust gases

at 346°C from marine diesel engines, as documented by Bombarda [25]. The baseline case cycle is a type of Kalina cycle which is common in the literature, among others documented by Leibowitz et al. [21] and Jonsson et al. [19]. The SC model presented in the present work maintains the same constraints and boundary conditions as the baseline case.

2. Kalina Split cycle

Ammonia-water is a *zeotropic* mixture, which means that vapour and liquid phases at equilibrium never have both identical temperatures and compositions. During evaporation and condensation processes, the liquid and vapour compositions of zeotropic mixtures will continually change, and the saturation temperatures of these two phases will vary in consequence. It is thus possible to affect the thermophysical properties of the Kalina working fluid either by changing the operating pressure or by varying the ammonia concentration of the mixture.

Ammonia, being more volatile than water, is the first component to evaporate. The ammonia concentration in the liquid phase progressively decreases, causing a continual rise of the boiling temperature. The existence of this temperature glide may lead to a better match between the temperature profiles of the heat source and the working fluid, reducing the internal irreversibilities of the heat recovery process.

In an attempt to further reduce them, Dr. Kalina proposed in his patent petitions an alternative arrangement of this power cycle, referred to as the Split Cycle [24]. Other work of the same author [26] suggested that this configuration could reach a 2^{nd} law efficiency of 75-80% for various heat sources.

The idea of the SC is to use two separate streams of ammonia-water, with different concentrations, running through a first evaporator. An important constraint proposed by Kalina is to have the ammonia-rich stream exit the first evaporator as saturated vapour (dew point) while the ammonia-lean stream exits as saturated liquid (bubble point). This proposed constraint is important for minimising thermodynamic losses and is therefore adopted in this work, leaving an investigation of the consequences of this assumption for future work. The constraint makes it harder to set initial parameters and to optimise the cycle and is thus providing motivation for developing the presented methodology. The two streams are then mixed into a composite stream and the newly formed two-phase mixture is evaporated and superheated before running through the turbine.

The modified Kalina SC is illustrated in Figure 1. The main differences from the conventional configuration are the use of additional mixers, splitters, pumps and recuperators between the separator and the turbine. In the simple Kalina cycle, the ammonia-rich vapour at the top outlet of the separator flows through a recuperator first and then a mixer before being condensed, while the ammonia-lean liquid at the bottom flows through another recuperator before being throttled.

In the SC, the very ammonia-rich vapour is first split into two sub-streams (19 and 26). Both are partly diluted in different proportions with fractions of the very ammonia-lean liquid flow and pass a succession of two recuperators where they are cooled down. The richer of these two streams (22) is then condensed (23) and pumped (24), before it is preheated (25) and flows through the heat recovery system. The leaner stream (29) is pumped (30) and preheated (31) before running through the first evaporator. These two streams are then mixed at the same temperature (1) before entering the second evaporator (2) and the superheater (3).

The very ammonia-lean liquid from the bottom of the separator is split into three substreams. Two (16 and 17) are used to adjust the concentration and mass flow rate of the

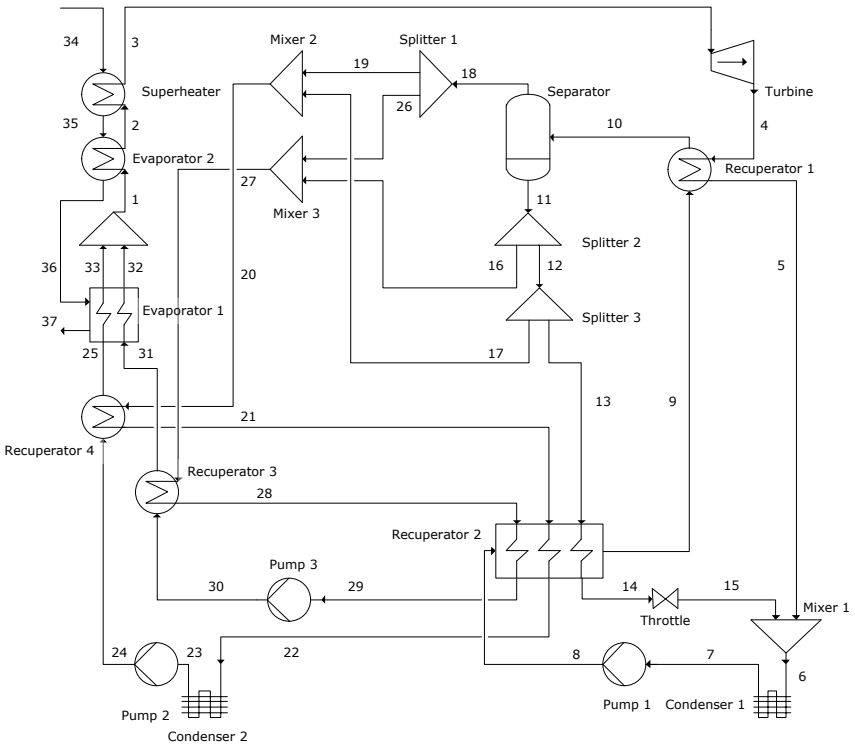

Figure 1: Process flowchart of the Kalina Split Cycle process

two rich vapour sub-streams from the top of the separator. The latter (13) runs through a recuperator where it is cooled down (14) before being throttled (15) and mixed with the ammonia-rich solution out of the turbine system.

Theoretical studies showed that, compared to the conventional configuration, the SC induces a lower entropy generation because of the better match between the temperature profiles of the two cold streams and the heat source [26]. The gradient of the evaporation temperature curve can to some degree be adjusted to the temperature profile of the heat source by selecting the optimal composition of each of the two streams, as illustrated in Figure 2. The line from (25,31) to the point ($T_{r,b}$) represent the preheating stage. From here to point (1), (2) and (3) the fully drawn line shows the heat transfer in the SC case. The upper dashed line show how the heat transfer would be if the stream were not split but instead the composite stream was used. The point (T_b) shows the boiling point of the composite stream, and it is clear that the pinch point temperature difference is much smaller and possibly violated in this case. The lower dashed line from ($T_{r,bub}$) to (2), shows how the heat transfer would happen if only the rich stream concentration was used. Evaporation would occur at lower temperatures and thus likely causing a lower thermal efficiency.

3. Methodology

Given the constraint of having identical temperatures and pressures of the rich and lean streams exiting the first evaporator, whilst also requiring the rich stream to be saturated vapour and the lean stream saturated liquid, initial parameter estimation and subsequent optimisation at full process level are not feasible. The choice was made to build two submodels which could accurately predict the op-

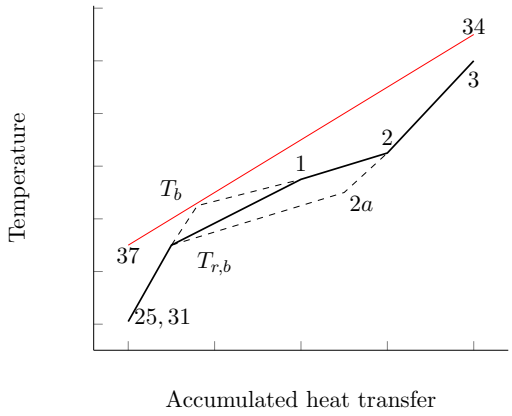

Figure 2: Theoretical T-Q diagram of the Heat Recovery System to explain the Split Cycle

timum performance of the full process and subsequently obtain full process validation. In the next sub-sections, three modelling levels are considered and presented: thermodynamic property level, governing subsystems at component level and full process level.

3.1. Thermodynamic property level

Tillner-Roth and Friend (TRF) presented their model of the ammonia-water system in 1998 [27]. Their motivation was the rising interest in modelling the Kalina cycle and thus the arising need for an accurate model for this working fluid mixture over a wide range of concentrations, temperatures and pressures. At the time, there was seemingly no model covering both the liquid, two-phase and vapour domains with satisfying accuracy [27]. Based on a thorough survey [28] of the publicly available experimentally obtained properties for the system, a fundamental equation of state (EOS) which is claimed to be accurate up to 40 MPa was derived.

Thorin et al. [29] compared in 1999 the Tillner-Roth and Friend model with both experimental data and two other EOS derived for the ammonia-water system (Stecco-Desideri and Ibrahim and Klein). Analysis showed that the TRF EOS is generally more accurate than the two other EOS because of an additional correction factor. Additionally the TRF EOS is valid up to higher pressures than the two others which are valid up to 11.5 and 20 MPa respectively. Thorin also compared the thermal efficiency of a Kalina cycle using boiler pressures between 10-18 MPa and found that the choice of EOS does influence the efficiency up to 1.5% points at high pressures.

For the above mentioned reasons and since the TRF EOS is included as a property model in Aspen and in Matlab with NIST REFPROP, this EOS was chosen for the sub- and full process models. A disadvantage of using this property model is its complexity. Except when the phase is specified, the model needs first to determine if the fluid is in the liquid, vapour or two-phase domain. As experienced by the authors and as also confirmed by personal communication with Eric Lemmon (NIST), the TRF model in REFPROP has occasional non-convergence issues (at certain random points in the thermodynamic domain). In Aspen Plus it is possible to specify phase and thereby to increase the convergence efficiency. When compared to the Peng-Robinson EOS, the TRF EOS seems to be significantly more accurate for the Kalina cycle. Consequently, the baseline model in the present work has minor deviances in the thermodynamic properties at some points in the process, compared to the model in the work of Bombarda (which is used as baseline) [25]. An advantage of the Peng-

Robinson EOS is that it is simpler and converges easily, a benefit traded in this work in order to obtain better accuracy.

3.2. Subsystem Level

A subsystem is here regarded as a system of components which is an integrated part of the whole process. In the following, two subsystems are discussed: firstly, the heat exchangers system described earlier, and secondly, the separation and mixing system. The motivation for making the models of these subsystems is to ease initial parameter estimations and optimisation of the process. Both subsystems were validated using corresponding subsystem models in Aspen Plus.

3.2.1. Heat exchanger system

The composite working fluid mass flow rate exiting the boiler can be used as a measure proportional to the process work output, since the thermodynamics state at the boiler outlet is held constant. The aim of the following methodology is thus to uncover the relation between the maximum possible mass flow rate and the composition of the two split streams.

Rich and lean streams entering and exiting the first evaporator should have identical temperatures and pressures, and leave as saturated vapour and liquid respectively. Any chosen composition of the rich stream (x_r) results therefore in only one possible composition of the lean one and only one ratio between the rich and lean mass flow rates.

Thus the final optimisation is based on the rich stream composition versus boiler mass flow.

Composition of the lean mass flow (x_l) is calculated from the rich stream composition by solving the following equation system:

$$T_{r,d} = T(p = p_w, Q = 1, x = x_r) \quad (1)$$
$$T_{l,b} = T(p = p_w, Q = 0, x = x_l) \quad (2)$$
$$T_{r,d} - T_{l,b} = 0 \quad (3)$$

where $T_{r,d}$ is the dew point temperature of the rich stream, $T_{l,b}$ is the bubble point temperature of the lean stream, p_w is the working fluid pressure and Q is vapour quality. Then, the mass flow ratio between the rich and lean streams are found by solving the following mass balance equations (note that the actual mass flow of the composite stream ($\dot{m}_c$) is not known at this stage):

$$\dot{m}_c - \dot{m}_r + \dot{m}_l = 0 \quad (4)$$
$$x_c\dot{m}_c - x_r\dot{m}_r - x_l\dot{m}_l = 0 \quad (5)$$

where $\dot{m}_r$ and $\dot{m}_l$ are the mass flow rates of the rich and lean streams and x_c is the composite stream composition, i.e. the stream exiting the boiler. Using an energy balance over the entire boiler, the mass flow of the (composite) working fluid, can be found. The hot source mass flow, pressure and temperature at the outlet and inlet are known parameters. Also known is the superheater approach, the pressure of the working fluid as well as the inlet states (pressure, temperature and composition) of the working fluid streams:

$$\dot{m}_c = \dot{m}_e \frac{h_{e,i} - h_{e,o}}{h_{w,o} - \frac{\dot{m}_r}{\dot{m}_r+\dot{m}_l}h_{r,i} - \frac{\dot{m}_l}{\dot{m}_r+\dot{m}_l}h_{l,i}} \quad (6)$$

where $\dot{m}_e$, $h_{e,i}$ and $h_{e,o}$ are the mass flow rate and enthalpies in and out of the boiler respectively. $h_{w,o}$, $h_{r,i}$ and $h_{l,i}$ are the enthalpies of the working fluid exiting the boiler and the rich and lean stream entering. All enthalpies in the above equation are found using $h = h(T, p, x)$. Upon finding the mass flow of the composite stream, the rich and lean mass flows can be calculated. In order to estimate the minimum temperature difference in the boiler, both heat exchangers are divided into a number of steps (n). The first evaporator (including preheater) is modelled by dividing the temperature between outlet and inlet into steps ΔT_s and assuming temperature equilibrium between the

lean and rich streams in each division. Hereby the enthalpy in each step is found:

$$\Delta T_s = \frac{(T_{l,b} - T_{w,i})}{n} \quad (7)$$

$$T_{r,i} = T_{l,i} = T_{w,i} + (i-1)\Delta T_s \quad (8)$$

$$\Delta H_{s,j} = \dot{m}_r(h_{r,j} - h_{r,1}) + \dot{m}_l(h_{l,j} - h_{l,1}) \quad (9)$$

where $i = [2, 3, ...(n+1)]$ and $j = [2, 3, ...n]$, $T_{w,i}$ is the working fluid temperature, ΔH_s the difference in enthalpy between two steps with i and j representing the step number. Since the enthalpy increase numerically in each step is the same for working fluid and heat source, the temperature of the hot source at each step is thus found from the enthalpies, $T = T(h, p, x)$. The minimum temperature difference can now be found and a similar approach is used for the second evaporator. By varying x_r the maximum working fluid mass flow rate is found, but still the question remains whether the mixing system can deliver the corresponding rich and lean streams.

3.2.2. Mixing system

Desired outputs from the mixing system model are the mass flow fractions of the three splitters (S_1, S_2 and S_3 respectively), as shown in figure 1, and the mass flow feeding the separator ($\dot{m}_f$). Inputs are the mass flow rates and compositions found in the heat exchanger subsystem model. Being fed by the separator, the mixing subsystem model includes this component beginning from the inlet of the separator, a stream which composition (x_f) is chosen to be the same as the baseline case for comparison reasons. Other inputs to the model are p_w, x_c and $\dot{m}_c$. Assuming an isothermal adiabatic process, the single stage separator can be modelled with the use of the EOS and an ammonia mass balance. The equilibrium concentrations of the liquid and vapour phases (x_l and x_v) are found using a REFPROP function, provided an assumed temperature and pressure (T_f and p_f) similar to the baseline case (from the Bombarda article [25]):

$$[x_L, x_V] = X(T = T_f, p = p_f, x = x_f) \quad (10)$$

where $x_{18} = x_V$ and $x_{11} = x_L$ (figure 1). Solving the following equation system of mass balances, provides the liquid and vapour mass flows from the separator:

$$\dot{m}_{11} = \dot{m}_f - \dot{m}_{18} \quad (11)$$

$$x_f\dot{m}_f - x_{18}\dot{m}_{18} - x_{11}\dot{m}_{11} = 0 \quad (12)$$

The following equations are common for the three splitters, here splitter 1:

$$x_{26} = x_{18} \quad (13)$$

$$x_{19} = x_{18} \quad (14)$$

$$\dot{m}_{26} + \dot{m}_{19} = \dot{m}_{18} \quad (15)$$

$$\dot{m}_{26} = S_1\dot{m}_{18} \quad (16)$$

Where S_1 is the ratio to be found and used in the full process model. The mixers are described by both a mass balance and an ammonia mass balance:

$$\dot{m}_{27} = \dot{m}_{16} + \dot{m}_{26} \quad (17)$$

$$x_{27}\dot{m}_{27} = x_{16}\dot{m}_{16} + x_{26}\dot{m}_{26} \quad (18)$$

This equation system is solved iteratively and returns the separator feed mass flow and the splitter fractions, thereby producing the desired rich and lean streams characteristics ($\dot{m}, x$). Coupling of the two sub models described here provides an accurate tool needed to optimise the full process of the Kalina Split cycle within the boundary conditions given.

3.3. Process modelling

3.3.1. Available models

Aspen Plus is a widely used commercial process simulation software, which is based on several methods and packages for estimations of

thermodynamic properties. Modelling of the overall Kalina cycle was carried out using Aspen Plus(R) v7.2, based on the REFPROP property method for consistency.

This process flow-sheet program also includes several sets of modules for simulating unit operations such as compressors and turbines, heat exchangers and separators, pumps and throttles, etc. Calculations are based on physical relations (mass and energy balances, heat transfer and fluid dynamics) and are conducted iteratively.

Aspen Plus is a sequential modular program, meaning that the sets of equations used to model the overall system are solved in a certain order, in contrast to equation-oriented programs which solve the equation sets simultaneously. In case of processes with internal loops (e.g thermodynamic cycles), equation sets are solved iteratively and the implementation of initial guess values and constraints is needed to avoid convergence issues and accelerate the problem resolution.

It is possible to implement kinetic-rate models (e.g kinetic mechanisms for chemical reactions and rate-based models for separation and distillation). However, it is assumed that an equilibrium-based separator module can rigorously model the two-phase separator used in Kalina cycles.

3.3.2. General modelling assumptions

The simulations of the simple Kalina cycle and of the Split Cycle were both based on the following assumptions and data, adopted from the baseline case, which is based on work presented by Bombarda [25]. The chemical compounds considered in the simulations are: N_2, O_2, H_2O, CO_2, Ar and NH_3. The heat source considered in this study are exhaust gases from two marine diesel engines, with the following molar composition 74.6% N_2, 11.7% O_2, 6.7% H_2O, 5.9% CO_2 and 1.1% Ar and a total mass flow rate of $35\frac{kg}{s}$. The ammonia-water mixture enters the heat recovery system at a temperature of 83.5°C and has the following mass composition at the inlet of the turbine 77.2% NH_3, 22.8% H_2O. Assumptions on the process design are listed below:

- Exhaust gas pressure and temperature: 2 bar and 346°C
- Stack temperature: 127.7°C
- Minimum allowable pinch point temperature difference in boiler: 21.9°C
- Super heater approach: 16°C
- Minimum allowable pinch point temperature difference in low and intermediate pressure (IP) recuperators: 4.5°C
- Minimum allowable pinch point temperature difference in high pressure recuperator: 16.5°C
- Pressure levels: 5.94, 10, 100 bar
- Separator temperature: 100°C
- Cooling water temperature: 20°C
- Adiabatic separator
- Homogeneous fluid flow and temperatures
- Turbine mechanical and isentropic efficiency: 96% and 75%
- Pumps driver efficiency and isentropic efficiency: 95 % and 70%
- Ammonia concentration in composite stream, y_3: 78.6%
- Heat to the environment and pressure losses in heat exchangers are neglected

3.3.3. Specific modelling assumptions

Specific assumptions related to the design of the Kalina process without Split Cycle are listed below:

- IP condensation temperature: 33°C
- IP recuperator: 2 streams

Specific assumptions related to the design of the Kalina process with Split Cycle are listed below:

- Additional pumps have the same efficiency
- Additional mixers and splitters are adiabatic
- IP condensation temperature: 26°C

- IP recuperator: 4 streams

One of the main differences between the conventional Kalina process and the Split Cycle is the ammonia concentration of the rich mixture at the inlet of the heat recovery system. In the first case, the ammonia content is between 70-75%$_{wt}$, which corresponds to a condensing temperature of about 33°C at a pressure of 10 bar. In the second case, the ammonia content of the rich stream is 10 percentage points higher, which corresponds to a condensing temperature of 26°C.

In order to fully condense the ammonia-rich stream in the Split Cycle, the operating temperature of the condenser should be decreased from 33°C to 26°C (effectuated by larger cooling water flow rate). As a consequence, the operating parameters of the cooling system and of the condenser are slightly different compared to the baseline case.

3.3.4. Optimisation

Optimisation of the Split Cycle is conducted by changing the pressure level to reach the same pinch point temperature difference in the heat recovery system (21.9°C) while keeping the same temperature inlet and outlet conditions, and an identical ammonia concentration at the boiler outlet (point 3 Figure 1).

4. Results and discussion

By varying the rich (and lean) stream compositions, the temperatures of the working fluid in the first evaporator changes and thus also the pinch point. This variation is shown in Figure 3 at pressures from 100 to 140 bar. The constraint of pinch point temperature difference of 21.9°C is not respected at any concentration at 140 bar pressure and above and the maximum net work output without any violation is found at 138 bar and an x_{rich} of 0.90. It is also shown in the figure how the pinch point temperature difference is larger than the baseline case of 21.9°C, when using SC at baseline pressures and high rich stream concentrations.

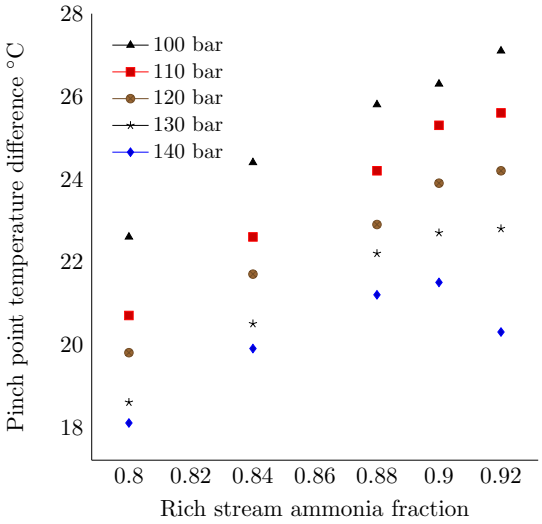

Figure 3: Rich stream composition versus pinch point temperature difference

Changing the rich and lean streams compositions does not enable significant changes in the maximum mass flow rate and consequently the turbine work output. The maximum obtainable turbine work output at various concentrations and pressures is shown in Figure 4. The maximum output is, in most cases, found at rich stream compositions of about 0.90.

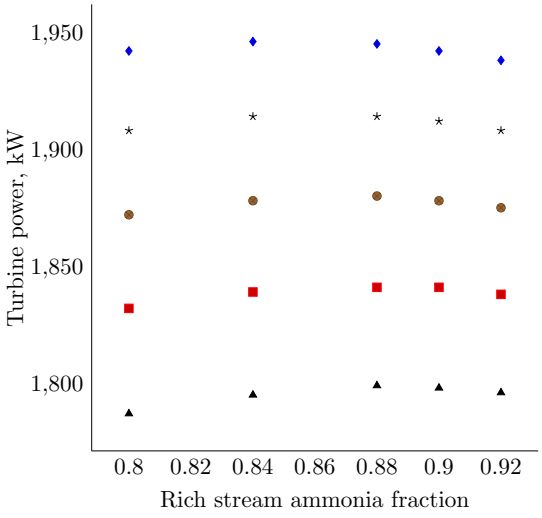

Figure 4: Rich stream composition versus turbine power

In Figure 5 the temperatures as a function of the accumulated heat transfer in the entire heat

recovery system, as seen from the hot source side, is shown. Looking at the SC case at 100 bar, it is seen that the alignment of temperatures of the hot and cold streams, is deteriorated compared to the baseline case. Despite that, the turbine work output is slightly higher because the early evaporation of the rich stream enables a higher mass flow rate, a parameter limited by the pinch point temperature difference. Compared to the baseline case, the optimised case at 138 bar shows a visibly closer alignment of temperatures of the hot and cold streams, while the pinch point temperature difference is not changed from that of the baseline case. The average temperature in the heat uptake is clearly higher in this case. Although the Split Cycle streams are only separated in the first evaporator, the improved match continues through the second evaporator.

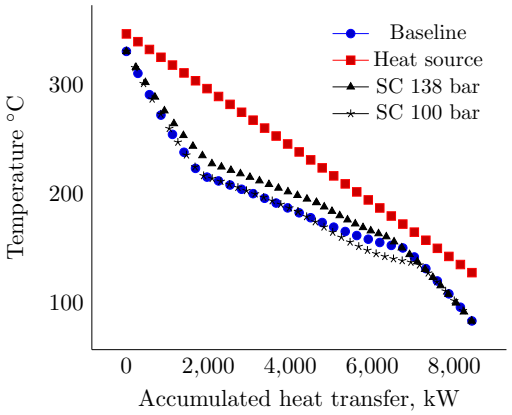

Figure 5: T-Q diagram of the boiler

Using the SC configuration is thus seen to enable an increased maximum pressure in the cycle without violating the pinch point temperature difference constraint. Reversely, the baseline case does not allow higher pressures without a pinch point temperature difference violation, indicating that the baseline cycle parameters are indeed optimised. Figure 6 shows how the turbine work, cycle net work and thermal efficiency increase with higher boiler pressure. The shown cases were optimised in terms of concentrations and mass flows of the rich and lean streams, aiming at maximum power. Even more power could be obtained with a smaller pinch point temperature difference. Temperature and vapour quality at the turbine outlet decrease slightly as the inlet pressure increases without affecting the rest of the process markedly. The vapour quality at 138 bar is 96% compared to 99% in the baseline case.

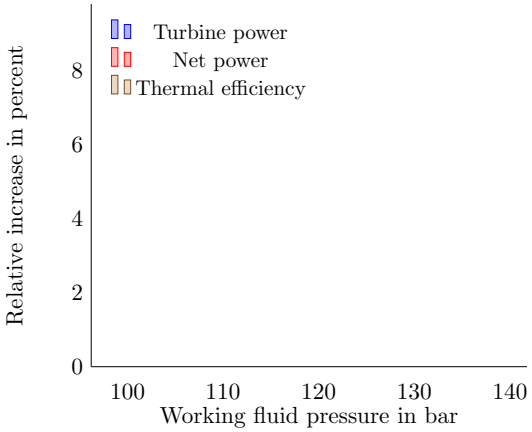

Figure 6: Cycle output versus maximum pressure

As should be expected, the relative increases in thermal efficiency of the cycle and the net work output are identical and in the baseline case the thermal efficiency is 20.1% while at 138 bar in the optimised SC case 21.5 % is achieved. States of all the points in the optimised Split Cycle are shown in the appendix.

5. Conclusion

A thermodynamic model of the Kalina Split Cycle and a methodology for optimising the cycle was presented. The methodology, consisting of two subsystem models, has made it possible to optimise the entire cycle effectively. It has been shown that the concept of using two different streams instead of one running through the evaporator does bring some advantages. The temperature development of the working fluid can be altered by changing the composition and mass flow rates of the two streams, in order to obtain a better alignment

of temperatures of the hot and cold streams in the heat exchanger.

Since the richer stream evaporates first and thus results in a larger pinch point temperature difference, higher boiler pressures and work outputs are enabled without violating the pinch point temperature difference limitation.

Results suggest a turbine power output increase of about 9% can be achieved resulting in an increase in thermal efficiency of 7%, or an increase from 20.1 to 21.5% thermal efficiency for the cycle.

Acknowledgements

The authors wish to thank Brian Elmegaard of the Technical University of Denmark and Cecilia Gabrielii of Chalmers University of Technology, Göteborg, Sweden for inspiration and support. The competence and research centre Lighthouse (http://www.lighthouse.nu) is acknowledged for the financial support.

References

[1] The International Maritime Organisation, IMO . The International Maritime Organisation. 2012.

[2] Kalina A. Combined cycle and waste heat recovery power systems based on a novel thermodynamic energy cycle utilizing low-temperature heat for power generation. Am Soc Mech Eng, (Pap); (United States) 1983;83-JPGC-GT.

[3] Kalina A, Leibowitz H, Lazzeri L, Diotti F. Recent development in the application of Kalina cycle for geothermal plants, geothermal-energy.org. 1995.

[4] Lazzeri L, Diotti F, Bruzzone M, Scala M. Application of Kalina Cycle to Geothermal Applications. Proceedings of the American Power Conference 1995;57(V1):370–3.

[5] Madhawa Hettiarachchi HD, Golubovic M, Worek WM, Ikegami Y. The Performance of the Kalina Cycle System 11(KCS-11) With Low-Temperature Heat Sources. Journal of Energy Resources Technology 2007;129(3):243–.

[6] Koroneos CJ, Rovas DC. Electricity from Geothermal Energy with the Kalina Cycle An Exergy Approach. In: International Conference on Clean Electrical Power, 2007. ICCEP '07. 2007, p. 423–8.

[7] Kalina AI. Application of recent developments in Kalina Cycle technology to the utilization of high temperature geothermal sources. Transactions - Geothermal Resources Council 2008;32:346–50.

[8] Nasruddin D, Usvika R, Rifaldi M, Noor A. Energy and exergy analysis of kalina cycle system (KCS) 34 with mass fraction ammonia-water mixture variation. Journal of Mechanical Science and Technology 2009;23(7):1871–6.

[9] Ogriseck S. Integration of Kalina cycle in a combined heat and power plant, a case study. Applied Thermal Engineering 2009;29(14-15):2843–8.

[10] Valdimarsson P. Geothermal power plant cycles and main components. Tech. Rep.; University of Iceland; Reykjavik; 2011.

[11] Jonnson M, Thorin E, Svedberg G. Gas Engine Bottoming Cycles With Ammonia-Water Mixtures as Working Fluid. ASME -Publications- PWR 1999;34(NO 2):55–66.

[12] Jonsson M, Yan J. Exergy and Pinch Analysis of Diesel Engine Bottoming Cycles with Ammonia-Water Mixtures as Working Fluid 2000;3(2):57–71.

[13] Jonsson M, Yan J. Ammonia-water bottoming cycles: a comparison between gas engines and gas diesel engines as prime movers. Energy 2001;26(1):31–44.

[14] Xia B, Tanaka S, Nakazawa T, Sugita H. Research on the application of the combined cycle used in the power plant for ship propelling systems. Proceedings of the International Conference on Power Engineering : ICOPE 2003;2003(3):3–162.

[15] He M, Zhang X, Zeng K, Gao K. A combined thermodynamic cycle used for waste heat recovery of internal combustion engine. Energy 2011;36(12):6821–9.

[16] Marston CH. Parametric Analysis of the Kalina Cycle. Journal of Engineering for Gas Turbines and Power 1990;112(1):107–.

[17] Marston CH, Hyre M. Gas Turbine Bottoming Cycles: Triple-Pressure Steam Versus Kalina. Journal of Engineering for Gas Turbines and Power 1995;117(1):10–.

[18] Nag P, Gupta A. Exergy analysis of the Kalina cycle. Applied Thermal Engineering 1998;18(6):427–39.

[19] Jonsson M, Yan J. Gas turbine with Kalina bottoming cycle versus evaporative gas turbine cycle. In: Proceedings of the International Joint Power Generation Conference. New Orleans: ISSN 1537-6753; 2001, p. 77–85.

[20] Zhang Y, He M, Jia Z, Liu X. First law-based thermodynamic analysis on Kalina cycle. Frontiers of Energy and Power Engineering in China 2008;2(2):145–51.

[21] Leibowitz HM, Zervos N. Installation and Early Test Results of a 3 MW Kalina Cycle Demonstration Plant. SAE International 1992;1992-08-03.

[22] Zervos NG, Leibowitz HM, Robinson K.

Innovative Kalina cycle promises high efficiency [combined cycle power stations]. Power 1992;136(4):177–9.

[23] Zervos NG, Leibowitz HM, Robinson K. Startup and operating experience of the Kalina cycle demonstration plant. American Society of Mechanical Engineers, International Gas Turbine Institute (Publication) IGTI 1992;7.

[24] Kalina A. Website of Rex Research, US Patent # 4,548,043. 1985.

[25] Bombarda P, Invernizzi CM, Pietra C. Heat recovery from Diesel engines: A thermodynamic comparison between Kalina and ORC cycles. Applied Thermal Engineering 2010;30(2-3):212–9.

[26] Kalina A. A Kalina cycle technology and its applications. In: American Institute of Chemical Engineers, New York, NY. American Institute of Chemical Engineers, New York, NY; 1986, p. 1–13.

[27] Tillner-Roth R, Friend D. A Helmholtz free energy formulation of the thermodynamic properties of the mixture {water+ammonia}. Journal of Physical and Chemical Reference Data 1998;27(1):63–96.

[28] Tillner-Roth R, Friend DG. Survey and Assessment of Available Measurements on Thermodynamic Properties of the Mixture {Water + Ammonia}. Journal of physical and chemical reference data 1998;27(1):45–62.

[29] Thorin E. Comparison of Correlations for Predicting Thermodynamic Properties of AmmoniaWater Mixtures. International Journal of Thermophysics 2000;21(4):853–70.

Appendix A. States in the Kalina Split Cycle referring to Figure 1

Point	p, bar	T, $°C$	x	$\dot{m}$, $\frac{kg}{s}$	Q
1	138.0	191.8	0.772	4.48	0.458
2	138.0	227.9	0.772	4.48	1.000
3	138.0	330.0	0.772	4.48	-
4	5.9	108.7	0.772	4.48	0.958
5	5.9	75.7	0.772	4.48	0.713
6	5.9	73.0	0.600	7.14	0.426
7	5.9	25.0	0.600	7.14	0.000
8	10.0	25.1	0.600	7.14	-
9	10.0	75.0	0.600	7.14	0.316
10	10.0	100.0	0.600	7.14	0.479
11	10.0	100.0	0.308	3.78	0.000
12	10.0	100.0	0.308	2.76	0.000
13	10.0	100.0	0.308	2.65	0.000
14	10.0	44.0	0.308	2.65	0.000
15	5.9	44.1	0.308	2.65	-
16	10.0	100.0	0.308	1.02	0.000
17	10.0	100.0	0.308	0.11	0.000
18	10.0	100.0	0.928	3.35	1.000
19	10.0	100.0	0.928	1.93	1.000
20	10.0	100.0	0.895	2.04	0.948
21	10.0	75.0	0.895	2.04	0.848
22	10.0	29.9	0.895	2.04	0.248
23	10.0	26.0	0.895	2.04	0.000
24	138.0	30.4	0.895	2.04	-
25	138.0	83.5	0.895	2.04	-
26	10.0	100.0	0.928	1.42	1.000
27	10.0	100.0	0.669	2.44	0.590
28	10.0	83.3	0.669	2.44	0.493
29	10.0	35.0	0.669	2.44	-
30	138.0	38.2	0.669	2.44	-
31	138.0	83.5	0.669	2.44	-
32	138.0	191.8	0.669	2.44	0.000
33	138.0	191.8	0.895	2.04	1.000
34	2.0	346.0	-	35.00	-
35	2.0	254.8	-	35.00	-
36	2.0	227.1	-	35.00	-
37	2.0	127.8	-	35.00	-

Automatic Chromatogram Analysis

Jani Tomperi*, Esko K. Juuso*, Kauko Leiviskä*

*University of Oulu, Control Engineering Laboratory,
P.O.Box 4300, FIN-90014 University of Oulu, Finland.
(e-mail: Jani.Tomperi | Esko.Juuso | Kauko.Leiviska @oulu.fi)*

Abstract: Chromatography has been found an efficient tool for analysing the water quality, especially natural organic matter (NOM) content, in water treatment processes. Information of the fast and relatively easy chromatography measurements can be used, by itself or together with other process measurements, for process control and improving the water quality. Unfortunately, some chromatography measurement results are available only as graphical chromatograms or in software specific data file and cannot be transmitted to other software for more detailed mathematical analysis, or to the automation system of the water treatment plant. In this paper, the automatic chromatogram analysis method is developed using Matlab. Graphical chromatograms are converted to numerical data for easier and more efficient processing and analysing. The automatic analysis method calculates the significant values (e.g. peak maximums, peak areas) of the chromatograms, and provides an effective and fast way to monitor the water quality.

***Keywords**: Drinking Water; High-Pressure Size Exclusion Chromatography; Matlab; Natural Organic Matter; Water quality.*

1. INTRODUCTION

Water quality consists of biological, chemical and physical characteristics of water. The quality of drinking water is affected by many factors, for example raw water source, water treatment techniques (sedimentation, filtration, disinfection), distribution network material and biofilm, etc. Natural organic matter (NOM) has become a significant issue in drinking water treatment processes since the negative health effects were discovered. NOM causes colour, taste and odour problems to drinking water, leads to the formation of disinfection by-products and increase chlorine demand, and promotes bacterial re-growth. The NOM affects also the water treatment operations: coagulant and disinfectants are dosed based on the amount of NOM, it blocks active carbon pores and is one of the major membrane foulants. The amount of NOM depends on climate, water source and season of the year. (Teixeira and Nunes 2011, Vuorio et al. 1998)

The most important water quality indicators pH, colour, taste and odour, dissolved metals and organics, salts and microorganisms, are measured frequently from a water treatment process. With basic measurements the general condition of the water treatment process and water quality can be achieved, but using chromatography techniques have been found to give more detailed information. Chromatography technique can be used to analyse the qualitative changes in the water treatment process. Changes in molecular size fractions can be measured from raw water, after different purification steps and from drinking water. In addition to analysing the quality of the water treatment process, chromatography technique can be used to assist the process control.

Chromatography is an analytical technique which can be used for separating chemical substances into its components for analysis or identification. There are e.g. paper, liquid, gas and ion-exchange chromatography techniques which all function in the same way: mobile phase (a liquid or a gas) flows through the stationary phase (solid, or liquid supported on solid) and carries the components of the mixture with it. Different components travel at different rates and the time that a compound travels to the output of the chromatography column is called a retention time. Different components of the analysed mixture are shown as separate peaks or patterns on the visual output, the chromatogram. Concentrations of substance components are measured as the peak area and peak height.

Fast, easy and practical High-Pressure Size Exclusion Chromatography (HPSEC) has been found to be a highly effective and precise analytical method of evaluating the molecular size and molecular weight (MW) distributions of dissolved humic substances in drinking water (Conte and Piccolo 1999, Matilainen et al. 2002, Teixeira and Nunes 2011, Zhou et al. 2000). The HPSEC method provides useful information about the quality of water and the amount of NOM. Correlation among HPSEC and traditional analytic methods like TOC and UV absorbance have been found but in comparison with traditional

analytical methods, HPSEC yields additional information on the removal and transformation of NOM.

In HPSEC analysis, humic molecules are separated on the basis of the different molecular size so that the largest molecules elute first and the smallest molecules elute last in the column (Matilainen et al. 2002). The amount of NOM in one molecular size fraction can be calculated as the height of the peak or the peak area. The peak area is less sensitive to the influence of peak dispersion mechanisms and thus is more reliable and corresponds better to the quantity of the component. Due to dispersion, the peaks may become shorter, broader and more asymmetrical but the total area under the peak remains nearly equal. Sometimes in chromatographic analysis the area under the individual peak curve cannot be resolved. The width of the base, wide of the half of the peak and the height of the peak are also often studied indicators. The total amount of the NOM in a measured water sample is calculated as the sum of all peak areas or peak heights.

Usually from five to seven, even eight different peaks (molecular size fractions) can be found in the chromatography measurement of the Finnish surface water sample. Peaks can be separated to high molecular weight (HMW), which has the lowest retention time, intermediate molecular weight (IMW) and low molecular weight (LMW), which has the highest retention time. Raw water consists mostly of large molecules and generally, high molecular weight matter is easier to remove than low molecular weight matter. (Matilainen et al. 2002, Vuorio et al. 1998)

However, usually chromatography measurement results are stored in software specific data and cannot be transferred or used in other software or systems e.g. Matlab or in the automation system of the water treatment plant. In the worst case only graphical chromatograms are available. In this study, the automatic chromatogram analysis method which converts images to numerical data and analyses the data is created. HPSEC measurements of water samples taken from one Finnish water treatment plant are used to demonstrate the functionality of the developed method. Water samples are collected from several stages of the water treatment process, from raw water to the distribution system. The automatic chromatography analysis method is programmed in Matlab and it consists of image processing of graphical chromatograms and analysis of the resulting data.

2. IMAGE DIGITIZATION

The image digitization is done using familiar methods and Matlab functions. In the first step of image processing all images containing the graphical chromatograms are loaded automatically from a specific folder using Matlab function ‘imread’. Image data is converted to class ‘double’ and converted to gray-scale intensity image by eliminating the hue and saturation information while retaining the luminance. Same processing is done to the background image which is subtracted from the original image. After subtraction all values in image data greater than 1 are converted to value 1 and all values lower than 0 are converted to 0 to ensure the binary black and white image. Pixels with value 0 are displayed as black and pixels with value 1 are displayed as white. In the final step, the contrast of the image is adjusted using ‘imadjust’-function and enhanced using ‘adapthisteq’-function, and the intensity of the image is converted to double precision. (Matlab 2012)

After removing the background and processing the original image, numerical data of the image is stored to a mat-file where every pixel has its specific value, in this case between 0 and 1. The spectrum can now be found by reading the pixel values. After image processing some sporadic values of the spectrum may be missing, but they can be replaced by linear interpolation. Y-values of the spectrum are scaled to real values by reading the minimum and maximum values of the original spectrum from a separate file. For relative comparison, scaling can be also done, for instance, between 0 and 1. The main steps of image digitization are shown in Figure 1.

Locations of studied spikes are case specific and determined beforehand. The time/pixel -relation is used to select the specific spike for area and height calculation and analysis. The area of the spike is calculated using Matlab’s ‘trapz’ integration method, which computes an approximation of the integral of the spectrum via the trapezoidal method. In the analysis, a single spike can be studied and the height of peak(s) or the total area of all peaks can be calculated. Chromatogram can also be divided into, for example, three molecular size fraction areas, which are studied.

3. RESULTS AND DISCUSSION

In this study water samples are taken from eight different process stages of a Finnish water treatment plant and measured using the HPSEC method. Block diagram of the water treatment plant is shown in Figure 2. Water samples are taken from raw water (#1), after adding flocculation chemical (#2), at slow mixing stage (#3), after clarification by flotation (#4), after active carbon filtration (#5), after disinfection using UV radiation (#6) and chlorine (#7) and from the distribution system (#8). Eight peaks are found and analysed in every measured spectrum.

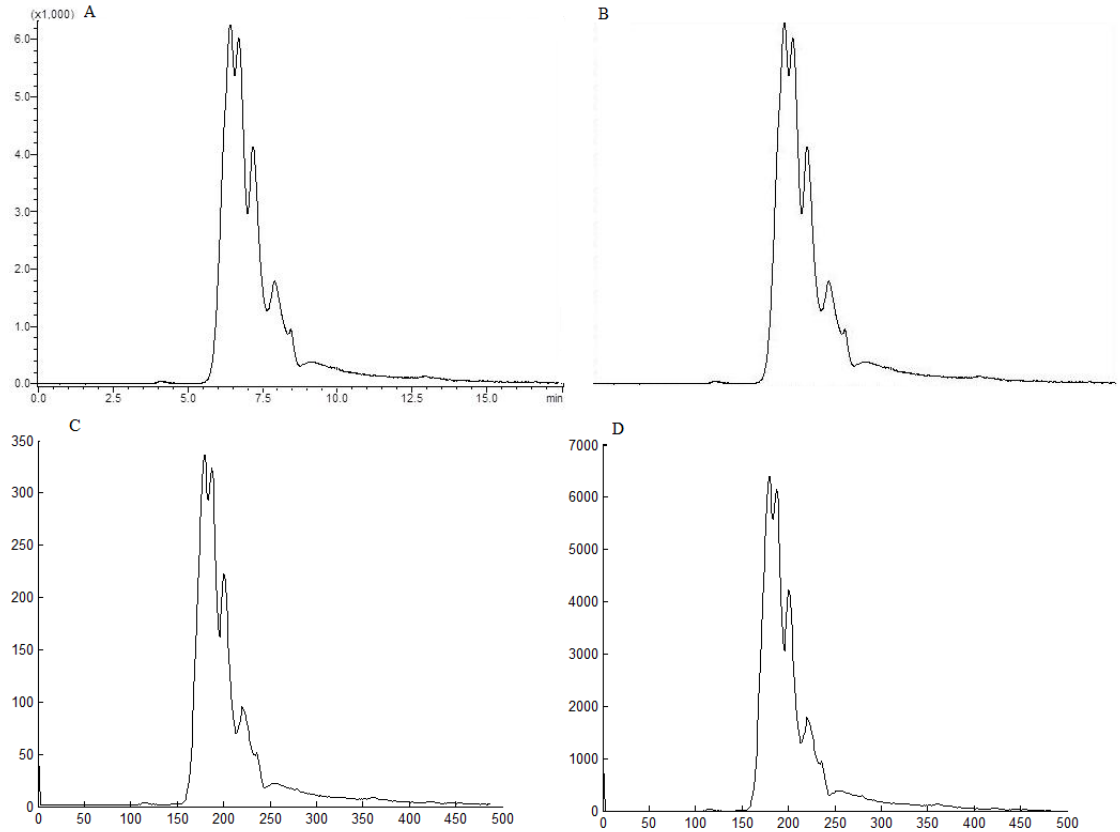

Figure 1. Digitization of a chromatograph: (A) The original chromatograph, (B) Chromatograph after the background is removed, (C) Image has been processed, stored to mat-file and after interpolation plotted, (D) Spectrum values have been scaled to real values.

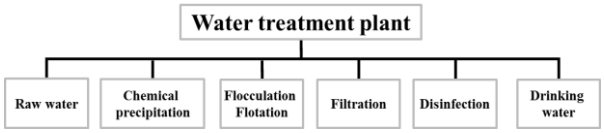

Figure 2. Block diagram of the Finnish water treatment plant.

The automatic chromatogram analysis can process hundreds of images in relatively short time. All results can be listed in numerical form or plotted to various figures. Analysis can be done by comparing different samples at the same process stage, samples from different (or consecutive) process stages, separate peaks in one spectrum etc. Examples of calculated peak heights and areas of raw water and drinking water samples in the numerical form are shown in Table 1. Eight different molecular size fractions are listed from high (#1) to low (#8). Using numerical data, the exact comparison between samples, process stages or peaks is more easy and precise than comparing several plotted spectra.

Table 1. Height and area of peaks analysed from raw water and drinking water samples.

	Raw water		Drinking water	
Peak	Peak height	Peak area	Peak height	Peak area
1	6400	129121	1051	12686
2	4226	54957	1600	17798
3	1798	22394	831	9392
4	947	5850	349	1822
5	382	18081	119	5502
6	134	2983	1072	10975
7	134	2706	57	1232
8	76	1210	81	1327

For visual examination, different figures can be plotted. In Figure 3 peaks are separated to HMW, IMW and LMW organic matter areas. Principles of separation can differ, but in this case the first two peaks are selected as HMW, the next three as IMW and last three as LMW. Figure shows that raw water (process stage #1) consists mostly of large molecules which are removed efficiently, but low molecular weight matter is harder to remove.

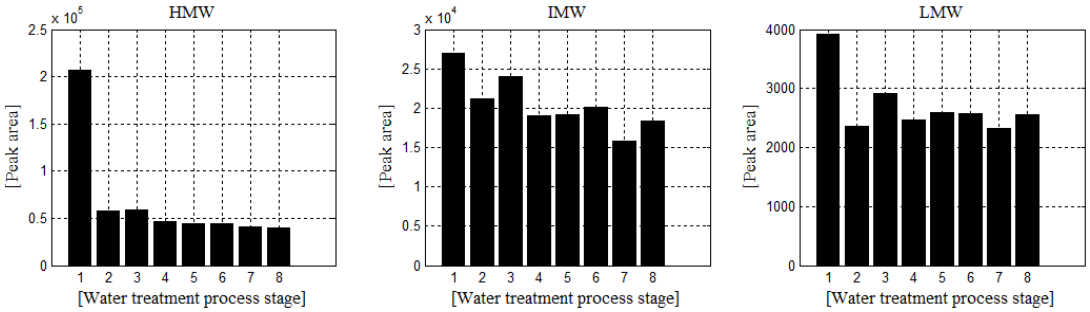

Figure 3. Molecular size fractions are examined as high, intermediate and low molecular weight areas.

In Figure 4, total areas of all peaks in every stage of the water treatment process are presented as bars. Total peak area is the highest in raw water (#1) and decreases towards the sample taken from the distribution system (#8). Thus the water treatment process is efficient and the amount of NOM diminishes.

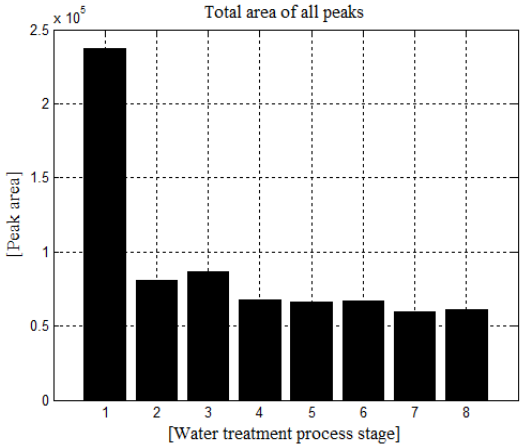

Figure 4. Total peak area of the water samples.

4. CONCLUSIONS

In this paper, a method for digitizing graphical chromatograms describing the operation of the water treatment plant has been developed. Methods familiar from image processing have been used. The digitized data is used in calculating peak heights and areas in the chromatogram that correspond the molecular size distribution of the flow in question.

The paper shows an example, how to use the calculated values in analysing how the water purification proceed in different stages of the plant and what happens to the water quality and NOM in different stages of water treatment. The example comes from one Finnish drinking water purification plant. In this case, NOM is divided into low, intermediate and high molecular weight areas and changes in these are followed through the eight stages of the plant. The results are logical compared with the practical experience.

In the future, the calculations of essential indicators, inter alia the peak area, are improved and the automatic chromatogram analysis method is used for processing and analysing multiple chromatography measurement series from Finnish water treatment processes. Results are compared to each other and with other process measurements to analyse the water quality and functionality of the water treatment process.

ACKNOWLEDGEMENTS

This work was done as a part of the project “Development of a comprehensive water quality management system (POLARIS)”. The funding of the TEKES (the Finnish Funding Agency for Technology and Innovation) and other partners of POLARIS is acknowledged. High-Pressure Size Exclusion Chromatography measurements were done by Mr Jaakko Pellinen who is also acknowledged.

REFERENCES

Conte P. and Piccolo A. (1999). High Pressure Size Exclusion Chromatography (HPSEC) of humic substances: molecular sizes, analytical parameters, and column performance. *Chemosphere*, Vol. 38, No 3, pp. 517-528.

Matilainen A., Lindqvist N., Korhonen S. and Tuhkanen T. (2002). Removal of NOM in the diffrent stages of the water treatment process. *Environment International*, Vol. 28, pp. 457 – 465.

MATLAB. (2012). Image Processing Toolbox User's Guide. *Matlab MathWorks Inc*. web document.

Teixeira M.R. and Nunes L.M. (2011). The impact of natural organic matter seasonal variations in drinking water quality. *Desalination and Water Treatment*, Vol 36, pp. 344 – 353.

Vuorio E., Vahala R., Rintala J. and Laukkanen R. (1998). The evaluation of drinking water treatment performed with HPSEC. *Environment International*, Vol. 24, No 5/6, pp. 617 – 623.

Zhou Q., Cabaniss S. E. and Maurice P.A. (2000). Considerations in the use of High-Pressure Size Exclusion Chromatography (HPSEC) for determining molecular weights of aquatic humic substances. *Water Research*, Vol. 34, No 14, pp. 3505-3514.

Dynamic Operations of the Stripping Column of a CO_2 Capture Plant

Sanoja A Jayarathna[†], Achini Weerasooriya[†], Bernt Lie[†], Morten C Melaaen[†‡]

[†] *Faculty of Technology, Telemark University College, Porsgrunn, Norway*

[‡] *Telemark Technology Centre, Porsgrunn, Norway*

Abstract

Post combustion CO_2 capturing holds an important position in the area of carbon capture and sequestration (CCS). Research is operating in this area ranging from experimental work to modelling work. Dynamic models are interesting since these describe the plant operation during variations, up-stream or down-stream. A model for the stripping column of a capture plant is developed following the rate based approach to represent the heat and mass transfer. Sensitivity of the model for different physiochemical property correlations is analyzed. The predictions of the dynamic model for the stripping column of the capture plant under varying operating conditions in the re-boiler are presented. Predictions of the transient behaviour of the developed stripper model appear realistic.

Keywords: CO_2 capture; Dynamic model; Stripping column; MATLAB

1. Introduction

Achieving a sound solution for the CO_2 emission reduction is of interest and a challenge for the researchers who are actively involved in dealing with the climate issue.

Power generation via fossil fuel-fired power plants is known to be the largest single source of CO_2 emission [1]. The development of capture technologies targeting such sources therefore is important for achieving the goals in CO_2 emission reduction. Post-combustion capture, pre-combustion capture and oxy-fuel combustion are the three main technologies available at present [2], and much research is done with the prospect of developing those techniques further. Post combustion capture is still the best known technique, possibly due to the large number of existing power plants, and the promising developments that are available. CO_2 capture by amine absorption and stripping is currently considered to be the most feasible option for the removal of carbon dioxide from the power plants' exhaust gases [3].

Modelling work related to CO_2 capture technologies plays an important role with respect to the design, control and optimization of the capture process. Several steady state models are already in use for design and optimization purposes, but dynamic simulation models are scarce. Development of dynamic models is important since there is a demand for information related to the dynamics of a plant, such as the transient conditions during the start-up and shut-down and the operation of the plant under varying loads.

A CO_2 capture plant with solvent absorption (absorber/ stripper process) consists of several units which will interact and eventually influence the control and optimization of the process. The operation of a power plant always depends on the power demand and availability of other utilities which can lead to variations in its load. The load variations in the up-stream power plant cause varying exhaust gas rates which may cause operating challenges for the CO_2 capture plant. A dynamic simulation model should predict the influence of the components of the capture plant on each other. Further, the model should predict the influence from the up-stream power plant on the operation of the capture plant, when the power plant is running under varying load conditions.

In recent years, the popularity of the non-equilibrium rate based approach (NEQ) for column modelling has surpassed that of the equilibrium stage approach (EQ), where the liquid and vapour phases are assumed to be in equilibrium. The EQ stage and efficiency based approaches are not very accurate because columns rarely, if ever, operate at equilibrium in actual operation. Further, heat and mass transfer are actually rate based processes that are driven by the gradients of temperature and chemical potentials. In the NEQ approach, the finite mass transfer rates across the liquid-vapour interface are considered. The NEQ approach has been introduced in steady state simulators like Aspen Plus [4] and is even more appropriate for dynamic models.

The dynamic models developed for representing industrial stripping processes have to be accurate and rigorous in order to give insight in the complex transient conditions, and simple to ensure the feasibility of the process simulations [5]. Simplicity will ensure higher execution speed, which is an important factor since simulation of transient conditions is much more complex than steady state simulations. Therefore, it is important to make the model as simple as possible yet good enough to be used in a dynamic simulator. Use of simple thermodynamics can be considered as a wise strategy for developing a dynamic model to ensure simplicity. Inclusion of simple equilibrium models such as the Kent-Eisenberg model [6] instead of much more complex models like e-NRTL [7] in a dynamic model is a good example where the proposed simple equilibrium model will introduce simplicity to the model as well.

Validation of the predictions of the dynamic model still remains a challenge due to the absence of appropriate experimental data. Comparing the predicted steady states from such a dynamic model with the experimental data available in the literature is a possible first step in validating the model.

Little work exists on the development of dynamic models of the stripping tower of a post combustion CO_2 capture plant [8]-[11]. The majority of the existing models have used a complex thermodynamic model which increases the complexity of the models.

In the present work a dynamic model is developed for a stripping tower of a MEA (Mono-Ethanol-Amine) based CO_2 capture plant from the flue gas, following the NEQ approach, and implemented in MATLAB. The structure of the stripping tower considered for modelling is given in Figure 1.

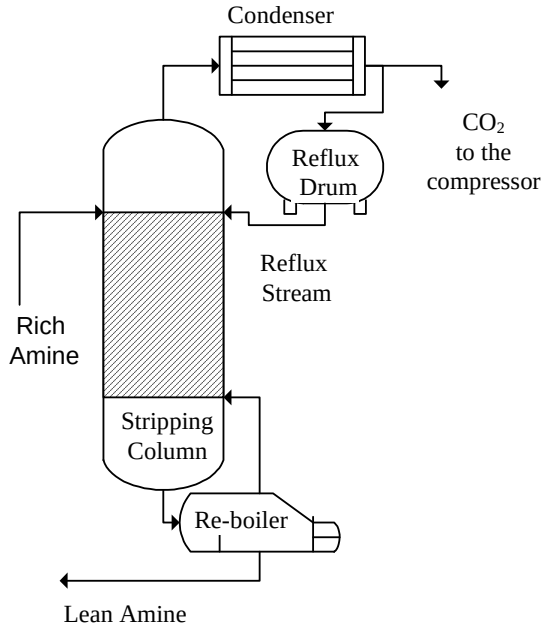

Figure 1. Diagram of a Stripping column

Some steady state results and dynamic predictions are found and recorded. The results are compared with experimental data found in the literature [12]. The sensitivity of the model for different physiochemical correlations is analyzed. Effect on the predictions of the model from the inclusion of minor reactions is also analyzed.

2. Dynamic model

A dynamic model for the stripping column of a CO_2 capturing system is developed and implemented in MATLAB. The stripping column is modelled as a combination of the main tower, the re-boiler and the condenser. The main column is discretized along the height and a set of time dependant equations are developed. Each control volume consists of a separate liquid and vapour phase. Physics and thermodynamics of each phase and interfacial heat and mass transfer are considered with assumptions for developing the set of equations.

The important model assumptions are summarized below.

1. Each phase in a control volume behaves as a continuous stirred tank (CST)
2. Ideal gas phase and ideal liquid phase
3. Interfacial mass transfer of only H_2O, CO_2 and MEA are considered
4. Only the reactions in the liquid phase are of importance
5. Linear pressure drop along the column
6. The packing height of the column is considered
7. Constant volumetric flows of vapour and liquid are considered
8. Heat loss to the surroundings is neglected

1.1. Main model equations

The main model equations consist of the molar (component) and energy balances for the liquid and vapour phases. The component balances for the gas and liquid phases are given by eqs. 1 and 2, respectively,

$$\frac{dc_i^l}{dt} = \frac{u^l}{\lambda}\frac{dc_i^l}{dz} + \frac{1}{\lambda}\dot{n}_{i,trans}''' + \dot{n}_{i,gen}''' \quad (1)$$

$$\frac{dc_i^v}{dt} = -\frac{u^v}{(1-\lambda)}\frac{dc_i^v}{dz} - \frac{1}{(1-\lambda)}\dot{n}_{i,trans}''' \quad (2)$$

where c_i is the concentration of component *i*, *t* is the time, *u* is the velocity, λ is the liquid hold up of the column, *dz* is the height of a control volume and $\dot{n}_i'''$ is the volumetric molar flow or generation. The superscripts "*l*" and "*v*" and the subscripts "*trans*" and "*gen*" stand for the liquid and vapour phases, and the interfacial transfer and the rate of generation, respectively.

Only the main reaction between CO_2 and MEA, which is given by reaction R1, is considered for computing the rate of generation of species.

$$CO_2 + 2MEA \longleftrightarrow MEAH^+ + MEACOO^- \quad (R1)$$

Here $MEAH^+$ is the protonated MEA and $MEACOO^-$ is the carbamate ion formed by the reaction.

The energy balances for the liquid and vapour phases are given by the eqs. 3 and 4, respectively.

$$\frac{dT^l}{dt} = \frac{u^l}{\lambda}\frac{dT^l}{dz} + \frac{h_{ov}A_w}{\lambda\tilde{C}_p^l \Sigma c_i^l}(T^v\text{-}T^l) + \frac{\dot{n}'''_{CO_2,trans}}{\lambda\tilde{C}_p^l \Sigma c_i^l}(-\Delta\tilde{H}_{ab}) + \frac{1}{\lambda\tilde{C}_p^l \Sigma c_i^l}\sum \dot{n}'''_{i,trans}(-\Delta\tilde{H}_{i,vap}) \quad (3)$$

$$\frac{dT^v}{dt} = -\frac{u^v}{(1-\lambda)}\frac{dT^v}{dz} - \frac{h_{ov}A_w}{(1-\lambda)\Sigma(c_i^v\tilde{C}_{p,i}^v)}(T^v\text{-}T^l) \quad (4)$$

Here T is the temperature, h_{ov} is the overall heat transfer coefficient between the two phases, A_w is the effective contact area between the phases and C_p is the specific heat capacity. Decoration "~" denotes molar basis, while $(-\Delta H_{ab})$ and $(-\Delta H_{i,vap})$ represent heat of absorption of CO_2 and heat of condensation of specie i.

The reflux flow, which enters the column in the first control volume from the top of the stripping tower, introduces the following changes (given by eqs. 5 and 6) into eqs. 1 and 3.

$$\frac{u^l}{\lambda}\frac{dc_i^l}{dz} = \frac{u_1^l}{\lambda}\left(\frac{c_{i,1}^l - c_i^l}{\Delta z}\right) + \frac{u_2^l}{\lambda}\left(\frac{c_{i,2}^l - c_i^l}{\Delta z}\right) \quad (5)$$

$$\frac{u^l}{\lambda}\frac{dT^l}{dz} = \frac{u_1^l}{\lambda}\left(\frac{T_1^l - T^l}{\Delta z}\right) + \frac{u_2^l}{\lambda}\left(\frac{T_2^l - T^l}{\Delta z}\right) \quad (6)$$

Here u_1^l and u_2^l are the velocities of the amine flow from the absorption tower and the reflux flow from the reflux drum. Concentrations $c_{i,1}^l$ and $c_{i,2}^l$ represent the concentrations of the rich amine leaving the absorption tower and the reflux stream, respectively. Temperatures T_1^l and T_2^l are correspondent to the rich amine flow and the reflux flow at the inlet to the stripping tower.

The MEA solvent system is considered for analysis, and the thermodynamic and physical parameters are given accordingly. The interfacial mass transfer, reaction kinetics, and phase equilibrium formulations used are the same as presented by Jayarathna et al. [13].

The model is implemented in MATLAB and solver ODE15s is used to solve the set of differential and algebraic equations.

1.2. Condenser and re-boiler models

The condenser of the stripping column is modelled with a reflux drum to hold the liquid until it is refluxed. A flash calculation is performed (the feed stream to the condenser is flashed at constant pressure and temperature) in the condenser to find the liquid and vapour fractions leaving the condenser and their compositions. The liquid flow leaving the condenser enters the reflux drum, and the gas flow leaves for the CO_2 compressor.

The reflux drum is assumed to have constant cross sectional area. The temperature inside the drum and the liquid phase density (which is dominated by water) are also assumed to be constants. An overall mass balance and specie balances are performed for the liquid phase inside the tank in order to find the rate of change of the liquid height and the liquid phase composition (given by eqs. 7 and 8).

$$\frac{dH^{l}_{RD}}{dt} = \frac{1}{A_{RD}\rho^{l}}\left(\dot{m}^{l}_{RD,in} - \rho^{l}\dot{V}^{l}_{RD}\right) \qquad (7)$$

$$\frac{dc^{l}_{i.RD}}{dt} = \frac{1}{A_{RD}H^{l}_{RD}}\left(\dot{n}^{l}_{i,RD,in} - \frac{c^{l}_{i.RD}}{\rho^{l}}\dot{m}^{l}_{RD,in}\right) \qquad (8)$$

Here $\dot{m}^{l}_{RD,in}$ is the mass flow rate of liquid into the reflux drum, which is found from the molar flow into the reflux drum: $\dot{m}^{l}_{RD,in} = \sum (\dot{n}^{l}_{i,RD,in} \cdot M_i)$ where M_i is the molar mass of specie *i*. Liquid height, specie concentration, liquid density and cross sectional area of the reflux drum are given by H^{l}_{RD}, $c^{l}_{i.RD}$, ρ^{l} and A_{RD}. Liquid height of the reflux drum is controlled between an upper and a lower boundary by manipulating the flow rate of the liquid from the reflux drum ($\dot{V}^{l}_{RD}$). When the liquid phase composition and the mass flow rate from the reflux drum are known, the conditions of the reflux stream are known.

The re-boiler is modelled using a fixed vapour to feed fraction. Ideal temperature and pressure control in the re-boiler is assumed. The re-boiler heat duty ($\dot{Q}_{RB}$) is calculated using:

- the energy required to heat up the feed ($\dot{m}^{l}_{RB,in}\hat{c}^{l}_{p}\Delta T_{RB}$),
- energy required to vaporize the pre-defined fraction of the feed ($\sum\left(\dot{n}^{v}_{i.RB}\Delta\tilde{H}_{Vap,i}\right)$), and
- heat of desorption of CO_2 (ΔH_{ab}), which leads to eq. 9,

$$\dot{Q}_{RB} = \dot{m}^{l}_{RB,in}\hat{c}^{l}_{p}\Delta T_{RB} + \sum\left(\dot{n}^{v}_{i.RB}\Delta\tilde{H}_{Vap,i}\right) + \Delta H_{ab} \qquad (9)$$

where $\Delta T_{RB} = T_{RB} - T^{l}_{RB,in}$. The feed flow into the re-boiler, specific heat capacity of the liquid and the molar rate of vapour leaving the re-boiler are given by $\dot{m}^{l}_{RB,in}$, $\hat{c}^{l}_{p}$ and $\dot{n}^{v}_{i.RB}$.

1.3. Physical properties and other parameters

Physical properties and other parameters are introduced to the model either as correlations or constant values found in the literature, or else using well known calculation methods. Some of the important physical properties and other parameters are given in Table 1 with their literature sources.

1.4. Numerical method

The model is implemented in MATLAB and the solver ODE15s is used to solve the set of differential and algebraic equations. Each tower model is discretized into 50 control volumes using the method of lines. The 50 control volumes are of uniform size.

Table 1. Physical properties and other parameters used in the MATLAB stripper model.

Property	Source	Comments
Enhancement factor	Hoff et al. [14]	
Forward reaction rate coefficient	Jamal et al. [15]	
Heat of absorption of CO_2	Kohl et al. [16]	
Heat of vaporization (H_2O and MEA)	Gáspár et al. [10]	
Liquid density	Weiland et al. [26]	
Liquid diffusivity of CO_2	Versteeg et al.[18]	N_2O analogy is used.
Liquid hold-up	Billet et al. [19]	
Liquid viscosity	Cheng et al. [17]	
Mass transfer coefficients	Hanley et al. [20]	Has developed for Flexipac1Y packing.
Overall heat transfer coefficient between phases	Cussler et al.[21]	Chilton-Colburn analogy is used.
Phase and reaction equilibrium	Kent et al. [6]	Simple and easy to apply.
Saturation pressure of water	Hoff et al. [14]	Clausius Clapeyron model is used
Thermal conductivity of N_2	Incropera et al.[22]	Value of N_2 is used for the gas mixture.
Vapour diffusivity	Poling et al. [23]	Fuller equation is used together with Blanc's law.
Vapour viscosity	Perry et al. [24]	Mixture viscosity is found by combining the individual component values.
Wetted area of packing	R.E.Dugas. [12]	Constant value, specific for Flexipac1Y packing.

1.5. Model predictions

The MEA solvent system is considered for the analysis, and the thermodynamic and physical parameters are given accordingly. Several pilot plant cases from the Separations Research Program at the University of Texas at Austin are used for the validation of the dynamic model [12]. The stripping column in the pilot plant is a packed column with Flexipac 1Y type of structured packing. This column consists of two 3.05m packing sections with a collector plate and redistributors in between. Applied flow rates and packing properties are taken from the literature [12], [25]. The model prediction is satisfactory, and details are given in Table 2 and Figure 2.

Table 2. Inputs and predictions for the Texas cases 25, 28, 30 and 32.

Case no:	Inlet liquid temp: [K]	Inlet liquid rate [L/min]	Re-boiler temp: [K]	Inlet rich CO_2 loading	Lean CO_2 loading		Re-boiler duty [kW]	
					Pilot plant data	Simulated	Pilot plant data	Simulated
25	342	104.1	390	0.386	0.277	0.280	469	433
28	345	82.1	393	0.412	0.282	0.284	366	387
30	349	54.9	394	0.453	0.280	0.276	255	259
32	359	40.7	400	0.428	0.272	0.268	152	164

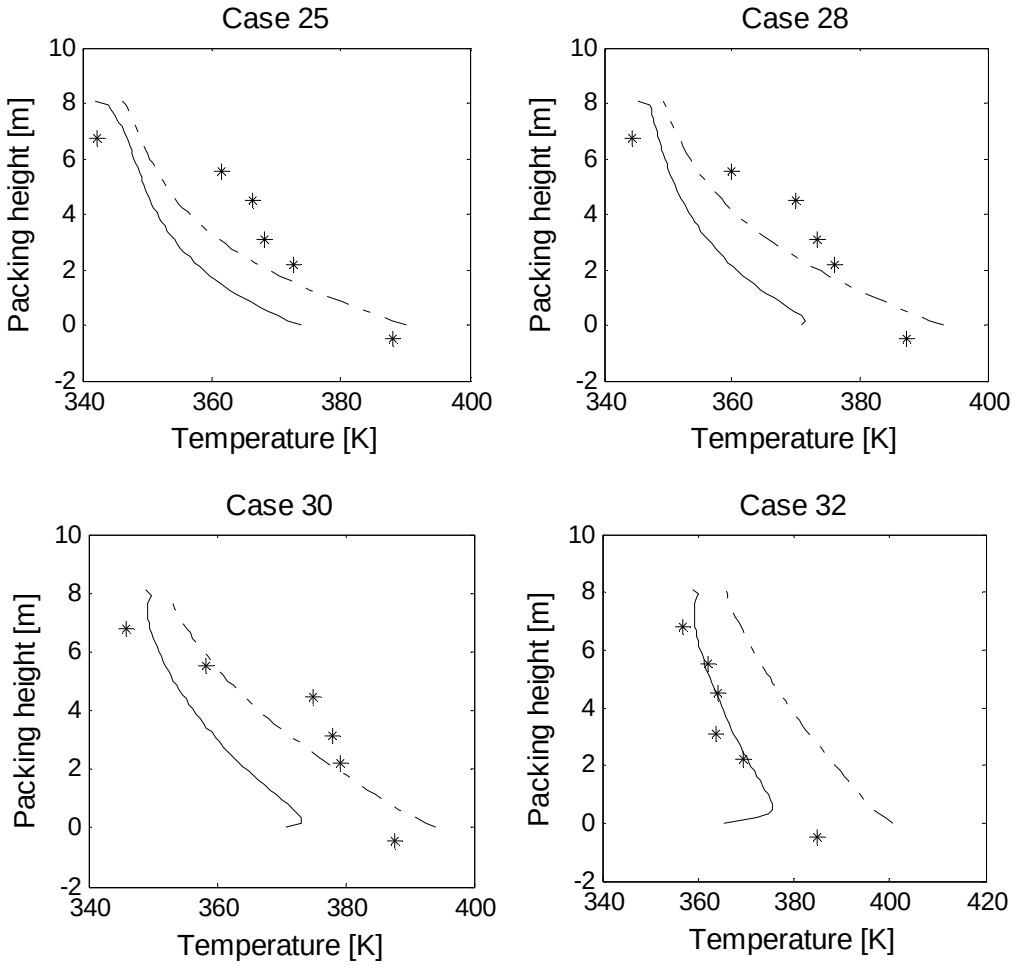

Figure 2. Temperature profiles inside the stripping column at the steady state. — is the liquid phase temperature, -.-. is the vapour phase temperature, * is the experimental data.

3. Sensitivity analysis

Sensitivity of the model for different physiochemical correlations and inclusion or exclusion of the minor reactions is analyzed. Eleven different cases are simulated and the predictions of the steady state are compared with the steady state results of the base case. Pilot plant case 32 is selected for the analysis. The combination of the physical properties and other parameters given in Table 1 are used for the base case simulation. Each case analyze the effect on the re-boiler heat duty, lean CO_2 loading and prediction of the temperature profiles inside the stripping tower.

Details of the cases with the alterations made, the predicted re-boiler heat duties and lean CO_2 loadings are given in Table 3.

Table 3. Details of the simulations performed for the sensitivity analysis.

Case number	Amendment	Re-boiler hear duty [kW]	Lean CO_2 loading
Pilot plant 32	-	152.2	0.272
Base case	-	164	0.268
1	Density model from Cheng et al. [17] is used	164	0.268
2	Viscosity model from Poling et al. [23] is used	164	0.268
3	Viscosity model from Weiland et al. [26] is used	164	0.268
4	Specie generation is presented with additional set of minor equations	166	0.259
5	Model for wetted specific area is taken from Billet et al. [19]	178	0.343
6	Model for wetted specific area is taken from Onda et al. [27]	169	0.293
7	Model for wetted specific area is taken from Hanley et al. [20]	169	0.294
8	Correlation for local mass transfer coefficients is taken from Onda et al. [27]	151	0.281
9	Correlation for Henry's law is taken from Jiru et al. [28]	159	0.313
10	Saturation pressure of H_2O is calculated from Antoine equation	145	0.316
11	Saturation pressure of H_2O is calculated from the Clausius Clapeyron relation	147	0.319

Cases 1 – 3 analyse the effect on the prediction of the stripper model by the correlations for computing the liquid phase density presented by Cheng et al. [17], liquid phase viscosity presented by Poling et al. [23] and liquid phase viscosity presented by Weiland et al. [26], respectively. Case 4 considers the effect by including the minor reactions into the model. The term minor reactions refer to the set of reaction presented by Liu et al. [29] for the system of CO_2-MEA-H_2O. Cases 5 to 7 analyse the effect from different correlations available for calculating the wetted specific area of the packing that are presented by Billet et al. [19], Onda et al. [27] and Hanley et al. [20], respectively. Case 8 considers the effect on the model predictions by the inclusion of the correlation presented by Onda et al. [27] to predict the local mass transfer coefficients of the species. Changes of the model predictions when the phase equilibrium of CO_2 is calculated using Henry's law constant presented by Jiru et al. [28] is examined by case 9. Cases 10 and 11 show the effect on the model predictions by inclusion of the different methods, such as the Antoine equation and the Clausius Clapeyron relation, to calculate the saturation vapour pressure of H_2O.

The predictions of the temperature profiles inside the stripping tower, re-boiler heat duties and lean CO_2 loadings for the cases 1 to 4 are very similar to the predictions by the base case simulation, showing that there is no significant effect from the alterations made in the cases 1 to 4 on the model predictions.

Comparison between the experimental data (from Pilot plant case 32), temperature profiles from the base case simulation and the temperature profiles from the simulations of the cases 5 to 7 and 8 to 11 are given in Figure 3 and Figure 4, respectively.

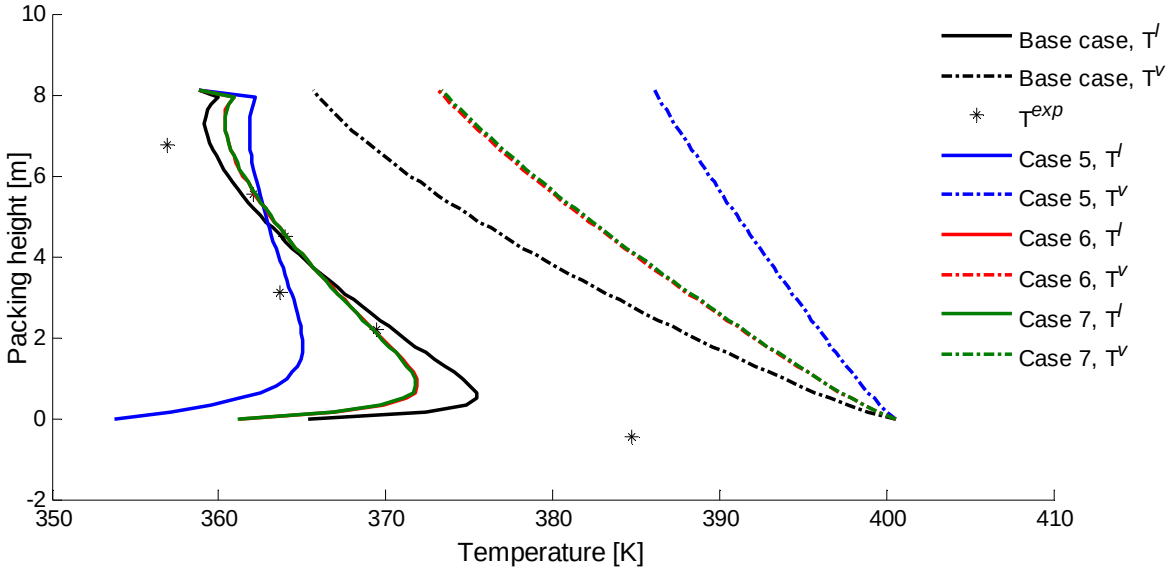

Figure 3. Temperature profiles predicted by the simulations of the base case and the cases 5 to 7, and the experimental data.

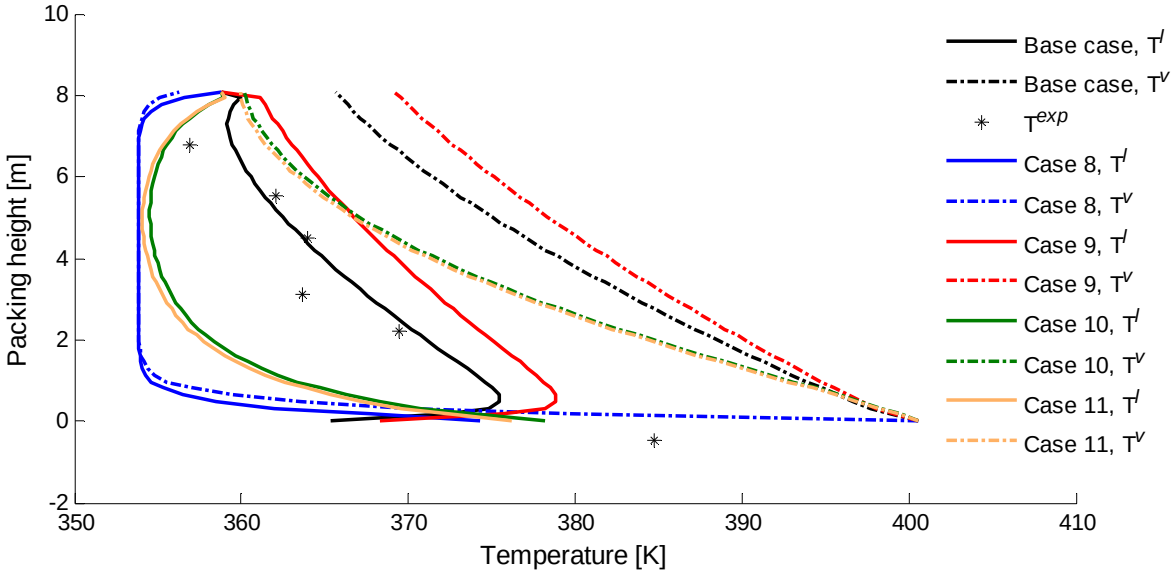

Figure 4. Temperature profiles predicted by the simulations of the base case and the cases 8 to 11, and the experimental data.

In Figure 3, the temperature curves predicted by the simulations of the base case, case 5, case 6 and case 7 for the liquid and the vapour phases, and the experimental data points are presented. Predicted curves from the cases 6 and 7 are very much the same for each phase along the tower height. Liquid

phase temperature profiles predicted by the cases 6 and 7 lie close to the liquid phase temperature profile from the base case. Vapour phase temperature profiles predicted by the cases 6 and 7 show an increasing deviation which starts from the bottom of the tower, from the vapour phase temperature profile of the base case, with a maximum deviation of about 7 K at the top of the tower. The temperature profile predicted for the liquid phase by case 5 has a considerable deviation from that of the base case up to about 4 m along the column height. The vapour phase temperature profiles from the base case simulation and the case 5 simulation have an increasing deviation with a maximum of about 12 K at the top of the tower.

Wetted specific area predictions from the correlations used in the cases 5 to 7 are lower than that of the base case, resulting increased re-boiler duties and lean loadings. As a result of the reduced transfer area followed by the reduced heat and mass transfer, deviation between the liquid and vapour phase temperature profiles in each case has also increased.

In Figure 4, the temperature curves predicted by the simulations of the base case, case 8, case 9, case 10 and case 11 for the liquid and the vapour phases, and the experimental data points are presented. Liquid and vapour temperature profiles predicted by case 8 lie very close to each other and consist of a steep curve (almost constant temperatures) from about 1 m to the top of the tower, while being very much different from the results of the base case and the experimental data. Curves predicted by case 9 have shifted towards higher temperatures than in the base case, but lie closer to the curves from the base case. The predictions of case 10 are very similar to those of case 11. The liquid phase profiles from cases 10 and 11 have predicted lower temperatures than the base case simulation all the way to the top of the tower from about 0.5 m and the predicted temperature is higher than the base case up to about 0.5 m from the bottom of the tower.

The correlation by Onda et al. [27] used in the case 8, has predicted higher values for the local mass transfer coefficients compared to the base case. The effect on the overall mass transfer coefficient from the over-prediction of the local mass transfer coefficients is dampening by the effect on the enhancement factor from the same alteration. Temperature profiles inside the tower have been predicted very similar to each other as a result of the over-prediction of the gas side local mass transfer coefficient. The gas side local mass transfer coefficient has a direct effect on the overall heat transfer coefficient according to the Chilton-Colburn analogy [21]. The re-boiler heat duty has reduced as a result of the increased temperature of the liquid leaving the stripping columns. Lower temperature values inside the tower compared to the base case may have increased lean CO_2 loading value due to the reduced reversed reaction rate.

The correlation by Jiru et al. [28] have predicted higher solubility of CO_2 in amines compared to the base case, which in return have predicted higher lean CO_2 loading value. As a result of the reduced CO_2 transfer the H_2O transfer may also have reduced causing higher temperature values inside the tower compared to the base case. The increased temperature of the liquid entering the re-boiler has reduced the re-boiler heat duty.

The correlations used in the cases 10 and 11 for predicting the saturation pressure of water have predicted higher values compared to the correlation by Hoff et al. [14], which is used in the base case. Higher saturation pressure values have resulted in increased vaporisation of water (or reduced condensation), which can be considered as the reason for reduced temperature values inside the tower. The reduced temperature values have resulted in increased lean CO_2 loading. The re-boiler duty has reduced as a result of the increased temperature of the liquid leaving the stripping tower.

4. Dynamic analysis

The predictions of the transient conditions from the dynamic model are analysed via a simulation with varying re-boiler temperature.

The steady state results from the base case simulation are used as the initial conditions for this simulation. Firstly, the re-boiler temperature can be increased gradually as an attempt to introduce a varying heating load condition. Secondly, the re-boiler temperature can be reduced gradually in order to achieve the temperature set-point of the re-boiler, which represents the action of a temperature controller to reassure the stability of the process.

The simulation procedure is given below.

- The base case is simulated for 10 minutes
- The re-boiler temperature is increased from 400.5 K to 405.5 K in 5 minutes (until t = 15 min)
- Then, the re-boiler temperature is reduced from 405.5 K to 400.5 K in 5 minutes (until t = 20 min)
- The simulation keeps on for another 10 minutes (until t = 30 min)

The temperatures are changed linearly for the simulation rather than introducing a step change, which represents a more sudden change and more challenging operation.

Figure 5-(a) and 5-(b) demonstrate the change of the temperature profiles of the liquid and vapour leaving the stripping column with respect to the time. Figure 5-(c) and 5-(d) show the change of the re-boiler heat duty and the CO_2 loading in the liquid leaving the stripping column during the transient situation.

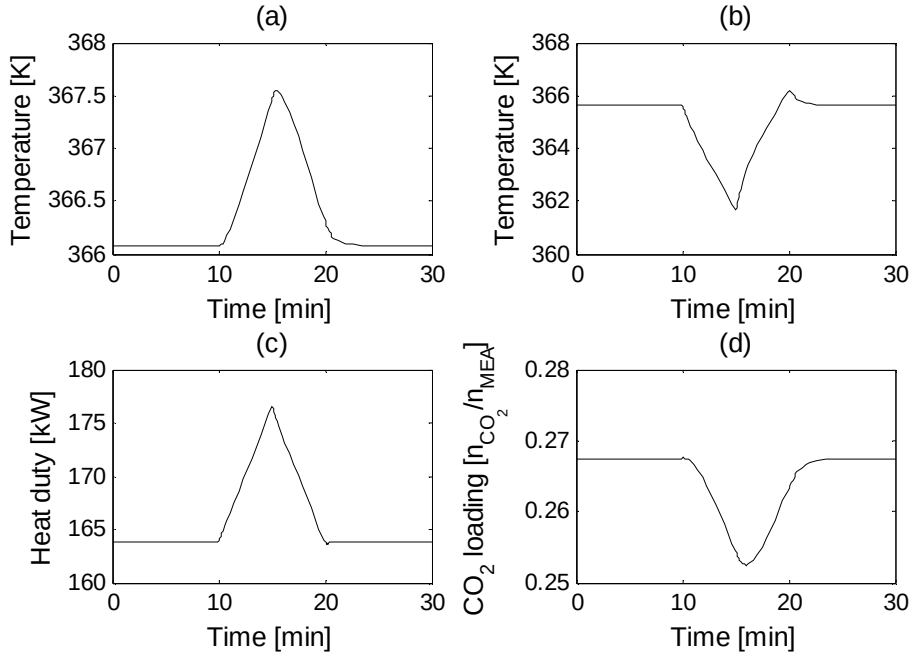

Figure 5. Predictions from the dynamic simulation. (a). Temperature of the vapour leaving the stripping column to the condenser, (b). Temperature of the liquid phase leaving the stripper to the re-boiler, (c). Re-boiler heat duty and (d). CO_2 loading in the amine leaving the stripping column.

The heat duty shows an increase as the re-boiler temperature increases (Figure 5-(c)), obviously due to the increased heat demand to raise the temperature. The vapour temperature appears to be increasing as the re-boiler temperature increases (Figure 5-(a)), which is a direct effect from the increasing temperature of the inlet vapour to the stripping column. The liquid phase temperature decreases as the re-boiler temperature increases (Figure 5-(b)), even though one may expect an increase as the inlet temperature of the vapour increases. A possible reason for this observation is the increased vapour rate as a result of the increased temperature in the re-boiler, which may then limit the heat transfer from the vapour to the liquid. Increased vapour rate has increased the mass transfer between phases and increase the rate of the reversed reactions in the liquid phase (this can be seen from the figure 5-(d)), which leads to a reduction in the liquid phase temperature as well.

During the attempt to bring the temperature of the re-boiler back to the temperature set-point, the curves show a reversed effect as expected.

5. Conclusions

A good dynamic model provides the possibility to study the effect of various disturbances on the operating conditions of a plant and to apply improvements. Further, a dynamic model is useful for implementing a control system for the plant and to perform optimization. Development of dynamic models is vital for the understanding and improvement of the CO_2 capture process.
A dynamic simulation model for the stripper of a CO_2 capture plant has been developed in order to predict the transient conditions during various operating scenarios. The simplicity of the model has been maintained by use of simple models such as the Kent-Eisenberg model.

The steady state results from the simulation of the stripping column have shown acceptable accordance with the pilot plant data from the Separations Research Program at the University of Texas at Austin, which is taken as a primary validation of the model.

Simulations are performed to analyze sensitivity of the model predictions to different physical property correlations and inclusion of the minor reactions. The model predictions are not effected by the inclusion of the minor reactions, different density correlation for the liquid phase or different viscosity model for the liquid phase. Significant effect could be seen by the selected correlation for calculating the wetted specific area of the packing, Henry's law coefficient or saturation vapour pressure of water.
A simulation is performed to analyse the model predictions under varying operating conditions. The model predictions of the transient conditions seem reasonable.

Further validation of the model will be performed by comparing it with the behaviour of a real plant. This is not included in the current work due to the limitation in available data. The model will be expanded to cover the whole CO_2 capture plant, which can be used for developing a control system for the capture process.

Acknowledgement

Financial support for this project from the Norwegian Research Council is gratefully acknowledged.

References

[1] P. Freund, Making deep reductions in CO_2 emissions from coal-fired power plant using capture and storage of CO_2, Proc IMechE Part A, J Power Energy. 217 (2003) 1-7.

[2] A. M. Cormos, J. Gáspár, A. Padurean C. C. Cormos, Techno-economical analysis of carbon dioxide absorption in mono-ethanolamine by mathematical modelling and simulation, in Proc. ESCAPE20, Ischia, Italy. (2010) 81-1 - 81-6.

[3] J. M. Plaza, D. V. Wagener, G. T. Rochelle, Modelling CO_2 capture with aqueous monoethanolamine, Energy Procedia. 1 (2009) 1171-1178.

[4] I. Tönnies, H. P. Mangalapally, H. Hasse, Sensitivity study for the rate-based simulations of reactive absorption of CO_2, Energy Procedia. 4 (2011) 533-540.

[5] R. Schneider, F. Sander, A. Górak, Dynamic simulation of reactive absorption processes, Chem. Eng. and Processing. 42 (2003) 955-964.

[6] R. L. Kent, B. Eisenberg, Better Data for Amine Treating, Hydrocarbon Processing. (1976) 87-90.

[7] E. T. Hessen, T. Haug-Warberg, H. F. Svendsen, The refined e-NRTL model applied to CO_2-H_2O-alkanolamine systems, Chemical Engineering Science. 65 (2010) 3638-3648.

[8] S. Ziaii, G. T. Rochelle, T. F. Edgar, Dynamic modelling to minimize energy use for CO_2 capture in power plants by aqueous Monoethanolamine, Ind. Eng. Chem. Res. 48 (2009) 6105–6111.

[9] A. Lawal, M. Wang, P. Stephenson, G. Koumpouras, H. Yeung, Dynamic modelling and analysis of post-combustion CO_2 chemical absorption process for coal-fired power plants, Fuel. 89 (2010) 2791–2801.

[10] J. Gáspár, A. M. Cormos, Dynamic modelling and validation of absorber and desorber columns for post-combustion CO_2 capture, Computers and Chemical Engineering. 35 (2011) 2044–2052.

[11] K. Prölß, H. Tummescheit, S. Velut, J. Åkesson, Dynamic model of a post combustion absorption unit for use in a non-linear model predictive control scheme, Energy Procedia. 4 (2011) 2620-2627.

[12] R. E. Dugas, Pilot plant study of carbon dioxide capture by aqueous monoethanolamine, Revision of MSE thesis, Texas Univ., Austin, 2006.

[13] S. A. Jayarathna, B. Lie, M. C. Melaaen, NEQ rate based modelling of an absorption column for post combustion CO_2 capturing, Energy Procedia. 4 (2011) 1797-1804.

[14] K. A. Hoff, Modelling and experimental study of carbon dioxide absorption in a membrane contactor, Ph.D. dissertation, NTNU, Norway, 2003.

[15] A. Jamal, A. Meisen, C. J. Lim, Kinetics of carbon dioxide absorption and desorption in aqueous akanolamine solutions using a novel hemispherical contactor-11: Experimental results and parameter estimation, Chem. Eng. Sci. 61 (2006) 6590-6603.

[16] A. Kohl, R. Nielsen, Gas purification. fifth ed. Gulf, Houston, USA, 1997.

[17] S. Cheng, A. Meisen, A. Chakma, Predict amine solution properties accurately, Hydrocarbon Processing. (1996) 81-84.

[18] G. F. Versteeg, W. P. M. Van Swaaij, Solubility and diffusivity of acid gases (CO_2, N_2O) in aqueous alkanolamine solutions, J. Chem. Eng. Data. 33 (1988) 29-34.

[19] R. Billet, M. Schultes, Prediction of mass transfer columns with dumped and arranged packings: updated summary of the calculation method of billet and schultes, Trans IChemE. 77 (1999) 498-504.

[20] B. Hanley, C. C. Chen, New mass-transfer correlations for packed towers. AIChe Journal. doi: 10.1002/aic. 12574. 58 (2012) 132-152.

[21] E. L. Cussler, Diffusion: Mass transfer in fluid systems. third ed. Cambridge University Press, UK, 2009.

[22] T. P. Incropera, D. P. Dewitt, T. L. Bergman, A. S. Lavine, Fundamentals of Heat and Mass transfer, sixth ed. John Wiley & Sons, USA, 2007.

[23] B. E. Poling, J. M. Prausnitz, J. P. O'Connell, The properties of gases and liquids. fifth ed. New York, McGraw-Hill, 2001.

[24] R. H. Perry, D. W. Green, Chemical engineers handbook, seventh ed. New York, McGraw-Hill, 1999.

[25] C. F. Petre, F. Larachi, I. Iliuta, B. P. A. Grandjean, Pressure drop through structured packings: Breakdown into the contributing mechanisms by CFD modeling, Chemical Engineering Science. 58 (2003) 163–177.

[26] R. H. Weiland, J. C. Dingman, D. B. Cronin, G. J. Browning, Density and viscosity of some partially carbonated aqueous alkanolamine solutions and their blends, J. Chem. Eng. Data. 43 (1998) 378-382.

[27] K. Onda, H. Takeuchi, Y. Okumoto, Mass transfer coefficients between gas and liquid phases in packed columns, J. Chem. Eng. Jap. 1 (1968) 56-62.

[28] Y. Jiru, D. A. Eimer, Y. Wenjuan, Measurements and correlation of physical solubility of carbon dioxide in (Monoethanolamine + Water) by a modified technique, Ind. Eng. Chem. Res. 51 (2012) 6958–6966.

[29] Y. Liu, L. Zhang, S. Watanasiri, Representing vapour-liquid equilibrium for an aqueous MEA-CO2 system using the electrolyte Non-random-Two-Liquid model, Ind. Eng. Chem. Res. 38 (1999) 2080–2090.

Assess proper drag coefficient models predicting fluidized beds of CLC reactor by utilizing computational fluid dynamic simulation

Milad Mottaghi[1,a], Hooyar Attar[b] , Mehrdad Torabzadegan[a]

[a] Master student in Department of Process , Energy, and Environmental Technology, Telemark University College, Norway

[b] PhD Student in Department of Chemical Engineering, Edith Cowan University, Australia

ABSTRACT:

A two dimensional simulation fluidized beds of CLC reactor were carried out by using Eulerian-Eulerian multi phase flow approach in the OpenFOAM v2.1.1 CFD software package. Data obtained from simulation part compared with the fuel reactor of a pilot CLC rig at the Vienna University of Technology. Different drag correlation were tested for varying size of particles: Ergun, Gibilaro, Gidaspow, WenYu, SchillrNaumann , in order to find the model that exhibit flow behavior of gas and particles in the fuel reactor precisely. Slightly discrepancy between these models were detected, however the Gidaspow model captured experimental trend accurately more than the other models for the all range of particles size.

1. Introduction

According to the Statistics from IPCC, the last decade is ranked among warmest years recorded since 1850[1]. One of the main causes of this Global Warming is Greenhouse gases (GHG) like: H_2O, CO_2, CH_4, N_2O, CFC's and SF_6. Among these gases, CO_2 is considered making largest contribution to the GHG effect, since it represents the largest emissions of the global anthropogenic GHG emissions, and also it has a high residence time in atmosphere. CO_2 emission attribute to human activity as a result of the dependency on fossil fuels for energy production. Until now, intensive investigations have been performed in order to reduce net CO_2 emission, in instance a) increasing the efficiency of conversion of fuel to energy b) substituting the fossil fuel with renewable energy or nuclear energy c) utilizing techniques for capturing CO_2 from exhaust gas and storing it. It appears that Carbon Capture and storage (CCS) is one of the promising approaches for reducing concentration of CO_2 in atmosphere and as a consequence mitigating GHG effects.

Three main methods have been considered to industrial and power plant for sequestering CO_2 from exhaust gas: post-combustion systems, oxy-fuel combustion, and pre-combustion systems[2]. All of these technologies have been reached to a good progress, and they can be available in commercial scale. The foremost drawback of these techniques is, they contain a high energy penalty, which has effects on efficiency of the whole process. Therefore, great efforts have been carried out to eliminate this defect, Chemical Looping Combustion (CLC) is an alternative that can reduce the cost of CO_2 capturing significantly[1]. CLC has not been attained to maturity but it has experienced a great development. Typical CLC system is made from two fluidized bed reactors, oxidizer for combustion process is provided indirectly by means of oxygen carrier materials in absence of air. The solid particles that contain oxygen require for combustion lose their oxygen in fuel reactor, the oxygen depleted particles must re-generated before beginning new cycle, and this can be carried out in the second reactor through passing air among solid particles. Through this procedure the exhaust gases in fuel reactor are just H_2O and CO_2, hence energy demand for separating these two gases from each other reduces considerably.

[1] Corresponding author:
M. Mottaghi, Department of Process Technology, Telemark University College, N-3901 Porsgrunn Norway. Tel:+47 45117245
E-mail address: 113811@student.hit.no

The efficiency of chemical-looping system is dependent on flow behavior of oxygen-carrier from one reactor to other one and awareness of it affects on scaling and designing steps[3]. CFD depicted that it can provide a precious insight into the system behavior. For simulating CLC, different techniques can be applied, among them multiphase fluid dynamic models supply more satisfactory level of details as result. In this method the solid and fluid phases are modeled in the framework of the coupled Navier-Stokes equations through spatially and temporally averaged quantities[4]. Since gravity and drag forces play great roles in fluidized bed system (bed expansion, distribution of particles in vessel), so it require more consideration. Kinetic Theory of Granular Flows (KTGF) is a promising approach for simulating gas-particle systems. The properties of solid phase like pressure and viscosity are derived from KTGF[5].

This study is investigated on various drag models and compared the results in order to obtain best model that predict the behavior of fluid and particles in CLC system.

2. Simulation

2.1. Model Equation

In this study, it was assumed that an isothermal fluid passing through particles and no reaction occurred so the energy equation has not been included among conservation equations. In Eulerian-Eulerian multiphase framework separate conservation equations in combination with various constitute models as complementary are calculated for the gas and the solids phases. A brief outline is provided as follow.

2.2. Conservation equations

The continuity equations for both phases are solved as follow:

$$\frac{\partial}{\partial t}\left(\alpha_g \rho_g\right) + \nabla \cdot \left(\alpha_g \rho_g v_g\right) = \alpha_g S_g \quad (2\text{-}1)$$

$$\frac{\partial}{\partial t}\left(\alpha_s \rho_s\right) + \nabla \cdot \left(\alpha_s \rho_s v_s\right) = \alpha_s S_s \quad (2\text{-}2)$$

Right hand terms in both equations are source terms and account for mass transfer according to reaction but since there is no reaction in this study, their values will be equal to zero.

Momentum conservation for the gas is provided as

$$\frac{\partial}{\partial t}\left(\alpha_g \rho_g \vec{v}_g\right) + \nabla \cdot \left(\alpha_g \rho_g \vec{v}_g \vec{v}_g\right) = -\alpha_g \nabla p + \nabla \cdot \bar{\bar{\tau}}_g + \alpha_g \rho_g \vec{g} + K_{sg}\left(\vec{v}_s - \vec{v}_g\right) + S_g \quad (2\text{-}3)$$

And for solid as

$$\frac{\partial}{\partial t}\left(\alpha_s \rho_s \vec{v}_s\right) + \nabla \cdot \left(\alpha_s \rho_s \vec{v}_s \vec{v}_s\right) = -\alpha_s \nabla p - \nabla \mathrm{p_s} + \nabla \cdot \tau_s + \alpha_s \rho_s \vec{g} + K_{gs}\left(\vec{v}_g - \vec{v}_s\right) + S_s \quad (2\text{-}4)$$

Where K is the interfacial momentum exchange or drag, τ is stress-strain tensor. Similar to continuity equation, source terms in momentum equations are also zero. In KTGF the random motion of granular particles are addressed to gas molecules motion where kinetic theory of gas will be applied. Through this analogy fluid properties as previously mentioned can be determined, the granular temperature is written in conservation form as follow[6]:

$$\frac{3}{2}\left[\frac{\partial}{\partial t}\left(\alpha_s \rho_s \Theta_s\right) + \nabla \cdot \left(\alpha_s \rho_s \vec{\mathrm{v}}_s \Theta_s\right)\right] = \left(-p_s \bar{\bar{I}} + \bar{\bar{\tau}}_s\right) : \nabla \vec{v}_s + \nabla \cdot \left(K_{\Theta_s} \nabla \Theta_s\right) - \gamma_{\Theta_s} + \emptyset_{gs} \quad (2\text{-}5)$$

Further details about conservation and constitute equations can be found in[7].

3. Drag models

The most drag models use values of Reynolds number, phase fraction, relative velocity between phases, and drag coefficient. Also various expressions are used for calculating C_d depending on the Reynolds number. For dispersed multiphase flow different drag correlations can be utilized. Some of them are investigated in this section.

3.1. Schiller Naumann drag model

There is a transitional region between Stoke drag and Newtonian drag, where predicting analytical solution for a falling sphere is so sophisticated. For tackling this obstacle, empirical expressions are applied to compute drag in this regime. Schiller Naumann drag model is one such equation.

$$\boldsymbol{F = C_D \rho_f \frac{U^2}{2} A} \quad \textbf{(3-1)}$$

$$\boldsymbol{C_D = \frac{24}{Re}(1 + 0.15 Re^{0.687})} \quad \textbf{(3-2)}$$

3.2. Wen Yu drag Model (Densely Distributed Solid Particles)

This model has similarity form as Schiller Naumann, just with one modification in Reynolds number and power law correlation. Both of them are functions of the continuous phase volume fraction r_c [6].

$$\boldsymbol{C_D = r_c^{-1.65} max\left(\frac{24}{Re}(1 + 0.15 Re'^{0.687}), 0.44\right)} \quad \textbf{(3-3)}$$

$$\boldsymbol{Re' = r_c Re} \quad \textbf{(3-4)}$$

$$\boldsymbol{K_{sg} = \frac{3\rho_g \alpha_g (1-\alpha_g)}{4 d_p} C_D \left|\vec{u}_s - \vec{u}_g\right| \alpha_g^{-2.65}} \quad \textbf{(3-5)}$$

3.3. Gidaspow drag model

This model is a combination of Wen Yu correlation for low solid volume fraction, and Ergun's law for larger solid volume fractions[6].

Ergun equation is shown as follow[8]

$$\boldsymbol{K_{sg} = 150 \frac{\mu_g (1-\alpha_g)^2}{\alpha_g (d_s \emptyset)^2} + 1.75 \frac{\rho_g (|\vec{u}_g - \vec{u}_s|)(1-\alpha_g)}{d_s \emptyset}} \quad \textbf{(3-6)}$$

The constant ϕ is a shape factor for particles.

So Gidaspow drag model is like

$$\boldsymbol{K_{sg} = \begin{cases} K_{sg}(Wen\ Yu) & \alpha_g \geq 0.8 \\ K_{sg}(Ergun) & \alpha_g \leq 0.8 \end{cases}} \quad \textbf{(3-7)}$$

4. Simulation

4.1. Geometry and boundary conditions

3D Cylindrical fuel reactor had to be simulated on 2D plane due to computational effort (computational cost) required. Reactor diameter is 0.16 m and height is 4.1, tangential and normal velocity of gas phase are set to zero at the wall of reactor (no-slip), the gas outlet from top of reactor is defined as pressure outlet, and the gas inlet is specified as velocity inlet. The particle size is investigated in two diameters 120, 290μm[9].

4.2. Solver setting

OpenFOAM v2.1.1 CFD software package was used as solver. This software allows implementation of extra equation and boundary conditions according to the requirements of the problems in comparison to other software like Fluent, which make this software more flexible. Mesh generation was accomplished with "blockMesh" Utility[4]. A summary of solver setting provided in Table 1.

Table 1: Summary of solver setting

Temperature	1173 (K)
Superficial gas velocity	1.8 (m/s)
Particle diameter	120, 290 (μm)
Particle density	2800 (kg/m^3)
Static bed height	0.6 (m)
Gas viscosity	1.789×10^{-5} (kg/m.s)
Restitution coefficient	0.9
Specularity coefficient	0.5

5. Result and discussion

Four sets of numerical experiments were performed; in the first three the effects of different drag models on hydrodynamic behavior of the system were investigated. Finally, the proper drag model was selected for comparing behavior of two sizes of particles. Solids volume fraction and solids axial velocity as a function of dimensionless lateral distance were utilized for comparing different models. Data of Volume fraction and axial velocity of particles were collected from 0.5 m and 1.5 m, vertical levels of fuel reactor. The results were depicted in Figure 1, and Figure 2. As the graphs show, the Gidaspow and Wen Yu drag model lines are in the vicinity of each other in comparison to Schiller Naumann, which can be referred to that Gidaspow model originated from Wen Yu. In addition, by contrasting the data gained through simulation (following graphs) and ref [3, 5], it can be deduced that by implementing Gidaspow drag model in gas-particle momentum exchange equation, more precisely results can be achieved.

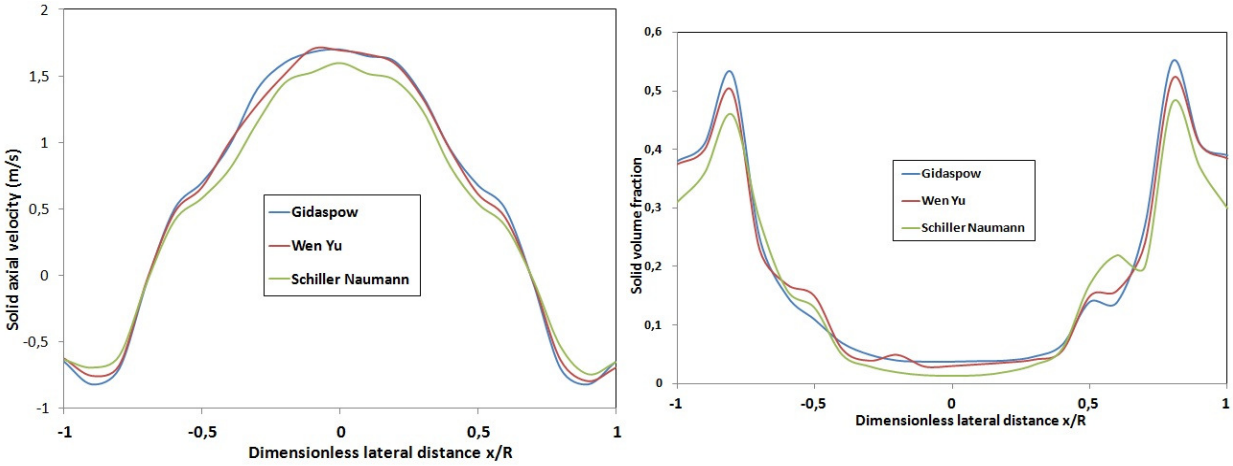

Figure 1: Solids axial velocity and volume fraction along the diameter of the reactor at axial position 0,5m for three drag models: Gidaspow, Wen Yu, and Schiller Naumann

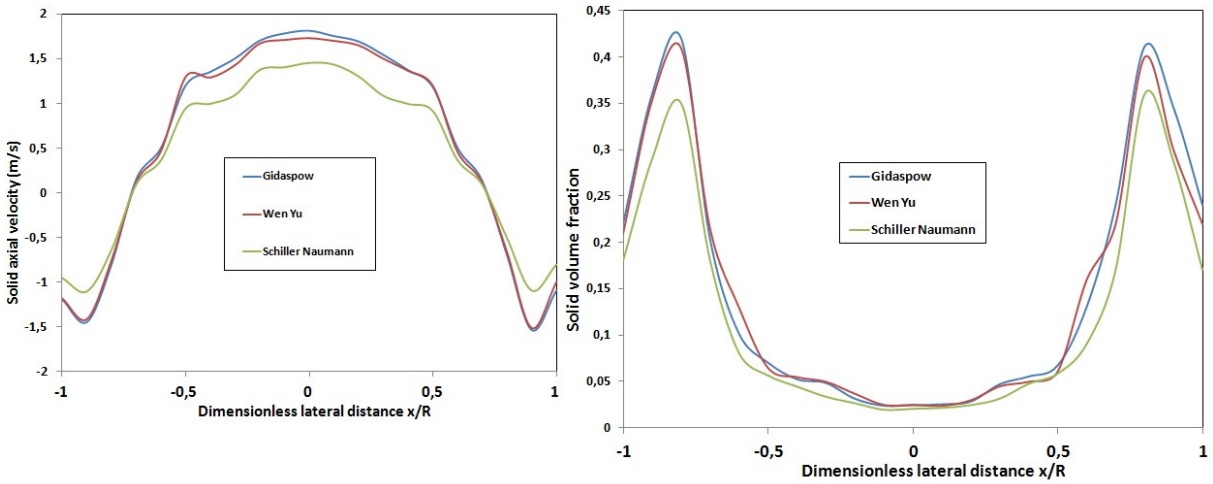

Figure 2: Solids axial velocity and volume fraction along the diameter of the reactor at axial position 1,5m for three drag models: Gidaspow, Wen Yu, and Schiller Naumann

In Figure 3, the time averaged volume fraction of particles with two sizes was compared with each other. The particles concentration for fine particles is higher near to the wall but particles with bigger scale size distributed more uniformly along width of reactor, just like in the real flow, the particle concentration is highest at the bottom and on average the solid particles rise in the middle and come down as clusters near the walls[10].

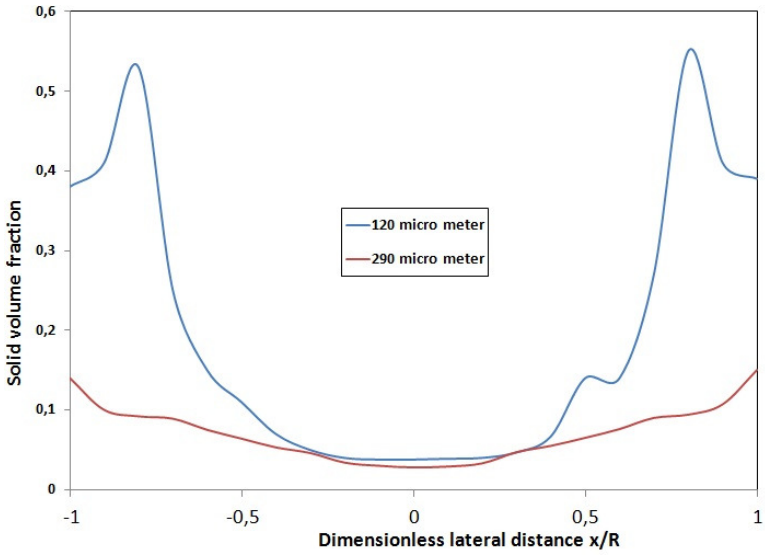

Figure 3: Particles volume fraction along the diameter of the reactor at axial position 0,5m acquired from Gidaspow drag models

6. Conclusion

Various drag models are examined in 2 dimensional CFD simulation for a fuel reactor of a CLC system, the distribution of concentration of particles and their velocities are obtained, the computed results are also compared with experimental data[5, 11] that depict similar behaviors for the particles along height of the column in this paper and [5], the Gidaspow model gives better agreement with experimental data, even if there is a negligible differences between these models. Particularly, Gidaspow drag model is applied for two particle sizes, and it demonstrates that at the height of 0.5 m from bottom of the reactor the volume fraction of large particles are fewer than small ones which is in agreement with real experiments.

7. Reference

[1] A. A. Juan Adanez, Francisco Garcia-Labiano, Pilar Gayan, Luis F. de Diego, "Progress in chemical-looping combustion and reforming technologies," *progress in energy and combustion science,* vol. 38, p. 215, 2012.

[2] V. S. Harald Kruggel-Emden, "Heat and mass flow control in an interconnected multiphase CFD model for chemical looping combustion," *chemical engineering and technology,* vol. 34, p. 1259, 2011.

[3] E. Wopienka, "Hydrodynamic investigation of a dual fluidised bed chemical-looping combustor experiments and mathematical modelling," vienna university, vien, 2004.

[4] (2012). *OpenFOAM user guide*. Available: http://www.openfoam.org/docs/user/

[5] S. T. J. Schalk Cloete, Shahriar Amini, "An assessment of the ability of computational fluid dynamic models to predict reactive gas-solid flows in a fluidized bed," *Powder Technology,* vol. 215-216, pp. 15-25, 2012.

[6] D. Gidaspow, *Multiphase Flow and Fluidization: Continuum and Kinetic Theory Descriptions*. San Diego: Academic press, 1994.

[7] S. Patankar, *Numerical heat transfer and fluid flow*: Hemisphere Publishing Corporation, 1980.

[8] B. M. H. Joachim Lundberg, "A review of some exsisting drag models describing the interaction between phases in a bubbling fluidized bed," *International Journal of Engineering Science and Technology,* vol. 2, p. 1047, 2010.

[9] Y. Y. Wang Shuai, Lu Huilin, Xu Pengfei, and Sun Liyan, "Computational fluid dynamic simulation based cluster structures-dependent drag coefficient model in dual circulating fluidized beds of chemical looping combustion," *Industrial and engineering chemistry research,* vol. 51, p. 1396, 2011.

[10] T. Niemi, "Simulation of Gas-Particle Flows," Master thesis, School of Science, Aalto University, 2012.

[11] P. K. Tobias Proll, Johannes Bolhar-Nordenkampf, Hermann Hofbauer, "A novel dual circulating fluidized bed system for chemicla looping processes," *AICHE journal,* vol. 55, p. 3255, 2009.

ORKUSTOFNUN